Faculty of Science

Department of Applied Physics
and
Department of Applied Chemistry

Determination of the Structure of γ-Alumina using Empirical and First Principles Calculations combined with Supporting Experiments

Gianluca Paglia

This thesis is presented for the Degree of
Doctor of Philosophy
of
Curtin University of Technology

February 2004

Declaration

This thesis contains no material which has been accepted for the award of any other degree or diploma in any university.

To the best of my knowledge and belief this thesis contains no material previously published by any other person except where due acknowledgement has been made.

Signature: 

Date: February 2nd 2004

Acknowledgments

One can never know how difficult putting together a PhD thesis can be until one actually goes through the process. I myself did not appreciate this until I tried it myself. And now a days there is enormous pressure to complete the work within three odd years. I am enormously proud of the work which constitutes this thesis. It can be justifiably split up into two projects. However, such a task could not be achieved without the valuable aid of many people, without which I would not have been able to do this at all.

Before mentioning the people directly I would like to thank several institutions for providing financial support. Firstly, the Australian government for awarding me with an Australian Post-Graduate Award with Stipend (APAWS). The Australian Institute of Nuclear Science and Engineering (AINSE) for awarding me with a Post-Graduate Research Award (PGRA) which includes a scholarship and a grant to travel to the Australian Nuclear Science and Technology Organisation (ANSTO), Lucas Heights, Sydney to perform key experiments for the project. The staff at AISNE were very friendly and always accommodating to my needs. I thank them kindly. Thanks also goes to the Western Australian Interactive Virtual Environments Centre (IVEC) and the Australian Partnership for Advanced Computing (APAC) for provision of allocation time on their computational facilities. IVEC also kindly awarded me with a Western Australian IVEC Doctoral Scholarship (WAIDS).

The most important people to thank are my two supervisors, Associate Professors Craig Buckley (Materials Research Group) and Andrew Rohl (Nanochemistry Research Institute). The project was originally Craig's idea. He, in partnership with Andrew won an ARC Small Grant to purchase some of the software and equipment necessary to carry out the work. Craig taught me much about concepts in physics that I was yet to grasp properly. He also helped me enormously in getting started with computer programming. In spite of his own enormously busy schedule, time was always made for me to seek advice, without having to make an appointment in advance. I sought advice frequently. He also provided advice that extended beyond issues pertaining to the project work, such as career and personal concerns. Importantly, both he and Andrew allowed me to take control of the project

and do things how I saw best, which facilitated a casual, yet productive, atmosphere. I consider him to be an excellent friend and mentor.

Andrew's assistance in the project was invaluable. Without his assistance and the resources already under his control, the degree of modelling that was performed would not have been achieved. It was through Andrew that I learnt most about the concepts of molecular modelling. He was also the person I came to rely on most with developing my programming skills. As with Craig, I frequently sought his assistance because the learning curve for both the modelling and programming was enormous. Like Craig, he has become an excellent friend and mentor.

The computational work was carried out using two simulation codes, GULP and SIESTA, which were acquired through Professor Julian Gale, who has recently moved to Curtin University from Imperial College, London. He is the author of the former program and a co-developer of the latter. Julian's assistance has been invaluable. He provided a lot of assistance with the use of both codes and helped me to understand a lot of the concepts behind the programs.

Professor Brian O'Connor was the main person who motivated me to undertake my Ph.D. The project was jointly his conception, with Craig. It was Brian's idea to make γ-alumina as the subject of this modelling-based project. Brian has produced a wealth of research on transition aluminas so his advice was very useful and greatly appreciated. Although we did not always agree, a compromise was always achievable. I have enormous respect for his scientific achievements.

Most of the assistance I received for my experimental work was provided by Dr Robert Hart and Karsten Winter from the Materials Research Group and Dr's Brett Hunter and Andrew Studer from the Bragg Institute at ANSTO. Robert was with me every minute while performing electron microscopy. He did most of the difficult fine-tuning required to obtain high quality images and diffraction patterns, saving me an enormous amount of time. He taught me how to analyse the patterns and about the associated crystallography. He also helped me improve my scientific writing and reduce the amount of words used. In this area, I was certainly in need of improvement. The electron microscopy work could not have been done without the contribution made by Professor Arie van Riessen. Arie was an associate supervisor to the project. While the nature of the project was such that he was not able to provide much direct assistance he is the person behind the obtainment of the state of the art

electron microscopy equipment for the physics department. He is also responsible for the appointment of Robert Hart to the run the equipment. He is the first scientist I had respect for and always made himself available for discussion when I sought advice on matters.

Karsten Winter was an integral part of this project. Although he is a fellow PhD student he has over 15 years experience in crystallography. He helped me understand vital crystallographic concepts which I had never before been properly exposed to nor could I have hoped to learn it without many years of hard reading. This facilitated rapid output of written work on my part. Without this help, the project would easily have take up to a year longer. He is an excellent mentor.

Brett Hunter, my AINSE supervisor, and Andrew Studer assisted me in performing the neutron diffraction experiments at ANSTO. Their assistance was therefore imperative. Andrew taught me how to use the processing software developed at ANSTO to convert the data to the correct format and perform all the necessary precursory analysis before performing Rietveld analysis. He also did much of the legwork to keep the experiments running smoothly. Brett is the author of Rietica and taught me most of what I know about Rietveld Analysis. Dr Margaret Elcombe, from the Bragg Institute, was also a key factor in helping me to understand Rietveld analysis. In all, I spent about seven to eight weeks conducting experiments at ANSTO. All of the staff made me feel very welcome. Professor Robert Robinson gave me great advice on my future. Spending time working at another institution was an excellent experience.

Other people from ANSTO, from the Materials Division, also made extremely important contributions. John Hanna performed the high-resolution NMR experiments and David Cassidy performed the BET and pycnometry.

Dr Lindsey Byrne from the NMR facility at the University of Western Australia collected my initial NMR data and facilitated my analysis of the all the data by providing me with access to the appropriate software. Nigel Kirby and Geoff Carter from the Materials Research Group also helped with BET work.

Clinton Maitland and Dr Joan Connolly from the Materials Research Group and Dr Terry Udovic of the National Institute of Standards and Technology (NIST), USA also deserve a big thank you. Clinton and Joan performed small angle X-ray scattering on my samples and Clinton did the modelling analysis. Terry performed the neutron vibrational spectroscopy and prompt-gamma activation analysis. They

made life very easy for me as they supplied the results and all I had to do was interpret the significance.

Special thanks goes to Professor Li Deyu of the Materials Research Group. Li helped me to get started with the basics of Rietveld analysis. He provided me with insight regarding what had been previously done on γ-alumina within the department and supplied me with the conference paper he, Brian and co. authored in 1990.

There have been several other people who have provided valuable assistance. Dr Franca Jones, Nanochemistry Research Institute, helped me to conduct the infrared analysis of my samples. Dr Andrew Fogg, formerly of the Nanochemistry Research Institute, allowed me to use his Bayer labs to synthesise my gibbsite and boehmite starting materials. Dr Joanne Loh, formerly a Ph.D. student with the Nanochemistry Research Institute provided useful comments and taught me how to synthesise hydrogenated and deuterated gibbsite. John Cornell of ALCOA World Alumina supplied me with commercial boehmite from the Alumina and Ceramics Laboratory, Malakoff Industries, Arkansas, USA. Professor Andrew Johnson of the Centre for Microscopy and Microanalysis at the University of Western Australia provided valuable advice and helped me obtain my first electron diffraction pattern of γ-alumina. Dr Sean Fleming, helped me with IT issues pertaining to the molecular modelling. I must also thank Professor Javier Junquera for kindly generating the optimized basis sets used in this work.

I was also given tremendous help from two good friends of mine, Damien Carter, fellow Ph.D. student from the Nanochemistry Research Institute, and Dr Justin Hoffman, formerly a Ph.D. student of the Department of Applied Physics. These gentlemen helped me with many IT issues.

Every one of these people has taught me something. They have all made some form of impact on my life. I thank them and all my other colleagues for their friendship and encouragement. The road certainly would have been much harder if they weren't there. I am extremely grateful.

I must also thank my fiancé, Vanessa Di Falco, for all her support. She has been very understanding with all the long hours that I have had to put in and has kept my belly fully on many occasions. She has taken my aloofness and many nights spent indoors with a notebook computer on my lap surprisingly well. Her love has been unconditional. I dedicate this work to her and our future together.

29/11/2003

Abstract

Aluminas have had some form of chemical and industrial use throughout history. For little over a century corundum (α-Al_2O_3) has been the most widely used and known of the aluminas. The emerging metastable aluminas, including the γ, δ, η, θ, κ, β, and χ polymorphs, have been growing in importance. In particular, γ-Al_2O_3 has received wide attention, with established use as a catalyst and catalyst support, and growing application in wear abrasives, structural composites, and as part of burner systems in miniature power supplies. It is also growing in importance as part of the feedstock for aluminium production in order to affect both the adsorption of hydrogen fluoride and the feedstock solubility in the electrolytic solution. However, much ambiguity surrounds the precise structure of γ-Al_2O_3. Without proper knowledge of the structure, understanding the properties, dynamics and applications will always be less than optimal.

The aim of this research was to contribute towards settling this ambiguity. This work was achieved through extensive computer simulations of the structure, based on interatomic potentials with refinements of promising structures using density functional theory (DFT), and a wide range of supporting experiments. In addition to providing a more realistic representation of the structure, this research has also served to advance knowledge of the evolution of the structure with changing temperature and make new insights regarding the location of hydrogen in γ-Al_2O_3.

Both the molecular modelling and Rietveld refinements of neutron diffraction data showed that the traditional cubic spinel-based structure models, based on $Fd\bar{3}m$ space group symmetry, do not accurately describe the defect structure of γ-Al_2O_3. A more accurate description of the structure was provided using supercells of the cubic and tetragonal unit cells with a significant number of cations on *c* symmetry positions. These *c* symmetry based structures exhibited diffraction patterns that were characteristic of γ-Al_2O_3.

The first three chapters of this Thesis provide a review of the literature. **Chapter One** provides a general introduction, describing the uses and importance of the aluminas and the problems associated with determining the structure of γ-Al_2O_3. **Chapter Two** details the research that has been conducted on the structure of

γ-Al_2O_3 historically. **Chapter Three** describes the major principles behind the computational methods employed in this research.

In **Chapter Four**, the specific experimental and computational techniques used to investigate the structure of γ-Al_2O_3 are described. All preparation conditions and parameters used are provided.

Chapter Five describes the methodology employed in computational and experimental research. The examination of the ~ 1.47 billion spinel-based structural possibilities of γ-Al_2O_3, described using supercells, and the selection of ~ 122,000 candidates for computer simulation, is detailed. This chapter also contains a case study of the structure of κ-Al_2O_3, used to investigate the applicability of applying interatomic potentials to solving complex structures, where many possibilities are involved, and to develop a systematic procedure of computational investigation that could be applied to γ-Al_2O_3.

Chapters Six to **Nine** present and discuss the results from the experimental studies. Preliminary heating trials, performed to determine the appropriate preparation conditions for obtaining a highly crystalline boehmite precursor and an appropriate calcination procedure for the systematic study of γ-Al_2O_3, were presented in **Chapter Six**.

Chapter Seven details the investigation of the structure from a single-temperature case. Several known structural models were investigated, including the possibility of a dual-phase model and the inclusion of hydrogen in the structure. It was demonstrated that an accurate structural model cannot be achieved for γ-Al_2O_3 if the cations are restricted to spinel positions. It was also found that electron diffraction patterns, typical for γ-Al_2O_3, could be indexed according to the $I4_1/amd$ space group, which is a maximal subgroup of $Fd\bar{3}m$. Two models were presented which describe the structure more accurately; Cubic-16*c*, which describes cubic γ-Al_2O_3 and Tetragonal-8*c*, which describes tetragonal γ-Al_2O_3. The latter model was found to be a better description for the γ-Al_2O_3 samples studied.

Chapter Eight describes the evolution of the structure with changing calcination temperature. Tetragonal γ-Al_2O_3 was found to be present between 450 and 750 °C. The structure showed a reduction in the tetragonal distortion with increasing temperature but at no stage was cubic γ-Al_2O_3 obtained. Examination of the progress of cation migration indicates the reduction in the tetragonal nature is due

to ordering within inter-skeletal oxygen layers of the unit cell, left over from the breakdown of the hydroxide layers of boehmite when the transformation to γ-Al_2O_3 occurred. Above 750 °C, δ-Al_2O_3 was not observed, but a new phase was identified and designated γ′-Al_2O_3. The structure of this phase was determined to be a triple cell of γ-Al_2O_3 and is herein described using the $P\bar{4}m2$ space group.

Chapter Nine investigates the presence of hydrogen in the structure of γ-Al_2O_3. It was concluded that γ-Al_2O_3 derived from highly crystalline boehmite has a relatively well ordered bulk crystalline structure which contains no interstitial hydrogen and that hydrogen-containing species are located at the surface and within amorphous regions, which are located in the vicinity of pores. Expectedly, the specific surface area was found to decrease with increasing calcination temperature. This trend occurred concurrently with an increase in the mean pore and crystallite size and a reduction in the amount of hydrogen-containing species within the structure. It was also demonstrated that γ-Al_2O_3 derived from highly crystalline boehmite has a significantly higher surface area than expected, attributed to the presence of nano-pores and closed porosity.

The results from the computational study are presented and discussed in **Chapter Ten**. Optimisation of the spinel-based structural models showed that structures with some non-spinel site occupancy were more energetically favourable. However, none of the structural models exhibited a configuration close to those determined from the experimental studies. Nor did any of the theoretical structures yield a diffraction pattern that was characteristic of γ-Al_2O_3. This discrepancy between the simulated and real structures means that the spinel-based starting structure models are not close enough to the true structure of γ-Al_2O_3 to facilitate the derivation of its representative configuration. Large numbers of structures demonstrate migration of cations to *c* symmetry positions, providing strong evidence that *c* symmetry positions are inherent in the structure. This supports the Cubic-16*c* and Tetragonal-8*c* structure models presented in **Chapter Seven** and suggests that these models are universal for crystalline γ-Al_2O_3. Optimisation of *c* symmetry based structures, with starting configurations based on the experimental findings, resulted in simulated diffraction patterns that were characteristic of γ-Al_2O_3.

LIST OF ABBREVIATIONS

γ-Al_2O_3	Gamma alumina
γ'-Al_2O_3	Gamma-prime alumina
α-Al_2O_3	Alpha alumina
δ-Al_2O_3	Delta alumina
θ-Al_2O_3	Theta alumina
κ-Al_2O_3	Kappa alumina
η-Al_2O_3	Eta alumina
χ-Al_2O_3	Chi alumina
AINSE	Australian Institute of Nuclear Science and Engineering
ANSTO	Australian Nuclear Science and Technology Organisation
APW	Augmented plane waves
BFGS	Broyden-Fletcher-Goldfarb-Shanno minimisation algorithm
CBED	Convergent beam electron diffraction
Cheby I	Non-shifted type 1 Chebyshev function
CSD	Coherently scattering domains
DRIFT	Diffuse Reflectance Infrared Fourier Transform
DTA	Differential thermal analysis
DZ	Double-zeta
DZP	Double-zeta plus polarisation
EDS	Energy dispersive spectrometry
FANS	Filter Analyser Neutron Spectrometer
FLAPW	Full-potential linear augmented plane waves
FWHM	Full-width-at-half-maximum
GEA	Gradient expansion approximation
GGA	Generalised gradient approximation
Gnorm	Normal to the energy gradient in GULP.
GTO	Gaussian-type-orbital
GULP	General utility lattice program
HF	Hartree-Fock
HRPD	High-resolution powder diffractometer
ICDD	International Centre for Diffraction Data

INS	Inelastic neutron scattering
IR	Infrared
ISIS	Name of the Spallation Neutron Source, UK.
LAPW	Linear augmented plane waves
LCAO	Linear combinations of atomic orbitals
LDA	Local density approximation
LSD	Local spin density approximation
MAS-NMR	Magic angle spinning nuclear magnetic resonance
MRPD	Medium-resolution powder diffractometer
NCNR	NIST Center for Neutron Research
ND	Neutron diffraction
NIST	National Institute of Standards and Technology, USA
NMR	Nuclear magnetic resonance
NVS	Neutron vibrational spectroscopy ≡ INS
OLCAO	Orthogonalized linear combinations of atomic orbitals
PDF	Powder diffraction file
PGAA	Prompt gamma activation analysis
PW	Plane waves
RFO	Rational function optimisation
SAD/SAED	Selected area electron diffraction
SEM	Scanning electron microscopy
SIESTA	Spanish initiative for electronic simulations of thousands of atoms
STO	Slater-type-orbital
TED	Transition electron diffraction
TEM	Transition electron microscopy
TGA	Thermogravimetric analysis
XRD	X-ray diffraction

Contents

List of Figures

List of Tables

Chapter 1

Introduction

Alumina, also called aluminium oxide, is the only solid oxide of aluminium and has the chemical formula Al_2O_3. Aluminas, or more precisely, aluminous materials have been technologically significant ceramic materials throughout human history. Before 5000 BC aluminous clays were being used in Mesopotamia for the manufacture of fine pottery. After 3000 BC the Babylonians and Egyptians began employing aluminium compounds in various chemicals, such as perfumes and dyes, and medicines (van Horn *et al.* 2002). Upon these uses the Romans utilised aluminous materials in the manufacture of cosmetics. Emerald, sapphire and ruby, which are crystalline forms of alumina coloured by various impurities, were utilised in jewellery from about 800 BC, no more extensively than during ancient Roman times.

Etymology shows that the word alumina, like the word aluminium, comes from the term *alumen* (Simpson and Weiner 1989), which is Latin for alum (potassium aluminium sulphate, $K_2SO_4.Al_2(SO_4)_3.12H_2O$). The Romans used alum as a styptic or astringent, perfume, and as a mordant in the dyeing process. The earliest extant literature documenting the use and manufacture of alum was by the Roman naturalist Pliny the Elder (*Gaius Plinus Secundus*) in his '*Historia Naturalis*' (77 AD), Books XXXIII & XXXIV). Note that the earliest mention of the word alum was in Herodotus' 'The Persian Wars' (425 BC), Book II), but the word's appearance is only in Latinised translations made by Roman scholars in later centuries, and its reference is to a form of currency, not a description of the material or its uses. In 1781, de Morveau proposed the new-Latin term *alumine* (alumina in English) for the base in alum. In 1787 Lavoisier suggested that *alumine* was the oxide of a previously undiscovered metal. The word aluminum, later aluminium, was proposed by Davy in 1807, who confirmed that alumina has a metallic base.

Bauxite, the most common ore of aluminium, was discovered in 1821 by Berthier near the village of Les Baux, France. However, it was not until the end of the 19th century that bauxite was recognised as containing $Al(OH)_3$ and AlO.OH and

various quantities of aluminium silicate, titanium dioxide and iron mineral impurities (Wefers and Misra 1987). It has since been determined that various crystallographic forms of the aluminium hydroxides including gibbsite, bayerite, boehmite, and diaspore may be present in the aluminium ores. It is from naturally occurring aluminium hydroxides, such as those found in bauxite, that alumina (Al_2O_3) is most commonly produced. This is primarily achieved using the Bayer process, developed in 1889 by Karl Bayer (Hind *et al.* 1999), which today remains the most economic thermal treatment for the synthesis of alumina.

Although aluminium is generally accepted to have been first isolated in 1825 by Hans Christian Oersted, Pliny may have unknowingly provided us with some curious insight into the history of alumina and aluminium with this excerpt from *Historia Naturalis* (77 AD, Book XXXV):

> "*One day a goldsmith in Rome was allowed to show the Emperor Tiberius a dinner plate of a new metal. The plate was very light, and almost as bright as silver. The goldsmith told the Emperor that he had made the metal from plain clay. He also assured the Emperor that only he, himself, and the gods knew how to produce this metal from clay. The Emperor became very interested, and as a financial expert he was also a little concerned. The Emperor felt immediately, however, that all his treasures of gold and silver would decline in value if people started to produce this bright metal from clay. Therefore, instead of giving the goldsmith the regard expected, he ordered him to be beheaded.*"

It can be conjectured that the metal is aluminium and the clay is an aluminium ore, such as bauxite, most likely from the now known deposits around the northern Mediterranean, once a part of ancient Rome's massive empire. Tiberius' (42 BC – 37 AD) rashness appears to have deprived ancient Rome of a precious commodity with which to trade and the world of a long history of alumina and aluminium use. However, conclusive evidence of widespread Roman knowledge of alumina may yet be uncovered. It was not until the 18th and 19th centuries that the Western world only began to catch up to the Romans in most areas, including education, technology and administration. Moreover, new discoveries are being made about the Romans every

day. It has, for example, only recently been realised that Roman medical and surgical procedures, including eye, cosmetic and brain surgery, were on par with their modern counterparts, at least to the mid 20th century (Jackson 1991; Adkins and Adkins 1994; Shelton 1997). A future discovery of direct evidence of Roman knowledge of alumina and aluminium may not be surprising.

Today the word "alumina" is still vaguely used in literature to denote anything from the entire group of aluminous materials, including aluminium hydroxides. The definition of alumina by the Oxford English Dictionary (1989) illustrates some of the ambiguity in the use of the word: "*one of the earths, a white, insoluble, tasteless, amorphous substance; the only oxide (Al_2O_3) of the metal aluminium, the basis of alum, the chief constituent of all clays, and found crystallised as the sapphire*." A quick browse through several dictionaries will show that most also refer to alumina as "*a mineral occurring in nature as corundum*." The absence of universal standard nomenclature contributes to the confusion which has arisen in literature for the naming of aluminium compounds. Only one attempt has been made at implementing standardised nomenclature so far (Ginsberg *et al.* 1957). One of the outcomes of this attempt is that the prefix α is applied to hexagonal close packed and related structures while γ signifies cubic close packed and related structures.

Although there is loose and varied use of "alumina" as a naming tool, it definitively only applies to substances with the Al_2O_3 stoichiometric formula. Early research into aluminium compounds resulted in the discovery of aluminium ores, chiefly comprised of aluminium hydroxides. These aluminium hydroxides are sometimes, and incorrectly, referred to as hydrated aluminas. This misconception has resulted from the representative stoichiometric formulae; gibbsite, for example, is a trihydroxide compound ($Al(OH)_3$) which has been represented as $Al_2O_3.3H_2O$ and named alpha aluminium hydrate by Alcoa (Wefers and Misra 1987).

The Transition Alumina's

It was eventually discovered that alumina itself also exists in a variety of 'transition' structures which are reproducible and stable at room temperature. The term 'transition,' as opposed to 'metastable,' applies as the phase transition between them is irreversible and occurs only with increasing temperature. The transition

aluminas occur within several pathways when dehydrating the aluminium hydroxides, such as gibbsite, to form *corundum* (α-Al_2O_3), a name that lends itself from the mineral of composition Al_2O_3 identified in India by Greville in 1798 (van Horn *et al.* 2002). The α phase is the only thermodynamically stable oxide of aluminium and is the final product of the calcination process which follows the Bayer treatment. The nature of these phase transformations has now been studied for many years, and the pathways involved in the calcination include gibbsite $\rightarrow$ boehmite (γ-AlOOH) $\rightarrow$ γ-alumina (γ-Al_2O_3) $\rightarrow$ δ-alumina (δ-Al_2O_3) $\rightarrow$ θ-alumina (θ-Al_2O_3) $\rightarrow$ α-alumina (Figure 1.1), with each transition phase exhibiting a distinct powder X-ray diffraction pattern. These phase transformations are of fundamental importance in designing ceramic processing procedures that use partially-calcined starting material.

Initial classification of the transition aluminas was by Ulrich (1925) who used the prefix γ for an undescribed alumina compound. This prefix has subsequently been used for all newly encountered and undescribed aluminas, all of which were found to form at low calcination temperatures during the thermal treatment of aluminium hydroxides. As new forms have been identified they have been assigned a unique Greek letter prefix. The γ prefix has since been restricted to the name of the structure obtained for the dehydration sequence of boehmite from 400 °C. Several other transitions have now been identified including the η, θ, κ, β, and χ aluminas. They are designated as oxides but it is not yet certain that they are anhydrous and several of the structures exhibit some amorphous content, hence they are commonly referred to as partially-calcined or partially dehydrated. A summary of the transformation transition aluminas and their occurrence in the calcination pathways is provided in Figure 1.1. Diagrams such as this serve only as a guide because they do not elucidate that the exact temperature of formation depends on parameters such as pressure and that overlap of phases can occur at certain temperatures.

The original purpose for the production of α-Al_2O_3 was as a precursor in the production of aluminium metal which is the third most abundant element in the earth's crust, comprising 8.13%, and has almost limitless applications in transport, packaging, electrical, construction and medicine. In 2001, 48,488,000 metric tons of alumina was produced (Report 2001b). Of this figure 3,997,000 metric tons represents the amount of all phases of alumina produced for uses other than the

production of aluminium metal. The remaining alumina produced was used to synthesise 20,551,000 metric tons of aluminium (Report 2001a; Report 2001b).

Corundum itself has since found an enormous range of technological and industrial applications as a result of its hardness, abrasion resistance, mechanical strength, corrosion resistance, and good electrical insulation (Stumpf *et al.* 1950; Kingery *et al.* 1976). It is the most widely used form of alumina with structural, refractory, abrasive, optical, and electronic applications. Many of its applications are commonly known, such as its incorporation in composites (Green *et al.* 1989), while others are more obscure, such as its use in ballistic armour (Badmos and Ivey 2001).

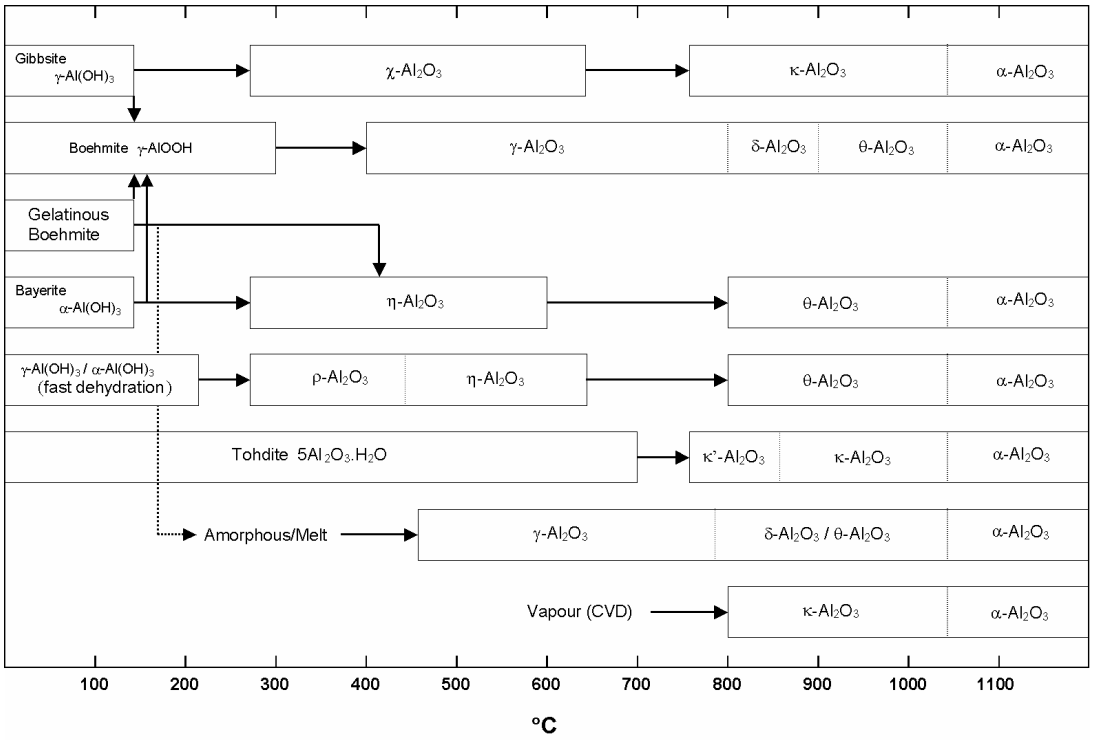

Figure 1.1. Commonly accepted transition sequences of the aluminas from hydroxides to corundum during thermal treatment (Wefers and Misra 1987; Levin and Brandon 1998a; Ruberto 2001).

The industrial importance of transition aluminas is increasing as more becomes known about them. This group of materials have a variety of niche applications, many overlapping with those of α-Al_2O_3, depending on the properties of the specific polymorph. κ-Alumina (κ-Al_2O_3), for example, finds use in wear-resistant coatings on cemented carbide cutting-tools (Lux *et al.* 1986; Vuorinen and Skogsmo 1990). δ-Alumina has been incorporated in bioactive bone cement

composites as a replacement for α-Al_2O_3 (Nishio *et al.* 2001). It was found to be superior for incorporation in bone cement as it allowed for greater osteoblastic differentiation than α-Al_2O_3, allowing for *in-vivo* bone formation. θ-Alumina is used as a precursor for the production of ultra-high purity α-Al_2O_3 with reduced particle agglomeration (Wei *et al.* 1996; Kao and Wei 2000). All the transition aluminas have chemical functions including use as adsorbents, desiccants and binders. They are also widely used in heterogeneous catalysis, (Knözinger 1985) both as catalysts and support material for monolayer catalysts (Poncelet *et al.* 1991).

The transition aluminas are also of great importance in aluminium metal production. The α phase is not as soluble as the transition aluminas in the electrolytic solution (cryolite – Na_3AlF_6) from which aluminium metal is produced. Hence the processed alumina used for aluminium metal production contains a high amount of various transition phases (Homsi 1989; Hind *et al.* 1999). The high surface area, and corresponding adsorption properties, of some of the transition phases allows the alumina product to also be used as a HF (hydrogen fluoride) 'scrubber', during aluminium refinement in order to reduce HF pollution (Gillespie *et al.* 1999). Alumina has traditionally been formed by calcining aluminium trihydrate (gibbsite) in a rotary kiln at typically 1000 °C. More recently, fluidised bed furnaces have been used as they have more flexible calcination parameters, therefore exerting more influence on the amount of transition phases produced within the alumina product.

There still exists considerable controversy over the definitive structures of many of the alumina phases. In the case of δ-Al_2O_3, there is speculation as to whether it exists at all. Studies by Zhou and Snyder (1991) and Gan (1996) have not reported the presence of δ-Al_2O_3 in the transformation sequence of γ-Al_2O_3 to θ-Al_2O_3. Also, Pecharroman (1999) suggests that while δ-Al_2O_3 was detected using X-ray diffraction, it is actually a heterogeneous mixture of well crystallised γ-Al_2O_3 and θ-Al_2O_3 instead of a single δ-phase. Furthermore, many researchers who develop Al_2O_3-based applications have not or are unable to ascertain the exact Al_2O_3 phase present. An example of this scenario is in the development of nanosized Al_2O_3 fibres. Two variants of Al_2O_3 nanofibres were developed by Tepper, Lerner and Ginley (2001) for improved catalysis, chemisorption of metals, use in nanocomposites, ceramic substrates, filters and membranes, and chemisorption and biomedical applications. These authors, however, have not identified a specific Al_2O_3

phase beyond the presence of amorphous Al_2O_3. Without adequate knowledge of the structural form, research into the properties, dynamics and applications of these materials will always be less than optimal.

γ-Alumina

γ-Alumina, the subject of this thesis, is a material of immense industrial significance and is the subject of considerable research. It is used as a catalyst support for automotive (Satterfield 1980; Taylor 1993; Gates 1995) and industrial catalysts (Che and Bennett 1989; Xu *et al.* 1994), for example, the production of bulk and fine chemicals (Shi and Davis 1995), and as a catalyst in hydrocarbon conversion for petroleum refining (Tung and Mcininch 1964; Knözinger and Ratnasamy 1978). Supported catalysts are typically made by impregnating a porous material with an aqueous catalytic salt followed by calcination. Porosity is the property which makes γ-Al_2O_3 appealing as a catalyst support. Also, porosity (and therefore high surface area), combined with the removal of water and/or hydroxyl ligands at the surface, resulting in the exposure of Al^{3+} ions, are why γ-Al_2O_3 is also used directly as a catalyst.

Catalytic processes account for the majority of applications of γ-Al_2O_3. However, there are a growing number of other uses for γ-Al_2O_3. Like other transition aluminas, it is widely used as a polishing abrasive and in ceramic coatings, which provide corrosion, thermal and wear protection (McPherson 1980). NASA utilised it in γ-Al_2O_3/epoxy composite struts to attach a cryogenically cooled solid-hydrogen telescope to its Wide-Field Infrared Explorer (WIRE) spacecraft because of its low thermal conductivity and relatively high mechanical strength (Rosanova 1998; Everett *et al.* 2000). Also, the high surface area of γ-Al_2O_3 makes it useful as platinum-coated combustion burners in recently investigated miniature power supplies (Drost *et al.* 1997; Koeneman *et al.* 1997). Furthermore, γ-Al_2O_3 has also been shown to be thermodynamically stable relative to α-Al_2O_3 when a critical surface area is achieved (McHale *et al.* 1997). The outcomes of this research can open up endless possibilities for applications of γ-Al_2O_3.

The Uncertainty Surrounding γ-Alumina

Despite the industrial significance of γ-Al_2O_3, controversy still exists over its definitive structure. Not even the mechanisms by which γ-Al_2O_3 behaves as a catalyst (or support) are clearly understood (Sohlberg *et al.* 1999; Xia *et al.* 1999). Over 67 years have passed since the first description of its structure, which was as a cubic spinel-type ($MgAl_2O_4$) structure (Verway 1935a), and over 52 years since it was identified as a direct product of the calcination of boehmite (Stumpf *et al.* 1950). Yet there are still many questions regarding its formation, structure, and even stoichiometry. It was initially determined to occur at a calcination temperature of > 525 °C, though now it is thought to occur between 400 and 950 °C (Stumpf *et al.* 1950; Saalfeld 1958; Lippens and de Boer 1964). These early studies have tended to shed light on the configuration of the oxygen sublattice, however the major uncertainty arises in the positions of the aluminium ions within the unit cell. Analysis of neutron, X-ray, and electron diffraction data, has led to conclusions that the vacancies are situated entirely on octahedral (Sinha and Sinha 1957; Jagodzinski and Saalfield 1958; Li *et al.* 1990; Wang *et al.* 1998; Kryukova *et al.* 2000) or tetrahedral (Saalfeld 1958; Saalfeld and Mehrotra 1965; Jayaram and Levi 1989) sites, or distributed over both spinel site positions (Wilson 1979; Wang *et al.* 1999). The occupation of a highly distorted Wyckoff 32*e* site has also been reported (Zhou and Snyder 1991; Gan 1996), which coincides with reports of 'pentahedrally' coordinated Al by several NMR studies (Dupree *et al.* 1986; Chen *et al.* 1992; Pecharroman *et al.* 1999; Wang *et al.* 1999). Furthermore, there is the issue of hydrogen and/or water content in the lattice, which remains unsolved.

Three space groups have been attributed to the γ-Al_2O_3 structure; $Fm\bar{3}m$, $Fd\bar{3}m$ and $I4_1/amd$. It is traditionally thought to be a cubic spinel structure, but tetragonally-distorted structures have been reported (Stumpf *et al.* 1950; Lippens and de Boer 1964). Wilson (1979) and Wilson and McConnell (1980) also observed a tetragonally-distorted spinel structure for γ-Al_2O_3, but found that distortion of the spinel lattice decreases with increasing time or temperature of heat treatment. They found this decrease of tetragonal γ-Al_2O_3 coincide with the formation of cubic γ-Al_2O_3. Zhou and Snyder (1991) found the structure to be a cubic spinel, reporting no tetragonal distortion. Later, Gan (1996), suggested tetragonal and cubic γ-Al_2O_3 to

be simultaneously present at all temperatures with the tetragonal form dominating at lower temperatures. The amount of cubic γ-Al_2O_3 was suggested to increase with increasing temperature, at the expense of tetragonal γ-Al_2O_3.

Through extensive reading one can see that many subtle, confusing and contradictory variations of the structure of γ-Al_2O_3 (and δ-Al_2O_3) have been reported. There has even been one study which has reported a supercell lattice parameter of 15.790 Å as opposed to the traditionally known ~ 7.9 Å (Kordes 1935). One can see that there is a myriad of preparation routes. Further confusion has been added by the terminology used to describe these structures. For example, Rooksby and Rooymans (1961) labelled the tetragonally distorted γ-Al_2O_3 structure described by Saalfeld (1958) as δ-Al_2O_3 which was later confirmed, by Lippens and de Boer (1964) to be γ-Al_2O_3. It appears that the exclusive use of traditional experimental techniques will fall short of providing a decisive answer. Understanding the structure of γ-Al_2O_3 has far reaching implications. Some researchers, in their study of the structure and phase transformation to δ-Al_2O_3 and, subsequently, θ-Al_2O_3, have assumed a structure for γ-Al_2O_3 (Levin *et al.* 1997; Levin and Brandon 1998b; Levin *et al.* 1998). The advantage in knowing the structure of γ-Al_2O_3 for such a study is obvious. It is an imperative step towards understanding mechanisms of phase transformation. It will assist in the subsequent understanding of the surface structure of γ-Al_2O_3. Furthermore, it will ultimately assist in understanding the mechanism by which γ-Al_2O_3 behaves as a catalyst, and will allow for synthesis techniques to be refined and lead to further development of applications.

Problems Associated with Solving γ-Alumina

The predominant factor hindering attempts to solve the γ-Al_2O_3 structure is that it is poorly ordered. This makes it difficult to obtain single crystals of suitable size (coherently scattering domains do not usually exceeding 300 nm), and hence, unsuitable for single-crystal diffraction studies. Furthermore, powder diffraction patterns exhibit high backgrounds and diffuse peaks. The structural disorder makes it difficult to obtain electron diffraction patterns as kikuchi bands, which are used to

identify zone axes, are generally not observed. These complications make it difficult to determine the structure unambiguously.

The traditionally used powder X-ray diffraction and electron microscopy are at a disadvantage when examining the complicated structures of the Al_2O_3 polymorphs. These structures have similar d-spacings and the transformations appear to occur continuously, with several phases coexisting in some instances. Furthermore, factors such as the degree of crystallinity, the presence of impurities, particle size and pressure can alter when a transformation occurs and affect what variant of the structure will be found. Powder X-ray diffraction, where the analysis is 'averaged' over thousands of crystals cannot adequately overcome these problems, while the use electron microscopic techniques may sometimes be too arduous to cover the scope of all possibilities. A possible solution is offered by the use of computational molecular modelling techniques, in conjunction with suitable experimental analysis.

In recent years rapid advancement has occurred in the field of computational materials science. Huge advances in computing power during this period have made it possible to apply the laws of quantum mechanics to the study of macroscopic properties of real materials at the atomic level. Predicting the properties of materials by theoretical means can achieve high accuracy and complements the traditional experimental approaches. In many cases, time and money can be saved by conducting theoretical simulations on a material before conducting experimental tests.

Ab initio quantum mechanical calculations of a single configuration of complex structures like γ-Al_2O_3 can take many days or weeks, whereas the empirical modelling methods, which are based on classical physics, typically only involve a few minutes of computation time. This allows for many more possible structural candidates to be examined, in order to thoroughly sample configuration space, for disordered materials. Although modelling techniques based on interatomic potentials cannot yield accurate data with regards to electronic properties of materials, they can produce reasonably accurate structural data in a fraction of the time taken by quantum mechanical calculations. This means that interatomic potentials can be used to reduce the number of likely candidates before utilising a first principles approach. A key advantage to theoretical investigations is the ability to directly examine many

possible structures of the material, whereas traditional experimental techniques usually correspond to one general model being conceptualised. Hence, this research will involve the combined use of interatomic potentials and first principles calculations, by means of density functional theory (DFT), to investigate possible structures of γ-Al_2O_3 and yield highly accurate results.

Whereas structure determination problems are traditionally approached by obtaining a diffraction pattern and working backwards to determine the unit cell, with interatomic potentials and DFT the process of structure determination begins with construction of the unit cell which is then optimised. The final possible structures determined are then compared with experimental data to obtain consensus. The theoretical modelling will provide a representative structure for γ-Al_2O_3 with precise cation coordinates. To date no experimental study has provided precise cation coordinates for γ-Al_2O_3, a limiting factor brought about by the nature of the material.

1.1 Objectives

The aim of the work contained within this thesis is to advance knowledge of and make new insights into the structure of γ-Al_2O_3. Research will be primarily geared towards elucidating the definitive structure and settling the ambiguity surrounding the γ-Al_2O_3 system. The primary technique to be used is computer simulations based on both interatomic potentials and first principle calculations. This will be combined with the following supporting experimental techniques:

- Neutron diffraction
- X-ray diffraction
- Transmission electron microscopy and electron diffraction
- Nuclear magnetic resonance spectroscopy
- Differential scanning calorimetry and thermogravimetric analysis
- Infra-red spectroscopy
- Inelastic neutron Scattering
- Prompt-gamma activation analysis
- Small angle X-ray scattering
- BET and pycnometry
- Loss on ignition

- The computational work will involve the development of a methodology which will allow all structure possibilities to be examined and do so in reduced time. This is contrast to previous computational studies which have been time consuming and, because of this, have not been able to examine all possible structures.
- Focus will be directed towards accurately determining the unit cell and assessing the possibility of a dual-phase structure.
- Attention will be paid to ascertaining the distribution of vacancies and the precise cation coordinates.
- Once a satisfactory structural model is established annealing time and temperature effects on the system will be examined.
- Research will also involve understanding the evolution of the structure as the transition sequence progresses. The nature of hydrogen and its role in the structure of γ-Al_2O_3 will also be investigated.
- An understanding of the possible synthesis techniques and kinetic effects will be developed with the view of employing a common approach to produce a systematic set of samples within the temperature range of the occurrence of γ-Al_2O_3 for study using experimental techniques.

In addition to the extension of the current understanding the results will offer a platform for further study of the system and other similar and related systems, such as η and δ-Al_2O_3.

Chapter 2

The Structure of γ-Alumina Explored: Historical Review

2.1 Preparation and Reaction Kinetics

The summary of the preparation routes for the transition aluminas provided in Figure 1.1 indicates that γ-Al_2O_3 occurs both from the dehydration of a precursor (boehmite or gibbsite), and the crystallisation of amorphous Al_2O_3. The former is more industrially important. The formation of γ-Al_2O_3 has been reported to occur at temperatures as low as 350 and 400 °C (Lippens and de Boer 1964) and remains present at temperatures as high as 1200 (Chou and Nieh 1991) and 1000 °C (O'Connor *et al.* 1997) when derived from amorphous and boehmite precursors respectively. It should be noted that the transformation sequences for the transition aluminas are approximate. Both of the transformation sequences in which γ-Al_2O_3 occurs indicate evolution to the δ polymorph followed by the θ polymorph. However, there is no direct experimental evidence confirming the existence of a direct $\delta \rightarrow \theta$ transformation or disproving a direct $\gamma \rightarrow \alpha$ transformation (Levin and Brandon 1998a).

Research into the preparation of γ-Al_2O_3 indicates the reaction sequence and kinetics depends on the properties of the precursor (Wilson 1979; Tsuchida *et al.* 1980; Wilson and McConnell 1980). This applies not only to different forms of boehmite, such as the gelatinous and highly crystalline type, but also the conditions under which the boehmite was prepared. Tsuchida *et al.* (1980) reported activation energies for the transformation of boehmite to γ-Al_2O_3 between 220 and 235 kJ $mole^{-1}$. This variation in activation energy was found to correspond to boehmite samples hydrothermally prepared at a range of different temperatures (147 – 297 °C) and different vapour pressures during calcination. Under similar preparation conditions, Wilson and McConnell (1980) reported lower phase transition activation energies of between 185 and 205 kJ $mole^{-1}$.

It can be seen from Figure 1.1 that heating gibbsite results in its transformation to boehmite and χ-Al_2O_3 concurrently. Likewise, heating bayerite results in transformation to both boehmite and η-Al_2O_3. Therefore, when $Al(OH)_3$ is used as the starting material it is imperative to ensure 100% conversion to boehmite before calcining to achieve a pure γ-Al_2O_3 product.

The concurrent formation of boehmite and χ-Al_2O_3 occurs between 200 and 300 °C when heated under atmospheric conditions. Wefers and Misra (1987, pp.46-47) illustrate that boehmite is formed due to the hydrothermal conditions which eventuate inside coarse gibbsite particles from which water cannot rapidly evaporate. When the particle size is small enough to let water escape without significant elevation in pressure, boehmite does not form. Wefers and Misra further indicated that the temperature of formation of boehmite can be separated from that of χ-Al_2O_3. Observation of the differential thermal analysis (DTA) curves in Figure 2.1 indicates a single endotherm at approximately 340 °C, representing transformation to χ-Al_2O_3 (predominantly) and boehmite, for gibbsite starting material with small particle size (< 5 μm). However, for the starting material with large particle size (> 80 μm) a smaller endotherm, at approximately 230 °C, represents the onset of boehmite formation, followed by the larger endotherm at 350 °C, where χ-Al_2O_3 begins to form concurrently. These outcomes were supported by Gan (1996, p.78) who investigated two different commercial gibbsite products with median particle sizes of 50 and 1.5 μm. Gan observed that the fine grained material yielded a DTA curve with a single endotherm at 290 °C representing concurrent evolution to boehmite and χ-Al_2O_3 while the coarse material produced a small endotherm at 240 °C and a larger one at 295 °C.

Heating rate is also a factor. A faster heating rate aids in creating a hydrothermal process within coarse gibbsite crystals, therefore promoting the formation of boehmite (Tertian and Papee 1958). These authors further suggested that the rate of dehydration determines the space group structure of the γ-Al_2O_3 (*refer to section 2.2*). They claimed that a slow dehydration rate using a slow heating rate leads to the tetragonal form of γ-Al_2O_3, whereas a more drastic treatment, using a fast heating rate, gives rise to the cubic spinel γ-Al_2O_3. Wilson (1979) determined

that prolonged heating periods result in reductions in the tetragonal distortion of the lattice; it becomes increasingly 'cubic'.

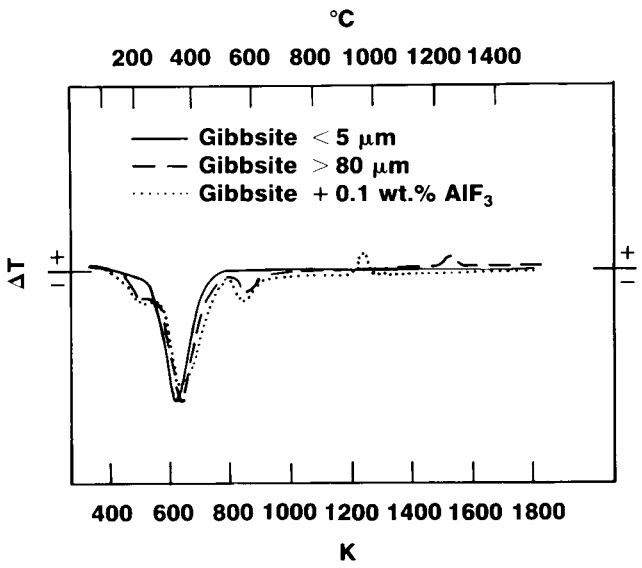

Figure 2.1. DTA curves of gibbsite for different particle sizes (Wefers and Misra 1987, p.49).

Gan (1996, p.178) also determined that while particle size does affect the reaction kinetics and pathway from a gibbsite precursor, these parameters have no influence on the reaction kinetics and pathway from boehmite. This is contrary to the findings of Tsuchida *et al.* (1980) and Garn (1965, p.95) who found the boehmite to γ-Al_2O_3 transformation temperature depends on the crystallite size within the particles; larger crystals have higher stability.

Tsuchida *et al.* (1980) went further to illustrate that the kinetics of the boehmite to γ-Al_2O_3 transformation is extremely complex and that the kinetics depends on the rate-controlling step in the transformation mechanism. The mechanism initially involves the nucleation of γ-Al_2O_3 crystals at active sites on the boehmite surface. The nuclei overlap each other as they grow larger, eventually covering the entire surface of the boehmite particles with a continuous layer of γ-Al_2O_3. After this point, the water given off in the dehydration reaction must diffuse through the γ-Al_2O_3 surface layer. As the diffusion rate increases, the reaction eventually becomes phase-boundary controlled. The fewer structural imperfections and active sites (potential nucleation sites) on highly crystalline boehmite means the

dehydration reaction is nucleation controlled. On the other hand, the dehydration of poorly crystalline boehmite is diffusion controlled. Poorly crystalline boehmite has higher porosity, and therefore more imperfections and active sites, resulting in an instantaneous nucleation step. Consequently, a compact and impermeable product layer envelops the boehmite particles which restricts further formation of γ-Al_2O_3. The rate of increase in surface area during the dehydration of boehmite is much higher for the highly crystalline material. This confirms that nucleation and diffusion are the rate-determining steps for highly crystalline and poorly crystalline boehmite precursor respectively.

Tsuchida *et al.* (1980) also determined that the crystallinity of the boehmite precursor affects the X-ray diffraction (XRD) pattern of γ-Al_2O_3. A more crystalline boehmite yields a sharper peak splitting about the (400) ($\equiv$ (004)) line, coinciding with γ-Al_2O_3 of higher crystallinity. This splitting becomes obscure for poorly crystalline precursors. In fact, poorly crystalline boehmite has been reported in one case to form η-Al_2O_3 and amorphous alumina upon dehydration (Abrams and Low 1969). The latter, in turn, concurrently dehydrates to both η-Al_2O_3 and γ-Al_2O_3. Abrams and Low (1969) and Tsuchida *et al.* (1980) therefore showed that the crystallinity of boehmite affects the yield of crystalline γ-Al_2O_3 produced. This was illustrated most clearly by DTA traces where the endotherms corresponding to the boehmite to γ-Al_2O_3 transformation became more pronounced and distinct with increasing crystallinity.

Vapour pressure can play a key role in ensuring complete conversion of $Al(OH)_3$ to boehmite. Stumpf *et al*. (1950) determined that heating in a high pressure environment results in lower formation temperatures of the next transition phase. But as the temperature increases, the influence of vapour pressure becomes negligible. The implication here is that hydrothermal treatment of $Al(OH)_3$ in pressurised vessels can result in boehmite synthesis. Several studies have been conducted which confirm this and show that pure, highly crystalline boehmite forms as low as 150 °C (Laubengayer and Weisz 1943; Ervin and Osborn 1951). Particle size only serves to affect the duration required for hydrothermal conversion. Wilson *et al*. (1980) and Wilson and McConnell (1980) found that vapour pressure can determine whether or not intermediate phases in the boehmite to α-Al_2O_3 sequence occur.

According to Tertian and Papee (1958), Sato (1962), Lippens and de Boer (1964) and Wilson (1979) δ-Al_2O_3 occurs as an intermediate between the γ and θ polymorphs. However, Saalfeld (1960), Abrams and Low (1969), Zhou and Snyder (1991), Wang *et al*. (1999) and O'Connor *et al*. (1997) reported no occurrence of the δ phase. MacKenzie *et al*. (2000) determined that neither δ nor θ-Al_2O_3 occur when the boehmite precursor is ground before calcination and that grinding led to an increased amorphous content. Despite the ambiguity surrounding the occurrence of a δ-Al_2O_3 intermediate, all of these researchers, with the exception of Abrams and Low (1969) and Wang *et al*. (1999), used similar methods to obtain the boehmite precursor; a pressurised hydrothermal treatment of gibbsite which yields highly crystalline boehmite. In the case of Abrams and Low (1969) γ-Al_2O_3 was found to evolve from the well-crystallised part of fibrous boehmite made from the sol-gel method of Bugosh (1959). Wang *et al*. (1999) also used the sol-gel method and found the onset of θ-Al_2O_3 to occur as early as 600 °C.

Wilson and McConnell (1980) described δ-Al_2O_3 as a triple cell of γ-Al_2O_3, resulting in the appearance of a spinel superstructure. It was concluded by Wilson and McConnell that there is no distinct difference between δ and γ-Al_2O_3. This conclusion was supported by the electron energy loss spectroscopy (EELS) of French *et al.* (1998) who found the spectra for the two polymorphs to be almost indistinguishable. However, the results of Pecharroman *et al*. (1999), through comparison of infrared (IR) and nuclear magnetic resonance (NMR) spectra of a proven triple cell material (γ-Fe_2O_3), do not agree with the triple cell hypothesis and suggest it can be explained as a mixture of γ and θ-Al_2O_3.

Lippens and de Boer (1964), Saalfeld and Mehrota (1965) and Wilson (1979) showed, by electron diffraction, that the transformation from boehmite to θ-Al_2O_3 is topotactic (proceeds via short-range in-situ structure rearrangement). This indicates that there is an orientational relationship of the lattice axes between boehmite and its transition derivatives. The crystals of each polymorph, therefore, exhibit the same shape as its precursor, which is usually sheet-like or lamellar. Zhou and Snyder (1991) refer to this as a pseudomorphic transformation. As the boehmite is heated, its hydroxide layers are destroyed but the oxygen layers remain unaffected, creating the skeleton for γ-Al_2O_3 which converts from hexagonal ABABAB…. stacking to cubic ABCABC… stacking of the oxygen layers (Wang *et al.* 1999). Wilson and

McConnell (1980) concluded the transformation sequence from the γ phase to the θ phase to be energetically favourable because of the structural similarities of the phases concerned.

The above discussion is illustrated in Figure 2.2, which is a summary of the reaction pathways when considering the formation of γ-Al_2O_3 from aluminium trihydroxide and monohydroxide precursors of varying degrees of crystallinity. It should be noted that γ-Al_2O_3, and the subsequent δ and θ phases, can be obtained by calcining reagent grade ammonium alum ($NH_4Al(SO_4)_2.H_2O$) in air at 1000 °C (Plummer 1958; Dynys and Halloran 1982). Recently, an alternative sol-gel route that did not use boehmite as a precursor was developed for γ-Al_2O_3 (Fu *et al.* 1999). It has also been observed upon the separation of alumino-silicate compounds during heating (Sanz *et al.* 1991).

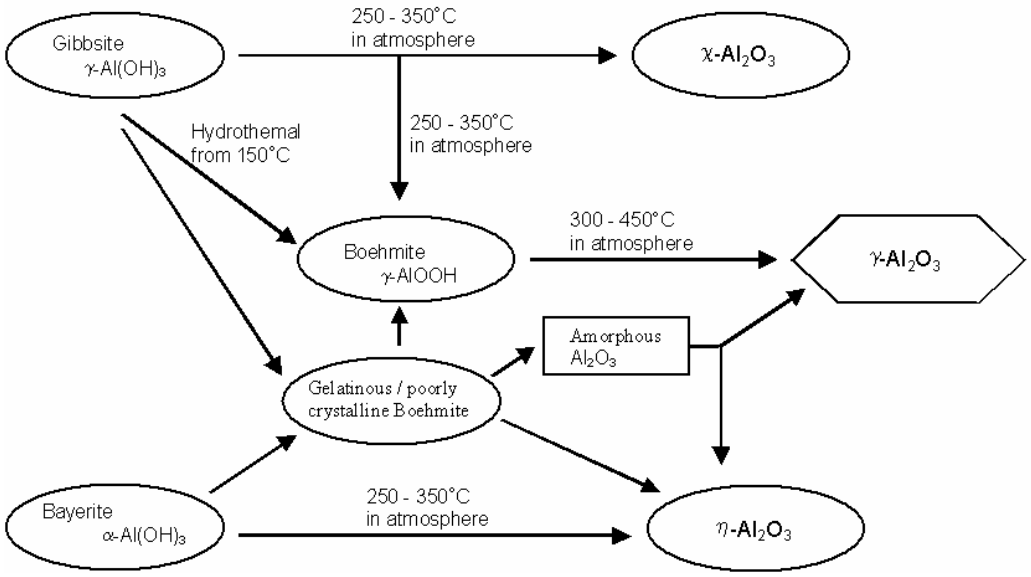

Figure 2.2. Possible reaction pathways from alumina hydrates to the formation of γ-Al_2O_3.

Highly crystalline boehmite usually produces γ-Al_2O_3 with lower surface area, usually less than 100 $m^2\ g^{-1}$, compared to boehmite of a lower crystallinity (Wefers and Misra 1987, pp.58-59). It is the γ-Al_2O_3 that is of higher surface area, and poorer crystallinity, usually made from either gelatinous or poorly crystalline boehmite, which is used as a catalyst (Taylor 1984; Knözinger 1985; El-Katatny *et al.* 1998). The surface area of gelatinous boehmite-derived γ-Al_2O_3 is typically

between 150 and 230 m^2 g^{-1} (Soled 1983) and can exceed 600 m^2 g^{-1} (Wefers and Misra 1987, p.59). A detailed description of the sol-gel method, which involves the preparation of fibrillar, gelatinous boehmite from acidic anion solution, is provided by Bugosh (1959).

In addition to direct calcination, and hydrothermal treatment of gibbsite, there are other methods of producing boehmite precursors to γ-Al_2O_3 that are closely related to the sol-gel method. Synthesis of boehmite from acid neutralisation of sodium aluminate solutions with CO_2 has been reported (Leech 1984). Boehmite can also be produced from hydrothermal treatment (hydrolysis) of urea-aluminium anion solutions (Hille *et al.* 1989). Mishra *et al*. (2002) investigated the effect of the type of aluminium salt used ($AlCl_3$, $Al(NO_3)_3$, $Al_3(SO_4)_3$) on the precipitation of boehmite. The boehmite produced from this method is relatively well crystalline but has some gelatinous boehmite content, with little water, and results in a high surface area γ-Al_2O_3 suitable for use as a catalyst. The type of anion used was found to influence the formation temperature of both boehmite and the γ-Al_2O_3 produced from calcination of the boehmite. Once γ-Al_2O_3 was formed, no other phase transformation was found to occur before 1000 °C, according to DTA results, indicating enhanced thermal stability in the alumina product. El-Katatny *et al*. (1998) produced a similar boehmite product using a technique involving precipitation of boehmite from sodium aluminate solution using H_2O_2. Unlike every other method by which boehmite is produced, this method is carried out at or near room temperature, with the critical parameter being the pH level. It also has another advantage over other precipitation techniques, in that there are no extraneous anions to deal with.

2.1.1 Amorphous Precursors

Transition aluminas designated with the γ, δ and θ prefixes have also been observed to occur during nucleation and crystallisation in vapour deposited ceramic coatings derived from alumina melts (Plummer 1958; Dragoo and Diamond 1967; Barry *et al.* 1968; Bonevich and Marks 1992; Larsson and Ruppi 2001). This is done by either flame or plasma melting of powders or by the condensation of vapour from arcs. Ceramic films have also been derived from amorphous sols (Fukuda *et al.*

1996) and either electrolytic or thermal oxidation of aluminium substrates (Verwey 1935b; Morrissey *et al.* 1985; Ealet *et al.* 1994).

The dominant phase which occurs depends on the temperature of the substrate, or the temperature that the film itself is heated to, and can be influenced by the presence of a nucleation agent. After deposition, at below 150 °C, Dragoo and Diamond (1967) observed the film to remain amorphous until between 570 and 670 °C, where it transformed to a poorly crystalline material. Nukui *et al*. (1976) determined the structure of amorphous alumina to be similar to that of γ-Al_2O_3. Between 670 and 1200 °C the $\gamma \rightarrow \delta \rightarrow \theta \rightarrow \alpha$-$Al_2O_3$ sequence was observed as well as the concurrent crystallisation of θ-Al_2O_3 alongside γ-Al_2O_3. When the melt is immediately calcined or quenched at temperatures over 1000 °C all three transition phases, and α-Al_2O_3, were found to be simultaneously present (Plummer 1958; Morrissey *et al.* 1985). Jayarem and Levi (1989), who used electron oxidation of pure aluminium to prepare their samples, also observed the concurrent formation of each of the above phases directly from the melt. However, in the case of α-Al_2O_3 direct nucleation from the melt depends on the presence of an α-Al_2O_3 seed. Additionally, δ-Al_2O_3 has been found to be the dominant phase present in several studies, particularly at higher calcination temperatures of the amorphous film (Morrissey *et al.* 1985; Jayaram and Levi 1989; Bonevich and Marks 1992). Furthermore, it is usual that the phase present is related to the size of the particle upon which nucleation occurred, with γ-Al_2O_3 occurring in the smaller particles and α-Al_2O_3 in the largest. Pertaining to γ-Al_2O_3, several regions of symmetry related variants, both fully crystallised and partially disordered, have been observed within the same grain, creating a subgrain-like appearance (Morrissey *et al.* 1985; Jayaram and Levi 1989).

However, there are differences between the transformation sequences derived from the boehmite and amorphous alumina precursors. In the sequence beginning with boehmite, the presence of the δ–phase is not always observed. But for amorphous precursors, the presence of δ-Al_2O_3 has always been reported, with the exception of Chou and Nieh (1991) who do not consider the presence of δ or θ-Al_2O_3. There is also a distinction in the unit cell structure observed for δ-Al_2O_3; *tetragonal*, in many cases, when derived from boehmite and *orthorhombic*

when derived from the melt or by oxidation. Furthermore, three extra phases, λ, θ',θ" have been reported for the transformation sequence originating from the melt which have not been observed form the hydrate (Levin *et al.* 1997; Levin and Brandon 1998b; Levin *et al.* 1998). There are also differences in the observed structure of γ-Al_2O_3 in the two sequences which are discussed in *section 2.2*.

2.2 Characterisation of the Crystallographic Structure

The γ-Al_2O_3 phase (along with the δ and η phases) is generally believed to be a cubic spinel ($MgAl_2O_4$) based structure in accordance with the $Fd\bar{3}m$ space group (Sickafus *et al.* 1999). The unit cell contains 32 oxygen ions in 32*e* Wyckoff positions, which are approximately close packed in a face centred cubic (fcc) arrangement, with ABCABC… stacking. The cation:anion ratio in γ-Al_2O_3 is 2:3, as opposed to 3:4 for spinel structures, so to maintain stoichiometry there must be 21⅓ aluminium cations in the unit cell. This creates a defect spinel structure because of the vacancies imposed by such an arrangement. The consideration of a spinel structure restricts the aluminium cations to occupying 8*a* (tetrahedral) and 16*d* (octahedral) Wyckoff positions, which are termed the spinel sites. Hence the stoichiometry can be represented as $Al_{21⅓}□_{2⅔}O_{32}$, where □ represents a vacancy among the spinel positions. This can be simplified to $Al_{8/3}□_{⅓}O_4$. Note that the $Fd\bar{3}m$ space group also possesses other tetrahedral (8*b* and 48*f*) and octahedral (16*d*) site positions.

Since Ulrich's assignment of the prefix γ to any undescribed alumina in 1925 (Ulrich 1925), the term has been used in many cases to describe all the transition forms. It can therefore be difficult to determine when researchers began to describe γ-Al_2O_3 as the spinel-type structure it is thought of today. The first description came in 1935 (Verway 1935a; Verwey 1935b). Verway determined the unit cell to contain 32 oxygen atoms with a lattice parameter, *a*, equal to 7.90 Å, the symmetry relations for the structure to conform to $Fm\bar{3}m$ space group symmetry, and Al sublattice coordination of 70% in octahedral site positions and 30% in tetrahedral site positions. Rooksby (1951, p.264) determined that the $Fd\bar{3}m$ space group, a subgroup of the

$Fm\bar{3}m$ (Hahn 1995) space group, more correctly described spinel structures with lattice parameters of 7.90 Å.

The structure of γ-Al_2O_3 is, in fact, analogous to that of η-Al_2O_3. The latter is distinguished from γ-Al_2O_3 because it is derived from bayerite (Figure 1.1). Both of these structures have XRD patterns that exhibit a small number of broad lines. The δ and θ-Al_2O_3 phases, both derived from γ and the latter also from η-Al_2O_3, display a large number of sharp lines in their diffraction patterns signifying that their structures are more ordered. Given that the oxygen lattice remains relatively undisturbed during the transformations the higher-order ordering stems from the cation sublattice (Jayaram and Levi 1989). All of these structures share similarities. Each of the γ, δ, and η-Al_2O_3 polymorphs have common reflections; $d_{400} \approx 1.99$ Å, $d_{440} \approx 1.40$ Å (Lippens and de Boer 1964). A further example of the structural similarities is seen in the lattice parameters with $a_\gamma \approx a_\theta$ and $a_\gamma = a_\delta = b_\delta$ (Rooksby and Rooymans 1961; Lippens and de Boer 1964; Wilson 1979). Although θ-Al_2O_3 is monoclinic it is also based on a near cubic close-packed lattice with the (440) plane in the spinel-based structures represented by the (204) plane ($d_{440} \approx d_{204}$) in the θ phase (Yamaguchi *et al.* 1970).

The oxygen lattice for γ and δ-Al_2O_3 are the same, the difference is in the ordering of the Al atoms (Morrissey *et al.* 1985). Wang *et al*. (1998), for example, suggest that aluminium cation rearrangement occurs with vacancies being distributed among octahedral and tetrahedral sites in γ-Al_2O_3 to ordering solely on octahedral sites in δ-Al_2O_3. The structure of δ-Al_2O_3 is still not well known but descriptions have been offered (Wilson 1979; Wilson and McConnell 1980; Jayaram and Levi 1989; Repelin and Husson 1990). Lippens and de Boer (1964), Wilson (1979) and Repelin and Husson (1990) reported a tetragonal unit cell for δ-Al_2O_3 with $c = 3a_\gamma$ from boehmite precursors. Repelin and Husson (1990), however, reported different *a* and *b* parameters for δ-Al_2O_3 than what is traditionally believed with $a_\delta \approx a_\gamma/\sqrt{2}$ and provided a description of the symmetry. From an amorphous precursor, Rooksby and Rooymans (1961) also reported a tetragonal structure for δ-Al_2O_3 with $c = 1.5a_\gamma$. Jayarem and Levi (1989) on the other hand, reported an orthorhombic unit cell for amorphous derived δ-Al_2O_3.

According to Zhou and Snyder (1991) the initial cation disorder of the low-temperature forms of alumina depend upon the precursor used. The phases become more ordered with increasing heat treatment. Both δ, and θ-Al_2O_3 are more ordered than γ-Al_2O_3 (Wilson 1979; Wilson and McConnell 1980; Jayaram and Levi 1989). This is accompanied by a reduction in pore size, an increase in particle size and bulk density, and a gradual annihilation of vacancies (Soled 1983). The formation of γ, δ, and θ-Al_2O_3 may therefore be seen as part of the gradual transition from disordered to fully ordered structures with decreasing undercooling of the melt in the case of amorphous precursors, and increasing dehydration in the case of boehmite precursors. Wilson and McConnell (1980) found no obvious variations in microstructure for γ, δ, or θ-Al_2O_3 samples, with other samples of the same phase, prepared under different conditions from the same well-crystalline boehmite precursor.

2.2.1 Structural Characteristics from Diffraction Patterns

Lippens and de Boer (1964) identified and described three types of reflection which occur in electron diffraction patterns of γ-Al_2O_3:

Type a: Sharp reflection with broadened base. After division of the Miller indices of these reflections by two they still belong to a fcc lattice.

Type b: Reflections not as sharp as *type a*, length about twice the breadth. The indices of these reflections are all odd.

Type c: Reflections without a sharp maximum, length more than three times the breadth. These reflections have even indices, which upon division by two no longer belong to a fcc lattice.

Type a reflections originate predominantly from the oxygen lattice, but also the entire cation sublattice. *Type b* reflections stem from the cation sublattice and *type c* originate only from cations in tetrahedral positions. Figure 2.3 illustrates a typical selected area electron diffraction (SAED) pattern observed form γ-Al_2O_3 depicting the reflection positions and the locations of each type of reflection. These patterns are viewed down the [0kl] zone axis, showing the *c* axis and the *hk0* plane (Wilson 1979).

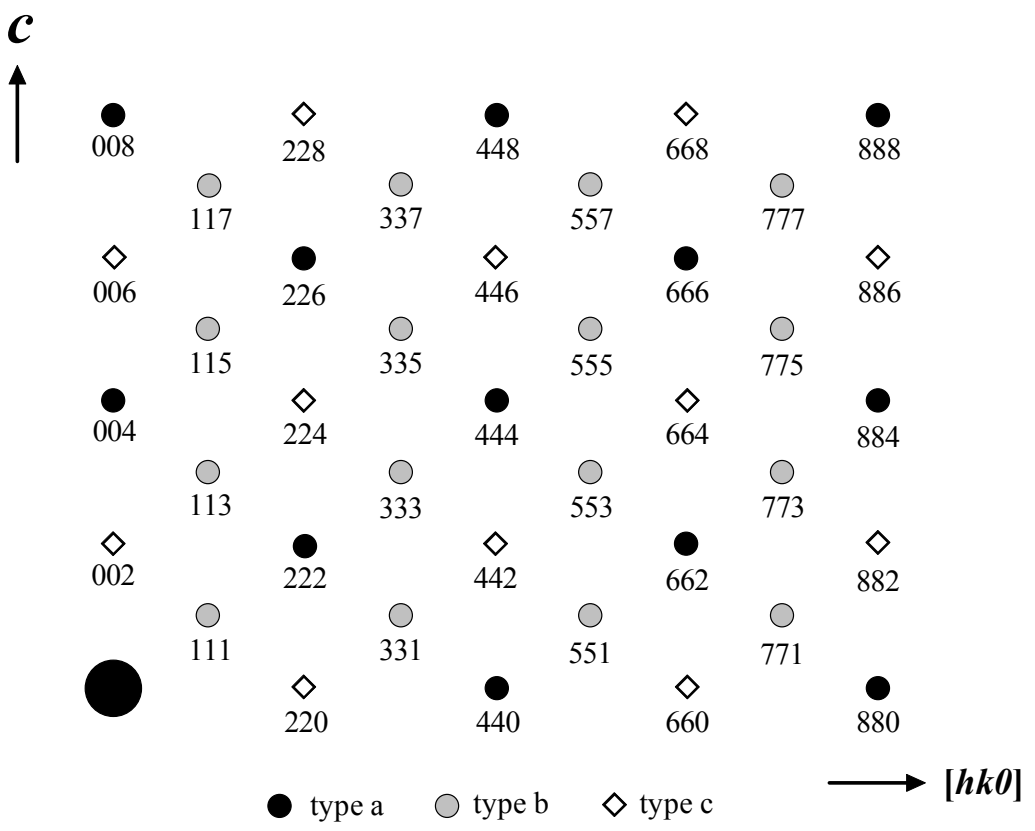

Figure 2.3. Most common electron diffraction pattern observed for γ-Al_2O_3, [0*kl*] zone axis, depicting the position of reflections and each reflection type. Reflections indexed according to $Fd\bar{3}m$ space group. (After Lippens and De Boer (1964).)

Observing the change in these diffraction patterns has, historically, been the most direct way to understanding the microstructure of γ-Al_2O_3. For example, because the *type a* reflections are sharper for γ-Al_2O_3 than the equivalent reflections in η-Al_2O_3, it is known that the oxygen sublattice is more ordered for the former. The observation of streaking, associated with *type b* and to a larger extent *type c* reflections has been attributed to stacking faults at positions where the cation vacancies are located (Cowley 1953). As the structure becomes more ordered with increasing heat treatment streaking in the *00l* direction is increased (Jayaram and Levi 1989). The reflection types can provide an indication of which sites vacancy ordering occurs on. If there is streaking from *type c* reflections and not *type b* then the vacancy ordering is exclusive to tetrahedral sites in the spinel lattice. Conversely, if there is streaking from *type b* reflections and not *type c* then the vacancy ordering is exclusive to octahedral sites. These streaks are perpendicular to the orientations of

pores in the microstructure and their size is consistent with the pore spacing (Wilson 1979).

Similar trends in the types of reflections observed in electron diffraction patterns can be seen in XRD patterns (Figure 2.4). As with streaking in the electron diffraction pattern the degree of line broadening reflects the pore spacing.

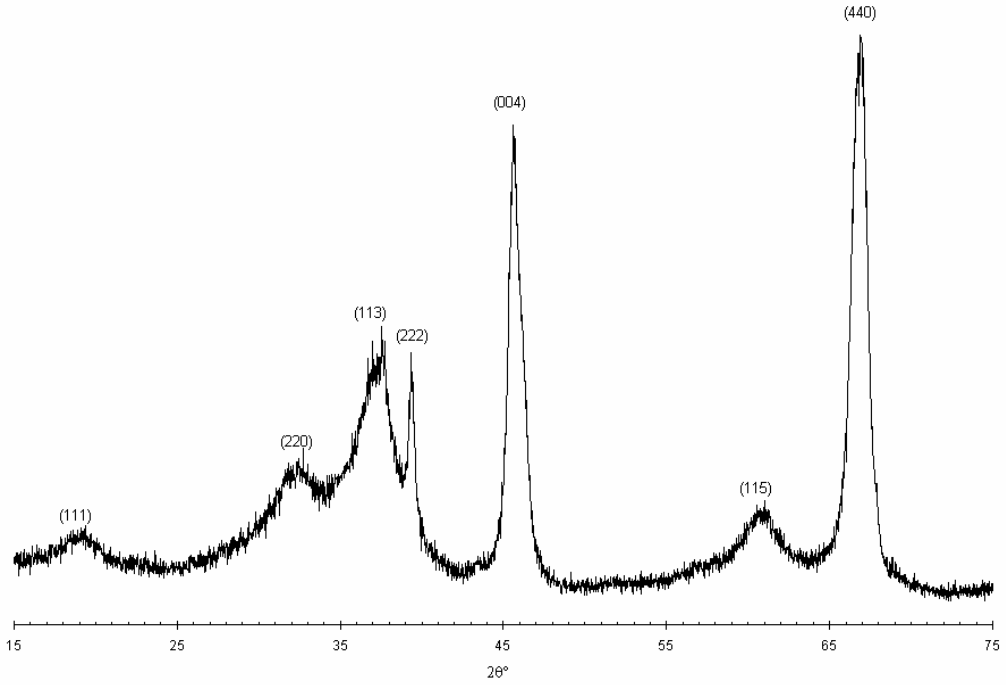

Figure 2.4. Typical X-ray diffraction pattern for γ-Al_2O_3, indexed according to the $Fd\bar{3}m$ space group.

2.2.2 Discrepancies in Cation Occupation

The greatest confusion surrounding γ-Al_2O_3 concerns the distribution of vacancies in the structure. Analysis of neutron and X-ray diffraction, and electron microscopy data, has led to conclusions that the vacancies are situated entirely on octahedral (Sinha and Sinha 1957; Jagodzinski and Saalfield 1958; Li *et al.* 1990; Wang *et al.* 1998; Kryukova *et al.* 2000) or tetrahedral (Saalfeld 1958; Saalfeld and Mehrotra 1965; Jayaram and Levi 1989) sites, or distributed over both spinel site positions (Wilson 1979; Wang *et al.* 1999). Sinha and Sinha (1957), as well as Jagodzinski and Saalfield (1958), based their conclusions on the absence of the (111) reflection in XRD patterns. Li *et al*. (1990) used Rietveld pattern-fitting, as did Wang *et al*. (1999). From electron microscopy images, Kryukova *et al*. (2000) observed

hexagonal loop defects bounded by the {111} and {110} type crystal planes which they assumed to represent the coalescence of octahedral vacancies. Saalfeld (1958) supposed full octahedral occupation, and hence tetrahedral vacancies, because of the intensity of the 400 and 440 reflections, while Saalfeld and Mehrota (1965) performed Fourier analysis to reach the same conclusion. Jayarem and Levi (1989) concluded that ordering on tetrahedral sites from direct comparison of the (220) and (400) reflection intensity ratio (I_{220}/I_{400}) for γ-Al_2O_3 and $MgAl_2O_4$, the (220) reflection stemming solely from the tetragonal sublattice. I_{220}/I_{400} was observed to be lower for γ-Al_2O_3. Wilson (1979), following on from the observations of Cowley (1953) and Lippens and de Boer (1964), concluded a distribution of vacancies on both octahedral and tetrahedral site positions from the streaking of reflections which originate from both the total cation lattice and cations only in tetrahedral positions. Wang *et al*. (1998) arrived at their conclusion from consideration of a transformation mechanism to δ-Al_2O_3.

The ordering of vacancies on octahedral sites is supported by several computational studies (Mo *et al.* 1997; Streitz and Mintmire 1999; Wolverton and Hass 2001; Gutiérrez *et al.* 2002). Vacancy ordering on tetrahedral sites is supported by the NMR study of John *et al.* (1983) and the molecular dynamics simulation of Blonski and Garofalini (1993). However, the NMR and computational work of Lee *et al*. (1997) supports vacancy distribution among both octahedral and tetrahedral positions.

Departure from Spinel Position Exclusivity

Some studies have suggested that the cation sublattice is not restricted to the occupation of spinel positions only. This departure from the traditional belief was first proposed for η-Al_2O_3 by Shirasuka *et al*. (1976) who suggested, from powder XRD data, that the cations were distributed over all possible sites in the $Fd\bar{3}m$ space group, with 62.5% in octahedral and the remainder in tetrahedral positions. Ushakov and Moroz (1984) could not index XRD of γ-Al_2O_3 data with only spinel sites being occupied. This work was followed by Zhou and Snyder (1991) who, from Rietveld analysis of neutron diffraction data, reported cation occupation of a highly distorted Wyckoff 32*e* site and designated it pseudo-octahedral, which they proposed exits at

the surface of the structure. The model proposed by Zhou and Snyder provides the best fit to date for diffraction data. The reporting of the Wyckoff 32*e* site coincides with reports of what has been labelled pentahedrally coordinated Al in several NMR studies on γ-Al_2O_3 (Komarneni *et al.* 1985; Dupree *et al.* 1986; Chen *et al.* 1992; Pecharroman *et al.* 1999; Wang *et al.* 1999) and molecular dynamics studies (Álvarez *et al.* 1992; Álvarez *et al.* 1995). A pentahedral or 'five-coordinated' Al is characterised by the occurrence of a peak in the NMR data situated between the octahedral and tetrahedral peaks. These types of peaks have also been observed in studies of other spinel-type structures and alumino-silicate gels (Grobet *et al.* 1987; Man and Klinowski 1988; Pellet *et al.* 1988; Sanz *et al.* 1988; Sanz *et al.* 1991).

The reasons for the occurrence of pentahedral peaks are still not confirmed. Komarneni *et al*. (1985) suggest pentahedral peaks result from the migration of Al in octahedral to tetrahedral sites. Wang *et al*. (1999) proposed that it is due to substitution of oxygen ions in the lattice with hydroxyl groups. In work on other materials containing Al where more peaks have been observed than expected, distortions in the symmetry position where the Al is located are the suggested cause (Grobet *et al.* 1987; Man and Klinowski 1988). Significant pentahedral peaks have only been observed for γ-Al_2O_3 produced from gelatinous (poorly crystalline) boehmite (Komarneni *et al.* 1985; Wang *et al.* 1999) or well ground boehmite (Chen *et al.* 1992). Chen *et al.* did not observe a pentahedral peak for a boehmite precursor that was left unground. Also, Sanz *et al*. (1991) found significant amounts of pentahedral peaks in gelatinous alumino-silicate materials. However, they did not observe such peaks in the anhydrous γ-Al_2O_3 produced from the separation of Al_2O_3-SiO_2 at high temperature.

2.2.3 Tetragonal Deformation in Boehmite Derived γ-Alumina

When derived from amorphous precursors, γ-Al_2O_3 has always been reported as having a cubic lattice (Verway 1935a; Plummer 1958; Harvey *et al.* 1960; Dragoo and Diamond 1967; McPherson 1973; Dynys and Halloran 1982; Morrissey *et al.* 1985; Jayaram and Levi 1989; Chou and Nieh 1991; Bonevich and Marks 1992; Ealet *et al.* 1994; Levin *et al.* 1997). Boehmite derived γ-Al_2O_3 has been reported as exhibiting a cubic lattice (Stumpf *et al.* 1950; Rooksby 1951; Sinha and Sinha 1957;

Zhou and Snyder 1991; Liddell 1996; Wang *et al.* 1998; Wang *et al.* 1999) and as having a slight *tetragonal* distortion (Lippens and de Boer 1964; Saalfeld 1958; Tertian and Papee 1958; Saalfeld and Mehrotra 1965; Yanagida and Yamaguchi 1962; Yanagida and Yamaguchi 1964; Wilson 1979; Wilson and McConnell 1980) in the cubic lattice. These findings have been arrived at using diffraction techniques. The tetragonal nature is signified by greater than expected reflections for an ideal spinel. In electron diffraction patterns this is represented as extra spots, such as the (002) and (006) reflections (Figure 2.3). In XRD patterns, tetragonal nature is suggested by split or asymmetric peaks. When it occurs, the most notable splitting occurs in the (004) reflection (Figure 2.4). η-Alumina, for comparison, only experiences peak asymmetry, signifying a less pronounced tetragonal nature than γ-Al_2O_3. Structural variations may result from varied preparation history (Tsuchida *et al.* 1980; Wefers and Misra 1987). The most recent reports have either concluded or assumed in favour of a cubic lattice, though there has been a suggestion that γ-Al_2O_3 is a dual-phase system, consisting of cubic γ-Al_2O_3 *and* tetragonal γ-Al_2O_3 (Gan 1996; O'Connor *et al.* 1997). In the proposed dual-phase system the tetragonal phase is dominant at lower temperatures but the amount of cubic γ-Al_2O_3 increases with increasing temperature, at the expense of tetragonal γ-Al_2O_3.

Reports of tetragonal γ-Al_2O_3 found *c*:*a* ratios to be between 0.987 and 0.963 (Lippens and de Boer 1964; Yanagida and Yamaguchi 1964; Wilson and McConnell 1980). Lippens and de Boer (1964), Yanagida and Yamaguchi (1964) and Wilson (1979) found the degree of tetragonal distortion decreases with increasing preparation temperature. Wilson (1979) observed reduced tetragonal distortion with increased heating times. Tertian and Papee (1958) observed that rapid heating rates result in a cubic structure and slow rates lead to a tetragonal structure. Yanagida and Yamaguchi (1964) performed *in situ* XRD followed by room temperature measurements and found that the tetragonal distortion was reduced at room temperature. Tsuchida *et al*. (1980) determined that greater crystallinity of the boehmite precursor leads to tetragonal distortion, signified by sharper peak splitting about the (004) line.

Several reasons for a tetragonal structure have been proposed: shrinkage anisotropy in the *a* and *b* axes of boehmite during heating (Lippens and de Boer 1964), the distribution of residual water or hydroxyl ions (Yanagida and Yamaguchi

1964), and vacancy ordering on tetrahedral positions (Wilson 1979; Wilson and McConnell 1980; Zhou and Snyder 1991). The tetragonal distortion in γ-Al_2O_3 and δ-Al_2O_3 coincides with vacancy ordering on tetrahedral and octahedral sites, respectively, and the change in the tetragonal distortion relates to the cation migration between the sites (Wilson 1979; Wilson and McConnell 1980).

Regardless of these reports on the tetragonal distortion in its structure, γ-Al_2O_3 has continued to be ascribed to $Fd\bar{3}m$ symmetry (Lippens and de Boer 1964; Saalfeld and Mehrotra 1965). The tendency has been to simply assert a cubic structure and highlight a contracted *c* axis upon observation of a tetragonal distortion. Levin and Brandon (1998a) have asserted that the '*true*' symmetry of the tetragonally deformed structures should be described by a tetragonal space group, expectedly, a maximal subgroup of $Fd\bar{3}m$.

The tetragonal $I4_1/amd$ space group is a maximal subgroup of $Fd\bar{3}m$, with $a_{cubic} \approx \sqrt{2} \times a_{tetragonal}$. This space group was first suggested by Li *et al*. (1990), who proposed a structure with Al restricted to spinel sites with vacancy ordering on octahedral sites from analysis of ICDD pattern PDF data. The γ-Al_2O_3 structure representation provided by $I4_1/amd$ is analogous to the spinel representation except the unit cell contains half the number of atoms. In this space group, site positions analogous to the *spinel* sites in its supergroup are the 4*a* (≡ 8*a*) and 8*d* (≡ 16*d*) (Hahn 1995). The 16 oxygen ions of the unit cell are located in 16*h* Wyckoff positions and the 10⅔ Al cations were considered to be distributed among the 4*a* (tetrahedral) and 8*d* (octahedral) Wyckoff positions. As with $Fd\bar{3}m$, the $I4_1/amd$ space group formally has other site positions available for occupation; 8*c* (octahedral), and 4*b*, 8*e* and 16*g* (tetrahedral).

2.2.4 The Uncertain Role of Hydrogen

Structural Aspects

Hydrogen, whether in the form of water, hydroxyl groups, or discrete protons has been reported in the structure of boehmite-derived γ-Al_2O_3. However, traditional representations of γ-Al_2O_3 tend to ignore the nature of hydrogen and its implications

on the structure. According to Sohlberg *et al*. (1999b) the presence of hydrogen in the structure casts doubts over the validity of its spinel representation.

It is well known that water is present in the structure of γ-Al_2O_3, resulting from the dehydration of boehmite, following the reaction:

$$2\gamma\text{-AlOOH} \rightarrow \gamma\text{-}Al_2O_3 + H_2O \qquad (2.1)$$

The dehydration model described by Lippens and de Boer (1964) involves a breakdown of the layers in boehmite formed by OH groups while the oxygen layers remain in place to form a skeleton of the spinel/γ-Al_2O_3 lattice. This suggests that the presence of water and hydroxyl groups in the structure is possible. The water loss is typically traced, quantitatively, from DTA-TGA measurements (Tsuchida *et al.* 1980; Wefers and Misra 1987) and can be investigated qualitatively from the difference in background contribution in neutron diffraction patterns (Gan 1996, pp.105-107).

The first mention of hydrogen in the structure, not bound in water form, was made by Dowden (1950) who suggested that protons reside in the cation vacancies in the bulk structure, which are considered passive. Proton NMR results from gel-derived alumina showed 0.00888 g of hydrogen per gram of alumina within the structure, with 36.8% of these hydrogens residing within the bulk (Pearson 1971). These passive protons have been suggested to account for the catalytic properties of the transition aluminas (Tung and Mcininch 1964; Tsyganenko and Mardilovich 1996). De Boer and Houben (1952) suggested a hydrogen-spinel (protospinel) structure for γ-Al_2O_3 analogous to the lithium spinel described by Kordes (1935). The protospinel approach is supported by several other researchers (Ushakov and Moroz 1984; Tsyganenko *et al.* 1990; Saniger 1995; Sohlberg *et al.* 1999b). As a result several researchers have proposed the stoichiometric formula for γ-Al_2O_3 be written γ-$Al_2O_3.nH_2O$, with n reported to be between zero and 0.63 (de Boer and Houben 1952; Pearson 1971; Ushakov and Moroz 1984; Zhou and Snyder 1991). This notation, however, implies that γ-Al_2O_3 is a crystalline hydrate, which it is not, and that excess oxygen is involved.

Tung and Mcininch (1964) suggested a mechanism by which the protospinel structure occurs whereby a water molecule ionises after interaction with Lewis acid sites at the surface, most probably through coordination of the oxygen in water with an exposed Al ion. The ionisation of the water results in a hydroxyl group residing in

an anionic vacancy with the proton (H^+) migrating into a cationic vacancy in the layer below. This mechanism was based on energy considerations, whereby oxygen ions make up the outside layer and aluminium forms the layer below, and the pioneering surface structure model developed by Peri (1965c), which considers anionic defects. The anionic defects (absence of oxygen ions) at the surface expose cations from the aluminium layer below. Support for such a mechanism comes from Liu and Truitt (1997) who found surface hydroxyls adjacent to Lewis acid sites (Al^{3+} ions) and from Ealet *et al*. (1994) who found the surface to have differing stoichiometry to the bulk, suggesting exposure of Al ions at the surface. Tsyganenko *et al*. (1990) illustrated that hydroxyl groups can also form directly from the decomposition of boehmite.

Peri and Hannan (1960) found hydroxyl groups on the surface of γ-Al_2O_3 after all water was removed and found that these groups are removed by further heating or deuterium exchange. Several studies have since shown hydroxyl groups to be on the internal and external surfaces (Peri 1965b; Peri 1965a; Knözinger and Ratnasamy 1978; Soled 1983; McHale *et al.* 1997).

Soled (1983) hypothesized that hydroxyl ions are a necessary component of the γ-Al_2O_3 (and η-Al_2O_3) structures. His representation involved the substitution of O^{2-} ions in the structure with twice as many OH^- ions at the surface, but not in the bulk, and demonstrated how varying amounts of hydroxyl ions account for variations in physical properties such as pore and particle size, surface area, and density during the dehydration process. The resulting representative stoichiometry for γ-Al_2O_3 becomes $Al_{2½}□_{½}O_{3½}(OH)_{½}$. A considerable amount of amorphous content, most likely in the form of water, is implied by the Soled model.

Ushakov and Moroz (1984) found that XRD patterns could only be modelled if residual OH^- ions were substituted in place of O^{2-} ions within the bulk anion lattice of the spinel structure. However, it should be noted that hydrogen cannot be distinctly seen by X-rays. It is well known that hydrogen is better seen in bulk structures by neutrons, most suitably after deuterium exchange. Tsyganenko *et al*. (1990), investigated the presence of hydrogen in the bulk of γ-Al_2O_3 by exchanging D_2O with surface hydroxyls to eliminate their signal. Peaks were found in IR spectra of O-H vibrations, at ~ 3500 and 3300 cm^{-1}, originating from the bulk. These were attributed to protons trapped in octahedral and tetrahedral vacancies within the anion

lattice, respectively. This work is supported by the results of Saniger (1995) who, assuming a hydrogen spinel structure, assigned an absorption band from the bulk IR signal to a hydrogen translation. Wang *et al*. (1999) also supported the concept of OH^- groups in the bulk and they found more cation defects than could be explained with a simple defect spinel using XRD and NMR. Furthermore, protons were found to move to the surface with heating where they combine with OH^- ions to form water (Tsyganenko *et al.* 1990; Wang *et al.* 1999).

Consideration of a protospinel structure can result in an idealised spinel structure, with no vacancies, represented by HAl_5O_8, or $Al_2O_3.0.2H_2O$. This is the same composition that was established for tohdite (Yamaguchi *et al.* 1964). Sohlberg *et al*. (1999b), following from hitherto work favouring protospinels, proposed alternative notation to γ-$Al_2O_3.nH_2O$. This alternative notation is $H_{3m}Al_{2-m}O_3$, where $m = 2n/(n+3)$, which allows for a valid representation of the hydrogen content as opposed to the crystalline hydrate representation. It also accounts for the valency requirements of the dehydration mechanism whereby one Al atom enters the structure at the surface for every three protons driven out.

Contrary to the hydrogen spinel based structures reported, Zhou and Snyder (1991) found only small amounts of hydrogen in γ-Al_2O_3, one OH per unit cell. From this they specifically ruled out hydrogen spinel as a structural possibility. This finding is supported by the theoretical calculations of Wolverton and Hass (2001) who found HAl_5O_8 to be thermodynamically unstable with respect to boehmite and decomposition to an anhydrous defect spinel.

It should be noted that Zhou and Snyder (1991) performed their analysis on γ-Al_2O_3 synthesised from well crystalline boehmite. This is in contrast to studies that have concluded in favour of considerable quantities of hydrogen in the structure, such as Peri and Hannan (1960), Peri (1965a), Pearson (1971) and Wang *et al*. (1999) where gelatinous boehmite was the precursor.

Surface Structure

The majority of studies concerning hydrogen in the structure of γ-Al_2O_3 investigated its presence at the surface in the form of hydroxyl species. Several studies have been conducted on the surface structure for over 40 years in order to

elucidate both the nature of the surface structure itself and mechanisms of catalysis. However, the surface of γ-Al_2O_3 is very complicated and there is more controversy concerning the surface structure than the bulk. For example, molecular dynamics calculations have shown that the bulk structure of γ-Al_2O_3 is relatively well organized but the surface has many defects (Álvarez *et al.* 1995; Álvarez *et al.* 1993; Álvarez *et al.* 1992). The nature of the atomic scale catalytic sites is far from conclusively known. Although this study aims to determine the bulk structure of γ-Al_2O_3, the surface occupying atoms and their total area coverage can become significant considering that the average crystallite size tends to be small, as illustrated by Soled (1983).

It is generally supposed that the surfaces of aluminas are terminated at the (100), (110), and (111) crystal planes (Peri 1965c; Tsyganenko and Filimonov 1972; Tsyganenko and Filimonov 1973; Knözinger and Ratnasamy 1978; Morterra *et al.* 1979; Morterra and Magnacca 1996; Tsyganenko and Mardilovich 1996; Liu and Truitt 1997). The (100) and (110) planes are supposed to be the catalytic active planes for γ-Al_2O_3 (Knözinger and Ratnasamy 1978). This hypothesis was largely supported by the TEM work of Nortier *et al*. (1990). Surface models consider the bonding interaction of OH^- groups after cleavage of the bulk structure and hydration of the exposed surface. Upon cleavage two types of coordinatively unsaturated Al^{3+} ions are expected to appear at the surface following the crystal splitting, producing Lewis acid sites: Al from octahedral symmetry positions with a coordination number of five and Al from tetrahedral symmetry positions with a coordination number of three (Lippens and Steggerda 1970). The occurrence of penta and tri-coordinated Al^{3+} ions have been supported by several adsorption (Morterra *et al.* 1979; Morterra and Magnacca 1996), NMR (Majors and Ellis 1987; Huggins and Ellis 1992) and theoretical studies (Fleisher *et al.* 1991; Linblad and Pakkanen 1993; Tachikawa and Tsuchida 1995; Neyman *et al.* 1996). The OH^- groups result from the ionization of the hydrating water molecules. The OH^- groups occupy the positions where oxygens would be if the crystal planes were still part of an infinite lattice. It is also considered that the crystal remains unchanged right up to the surface (Tsyganenko and Filimonov 1972; Tsyganenko and Filimonov 1973). As the OH^- groups are driven off, the surface coordinatively unsaturated Al^{3+} and O^{2-} ions appear that play the role

of Lewis acids and bases, respectively (Lavalley and Benaissa 1984; Busca *et al.* 1991; Busca *et al.* 1993; Tsyganenko and Mardilovich 1996).

The γ-Al_2O_3 surface is known to have many possible types of OH^- group bonding, the number of which is dependent on the coordinated Al ions that appear at the surface (Morterra *et al.* 1976; Morterra *et al.* 1978; Zecchina *et al.* 1985; Liu and Truitt 1997) and the degree of dehydroxylation (Knözinger and Ratnasamy 1978; Tsyganenko and Mardilovich 1996). The nature of these OH^- groups is traditionally examined by IR spectroscopy, from which at least five absorption bands between 3700 and 3800 cm^{-1} are usually observed for OH^- groups on γ-Al_2O_3 (Peri and Hannan 1960; Peri 1965c; Knözinger and Ratnasamy 1978). The vibrational spectrum for OH^- groups is typical among several of the transition aluminas and is more complicated than that of any other known metal oxide (Morterra and Magnacca 1996). Adsorption and desorption of species such as CO, NH_3, pyridine and D_2O have been used to investigate the interaction of OH^- with the surface (Peri and Hannan 1960; Peri 1965b; Knözinger and Ratnasamy 1978; Morterra *et al.* 1979). Knözinger and Ratnasamy (1978) developed a surface model that was, until recently, the most complete approach to understanding the complex interactions of OH^- groups with the surface. This approach was consistent with the assignment system for OH^- groups introduced by Tsyganenko and Filimonov (1972; 1973), however, it only partly agrees with the description of Zecchina *et al*. (1985).

The Knözinger and Ratnasamy (1978) model of the (100), (110), and (111) crystal planes, describes five possible OH^- configurations, neglecting the orientation of the OH^- with respect to the cation(s) and hydrogen bonding, which virtually agree with the number of O-H frequencies actually observed. The model does not consider reconstruction effects, the presence of cation vacancies at the surface or in the bulk, and only takes into account the regular surface termination, i.e. the coordinatively unsaturated octahedral and tetrahedral Al^{3+} ions with coordination numbers five and three respectively (Morterra and Magnacca 1996; Tsyganenko and Mardilovich 1996). Since then, more possible configurations of OH^- groups and Lewis acids have been suggested (Morterra and Magnacca 1996; Tsyganenko and Mardilovich 1996; Liu and Truitt 1997). Morterra and Magnacca (1996) and Tsyganenko and Mardilovich (1996) considered the affect of cation vacancies and surface dehydroxylation. Morterra and Magnacca (1996) also considered the effect of

defective crystal orientations. Liu and Truitt (1997) incorporated a possible four-coordinated Al^{3+} Lewis acid site after the suggestion of its existence in NMR studies (Coster *et al.* 1994; Kao and Grey 1997). Lewis acid strength was determined to be related to the coordination of the Al^{3+} ion the hydroxyl group was binding to (Liu and Truitt 1997). Several previous experimental (Zecchina *et al.* 1987) and theoretical (Kawakami and Yoshida 1986; Hirva and Pakkanen 1992; Linblad and Pakkanen 1993; Neyman *et al.* 1996; Fleisher *et al.* 1991; Tachikawa and Tsuchida 1995) studies have shown that the Lewis acid strength of three-coordinated surface atoms is stronger than that of five-coordinated surface atoms. However, Coster (1994) did not observe three-coordinated Al at the surface and Solhberg *et al*. (1999a) theoretically determined this observation to result from the three-coordinated Al dropping from the surface into an octahedral vacancy in the layer below. Maresca *et al*. (2000) considered all three of these coordinated Al^{3+} ions in their theoretical study of the γ-Al_2O_3 surface. Also, another theoretical study determined the existence of four, six, and seven-coordinated Al at the surface (Álvarez *et al.* 1995). These outcomes indicate that the suggested occupancy of the 32*e* site position by Zhou and Snyder (1991) cannot account for the immense complexities of the γ-Al_2O_3 surface.

A detailed analysis of the surface structure and the nature of its interactions with hydroxyl groups is beyond the scope of study. Reviews of these types of interactions with existing surface models are presented by Morterra and Magnacca (1996), Tsyganenko and Mardilovich (1996) and Liu and Truitt (1997).

2.2.5 Computational Investigations into γ-Alumina

Research involving some form of theoretical calculation has been referred to throughout all previous sections. Computer simulations can, potentially, elucidate issues that continue to be controversial after an extensive history of experimental examination. The unit cell of γ-Al_2O_3 does not have an integer number of aluminium ions, therefore multiple cells are required to simulate the bulk structure with the correct stoichiometry. As computing power has increased, different approaches to simulating the unit cell have been adopted. Interatomic pair potentials are not as computationally expensive as quantum mechanics-based methods and allow for simulation of larger systems. Pair potentials have been used in early molecular dynamics simulations of supercells, with Al_2O_3 stoichiometry maintained, containing

1440 (Álvarez *et al.* 1992), 3600 (Blonski and Garofalini 1993), and 11520 (Álvarez *et al.* 1995) atoms to examine the bulk structure. More recently, interatomic potentials were used to perform a series of single-point calculations and optimisations of several structural models by Streitz and Mintmire (1999) and 750000 by Watson and Willock (2001). Both utilised supercells three times the size of the unit cell, $Al_{64}O_{96}$, to maintain the correct stoichiometry. The earliest use of quantum mechanics-based techniques involved *ab initio* plane-wave DFT calculations on a 20 atom orthorhombic cell of the asymmetric unit, using the local density approximation (LDA) and norm-conserving pseudopotentials, followed by Monte Carlo simulations on a 1440 atom supercell using a simple potential model (Lee *et al.* 1997). Mo *et al*. (1997) examined a series of non-stoichiometic $Al_{21}O_{32}$ cells to approximate Al_2O_3, using interatomic pair potentials and more computationally expensive *ab initio* DFT, based on the LDA. Sohlberg *et al*. (1999b) used *ab initio* DFT within the generalized gradient approximation (GGA) in order to study 14 atom primitive cells with hydrogen incorporated (HAl_5O_8). More recent DFT calculations have been performed by others on 40 atom supercells containing eight Al_2O_3 formula units (Wolverton and Hass 2001; Gutiérrez *et al.* 2002). To the author's knowledge, all hitherto computational studies on γ-Al_2O_3 have assumed that the structure is a cubic spinel (Rooksby 1951; Sickafus *et al.* 1999).

The results of these theoretical studies are as diverse as experimental research. For example, the molecular dynamics studies by Álvarez *et al*. (1992; 1995; 1993) showed that the bulk structure of γ-Al_2O_3 is relatively well organized and anhydrous but the surface has many defects. They also observed oxygen to have varied coordinations (Álvarez *et al.* 1992) and found penta (Álvarez *et al.* 1992) and heptacoordinated (Álvarez *et al.* 1995) Al to occur in addition to octahedral and tetrahedral coordination. Lee *et al*. (1997) observed only octahedrally and tetrahedrally coordinated Al. Sohlberg *et al*. (1999b) determined that hydrogen is present in varying amounts within the bulk structure. However, Wolverton and Hass (2001) found hydrogen spinel to be energetically unfavourable and therefore supported an anhydrous bulk structure. Several studies observed preferential location of cation vacancies on octahedral sites (Álvarez *et al.* 1992; Mo *et al.* 1997; Streitz and Mintmire 1999; Wolverton and Hass 2001; Gutiérrez *et al.* 2002), but one determined vacancies to reside on tetrahedral sites (Blonski and Garofalini 1993).

Watson and Willock (2001) observed structures that demonstrated a departure from cubic symmetry reflected in a small tetragonal distortion. These distortions were found to be symmetrically equivalent in the *a* and *b* directions and averaged out to give the initial cubic symmetry. Table 2.1 provides a summary list of computer simulation studies performed on the bulk structure of γ-Al_2O_3.

Table 2.1. Examples of computational studies that have been performed on the bulk structure of γ-Al_2O_3. (DFT = density functional theory, FLAPW = full-potential linearized plane-wave, GGA = generalised gradient approximation, LDA = local density approximation, OLCAO = orthogonalized linear combinations of atomic orbitals, NMR = nuclear magnetic resonance).

Author(s)	*Year*	*Calculation types*	*Outcomes*
Álvarez *et al*.	1992	Molecular dynamics using interatomic pair potentials	Found varying coordination's of O. Determined vacancies to reside in octahedral sites Found Al to also be pentahedrally coordinated
Blonski and Garofalini	1993	Molecular dynamics using interatomic pair potentials	Determined vacancies to reside on tetrahedral sites
Álvarez *et al*.	1995	Molecular dynamics using interatomic pair potentials	Found bulk structure to be more ordered than surface Also determined presence of heptacoordinated Al
Lee *et al*.	1997	*Ab initio* plane-wave DFT using LDA and pseudopotentials, followed by Monte Carlo simulation	Determined Al to be 70 ± 1% in octahedral positions, in excellent agreement with NMR spectra
Mo *et al*.	1997	Interatomic pair potentials and *Ab initio* DFT using OLCAO and LDA	Cation vacancies preferentially located in octahedral sites Density of states in good agreement with experiment
Sohlberg *et al*.	1999	*Ab initio* plane-wave DFT using GGA and pseudopotentials	Determined H to exist in varying amounts within the bulk and described according to the formula $H_{3m}Al_{2-m}O_3$, where $m = 2n/(n+3)$ and $0 \leq n \leq 0.6$
Streitz and Mintmire	1999	Interatomic pair potentials	Determined vacancies to reside in octahedral sites, but said tetrahedral vacancies possible
Wolverton and Hass	2001	*Ab initio* DFT using FLAPW method with LDA and GGA and pseudopotentials	Determined vacancies to reside in octahedral sites Found hydrogen spinel structure to be energetically unfavourable
Watson and Willock	2001	Interatomic pair potentials	Examined starting structure energies of all possible structures, assuming no octahedral vacancies Used thermodynamic probabilities to investigate relationship between starting energy ordering and lowest optimised energy
Gutiérrez *et al*.	2002	*Ab initio* plane-wave DFT using LDA	Determined vacancies to reside in octahedral sites

The majority of computational calculations, beginning with the Monte Carlo work of Peri (1965c), have been on the surface rather than the bulk structure of γ-Al_2O_3, with particular regard for its Lewis activity and the interactions with reactive species relating to catalytic applications. Some theoretical studies have involved interatomic potential based molecular dynamics simulations, including calculations of the bulk structure (Blonski and Garofalini 1993; Álvarez *et al.* 1995). The more recent studies were based on cluster models of the surface and utilised *ab initio* quantum mechanical methods including molecular orbital (MO) theory (Kawakami and Yoshida 1986; Fleisher *et al.* 1991; Tachikawa and Tsuchida 1995), semi-empirical quantum mechanical calculations (Fleisher *et al.* 1991; Cai and Sohlberg 2003), Hartree-Fock (HF) (Linblad and Pakkanen 1993; Maresca *et al.* 2000) and DFT (De Vito *et al.* 1999; Xia *et al.* 1999; Maresca *et al.* 2000; Digne *et al.* 2002; Maresca *et al.* 2003). Recent DFT studies used a series of infinitely repeating slabs to model the surface (Sohlberg *et al.* 1999a; Sohlberg *et al.* 2001).

Yourdshahyan *et al*. (1997a; 1997b; 1999) have compared the diffraction patterns of their computationally determined κ-Al_2O_3 structural models with experimentally determined patterns, and thereby showed that their simulated structures are close to the real structure. The current work investigates computationally derived γ-Al_2O_3 structures through comparison of both simulated and experimentally determined diffraction patterns (*Chapter 10*). It is the author's belief that this is imperative to ensure the plausibility of theoretical models and, in some cases, is a necessary step before a true comparison of properties can be made. It is also the most direct way to conclusively prove that a simulated structure is consistent with the crystallographic structure.

Chapter 3

Computational Techniques used *Abhinc*: Principles

3.1 Development of Atomic Theory

Developments in atomic theory, centered on the belief that matter is composed of atoms, have formed the basis of much of modern science since the landmark work of Dalton in the nineteenth century. Atomic theory of matter finds its roots in the 5th century BC with the ancient Greek philosophers Leucippus and his pupil Democritus (Brumbaugh 1981; Allen 1991). Democritus described matter as being made of tiny invisible particles, differing in shape and rapidly moving, that are indivisible. From this theory, the name *atom* was given, the ancient Greek word for uncuttable. This theory was largely ignored during the Middle Ages because of the repudiations of the ancient Greek philosophers Plato and Aristotle (Aristotle 350 BC; Allen 1991), whose theories dominated science and philosophy after the end of antiquity. They had rejected it because the motion was considered to be deterministic. However, Epicurus, in the 4th century BC, modified the theory to avoid the determinism. The Roman philosopher and poet, Lucretius, expounded this modified theory in the first century BC in a poem titled "*De Rerum Natura*" ("On the Nature of Things") (Lucretius 50 BC). Many features of modern molecular theory are found in this work. Despite the long dominance of Aristotlean philosophy in science (and religion) a few great scientists, such as Galileo, Bacon, Boyle and Newton, did refer to atomic phenomena to explain the properties of matter, during the interim years. However, none of these scientists provided any detailed or quantitative explanations in terms of atomic theory to account for the physical properties of matter. This breakthrough was accomplished by Dalton in 1803.

Dalton determined that each chemical element was composed of a unique type of atom. He also determined that heterogeneous compounds were made up of molecules, which themselves are composed of atoms in definite proportions. Dalton's work followed that of Lavoisier in the 1780's who began the process of making careful quantitative measurements**,** allowing the compositions of compounds

to be determined with accuracy, which culminated in the establishment of the Law of Constant Composition by Proust in 1799 (Dalton *et al.* 1906; Patterson 1970). Dalton used wooden ball and stick models to represent atoms and molecules connected by bonds. Wollaston, in 1813 considered that regular tetrahedra, octahedra and rhombohedra can be formed by the close packing of spheres of equal radii (Wollaston 1813). Additional work by Avogadro, Faraday and Mandeleev helped to pioneer the understanding of atoms and their classification (Krane 1988).

It was from Newton that the idea of matter interacting through force fields originated (Newton 1687). Following the Newtonian approach, Coulomb had developed his force law to quantify the electrostatic force between charged particles by 1787. However, the direct concept of attractive and repulsive forces between molecules was first formulated by Boscovich in 1783 (Maitland *et al.* 1981). Clairaut, Laplace and Gauss extended this idea, developing the modern view that atoms repel each other at small separations and attract each other at longer ranges (Torrens 1972; Maitland *et al.* 1981; Kaplan 1986). By 1918 the Madelung constant was being used for lattice energy calculations based on experimental models (Madelung 1918). Gauss also pioneered the method for the calculation of lattice energies by the summation of pair-potentials (Kaplan 1986). Interatomic potentials, such as the Lennard-Jones (Lennard-Jones 1937) and Buckingham (Buckingham 1938) potentials, are often incorporated into pair-potential functions for lattice energy calculations of inorganic solids using the Born-Mayer form (Born and Mayer 1932).

While Dalton believed that atoms were indivisible, it was suggested by Boscovich in 1750 that they were divisible. This was not confirmed until the work of Thomson in 1897 (Dahl 1997). It is now known from subsequent researchers such as Bohr, Rutherford and Pauli that atoms are composed of protons, neutrons, and electrons, which are in turn composed of smaller entities. By 1926 Heisenberg developed matrix mechanics which was found to agree with the non-relativistic wave equation, $H\Psi = E\Psi$, proposed by Shrödinger. A relativistic generalization of the wave equation was added by Dirac shortly after. The wave equation forms the mathematical basis of quantum mechanics, providing a description of nuclei and electrons in matter. It therefore determines, in principle, all properties of matter as highlighted by the famous comment by Dirac in 1929 (Pople 1999):

"*The fundamental laws necessary for the mathematical treatment of a large part in physics and the whole of chemistry are thus completely known, and the difficultly lies only in the fact that application of these laws leads to equations that are too complex to be solved.*"

As in indicated by Dirac, the computational expense of solving the Shrödinger equation for systems that contain only a few atoms has been the limiting factor in the use of *ab intio* methods. *Ab initio* methods are those in which first principles, *i.e.* quantum mechanics, are used; it literally means that you start from scratch and endeavor to determine a true answer. These have only been employed with the development of approximations to quantum descriptions and as computer power increases. In some cases classical approximations were incorporated in quantum calculations such as the use of the Coulomb potential in the Bohr model. As a result classical approaches to calculating the energetics and properties of physical systems have remained in use.

3.2 Computer Simulation of Atomic Structures

Over the past few decades, computer simulation of atomic structures has become increasingly important in interpreting experimental data and in producing structural models. These techniques can be used for structure prediction and the determination of reaction mechanisms and energetics, reducing the reliance on experiments, and hence costs. In particular, computer simulation can help elucidate structures where experimental techniques fail to provide a clear answer. γ-Alumina is an ideal candidate for such a study. Here, the simulation involves determining stable structural configurations which are then compared with experiment. Such an assessment can be made by generating diffraction patterns from the stable structures and comparing them with those obtained experimentally.

The process of obtaining stable structural configurations begins with defining starting structural configurations which closely correspond to what is experimentally observed. This is followed by total energy minimisation of the system with respect to structural variables, which include cell dimensions and atomic positions (Catlow *et al.* 1996). The minimisation is considered complete once the derivatives of the energy with respect to the structural variables are zero (Catlow *et al.* 1994). The

structure associated with the energy minimum is the structural model. Once the global and local minima, and the atomic positions, are determined then essentially all structural, mechanical, thermal, electrical, optical, magnetic and dynamic properties become predictable (Wimmer 1996).

The fundamental problem is selecting what method to use for the determination of the total energy of the system with respect to the positions of the atoms. This work involves the use of *ab initio* quantum mechanical techniques, based on DFT, and empirical force field calculations, based on interatomic and Coulombic potentials for short and long-range interactions, respectively. *Ab initio* approaches provide the greatest accuracy but are computationally very expensive. Although modelling techniques based on interatomic potentials cannot yield accurate data with regards to electronic properties of materials, it is expected that they can produce reasonably accurate structural data in a fraction of the time taken by quantum mechanical calculations. *Ab initio* calculations on complex structures like γ-Al_2O_3 can take many weeks or months for a single structural possibility whereas the empirical modelling methods typically only involve a dozen minutes of computation time. This allows for an extensive search of all possible structural candidates to be performed rather than an "educated guess" at a restricted number of structural candidates.

3.3 Empirical Force Field Molecular Mechanics

Molecular mechanics provides a description of the structure and energetics of organic and inorganic materials using the laws of classical physics. The method is a combination of two methods: the Central Force Field (CFF) method whereby molecular vibrations are fitted to a potential function which is a sum of pairwise interactions without reference to covalency, and the Vibrational Force Field (VFF) method where a potential function is fitted to the bond length and bond angle dependent terms (Grant and Richards 1995, p.32). With molecular mechanics, the nuclear motion is considered while the electron distribution associated with each atom is fixed to the ground state, an alternative approach to the Born-Oppenheimer approximation (Born and Mayer 1932). Chemical reactions cannot be investigated because the electrons are not explicitly represented.

The energy between two atoms is calculated by an expression which has four general terms:

$$E_{tot} = E_l + E_\theta + E_\omega + E_{nb}. \quad (3.1)$$

E_l accounts for bond stretching and can be generically represented as a harmonic spring by $E_l = \sum_{ij} k_{ij}(l_j - l_i)^2$, where l is the bond length. E_θ is the bond angle term, described by $E_\theta = \sum_{ij} k_{ij}(\theta_j - \theta_i)^2$, where θ represents the bond angle. The k_{ij} term in these equations is the force constant. E_ω accounts for bond rotation and is represented by $E_\omega = \sum_{ij} V_n(1 + \cos n\omega_i)^2$, where V_n is the rotational height barrier and n the periodicity of the rotation. The final term, E_{nb}, represents the non-bonded, Pauli repulsion, van de Waals and electrostatic interactions.

The first three terms of the total energy function are important for calculations involving molecular species, or where docking of molecules on inorganic, or ionic, surfaces is investigated (Carter *et al.* 2003). For ionic systems, such as γ-Al_2O_3, the first three terms are not significant. Hence the total energy calculation only requires consideration of the non-bonded interactions, which are accounted for by electrostatic (Coulombic) and van der Waals (dispersion) forces. The ions are treated as classical particles bearing an electronic charge corresponding to their oxidation number.

The non-bonded interactions can be determined exactly for a many-body system by a series of terms containing the *n*-body components (Gale 1996):

$$E(1,...,N) = \sum_i E(i) + \sum_{i,j} E(i,j) + \sum_{i,j,k} E(i,j,k) + \sum_{i,j,k,l} E(i,j,k,l) + ... \quad (3.2)$$

For ionic, close packed systems the two-body (second) term is the dominant contribution to the binding energy. The three-body and higher terms can be assumed negligible and ignored, as can the first term, which represents self interaction of individual ions (Bush *et al.* 1994). Considering only the two-body term follows the Born model (Tosi 1964) framework which assumes the potential depends only on the interatomic distance and has no angular dependence (Bush *et al.* 1994; Catlow *et al.* 1994). The model considers the ions to simply be charged closed shell atoms whose electronic properties are not affected by their environment. Analytical functions describing the two-body term most commonly follow the form of the Born-Mayer

potential (Lewis and Catlow 1985). For ions i and j, with charges q_i and q_j this can be written represented by the pair potential:

$$E(i,j) = \varphi_{ij}(r_{ij}) + \frac{1}{4\pi\varepsilon}\frac{q_i q_j}{\boldsymbol{r}_{ij}}, \qquad (3.3)$$

where ε is the dielectric constant *in vacuo*. This equation accounts for short-range interactions (first term), determined using interatomic potentials, and the long-range electrostatic interactions (second term) between two ions separated by the distance r_{ij}. The pair potential equation may be supplemented by three-body and higher order terms when covalency becomes a factor. The total energy of the system is obtained by summing *E(i,j)* for all ions in the system.

3.3.1 Interatomic Potentials

Interatomic potentials typically consist of two terms to account for the short-range interactions. One of these is a repulsive term, of the form $e^{-B\boldsymbol{r}}$, which accommodates for the electron cloud overlap due to finite atom radius, as expected from the Pauli exclusion principle (Rigby *et al.* 1986, p.15). This is the main factor counteracting the electrostatic term and determines the equilibrium lattice parameters for an ionic solid. The second term, of the form $C\boldsymbol{r}^{-n}$, where n is typically six or eight, models the dispersion interactions of the ions and is an attractive term acting at longer range. It represents the effect of perturbations from the electron distribution of one ion on that of a neighbouring ion. When n is six the term simulates a dipole-induced dipole moment. When it is eight a dipole induced quadrupole is simulated. Calculation of the interatomic potentials proceeds until the decay of the terms converge to a negligible value within the desired accuracy (Gale 1997; Gale and Rohl 2003). This is carried out in real space.

The best known interatomic potential function is the Lennard-Jones 12-6 potential (Lennard-Jones 1924a; Lennard-Jones 1924b; Lennard-Jones and Ingham 1925; Lennard-Jones 1937):

$$\varphi_{ij}(r_{ij}) = 4\Phi\left[\frac{\sigma}{\boldsymbol{r}_{ij}^{m}} + \frac{\sigma}{\boldsymbol{r}_{ij}^{n}}\right]. \qquad (3.4)$$

where $m = 12$ and $n = 6$. The collision parameter, σ, and well depth, Φ, are fitted to the function after parameterisation. The short-range energy has the form $A/\boldsymbol{r}^{12}$, in

contrast to the theoretically expected e^{-Br} form. As a result the Lennard-Jones 12-6 potential does not readily provide an accurate representation of the interactions between any known molecule (Rigby *et al.* 1986, p.20).

Another commonly used analytical function describing an interatomic potential, which does follow the theoretically expected form for the short-range term, is the Buckingham potential (Buckingham 1938):

$$\varphi_{ij}(r_{ij}) = A_{ij} e^{-\frac{r_{ij}}{\rho_{ij}}} - \frac{C_{ij}}{r_{ij}^6} \; . \qquad (3.5)$$

A_{ij}, ρ_{ij}, and C_{ij} require fitting by parameterisation for each particular type of material being modelled. The A_{ij} parameter controls the amplitude of the repulsion and is primarily dominated by the ionic radii. ρ_{ij} defines the radial shape of the ion wavefunctions and thus the range of the effective repulsion. The Buckingham potential has one setback, where the energy tends to minus infinity as the distance approaches zero. Therefore a significantly large energy barrier must be present to ensure this region is inaccessible (Gale 1997).

The procedure for parameterisation is typically empirical with the desired parameter being determined through fitting of calculated bulk properties to experimental values, such as lattice constants and elastic moduli. Optimum values for potential parameters are obtained by varying them to yield the smallest possible difference between calculated structural properties and those obtained from an experimental standard. This is traditionally done from least squares fitting, or by trial and error using single point energy calculations of simulated experimental standards (Grant and Richards 1995, p.41-42). When experimental standards are not available, *ab initio* simulations have been used (Maple *et al.* 1989). A relaxed fitting parameterisation technique can also be used where a full optimization of the structure is performed with a subsequent property calculation for each point during fitting (Gale 1997).

Polarization

A successful description of ionic crystals requires a portrayal of polarization of the ions in the electric field. This is commonly achieved by extension of the two-body terms of the Lennard-Jones or Buckingham potentials to incorporate the

dipolar shell model of Dick and Overhauser (1958). In the dipolar model the ionic charge is partitioned between the core and a massless shell, representing the electrons, which are coulombically screened from each other. A dipole moment is generated when the intra-atomic force field causes the shell to move relative to the core. The energy term representing the core-shell system employs a harmonic spring, $k_{core\text{-}shell}$, acting between the core and the shell separated by distance, r:

$$E_{core-shell} = \frac{1}{2} k_{core-shell} r^2 . \tag{3.6}$$

The resulting ion polarisabilty, α_i, follows (Bush *et al.* 1994):

$$\alpha_i = \frac{q_{shell}^2}{k_{core-shell} + f_{shell}}, \tag{3.7}$$

where f_{shell} represents the distorting forces caused by surrounding ions.

3.3.2 Electrostatic Interactions

In an ionic lattice the electrostatic energy is usually the dominant term, represented by Coulombs law:

$$E_{(q_i,q_j)} = \frac{1}{4\pi\varepsilon} \frac{q_i q_j}{\boldsymbol{r}_{ij}} . \tag{3.8}$$

The Ewald summation (Ewald 1921; Tosi 1964) most efficiently evaluates the electrostatic potential for systems of moderate size (less than 10000 ions) (Gale 1997). For larger systems, approaches such as the fast multipole (Peterson *et al.* 1994) and particle mesh (Essmann *et al.* 1995) methods are more time-efficient, with $N.\log N$ scaling as opposed to the $N^{3/2}$ scaling (Perram *et al.* 1988) for the Ewald summation. However, most system sizes, including γ-Al_2O_3, are well below this size, leaving the Ewald summation the most efficient for electrostatic evaluations. In the Ewald summation, the inverse distance is converted to its Laplace transform and then split into two rapidly convergent series. One of these series is in real space and the other in reciprocal space, with their respective energy expressions as follows (Gale 1997):

$$E_{real} = \frac{1}{2} \sum_{i,j} \frac{q_i q_j erfc(\eta^{\frac{1}{2}} \boldsymbol{r}_{ij})}{4\pi\varepsilon \boldsymbol{r}_{ij}}, \tag{3.9}$$

$$E_{recip} = \frac{1}{2}\frac{4\pi}{V}\sum_{G}\frac{e^{-\frac{G^2}{4\eta}}}{G^2}\sum_{i,j}\frac{q_i q_j e^{-iG.r_{ij}}}{4\pi\varepsilon}. \qquad (3.10)$$

In these equations G is a reciprocal lattice vector and *erfc* is the complementary error function, V is the unit cell volume, and η is the control parameter which distributes the summation between real and reciprocal space. Selection of the optimum η value can be facilitated by weighting the relative computational expense of operations involved to minimize amount of terms evaluated in real and inverse space (Jackson and Catlow 1988; Gale 1997).

3.3.3 Energy Minimization

The description above describes the total internal energy of a system, termed the potential energy. For models constructed to represent the coordinates of a system, the energy obtained from empirical force fields is likely to be high and not at a minimum. The energy must therefore be minimized so that the representative forces, strain and pressure acting on the calculated system are zero, resulting in an optimised structure. This is achieved by gradual adjustments of the system's coordinates using numerical methods to generate modified configurations with lower energies until a minimum is found. Energy minimisation is usually a prerequisite for most other types of calculations used to determine the properties of materials (Gale and Rohl 2003). The minimum is identified when the first derivative of the energy is zero and the second derivative is greater than zero.

The way in which energy varies with the coordinates of a system is termed the potential energy surface or hypersurface. In a three-dimensional ionic system of N atoms, where there are $3N$ Cartesian coordinates, the task of finding the minimum energy is complicated by the presence of many local stationary points on the potential energy surface, which by definition have zero gradients. These stationary points can be local minima (energy troughs), maxima or saddle points which are higher in energy than the lowest energy state, or global minimum (Grant and Richards 1995, p.38; Gale and Rohl 2003). The energy surface, containing multiple stationary points, can be visualized as a roller coaster or a series of hills and valleys. Energy minimisation requires a search procedure that traces the energy surface morphology down hill to find minima. Global minima can be sought out specifically

using genetic algorithms (Holland 1975; Bush *et al.* 1995) and simulated annealing (van Laarhoven and Aarts 1987). However, global minima have most commonly been sought out using iterative techniques, which also yield local minima, and can provide information about transition states (Gale and Rohl 2003). Iterative procedures are being utilized here and will be the focus of the following discussion.

Derivative Methods

Because the functions used in force field calculations are continuous they are differentiable. The most common minimisation algorithm based on derivatives is the Newton-Raphson method (Press *et al.* 1992, pp.355-360), which requires first and second derivative information of the energy surface. For a one-dimensional case, at any given point, x, which is δx from the minimum, the energy can be expanded as a Taylor series:

$$E(x+\delta x) = E(x) + f'(x)\delta x + \frac{1}{2!} f''(x)(\delta x)^2 + ... \qquad (3.11)$$

The first derivative can be similarly expanded:

$$f'(x+\delta x) = f'(x) + f''(x)\delta x + \frac{1}{2!} f'''(x)(\delta x)^2 + ... = 0\,. \qquad (3.12)$$

These can be truncated after the second order terms to give:

$$f'(x) + f''(x)\delta x = 0\,, \qquad (3.13)$$

and can be rearranged to give

$$\delta x = -\frac{f'(x)}{f''(x)}\,. \qquad (3.13)$$

Truncating the Taylor series means the minimum is assumed to be quadratic in nature (Grant and Richards 1995, p.39). This approximation becomes more accurate as the energy moves closer to the minimum. The inaccuracy of the approximation when starting in a region far from the minimum means it cannot be reached in one step. The calculation must therefore be carried out iteratively, until the energy converges to the minimum.

When considering three-dimensions, the first derivative is written as a $3N\times1$ matrix, containing the derivatives of the internal energy with respect to a change in coordinate, $\delta E/\delta x_i$, and is called the gradient vector, $\boldsymbol{g}$, or the force gradient. The

second derivative is known as the Hessian matrix, *H*. Equation 3.13 can now be rewritten as

$$\Delta \boldsymbol{x} = -H^{-1}\boldsymbol{g}, \qquad (3.14)$$

where Δx is the translation vector from the current position to the minimum. The Hessian may be diagonalised to obtain eigenvalues and eigenvectors which are updated with each iteration to map to a different set of geometric variables that relate to combinations of atomic coordinates. It follows, from the quadratic approximation to the Taylor series, that Equation 3.14 is also approximate; it is only exact for a harmonic surface (Gale and Rohl 2003). As a result, the use of Equation 3.14 in the iterative procedure can result in convergence to a maximum on the energy surface, a transition state being obtained instead of a stable ground state. This typically occurs when a maximum is close to a minimum, but can be overcome by ensuring that the Hessian is positive definite; all eigenvalues being positive. Achieving a positive definite Hessian can be facilitated by including a scalar, α, determined by performing a line search to find a minimum in the search direction before proceeding with the next iteration (Gale and Rohl 2003), as per conjugate gradients (Press *et al.* 1992, pp.77-82):

$$\Delta \boldsymbol{x} = -\alpha H^{-1}\boldsymbol{g}. \qquad (3.15)$$

As the system size increases from *N* to *N*+1 atoms the corresponding increase in Hessian matrix elements $(N+1)^2/N$. The calculation of the inverse Hessian slows down as a result, leading to approximations to the Hessian, such as ignoring off-diagonal elements (Leach 2001, p.268). Another approach is not to update the Hessian at every step. Instead, updating formulae that use the change in gradient and variables between cycles to modify the inverse Hessian such that it approaches the exact matrix (Gale and Rohl 2003). One of the most widely used means of updating the inverse Hessian in such a way is the Broyden-Fletcher-Goldfarb-Shanno (BFGS) algorithm (Shanno 1970):

$$H_{i+1}^{BFGS} = H_i^{BFGS} + \frac{\Delta \boldsymbol{x} \otimes \Delta \boldsymbol{x}}{\Delta \boldsymbol{x}.\Delta \boldsymbol{g}} - \frac{(H_i^{BFGS}.\Delta \boldsymbol{g}) \otimes (H_i^{BFGS}.\Delta \boldsymbol{g})}{\Delta \boldsymbol{g}.H_i^{BFGS}.\Delta \boldsymbol{g}} + [\Delta \boldsymbol{g}.H_i^{BFGS}.\Delta \boldsymbol{g}]\boldsymbol{v} \otimes \boldsymbol{v}\,, \qquad (3.16)$$

where $\otimes$ means that a matrix is to be formed between the two vectors either side of the symbol, and

$$v = \frac{\Delta \boldsymbol{x}}{\Delta \boldsymbol{x}.\Delta \boldsymbol{g}} - \frac{H_i^{BFGS}.\Delta \boldsymbol{g}}{\Delta \boldsymbol{g}.H_i^{BFGS}\Delta \boldsymbol{g}}. \qquad (3.17)$$

The Hessian can be explicitly recalculated when the angle between the gradient and the search vectors becomes too large or when the energy drops by more than is allowable in one step (Gale 1997). Once the gradient has dropped below the desired threshold the exact threshold is calculated.

When searching for a minimum energy it is imperative to check that one has in fact been reached. The above approaches are usually satisfactory except where the Hessian has soft modes; eigenvalues that have low or negative values (Gale 1997). Rational Function Optimisation (RFO), or eigenvector following (Banerjee *et al.* 1985), is a method which attempts to remove imaginary modes (negative eigenvalues) from the Hessian, forcing it to be positive definite, hence guaranteeing that a real minimum is obtained, provided a final **Γ**-point[1] phonon calculation is also used for validation (Gale and Rohl 2003). It is therefore useful to introduce RFO when the minimum is close, *i.e.* when the gradients fall below a designated tolerance as the harmonic region is approached. In RFO, a Taylor expansion is used to define the energy as in the case of the standard Newton-Raphson approach, however it is in the form of a rational function. The inverse Hessian matrix is diagonalised at each step to obtain eigenvalues and eigenvectors. If imaginary eigenvalues are present, the spectrum is level-shifted to correct this (Gale and Rohl 2003). As this procedure is repeated the optimization moves up or down hill until the minimum is located. Because it can handle soft modes, RFO can lead to faster convergence than other minimisers, but it is computationally more expensive (Gale 1997). In principle the RFO method can also locate possible transition states. In this case, the eigenvalues are examined to confirm the correct numbers of imaginary points are present in the matrix, corresponding to the stationary point being sought.

When the energy is a considerable distance from the minimum, faster methods, which depend solely on first derivatives of the energy, can be employed. An example of such a method is the steepest descents method (Leach 2001, p.262). Here, the minimisation follows the direction of the force, which is defined by the search vector $\boldsymbol{s}_k$:

$$\boldsymbol{s}_k = -\boldsymbol{g}_k / |\boldsymbol{g}_k| . \qquad (3.18)$$

[1] A **Γ**-point calculation samples the cell in the first Brillouin zone.

Each direction in the steepest descents method is orthogonal to the previous direction. The minimum is determined by performing an arbitrary step or a line search in the direction of the force (Leach 2001, p.262-264). The steepest descents method continuously corrects itself as it oscillates along its paths to the minimum. Because there is no information of the local curvature of the energy surface, the minimisation slows down as the gradient decreases (Grant and Richards 1995, p.40). If a step takes the energy through the minimum and back up the energy surface, the method corrects itself by reducing the size of the step and going backwards over the path it has already taken to find the minimum.

Unlike the steepest descents method, the conjugate gradients method (Press *et al.* 1992, pp.77-82) is based on an updating scheme, using information from previous steps to modify the next move. Instead of the gradients and direction at each step being orthogonal, only the gradients are orthogonal, whereas the direction is conjugate. The effect is the prevention of a step retracing paths that have previously been explored. Each step refines the direction to the minimum, eliminating the possible oscillations that can be seen in the steepest descents method (Leach 2001, p.266). The first step is given by $\boldsymbol{s}_k = -\boldsymbol{g}_k$. The new direction from this step, taking into account the previous step, uses an additional search vector, $\boldsymbol{s}_{k-1}$, and a scaling factor, $\gamma_k = \boldsymbol{g}_{i+1} \bullet \boldsymbol{g}_{i+1} / \boldsymbol{g}_i \bullet \boldsymbol{g}_i$:

$$\boldsymbol{s}_k = -\boldsymbol{g}_k + \gamma_k \boldsymbol{s}_{k-1}. \qquad (3.20)$$

A key advantage to using conjugate gradients is that there is no requirement to use the Hessian at all and therefore less array space is used. This makes the conjugate gradients method useful for very large systems when all Hessian based techniques are too computationally expensive.

3.4 Density Functional Theory

3.4.1 Basic Quantum Mechanical Concepts

Because it is impossible to solve the Schrödinger equation for many-body systems, all quantum-based modelling methods provide a means by which the solution to the Schrödinger equation can be approximated. Density functional theory (DFT) is one such method. It is an alternative method to other quantum mechanical

techniques, namely the Hartree-Fock (HF) approximation (Hartree 1928; Slater 1929; Slater 1930b; Fock 1930).

The time-independent form of Schrödinger equation can be written in short-hand as follows:

$$H\Psi = E\Psi. \tag{3.21}$$

This is a second-order partial differential eigenvalue equation where H is short-hand for the Hamiltonian operator which acts on a mathematical 'wavefunction', Ψ, or eigenfunction, that characterizes the motion of particles in the system. E is the energy of the system, the eigenvalue. The Schrödinger equation is solved when a Ψ is determined such that it can be operated upon by the Hamiltonian to return the Ψ multiplied by the energy.

The Hamiltonian operator is comprised of terms which describe the kinetic and potential energy of the system. For a one particle system:

$$H = -\frac{\hbar^2}{2m}\left(\frac{\partial^2}{\partial x^2}+\frac{\partial^2}{\partial y^2}+\frac{\partial^2}{\partial z^2}\right)+U\,. \tag{3.22}$$

The first term of Equation 3.22 describes the kinetic energy operator where m is the mass of the particle and $\hbar$ is Plank's constant divided by 2π. U represents the potential energy operator which involves the use of an appropriate expression for the electrostatic energy. In the case of a many body system, the potential operator involves terms describing the electrostatic interactions between nuclei and electrons, electrons and other electrons, and nuclei and other nuclei. Del-squared, ∇^2, can be used as short-hand representation of second-order partial derivatives of the Cartesian coordinates, and is termed the Laplacian operator:

$$\nabla^2 = \frac{\partial^2}{\partial x^2}+\frac{\partial^2}{\partial y^2}+\frac{\partial^2}{\partial z^2}\,. \tag{3.23}$$

Therefore, for a single particle, the time-independent form of the Schrödinger equation can be written

$$\left\{-\frac{\hbar^2}{2m}\nabla^2+U\right\}\psi(\boldsymbol{r}) = E\psi(\boldsymbol{r})\,, \tag{3.24}$$

where $\boldsymbol{r}$ is the position vector for the particle, $\boldsymbol{r} = x_{\mathbf{i}} + y_{\mathbf{j}} + z_{\mathbf{k}}$.

The Born-Oppenheimer approximation is used to simplify the many body Schrödinger equation (Born and Oppenheimer 1927). Due to the large difference in mass and mobility between the nuclei and electrons, it is assumed the atom cores are

stationary whilst the electrons are mobile. This eliminates the kinetic energy terms for nuclei and reduces the potential energy due to the nucleus-nucleus repulsion to a constant which can simply be added to the electronic energy determined by the Schrödinger equation. Therefore, for a given system the ground state wavefunction is wholly determined by N, the number of electrons, and V_{ext}, the external potential, itself uniquely determined by Z, the nuclear charge and $\boldsymbol{R}$, the interatomic distances (Koch and Holthausen 2000, p.6,8). In an N-electron system there are N wavefunctions, one for each electron. Consequently, the Hamiltonian contains N equations.

Reasonable approximations (trial wavefunctions, ψ_{trial}) to the true ground state wavefunction must be employed in a systematic search for the lowest energy because it is impossible to search through all N-electron wavefunctions physically. This is facilitated by the variational principle which implies the energy determined from a trial wavefunction is an upper bound on the true ground state energy (Pople 1999; Koch and Holthausen 2000, p.7):

$$\left\langle \psi_{trial} \middle| H \middle| \psi_{trial} \right\rangle = E_{trial} \geq E_o \equiv \left\langle \psi_o \middle| H \middle| \psi_o \right\rangle, \tag{3.24}$$

where the subscript o denotes a wavefunction and energy corresponding to the ground state. The brackets in Equation 3.24 denote Dirac notation representing product of the complex conjugate of the wavefunction, ψ^*, by the Hamiltonian, followed by the wavefunction (Dirac 1958).

3.4.2 Components of the Total Energy in DFT

In DFT the total energy can be broken down into kinetic (T) and electrostatic terms, of which the latter is decomposed into ion-election potential energy ($U_{n\text{-}e}$), ion-ion potential energy ($U_{n\text{-}n}$), and electron-electron potential energy ($U_{e\text{-}e}$), which has separate treatment for exchange-correlation (E_{xc}) interactions. Mathematical definitions of these functionals are provided in *section 3.4.3*. All of these terms, except the correlation component from the exchange-correlation term, are incorporated in the HF approximation.

In atomic systems, one electrons motion is strongly coupled to that of another, making calculation of the electrostatic terms within the Schrödinger equation analytically impossible. This was overcome by Hartree (1928) who used the

variational principle to determine the Hamiltonian form that defined a *N*-electron system in terms of *N* wavefunctions. The resulting Schrödinger equation generated a potential that was no longer coupled to the motions of other electrons, known as the Hartree potential. The determination of this potential allows each electron to be treated as a single particle moving in an external field. Mathematically, the product wavefunction of the Hartree potential was symmetric instead of antisymmetric; antisymmetry is required by the Pauli exclusion principle (Koch and Holthausen 2000, p.5-9). An antisymmetric wavefunction ensures that fermions (electrons) of identical energy have opposite spins. This is accommodated by the HF approximation, which incorporates a normalized wavefunction termed a Slater determinant (Slater 1929; Slater 1930b; Pople 1999):

$$\psi = \frac{1}{\sqrt{N!}} \det\{\chi_m(\boldsymbol{r}_1)\alpha_1 \chi_m(\boldsymbol{r}_2)\beta_2 .....\}\,, \qquad (3.24)$$

where $\chi_m(\boldsymbol{r})$ is a general orthonormal molecular orbital and α and β denote up and down spin functions. Hence, the many electron wavefunction is represented as a sum of products (within the determinant) of one electron wavefunctions, termed molecular orbitals. Using an antisymmetrised wavefunction to account for the effects of the Pauli exclusion principle, results in an additional potential to the Hartree potential, the exchange potential (Jenkins 1995). This is physically represented by a region around an electron where the nearby like-spin electrons are repelled, creating a positively charged exchange hole.

Simple electrostatic processes mean that electrons of any kind should be repelled from each other resulting in a second type of hole, termed a Coulomb, or correlation hole. This effect is not directly taken into account with the HF Hamiltonian but is incorporated in DFT. It is currently not possible to analytically determine the exchange-correlation energy but it is approximated in DFT using the local density approximation (LDA) (Kohn and Sham 1965), detailed in *section 3.4.5*. The correlation component is the limiting factor which prevents accurate analytical calculation of the exchange-correlation energy in complex systems. Numerical quantum Monte Carlo simulations have been used for accurate determination of correlation energy for smaller systems (Ceperley and Alder 1980; Fahy *et al.* 1988; Li *et al.* 1991). However, these are currently intractable in total energy calculations for complex systems.

3.4.3 Hohenberg and Kohn Theorem

Treating the motion of each electron independently, as done in traditional *ab initio* quantum wavefunction methods, means that each electron's motion implicitly becomes a parameter requiring solution in the Schrödinger equation. Such techniques, like HF theory, are extremely accurate for small molecular systems but have been found lacking for larger solids. This is not surprising given the non-consideration of correlation effects and that the approximate forms for the wavefunctions are generally not adequate to begin with. According to Kohn (1999), an exponential wall, in terms of the number of parameters required to solve, is encountered for a system size upwards of 10 atoms. Hence implementation of traditional quantum methods for systems with N atoms, requiring a wavefunction dependent on $3N$ coordinates, become prohibitively expensive in terms of computer time and memory.

Density functional theory, formulated through the work of Hohenberg and Kohn (1964) and Kohn and Sham (1965), overcomes the hindrance of the exponential wall. The theory finds its roots in the concepts of Thomas-Fermi theory (Fermi 1927; Thomas 1927; Fermi 1928). By *reductio ad absurdum*, Hohenberg and Kohn (1964) found that "*the external potential, $V_{ext}(\mathbf{r})$, is (to within a constant) a unique functional of the electron density, $\rho(\mathbf{r})$; since, in turn $V_{ext}(\mathbf{r})$ fixes H we see that the full many particle ground state is a unique functional of $\rho(\mathbf{r})$*." This reduces the problem from requiring many wavefunctions, each based on the motion of individual electrons, to one wavefunction based on the electron density, and hence on three spatial variables, $\mathbf{r} = x, y, z$. Thus all properties of all states are formally determined by the ground state electron density. The energy functional describing the total energy of the system can be written (Payne *et al.* 1992)

$$E[\psi_i] = \sum_i \int \psi_i^*(\mathbf{r}) \left(-\frac{\hbar^2}{2m} \right) \nabla^2 \psi_i(\mathbf{r}) d^3\mathbf{r} + \int V_{ion}(\mathbf{r}) \rho(\mathbf{r}) d^3\mathbf{r} + \frac{e^2}{2} \int \frac{\rho(\mathbf{r}) \rho(\mathbf{r}')}{|\mathbf{r} - \mathbf{r}'|} d^3\mathbf{r} d^3\mathbf{r}' + E_{XC}[\rho(\mathbf{r})] + E_{ion}(\mathbf{R}), \tag{3.25}$$

where $\mathbf{r}$ and $\mathbf{r}'$ are electron positions, $\mathbf{R}$ the ion positions, and V_{ion} is the static electron-ion potential. Equation 3.25 can be written more lucidly:

$$E(\rho) = T(\rho) + U_{n\text{-}e}(\rho) + U_{e\text{-}e}(\rho) + E_{xc}(\rho) + U_{n\text{-}n}(\rho). \tag{3.25a}$$

$U_{e\text{-}e}$ is known as the Hartree potential. Hohenberg and Kohn (1964) also determined by the variation principle that the minimum value of the total energy functional is the ground state energy of the system, from which the electronic density is given:

$$\rho(\boldsymbol{r}) = \sum_i |\psi_i(\boldsymbol{r})|^2 \ . \tag{3.26}$$

This is, by construction, the exact many electron density (Freeman and Wimmer 1995).

3.4.4 Self Consistent Kohn Sham Equations

The Hohenberg and Kohn (1964) theorem provides a formally exact functional, with no approximations with respect to the many electron interactions, which only incorporates a one-particle wavefunction. Kohn and Sham (1965) showed that solving the Schrödinger equation for the ground state energy is equivalent to minimising the Hohenberg and Kohn total energy functional (Equation 3.25) with respect to an orthonormal set of single-particle wavefunctions. Therefore, the basic idea in density functional theory is to replace the Schrödinger equation for the interacting electronic system with a set of single-particle equations with the same density as the original system (Burke *et al.* 1995). The form of the Schrödinger equation for the ground state energy, called the Kohn-Sham equations, can be represented as (Kohn 1999)

$$\left[-\frac{\hbar^2}{2m}\nabla^2 + V_{eff}(\boldsymbol{r}) \right] \psi_i(\boldsymbol{r}) = \varepsilon_i \psi_i(\boldsymbol{r}), \tag{3.26}$$

where ε_i is the Kohn-Sham eigenvalue, and the effective field, $V_{eff}(\boldsymbol{r})$ is

$$V_{eff}(\boldsymbol{r}) = V_{ion}(\boldsymbol{r}) + V_H(\boldsymbol{r}) + V_{XC}(\boldsymbol{r}), \tag{3.27}$$

with the electron-ion term, $V_{ion}(\boldsymbol{r})$, given by

$$V_{ion}(\boldsymbol{r}) = -\frac{e}{4\pi\varepsilon} \sum_i \frac{Z_i}{|\boldsymbol{r} - \boldsymbol{R}_i|}, \tag{3.28}$$

where $\boldsymbol{R}_i$ and Z_i are the positions and atomic numbers of the nuclei. The Hartree potential, $V_H(\boldsymbol{r})$, of the electrons is given by

$$V_H(\boldsymbol{r}) = \frac{e^2}{4\pi\varepsilon} \int \frac{\rho(\boldsymbol{r}')}{|\boldsymbol{r} - \boldsymbol{r}'|} \boldsymbol{dr}^3 \ , \tag{3.29}$$

and the exchange-correlation potential, V_{XC}, while analytically undeterminable, is formally represented by

$$V_{XC}(\boldsymbol{r}) = \frac{\delta E_{XC}[\rho(\boldsymbol{r})]}{\delta \rho(\boldsymbol{r})} \ . \tag{3.30}$$

The exchange-correlation energy results from integration of the exchange-correlation potential. The form of this energy functional stems from the *near sightedness* of the Green's functions used to express the density matrices of the interacting and non-interacting system in the Kohn-Sham equations (Kohn 1996). The exchange-correlation energy accounts for unknown contributions to the total energy. This includes the expected self-interaction, exchange and correlation effects, $E_{nl}[\rho]$ and a residual portion of the kinetic energy, $T_c[\rho]$ (Koch and Holthausen 2000, Chapt. 4-6). Kohn and Sham (1965) recognized that because the true kinetic energy cannot be determined accurately by a functional only, the portion which can be calculated accurately was to be explicitly computed within the Kohn-Sham construction. This is the kinetic energy of the non-interaction reference system, T_s, which is lower in energy but has the same energy as the true, interacting kinetic energy. Hence, as a result of the Kohn-Sham construction

$$E_{XC}(\mathbf{r}) = T_c[\rho(\mathbf{r})] + E_{nl}[\rho(\mathbf{r})] \tag{3.31}$$

Various theoretical and computational methods are available to solve the Kohn-Sham equations. An overview of these is provided in Figure 3.1. Only the techniques pertinent to this study will be discussed in the following sections.

The dilemma in solving the Kohn-Sham equations (Equations 3.26 and 3.27) is that the exact solution is required to solve them (Freeman and Wimmer 1995). This is because $V_{eff}(\mathbf{r})$ depends on the charge density, which is constructed from the one particle wavefunctions. Also, variation of the wave function leads to a change in the electron density. To overcome this, the Kohn-Sham equations are solved iteratively by way of the variational principle (Freeman and Wimmer 1995; Koch and Holthausen 2000, Chapt. 4-5). The total energy is varied with respect to each different wave function used, leading to the ground state wave function and its corresponding electron density. Figure 3.2 provides and illustration of the procedure. Energy minimization during each iterative cycle is carried out using derivative methods such as those described in *section 3.3.3*.

It is important that the starting densities, determined from the starting configurations used, be as close to the real density as possible. For a given variational basis set the Hamiltonian and overlap matrix elements can be computed (Freeman and Wimmer 1995). The matrix diagonalisation results in a set of one-particle eigenvalues which are used to determine a new electron density and one-

particle eigenvalues. The new (output) electron density is then used as the input in the next cycle. Self-consistency is achieved when the output density equals the input density. Once this is achieved the total energy, forces on each atom, and other properties can be calculated.

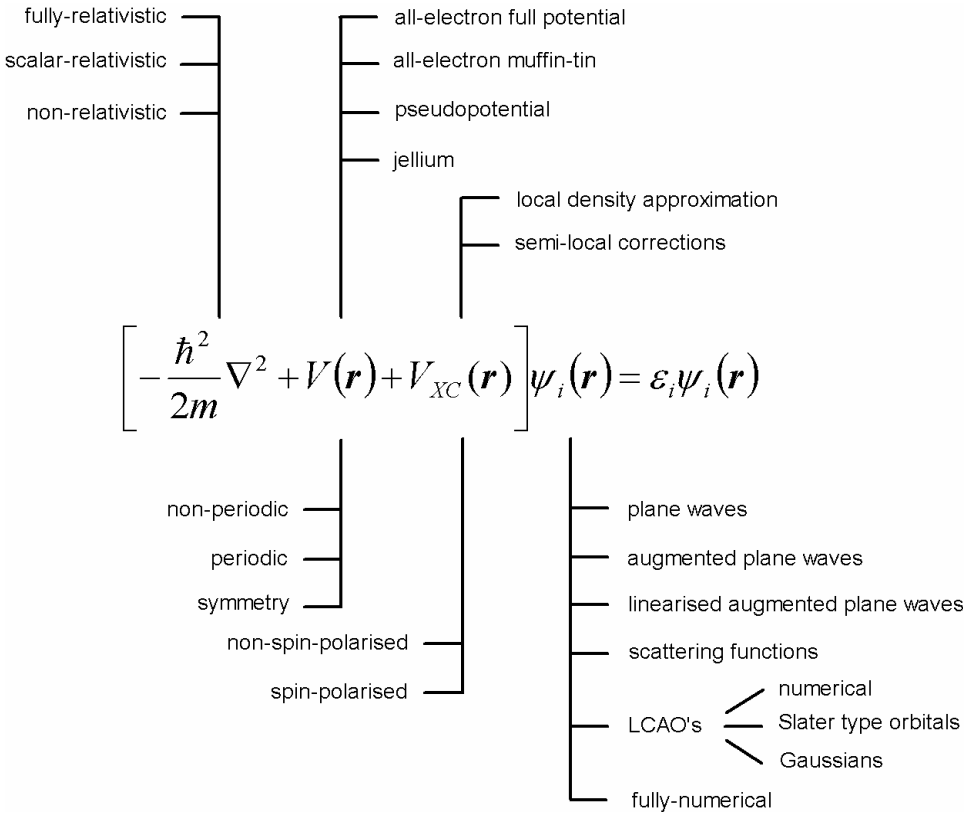

Figure 3.1. Overview of computational techniques available for solving the Kohn-Sham Equations; $V(\boldsymbol{r})$ represents $V_{ion}(\boldsymbol{r})$ and $V_H(\boldsymbol{r})$ (after Freeman and Wimmer 1995).

The diagonalisation procedure consumes most of the computational resources. For a system of N components, diagonalisation requires N^3 calculations during the procedure. This limits the size of systems which optimisations can be performed on to a few hundred atoms. In recent years, diagonalisation procedures have been developed which scale proportionally to system size (see for *e.g.* Ordejon *et al.* 1995; Kohn 1996; Stratmann *et al.* 1996; White *et al.* 1996; Goedecker 1999; Soler *et al.* 2002). These are called order-N methods.

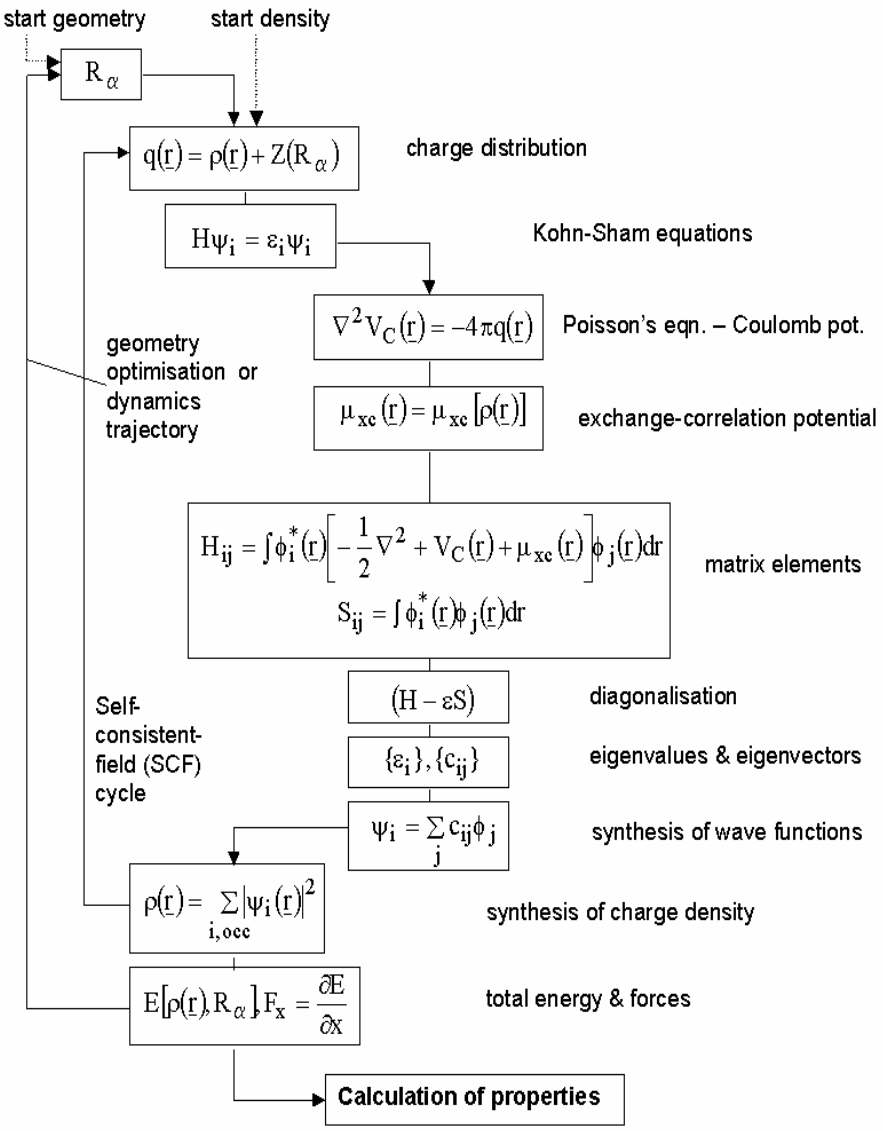

Figure 3.2. Schematic illustration of the self-consistent iterative procedure used to solve electronic structure calculations (after Freeman and Wimmer 1995).

3.4.5 Approximating Exchange and Correlation

The physics behind exchange and correlation, the approximation functionals describing them, and the means with which the approximations are derived, is far from being well understood. However, several approximations to exchange and correlation work surprisingly well. The simplest is the local density approximation (LDA), which was included in the original paper detailing the Kohn-Sham scheme (Kohn and Sham 1965) and finds itself the basis of most other approximations to exchange and correlation which have evolved since.

The LDA is based on the electron density of a homogeneous electron gas; the number of electrons and the volume of the gas are considered infinite so that the electron density ($\rho = N/V$) is constant throughout. It is also assumed that the exchange and correlation effects come predominantly from the immediate vicinity and are not dependent on inhomogeneities of the electron density away from any reference point, $\boldsymbol{r}$ (Wimmer 1996). The analytical expression for the LDA to the exchange-correlation energy is

$$E_{XC}^{LDA}(\rho) \approx \int \rho(\boldsymbol{r}) \varepsilon_{XC}[\rho(\boldsymbol{r})] d\boldsymbol{r}^3 \tag{3.31}$$

where $\varepsilon_{XC}[\rho(\boldsymbol{r})]$ is the exchange-correlation energy per particle of a uniform electron gas of density $\rho(\boldsymbol{r})$ (Koch and Holthausen 2000, p.71). $\varepsilon_{XC}[\rho(\boldsymbol{r})]$ is comprised of exchange, ε_X, and correlation, ε_C, contributions:

$$\varepsilon_{XC}[\rho(\boldsymbol{r})] = \varepsilon_X[\rho(\boldsymbol{r})] + \varepsilon_C[\rho(\boldsymbol{r})]. \tag{3.32}$$

The exchange term used is explicit and has the same form as the exchange approximation in HF theory

$$\varepsilon_X = -\frac{3}{4}\left(\frac{3[\rho(\boldsymbol{r})]}{\pi}\right)^{\frac{1}{3}} \tag{3.33}$$

and is called Slater exchange. There is no explicit expression for determining ε_C. These are usually derived through empirical fitting or derived analytically. The most commonly used representations for ε_C are those by Vosko *et al*. (1980), Perdew and Zunger (1981) and Perdew and Wang (1992).

The LDA also has unrestricted representation whereby the electron density is considered with respect to the electron spin-polarisation (spin-up, $\rho_\uparrow$ and spin-down, $\rho_\downarrow$), such that $\rho(\boldsymbol{r}) = \rho_\uparrow(\boldsymbol{r}) + \rho_\downarrow(\boldsymbol{r})$. Spin-polarisation is used for magnetic materials or dissociation reactions on surfaces involving unpaired electrons or radicals (Freeman and Wimmer 1995). When electron spin polarisation is considered the LDA becomes the local spin density approximation (LSD) and is formally written (Jones and Gunnarsson 1989)

$$E_{XC}^{LDA}(\rho) \approx \int \rho(\boldsymbol{r}) \varepsilon_{XC}[\rho_\uparrow(\boldsymbol{r}), \rho_\downarrow(\boldsymbol{r})] d\boldsymbol{r}^3 . \tag{3.34}$$

The degree of polarisation can be measured by the spin-polarisation parameter, ζ:

$$\zeta = \frac{\rho_\uparrow(\boldsymbol{r}) - \rho_\downarrow(\boldsymbol{r})}{\rho(\boldsymbol{r})} . \tag{3.35}$$

A value of 1 for ζ means full spin polarisation and 0 signifies spin compensation (Koch and Holthausen 2000, p.73). When $\rho_{\uparrow}(r) = \rho_{\downarrow}(r)$ spin-polarisation does not apply as the spin density becomes zero and LSD = LDA.

While the LDA assumes the electron density is constant and the interactions are local, in reality this is not the case. Even so the LDA is very accurate, more so, if not, at least comparable to the HF approximation. This is because the homogeneous electron gas model for exchange-correlation holes satisfies the important relations established for true holes (Koch and Holthausen 2000, p.74). LDA holes are spherically symmetric (Figure 3.3), unlike true holes. However, in a bonding environment the true exchange holes become more isotropic. This means the LDA representation of electron density is a relatively good approximation to the shape of the electron density around bonded atoms. Discrepancies between the LDA and real electron density arises from the true exchange hole being displaced towards the nucleus in a bonding environment while the LDA hole remains centred on the reference electron. Greater accuracy results for systems that have smaller distances between the reference electron and other electrons (Koch and Holthausen 2000, pp.74-75). The LDA typically overestimates binding energies by up to a factor of two (Wimmer 1996). A major reason for this is the exclusion of inhomogeneity (or gradient correction) to the exchange-correlation holes near the electron (Perdew and Kurth 1998).

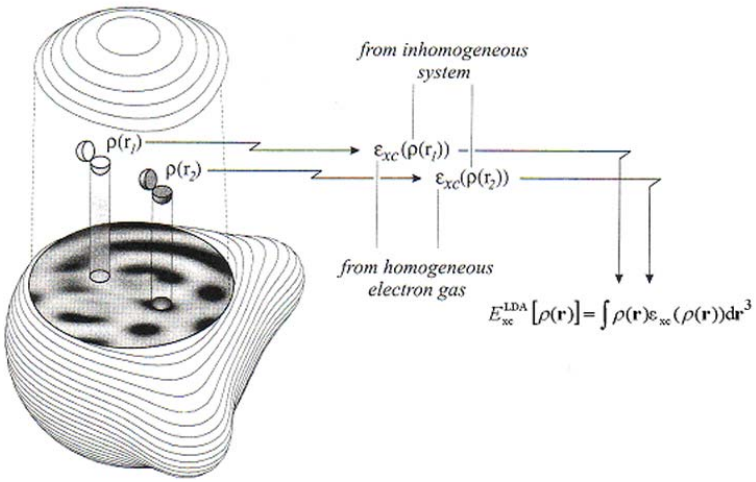

Figure 3.3. Pictorial representation of the local density approximation (Koch and Holthausen 2000, p.73)

Generalized Gradient Approximation

Non-uniform electron density, such as in chemical binary systems, detracts from the accuracy of the LDA. Improvement in accuracy results from including information about the gradient of the charge density, $\nabla\rho(\boldsymbol{r})$, to account for the non-homogeneity of the true electron density (Koch and Holthausen 2000, p.75). Early attempts at this assumed that the LDA was equivalent to the first term of a Taylor series expansion and account for the inhomogeneity by using lower order terms. This form of functional is known as gradient expansion approximation (GEA), but has been found to often perform worse than the LDA (Perdew 1991). The generalised gradient approximation (GGA), introduced by Becke (1986), Perdew (1986) and Perdew and Wang (1986) adopts a gradient expansion to the LDA more successfully. GGA's are generically written

$$E_{XC}^{GGA}(\rho) \approx \int f[\rho(\boldsymbol{r})\nabla\rho(\boldsymbol{r})]d\boldsymbol{r}^3 . \tag{3.36}$$

As with the LDA the functional can be modified to account for spin-polarised cases.

$E_{\mathrm{xc}}^{\mathrm{GGA}}$ is usually split into its exchange and correlation contributions and approximations for the two are separately derived:

$$E_{XC}^{GGA} = E_X^{GGA} + E_C^{GGA} \tag{3.37}$$

The gradient-corrected exchange energy is usually expressed in the general form shown below (Koch and Holthausen 2000, p.76):

$$E_X^{GGA} = E_X^{LDA} - \sum_\sigma \int F(s_\sigma)\rho_\sigma^{4/3} d\boldsymbol{r}^3 \tag{3.38}$$

where the argument F is the reduced density gradient for spin σ. s_σ is the enhancement factor:

$$s_\sigma(\boldsymbol{r}) = \frac{|\nabla\rho_\sigma(\boldsymbol{r})|}{\rho_\sigma^{4/3}(\boldsymbol{r})} . \tag{3.39}$$

The form of the precise functional can vary but there are two main classes for F. The first class involves performing least-squares fitting of functional parameters to exactly known exchange energies of rare gas atoms. This approach was developed by Becke (1986). The second class is the use of a rational function for F (see for *e.g.* Perdew 1986). The functionals tend to be mathematically complex and do not usually improve the understanding of the physics (Koch and Holthausen 2000, p.76). Gradient-corrected correlation functionals are usually more complicated. The

gradient expansion for exchange and correlation functionals is usually empirically parameterised and each customised functional designated an acronym derived from the name of the authors; *e.g.* LYP (Lee, Yang and Par 1988).

While GGA functionals generally offer improved accuracy over the LDA, they tend to underestimate binding energies. Semi-empirical GGA functionals are most successful for calculations on small molecules. However, they may fail for cases when electrons are delocalised in the uniform gas, such as metal oxides. There is also the issue that there can be large differences between various proposed GGA functionals, so the optimum choice of GGA is not always obvious. To account for these failings, Perdew *et al*. (1996) constructed a numerical GGA from first principles, called PBE. This functional involves a second-order density gradient expansion for the exchange-correlation hole surrounding the electron in a system of slowly varying density, then cutting of spurious long-range parts to satisfy the sum rules for the exact hole (Perdew *et al.* 1996). It is also possible to use hybrid functionals constructed using HF theory, the LDA and/or GGA (Chermette 1998).

3.4.6 Basis Sets

A basis set is the set of one-electron wavefunctions, $\psi_i(\boldsymbol{r})$, that describe the motion of the electrons of a system (valence electrons in cases where pseudopotentials are used - *section 3.4.7*). It can be typically expanded as a linear representation using a set of basis functions, χ_u:

$$\psi_i(\boldsymbol{r}) = \sum_u c_{u,i}\chi_u \qquad (3.40)$$

Exact orbital representation requires an infinite set of basis functions, which are summed over an infinite number of expansion coefficients, $c_{u,i}$. In order to make the calculation tractable the summations need to be truncated. There are two general approaches in the construction of basis sets. One is to consider atomic-like basis functions, which are derived from a real-space viewpoint and is the simplest and most natural approach. This is commonly called the linear combination of atomic orbitals (LCAO). The other is to construct a basis set using a momentum space description of the material, namely using plane-waves (PW). Other methods for determining basis functions include augmented plane-waves (APW), linear augmented plane-waves (LAPW), full potential linear augmented plane-waves

(FLAPW), scattering functions and fully numerical calculations (Freeman and Wimmer 1995).

Plane Waves

Plane-waves are an obvious choice for basis sets because Bloch's theorem (Bloch 1929) allows the electronic wavefunctions to be expanded in terms of a discrete set of plane-waves (Payne *et al.* 1992). This allows the plane-wave basis set to be truncated to only include plane-waves with kinetic energy below a chosen cut-off (Payne *et al.* 1992). Bloch's theorem can be written

$$\psi_{i,\mathbf{k}}(\boldsymbol{r}) = f_i(\boldsymbol{r})e^{i\mathbf{k}\cdot\boldsymbol{r}} \tag{3.41}$$

where $f_i(r)$ is the cell-periodic part, $e^{i\mathbf{k}\cdot\boldsymbol{r}}$ describes the wave motion, **k** is a continuous wavevector confined to the first Brillouin zone of the reciprocal lattice and the subscript i indicates a band index. The cell-periodic part is expressed in terms of a plane-wave basis set (Payne *et al.* 1992):

$$f_i(\boldsymbol{r}) = \sum_{\boldsymbol{G}} c_{i,\boldsymbol{G}} e^{(i\boldsymbol{G}\cdot\boldsymbol{r})} \tag{3.42}$$

where $\boldsymbol{G}$ is a wave vector that represents the reciprocal lattice vectors of the crystal, defined by $\boldsymbol{G}\cdot\boldsymbol{l} = 2\pi m$, m is an integer, $\boldsymbol{l}$ is a lattice vector, and $c_{i,G}$ are plane-wave coefficients. The set of one-electron wavefunctions can then be expressed in terms of a linear combination of plane-waves (Payne *et al.* 1992):

$$\psi_{i,\mathbf{k}}(\boldsymbol{r}) = \sum_{\boldsymbol{G}} \mathrm{c}_{i,\mathbf{k}+\boldsymbol{G}} e^{(i(\mathbf{k}+\boldsymbol{G})\cdot\boldsymbol{r})} \,. \tag{3.43}$$

Plane-waves offer a basis set that is independent of the type of crystal and treats all areas of space equally. This is in contrast to some other basis sets which use localised functions, such as Gaussians, that are dependent on the positions of the ions (Rushton 2002). In practice, a discrete set of **k** points are sampled from the Brillouin zone and the selection of **k** points depends on the shape of the system examined (Leach 2001, p.156). This is done because wavefunctions at points close to each other in **k** space can be almost identical and hence represented by a single point. The truncation of plane-wave basis sets can cause discontinuity in the basis states. This can make the description of wavefunctions with large curvature, typically in core regions of atoms, inefficient (Leach 2001, p.156). Such regions require a large

number of plane-waves for accurate description, which is computationally expensive, or may be overcome using pseudopotentials (*section 3.4.7*)

Atomic Orbitals

The two main classes of atomic orbital basis functions are Gaussian-type-orbitals, GTOs (Boys 1950) and Slater-type-orbitals, STOs, (Slater 1930a). STOs are the most natural choice for basis functions because they more accurately mimic exact wavefunctions. GTOs are the most commonly used because they can be readily used in calculations involving multicenter integrals that arise in polyatomic-molecule calculations and hence are less computationally expensive (Simons 1991).

GTOs have the general polar form:

$$\chi_{n,m,l,\alpha}(\boldsymbol{r},\theta) = NY_{l,m}\boldsymbol{r}^{(2n-2-l)}e^{-\alpha r^2} \tag{3.44}$$

where n, l and m are quantum numbers, N is a normalisation constant, $Y_{l,m}$ is a spherical harmonic function and α is an orbital exponent which governs the radial size of the basis function. The angular dependence of the wavefunction is contained within $Y_{l,m}$, where l and m determine the type of orbital (for example $l = 0$ is an s orbital, $l = 1$ is a p-orbital). In Cartesian form, GTOs can be expressed as

$$\chi_{\alpha,l_x,l_y,l_z}(\boldsymbol{x},\boldsymbol{y},\boldsymbol{z}) = N\boldsymbol{x}^{l_x}\boldsymbol{y}^{l_y}\boldsymbol{z}^{l_z}e^{-\alpha r^2} \tag{3.45}$$

where the sum of l_x, l_y and l_z determines the angular shape and direction of the orbital (*e.g.* $l_x + l_y + l_z = 1$ is a p-orbital).

STOs exhibit the correct cusp behaviour as $\boldsymbol{r} \to 0$ and the exponential decay as $\boldsymbol{r} \to \infty$. In comparison, GTOs have zero slope as $\boldsymbol{r} \to 0$ and decay sharply as $\boldsymbol{r} \to \infty$. To achieve the same level of accuracy three times as many GTOs as STOs are required (Koch and Holthausen 2000, p.98). The general form of STOs is

$$\chi_{n,m,l,\xi}(\boldsymbol{r},\theta) = NY_{l,m}\boldsymbol{r}^{n-1}e^{-\xi\boldsymbol{r}}, \tag{3.46}$$

where ξ is an orbital exponent which characterises the size of the basis function (Simons 1991).

The simplest construction for a basis set is to use only one basis function for each orbital of the simulated system. These are called *minimal* basis sets. Using two basis functions to describe each orbital produces a *double-zeta* (double-ζ or DZ)

basis set. Likewise, the use of three basis functions per orbital results in a triple-ζ basis. To reduce computation time a *split-valence* approach can be adopted whereby valence electrons are treated with double- or triple-ζ basis sets while core electrons are considered using minimal basis sets (Koch and Holthausen 2000, p.100). Polarisation functions have a higher angular momentum than occupied atomic orbitals, and ensure that orbitals can distort from their original atomic symmetry and better adapt to the molecular environment (Koch and Holthausen 2000, p.100). When polarisation is combined with a double-ζ basis set, a double-ζ plus polarisation (DZP) basis set is produced.

3.4.7 Pseudopotential Approximation

Simulations that require calculation of all-electronic wavefunctions in a system remain computationally expensive. Coulomb's law dictates that the electron-ion potential will tend to minus infinity at the core, creating a singularity or node (Jenkins 1995). This singularity can affect the convergence of the electron density and total energy. Increasing the basis set size does not necessarily aid in achieving convergence. As atom sizes increase the number of nodes in the wavefunctions increase, causing increased kinetic energy in the core region. This requires an increase in the required cut-off limits (Troullier and Martins 1991).

One way to deal with the interactions of the core regions, comprised of the core electrons and the nucleus, is to use pseudopotentials to represent them. The potential of the core region is replaced with the weaker pseudopotential, which acts on pseudo-wavefunctions (Troullier and Martins 1991). Figure 3.4 provides a schematic illustration whereby the pseudopotential and pseudo-wavefunction replace their all-electron counterparts of the core up to certain cut-off radius, r_c, and mimic the valence region exactly. The pseudo-wavefunctions replace the oscillations of the true wavefunctions within the core region with smoother oscillations. This allows the core of an atom to be described by the pseudopotential, and the valence electrons by basis functions. The pseudopotential approach is justified by the fact that most chemical properties are governed by the valence electrons. The tightly bound core electrons are usually shielded from interactions with other species. The use of pseudopotentials reduce the number of terms required in calculations and hence, the

computational expense (Leach 2001, p.156). The major drawback is that it introduces another approximation to the solution of the Schrödinger equation which can reduce accuracy (Porezag *et al.* 2000).

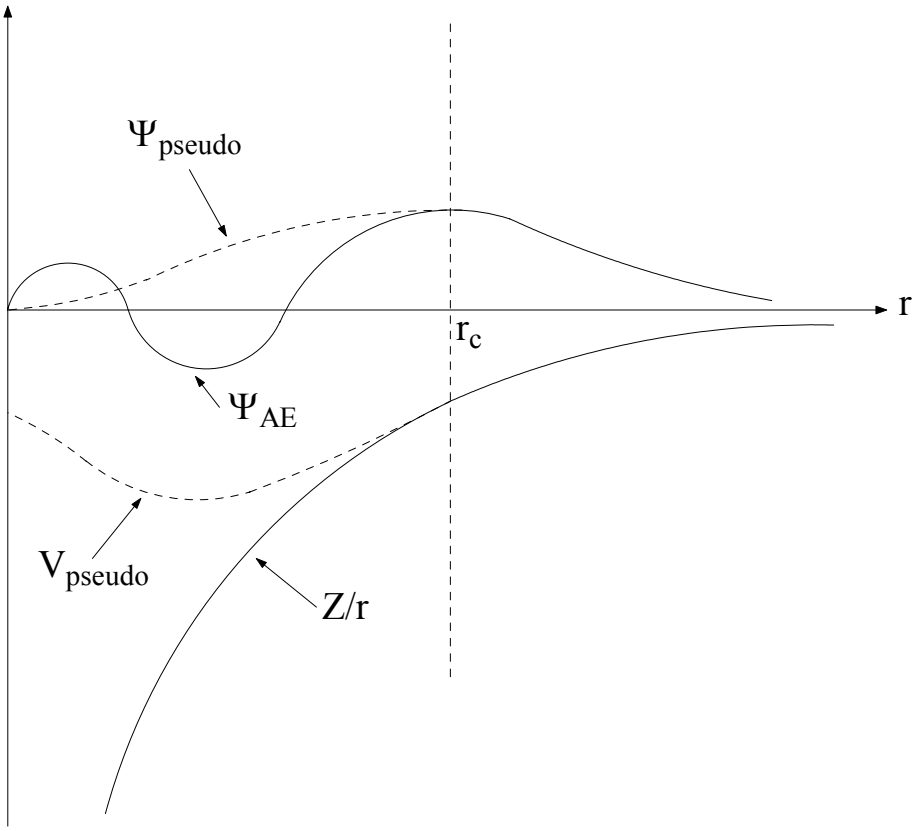

Figure 3.4. Illustration of the pseudo-wavefunction (Ψ_{pseudo}) and potential (V_{pseudo}) and how they compare to the all-electron wavefunction (Ψ_{AE}) and electronic potential ($V_{ext} = Z/r$) plotted against distance, r, from the atomic nucleus; r_c, denotes the radius at which the electron and pseudo-electron values are identical (after Payne 1992).

There is much to consider with pseudopotentials. Detailed discussions can be found in the literature (see for *e.g.* Bachelet *et al.* 1982; Kleinman and Bylander 1982; Troullier and Martins 1991; Furthmuller *et al.* 2000; Porezag *et al.* 2000, and references therein). Only a few key issues will be discussed here. Pseudopotentials are usually derived from all-electron calculations. They are typically constructed to satisfy four general conditions (Troullier and Martins 1991). The first is to ensure that the valence pseudo-wavefunction contains no nodes. This helps to ensure that the pseudo-wavefunction is smooth, with respect to the all-electron wavefunction, and maintains orthogonality between wavefunctions representing the core and valence electrons (Payne *et al.* 1992). Smooth functions aid in achieving rapid

convergence and can be achieved by increasing the cut-off radius at which the pseudopotential is generated, although this can compromise the transferability (Troullier and Martins 1990). Secondly, the normalised pseudo-wavefunction must be equal to the normalised all-electron wavefunction beyond the cut-off radius. Thirdly, the charge of the pseudo-wavefunction must be equal to that of the all-electron wavefunction inside the cut-off radius. If this criterion is met, norm conservation is achieved. Lastly, the eigenvalues of both wavefunctions must be equal.

A pseudopotential that uses the same potential for all the angular momentum components of the wavefunction is called a local pseudopotential (Payne *et al.* 1992). To produce an accurate approximation, it may be necessary to have different valence potentials for the different angular momenta (*e.g. s*, *p*, *d* and *f* orbitals). This produces a non-local pseudopotential (Troullier and Martins 1991). These kinds of pseudopotentials are capable of describing the scattering properties of an ion in a variety of atomic environments and hence are the most transferable (Soler *et al.* 2002).

Chapter 4

Deterministic Methods

4.1 Experimental

4.1.1 Materials and Sample Preparation

Several gibbsite samples of large particle size (> 80 μm) were employed in this research. Deuterated gibbsite was synthesised by dissolving 74.09 g L^{-1} aluminium wire in 3.77 mole L^{-1} NaOD solution in a stainless steel beaker to produce a liquor. The liquor was then placed in a bottle roller and rolled end over end at 10 rpm for one week at 80 °C whilst the gibbsite crystallised. Alcoa C31-grade hydrogenated gibbsite was also employed.

Powdered γ-Al_2O_3 was obtained from several highly-crystalline boehmite precursors. Heating trials were conducted to investigate the most appropriate method to attain the highly-crystalline boehmite precursors (*section 6.1*) and to establishing suitable calcination procedures for systematic study (*section 6.2*).

Hydrogenated boehmite was obtained from the Alumina and Ceramics Laboratory, Malakoff Industries, Arkansas, USA. Deuterated boehmite was prepared by hydrothermal treatment of synthesised deuterated gibbsite with D_2O for 10 days at 158 °C in a Barc bomb (~ 150 kPa pressure). A further deuterated boehmite precursor was prepared by hydrothermal treatment of Alcoa C31 hydrogenated gibbsite with D_2O for 10 days at 158 °C in a Barc bomb. The preparation temperature selected has been found to be the most effective for facilitating deuterium exchange (Gan 1996, p.53). Approximately 10 - 15 g of each boehmite precursor was calcined at temperatures between 400 and 1000 °C, at 50 ± 5° intervals, in air. The heating rate was 5 ° per minute. Each sample was calcined for seven hours at each temperature. In the case of one hydrogenated sample, calcination was undertaken for 13 hours at each temperature. After calcination, the furnace was switched off and each sample allowed to cool to room temperature.

The composition of the gibbsite and boehmite samples was confirmed with XRD. The XRD patterns for all gibbsite and boehmite samples were identical. Energy dispersive spectrometry (EDS) was used to ensure that no contaminants were present.

4.1.2 Particle Size Analysis

Particle size analysis was performed on boehmite and gibbsite precursors using a Malvern Instruments Mastersizer MS2000 instrument at CSIRO Minerals, Waterford, Perth, Australia. Between 1 – 2 g of powder was dispersed in approximately 75 mL of 1000 ppm sodium hexametaphosphate (Calgon) using a Cole-Palmer ultrasonic bath for 15 minutes, producing a slurry. The slurry was then homogenised and placed in a presentation chamber for analysis with the diffraction system of the MS2000 instrument, using a single optical lens with two laser optical sources. This provides two size ranges which the software blends together to give reporting range between 0.02 to 2000 μm. The particle size results are located in *Appendix I*, and the implication of particle size is discussed in *Chapter 6*.

4.1.3 Thermal Analysis

Thermogravimetric analysis (TGA) and differential thermal analysis (DTA) were employed to provide; (i) details on weight loss with temperature due to dehydration of the transition aluminas from the starting material gibbsite, and (ii) to extract endothermic and exothermic details to determine the temperatures at which transitions occur (Pope and Judd 1977). Experiments were performed with a Stanton Red-Croft model STA 780 simultaneous DTA-TGA machine in the School of Applied Chemistry, Curtin University of Technology. Approximately 15 mg of material was placed in an alumina crucible with a height of 3.0 mm and an internal diameter of 3.8 mm. The sample was then heated in air (flow rate of 35 mL min^{-1}) from room temperature to 1300 °C. The heating rate was 20 ° min^{-1}. The DTA-TGA results are presented in *Chapter 6*.

4.1.4 X-ray Diffraction

XRD data were obtained at room temperature for hydrogenated boehmite samples which had been pre-calcined (calcined before data collection) at 50 ± 5 ° intervals between 400 and 1000 °C, for seven hours in air at each temperature. The XRD data were collected with a Siemens D500 Bragg-Brentano instrument, using collimated monochromatic radiation. The specimen, X-ray source, and detector (counter) are all coplanar. The detector was moved about the central axis on a goniometer at a constant angular velocity in terms of the diffraction angle 2θ. Collection conditions are provided in Table 4.1.

XRD was used for phase identification, which had three areas of application in this work. Firstly it was used for the furnace trials (*section 6.1*), performed to establish how pure boehmite could be produced by calcining gibbsite. Secondly, it was utilised to qualitatively examine the dependence of the calcination of boehmite to form γ-Al_2O_3 on particle size and time (*section 6.2.2*). Finally, it was used to examine the structural evolution of calcination products of boehmite with temperature (*Chapter 8*).

Table 4.1. X-ray Diffractometer Specifications.

Parameter	***Settings***
Radiation	Cu K_α radiation (λ = 1.5418 Å)
Acceleration Voltage	40 kV
Filament Current	30 mA
Slits (1/2/3)	1 °/1 °/0.15 °
Goniometer Setting	10 – 70 °
Step Size	0.02 ° - 0.2 °
Counting Time	0.5 – 1 second

4.1.5 Neutron Diffraction

Neutron diffraction data was collected *in-situ* during calcination of deuterated and hydrogenated boehmite samples (*section 4.1.1*) using the medium-resolution powder diffractometer (MRPD) at the High Flux Australian Reactor (HIFAR), operated by the Australian Nuclear Science and Technology Organisation (ANSTO),

Lucas Heights Laboratories, Sydney, Australia. The *in-situ* data was collected at the selected temperatures in hourly intervals, yielding one complete neutron diffraction pattern every hour over the duration of calcination, so that kinetic effects could be investigated. Neutron diffraction data, using MRPD and the high-resolution powder diffractometer (HRPD), were also obtained at room temperature for hydrogenated boehmite samples which had been pre-calcined at 50 ± 5 ° intervals between 400 and 1000 °C, for 7 hours in air at each temperature. Wavelengths of ~ 1.66 Å and ~ 1.49 Å were used for MRPD and HRPD respectively. Data was collected for National Institute of Standards and Technology, USA (NIST) Standard Reference Material 676 (α-Al_2O_3) prior to data collection from γ-Al_2O_3 samples for calibration of wavelength and instrument parameters (see *section 4.1.6*). Results are presented in *Chapters 7* and *8* and *Appendices II* and *III*.

4.1.6 Rietveld Analysis of Neutron Diffraction Data

Rietveld analysis (Rietveld 1969; Young 1993b) of the neutron diffraction data from powdered γ-Al_2O_3 was performed using the LHPM Rietveld code with the Rietica 1.7.7 interface (Hunter 1998). Rietveld analysis is an established method for iterative non-linear least squares refinement that aims to determine the best fit between a calculated diffraction pattern and one which was experimentally obtained (McCusker *et al.* 1999). The analysis involves the input of a structural model from which a calculated diffraction pattern is generated. It is important that the structural model is relatively accurate otherwise convergence is not achieved. The model is modified during refinement until, ideally, the calculated pattern becomes identical to the measured diffraction pattern. The resulting model should then have structural characteristics that are representative of the true structure.

In the refinement procedure, the model is assumed optimum when the sum of the squares of the differences in the two patterns, R, is lowest according to

$$R = \sum_{i=1}^{n} w_i \left(y_i - y_{ic} \right)^2 , \qquad (4.1)$$

where y_i are the measured intensities, y_{ic} are the calculated intensity profiles and w_i is the statistical weighting assigned to each observation, which is typically set as the reciprocal of the variance. The calculated intensity profile is derived by summing the

contribution from the neighbouring reflections and the background, assuming random orientation of the crystallites. More precisely it is determined according to (Young 1993a, p.4)

$$y_{ic} = s\sum L_j \cdot \left|F_j\left(hkl\right)\right|^2 \cdot \varphi\left(2\theta_i - 2\theta_j\right) \cdot P_j A + y_{ib}, \qquad (4.2)$$

where s is the phase scale factor, L_j is the Lorentz-polarisation-multiplicity factor, $|\boldsymbol{F}_j(hkl)|$ is the structure amplitude for the structure factor $\boldsymbol{F}_j(hkl)$, $\varphi(2\theta_i - 2\theta_j)$ is the peak profile function describing the line broadening, P_j is the preferred orientation correction, A is an adsorption factor, and y_{ib} is the pattern background function. The scale factor is essentially an error factor which is used to scale a phase of the calculated pattern to the measured pattern. The structure amplitude determines the amplitude of the wave F_j scattered by the contents of a unit cell.

The Lorentz-polarisation-multiplicity factor is the product of three factors:

$$L_j = Lr_j \cdot p_j \cdot m_j, \qquad (4.3)$$

where Lr_j is the velocity factor, $Lr_j = 1 / (\sin 2\theta \cdot \sin\theta)$, p_j is the polarisation factor, $p_j = ½ (1 + \cos^2 2\theta)$, and m_j is the multiplicity (Kisi 1994). The multiplicity accounts for the number of equivalent reflections contributing to a Bragg peak.

The structure factor is defined as (Kisi 1994):

$$\boldsymbol{F}_j(hkl) = \sum_k f_k \cdot {o_k}^2 \cdot e^{2\pi i(hx_k + ky_k + lz_k)} \cdot T_k \qquad (4.4)$$

where f_k is the scattering factor for atom k, o_k is the site occupancy factor which varies according to site occupancy, (hx_k, ky_k, lz_k) are the positional coordinates for atom k within the unit cell, and T_k is the Debye-Waller factor, $T_k = \exp(-B_k \cdot \sin^2 2\theta / \lambda^2)$, and B_k is the temperature factor.

Several peak profiles can be used depending on various factors such as radiation source, instrument settings, and the specimen itself. In this case the Voigt profile was used because it is the most appropriate function for neutron scattering (Kisi 1994). The function is defined (Hunter and Kisi 2000):

$$V_{jk} = \frac{C_1^{\frac{1}{2}}}{H_{GK}\pi^{\frac{1}{2}}} \mathrm{Re}\left[\omega\left(C_1^{\frac{1}{2}} X_{jk} + iC_2 \frac{H_{LK}}{H_{GK}}\right)\right] \qquad (4.5)$$

where Re denotes the real part, ω is the complex error function, $\omega(z) = \exp(z^2)\mathrm{erfc}(z)$, $C_1 = 2ln2$, $C_2 = (\ln 2)^{½}$, and X_{jk} is the Bragg reflection, $X_{jk} =$

$(2\theta_i - 2\theta_k)/H_k$. H_k is the full-width-at-half-maximum (FWHM) of the kth Bragg reflection given by the function described by Caglioti *et al*. (1958):

$$H_k = U\tan^2\theta + V\tan\theta + W. \tag{4.6}$$

H_k is dependent on 2θ and is determined in accordance with three refinable parameters, U, V & W. H_{Gk} and H_{Lk} in Equation 4.5 represent the FWHM components of H_k contributed from Gaussian and Lorentzian functions, respectively.

Preferred orientation was refined using the March model (March 1932), which can correct for spherical, cylindrical or needle-like particles and agglomerations. It is determined using

$$P_j = \left(r^2 + \cos^2\alpha_j + r^{-1}\sin^2\alpha_j\right)^{-\frac{3}{2}} \tag{4.7}$$

where α is the angle between the *hkl* plane generating the Bragg reflection and the preferred orientation vector, and r is a refinable parameter (Hill 1993).

The pattern background was modelled using a non-shifted type 1 Chebyshev function (Cheby I) (Hunter and Kisi 2000)

$$y_{ib} = \sum_{m=0}^{n} B_m T_m(2\theta), \tag{4.8}$$

where B_m is one of up to 24 refinable parameters (a maximum of six were used for refinements of γ-Al_2O_3) and T_m is the Chebyshev function, defined by

$$2xT_n(x) + T_{n-1}(x) = 0, \tag{4.9}$$

where $T_0 = 1$ and $T_1 = x$.

The quality of the fit of the refined structure models to the data was determined by visual inspection of the difference plot and statistically by figures-of-merit of the estimated standard deviation of individual parameters. The figures-of-merit provided here are the profile factor (R_p), 'goodness-of-fit' (χ^2) and 'Bragg factor' (R_B), defined by Eqns 4.10 to 4.12 (Young and Wiles 1982):

$$R_p = \frac{\sum |y_{io} - y_{ic}|}{\sum y_{io}} \tag{4.10}$$

$$\chi^2 = \frac{\sum w_i (y_{io} - y_{ic})^2}{N - P} \tag{4.11}$$

where w_i is the weight assigned to each observation, y_{io} and y_{ic} are the observed and calculated intensities at the ith step, respectively, N is the number of observations and

P is the number of least-squares parameters refined. The goodness-of-fit represents the square of the ratio of the weighted-profile factor, R_{wp}, over the expected-profile factor, R_{exp}. Although not presented with the data here R_{wp} was also checked to ensure there was minimal difference between R_p and R_{wp}. These parameters provide an indication of the fit between the calculated diffraction pattern and the data.

$$R_B = \frac{\sum |I_{ko} - I_{kc}|}{\sum I_{ko}} \tag{4.12}$$

where I_{ko} and I_{kc} are the observed and calculated intensities for Bragg reflection k, respectively. The Bragg factor represents how well a particular phase in the structural model fits to the data.

Rietveld analysis requires that instrument parameters, in particular the wavelength of the radiation, are accurately known. This was achieved by refinement of calibration data (NIST Standard Reference Material 676). The calibrated wavelength and V and W parameters were then fixed during refinements of the γ-Al_2O_3 structure. Rietveld refinement data, and related results, are presented in *Chapters 7* and *8*, and *Appendices II* and *III*.

4.1.7 Transmission Electron Microscopy and Electron Diffraction

Dispersed samples of boehmite and γ-Al_2O_3 on carbon film were investigated using Jeol 2011 and Philips 430 transmission electron microscopes (TEM) fitted with LaB_6 filaments and operated at 200 kV and 300 kV respectively. Selected area electron diffraction (SAED) patterns were obtained using a 150 cm and 660 cm camera length for the Jeol and Philips microscopes, respectively. The camera length was calibrated by comparison with diffraction patterns from pure silicon for the Joel machine and gold for the Philips instruments. The absence of Kikuchi bands in γ-Al_2O_3 samples, attributable to the disorder in the structure, made it difficult to discern zone axes and difficult to obtain useful information using convergent beam electron diffraction (CBED). TEM images are presented in *sections 8.1 and 9.1*. SAED patterns are presented in *sections 7.2.1 and 8.2*.

4.1.8 Nuclear Magnetic Resonance

^{27}Al MAS-NMR (magic angle spinning nuclear magnetic resonance) spectra were recorded at ambient temperature for the γ-Al_2O_3 prepared by calcining hydrogenated boehmite for seven hours at 500, 600, 700, 800 and 900 °C. The spectra were obtained using a Bruker MSL-400 spectrometer (9.4 T) operating at a ^{27}Al frequency of 104.23 MHz. The solid sample was spun around an axis inclined at 54°44' (the magic angle) with respect to the magnetic field, at a rate of 15 kHz using a Bruker 4 mm double-air-bearing probe. The MAS-NMR spectrum was obtained after a 3 μs 90, and a 0.6 μs 90, pulse length on the solution and sample, respectively. A 1.0 M $Al(NO_3)_3$ solution was employed as the chemical shift reference (set to 0.0 ppm), and for calibrating the experimental pulse lengths.

The baselines of the MAS-NMR spectra were corrected before peak deconvolution and integration was performed to obtain the coordination distribution of Al. This baseline correction was repeated 20 times to obtain an indication of its contribution to the uncertainty in the measurements. Results are presented in *Chapters 7* and *8*.

4.1.9 Small Angle X-ray Scattering

The small-angle intensities were measured with a NanoSTAR small angle X-ray scattering (SAXS) instrument, equipped with a 2-dimensional detector. Scattered photons were counted with a 2-D multiwire detector over a period of three hours. Instrumental settings were as follows; λ = 1.5418 Å (CuK_α), sample detector distance of 65 cm, and 2θ range between 0.04 and 4.4 degrees. The raw data had the background subtracted and was radially averaged. Resulting intensities after discarding low q data points affected by the beam stop, spanned a q range between 0.01138 – 0.31287 Å^{-1} $\left(q = 4\pi \sin(\theta)/\lambda\right)$. The SAXS results are presented in *Chapter 9*.

4.1.10 Method of SAXS Analysis

This section was predominantly written by Clinton Maitland in the following published papers:

G. Paglia, C.E. Buckley, T.J. Udovic, A.L. Rohl, F. Jones, C.F. Maitland and J. Connolly 2004, "The boehmite derived γ-alumina system, 2: Consideration of hydrogen and surface," Chemistry of Materials, ***16****, pp. 1914-1923.*

Maitland, C.F., Buckley, C.E., Paglia G., and Connolly, J. 2004 "Determination of the specific surface of γ-alumina using small angle x-ray scattering," Proceedings of the Second Annual Conference of Asian Pacific Nanotechnology Forum (APNF) 2003, Cairns, Australia, November 19-21, 2003, pp. 113-120.

The approach taken for analysis of the SAXS data was adapted from Spalla *et al*. (2003). This approach allows for determination of the volume fraction, φ, of nano-sized porosity and specific surface, Σ_S, of specimens in powder form. This analysis is valid when the size of the powder grains is more than ten times the size of the porosity. Transmission electron microscopy (TEM) images of the nanoporosity and the powder grains confirmed that this was the case (*section 8.1*).

The raw intensity, *I(q)*, was converted to an absolute scale, $I_1(q)$, called the 'measurable' intensity. In this form, $I_1(q)$ represents the differential scattering cross section per unit volume of solid. The measurable intensity can be determined directly (Spalla *et al.* 2003):

$$I_1(q) = \frac{C(q)}{C_0 \Delta\Omega(q) T d_B} \tag{4.13}$$

where T is transmission of the powder sample and d_B is the length of solid traversed by the incident beam. This method requires the measurement of the number of incident photons per second, C_0, and number of photons per second, $C(q)$, scattered into a solid angle, $\Delta\Omega(q)$. The NanoStar SAXS instrument does not measure the intensity directly. Instead a highly cross-linked polyethylene S-2907 standard supplied from Oak Ridge National Laboratories was used to determine the measurable intensity:

$$I_1(q) = I_{abs,st} \frac{I(q)}{I_{st}} \frac{t_{st}}{t} \frac{d_{st}}{d_B} \frac{T_{st}}{T} \tag{4.14}$$

where $I_{abs,st}$ is the differential scattering cross section per unit volume of the standard at q = 0.0227 Å^{-1}, I_{st} is the average number of photons detected in time t_{st} (transmission of the standard) at q = 0.0227 Å^{-1} and d_{st} is the measured thickness of the standard. The solid thickness was calculated from the measured transmission, T, and the linear attenuation coefficient of the solid ($d_B = -lnT/\mu$). The use of a standard allows the measured intensity to be converted to absolute scale, eliminating the need to determine the count rate and the solid angle required in the Spalla *et al*. (2003) method.

Using the Porod law (Porod 1982, p.17), the specific surface area can then be determined from the following expression (Spalla *et al.* 2003):

$$\Sigma_S = \frac{1}{\rho_m}\frac{\lim_{q\to\infty}\left[I_1 q^4\right]}{2\pi\Delta\rho^2} = \frac{1}{\rho_m}\frac{K}{2\pi\Delta\rho^2} \qquad (4.15)$$

where ρ_m is the mass density of the solid and $\Delta\rho$ is the scattering length density difference between the pore and solid. The specific surface area, calculated using Equation 4.15, includes all interfacial surface area between pores and solid, plus that between the surface of the grains and air. The Porod constant, K, was determined by fitting a constant to plots of $I_1 q^4$ vs q over appropriate ranges of q (Figure 9.3).

To calculate the pore volume fraction, scattering from the 'envelopes' of the grains needs to be subtracted. The 'envelopes' are conceptualized as smoothed micron sized grains. After smoothing of the grain, the envelope surface is free from any small-scale structure and porosity. The measurable intensity after subtraction of scattering from the grains is denoted by I_1^{corr}. The pore volume fraction was then calculated using the following expression (Spalla *et al.* 2003):

$$\int_0^\infty I_1^{corr} q^2 dq = 2\pi^2 \varphi \Delta\rho^2 \qquad (4.16)$$

I_1^{corr} is only known over a finite q range, thus, to perform this integration, extrapolation of I_1^{corr} is required (Figure 9.2). At low q I_1^{corr} was estimated by a constant value. At high q the corrected intensity was estimated using the Porod law (Porod 1982, p.17). Pore sizes were calculated using a spherical approximation to the pore shape:

$$r = \frac{3\varphi}{\Sigma_S(1-\varphi)\rho} \qquad (4.17)$$

where r is the pore radius. The spherical approximation was used so that comparison could be made with the BET method, which also assumes spherical pores.

4.1.11 Multipoint BET Adsorption and Density Measurements

Surface area and pore distribution of γ-Al_2O_3 samples were determined using a Micrometrics 2400 instrument operated by the Australian Nuclear Science and Technology Organisation (ANSTO), Sydney, Australia. Known amounts of sample were conditioned under vacuum at a temperature of 120 °C for 16 hours for degassing before re-weighing and transfer to the measuring manifold. Nitrogen gas adsorption/desorption isotherms were then recorded at various pressures, followed by analysis to determine surface area and pore size.

Density was measured using a Quantachrome Helium Pycnometer. Helium was passed through pre-weighed samples in a micro-sample container to displace the air within the samples. The sample was then re-weighed and the total volume recorded, along with a reference volume, to yield the necessary parameters for density calculation. The density was then used to calculate the pore volume fraction:

$$\varphi = 1 - \frac{\rho_m}{\rho_i} \tag{4.18}$$

where φ is the volume fraction, ρ_m is the measured density and ρ_i is the ideal crystallographic density. BET and pycnometry results are presented in *section 9.1*.

4.1.12 Loss on Ignition

One-shot ignition-loss was performed on the γ-Al_2O_3 samples to determine the amount of hydrogen in the bulk of the sample examined here. The sample was initially heated to 200 °C for 2 hours, to drive off surface adsorbed water, and cooled in a desiccator. The sample was then weighed to ± 1 mg precision, heated to 1200 °C for 1 hour to drive off all residual hydroxyl ions from the bulk, cooled, and weighed again. The measured mass loss was then used to determine the amount of hydrogen-containing species in the material. Ignition-loss results are presented in *section 9.2*.

4.1.13 Prompt-Gamma Activation Analysis

Data for prompt-gamma activation analysis (PGAA) were collected from the γ-Al_2O_3 samples using the PGAA spectrometer at the National Institute of Standards and Technology (NIST) Center for Neutron Research (NCNR), Gaithersburg, USA. Cold neutrons were filtered through Be and Bi at 77 K and collimated using Li-6 glass. Prompt-gamma rays were detected using a high-resolution Ge gamma-ray spectrometer.

Typically, 1 g samples (~2 cm × 2 cm × 1 cm in size) were placed in Teflon pouches and pre-dried in air at 150 °C for 2 hours each. After drying, the pouches were immediately melt-sealed. Each PGAA sample was irradiated with a beam of cold neutrons for 1 - 2 hours. The constituent elemental nuclei absorb some of these neutrons and emit prompt-gamma rays, which are measured with the gamma ray spectrometer. The energies of these gamma rays identify the neutron-capturing elements, while the intensities of the peaks at these energies reveal their concentrations within the sample. H/Al ratios were determined from the integrated intensities of the 2223 keV prompt-gamma radiation from H and the 1778 keV decay gamma radiation from ^{28}Al. The integrated intensity of the ^{28}Al decay gamma radiation was corrected to reflect steady-state decay intensity. PGAA results are presented in *section 9.2*.

4.1.14 Inelastic Neutron Scattering

Neutron vibrational spectroscopy (NVS) measurements were performed on each γ-Al_2O_3 sample for 24 h at low temperature (~15 K) using the filter analyser neutron spectrometer (FANS) at the NCNR. A Cu (220) monochromator was used with horizontal beam collimations of 60′ and 40′ of arc before and after the monochromator, respectively. Hydrogen-related phonon energies over the range of 30 - 260 meV (1 meV = 8.065 cm^{-1}) were measured with a liquid-nitrogen-cooled Be-graphite-Be composite filter analyser. Samples between 9 and 12 g were placed in tubular aluminium sample cells (2.5 cm diameter × 5 cm tall) and pre-dried in air at 150 °C for 2 hours each. After drying, the samples were immediately sealed with a lid, using an indium o-ring. All spectra were measured for 24 h at ~15 K and were

normalized with respect to sample mass. The resulting spectra revealed details of the vibrational motion of hydrogenous species associated with the γ-Al_2O_3 samples and reflected the bonding environment of the hydrogen involved. NVS results are presented in *section 9.3*.

4.1.15 Infrared Analysis

Infrared (IR) spectra were obtained on a Bruker IFS 66 instrument using the Diffuse Reflectance Infrared Fourier Transform (DRIFT) and transmission accessories. The resolution was 4 cm^{-1} for both techniques and an MCT (Mercury Cadmium Telluride) detector was used. An aperture of 8 mm was used for DRIFT and transmission IR, with 256 and 32 scans obtained, respectively. The evanescent wave penetrates at most 1μm into the sample and therefore DRIFT measures predominantly surface species. Samples of KBr mixed with 2.5% γ-Al_2O_3 were prepared for both techniques, and were pelletised for transmission IR. Spectra were taken from γ-Al_2O_3 samples where surface water was driven off by heating to 200 °C for one hour. The IR results are presented in *section 9.4*.

4.2 Computational

4.2.1 Interatomic Potential Calculations

Four different potential models applicable to aluminium oxides, all based on the Born ionic model, were employed (Table 4.2), namely those of Bush *et al*. (1994), Catlow *et al*. (1982), Minervini *et al*. (1999) and Mackrodt and Stewart (1979). These models were used in the preliminary computational study on κ-Al_2O_3 (*section 5.3*). Only the Catlow *et al*. (1982) potential model was used for γ-Al_2O_3. All models consisted of short-range repulsive interactions, longer-range attractive interactions, long-range Coulombic interactions and atomic polarization. The first two types of interaction, describing the repulsion between atoms at short distances and the van der Waals attraction at longer distances, utilised a Buckingham potential (Equation 3.5) in three of the four models. The Mackrodt & Stewart (1979) model used electron gas methods to describe the short-range interactions, using a cubic

spline to interpolate the value of the potential (Press *et al.* 1992, pp.107-110). The long-range electrostatic energy for all models was evaluated using the Ewald method (Ewald 1921; Tosi 1964). Atomic polarisation was incorporated via the core-shell model where a massless shell is coupled to a core by a harmonic spring, described by Equation 3.6 (Dick and Overhauser 1958). It should be noted that only the Bush model employed the shell model for both aluminium and oxygen ions, while the other three assume that the aluminium ion is not polarisable.

More accurate structural information can be obtained from interatomic potentials by scaling them to suit cations in specific types of site positions (Lewis and Catlow 1985). This approach was not adopted here because it requires prior knowledge of which site positions the cations reside in after minimisation. Since this is not known where the cations are precisely located in γ-Al_2O_3, it is more sensible to use the same potential for all Al ions and allow for the possibility of cation migration to different sites throughout the structure. It has been shown that the structural information obtained from this approach is relatively accurate and the relative energies of different structures appear to be valid (*section 5.3*). Moreover, the accuracy is invariably improved once DFT is applied.

Constant volume simulations were performed using conjugate gradients minimisation of the total energy. This was employed in conjunction with the rational function optimisation (RFO) (Banerjee *et al.* 1985) algorithm to ensure that the final hessian is positive definite. On structures where the minimiser stopped due to discontinuities in the energy surface, other methods such as the introduction of a spring constant to stiffen the polarisation between the oxygen cores and shells, switching to the Broyden-Fletcher-Goldfarb-Shanno (BFGS) (Shanno 1970) minimisation algorithm, and including a Lennard-Jones 12-6 potential (Lennard-Jones 1924a; 1924b; 1925; 1937) were employed. The original optimising method was resumed once the discontinuities were overcome. The software employed for these calculations was the General Utility Lattice Program (GULP) (Gale 1996; Gale 1997; Gale and Rohl 2003). For the κ-Al_2O_3 case study, constant pressure minimisations were performed on the lowest energy structures determined by the constant volume minimisations.

Table 4.2. Potentials incorporated into the Buckingham Model for this study. Note: e = charge of an electron (1.602×10^{-19} C).

Authors		*A* (*eV*)	*ρ* (*Å*)	*C* (*eV Å^{-6}*)	*Truncation* (*Å*)	*q(core)* (*e*)	*q(shell)* (*e*)	*k* (*eV Å^{-2}*)
Bush *et al*	Al^{3+}-O^{2-}	2409.50	0.2649	0.0	15.0	0.043	2.957	403.98
	O^{2-}-O^{2-}	25.41	0.6937	32.32	15.0	0.513	-2.513	20.53
Catlow *et al*	Al^{3+}-O^{2-}	1460.3	0.29912	0.0	10.0	3.000	-	-
	O^{2-}-O^{2-}	22764.0	0.14900	27.8790	12.0	0.86902	-2.8690	74.92
Minervini *et al*	Al^{3+}-O^{2-}	1725.20	0.28971	0.0	20.0	3.000	-	-
	O^{2-}-O^{2-}	9547.96	0.2192	32.0	20.0	0.04	-2.04	6.30
Mackrodt & Stewart	Al^{3+}-O^{2-}	Cubic reverse spline used				3.000	-	-
	O^{2-}-O^{2-}					-0.0260	-1.974	16.00

The interatomic potential calculations were performed in a 15 node Beowulf cluster consisting of 12×600 MHz Dec Alpha EV56 processors and 3×1.2 GHz Athlon processors. Results are presented in *section 5.3* and *Chapter 10*.

4.2.2 First Principles Calculations

The first principles calculations were performed with the SIESTA (Spanish Initiative for Electronic Simulations of Thousands of Atoms) code (Ordejon *et al.* 1993; Ordejon *et al.* 1995; Ordejon *et al.* 1996; Artacho *et al.* 1999; Ordejon *et al.* 2000; Ordejon 2000; Sanchez-Portal *et al.* 1997; Soler *et al.* 2002), which implements density functional theory (Hohenberg and Kohn 1964; Kohn and Sham 1965; refer to *section 3.4*). The exchange-correlation contribution to the total energy was treated within the PBE generalised gradient approximation (GGA) of Perdew *et al*. (1996). Norm-conserving pseudopotentials were used to describe the non-local potential due to the atom core (Kleinman and Bylander 1982; Troullier and Martins 1991). The valence electrons were described within the framework of linear combination of atomic orbitals (LCAO) theory (Sankey and Niklewski 1989). A numerical double-ζ basis set with polarisation parameters was employed with soft

radial confinement. Here the basis set was variationally optimized at the experimental structure of α-Al_2O_3 (Junquera *et al.* 2001). The quality of the basis set and pseudo potentials used was assessed on rhombohedral α-Al_2O_3 using between 1 (**Γ**-point) and 10 **k**-points and mesh sizes between 120 and 200 Ry. The *a* and α parameters were within 1.3 and 0.7 % of the experimental values respectively. All structural configurations of γ-Al_2O_3 were optimised until all remnant forces were less than 0.01 eV $Å^{-1}$, using a mesh cutoff of 200 Ry (1 Ry = 13.6 eV) and an energy shift of 0.01 Ry, unless stated otherwise. The energy shift defines the radial confinement that is used to localise the orbital. These DFT calculations were performed using 4 **k**-points for the 1×1×3 supercells of the $Fd\bar{3}m$ system and 2 **k**-points for the 2×1×3 supercells of the $I4_1/amd$ system. Given the size of the supercells and the **k**-points used to sample them, this is the equivalent of using 12 **k**-points to sample a single unit cell. The unit cell parameters were kept fixed during the optimisations of γ-Al_2O_3 to decrease computational time and facilitate comparison with experimental data and significantly reduce the calculation time.

The DFT calculations were performed on a 15 node Beowulf cluster (*section 4.2.1*), and the facilities at the Australian Partnership for Advanced Computing (APAC) and the Western Australian Interactive Virtual Environments Centre (IVEC). APAC has 127 HP AlphaServer SC ES45 nodes, each with four 1 GHz processors and a peak processing power of over 1 teraflop. The total available RAM is 696 Gb. The IVEC facilities includes a Compaq SC40 server with 4 nodes, each with four 600 MHz processors and 4 Gb RAM. Results are presented in *section 5.3* and *Chapter 10*.

Chapter 5

Methodology

Material in this chapter has been published in the following papers:

G. Paglia, A.L. Rohl, C.E. Buckley & J.D. Gale 2001 "A computational investigation of the structure of κ-alumina using interatomic potentials," Journal of Materials Chemistry, ***11****, pp. 3310-3316.*

G. Paglia, C.E. Buckley, A.L. Rohl, B.H. O'Connor, A. van Riessen and J.D. Gale. 2001 "The determination of the structure of γ-alumina using empirical and first principle calculations and supporting experiment." Proceedings of the 2001 Joint Conference: Australian X-Ray Analytical Association (WA) Inc. and WA Society for Electron Microscopy, Mandurah, Australia, September 21-23, pp. 143-156.

and submitted to:

G. Paglia, A.L. Rohl, C.E. Buckley & J.D. Gale 2004 "Determination of the structure of γ-alumina from interatomic potential and first principles calculations - The requirement of significant numbers of non-spinel positions to achieve an accurate structural model," Physical Review B.

Preamble

The research program presented in this thesis involves essentially two projects conducted in parallel; a computational investigation and series of experiments. The overall methodology is summarised in Figure 5.1.

The computational investigation is based on the optimisation of structure candidates using interatomic potentials and first principles calculations based on DFT. It comprises of generation of possible structures that are consistent with the known crystallographic data and subsequent generation of all structural possibilities. For γ-Al_2O_3, the number of structural possibilities is approximately 1.47 billion. This is an excessive number of structures to optimise therefore selection criteria were developed to reduce the total sample pool to a workable quantity of candidates. The selection criteria were based on nearest-neighbour cation distances. The assumption was that structures with most sparsely distributed cation sublattice should have lower energies. Hence the selection criteria were used to select a group of initial low energy

structures which were subsequently optimised using interatomic potentials while the remainder were discarded.

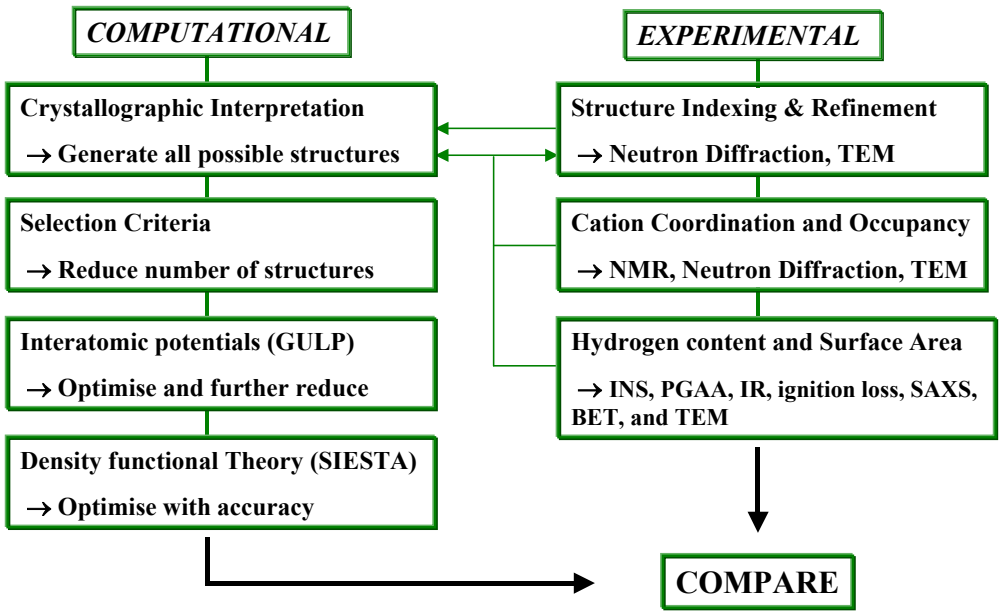

Figure 5.1. Flowchart depicting the general methodology adopted in this research.

Although modelling techniques based on interatomic potentials cannot yield accurate data with regards to electronic properties of materials, they can produce reasonably accurate structural data in a fraction of the time taken by quantum mechanical calculations. *Ab initio* calculations of a single configuration of complex structures like γ-Al_2O_3 can take many weeks whereas the empirical modelling methods typically only involve a few minutes of computation time. This allows for an extensive search of all possible structural candidates to be performed, without prior assumptions being made, before applying high accuracy quantum mechanical methods to a subset of the more favourable configurations. Once the interatomic potential calculations are complete and some likely structures are generated, the more accurate DFT calculations are carried out to achieve high accuracy. The outcome is a high accuracy result achieved in reduced time. While experimental studies yield information on the relative occupancy of the cations, these represent only an average distributed over the possible symmetry related positions. A major advantage of computational simulations of γ-Al_2O_3 is that the optimised

configurations provide precise cation coordinates. Therefore, further information regarding cation ordering and lattice distortions can be obtained.

Before attempting an investigation of this magnitude, it is important to establish if the approach of using interatomic potentials as a screening process before employing DFT works. Therefore a preliminary case study was performed on κ-Al_2O_3, whose structure has recently been definitively determined both from experiment and DFT calculations.

When using empirical and first principal calculations to determine the structure of the material it is important ensure that the starting model is as close to the actual structure as possible. It can be difficult to predict structures accurately without taking into account structural attributes obtained from experiment, but this is an area of extensive research. Hence it is useful to use experimental data, not only to provide appropriate starting parameters, but also to verify the integrity of the structural configurations obtained from the computer simulations.

To be able to start the simulations at the beginning of this project, the starting parameters used in the computer simulations were taken from experimental findings in the literature. As a result, the experimental research is initially conducted separately in parallel to the computational work. However, the experimental work is vital to the computational study because as it progresses it provides information which can be fed back into the simulations, or it can provide justification for the assumptions already made. For example, the choice to not include hydrogen in the simulation models was supported by Rietveld results obtained in this work. Most importantly, the experimental research provides a body of data which can be compared to the set of optimised structures to elucidate the structure of the material.

The experimental study involved a wide range of techniques. In addition to being used to provide information for comparison with simulation results for the determination of the structure, experiments were conducted to gain further insight into the nature of γ-Al_2O_3. The evolution of the structure was systematically investigated, detailing the crystallographic and nano-structure with changing calcination temperature. Among the findings is a new transition alumina phase, γ'-Al_2O_3. Hydrogen, its nature within the structure and the quantity was also investigated systematically, along with surface characteristics.

5.1 Experimental Methodology

The experimental work involves the selection of an appropriate precursor from which suitable samples of pure γ-Al_2O_3 can be synthesised, determination of an appropriate crystallographic model to describe the structure, followed by an investigation of the changes in the structure with varying treatment conditions. Thermal analysis was employed to obtain an indication of when phase transformation occurs. XRD was also performed for the purpose of phase identification and to qualitatively observe changes in structural characteristics with changing calcination temperature. XRD was not used in any crystallographic determination because of the extreme diffuse nature of some of the peaks in the diffraction pattern. This is a result of the disordered nature of the materials being examined, and the fact that X-ray signals do not deeply penetrate the sample and only interacts with the electron density around atoms. Obtaining information about the relative occupancies of Al ions is not reliable when performing Rietveld analysis on XRD data for powdered materials like γ-Al_2O_3. This is because it contains multiple partially occupied sites within a symmetric framework, leading to very similar scattering. Furthermore, hydrogen is not visible with XRD. Instead, neutron diffraction, the only true bulk penetrating technique, was performed. This was for the primary purpose of performing Rietveld analysis. The neutron diffraction data was obtained at ambient temperature from samples which were pre-calcined at temperatures between 400 and 1000 °C. Neutron diffraction data was also obtained from samples that were calcined *in situ* between 400 and 1000 °C. This was carried out to distinguish any possible kinetic effects, identify phase transformation boundaries, and to provide comparison data obtained at room temperature from pre-calcined material in order to establish any possible structural differences.

Rietveld analysis of neutron diffraction data was employed to obtain a suitable structural model for γ-Al_2O_3, comprising lattice dimensions, and elemental species information, *e.g*. the presence of hydrogen, and information concerning the relative site occupancy of cations. The Rietveld analysis can also provide information on the coordination distribution of the cations, *i.e*. indicate the proportion of cations with a particular coordination, which are typically octahedral and tetrahedral but could also be trihedral and pentahedral.

The coordination distribution of the cations was definitively determined using ^{27}Al MAS-NMR. This is used in conjunction with Rietveld analysis to verify the structural integrity of the models used in the refinements. Electron diffraction was also used to verify the structural integrity of the structural models. Electron diffraction is the only experimental technique that can directly yield the space group under which the symmetry is described. Used together, Rietveld analysis, ^{27}Al MAS-NMR and electron diffraction are a powerful combination of techniques that can yield accurate crystallographic information. Because all three techniques were performed on data collected at every temperature they can provide information on how the structure evolves with varying treatment conditions.

In addition to diffraction, TEM was incorporated to investigate the morphology of the materials produced, providing information on the nature of the microstructure, grain shape, and the location of amorphous regions. This was carried out on all pre-calcined samples, allowing the evolution of the morphology to be investigated with respect to varying treatment conditions.

5.1.1 Consideration of Hydrogen and Surface Effects

Because water is a by-product of the dehydration of boehmite, and many of the applications of γ-Al_2O_3 are believed to involve hydrogen, it is important to investigate where hydrogen is situated within the structure. Ignition-loss and PGAA were employed to determine the amount of hydrogen species present in the material. While ignition-loss relies on mass loss differences, PGAA is a bulk technique that can detect hydrogen atoms and thus provide an absolute measurement of the amount of hydrogen in the material. BET, SAXS and porosity measurements were used to determine microstructure characteristics such as specific surface area and total pore volume fraction. This information can be used to determine the contribution of the surface to the total volume and therefore indicate how much surface is available, for hydrogen to bind to. The amount of hydrogen in the structure and the contribution of the surface to the total volume may have implications for the bulk structural model. SAXS in particular, can measure closed porosity, which cannot be determined using BET. The information obtained can be complementary to TEM.

Further evidence for the location of hydrogen in the sample was obtained using DRIFT, transmission IR and NVS. DRIFT provides surface information while the latter techniques yield information from the bulk structure. Like PGAA, NVS is a bulk structure technique which can detect hydrogen atoms. It provides all the phonon frequencies within a structure; both acoustic modes associated with heavier atoms of the lattice, and optical modes associated with lighter atoms, such as hydrogen. Due to the large neutron scattering cross section for hydrogen relative to other elements, NVS provides the hydrogen-weighted vibrational density of states, spectroscopic information that reflects the bonding states experienced by hydrogen in the sample material. Rietveld analysis was also used to investigate whether hydrogen was likely to be present in the bulk crystalline structure.

5.2 Computational Methodology

5.2.1 Summary of Structure

The structure of γ-Al_2O_3 is usually considered to be a cubic spinel, ascribed to $Fd\bar{3}m$ space group symmetry (Rooksby 1951; Sickafus *et al.* 1999). The unit cell contains 32 oxygen ions in 32*e* Wyckoff positions, which are approximately close packed in a face centred cubic (fcc) arrangement. The cation ratio in γ-Al_2O_3 is 2:3, as opposed to 3:4 for spinel structures, so to maintain stoichiometry there must be 21⅓ aluminium cations in the unit cell. This creates a defect spinel structure due to the vacancies imposed by such an arrangement. The consideration of a spinel structure restricts the aluminium cations to occupying 8*a* (tetrahedral) and 16*d* (octahedral) Wyckoff positions, which are termed the spinel sites. Hence the stoichiometry can be represented as $Al_{21⅓}□_{2⅔}O_{32}$, where □ represents a vacancy among the spinel sites. Note that the $Fd\bar{3}m$ space group also possesses other tetrahedral (8*b* and 48*f*) and octahedral (16*d*) site positions.

A tetragonal distortion of the cubic lattice has been reported for several studies of boehmite-derived γ-Al_2O_3 (*e.g.* Lippens and de Boer 1964; Saalfeld 1958; Tertian and Papee 1958; Yanagida and Yamaguchi 1962; Wilson 1979). The tetragonal $I4_1/amd$ space group, a maximal subgroup of $Fd\bar{3}m$, with $a_{cubic} \approx \sqrt{2} \times a_{tetragonal}$, has been suggested to describe the tetragonally distorted

structure (Li *et al.* 1990). The γ-Al_2O_3 structure representation provided by $I4_1/amd$ is analogous to the spinel representation except the unit cell contains half the number of atoms. In this space group, the site positions analogous to the spinel sites in its supergroup are 4*a* (≡ 8*a*) and 8*d* (≡ 16*d*) (Hahn 1995). The 16 oxygen ions of the unit cell are located in 16*h* Wyckoff positions and the 10⅔ Al cations are distributed among the spinel sites. As with $Fd\bar{3}m$, the $I4_1/amd$ space group has other site positions available for occupation; 8*c* (octahedral), and 4*b*, 8*e* and 16*g* (tetrahedral). Table 5.1 provides a summary of the octahedral and tetrahedral positions available in both space group representations.

Table 5.1. Summary of site positions available for occupation in the cubic, $Fd\bar{3}m$, and tetragonal, $I4_1/amd$, space groups used to describe the structure of γ-Al_2O_3. Note that the *a* and *d* symmetry positions are the spinel site positions that traditional models of γ-Al_2O_3 assume that the cations are restricted to.

	$Fd\bar{3}m$	$I4_1/amd$	*Generic label given in this study*
		Octahedral Site Positions	
Wyckoff Symmetry Position	16*c*	8*c*	*c* symmetry
	16*d*	8*d*	*d* symmetry
		Tetrahedral Site Positions	
Wyckoff Symmetry Position	8*a*	4*a*	*a* symmetry
	8*b*	4*b*	*b* symmetry
		8*e*	*e* symmetry
	48*f*		*f* symmetry
		16*g*	*g* symmetry

Here, all structural possibilities of γ-Al_2O_3, with Al ions in all possible spinel site positions are investigated for both the $Fd\bar{3}m$ and $I4_1/amd$ space groups. Note that during the optimisations, the cations are free to move to non-spinel sites. The room temperature lattice parameters used for the starting structure candidates were a = 7.911 Å for $Fd\bar{3}m$ (Zhou and Snyder 1991), and a = 5.600 Å, c = 7.854 Å for $I4_1/amd$ (Li *et al.* 1990). Based on the findings of Zhou and Snyder (1991) and Wolverton and Hass (2001) and the experimental results herein, it was decided not to incorporate hydrogen in the structural models.

5.2.2 Generation of Structural Candidates

In order to account for the fractional number of Al ions in the unit cell, supercells were employed which result in larger periodic systems with an integer number of atoms. A 1×1×3 tetragonal supercell was applied to the cubic $Fd\bar{3}m$ structure and a 2×1×3 orthorhombic supercell was applied to the tetragonal $I4_1/amd$ structure. The supercells for each structure contain 96 O and 64 Al atoms, *i.e.* a total of 160 atoms. In this work, the tetragonal and orthorhombic supercells are referred to as the $Fd\bar{3}m$, or cubic, and $I4_1/amd$, or tetragonal, systems respectively.

Supercells (based on primitive cells) containing as little as 40 atoms have been used to examine γ-Al_2O_3 due to earlier computational restrictions (Wolverton and Hass 2001; Gutiérrez *et al.* 2002). This limits the type of ordered configurations that are possible compared to the larger supercells used here. Larger supercells were adopted because defects are known to be present in γ-Al_2O_3. The presence of a single defect within a smaller cell can result in a high concentration of defects which may interact with periodic images.

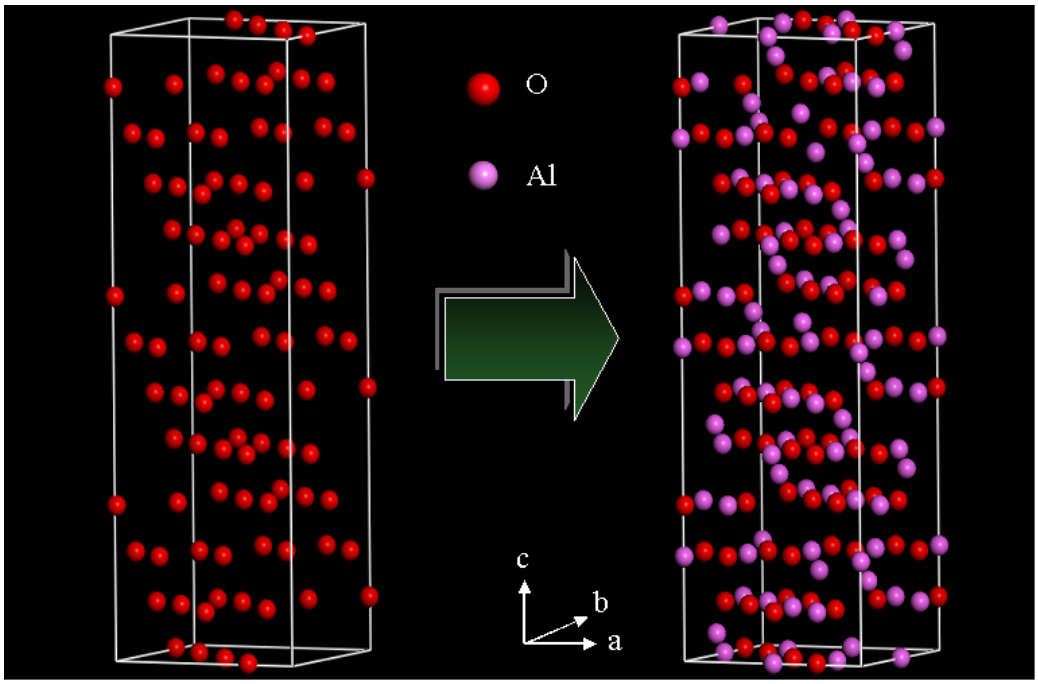

Figure 5.2. Illustration of how each starting structural configuration is generated. The oxygen sublattice of the supercell is fixed in idealised positions. Each different structural configuration results from a different arrangement of Al ions that is inserted into the oxygen sublattice.

As the oxygen sublattice of γ-Al_2O_3 is well known (Lippens and de Boer 1964), the oxygen ions can be fixed in idealised positions while the possible configurations are considered for the interstitial Al ions. This approach is illustrated in Figure 5.2. The Al ions are capable of occupying octahedral and/or tetrahedral site positions. *Appendix IV* contains the oxygen coordinates and the coordinates of possible cation site positions for both symmetry systems. The starting structure models assume that 70% of the Al atoms are distributed in octahedral site positions and the remaining 30% are in tetrahedral positions. This distribution of cations in the structures was based on the NMR spectroscopy and Monte Carlo simulations of Lee *et al*. (1997).

In the starting structure models, the Al ions were restricted to the spinel positions, 8*a* and 16*d* for $Fd\bar{3}m$, 4*a* and 8*d* for $I4_1/amd$. This approach was adopted because:

- Most researchers have reported cations to be exclusive to these sites.
- It reduces the number of possible starting structural configurations.
- The distances between 8*a* and 16*d* for $Fd\bar{3}m$, and 4*a* and 8*d* for $I4_1/amd$, are greater than the distances between any other pair of site positions. Restricting cations to the spinel positions should, in principle, yield lower starting lattice energies.
- Significant cation migration has been observed in aluminas during minimization using interatomic potentials (*section 5.3*). Consequently, if a departure from exclusive spinel site occupation is energetically favourable it may become apparent during optimisation.

Based on these assumptions, there are 48 octahedral and 24 tetrahedral site positions available in each supercell to distribute the cations. An occupancy of 70% of the 64 Al ions among the octahedral site positions yields 45 ions. Hence there are ${}^{48}C_{45}$ = 17,296 possible arrangements of the Al ions among the octahedral site positions. Likewise, an occupancy of 30% of the 64 Al ions among the tetrahedral site positions yields 19 ions, generating ${}^{24}C_{19}$ = 42,504 possible arrangements of amongst these sites. This yields ${}^{48}C_{45} \times {}^{24}C_{19}$ = 17,296 × 45,205 = 735,149,184 total starting structural possibilities for each space group structure under investigation, or a total of ~ 1.47 billion configurations overall. These starting structural

configurations were generated using simulated nested Fortran DO loops (Gentleman 1975).

Selection Criteria

Optimisation of each of the structural possibilities even using interatomic potentials was intractable with the available computing facilities. Selection criteria were developed to reduce the ~ 1.47 billion possible starting configurations to a manageable number of structures.

The procedure adopted was to reduce the number of starting structural configurations for optimisation to those with the most evenly (*i.e.* sparsely) distributed cation sublattice. This is expected to provide a group of starting structures that have energies that are amongst the lowest of all the possible configurations. The selection criteria were based on examining three different types of nearest neighbours in the cation sublattice and are catalogued in *Appendix V*:

- The number of nearest neighbour occupied octahedral positions to an occupied octahedral position (*oct-oct*) – for one occupied octahedral position there can be up to six surrounding nearest neighbour octahedrally coordinated atoms (Figure 5.3a).
- The number of nearest neighbour occupied tetrahedral positions to an occupied tetrahedral position (*tet-tet*) – for one occupied tetrahedral position there can be up to four surrounding nearest neighbour tetrahedrally coordinated atoms (Figure 5.3b).
- The number of nearest neighbour occupied octahedral positions to an occupied tetrahedral position (*tet-oct*) – for one occupied tetrahedral position there can be up to 12 surrounding nearest neighbour octahedrally coordinated atoms (Figure 5.3c).

During the generation of the configurations the number of *oct-oct*, *tet-tet* and *tet-oct* nearest neighbours for each occupied atom throughout the lattice were determined. The *oct-oct* and *tet-tet* criteria were implemented while applying the selection rule to obtain the possible cation arrangements among octahedral and tetrahedral positions, respectively. The structures with the lowest number of *oct-oct*

and *tet-tet* nearest neighbours were combined to form a pool of structure candidates to which the *tet-oct* selection criteria were then applied.

In terms of γ-Al_2O_3 described by $Fd\bar{3}m$ symmetry, the number of structure candidates was reduced to 58,558,564 before application of the *tet-oct* selection criteria. For the $I4_1/amd$ system structures the reduced number of structure candidates was 98,515,200. After application of the *tet-oct* selection criteria, the number of structures with the most sparsely distributed cation sublattice (*i.e.* the lowest mean number of nearest neighbours), with respect to all three selection criteria, was 56,064 and 502,752 for the $Fd\bar{3}m$ and $I4_1/amd$ systems, respectively. This process is summarised in Figure 5.4. A summary of the sample pools obtained from the application of the selection criteria is provided in Table 5.2. Each sample pool with a lower mean number of nearest neighbours should have a lower energy distribution, as illustrated by Figure 5.5.

The effectiveness of the selection criteria was examined by determining the single point energies[2] of each set of starting structures with a different mean number of nearest neighbour cations. Each set of structures exhibits a mean, maximum and minimum energy that are less than those of sets of structures with higher average numbers of nearest neighbour cations. Hence it was verified that the selection criteria were successful in providing a set of starting structural configurations for optimisation that had the lowest single point energies. Table 5.3 provides a summary of the energies for the starting structural configurations for the two lowest mean number of nearest neighbour cations.

The reduced number of starting structural configurations for the $I4_1/amd$ system was still a formidable quantity to optimise with the available computational facilities and consequently further criteria for reduction were sought. Watson and Willock (2001) suggested that perhaps the lowest energy starting structures optimise to the minimum energy structure. From the work on κ-Al_2O_3 this does not appear to be the case (*section 5.3*). When considering the calculations that involved the potentials of Catlow *et al*. (1982), of all the optimised structures 40% reached the minimum energy. Structures with starting lattice energies that were among the highest were found to optimise to the lowest energy, and those with the lowest

[2] The single point calculations were based only on the core potentials of the potential models employed.

starting lattice energies did not always optimise to the lowest energy. Furthermore, the differences between initial and final energies were examined for groups of structural configurations with starting energies less than the mean starting energy. The proportion of structures that optimised to the minimum energy decreased for groups of structures with lower starting energies. Based on this, a set of starting structures was randomly selected from the 502,752 most sparsely distributed structural configurations of the $I4_1/amd$ system (Press *et al.* 1992, pp272-273). The number of starting structural configurations randomly selected was 57,763. All Fortran codes used to generate the structures and perform analysis of the selection criteria are catalogued in *Appendix VI*.

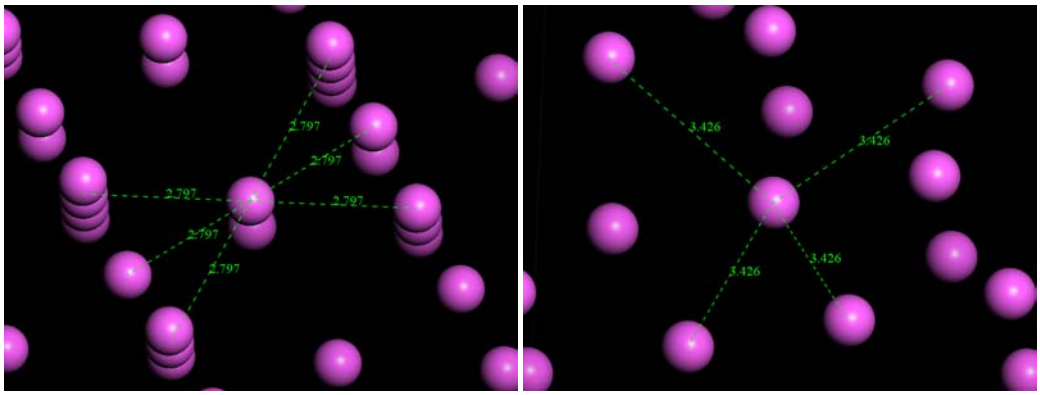

(a) (b)

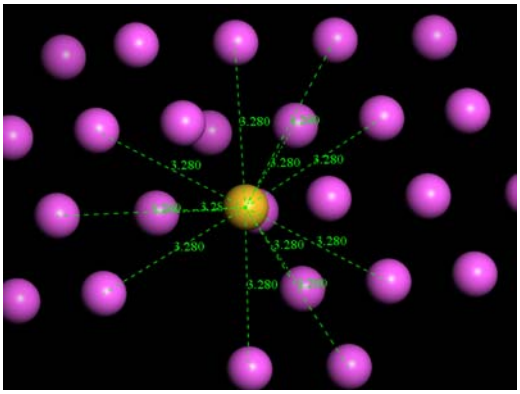

(c)

Figure 5.3. Illustration of the selection criteria; (a): *oct-oct*, (b): *tet-tet*, (c): *tet-oct*. The yellow atom in (c) indicates a tetrahedrally coordinated Al ion.

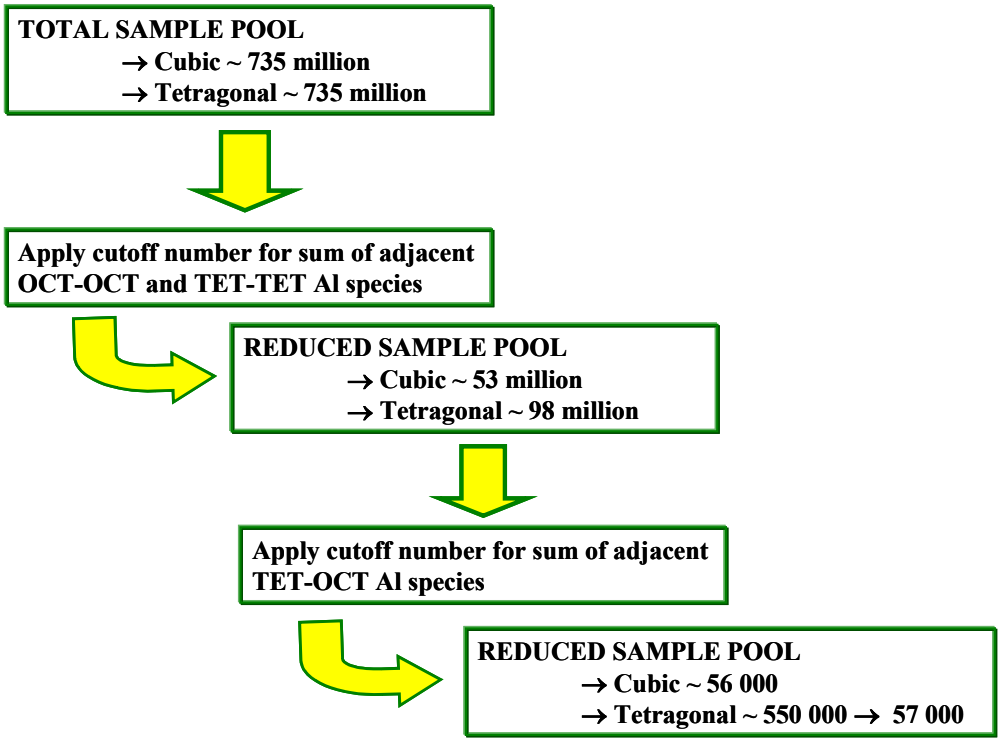

Figure 5.4. Flow chart illustrating how application of the selection criteria reduce the number of structure candidates

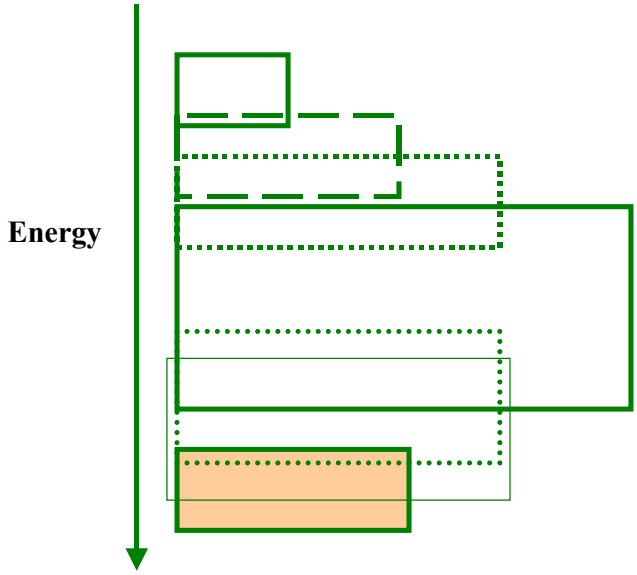

Figure 5.5. Representative illustration of the energy distribution of the groups of structures with different mean number of nearest neighbours. This figure is not to scale, it is intended to show the relative distribution of energies. Each rectangle is representative of the range in energies exhibited by a group of structures with the same mean number of nearest neighbour cations. The size of each box represents the relative amount of structures with the same mean number of nearest neighbour cations.

Table 5.2. Summary of the application of selection criteria to the total number of possible starting structures to obtain a reduced sample pool.

Application of *oct-oct* selection criteria to the 17,296 possible arrangements of 45 cations on 48 octahedral site positions			
		Number of structures for the $Fd\bar{3}m$ system	Number of structures for the $I4_1/amd$ system
Mean *oct-oct*	5.69	432	816
	5.64	5,472	4,656
	5.60	11,296	11,728
Application of *tet-tet* selection criteria to the 42,504 possible arrangements of 19 cations on 24 tetrahedral sites			
Mean *tet-tet*	3.58	48	192
	3.47	192	768
	3.37	1,464	3,240
	3.26	7,296	7,536
	3.16	16,608	10,992
	3.05	11,712	11,376
	2.95	5,184	8,400
Application of *tet-oct* selection criteria to the reduced cubic (11,296 × 5,184 = 58,558,564) and tetragonal (11,728 × 8,400 = 98,515,200) sample pool of staring structures			
Mean *tet-oct*	11.53	576	5,760
	11.47	20,736	160,896
	11.42	306,048	1,555,392
	11.37	2,592,768	7,529,664
	11.32	10,814,400	19,057,536
	11.26	20,957,568	28,162,176
	11.21	17,104,512	24,782,112
	11.16	5,802,624	12,985,632
	11.11	903,168	3,773,280
	11.05	56,064	502,752

Table 5.3. Summary of range of single point energies for the structures with the two lowest mean number of nearest neighbour cations.

		$Fd\bar{3}m$ system	
Mean oct-oct, tet-tet, tet-oct	***Mean Energy (eV)***	***Maximum Energy* (eV)**	***Minimum Energy (eV)***
5.60, 2.95, 11.11	-4955.63	-4829.72	-4982.59
5.60, 2.95, 11.05	-4968.38	-4915.85	-4989.80
		***$I4_1/amd$* system**	
5.60, 2.95, 11.11	-4898.22	-4748.19	-4934.10
5.60, 2.95, 11.05	-4915.07	-4801.09	-4944.17

Once the 56,064 cubic, $Fd\bar{3}m$, and the 57,763 tetragonal, $I4_1/amd$, system structures were optimised using interatomic potentials, their resulting structural configurations were analysed. Analysis of the structures was performed using Python code (*Appendices VII* and *VIII*). A select number of these structures were then further

optimised using first principles methods. The optimised structures were compared to experimental data by generating neutron diffraction patterns. This enables determination of the structural configuration(s) that correspond to a representative structure of γ-Al_2O_3.

Nomenclature

In order to distinguish between alternative possible configurations of structure, a system of notation is required. For both the $Fd\bar{3}m$ and $I4_1/amd$ systems, cation positions were named according to their Wyckoff position and the portion of the supercell in which they were located. For example, in the $Fd\bar{3}m$ space group, the 8*a* Wyckoff symmetry position corresponds to eight cation positions within the unit cell. Each of these positions is labelled 1, 2, 3,…., 8, with the letter *a* preceding it, to designate the site symmetry and the specific position it belongs to. The same notation is applied to all three segments of the 1×1×3 supercell. To distinguish which portion of the supercell the site position is situated in, the position label is followed by the letters a, b or c to designate the first, second and third segments of the cell. Hence the site positions corresponding to 8*a* Wyckoff symmetry are labelled *a*1a, *a*2a,….., *a*8a, *a*1b, *a*2b,….., *a*8b, *a*1c, *a*2c,….., *a*8c. This nomenclature is applied to all the possible site positions in the tetragonal supercell of the $Fd\bar{3}m$ system, such that the letters *b*, *c*, *d* and *f* are used to indicate site positions with 8*b*, 16*c*, 16*d* and 48*f* Wyckoff symmetry, respectively.

Slightly different nomenclature was used for the orthorhombic 2×1×3 supercell of the $I4_1/amd$ system. The unit cell is doubled along the *a* axis in addition to being tripled along the *c* axis. To account for the doubling in the *a* axis, the letters a and b are used following the position number label to differentiate whether the site position is located in the first or second half of the supercell, in the x direction. The letters a, b or c are then applied to distinguish which third of the unit cell, in the z direction, the site position is located. As an example, the site position nomenclature for 8*c* Wyckoff symmetry follows *a*1aa,….. *a*4aa, *a*1ba,….. *a*4ba, *a*1ab,….., *a*4ab, *a*1bb,….. *a*4bb, *a*1ac,….., *a*4ac, *a*1bc,….. *a*4bc. As per the $Fd\bar{3}m$ system, this nomenclature is applied to all the possible site positions in the $I4_1/amd$ system for

γ-Al_2O_3 such that the letters *b*, *c*, *d, e* and *g* are used to indicate site positions with 4*b*, 8*c*, 8*d*, 8*e* and 16*g* Wyckoff symmetry, respectively

5.3 Case Study: Testing the Computational Approach with κ-Alumina

5.3.1 Why κ-Alumina?

Unlike γ-Al_2O_3 and the accurately known α-Al_2O_3 phase, only a few experimental studies have been performed on κ-Al_2O_3 (Liu and Skogsmo 1991; Hansson *et al.* 1995; Halvarsson *et al.* 1995; Gross and Mader 1997; Halvarsson *et al.* 1999; Ollivier *et al.* 1997). Experimental determination of the structure of κ-Al_2O_3 was hampered by difficulty in obtaining significant amounts of pure sample and the poor degree of crystallinity.

Only recently have confident claims of the definitive κ-Al_2O_3 structure been made (Ollivier *et al.* 1997; Yourdshahyan *et al.* 1999). A study by Ollivier *et al*. (1997), based on XRD, TEM and NMR, concluded that the aluminium ions are inserted between the oxygen layers in both octahedral and tetrahedral positions, in a 3:1 ratio. The study, by Yourdshahyan *et al*. (1997a; 1997b; 1999), employed first principles calculations based on periodic density functional theory (DFT), with a plane wave basis set. This was the first study to attempt to look at several possible structures for κ-Al_2O_3 instead of just pointing towards a specific structure. The final structure determined for κ-Al_2O_3 by Yourdshahyan *et al*. (1999) exhibited lattice parameters differing by no more than ± 0.1 Å from those determined by Ollivier *et al*. (1997), and also found the aluminium ions to be octahedrally and tetrahedrally coordinated between the oxygen layers in a 3:1 ratio.

The purpose of the case study on κ-Al_2O_3 were two-fold. Firstly, to investigate the applicability of applying interatomic potentials to solving complex structures, where many possibilities are involved. Comparison with the results of Yourdshahyan *et al*. (1999) and Ollivier *et al*. (1997) provides a good indication of the accuracy achievable with interatomic potentials. If successful, interatomic potentials could be used as an efficient screening procedure prior to employing more accurate quantum mechanical calculations to a reduced set of structures. Although

modelling techniques based on interatomic potentials cannot yield accurate data with regards to electronic properties of materials, it is expected that they can produce reasonably accurate structural data in a fraction of the time taken by quantum mechanical calculations (Wimmer 1996). It is important to check if the speed gained by interatomic potentials does not have a detrimental effect on the quality of the optimised structure produced. κ-Alumina was chosen for this investigation because it is a far simpler structure than γ-Al_2O_3 and accurate structural details are now established in the literature to cross check against the interatomic potential optimisations. Proceeding with the methodology involving empirical calculations for γ-Al_2O_3 is dependent on the success of the optimisations for κ-Al_2O_3. The second purpose for studying κ-Al_2O_3 was therefore to develop a systematic procedure of computational investigation which could later be applied to γ-Al_2O_3.

5.3.2 Methodology

Recent TEM and XRD studies have shown κ-Al_2O_3 to belong to the space group *Pna2₁* (Liu and Skogsmo 1991; Halvarsson *et al.* 1995; Ollivier *et al.* 1997). Based on these experimental observations, the unit cell can be considered to be comprised of 40 atoms in total, 24 oxygen atoms and 16 aluminium atoms. There are four layers in the oxygen sublattice, each comprising six oxygen atoms, exhibiting a close-packed ABAC… stacking sequence along the *c*-axis of the unit cell. Due to the stoichiometry of κ-Al_2O_3, the aluminium sublattice has four layers with four atoms, lying interstitially between the oxygen layers. This structural configuration is illustrated in Figure 5.6. The Al atoms are capable of occupying octahedral and/or tetrahedral site positions.

The four symmetry related positions in the unit cell which arise due to the *Pna2₁* symmetry are as follows: (x, y, z), (½+x, ½-y, z), (-x, -y, ½+z), and (½-x, ½+y, ½+z). For κ-Al_2O_3 this means that the unit cell can be described using 10 independent atomic positions. For every independent starting coordinate, a second is generated within the same plane and a second pair is located two planes below, *i.e.* in the *n+2* plane.

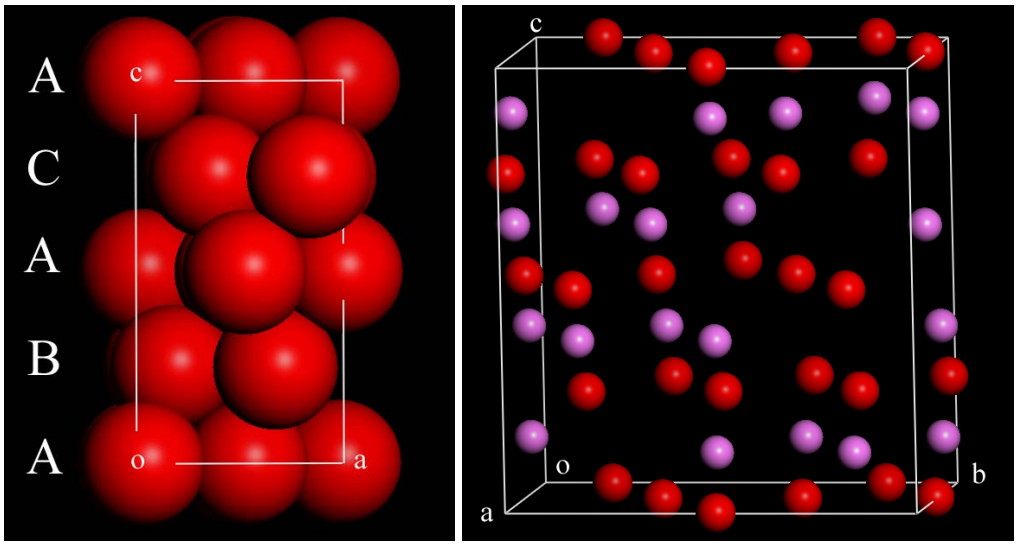

(a) (b)

Figure 5.6. (a): Illustration of the stacking sequence of the oxygen sublattice. (b): Idealised example of unit cell.

The room temperature lattice parameters of the κ-Al_2O_3 unit cell have been determined to be a = 4.8351 Å, b = 8.3109 Å, and c = 8.9363 Å by Halvarsson *et al*. (1995) using XRD. Using convergent-beam electron diffraction with a TEM these parameters were determined to be a = 4.8437 Å, b = 8.3300 Å, and c = 8.9547 Å by Liu and Skogsmo (1991).

5.3.3 Structure Notation and Candidates

In order to distinguish between alternative possible configurations of structure, a system of notation is required. In this examination of κ-Al_2O_3, the same structure notation scheme of Yourdshahyan *et al*. (1997a; 1997b; 1999) was used, where the oxygen and aluminium positions are described by the type of stacking. Because the oxygen sublattice is well known (Liu and Skogsmo 1991; Halvarsson *et al.* 1995; Halvarsson *et al.* 1999) it can be fixed in one position while the possible configurations are considered for the interstitial Al ions. Each structure candidate is labelled with notation of the type $Aa_{\alpha}c_{\gamma}Bc_{\alpha}c_{\gamma}$; the stacking and pair types of the first two oxygen and aluminium layers (layers n and $n+1$) in the unit cell, allowing each possible unit cell to be implicitly described. This is achieved as a consequence of the symmetry, which allows the structure to be described using 10 independent atomic positions as the starting coordinates for the symmetry operators.

A, B (and C) in the $Aa_{\alpha}c_{\gamma}Bc_{\alpha}c_{\gamma}$-type notation of Yourdshahyan *et al*. (1997a; 1997b; 1999) represent the layers of oxygen ions in accordance with the ABAC… stacking sequence. The lower case letters, a, b, and c, and their associated subscripts, α, β, and γ, represent Al pair positions within the layer, as shown in Figure 5.7, where the ideal positions for each pair between the A and B layers are illustrated. The $a_{\alpha}c_{\gamma}$ configuration representing the 2 Al pairs in the layer *n* are generated by applying the first two symmetry operators of the *Pna2₁* space group. Applying the remaining two symmetry operators yields $a_{\alpha}b_{\beta}$ in the *n+2* layer. Similarly, the $c_{\alpha}c_{\gamma}$ configuration in the *n+1* layer leads to $b_{\alpha}b_{\beta}$ pairs in the *n+3* layer. Hence the $Aa_{\alpha}c_{\gamma}Bc_{\alpha}c_{\gamma}$-type notation can be extended to $Aa_{\alpha}c_{\gamma}Bc_{\alpha}c_{\gamma}Aa_{\alpha}b_{\beta}Cb_{\alpha}b_{\beta}$ in order to explicitly describe the unit cell.

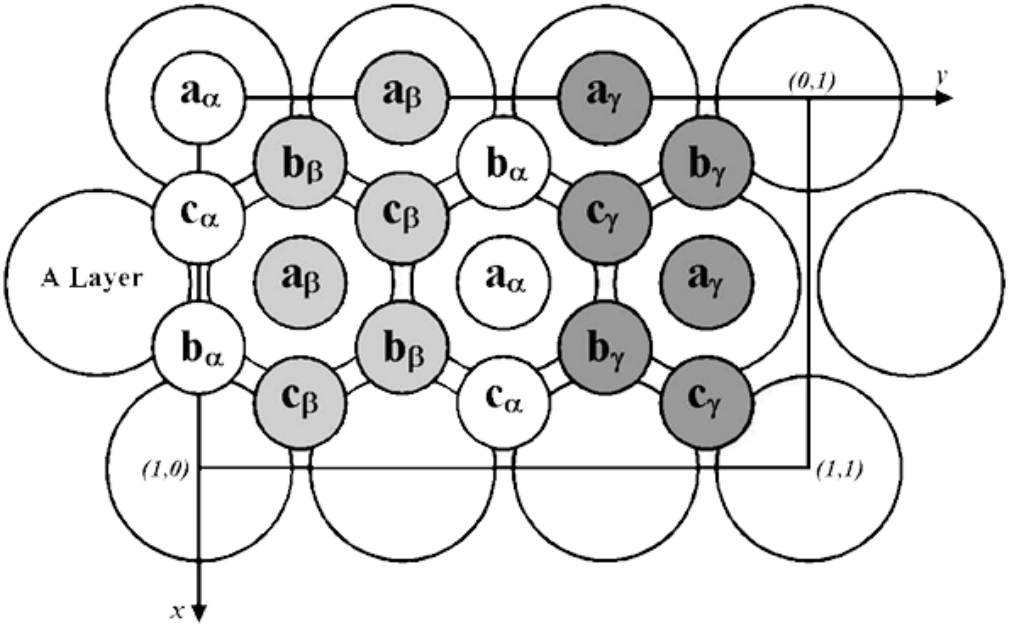

Figure 5.7. Illustration of aluminium pair positions (labelled circles) between the A and B stacking layers of oxygen (after Yourdshahyan *et al*. 1999).

The computational speed of the interatomic potentials used (Gale 1997) allows for a more rigorous investigation of the structural candidates than the Yourdshahyan *et al*. (1999) study. Yourdshahyan *et al*. (1999) excluded structural candidates where Al pairs are in adjacent sites on account of their presumed unfavourable energy. This left a total of 225 structure candidates which was then reduced to 60 after symmetry considerations. Such measures are necessary when

using quantum mechanical techniques due to the computational expense (Payne *et al.* 1992). In this study, the approach taken was to make no assumptions as to the likelihood of any configuration and to thus do an exhaustive search of all possible configurations.

For each independent layer there are 36 possible configurations for the two Al pairs. This gives rise to 36^2 = 1,296 different structures, after considering all possible combinations of the Al pairs between the two independent layers. This was reduced to 666 independent structural candidates after considering the artefact introduced by the structure notation; i.e. 630 of the 1,296 candidates were doubled up as a consequence of the notation system as noted by Yourdshahyan *et al*. (1999). These degenerate structures were related through symmetry, via a 180° rotation of the unit cell around [010] and the translation (½+x, ½+y, z) (Yourdshahyan *et al.* 1997b).

Remaining consistent with the nomenclature used by Yourdshahyan *et al*. (1997a; 1999), the aluminium layers can be categorised in accordance with their Al pair coordination. *O* reflects all Al ions being situated in octahedral sites, *T* indicates complete tetrahedral site occupancy, and *M* (mixed) represents one pair in octahedral and the other pair in tetrahedral positions. This allows independent structural possibilities to be grouped in six ways: *OO*, *OT*, *MO*, *MM*, *MT*, and *TT*, depending on the type of coordination in the first two layers.

In generating the 666 independent structural candidates, the oxygen sublattice was fixed at the same idealised positions for each possible structure, starting with the *A* stacking layer at the origin of the unit cell. Each subsequent stacking layer was positioned a fractional distance of 1/4 apart parallel to the *c*-axis of the unit cell. A program was used to generate the 666 possible independent configurations of the Al ions that were subsequently incorporated within the O sublattice, in accordance with the structure notation hitherto discussed, to complete each idealised unit cell. The *z*-axis positioning of the octahedrally and tetrahedrally coordinated Al ions was half and a quarter of the separation distance between the oxygen layers respectively. These 666 idealised independent candidates were then used as the starting configurations in the calculations. The same initial lattice parameters were used in this study as per the Yourdshahyan *et al*. (1999) study. These were (after

extrapolation to 0 K by Yourdshahyan *et al*. (1999), in Angstroms): a = 4.8041, b = 8.2543, and c = 8.8785.

5.3.4. Results and Discussion: Interatomic Potentials

For all potential sets used, every minimised structure is found to be considerably lower in energy than the starting configuration indicating that the atoms move away from their idealised positions. The starting and minimised energies of all the 666 configurations calculated using the Bush *et al*. (1994) parameters are illustrated in Figure 5.8 as an example. On this scale, the minimised configurations appear to have very similar energies. The lower energies of the starting structures towards the bottom right of Figure 5.8 are due to the higher separation distances between Al pairs, both within and between layers. Often the minimised structural configurations were different to the starting configuration from which they were derived. For example, structure number 662 exhibits an $Ac_{\alpha}c_{\gamma}Bc_{\alpha}c_{\beta}$ starting configuration (*OO*-type coordination). However, after minimisation its configuration was $Ac_{\alpha}c_{\beta}Bb_{\beta}c_{\gamma}$ (*MO*-type coordination) for all sets of potentials used. Focussing in on the minimised energies (Figure 5.9) shows that most starting configurations minimise to one of only seven local minima. This behaviour is observed for all of the potential sets used, except for the Bush *et al*. (1994) potential set where there were ten common local minima. Each minimised energy value represents the same optimised structural configuration. This was verified by examining the **Γ**-point phonon frequencies and structural configurations themselves. It was also observed that the majority of structure candidates minimised to one of the two lowest energy structures.

The starting configurations appeared to have little bearing on the minimised configurations achieved. All minimised structures tended towards either *OO*, *OT* or *MO* coordination. For these final structures, particularly *MO* and *OT*, the minimised configuration was obtained from starting structures of each type of coordination possibilities (*i.e*. *OO*, *OT*, *MO*, *MM*, *MT*, and *TT*).

The lowest energy structure for each of the four sets of potential parameters used all exhibited *MO* coordination, of identical structural configuration (Figure 5.10). The oxygen sublattice was found to remain in close proximity to the idealised starting coordinates upon optimisation, although sometimes a translation of the

sublattice, to varying degrees along any one of the three crystallographic axes was found. The resulting configuration was determined to be $Ac_{\alpha}c_{\beta}Bb_{\beta}c_{\gamma}Ab_{\alpha}b_{\gamma}Cb_{\beta}c_{\gamma}$. Cases existed where the minimised configuration was determined to be $Ac_{\alpha}c_{\gamma}Bb_{\gamma}c_{\beta}Ab_{\alpha}b_{\beta}Cb_{\gamma}c_{\beta}$, which is identical to the previous configuration through a 2_1 screw axis. The absence of imaginary values in the **Γ**-point phonon frequencies calculated at the lowest energy configuration for each potential set, combined with a search for higher symmetry within the Materials Studio software package, confirms that all potential sets predict that the space group is $Pna2_1$, in agreement with experimental observations (Liu and Skogsmo 1991; Halvarsson *et al.* 1995; Halvarsson *et al.* 1999).

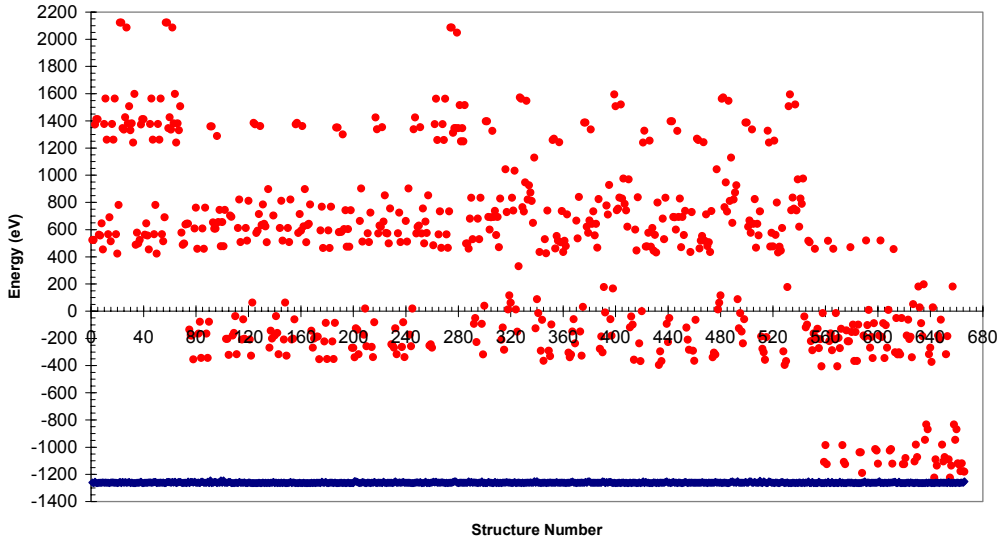

Figure 5.8. Starting and minimised energies for κ-Al_2O_3 candidate structures using the potentials of Bush *et al.* (1994); ● = starting structure energy, ♦= minimised structure energy.

Within the lowest energy structure, significant distortion was evident for the octahedrally coordinated Al ion within the *M* layer, which was accompanied by some perturbation of the immediately adjacent oxygen layers. To illustrate the degree of this distortion, the average Al-O bond length within the octahedra associated with the c_{β} aluminium pair of the *O* layers was typically 1.91 Å, with the bond lengths ranging from 1.90 to 1.97 Å. In contrast, the average Al-O bond length within the octahedra associated with the c_{γ} aluminium pair of the *M* layers was 1.96 Å. Here the range in bond lengths was 1.81 to 2.37 Å. In this instance, aside from the longest

bond length, 2.37 Å, the remaining five bond lengths averaged 1.88 Å, with the longest of these being 1.96 Å. This indicates that the distortion of the *M* layer octahedra is due to one extreme bond length.

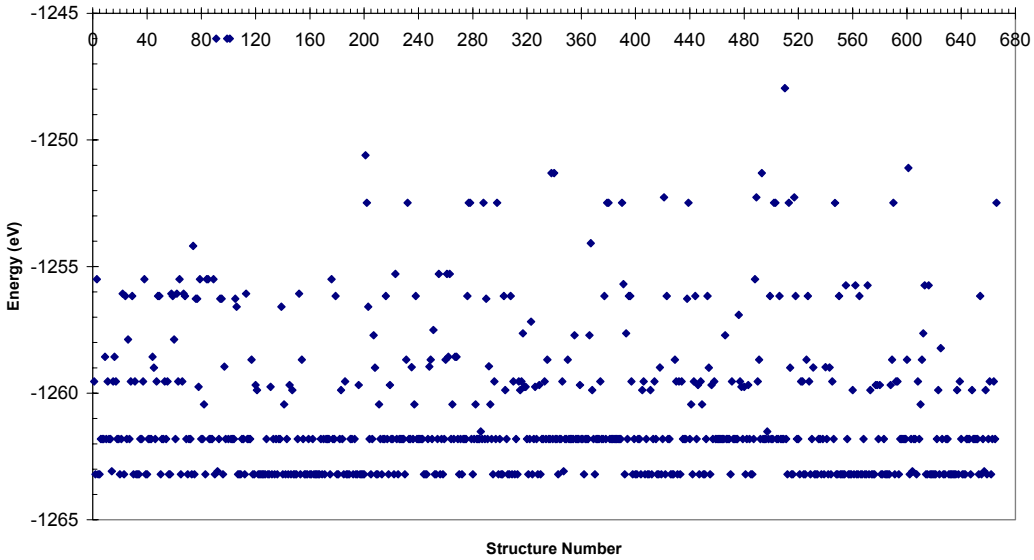

(a)

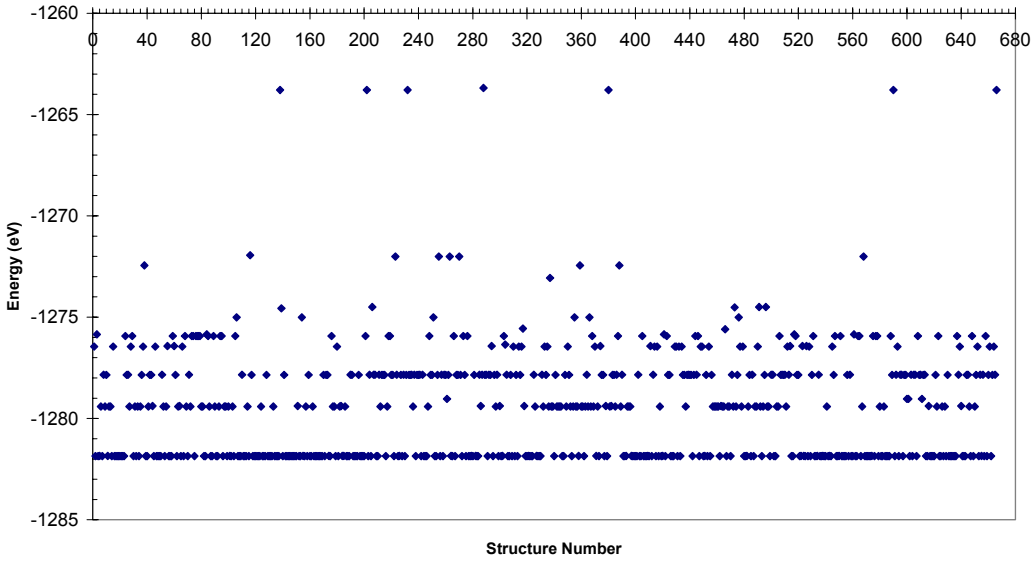

(b)

Figure 5.9. Minimised energies achieved for each of the potential models; (a): Bush *et al*. (1994), (b): Catlow *et al*. (1982).

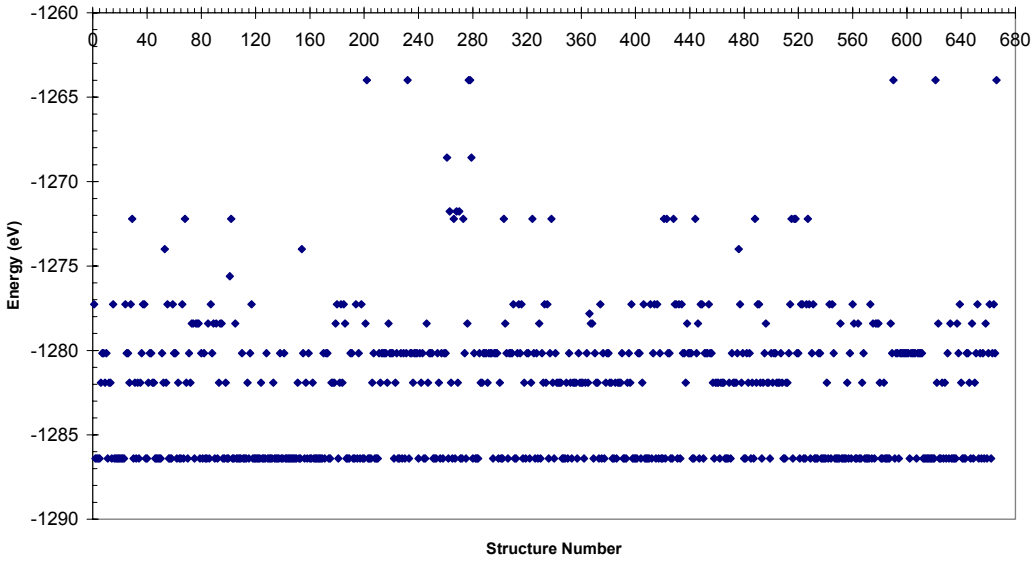

(c)

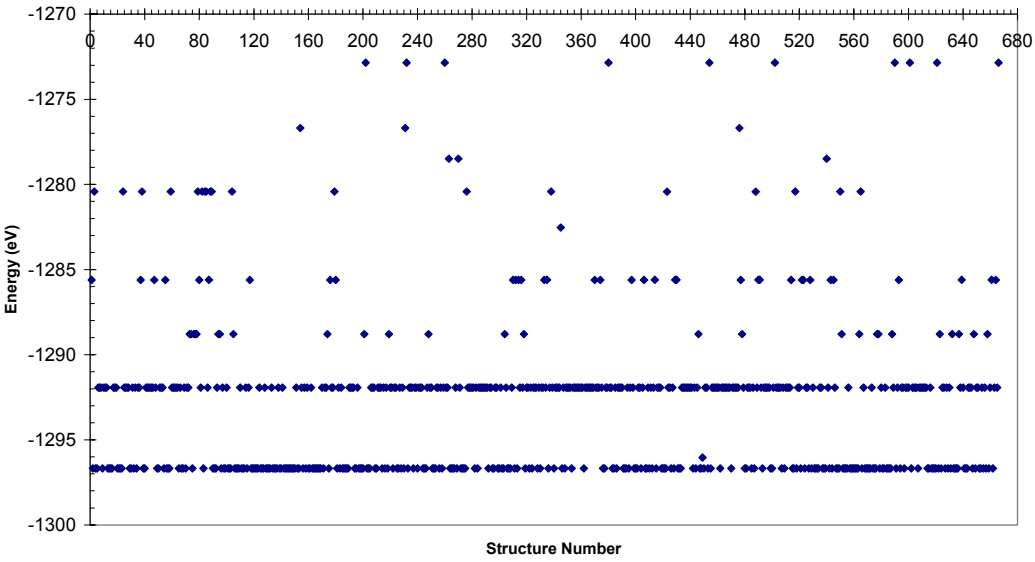

(d)

Figure 5.9 (cont'd). Minimised energies achieved for each of the potential models; (c): Minervini *et al*. (1999), (d): Mackrodt and Stewart (1979).

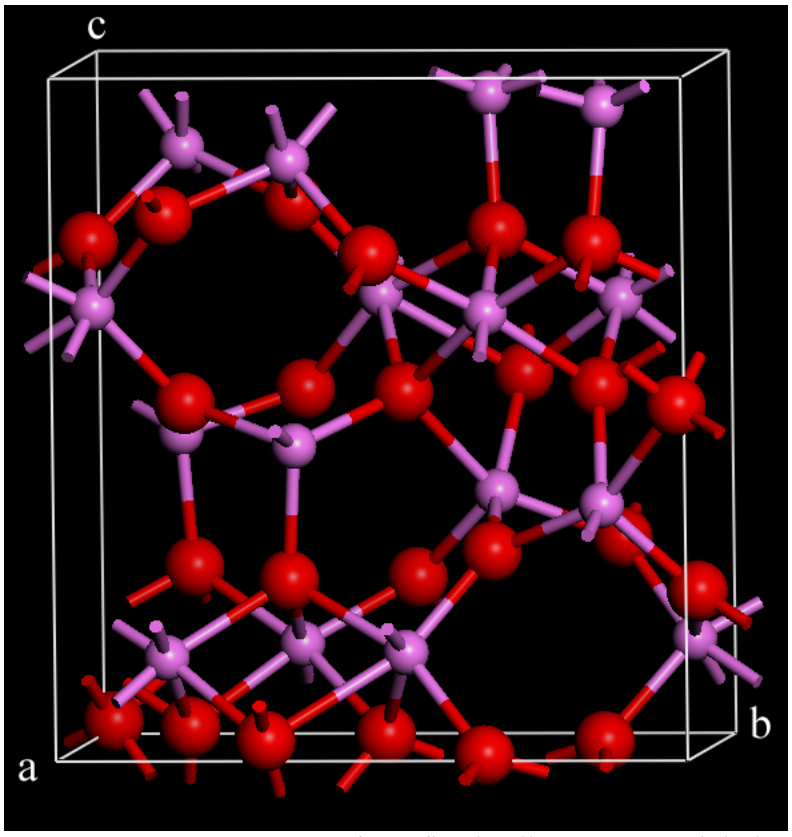

Figure 5.10. Lowest energy structure from fixed cell parameter minimisations; MO coordination; Atomic configuration: $Ac_{\alpha}c_{\beta}\,Bb_{\beta}c_{\gamma}\,Ab_{\alpha}b\gamma\,Cb_{\beta}c_{\gamma}$.

Within the oxygen sublattice, the slight distortion near the octahedrally coordinated Al ions of the *M* layer tended to be out-of-plane deviations in the *z*-direction. Aside from this slight deviation, the oxygen sublattice remained close to the idealised starting configuration provided for the oxygen layers.

The rigidity of the oxygen sublattice was also evident in the highest energy minimised structure (in Figure 5.9 this is the highest line of convergent energies) which exhibited *OO* coordination of the Al sublattice, the atom configuration being $Ac_{\beta}c_{\gamma}Bc_{\beta}c_{\gamma}Ac_{\beta}c_{\gamma}Cc_{\beta}c_{\gamma}$. This was consistently found for all the four potential parameters sets. Compared to the lowest energy structure of *MO*-type coordination, there was very little distortion of the oxygen sublattice (there was no departure from the starting positions in the z-direction), which is attributable to the complete octahedral bonding of the Al ions. Furthermore, the nature of the eigenvalues indicate that the $Ac_{\beta}c_{\gamma}Bc_{\beta}c_{\gamma}Ac_{\beta}c_{\gamma}Cc_{\beta}c_{\gamma}$ structure is stable within the $Pna2_1$ space group symmetry.

All stable structures with total energies between the highest and lowest values exhibit *MO* or *OT* coordination, depending on the potential parameters. For the Catlow *et al*. (1982) and Minervini *et al*. (1999) potential parameters these intermediate energy structures all exhibit *MO* coordination, while for the Bush *et al*. (1994) and Mackrodt and Stewart (1979) parameters, the intermediates were all of *OT* coordination. There was a general trend of increased structural distortion for intermediate structures of higher total energy. In some cases the distortion was severe, to the extent where both ion species occupied the same plane.

The oxygen lattice of the intermediate structures, although appearing to exhibit the correct configuration, demonstrated a general trend of greater distortion with increasing structure energy. As with the lowest energy structure, this distortion tended to be out-of-plane. To illustrate the degree of this, a typical example of the out-of-plane movement of the oxygen sublattice, adjacent to the octahedrally coordinated c_γ Al pair of the *M* layer, was 0.445 Å. In the structure with the second lowest energy this was typically 0.651 Å. As the energy of the structure increased, such distortions were more widespread throughout the lattice. It was not uncommon to see over ⅓ of the oxygen sublattice significantly deviating from their starting coordinates for many of the intermediate structures, while the remainder of the lattice remained in place.

It is understandable that the observed distortions in the structure have occurred given the conditions under which the calculations were performed. The starting structures themselves were highly strained. Cell volumes were fixed with dimensions extrapolated to 0 K during optimisations in order to be consistent with the Yourdshahyan *et al*. (1999) study, whereas the potential parameters used were fitted to ambient temperature data. However, the analysis has shown the lowest energy structure calculated here to be in good agreement with the lowest energy structure determined by Yourdshahyan *et al*. (1999).

Further optimisations were performed on the two most stable minimised structures and this time the lattice parameters were allowed to relax. For all potential sets, except those of Bush *et al*. (1994), this did not change the nature of the lowest energy configuration *i.e.* a *MO*-type structure with a $Ac_\alpha c_\beta Bb_\beta c_\gamma Ab_\alpha b_\gamma Cb_\beta c_\gamma$ configuration.

It is at this stage that the Bush *et al*. (1994) potential parameters can be discarded as unsuitable for the ionic crystal lattice calculations performed here. Although the Bush *et al*. potentials tended yield the same trends, the results were not entirely consistent with those of the other three sets of potential parameters. This can be seen in Figure 5.9 where there were 10 lines of convergent energies for Bush *et al*. (1994) (which were also more difficult to distinguish) as opposed to 7 for Catlow *et al*. (1982), Minervini *et al*. (1999) and Mackrodt and Stewart (1979). Furthermore, it can be seen from Figure 5.9 that the results obtained using the Bush *et al*. (1994) parameters contained, by far, the greatest number of anomalous energies. Finally, although the structure obtained from the second set of optimisations met the conditions of convergence, it was highly distorted and bore no resemblance to the structure from which it was derived or those which resulted for the other three potential parameters used. The calculated structural data for the Catlow *et al*. (1982), Minervini *et al*. (1999) and Mackrodt and Stewart (1979) sets of potential parameters can be found in Tables 5.4 and 5.5.

Assessment of the resulting stable structures (Figure 5.11) for each set of potential parameters and comparison of the unit cell parameters (Table 5.4) shows the Catlow *et al*. (1982) structure to be closest to that of the Yourdshahyan *et al*. (1999) study and experiment (Liu and Skogsmo 1991; Halvarsson *et al.* 1995). All lattice parameters determined in this study were within 1.7% of the experimental values (Table 5.4), with the exception of two from the Mackrodt and Stewart (1979) structure which were within 2.8%. In particular the lattice parameters determined from the Catlow *et al*. (1982) parameters were within 1% of the experimental lattice parameters (Liu and Skogsmo 1991; Halvarsson *et al.* 1995). Considering the approximations made by interatomic potentials, this compares extremely well to first principles calculations, which were also found to be within 1% of the experimental lattice parameters (Liu and Skogsmo 1991; Halvarsson *et al.* 1995).

Yourdshahyan *et al*. (1999) determined the lowest energy structure for κ-Al_2O_3 to also have *MO*-type coordination, with a $Ac_\beta b_\gamma Bc_\alpha c_\gamma Ab_\gamma c_\beta Cb_\alpha b_\beta$ configuration. This structure is related to that determined in this study, by symmetry, through a 180^o rotation about the [020] axis. These two resultant structures are compared in Figure 5.11. The quantum mechanical calculations make the lattice more rigid than the interatomic potentials. Yourdshahyan *et al*. (1999) also reported

anisotropy in the structure, where there was closer packing of the aluminium ions in the [100] direction than in the [010], confirming thermal expansion measurements (Halvarsson *et al.* 1995). This anisotropy was also observed here.

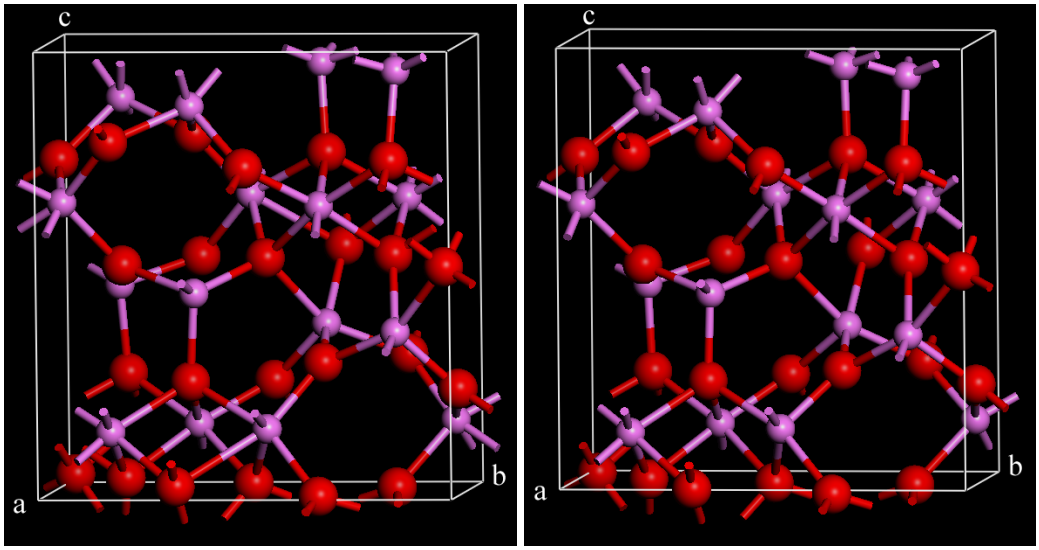

(a) (b)

Figure 5.11. (a): Lowest energy structure determined using the potential parameters of Catlow *et al*. (1982); MO coordination; Atomic configuration: $Ac_{\alpha}c_{\beta}$ $Bb_{\beta}c_{\gamma}$ $Ab_{\alpha}b\gamma$ $Cb_{\beta}c_{\gamma}$. (b): Lowest energy structure determined by Yourdshahyan *et al*. (1999); MO coordination; Atomic configuration: $Ac_{\beta}b_{\gamma}Bc_{\alpha}c_{\gamma}Ab_{\gamma}c_{\beta}Cb_{\alpha}$.

Table 5.4. Lattice Parameters for the κ-Al_2O_3 structure.

	Experimental		***Simulated***			
				This Study		
	Liu & Skogsmo	***Halvarsson et al.***	***Yourdshahyan et al.***	***Catlow et al.***	***Minervini et al.***	***Mackrodt & Stewart***
a (Å)	4.8437	4.8351	4.8041	4.8515	4.8473	4.8520
b (Å)	8.3300	8.3109	8.2543	8.1693	8.2124	8.5425
c (Å)	8.9547	8.9363	8.8785	8.8600	9.0119	9.1480
V (Å^3)	361.3044	359.09	352.07	351.15	358.75	379.17

The O-O distances ranged between 2.52 - 2.87 Å, 2.57 – 2.85 Å, and 2.67 – 2.94 Å, for the Catlow *et al*. (1982), Minervini *et al*. (1999) and Mackrodt and Stewart (1979) optimised structures, respectively. These compare well with the range of 2.52 – 3.00 Å in the final structure determined by Yourdshahyan *et al*. (1999) and also agrees with the empirical ionic radii of Pauling (1944, pp.396-400) and

Shannon[31]. These latter authors indicate that the O-O distance should be 2.8 Å, which lies within the range found here. Furthermore, Pauling (1944, pp.396-400) has indicated that O-O distances along edges shared by two polyhedra should be shorter, as was found to be the case here and in the work of Yourdshahyan *et al*. (1999).

Table 5.5. Calculated atomic coordinates (fractional) for the κ-Al_2O_3 structure.

	Catlow et al			***Minervini et al***			***Mackrodt & Stewart***		
Atom	***x***	***y***	***z***	***x***	***y***	***z***	***x***	***y***	***z***
O(1)	0.8492	0.8438	0.7500	0.8535	0.8415	0.7500	0.8704	0.8366	0.7500
O(2)	0.4794	0.5161	0.5192	0.4860	0.5132	0.5194	0.4843	0.5029	0.5131
O(3)	0.0296	0.6695	0.5279	0.0273	0.6704	0.5270	0.0291	0.6790	0.5198
O(4)	0.9544	0.6741	0.0052	0.9557	0.6769	0.0074	0.9794	0.6763	0.0021
O(5)	0.3457	0.3372	0.7938	0.3567	0.3336	0.7892	0.3614	0.3295	0.7758
O(6)	0.8484	0.4890	0.7323	0.8585	0.4935	0.7392	0.8630	0.4935	0.7332
Al(1)	0.3119	0.9601	0.1505	0.3072	0.9554	0.1500	0.3103	0.9501	0.1433
Al(2)	0.8082	0.1623	0.1447	0.8055	0.1604	0.1440	0.8012	0.1587	0.1369
Al(3)	0.2038	0.1393	0.4498	0.2073	0.1399	0.4450	0.1851	0.1489	0.4392
Al(4)	0.3036	0.6488	0.3665	0.2958	0.6474	0.3681	0.2917	0.6482	0.3583

In the case of the Al-O bond lengths within the octahedra of the lowest energy structure, Yourdshahyan *et al*. (1999) reported these to vary between 1.79 and 2.20 Å, with the average within each octahedron ranging from 1.90 to 1.94 Å. The ranges in the Al-O bond lengths calculated here were 1.79 – 2.33 Å, 1.79 – 2.36 Å, and 1.79 – 2.39 Å, for the structure determined using the Catlow *et al*. (1982), Minervini *et al*. (1999) and Mackrodt and Stewart (1979) potential parameters, respectively. Also, average bond lengths for each octahedron varied from 1.90 – 1.94 Å, 1.89 – 1.96 Å, and 1.90 – 2.00 Å. These values were averaged over the whole unit cell. However, there are three pairs of octahedra within the two independent layers of the κ-Al_2O_3 structure, two in the *O* layer and one in the *M* layer, and in Table 5.6 the results are given separately. Further comparison can be found in the Al-O bond lengths, within octahedra, of Shannon (1976), being between 1.895 and 1.925 Å.

Each of these pairs of octahedra was found to exhibit a different degree of distortion. It is therefore pertinent to examine the nature of the bonding and distortions more thoroughly (Table 5.6). To provide the appropriate comparison, the

same expression was used to quantify the distortion, Δ, as per Yourdshahyan *et al*. (1999):

$$\Delta = \frac{1}{N}\sum_{i=1}^{N}\left(\frac{R_i - R_{av}}{R_{av}}\right)^2 \qquad (5.1)$$

where N is the number of corners of the polyhedron, R_i is an individual Al-O bond length, and R_{av} is the average Al-O bond length within the polyhedron (Pauling 1944, pp.396-400). The relative size of the distortions in each of the octahedra was found to agree with those of Yourdshahyan *et al*. (1999).

Table 5.6. Al-O bond length data within the octahedra of the κ-Al_2O_3 structure.

				This Study		
	Al pair (This study)		***Yourdshahyan et al.***	***Catlow et al.***	***Minervini et al.***	***Mackrodt & Stewart***
O Layer	C_α	Range (Å)	1.79 -2.19	1.79 - 2.17	1.79 - 2.23	1.79-2.24
		Average (Å)	1.93	1.92	1.94	1.90
		Δ	51×10^{-4}	47×10^{-4}	72×10^{-4}	67×10^{-4}
	C_β	Range (Å)	1.79-1.94	1.79-1.94	1.80 -1.94	1.90 - 2.03
		Average (Å)	1.90	1.90	1.89	1.94
		Δ	7.2×10^{-4}	6.9×10^{-4}	8.0×10^{-4}	12×10^{-4}
M Layer	C_γ	Range (Å)	1.80 - 2.20	1.79 - 2.33	1.80 - 2.36	1.83 - 2.39
		Average (Å)	1.94	1.94	1.96	2.00
		Δ	55×10^{-4}	90×10^{-4}	94×10^{-4}	95×10^{-4}

The Al-O distances within the tetrahedra of the lowest energy structure ranged between 1.75 – 1.79 Å, 1.75 – 1.79 Å, and 1.74 – 1.79 Å for Catlow *et al*. (1982), Minervini *et al*. (1999) and Mackrodt and Stewart (1979), respectively, with averages of 1.78 Å, 1.78 Å, and 1.77 Å. The value reported by Yourdshahyan *et al*. (1999) was a range of 1.73 – 1.77 Å, and an average of 1.75 Å, for the Al-O lengths within the tetrahedra. Shannon (1976) provides the Al-O values between 1.75 and 1.77 Å for tetrahedra. In light of these results, it is concluded that in this study the Al-O bond lengths calculated for both octahedra and tetrahedra, agree with the results of Yourdshahyan *et al*. (1999) and the values provided by Shannon (1976).

Further comparison of the structures determined here shows that they are in good agreement with that determined by Ollivier *et al*. (1997) who found the Al-O bonds within the octahedra to vary between 1.72 and 2.27 Å. The lattice parameters were determined by Ollivier *et al*. (1997) to be a = 4.8437 Å, b = 8.3300 Å and c = 8.9547 Å. With the exception of the b lattice parameter of the Mackrodt and Stewart (1979) structure (which shows a 4.0% deviation) the largest difference between those of Ollivier *et al*. (1997) and the present work is 1.9% with an average deviation of 0.9%. A direct comparison with the parameters of Yourdshahyan *et al*. (1999) and those determined here shows average deviations of 0.7, 0.8 and 1.9% for the potentials of Catlow *et al*. (1982), Minervini *et al*. (1999) and Mackrodt and Stewart (1979), respectively.

5.3.5. Implementation of Quantum Mechanical Calculations

When a diffraction pattern is generated from the interatomic potential calculations and compared to one that was obtained experimentally (Figure 5.12), a small problem with the structures derived from empirical potentials becomes apparent. The more significant disorder in the optimised structure from interatomic potentials is signified by the split peaks, typical of a break in the symmetry of the structure with respect to experimental observation. Figure 5.13 highlights the most obvious examples of the splitting between the two diffraction patterns.

When the lowest energy stable structure from the interatomic potential calculations is viewed down the a axis, the cause of the reduced symmetry compared to experiment is apparent (Figure 5.14a). There is significant distortion out of the plane of the oxygen atoms immediately adjacent to the octahedrally coordinated Al ions from the *MO* layers. When DFT is applied, this distortion is reduced significantly (Figure 5.14b). The lattice parameters determined for the final structure, using first principles calculations, performed for this study differed by no more than ± 0.17 Å from those determined by Ollivier *et al*. (1997).

The agreement between the structure obtained in this study and the experimental study by Ollivier *et al*. (1997) can be seen by viewing the diffraction patterns of the respective structures (Figure 5.15). Not surprisingly, from Figure 5.15, it can be seen that peak positions are very similar because of the similarities between unit cell parameters. Furthermore, peak intensities, which are determined by

atom positions, are also similar, indicating a good match between the κ-Al_2O_3 structure determined through experiment and first principles calculations of this study. The calculated structural data from the DFT optimisation can be found in Table 5.7. The difference in the cell volumes between this study and the Yourdshahyan *et al*. (1999) study results from the method used to approximate the exchange-correlation energy. Yourdshahyan *et al*. (1999) employed the LDA, which results in a slight underestimation of the unit cell volume. Here, the GGA was used, which results in a slight overestimation of the unit cell volume. The calculated band gap energy was 5.3 eV, an exact match with the value calculated by Yourdshahyan *et al*. (1999).

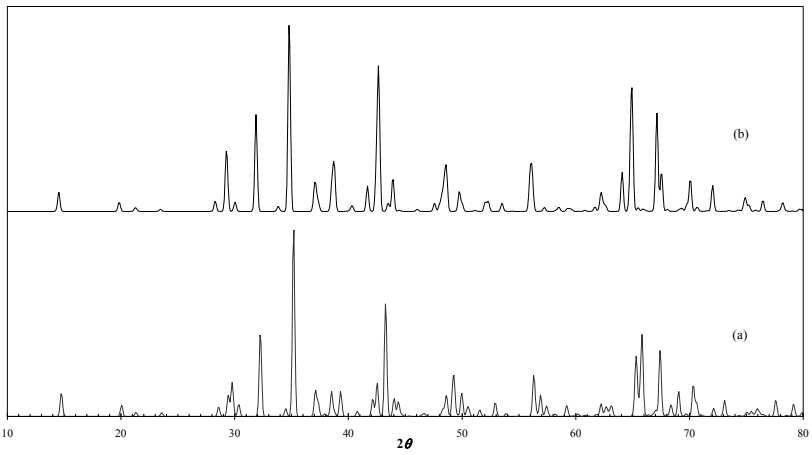

Figure 5.12. Powder XRD patterns; (a): generated from the optimised structure based on the potentials of Catlow *et al*. (1982), (b): Ollivier *et al*. (1997) experimental results.

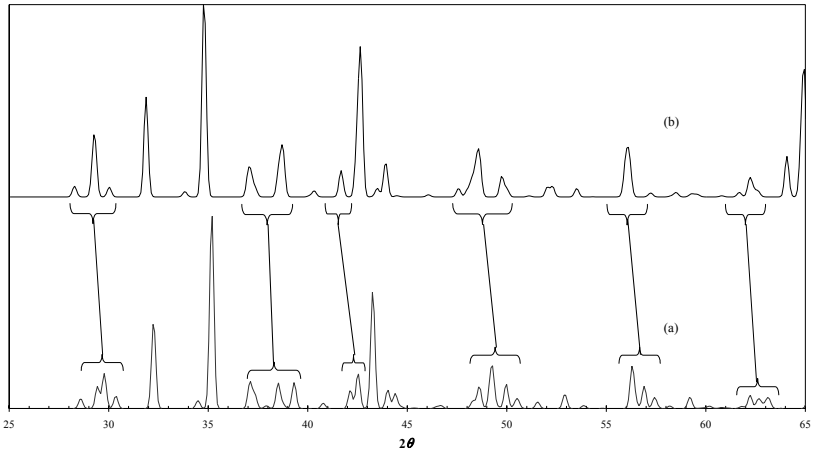

Figure 5.13. Closer view of powder XRD patterns from Figure 5.12. The brackets and adjoining lines indicate corresponding regions in (a) where the splitting occurs, representing a break in the symmetry compared to (b).

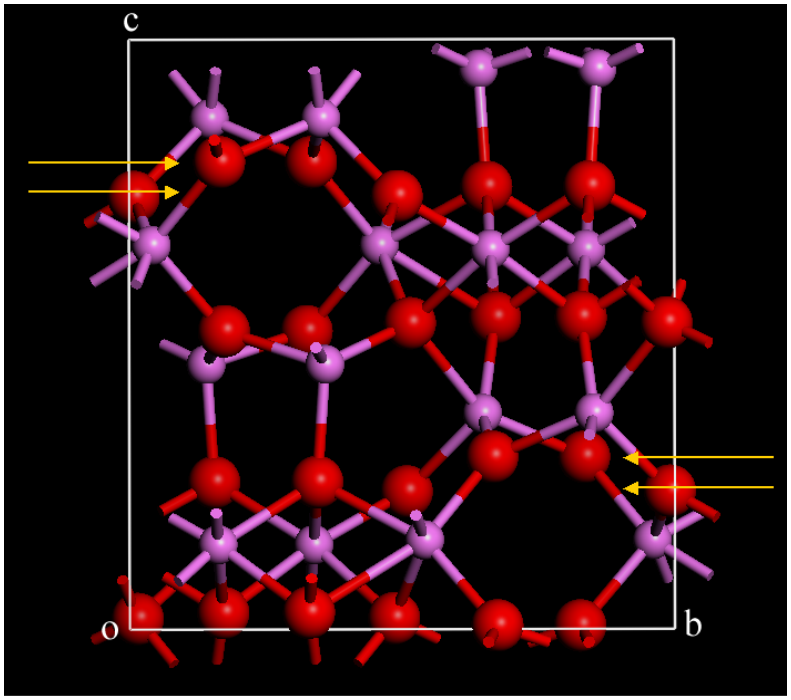

(a)

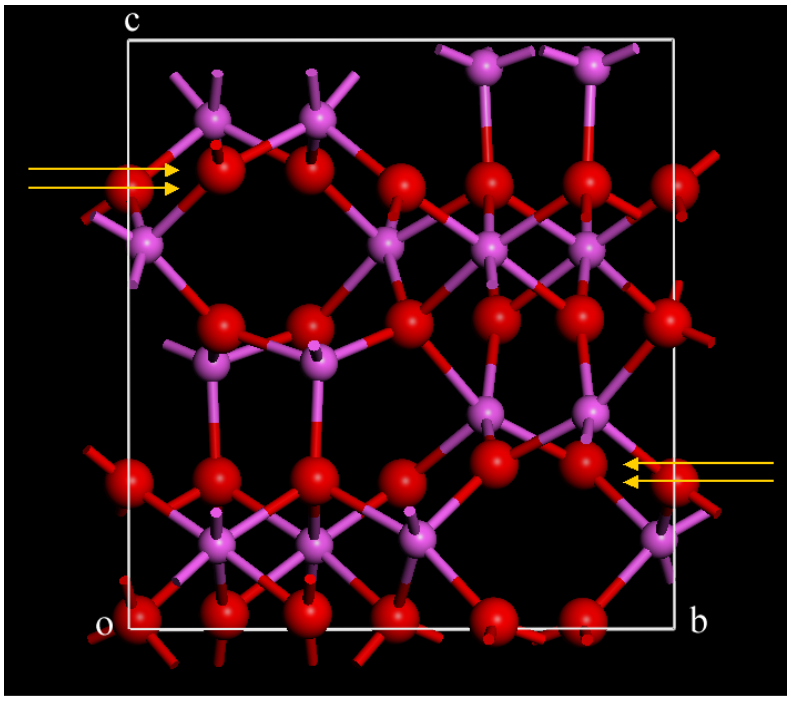

(b)

Figure 5.14. (a): Lowest energy stable structure determined using the potential parameters of Catlow *et al*. (1982) viewed down the *a* axis, (b): after optimisation with DFT. The arrows provide an indication of how far out plane the distorted oxygen atoms have moved. DFT clearly reduced the amount of distortion in the oxygen sublattice.

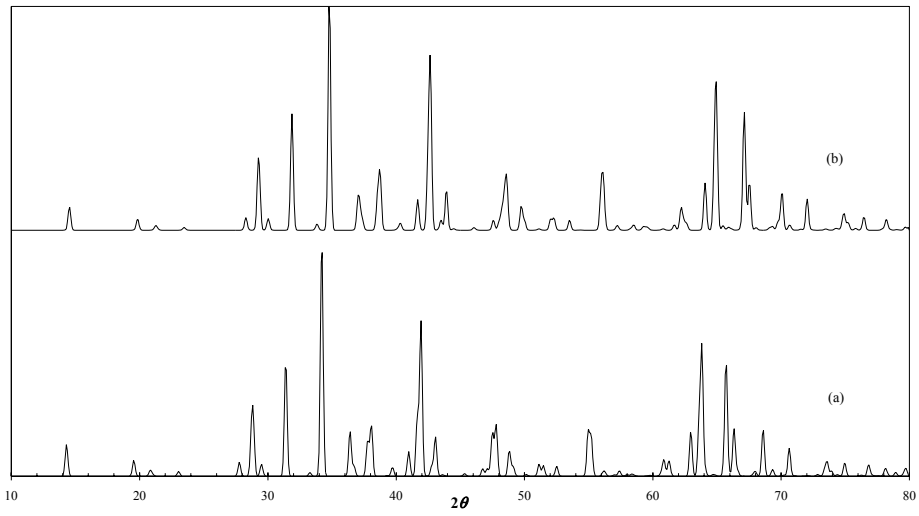

Figure 5.15. Powder XRD patterns; (a): generated from the lowest energy stable structure optimised using DFT, (b): Ollivier *et al*. (1997) experimental results.

Table 5.7. Calculated cell parameters and fractional atomic coordinates for the κ-Al_2O_3 structure using DFT. Calculation performed using 16 **k**-points, a 220 Ry mesh and an energy shift of 0.01 Ry.

a = 4.9312 Å, b = 8.4344 Å, c = 9.0686 Å, V = 377.1817 Å^3			
Atom	***x***	***y***	***z***
O(1)	0.84440	0.83969	0.75207
O(2)	0.480600	0.51348	0.51704
O(3)	0.02562	0.67386	0.52497
O(4)	0.97736	0.66843	0.01044
O(5)	0.34310	0.33146	0.77869
O(6)	0.84402	0.49954	0.74707
Al(1)	0.3258	0.97118	0.15179
Al(2)	0.81534	0.16050	0.14293
Al(3)	0.18047	0.15140	0.45194
Al(4)	0.31474	0.65370	0.36364

5.3.6. Outcomes from Case Study

The purpose of the case study was to investigate the structure of κ-Al_2O_3, using interatomic potentials, followed by a first principles calculation on the most stable structure, and compare the results with a large first principles study and experimental determinations. Of the four sets of potential parameters examined, only

one, those of Bush *et al* (1994), proved unsuitable for this particular study. The remaining three were found to predict the same most stable structure, which in turn was in close agreement to the first principles calculations of Yourdshahyan *et al*. (1999) and experiment (Ollivier *et al.* 1997). Furthermore, of these three sets of potential parameters, those of Catlow *et al*. (1982) were found to produce the results which most closely matched the first principles study. The structure obtained from the interatomic potential calculations was found to exhibit a more distorted oxygen sublattice compared to the true structure of κ-Al_2O_3. This distortion was reduced after optimisation using DFT. The resulting structure was found to be representative of the true structure of κ-Al_2O_3.

It can therefore be concluded that the stable structure of κ-Al_2O_3 is of *MO*-type coordination, with $Ac_\alpha c_\beta Bb_\beta c_\gamma Ab_\alpha b_\gamma Cb_\beta c_\gamma$ configuration. This is equivalent to $Ac_\beta b_\gamma Bc_\alpha c_\gamma Ab_\gamma c_\beta Cb_\alpha b_\beta$, reported by Yourdshahyan *et al*. (1999) through symmetry.

Interatomic potentials have therefore proven suitable for use in such investigations where stable structures need to be determined from an enormous number of possibilities. In this case, the speed of interatomic potentials has enabled every possible starting configuration of κ-Al_2O_3 to be investigated, four times over, in a fraction of the time compared to the DFT study by Yourdshahyan *et al*. (1999). Furthermore, the empirical method used also delivered an acceptable level of accuracy. With this in mind it makes sense to begin any computational study with a broad survey of possible structures, using faster methods, before striving to achieve high accuracy for a few cases.

Given the scale of the calculations required for γ-Al_2O_3, only the Catlow *et al*. (1982) potentials were used because they were the most accurate in this case study. The computational investigation of γ-Al_2O_3 will yield cation configurations with precise coordinates for every cation. This cannot be provided by any of the experimental techniques being employed here. This will provide a more detailed knowledge of the structure which, in turn, will aid future attempts to understand mechanisms of transition to other structure and the mechanisms by which applications of γ-Al_2O_3 work.

Chapter 6

Preliminary Experimental Findings: Heating Trials

Portions of this chapter have been published in:

G. Paglia, C.E. Buckley, A.L. Rohl, R.D. Hart, K. Winter, A.J. Studer, B.A. Hunter, and J.V. Hanna 2004, "The boehmite derived γ-alumina system, 1: Structural evolution with temperature, with the identification and structural determination of a new transition phase, γ'-alumina," Chemistry of Materials, ***16****, pp. 220-236.*

6.1 Procurement of Appropriate Boehmite Precursor

Before the experimental methodology, described in *section 5.1*, could be followed, preparation methods for suitable precursor were investigated. Based on the review in *Section 2.1*, it appears that the best way to ensure the formation of a 100% γ-Al_2O_3 sample is to ensure that the boehmite is highly-crystalline. Moreover, boehmite was chosen as the desired precursor as opposed to amorphous alumina for two reasons. Firstly, it is known that several transition phases can crystallise concurrently from the melt whereas they occur individually when derived from boehmite (Plummer 1958; Baraton and Quintard 1982; Morrissey *et al.* 1985; Jayaram and Levi 1989). The other consideration is the relative ease of obtaining and storing sufficient precursor.

From DTA, it was indicated by Wefers and Misra (1987, pp.46-47) and Gan (1996, p.78) that the formation of boehmite can occur separately to the formation of χ-Al_2O_3 when calcining gibbsite. These researchers suggested that this is facilitated by calcining gibbsite particles with larger particle sizes, resulting in an endotherm corresponding to the onset of boehmite formation at lower temperatures than χ-Al_2O_3. These findings were used as the basis of heating trials to investigate the best possible procedure for obtaining highly-crystalline boehmite precursor.

Gibbsite of high particle size, ≈ 211 μm volume weighted mean (*Appendix 1*), was synthesized according to the procedure outlined in *section 4.1.1* for use in the heating trials for boehmite synthesis. Alcoa C31 hydrogenated gibbsite, with

≈ 82 μm volume weighted mean (*Appendix 1*), was also used in the heating trials. These particle sizes were verified by visual inspection with scanning electron microscopy (SEM).

DTA-TGA (*section 4.1.3*) was performed on both gibbsite samples. The DTA-TGA curves were similar for both samples, and analogous to those described in the literature (Wefers and Misra 1987, pp.46-47; Gan 1996, p.78). Figure 6.1 shows the DTA-TGA curve obtained for the Alcoa C31 product. Both the synthesized and Alcoa C31 gibbsite displayed a small endotherm at ≈ 250 °C, with ≈ 4% associated weight loss, coinciding with the onset of formation of boehmite. The large endotherm at ≈ 326 °C corresponds to two concurrent processes: (i) transformation of gibbsite to χ-Al_2O_3 and (ii) further conversion of gibbsite to boehmite (Gan 1996, p.79). The endotherm at ≈ 541 °C in Figure 6.1 (≈ 539 °C for the synthesized gibbsite) represents the formation of γ-Al_2O_3.

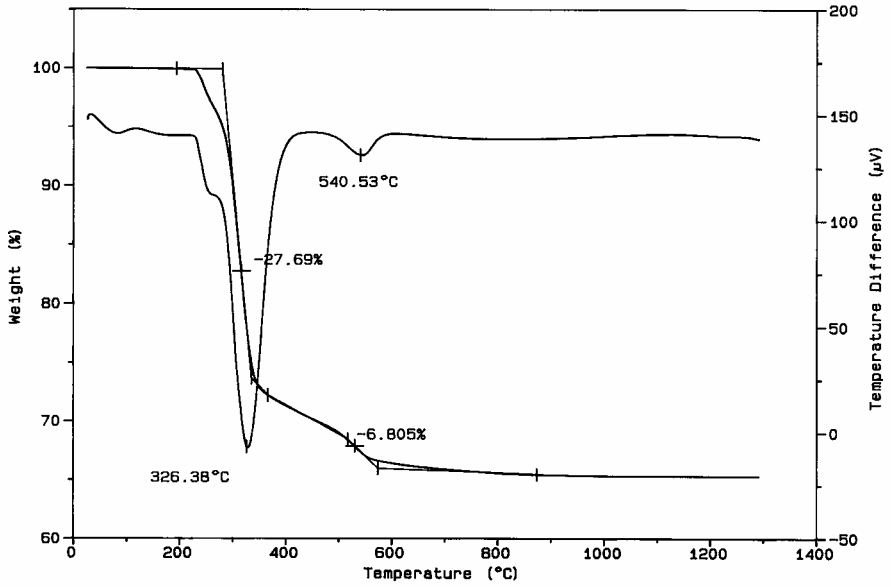

Figure 6.1. DTA-TGA results for Alcoa C31 gibbsite.

Based on the DTA-TGA, temperatures in the range of 200 to 320 °C were selected for calcination of gibbsite for the boehmite synthesis heating trials. The heating rate was 5 ° per minute and durations of calcination were between 4 and 16 hours.

Complete dehydration of gibbsite was not observed until the calcination was carried out at 285 °C for eight hours. However, it was found that the concurrent

formation of boehmite and χ-Al_2O_3 could not be avoided. Figures 6.2 and 6.3 show examples of calcination products where gibbsite dehydration was complete.

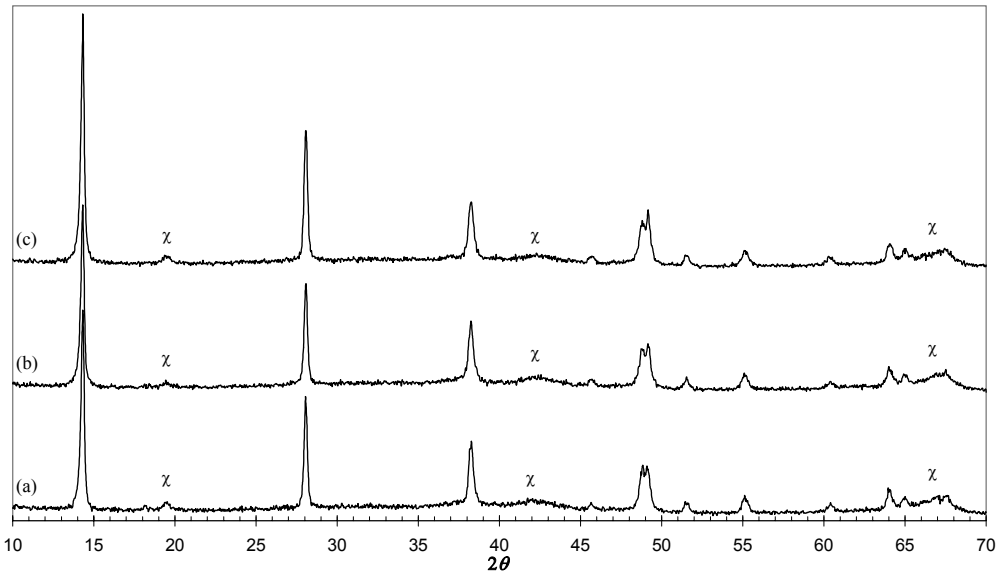

Figure 6.2. Example XRD scans of calcination products from (a): Alcoa C31 gibbsite calcined at 285 °C for eight hours, (b): Alcoa C31 gibbsite calcined at 315 °C for six hours, (c): synthesised gibbsite calcined at 315 °C for six hours. The broad lumps and diffuse peaks, indicated by χ, represent the χ-Al_2O_3 phase. All other peaks characterise boehmite.

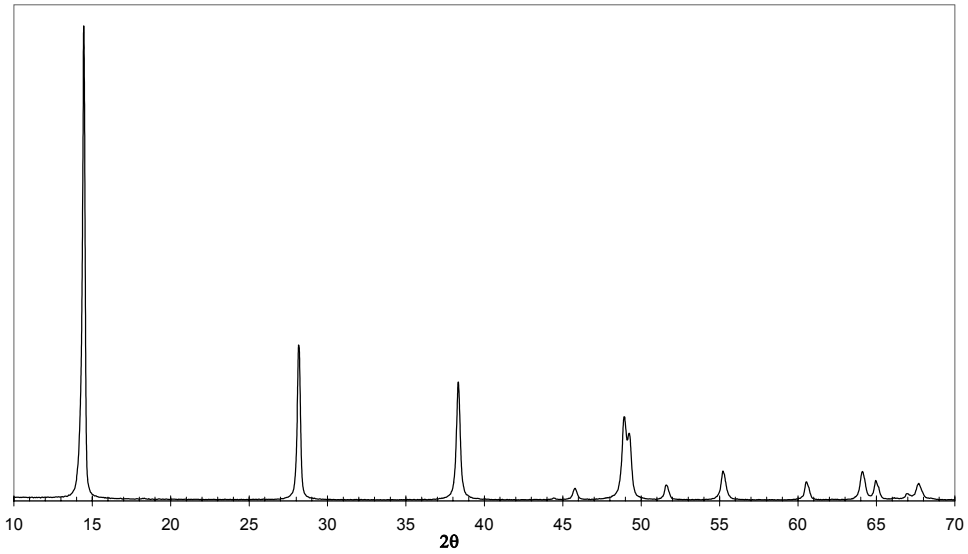

Figure 6.3. Example XRD scan of boehmite prepared by hydrothermal treatment of synthesised gibbsite at 158 °C for 10 days. The major peak intensities are much higher than those from Figure 6.2 and the background is lower.

Hydrothermal treatment of gibbsite at 158 °C in a Barc bomb, for periods between 7 and 10 days was then trialed (s*ection 4.1.1*), following from the work of Laubengayer and Weisz, (1943), Stumpf *et al*. (1950) and Ervin and Osborn (1951). XRD patterns of the hydrothermal product show a single phase consisting of boehmite (Figure 6.3). There was little or no background, in contrast to the higher, diffuse background observed for the calcination products (Figure 6.2). The hydrothermally produced boehmite was found to exhibit the same diffraction pattern as the highly-crystalline boehmite obtained from the Alumina and Ceramics Laboratory, Malakoff Industries, Arkansas, USA. Hence highly-crystalline boehmite precursor for the systematic study of γ-Al_2O_3 was obtained by hydrothermal treatment of gibbsite in accordance with the procedure detailed in *section 4.1.1*.

6.2 Establishing Suitable Calcination Procedures for Systematic Study of γ-Alumina

6.2.1 Thermal Analysis

DTA-TGA analysis of a hydrogenated boehmite sample (Figure 6.4a) shows an endotherm at ≈ 542 °C, which corresponds to the lattice changes coinciding with the transformation of boehmite to γ-Al_2O_3. A total of ≈ 16 wt. % was lost during the whole scan, the majority of which occurred with the formation of γ-Al_2O_3. The TGA curve also shows a less significant loss of mass before the major downward slope, between 400 and 500 °C, corresponding to the onset of transformation. DTA-TGA was also performed on a deuterated boehmite sample and exhibited a similar mass loss of ≈ 17 wt. % during the whole scan. The endotherm, representing the transformation to γ-Al_2O_3 occurred at a slightly lower temperature of ≈ 529 °C. Particle size appears to be the most obvious factor in the temperature differences, with the mean particle sizes being ≈ 16 μm and ≈ 4 μm for the hydrogenated and deuterated boehmite respectively. Beyond the conversion to γ-Al_2O_3 there are no endotherms indicating transformation to other phases and almost negligible mass loss.

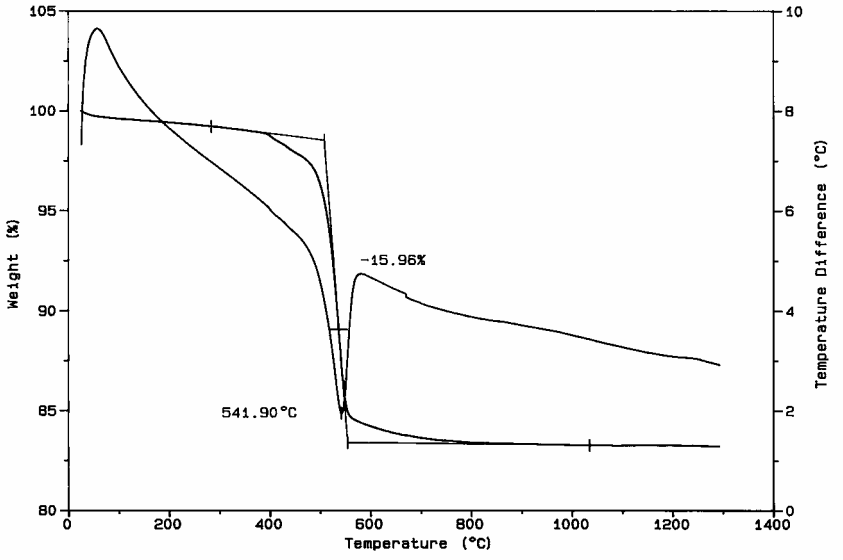

(a)

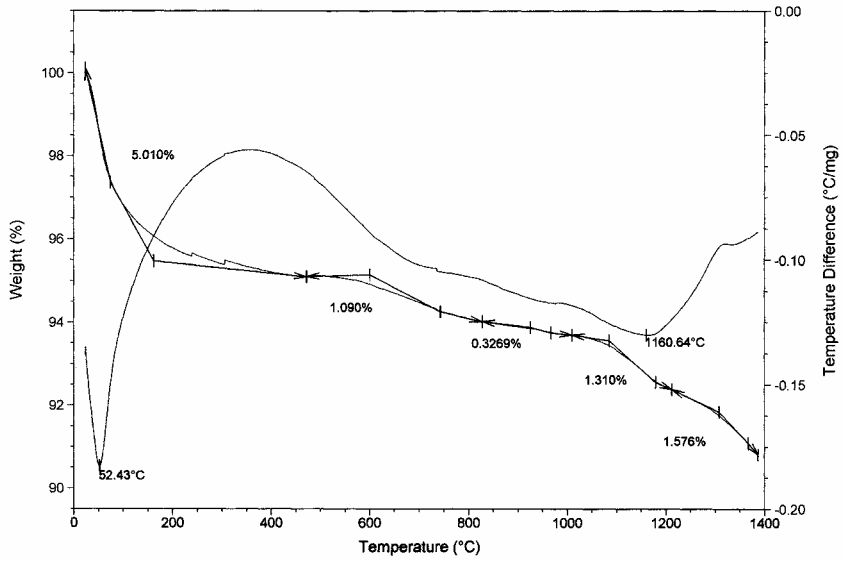

(b)

Figure 6.4. DTA-TGA results for (a): hydrogenated boehmite and (b): γ-Al_2O_3 sample resulting from the calcination of hydrogenated boehmite at 600 °C.

The relative scale of the endotherm, and corresponding mass loss (Figure 6.4a) makes it difficult to see events that occur beyond the transformation to γ-Al_2O_3. Hence DTA-TGA analysis was performed on a hydrogenated γ-Al_2O_3 sample calcined at 600 °C (Figure 6.4b). The endotherm at ≈ 52 °C and mass loss to ≈ 450 °C correspond to the loss of surface adsorbed water. A second endotherm at

≈ 1161 °C and mass loss of ≈ 2.8 wt. % corresponds to the formation of α-Al_2O_3. Preceding this temperature, there are no endotherms indicative of significant lattice changes. However, there are small inflection points in the TGA curve at ≈ 750 and 950 °C, which coincide with the approximate formation temperatures expected for the δ and θ phases (Wefers and Misra 1987). The lack of endotherms with marginal mass losses in DTA-TGA curves after the formation of γ-Al_2O_3 suggest a higher-order phase transformation. This implies continuous variation of the sub-cell parameters in the transformation from γ-Al_2O_3.

6.2.2 Heating Trials for the Effect of Milling and Calcination Time

As supplied hydrogenated boehmite was used for heating trials to investigate the effect of milling on the formation of γ-Al_2O_3 sample. The starting material had ≈ 16 μm particle size. This was compared with as supplied boehmite that was milled for 1 minute, resulting in a mean particle size between 4 and 5 μm. The material was calcined for intervals of 1.5, 3, 4, 7 and 10 hours. Milling was found to affect the diffraction patterns. It showed that less time and temperature was required to cause the formation of γ-Al_2O_3 from boehmite.

The onset of formation of γ-Al_2O_3 was 400 °C. This was only marginally apparent for both the milled and un-milled material, with the only discrepancy between the diffraction pattern of the 400 °C calcination product (Figure 6.5a) and parent material (Figure 6.3) being the increased diffuse nature of the peaks, particularly at $2\theta > 50$ °. This stage most likely represents initial loss of water associated with the break down of hydroxide layers of boehmite and the formation of pores (Lippens and de Boer 1964; Wilson 1979b). There was little difference in the diffraction patterns for the milled and unmilled material. The milled material exhibited a slightly higher increase in background with some increasingly diffuse peaks. This difference between the milled and un-milled material was consistent for all calcination intervals. Conversion to γ-Al_2O_3 did not occur in significant quantity for the calcination intervals used. Previous workers have required calcination for up to one week to effect full conversion to γ-Al_2O_3 from boehmite at 400 °C (Wilson 1979b; Wilson 1979a; Wilson and McConnell 1980).

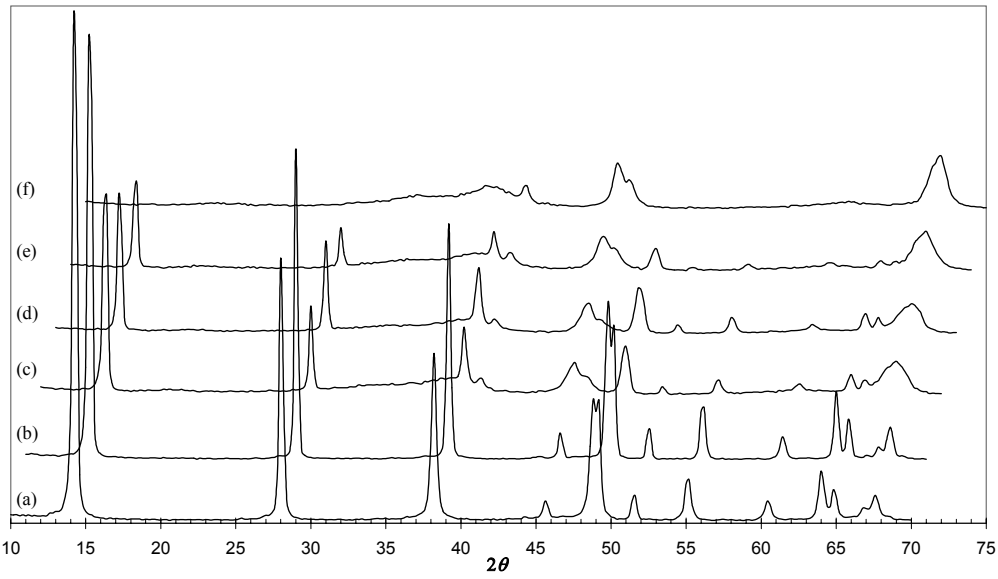

Figure 6.5. Example XRD scans from heating trials to investigate the effect of milling and calcination time, (a): milled boehmite calcined at 400 °C for seven hours, (b): unmilled boehmite calcined at 450 °C for seven hours, (c): milled boehmite calcined at 450 °C for seven hours, (d): unmilled boehmite calcined at 500 °C for one and a half hours, (e): milled boehmite calcined at 500 °C for one and a half hours, (e): unmilled boehmite calcined at 500 °C for seven hours. Plot (a) is almost entirely boehmite. Complete conversion to γ-Al_2O_3 is illustrated in plot (f). The plots are offset so that the change in peak intensities can be observed easily.

At 450 °C there was little difference between the diffraction patterns of the milled and un-milled materials for calcination intervals up to 4 hours. However, considerable change in the diffraction pattern was observed for milled material calcined for seven hours, with significant γ-Al_2O_3 peaks present. Diffraction patterns for both the milled and unmilled material calcined at seven hours are shown in Figure 6.5 (b and c). For the unmilled material, the diffraction pattern retains the major characteristics associated with boehmite (Figure 6.5b). However, there is considerable reduction in the intensity of the peak at $2\theta \approx 14$ °. The diffraction pattern is markedly different for the milled material (Figure 6.5c). There is a major reduction in the intensities of the peaks associated with boehmite and an increase in the intensity and diffuse nature of peaks associated with γ-Al_2O_3. Nonetheless, full conversion to γ-Al_2O_3 at 450 °C was not observed for the calcination intervals investigated. It has been found to require at least 20 hours to result in full conversion (*section 6.2.3*).

At 500 °C, 100% conversion to γ-Al_2O_3 occurred within three hours of calcination time, regardless of the particle size (Figure 6.5f is an example of 100% γ-Al_2O_3 powder). At lower calcination intervals the main boehmite peaks remain, however, the much higher background and greater diffuse nature of peaks show clear progression towards the formation of γ-Al_2O_3. Figure 6.5 (d and e) provides an example of milled and un-milled material calcined at 500 °C for 1.5 hours. The milled material exhibited considerably more diffuse peaks and greater reduction in boehmite peak intensity than the un-milled material. It should be noted that when calcination was performed *in situ*, *i.e.* with the boehmite precursor heated sequentially though the entire temperature range, full conversion to γ-Al_2O_3 at 500 °C was effected within half an hour.

For all temperatures above 600 °C, full conversion from boehmite to γ-Al_2O_3 was effected within one hour.

6.2.3 Kinetic Study of Neutron Diffraction Data Calcined *In Situ*

The differences between *in situ* neutron diffraction data obtained at each calcination temperature were examined to investigate at which temperatures lattice changes occur. This was accomplished by subtracting the neutron diffraction data collected in hourly intervals from the data collected during the final hour of calcination to yield a difference plot. Asymmetric spikes in the difference plot signify structural changes in the material.

The neutron data showed that conversion of boehmite to γ-Al_2O_3 was complete by 500 °C. Difference plots indicated that the greatest lattice changes during the whole calcination period occurred at 450 °C (Figure 6.6a) for both the hydrogenated and deuterated samples, indicating the phase transformation. For the deuterated boehmite, the onset of phase transformation occurred at 400 °C, with minor asymmetric spikes being observed. The earlier onset of phase transformation for neutron diffraction data may be explained by the slower heating rate and more prolonged heating times compared to the DTA-TGA (*section 4.1.3*). Each DTA-TGA scan, from ambient temperature to 1200 °C, was completed within one hour whereas the *in situ* heating of the samples during the collection of neutron diffraction data was carried out for seven to 13 hours at each calcination temperature.

Extended *in situ* calcination was carried out for prolonged periods at 450 °C. It was determined that kinetic effects (signified by asymmetric spikes in the difference plots) remained present for 16 and 20 hours for hydrogenated and deuterated boehmite respectively. This indicates that these were the minimum times required to effect full transformation from boehmite to γ-Al_2O_3 for the two materials investigated.

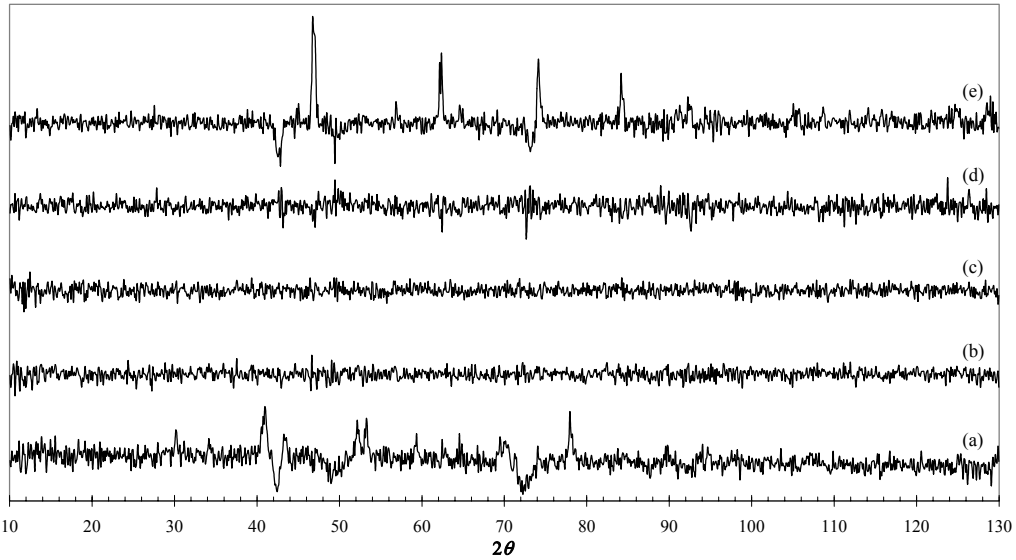

Figure 6.6. Example difference plots from neutron diffraction data collected *in situ* during calcination, of deuterated boehmite precursor, at (a): 450 °C, (b): 500 °C, (c): 700 °C, (d): 900 °C and (e): 950 °C.

The difference plots showed no further lattice changes beyond 450 °C until 900 °C (Figure 6.6) for the deuterated boehmite and 950 °C for the hydrogenated boehmite. The changes at these temperatures were marginal and become more significant at higher temperatures. As with occurrence of endotherms at different temperatures for the different materials investigated with DTA-TGA (*section 6.2.1*), particle size is the most obvious factor in the temperature differences between the occurrence of lattice changes for deuterated and hydrogenated boehmite respectively. The lattice changes at 900 °C and above correspond to the onset of formation of θ-Al_2O_3. The absence of lattice changes between 500 and 850 °C for the deuterated boehmite, and 900 °C for the hydrogenated boehmite, suggest that the δ-Al_2O_3 phase may not form.

For all temperatures between 500 and 900 °C no kinetic effects were observed after the first half hour of calcination. This was confirmed by Rietveld

refinements of hourly data sets, which showed negligible change in the lattice parameters and unit cell coordinates for the duration of calcination at each of these temperatures. This allowed for the addition of multiple hourly data sets to yield better statistics for the structure determinations by Rietveld refinement (*Chapters 7* and *8*).

6.2.4 Outcomes Pertinent to this Study

The objective of these heating trials was to elucidate an appropriate calcination procedure for obtaining a sufficient quantity of pure γ-Al_2O_3 in optimum time for systematic study using the various designated experimental procedures. The experimental studies involved investigation of γ-Al_2O_3 at room temperature after calcination and *in situ* while heating. Calcination for seven hours at any particular temperature between 500 and 900 °C was found to be sufficient to effect full conversion to γ-Al_2O_3. The reduced amount of calcination time required to form γ-Al_2O_3 caused by milling was not sufficient to warrant carrying out this procedure on the entire boehmite precursor. Thus the hydrogenated boehmite used was not milled, but instead used as-supplied to produce γ-Al_2O_3 for systematic study. Milling of the precursor was implemented for one deuterated boehmite sample used for data collection during *in situ* heating. The *in situ* heating was also used to investigate kinetic effects but these were found not to be present between 500 and 900 °C. Kinetic effects were observed above and below this temperature range, coinciding with changes in lattice parameters.

From these observations it was decided to perform a systematic study on highly-crystalline boehmite sample calcined for seven hours at temperatures between 500 and 900 °C (*section 4.1*). Initial analysis involved the solution of the structure of γ-Al_2O_3 for a single temperature case. The chosen temperature was 600 °C, the work is detailed in *Chapter 7*. This temperature was chosen to allow for further comparison with findings from other research based on similarly prepared samples (Li *et al.* 1990; Zhou and Snyder 1991; Gan 1996; O'Connor *et al.* 1997). *Chapter 8* considers the evolution of the bulk structural configuration of boehmite calcined between 500 and 900 °C. Hydrogen in the structure is considered in preliminary form in *Chapter 7* and systematically in *Chapter 9*.

Chapter 7

Experimental Findings: Establishing a Representative Structural Model

The material in this chapter has been published in:

G. Paglia, C.E. Buckley, A.L. Rohl and L.T. Byrne 2002, "Towards the determination of the structure of γ-alumina," Journal of the Australasian Ceramics Society, ***38****, 1, pp. 92-98.*

and

G. Paglia, C.E. Buckley, A.L. Rohl, B.A. Hunter, R.D. Hart, J.V. Hanna and L.T. Byrne 2003, "Tetragonal structure model for boehmite-derived γ-alumina," Physical Review B, ***68****, 14, pp. 144110, 1-11.*

Preamble

The overall objective of the experimental studies is to seek a representative structural model of γ-Al_2O_3 and then investigate the evolution of the structure with calcination temperature. Before a systematic study of the structural evolution can be performed, an appropriate model must be obtained first. Hence the structure of γ-Al_2O_3 was first investigated for a single temperature case. This was carried out for material calcined at 600 °C. This temperature was chosen to allow for further comparison with findings from other research based on similarly prepared samples (Li *et al.* 1990; Zhou and Snyder 1991; Gan 1996; O'Connor *et al.* 1997).

γ-Alumina is regarded as a cubic spinel structure but has also been reported as tetragonally distorted in some cases (*section 2.2.2*). This is the case for the boehmite-derived γ-Al_2O_3 obtained here. However, research journal papers have continued to index the structure under the cubic $Fd\bar{3}m$ space group and simply note that a tetragonal distortion of the structure occurs along one of the axes of the spinel cell.

It is important to describe the structure correctly. This means that a structure with tetragonal distortion should be described under the appropriate tetragonal space

group symmetry, most likely a maximal subgroup of $Fd\bar{3}m$. This is not merely an academic matter given that γ-Al_2O_3 already has significant industrial importance (*Chapter 1*). Correct knowledge of the structure is vital to the understanding of the mechanisms by which its applications work and can lead to the development of future applications.

7.1 Initial Rietveld Refinement Trials

7.1.1 Starting Structure Models for Rietveld Analysis

The overwhelming majority of reports on γ-Al_2O_3 in the literature report its structure as a cubic spinel, under $Fd\bar{3}m$ space group symmetry, with the cations restricted to the Wyckoff symmetry 8*c* and 16*d* site positions, *i.e.* the spinel site positions (*section 2.2*). This description follows even when a tetragonal distortion has been reported. Only in one case has a tetragonal space group be reported for γ-Al_2O_3 (Li *et al.* 1990). In this work, several structural models for γ-Al_2O_3 from the literature and newly created models based on findings from MAS-NMR studies were investigated for the neutron diffraction data obtained by calcination of boehmite at 600 °C. The investigation was carried out to determine the most suitable space group and cation distribution for γ-Al_2O_3.

Five structure models were selected to be used in Rietveld refinements on the neutron diffraction data obtained for the structure solution of γ-Al_2O_3. These are summarised in Table 7.1. Two of the starting models used were the final structure models determined from recent studies. One of these was from Zhou and Snyder (1991) who concluded the structure to be cubic with $Fd\bar{3}m$ space group. The other was taken from the conference paper of Li *et al*. (1990), who reported a tetragonal structure in the $I4_1/amd$ space group.

The final three starting models were based upon previous experimental results and consideration of vacancy spacing and space group symmetry. Distribution of the Al ions among octahedral and tetrahedral positions was based on findings from Lee *et al*. (1997) and Pecharromán *et al*. (1999). Lee *et al*. (1997), determined the Al ions to be 70% in octahedral and 30% in tetrahedral positions, using both MAS-NMR spectroscopy and computer simulations. This distribution was

incorporated in the Cubic-1 and Tetragonal-1 structure models implemented in this study. Pecharromán *et al*. (1999), using NMR, determined the distribution of Al ions, for boehmite calcined at 600 °C, to be 76% in octahedral and 21% in tetrahedral positions, while 3% displayed five-fold coordination. As a result, a second cubic model was constructed, Cubic-2, to incorporate these reported positions. In the cubic models, the octahedrally and tetrahedrally coordinated Al ions were placed exclusively within the 16*d* and 8*a* Wyckoff positions, respectively, for representation of the octahedrally and tetrahedrally coordinated atoms. This approach was taken because it yields a structure where Al-Al distances are the longest possible for $Fd\bar{3}m$ symmetry, as opposed to a structure with Al atoms distributed among other possible octahedral and tetrahedral site positions. It also is consistent with the belief that the cations in the phase are distributed only among the spinel site positions. In principle, this yields a structure of greater thermodynamic stability. Using the same approach for the tetragonal model, the octahedrally and tetrahedrally coordinated Al ions were placed exclusively within the 8*d* and 4*a* Wyckoff positions respectively. In the case of the five-fold coordinated Al ions for the Cubic-2 model, the same approach as Zhou and Snyder (1991) was followed. They consider the Al ions they determined to occur in the 32*e* site positions to be pseudo-octahedral (pentacoordinated).

Table 7.1. Structure models used in preliminary Rietveld structure refinements.

Model	***Space Group***	***Lattice Parameters (Å)***	***Atom species***	***Wyckoff site position***	***Occupancy***
Previous Studies					
Li *et al*.	$I4_1/amd$	a = 5.600 c = 7.854	O Al	16*h* 8*d* 4*a*	1 0.66 1
Zhou & Snyder	$Fd\bar{3}m$	a = 7.911	O Al	32*e* 32*e* 16*d* 8*a*	1 0.17 0.58 0.84
Modified from Previous Findings					
Tetragonal-1	$I4_1/amd$	a = 5.600 c = 7.854	O Al	16*h* 8*d* 4*a*	1 0.94 0.79
Cubic-1	$Fd\bar{3}m$	a = 7.911	O Al	32*e* 16*d* 8*a*	1 0.94 0.79
Cubic-2	$Fd\bar{3}m$	a = 7.911	O Al	32*e* 32*e* 16*d* 8*a*	1 0.02 1 0.58

7.1.2 Results from Initial Rietveld Analysis Trials

All neutron diffraction refinements were performed with manually fixed backgrounds before incorporation of Cheby I background parameters. This approach was adopted because the refinements, with the exception of the Zhou and Snyder (1991) and Cubic-2 models, often became unstable when incorporating background parameters from the onset. Furthermore, it was found that background parameters absorbed statistics from other parameters and lead to an increased statistical error in the final fit.

The acquired neutron data of γ-Al_2O_3 was first refined for the two literature models. Refinements on both of these models were performed with internal parameters both fixed and refined. The results are summarised in Table 7.2. Lattice parameters are larger than those from literature models. This is expected because the data was collected for material calcined *in situ*. A better fit to the data was obtained by refining internal parameters in both cases. The literature model of Li *et al*. (1990) indicates vacancy ordering in octahedral (8*d*) positions but refinement of these parameters leads to opposite findings, *i.e.* full occupancy of the octahedral positions and vacancy ordering among the tetrahedral sites. This agrees with the observations of Jayaram & Levi (1989) who found the intensity ratio of tetrahedral to octahedral reflections in γ-Al_2O_3 was smaller than in spinel ($MgAl_2O_4$). Refinement of the Zhou and Snyder (1991) model leads to an increase in octahedral (16*d*) and pseudo-octahedral (32*e*) occupancy at the expense of tetrahedral occupancy. The fits where the internal parameters are refined are illustrated in Figure 7.1. Comparison is made with the refinements of the three models created for this study.

The results of refinements performed on the present study models are summarised in Table 7.3. Comparison of these results with those for the previous study models, where the internal parameters were refined, and observation of the fits from Figure 7.1, show the refined tetragonal model of Li *et al*. (1990) to be equivalent to the refined Tetragonal-1 model of this study. Similarly for the data examined here, the refined cubic model of Zhou and Snyder (1991) is equivalent to the Cubic-2 model of the present study. These two models appear to have the most compelling fit for all the models used. The Bragg factors represent a reasonable fit for the type of structures examined here. This is confirmed by the difference plots. It

should be noted, however, that the thermal parameters became unstable in the refinement of the Cubic-2 and Zhou and Snyder (1991) models and had to be fixed to reasonable values. V and W parameters, which are shape parameters for the full-width-half-maximum of peaks, also showed a tendency to become physically unreasonable.

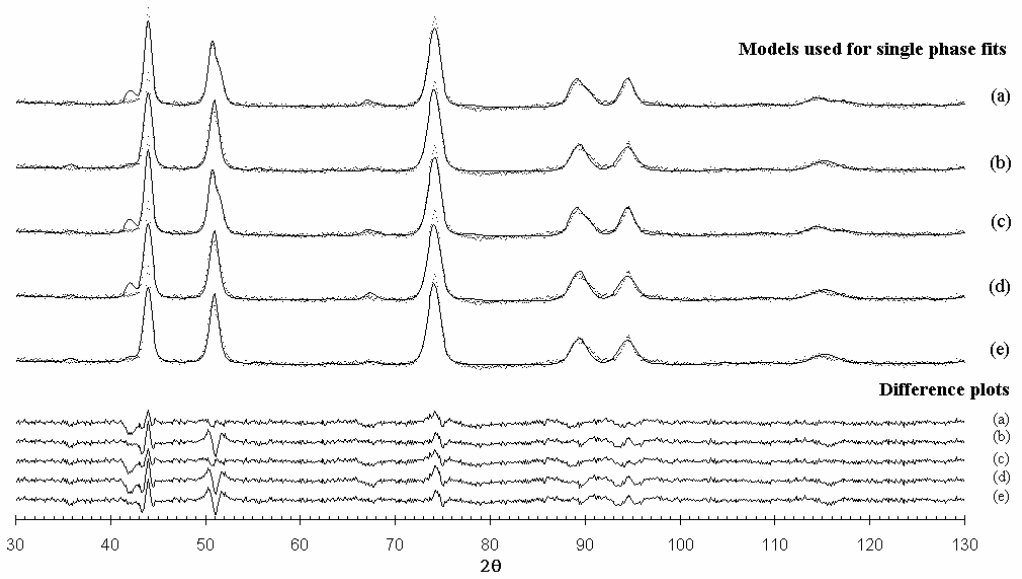

Figure. 7.1. Single-phase refinement plots for the models used, with internal parameters refined; (a): Li *et al*. (1990), (b): Zhou and Snyder (1991), (c): Tetragonal-1, (d): Cubic-1, (e): Cubic-2. Data shown is from γ-Al_2O_3 prepared by *in situ* heating of deuterated boehmite precursor.

Table 7.2. Refinement results for previous study models. Results are shown for refinements where backgrounds were manually fixed. Uncertainties are to 3 standard deviations.

Model	***Lattice Parameters (Å)***	***Al site positions***	***Occupancy***	***Goodness of Fit***	***Bragg Factor***
Internal Parameters Kept Fixed					
Li *et al*.	a = 5.653(2) b = 7.867(3)	8*d* 4*a*	0.66 1.00	5.89	15.53
Zhou & Snyder	a = 7.952(2)	32*e* 16*d* 8*a*	0.17 0.58 0.84	4.75	10.74
Internal Parameters Refined					
Li *et al*.	a = 5.653(1) b = 7.869(2)	8*d* 4*a*	1.000(3) 0.083(3)	3.89	10.57
Zhou & Snyder	a = 7.952(2)	32*e* 16*d* 8*a*	0.210(1) 0.595(1) 0.640(1)	4.35	8.64

Table 7.3. Refinement results for present study models. Results are shown for refinements where backgrounds were manually fixed. Uncertainties are to 3 standard deviations.

Model	*Lattice Parameters (Å)*	*Al site positions*	*Occupancy*	*Goodness of Fit*	*Bragg Factor*
Tetragonal-1	a = 5.653(2) b = 7.867(3)	8*d* 4*a*	1.000(3) 0.083(3)	3.88	10.59
Cubic-1	a = 7.952(2)	16*d* 8*a*	1.000(1) 0.083(1)	5.51	11.16
Cubic-2	a = 7.952(2)	32*e* 16*d* 8*a*	0.201(1) 0.590(1) 0.643(1)	4.35	8.73

However, all of the calculated fits exhibit peaks that are not present in the data. In particular, there is a significant peak immediately to the left of the first main peak ($2\theta \sim 42$ °) for the Cubic-1 and both tetragonal models. This suggests that these models are not correct. It is difficult to discern if these extra peaks are present in other refinements reported in literature where only spinel positions are assumed. To the author's knowledge, most of these papers do not show their calculated refinements (*e.g.* Li *et al.* 1990; O'Connor *et al.* 1997; Wang *et al.* 1999).

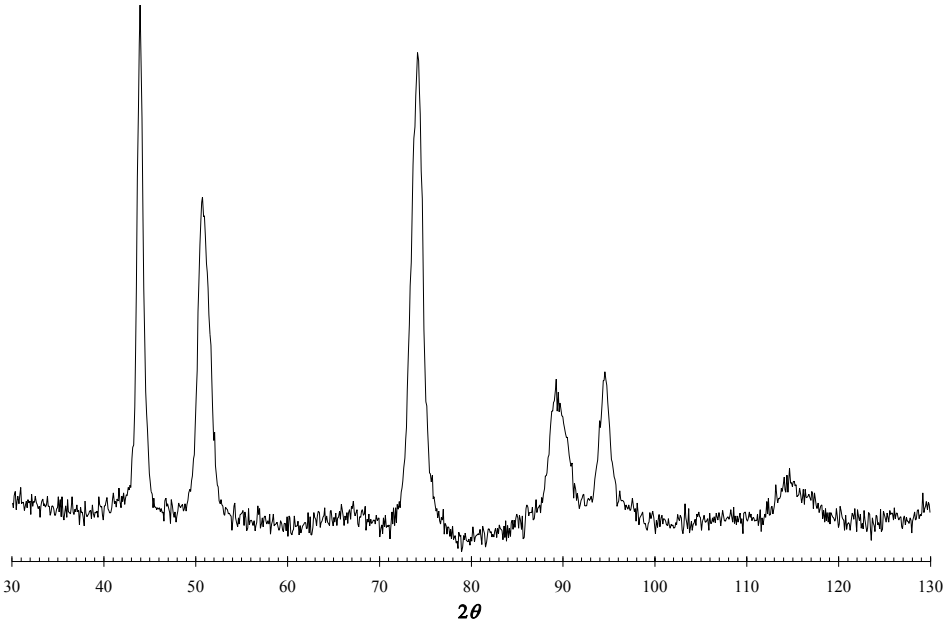

Figure 7.2. Neutron diffraction data obtained from γ-Al_2O_3 prepared by *in situ* heating of deuterated boehmite precursor at 600 °C. This data is shown to illustrate the peak characteristics more clearly than can be seen from figures which illustrate refinement fits. All the peaks, except that at $2\theta \sim 44$ °, show inconsistent anisotropic broadening.

The peak at $2\theta \sim 44$ ° is consistent with the most densely packed oxygen plane. The *hkl* depends on the determined phase ((222) for cubic, (022) for tetragonal). With the exception of this peak, all the experimental peaks show inconsistent, anisotropic broadening derived from uneven distribution of Al ions between the oxygen planes (the raw data is depicted in Figure 7.2). These are known to be true physical attributes because neutrons are being used here, as opposed to X-rays. This anisotropy in the peaks is also less likely to appear for data collected at room temperature, which is how the majority of other studies were conducted. Some of the peaks, particularly that at $2\theta \sim 51$ °, appear to be split. Profile analysis was performed on this peak using the CMPR program, distributed by NIST. The profile analysis was performed using one, two and three peaks. The goodness-of-fit for each of the profile refinements was 3.863, 0.883 and 0.849 respectively. The single-peak and two-peak profile refinements are representative of the single-phase cubic and tetragonal models respectively, where the plane contributing to the peak intensity is (004) for cubic and (220) and (004) for tetragonal. If one assumes that the Al vacancies are isotropically distributed among the possible sites, then these profile refinements on the $2\theta \sim 51$ ° peak suggest that the structure of γ-Al_2O_3 is tetragonal. This was supported by a better fit of this peak in the Rietveld refinement of the tetragonal models, compared to any of the cubic models. However, the best goodness-of-fit belongs to the profile refinement which considers a three peak contribution. This suggests that two phases may be present.

The idea of a dual-phase structural model originated from the work of Gan (1996, pp.150-158), who incorporated both the Li *et al*. (1990) and Zhou and Snyder (1991) models and observed the same peak splitting evident here. The final model of the Gan (1996, pp.150-158) study was examined for incorporation into this work but the stoichiometry of the tetragonal phase was incorrect, rendering this model unusable. However, the goodness-of-fit from the profile analysis described above suggests that the Gan approach has much merit. Here, the neutron data obtained were refined using two starting models for dual-phase presence. The first was the original Li *et al*. (1990) and Zhou and Snyder (1991) models, the second was the Tetragonal-1 and Cubic-1 models. The results of these refinements and their fits are displayed in Table 7.4 and Figure 7.3 respectively.

When examining the calculated profile to the peak at $2\theta \sim 51$ ° both of the dual-phase models provided a comparable fit which was better than any of those achieved in the single-phase refinements. This provides further support for the plausibility of a dual-phase structure. Whereas misfit, in terms of peak positioning, particularly at higher 2θ, was observed for all the single-phase refinements, this was not as obvious for the calculated dual-phase structures. However, for both dual-phase refinements the presence of significant calculated peaks where there are no equivalent peaks in the data still remains, suggesting the models are insufficient to describe the data being examined.

The dual-phase refinements resulted in phase concentrations of 78(4) wt. % tetragonal composition for the Li *et al*. (1990) with Zhou and Snyder (1991) dual-phase model and 89(6) wt. % tetragonal composition for the Tetragonal-1 with Cubic-1 dual-phase model. The greater apparent accuracy for the Li *et al*. (1990) with Zhou and Snyder (1991) dual-phase model is indicated by a better goodness of fit. However, better Bragg factors, signifying a better fit for the individual-phases, were obtained using the Tetragonal-1 with Cubic-1 dual-phase model. In the case of the Li *et al*. (1990) with Zhou and Snyder (1991) dual-phase model, instability in the cubic phase thermal parameters occurred during the refinement. Furthermore, the coordinates of 32*e* site position tended to diverge from physically plausible values.

Table 7.4. Results for dual-phase refinements. Results are shown for refinements where backgrounds were manually fixed. Uncertainties are to three standard deviations.

Model Combination	***Lattice Parameters (Å)***	***Al site positions***	***Occupancy***	***Goodness of Fit***	***Bragg Factor***
Li *et al*. (*Tetragonal*) + Zhou & Snyder (*Cubic*)	Tetragonal a = 5.659(2) b = 7.859(3) Cubic a = 7.947(3)	Tetragonal 8*d* 4*a* Cubic 32*e* 16*d* 8*a*	Tetragonal 0.970(5) 0.726(5) Cubic 0.398(4) 0.132(4) 0.823(4)	3.39	Tetragonal 9.78 Cubic 8.89
Tetragonal-1 + Cubic-1	Tetragonal a = 5.652(1) b = 7.864(2) Cubic a = 7.945(1)	Tetragonal 8*d* 4*a* Cubic 16*d* 8*a*	Tetragonal 1.000(5) 0.667(5) Cubic 0.833(7) 1.000 (7)	3.96	Tetragonal 9.18 Cubic 7.80

The Zhou and Snyder (1991) model depicts a distribution of the 32*e* site positions in eight groups of four positions distributed uniformly throughout the unit cell. The Al atoms of pseudo-octahedral coordination are distributed isotropically among these sites. Each group of four 32*e* positions closely surrounds an oxygen atom. The close proximity of these sites to the neighbouring oxygen means that it is only possible for one Al ion to be present among a group of four 32*e* positions. Therefore the maximum allowable occupancy of the pseudo-octahedral atoms is 0.25. This means that the occupancy of 0.398(4) calculated for the 32*e* site position in the cubic phase of the Li *et al*. (1990) with Zhou and Snyder (1991) dual-phase model is not physically possible.

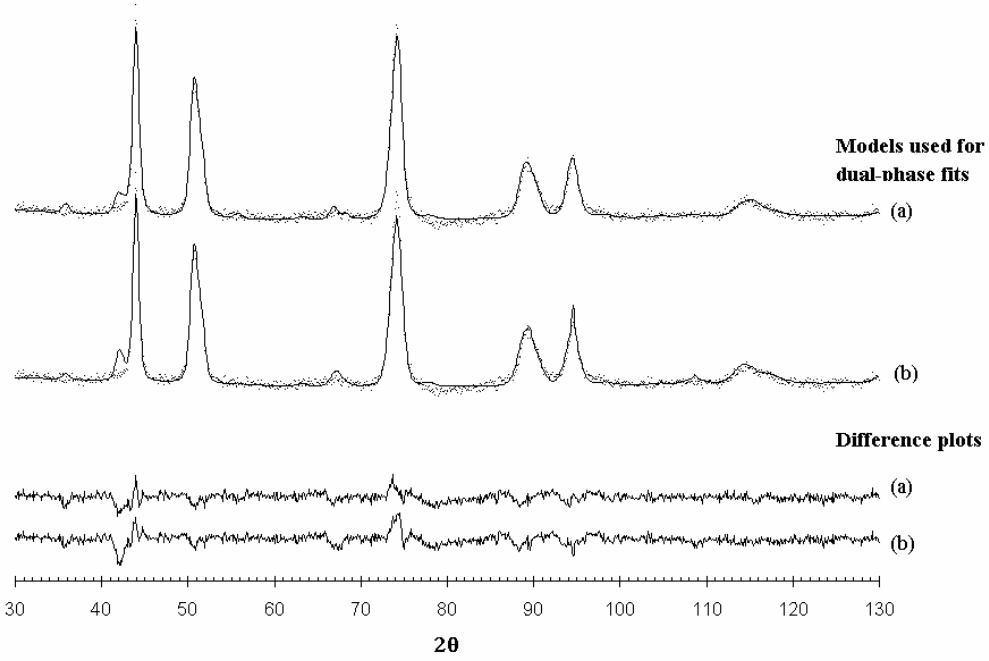

Figure 7.3. Refinement plots for dual-phase refinements; (a): Li *et al*. (1990) with Zhou and Snyder (1991), (b): Tetragonal-1 with Cubic-1. Data shown is from γ-Al_2O_3 prepared by *in situ* heating of deuterated boehmite precursor.

The above discussion shows the Zhou and Snyder (1991) and Tetragonal-1 with Cubic-1 models to provide the most probable structures of those inspected for single-and dual-phase structure possibilities respectively. These were examined using Hamilton's test (Giacovazzo 1992, p.103), which provides a statistical measure of whether a model suits the experimental data after refinement. For the Zhou and Snyder (1991) single-phase and Tetragonal-1 with Cubic-1 models T = 1.060 and the two $R_{m,n\text{-}m,\alpha}$ values are 1.021 and 1.006. (T is the ratio of the weighted Bragg R-

factors (R_w) obtained from respective refinements and $R_{m,n-m,\alpha}$ defines the significance of the weighted Bragg R-factors.) Because $T > R_{m,n-m,\alpha}$ both these models are in doubt.

The aluminium coordination distribution obtained from the Rietveld refinements compares reasonably with MAS-NMR data from the literature (Lee *et al*. 1997). Cation coordination from the refined Tetragonal-1 with Cubic-1 dual-phase model was 68(6)% and 32(6)% octahedral and tetrahedral respectively. The single-phase tetragonal refinements and the Cubic-1 refinement also yield comparable cation coordinations with 75(3)% being situated in octahedral sites. These coordination distributions are also in agreement with the MAS-NMR spectrum obtained for similarly prepared sample by Gan (1996, p.149), who used a spin rate of 15 kHz. The MAS-NMR data of Gan (1996, p.149) was integrated here to yield an Al coordination distribution of 72(3)% octahedral and 28(2)% tetrahedral. The proportion of pentacoordinated (32*e*) obtained from the refined (and literature) Zhou and Snyder (1991) model and the Cubic-2 model does not agree with the value of 3% from the Pecharromán *et al*. (1999) study. When comparing with the Zhou and Snyder (1991) model it is interesting to note that addition of the pseudo-octahedral and octahedral occupied sites yields ~ 75% after refinement and ~ 70% if the occupancies are kept fixed.

7.1.3 Conclusions from Preliminary Analysis

Because of the presence of additional calculated peaks in the refinement fits which have no corresponding peak in the data, none of the five single and two dual-phase structural models examined here was found to be suitable for describing the structure of γ-Al_2O_3 corresponding to the data obtained here. The Li *et al*. (1990), Tetragonal-1 and Cubic-1 single-phase and Tetragonal-1 with Cubic-1 dual-phase models were in reasonable agreement with MAS-NMR data for similarly prepared samples in the literature. However, these models, and the Li *et al*. (1990) with Zhou and Snyder (1991) dual-phase model, display the most drastic differences between the calculated fit and the data. This is irrespective of the improved profile fits for the peaks in the neutron data, particularly that at $2\theta \sim 51$ °, provided by the two dual-phase models, compared with the other models thus far examined.

The refined Zhou and Snyder (1991) and Cubic-2 models, which were equivalent after refinement, did not have coordination distributions in agreement with MAS-NMR data for similarly prepared samples in the literature. They also displayed the least adequate profile fits to the peaks of the neutron data of all the models investigated. However, these models exhibited the smallest overall residual differences between the calculated fits and the data.

7.2 Development of a New Structural Model

To date, the best model describing the structure of γ-Al_2O_3 is that by Zhou and Snyder (1991). The key difference between the Zhou and Snyder (1991) model and others is the incorporation of a *non-spinel* site position in the structural model, which follows from the work of Shirasuka *et al*. (1976) and Ushakov and Moroz (1984). However, there are two discrepancies between the Zhou and Snyder (1991) model and the data obtained here. The first relates to the report of the special Wyckoff 32*e* site position. The reported occupation of the highly distorted Wyckoff 32*e* site represents ~ 25% of the Al sublattice (Zhou and Snyder 1991), and ~ 32% when refined for the data analysed here (Table 7.5). Only one MAS-NMR study of γ-Al_2O_3 derived from highly-crystalline boehmite has reported pentahedrally coordinated Al, and this constituted no more than 6.5% of the Al sublattice (Pecharroman *et al.* 1999). The appearance of a peak representing *pentahedral* Al in such data can be debated. The occurrence of a 'five-coordinated peak' in MAS-NMR spectra of γ-Al_2O_3 is typically found for highly porous material made from poorly crystalline boehmite (Komarneni *et al.* 1985; Wang *et al.* 1999), or boehmite that is well ground (Chen *et al.* 1992), where higher surface areas result. From the literature, it seems that the appearance of obvious pentahedral peaks in MAS-NMR spectra predominantly occurs for γ-Al_2O_3 where there is a high content of amorphous material, or when there is a large amount of surface cleavage resulting from milling.

The MAS-NMR spectrum (Figure 7.4) obtained for the γ-Al_2O_3 sample examined herein shows two peaks, representing a cation sublattice with octahedral and tetrahedral coordination. There is no evidence of a 'five-coordinated,' or pentahedral, Al peak. What can only be said with certainty concerning this issue is that the asymmetric tailing of the peaks is indicative of short-range disorder in the

structure (Phillips *et al.* 1988; Kohn *et al.* 1989; Kohn *et al.* 1991; Kunath *et al.* 1992; Kunath-Fandrei *et al.* 1995). The spectrum is of similar appearance to those reported by Lee *et al*. (1997) and Pecharroman *et al*. (1999). Peak area integration of the data yields a distribution of 69(2)% octahedral and 31(2)% tetrahedral Al cation coordination, in excellent agreement with Lee *et al*. (1997).

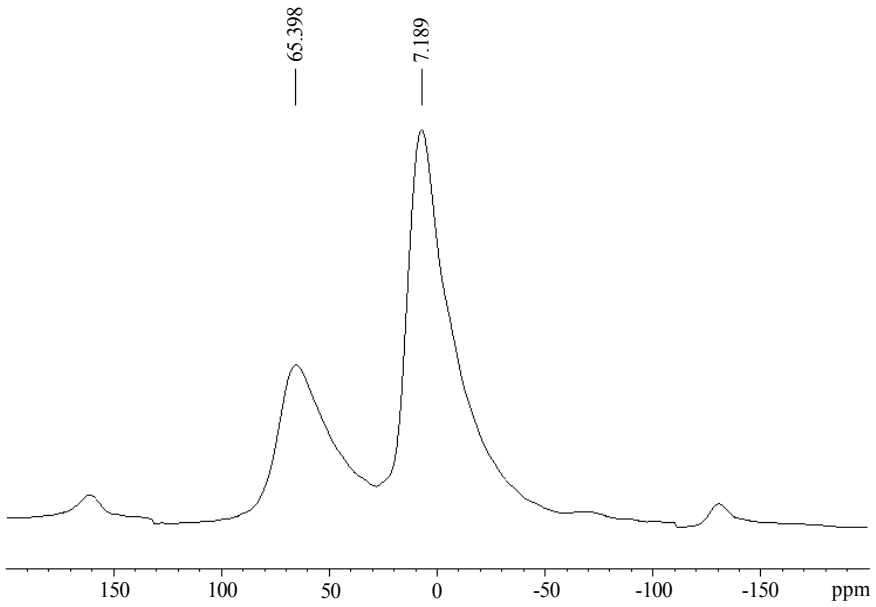

Figure 7.4. ^{27}Al MAS-NMR spectrum of γ-Al_2O_3 prepared from hydrogenated boehmite precursor; the octahedral peak is at 7.189 ppm, and the tetrahedral peak at 65.398 ppm.

Distorted octahedra, such as those described by Zhou and Snyder (1991), which may be regarded as pentahedral, have also been observed for κ-Al_2O_3 (Yourdshahyan *et al.* 1999; *section 5.3*). This was the result of a slight distortion in the neighbouring region of the oxygen sublattice. These distortions have not been found to result in a peak between the octahedral and tetrahedral peaks in the MAS-NMR spectra for κ-Al_2O_3 (Ollivier *et al.* 1997). The greatest significance of the distorted octahedra in κ-Al_2O_3 is that the Al remains in an octahedral site position which is consistent with the space group symmetry. In the $Fd\bar{3}m$ space group these can only be the 16*c* or 16*d* site positions. From crystallographic considerations, cleavage of the oxygen sublattice across an octahedra results in Al with a coordination number of five at a surface (Lippens and Steggerda 1970). These cations, distorted or not, remain effectively in an octahedral position, which is more

energetically favourable than the highly distorted 32*e* position. The proportion of Al in octahedral positions for the Zhou and Snyder (1991) model is ~ 44%, well below the quantity given by MAS-NMR studies. Added to the quantity of Al in the Wyckoff 32*e* site position this yields a proportion of Al sublattice equivalent to ~ 69%. Hence, the author believes it is more appropriate to incorporate the 16*c* position for Al in the model as opposed to the 32*e*. This belief is supported by Wolverton and Hass (2001), who found some spontaneous non-spinel occupation on the 16*c* site for some of the theoretical structures they optimised.

Figure 7.5 illustrates the Rietveld refinements of the Zhou and Snyder (1991) model and a cubic structural model incorporating the Wyckoff 16*c* site position in the Al sublattice, designated the Cubic-16*c* model. A cubic structural model with Al's restricted to the spinel site positions, designated Cubic-1 (*section 7.1*), is also shown to illustrate the misfit between the calculated pattern and the data. The Zhou and Snyder (1991) and Cubic-1 models were refined with background parameters incorporated rather than fixed (as in s*ection 7.1*). When considering only spinel sites in the structural model, the vacancies were ordered on tetrahedral sites. In all other cases, the occupied site positions were all partially occupied. Table 7.5 displays the results of these refinements. The Zhou and Snyder (1991) model, when refined here, yields an increase in the 32*e* occupancy at the expense of the 16*d* and a slight change in the 32*e* position Al from $x = 0.027$ to $x = 0.019$. Refinement of the 32*e* position tended to make the refinement unstable, with its coordinates approaching either $x = 0$ (the coordinates of the 16*c* position) or $x = 0.25$ (the coordinates of the O sublattice). The refinement fits to the data of the Zhou and Snyder (1991) and Cubic-16*c* models are very similar. However, the statistical indicators (Table 7.5) indicate a slightly better fit for the latter model. Hence it is concluded that the Cubic-16*c* model is equally as plausible as the Zhou and Snyder (1991) model for representation of the average bulk structure of boehmite derived γ-Al_2O_3.

Although the fits of the Zhou and Snyder (1991) and Cubic-16*c* models are similar, the unit cell structures are considerably different. The 16*c* positions in the Cubic-16*c* structure are uniformly dispersed, whereas the Zhou and Snyder (1991) model depicts a distribution of the 32*e* site positions in eight groups of four positions uniformly throughout the unit cell, as described in *section 7.1.2*.

Table 7.5. Refinement results for cubic model fits against neutron data obtained from deuterated boehmite heated *in situ* to form γ-Al_2O_3. Results are shown for refinements where background functions were incorporated (Cheby I), in contrast to Tables 7.2 - 7.4 in *section 7.1.2* where backgrounds were manually fixed. Uncertainties are to three standard deviations.

Model	*Lattice Parameters (Å)*	*Al site positions*	*Occupancy*	*Rp*	*Goodness of Fit*	*Bragg Factor*
Cubic-1	a = 7.952(2)	8a 16d	0.83(1) 1.00(1)	3.45	4.40	2.48
Zhou & Snyder	a = 7.952(2)	8a 16d 32e	0.83(2) 0.53(1) 0.20(1)	3.18	3.42	1.65
Cubic-16*c*	a = 7.953(2)	8a 16c 16d	0.78(2) 0.34(1) 0.60(1)	3.07	3.16	1.35

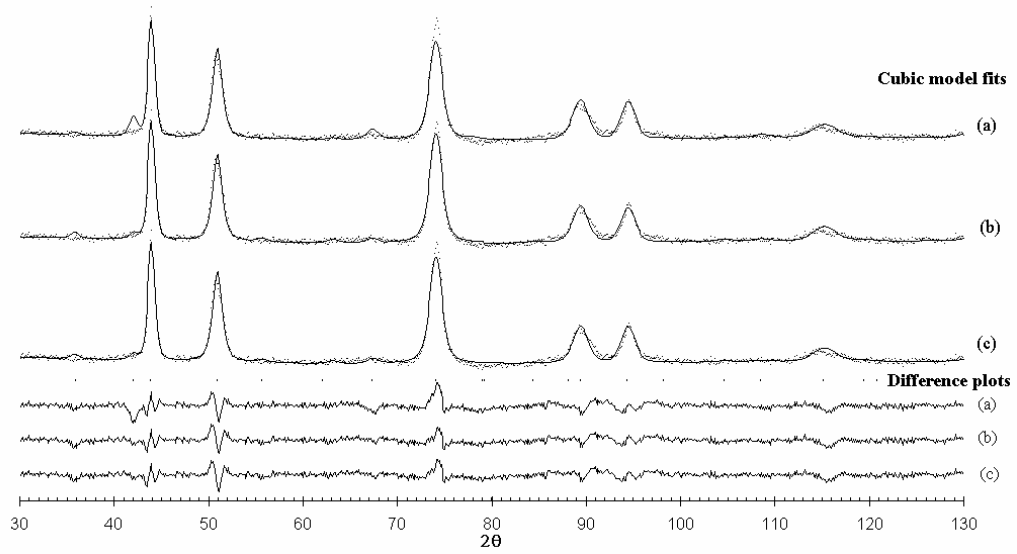

Figure 7.5. Refinements for cubic models against neutron data obtained from deuterated boehmite heated *in situ* to form γ-Al_2O_3; (a): Cubic-1, incorporating only *spinel* site positions, (b): Zhou and Snyder (1991), (c): Cubic-16*c*. The solid lines in the diffraction patterns represent the calculated fit.

The second discrepancy between the Zhou and Snyder (1991) model and the data examined here more specifically relates to the consideration of a cubic space group in general. All of the peaks in the diffraction pattern, with the exception of the peak at $2\theta \sim 44$ °, appear to be split. This was observed for all the neutron diffraction patterns collected from every sample. This splitting is most obvious for the peak at $2\theta \sim 51$ ° (see Figure 7.6). Profile analysis shows a much better goodness-of-fit when

multiple peaks are considered as opposed to one peak (*section 7.1.2*). The appearance of these split peaks, exhibiting an improved profile when considering two or more peaks, is characteristic of a structure of lower symmetry than cubic, such as a *tetragonal* structure. Rietveld refinement of both tetragonal and dual-phase structure models (discussed later in *section 7.2.2*) provides better profile fits to the peaks than the cubic models (Figure 7.6).

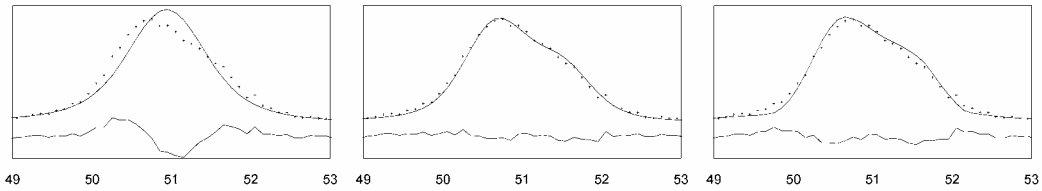

(a) (b) (c)

Figure 7.6. Resulting profiles of the peak at $2\theta \sim 51$ ° generated by refinement of structure models; (a): cubic, based on the Zhou and Snyder (1991) and Cubic-16*c* models, (b): tetragonal, based on the model designated Tetragonal-8*c*, (c): dual-phase, based on Cubic-16*c* combined with Tetragonal-8*c* models.

7.2.1 Space Group Identification from TEM

A systematic TEM examination revealed a granular morphology consisting of layered triangular and rhombohedral-like plates, consistent with previous observations (Lippens and de Boer 1964; Saalfeld and Mehrotra 1965). Selected area electron diffraction of individual plates showed only one type of pattern, indicative of a single-phase material. The diffraction patterns observed are depicted in Figure 7.7. Figure 7.7a, imaged from the plate surface, is consistent with the diffraction patterns observed by Lippens and de Boer (1964) and Saalfeld and Mehrotra (1965). Lippens and de Boer (1964) observed that the electron diffraction patterns of boehmite-derived γ-Al_2O_3 contained more spots than expected from the spinel structure, and a contracted *c* lattice parameter. Irrespective of the obvious tetragonal nature of boehmite-derived γ-Al_2O_3 researchers have continued to index the structure in accordance with the $Fd\bar{3}m$ space group. The tetragonal $I4_1/amd$ space group is a maximal subgroup of $Fd\bar{3}m$, with $a_{\text{cubic}} \approx \sqrt{2} \times a_{\text{tetragonal}}$. These patterns can be described by $I4_1/amd$ symmetry as opposed to $Fd\bar{3}m$ (Figure 7.7). In the $I4_1/amd$ representation the *a* parameter is equivalent to d_{110} (~ 5.62 Å) in the cubic representation. Using this representation, the data yields $a \sim 5.60$ Å and $c \sim 7.83$ Å,

which is consistent with the Rietveld data. Indexing by $I4_1/amd$ symmetry satisfies the reflection conditions of the space group (Hahn (Ed.) 1995) and remains consistent with the three types of reflections described by Lippens and de Boer (1964). The significance of the types of reflections observed have been discussed previously (Lippens and de Boer 1964; Saalfeld and Mehrotra 1965; Wilson 1979). A conversion table from reflections based on $Fd\bar{3}m$ to $I4_1/amd$ symmetry is provided in Table 7.6.

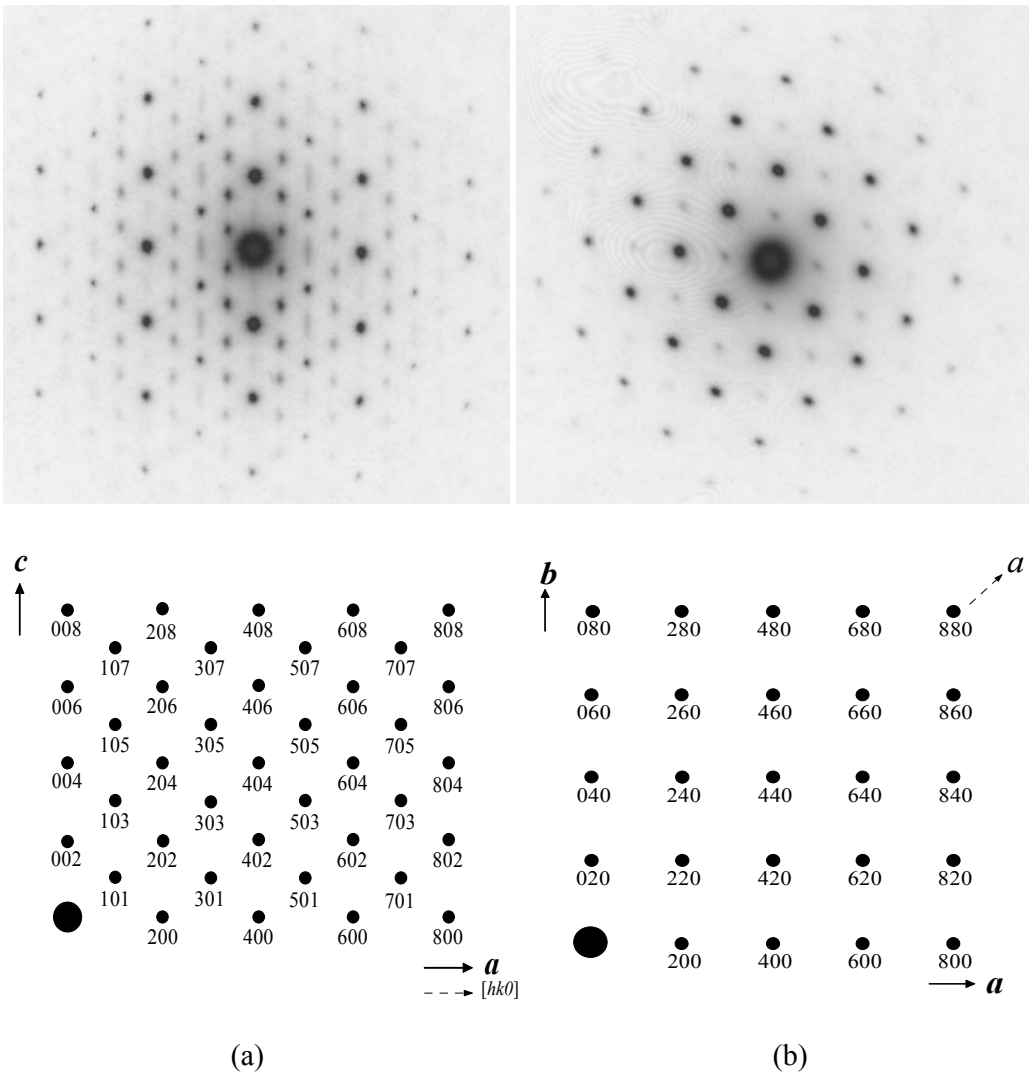

Figure 7.7. SAED patterns, with tetragonal, $I4_1/amd$, indexing diagrams below, looking down the (a) [0k0] and (b) [00l] zone axes. Dashed lines indicate the axis if the traditional cubic representation were followed.

Table 7.6. Equivalent Miller indices for the cubic and tetragonal, *I4₁/amd*, representations of the structure of γ-Al_2O_3.

From Figure 7.7a* - [0k0] *zone axis						***From Figure 7.7b* – [00l] *zone axis***					
Cubic			***Tetragonal***			***Cubic***			***Tetragonal***		
h	*k*	*l*	*h*	*k*	*l*	*h*	*k*	*l*	*h*	*k*	*l*
0	0	4	0	0	4	2	-2	0	0	2	0
0	0	8	0	0	8	2	2	0	2	0	0
0	0	12	0	0	12	4	0	0	2	2	0
1	1	1	1	0	1	4	-4	0	0	4	0
1	1	3	1	0	3	4	4	0	4	0	0
1	1	5	1	0	5	6	-6	0	0	6	0
1	1	7	1	0	7	6	-2	0	2	4	0
2	2	0	2	0	0	6	2	0	4	2	0
2	2	2	2	0	2	6	6	0	6	0	0
2	2	4	2	0	4	8	-8	0	0	8	0
2	2	6	2	0	6	8	-4	0	2	6	0
2	2	8	2	0	8	8	0	0	4	4	0
3	3	1	3	0	1	8	8	0	8	0	0
3	3	3	3	0	3	8	4	0	6	2	0
3	3	5	3	0	5	10	-6	0	2	8	0
3	3	7	3	0	7	10	-2	0	4	6	0
4	4	0	4	0	0	10	2	0	6	4	0
4	4	2	4	0	2	10	6	0	8	2	0
4	4	4	4	0	4	12	-4	0	4	8	0
4	4	6	4	0	6	12	4	0	8	4	0
4	4	8	4	0	8	12	0	0	6	6	0
5	5	1	5	0	1	14	-2	0	6	8	0
5	5	3	5	0	3	14	2	0	8	6	0
5	5	5	5	0	5	16	0	0	8	8	0
5	5	7	5	0	7						
6	6	0	6	0	0						
6	6	2	6	0	2						
6	6	4	6	0	4						
6	6	6	6	0	6						
6	6	8	6	0	8						
7	7	1	7	0	1						
7	7	3	7	0	3						
7	7	5	7	0	5						
7	7	7	7	0	7						
8	8	0	8	0	0						
8	8	2	8	0	2						
8	8	4	8	0	4						
8	8	6	8	0	6						
8	8	8	8	0	8						

7.2.2 Proposed Tetragonal Model

$I4_1/amd$ symmetry was first suggested by Li *et al*. (1990) who proposed a structure with Al restricted to spinel sites and vacancy ordering on octahedral sites. In this space group, the site positions analogous to the spinel sites in its supergroup are the 4*a* (≡ 8*a*) and 8*d* (≡ 16*d*) sites (Hahn (Ed.) 1995). This space group was utilised in a new structural model for Rietveld analysis, adopting the same approach as Cubic-16*c*, and designated Tetragonal-8*c*. The resulting unit cell has 16 oxygen ions, on the 16*h* site position, and 10⅔ aluminium cations to maintain 2:3 stoichiometry. The starting occupancies used for the Tetragonal-8*c* model were those resulting from the refinement of the Cubic-16*c* model (Table 7.5). Results of the refinements of this model are summarised in Tables 7.7 and 7.8, with an example of the fit illustrated in Figure 7.8. In every case, a significantly better fit resulted for the Tetragonal-8*c* model than for any of the cubic models examined. Table 7.7 illustrates consistency of the model data for all specimens examined, with the spread in the occupancy no greater than 0.04 between all samples. The distribution of the Al ions between octahedral and tetrahedral positions agrees with the MAS-NMR data in every case. Consistency of the model also pervaded through the interatomic distances, which showed a deviation no larger than 0.1 Å for any equivalent distance between all samples.

For all models examined, the Al ions were linked while they were refined to maintain the 2:3 ratio required by the formula Al_2O_3. However, to test the stability of the Tetragonal-8*c* model, the Al ions were also refined unlinked. Individual occupancies deviated less than 0.5% from their linked counterparts and the overall stoichiometry remained within 1% of the ideal 2:3 ratio for alumina. A summary of the structure is presented in Table 7.8.

The consistency of the structural model between *in situ* heating and room temperature data strengthens the argument against a special pentahedral Al. It is also indicative of the stability of the phase at both ambient and calcination temperatures. The disorder evident in the MAS-NMR data indicates that a good fit to the diffraction data can be difficult to achieve. However, the structural model accounts for this by using larger thermal parameters than seen in a more ordered structure such as α-Al_2O_3.

Table 7.7. Refinement results for the Tetragonal-8*c* model of γ-Al_2O_3 from the various precursors; 1: deuterated boehmite prepared hydrothermally from deuterated gibbsite and calcined *in situ*, 2: deuterated boehmite prepared hydrothermally from hydrogenated gibbsite and calcined *in situ*, 3: hydrogenated boehmite calcined *in situ*, 4: pre-calcined hydrogenated boehmite with data collected at room temperature. All refinements were made for MRPD data except where indicated. Uncertainties are to three estimated standard deviations.

Precursor	*Lattice Parameters (Å)*	*Al site positions*	*Occupancy*	*Rp*	χ^2	R_B
1	a =5.652(1) c=7.871(5)	4a 8c 8d	0.78(2) 0.36(1) 0.58(1)	2.47	1.96	0.99
2	a =5.660(2) c=7.866(5)	4a 8c 8d	0.78(2) 0.35(1) 0.59(1)	3.12	2.59	0.90
3	a =5.639(2) c=7.867(2)	4a 8c 8d	0.77(2) 0.36(1) 0.58(1)	2.94	2.25	0.97
4	a =5.616(3) c=7.836(6)	4a 8c 8d	0.75(2) 0.37(1) 0.59(1)	3.08	2.06	1.28
4 (HRPD)	a =5.615(2) c=7.835(4)	4a 8c 8d	0.79(2) 0.35(1) 0.59(1)	3.35	1.73	1.34

Table 7.8. Structural parameters of boehmite derived γ-Al_2O_3. Data taken from the refinement of neutron data of deuterated boehmite prepared hydrothermally from deuterated gibbsite and calcined *in situ*. Uncertainties are to three standard deviations.

Space group $I4_1/amd$, a = 5.652(1), c = 7.871(5), R_p = 2.47, χ^2 = 1.96, R_B = 0.99.

Site	x	y	z	B(Å^2)	occupancy
O (16*h*)	0.0000	0.0076(30)	0.2516(40)	1.4(3)	1.0
Al (4*a*)	0.0000	0.7500	0.1250	2.2(3)	0.78(2)
Al (8*c*)	0.0000	0.0000	0.0000	2.3(3)	0.36(1)
Al (8*d*)	0.0000	0.0000	0.5000	2.3(3)	0.58(1)

Core geometries (distances in Å, angles in °) around Al ions

Al (4*a*)─O	1.764(33)		
Al (8*c*)─O	1.981(33)	2.029(18)	
Al (8*d*)─O	1.956(32)	1.968(18)	
O─Al(4a)─O	111.23(1.47)	108.60(72)	
O─Al(8*c*)─O	180.00	91.22(1.26)	88.78(1.26)
O─Al(8*d*)─O	180.00	91.27(1.35)	88.73(1.35)

A dual-phase model was also refined against the data. This approach was first suggested by Gan (Gan 1996, pp.150-158; O'Connor *et al.* 1997) and investigated in *section 7.1*. Here, the Tetragonal-8*c* and Cubic-16*c* models were combined to form

the dual-phase model. Although the refinement was successful as opposed to previous attempts (Gan 1996) the figures of merit were higher than for any single-phase Tetagonal-8c refinement, with a profile factor of 2.79, a goodness-of-fit of 2.39, and Bragg factors of 1.89 and 0.56 for the tetragonal and cubic phases respectively. This is in spite of the greater number of parameters refined for the dual-phase model which usually result in better figures-of-merit. The dual-phase refinement also demonstrated unrealistic instability in site occupancy parameters due to high correlation between the phases. An example refinement is shown in *Appendix II*. In the example, unrealistically high thermal parameters resulted once the occupancies were restricted to physically reasonable values. Based on these results and the observations from TEM, a dual-phase model is discounted for the boehmite-derived γ-Al_2O_3 examined here. Consistency of the Tetragonal-8*c* model for all data sets strengthens the argument for one phase as opposed to two phases.

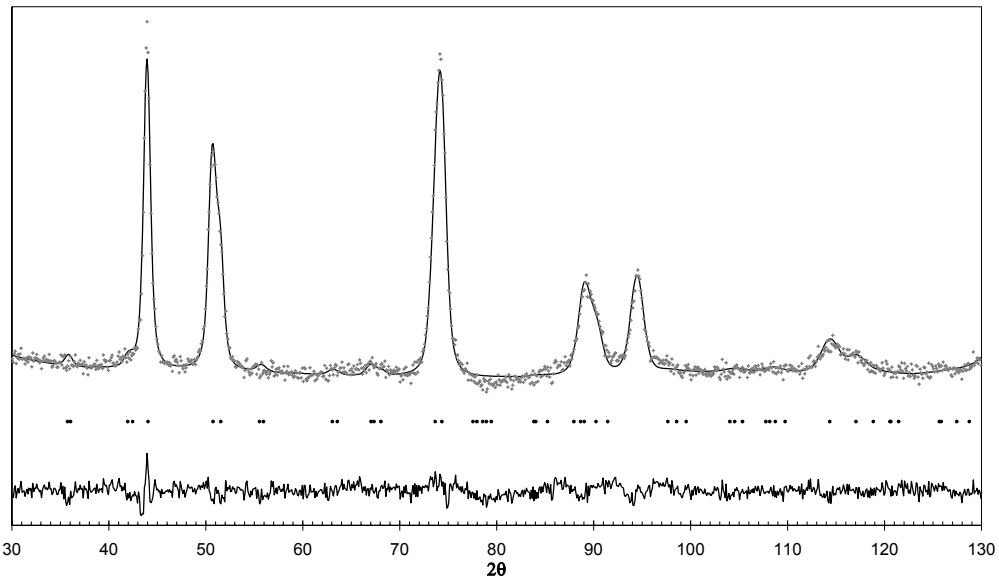

Figure 7.8. Rietveld refinement of the Tetragonal-8*c* model for γ-Al_2O_3 prepared by heating *in situ* from deuterated boehmite precursors.

7.2.3 Consideration of Hydrogen

From the literature it appears that the occurrence of hydrogen within the bulk structure is dependent on the precursor material used. For all the refinements attempted above there remains some differences between the data and the calculated pattern, particularly at $2\theta \sim 44$ °. This difference also remains in the refinement

determined by Zhou and Snyder (1991). This is the peak which draws the greatest intensity contribution from the oxygen sublattice. From suggestions in the literature that there is some hydroxyl substitution for oxygen in the bulk structure (Tsyganenko *et al.* 1990; Wang *et al.* 1999), it was decided to consider hydrogen in Rietveld refinements to investigate if this would account for the intensity mismatch at $2\theta \sim 44$ °. This was done by measuring the amount of hydrogen in the samples and incorporating this amount as deuterium in refinements of deuterated samples. Deuterated samples were used for the refinements instead of hydrogenated samples due to the high incoherent background caused by hydrogen. In the following discussion concerning the Rietveld refinements the word hydrogen is used instead of deuterium for clarity.

To determine the amount of hydrogen in the sample examined here, one-shot ignition-loss was performed on the hydrogenated γ-Al_2O_3 sample. For the ignition-loss, the sample was initially heated to 200 °C for 2 hours to drive off surface adsorbed water and cooled in a desiccator. The sample was then weighed to ± 1 mg precision, heated to 1200 °C for one hour to drive off all residual hydroxyl ions from the bulk, cooled and weighed again. From this procedure the residual amount of hydrogen species in the bulk was determined to be 2.26(3) wt. %. This is assumed to be in the form of water from the decomposition reaction of boehmite (Wefers and Misra 1987). From the ignition-loss $n = 0.131(2)$, giving the traditional protospinel stoichiometry as γ-$Al_2O_3.0.131H_2O$, which equates to 1.39(8) hydrogens per tetragonal unit cell. The treatment of Sohlberg *et al*. (1999) gives $H_{0.251}Al_{1.916}O_3$.

The incorporation of the measured amount of hydrogen in the sample via Rietveld refinement followed two approaches, designated approach one and approach two. Approach one involved sampling the hydrogen in various interstitial octahedral and tetrahedral positions, consistent with space group symmetry, following from the findings of Tsyganenko *et al*. (1990) and Sohlberg *et al*. (1999) Approach two was more generic, the hydrogen was given starting coordinates which placed it at a physically reasonable distance from oxygen, using the same symmetry position used for oxygen. These two procedures were systematically employed for all structural models tested, which included the cubic and tetragonal models with Al's restricted to spinel site positions, in addition to those where Al's were refined on non-spinel site positions.

The Rietveld refinements carried out for approaches one and two were conducted under two further conditions. The first was to maintain Al_2O_3 stoichiometry and incorporate the hydrogen as additional material within the bulk, consistent with γ-$Al_2O_3.nH_2O$ representation. The second was to incorporate the hydrogen according to the resulting stoichiometry of the Sohlberg *et al*. (1999) representation. The refinement trials for examining hydrogen content in the crystalline bulk structure are depicted in Figure 7.9.

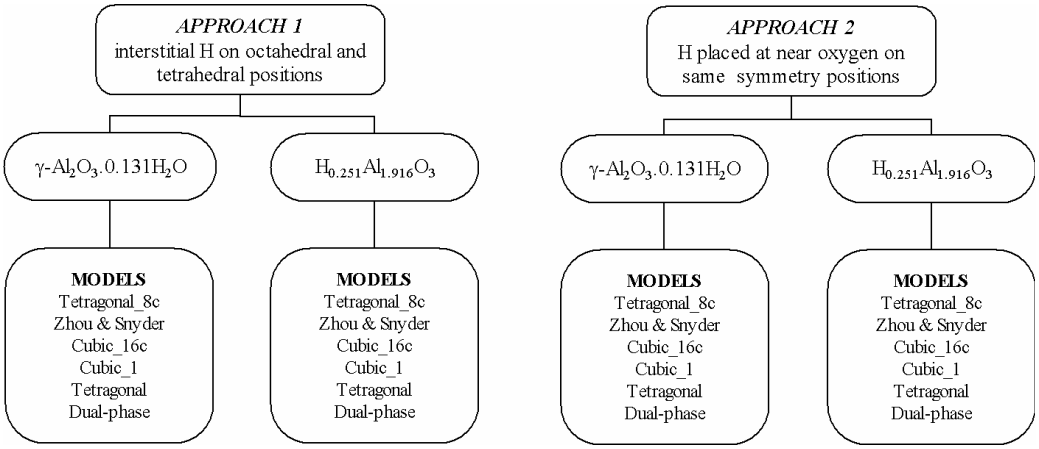

Figure 7.9. Illustration of the procedure employed in the hydrogen refinement trials.

For refinements where Al_2O_3 stoichiometry was maintained, refinements were more favourable when using approach two. Sustaining a stable refinement was extremely difficult when the occupancy of hydrogen was fixed to physically reasonable values for approach one. When catastrophic divergence in the refinement was avoided, the resulting fit was poor with high figures-of-merit relative to any of those obtained from the corresponding models that did not incorporate hydrogen (the anhydrous models). When the occupancy of hydrogen was refined, negative values always resulted indicating that the hydrogen did not prefer any of the assigned interstitial occupations. Unstable thermal parameters also resulted.

This was not the case for approach two. Refinements were stable for hydrogen occupancy fixed to physically reasonable values. Moreover, hydrogen occupancy generally remained physically reasonable when allowed to refine. Only in some cases did the hydrogen occupancy tend to become unreasonably large. The thermal parameters tended to become either uncharacteristically large, suggesting considerable migration of hydrogen through the structure, or negatively unstable. In

all cases, the best results were obtained when the hydrogen was incorporated in the Tetragonal-8*c* model, as opposed to any other tetragonal, cubic or dual-phase model. The best stable refinement yielded a profile factor of 2.75, a goodness-of-fit of 2.50, and a Bragg factor of 2.42. The fit for this refinement is illustrated in Figure 7.10a.

Refining using the stoichiometry implied by the Sohlberg *et al*. (1999) representation also resulted in the best fits being obtained for incorporation of hydrogen in the Tetragonal-8*c* model. Maintaining $Al_{1.916}O_3$ stoichiometry results in 10.21 Al's in the unit cell as opposed to 10⅔, to allow for the residual hydrogen. The same trends in instabilities, including the greater success in refining using approach two were observed, as per the refinements where Al_2O_3 stoichiometry was maintained. When the parameters were maintained within physically reasonable limits the best stable refinement yielded a profile factor of 2.68, a goodness-of-fit of 2.32, and a Bragg factor of 2.04. The fit for this refinement is illustrated in Figure 7.10b. These results suggest that the protospinel representation of Sohlberg *et al*. (1999) is more appropriate than the traditional γ-$Al_2O_3.nH_2O$ representation.

The figures of merit of the best protospinel refinements for the γ-Al_2O_3 examined here show fits that are not as good as those obtained for either the anhydrous Tetragonal-8*c* (Table 7.8) model or the Zhou and Snyder (1991) and Cubic-16*c* models. In addition, there were significant residual differences between calculated peaks and the data. These were reflected in poor profile fits when compared to the anhydrous Tetragonal-8*c* model and, in some cases, additional calculated peaks were present with none corresponding in the data. It was also found that none of the protospinel models trialed improved the calculated to data intensity mismatch at $2\theta \sim 44$ °.

To further test the stability of the most successful protospinel refinement models trialed for the present data, they were allowed to refine with the Al ions unlinked, as per the anhydrous Tetragonal-8*c* model. This improved the visual appearance of the peaks but at the expense of the crystallographic integrity of the models. In cases where the Al ions were restricted to spinel positions the overall stoichiometry deviated up to 40% below the ideal stoichiometry. For non-spinel site Al occupation in the protospinel models, the deviation from ideal stoichiometry was up to 30%. This is in distinct contrast to the anhydrous Tetragonal-8*c* model tested above (*section 7.2.2*).

The results from the protospinel trials suggest that there is no interstitial hydrogen within the crystalline bulk structure of the boehmite-derived γ-Al_2O_3 examined here. Its presence appears to be limited to the surface, as expected, and in the form of water within the amorphous content of the material. The presence of water and hydroxide groups within the structure is further investigated using PGAA (Paul *et al.* 1994), NVS (Rush and Udovic 2002), and IR analysis in *Chapter 9*.

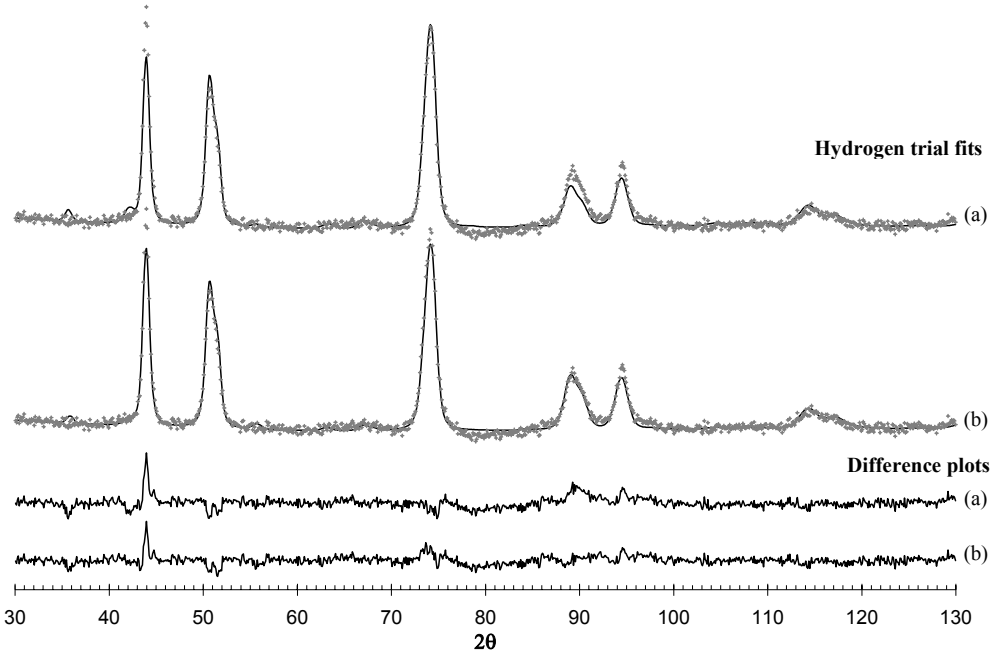

Figure 7.10. Best fits for the refinement trials incorporating hydrogen in the structure of γ-Al_2O_3; (a): using traditional protospinel stoichiometry as γ-Al_2O_3.0.131H_2O, (b): using Sohlberg *et al*. (1999) stoichiometry, $H_{0.251}Al_{1.916}O_3$. In all cases the best fits were obtained by incorporating hydrogen by approach two in the Tetagonal-8c model. Note that these fits are not as good as that for the anhydrous Tetagonal-8c model (Figure 7.8).

7.2.4 Outcomes from Study of Single Temperature Case

The research conducted here has successfully resulted in a new model, Tetragonal-8*c*, to describe the structure of boehmite-derived γ-Al_2O_3. The main outcomes of the single temperature case study are summarised below:

- The Tetragonal-8*c* model provides the correct crystallographic description of the structure of γ-Al_2O_3 when a tetragonal distortion is observed. This is the

first body of work to do so. This is a significant contribution to the portion of the scientific and industrial communities interested in structure and structural phase transitions. γ-Al_2O_3 is extremely important industrially, particularly in its role as a catalyst (and catalyst support). Accurate knowledge of the structure is vital to the understanding of the mechanisms by which its applications work and can lead to the development of future applications.

- It was demonstrated how electron diffraction patterns, typical of γ-Al_2O_3, that have consistently been indexed according to the cubic $Fd\bar{3}m$ space group can be indexed according to the tetragonal $I4_1/amd$ space group, under which the Tetragonal-8*c* model is described.
- The structure could not be accurately modelled by restricting the Al ions to spinel positions. As a result, occupation of the 8*c* Wyckoff position in addition to the 4*a* and 8*d* is proposed.
- No evidence of five-coordinated Al atoms within the structure was found in the MAS-NMR data obtained in this study. This and the subsequent Rietveld analysis suggest that the Al ions can only be situated in octahedral or tetrahedral positions.
- The presence of hydrogen in the crystalline bulk structure of γ-Al_2O_3 was also investigated. Importantly, the evidence suggests the crystalline bulk to be anhydrous. This implies that the hydrogen within the structure of γ-Al_2O_3 is situated at the surface and/or within the amorphous content. This is further investigated in *Chapter 9*.

The Tetragonal-8*c* model accommodates the observed peak splitting better than all other models investigated. The distribution of Al ions determined from the proposed Tetragonal-8*c* structural model is in agreement with the distribution obtained from MAS-NMR data. Consistency of this model for all data sets strengthens the argument for one phase as opposed to two phases. In this model there is ordering of vacancies on all the site positions, tetrahedral and octahedral. From this it can be seen why ambiguity has arisen in early work as to which sites the vacancies prefer to reside in.

Cubic γ-Al_2O_3 exhibits a diffraction pattern with the same peak positions as tetragonal γ-Al_2O_3 but no splitting and peak anisotropy. Hence, it is also proposed

that the Cubic-16*c* model, which is analogous to Tetragonal-8*c*, is appropriate to describe the structure of γ-Al_2O_3 when no tetragonal distortion is observed.

There still remains some differences between the data and the calculated pattern, particularly at $2\theta \sim 44$ °, which, to date, no model has been able to accommodate. It is anticipated that this will be elucidated by computer simulations of the structure (*Chapter 10*).

Chapter 8

Experimental Findings: Structural Evolution with Temperature

The material in this chapter has been published in:

G. Paglia, C.E. Buckley, A.L. Rohl, R.D. Hart, K. Winter, A.J. Studer, B.A. Hunter, and J.V. Hanna, 2004, "Boehmite derived γ-alumina system, 1: Structural evolution with temperature, with the identification and structural determination of a new transition phase, γ′-alumina," Chemistry of Materials, ***16****, pp. 220-236.*

Preamble

The previous chapter focused on the determination of a representative structural model for γ-Al_2O_3 from a single-temperature case. The work presented in this chapter follows on from similar work done previously within our research group (Gan 1996; O'Connor *et al.* 1997). There, the transformation pathways from gibbsite to α-Al_2O_3 were examined. Part of that work also involved examining the evolution of γ-Al_2O_3 with increasing calcination temperature using neutron diffraction. A novel description was offered, in that γ-Al_2O_3 was a dual-phase material, consisting of both cubic and tetragonal γ-Al_2O_3, which coexist at all temperatures between 400 and 900 °C. The tetragonal structure was suggested to dominate at lower temperatures with the cubic phase becoming dominant from 750 °C onward. Here, the findings are different.

A systematic study of the structural evolution with temperature is an important contribution to the understanding of the γ-Al_2O_3 system, particularly as a large number of the research papers on γ-Al_2O_3 examine materials from a single temperature case only. It is also important to investigate it using the correct crystallographic description. In this chapter the variation in the structure of γ-Al_2O_3 is investigated with changing calcination temperature. This is done using the new model determined in *Chapter 7*, which provides the correct crystallographic description of the structure of tetragonally distorted γ-Al_2O_3. The other structural

models investigated in *Chapter 7*, including the refinement trials of models incorporating hydrogen, were also trialed for data collected at all calcination temperatures, but not found to adequately describe the structure for any of the calcination products.

The investigation carried out in this chapter is for highly-crystalline boehmite calcined between 500 and 900 °C. These conditions were established in *Chapter 6*. In discussing the structural evolution a mechanism, involving short-range ordering processes, for the change in tetragonal nature with calcination temperature is suggested.

It is also demonstrated, for the material examined here, that the expected δ-Al_2O_3 phase does not form during the $\gamma \rightarrow \theta$ phase transformation sequence. A different phase, not mentioned before in the literature, is observed instead. This phase is herein designated γ'-Al_2O_3, its crystallographic structure is determined, and its evolution with temperature is detailed.

8.1 Morphology of Samples

The samples exhibited a plate-like morphology, similar to that observed by previous researchers (Wilson *et al.* 1980; Souza Santos *et al.* 2000). The plates had triangular, rectangular and rhombic-type morphologies and ranged between 0.1 and 4 μm along the longest dimension, with thicknesses between 0.1 and 0.6 μm for the larger grains (Figure 8.1). These plates are not single crystals; they are grains composed of lamellar crystallites (Wilson 1979c; 1979a; 1979b). Rietveld analysis, assuming ellipsoid crystallites, returns dimensions between 100 and 800 Å. It was determined that the differences between the data and the calculated patterns mentioned in *section 7.2.3*, particularly at $2\theta \sim 44$ °, the (220) direction, results from the inadequacy of currently available profile functions to model the crystallite shapes and sizes characteristic of these materials. Although there has recently been promising research to overcome these difficulties (Balzar *et al.* 1998; Stephens 1999), the available Rietveld codes still do not accommodate the inherent anisotropic broadening due to stacking faults and anisotropic strain. The discrepancy between the data and the calculated pattern was found for all data sets examined by Rietveld refinement at every calcination temperature. As a result, the Scherrer equation, which

ignores strain, was manually applied to the full-width-half-maximum, determined by Warren's method (Cullity 1978, pp.284-285), of the only non-overlapping peak, at $2\theta \sim 44$ °, yielding an average crystallite size of ≈ 150 Å for all samples calcined to and including 750 °C, ≈ 185 Å for samples calcined to 800 °C and ≈ 210 Å for samples calcined at 900 °C. TEM images of γ-Al_2O_3, where material appears to be decomposing at the edges of the grain, due to the electron beam intensity, indicate crystallite sizes up to 300 Å. Most crystallites appeared to be rectangular but some looked spherical.

Most of the grains were composed of multiple sheet-like layers. Overlapping SAED patterns, and CBED patterns that 'wobbled' as the beam was moved over individual grains, provided further evidence of this. It was difficult to find isolated grains which were not layered. Twinning of the grains was observed ubiquitously throughout the samples and this was also reflected in the SAED patterns. The layered nature of the grains and their twinning made it difficult to obtain non-overlapping diffraction patterns. Smaller grains tended to become unstable under the beam. The electron beam was found to cause lattice expansion in γ-Al_2O_3 when focussing for diffraction. Deliberate heating from the beam in the high vacuum environment caused fast dehydration of boehmite to form γ-Al_2O_3 as seen by previous researchers (Wilson 1979a; Kogure 1999).

The plate-like shapes of all calcination products are consistent with the boehmite precursor (Figure 8.1), until the formation of θ-Al_2O_3, indicating phase transformations within isovolumetric environments. This confirms the topotactic nature of the transformation from boehmite to θ-Al_2O_3 suggested by earlier researchers (Lippens and de Boer 1964; Saalfeld and Mehrotra 1965; Wilson 1979a).

A lamellar porous microstructure, similar to that observed by Wilson (1979c; 1979a; 1979b), Wilson *et al*. (1980) and Lippens and De Boer (1964), was observed for the calcination products (Figure 8.2). This is in contrast to the more ordered and featureless microstructure of boehmite. Hexagonal facets, much larger than those observed by others (Kogure 1999; Kryukova *et al.* 2000), were observed on the surface of all calcination products. The calcination products obtained over 800 °C showed more microstructure ordering than those obtained between 500 and 700 °C. Regions of dark contrast were observed intermittently within the grains (Figure 8.2d and g). Their occurrence is reduced with increasing calcination temperature and it is

believed here that they correspond with the location of amorphous content. Bulk structure hydrogen is likely to reside within these regions (*Section 7.2.3, Chapter 9*).

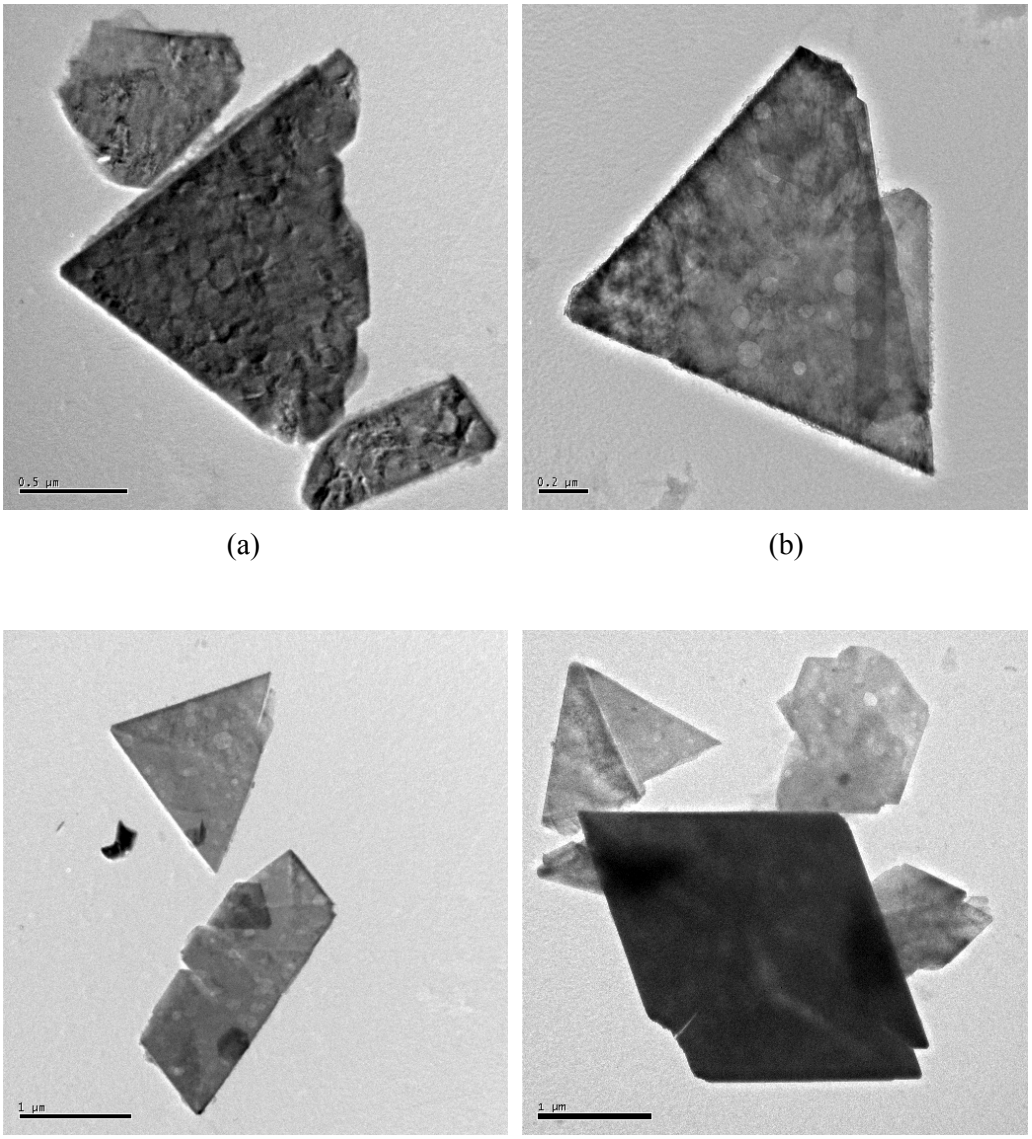

(a) (b)

(c) (d)

Figure 8.1. Examples of grain shapes; (a): boehmite, (b): γ-Al_2O_3 formed from boehmite calcined at 500 °C, (c): γ-Al_2O_3 formed from boehmite calcined at 600 °C, (d): γ-Al_2O_3 formed from boehmite calcined at 800 °C.

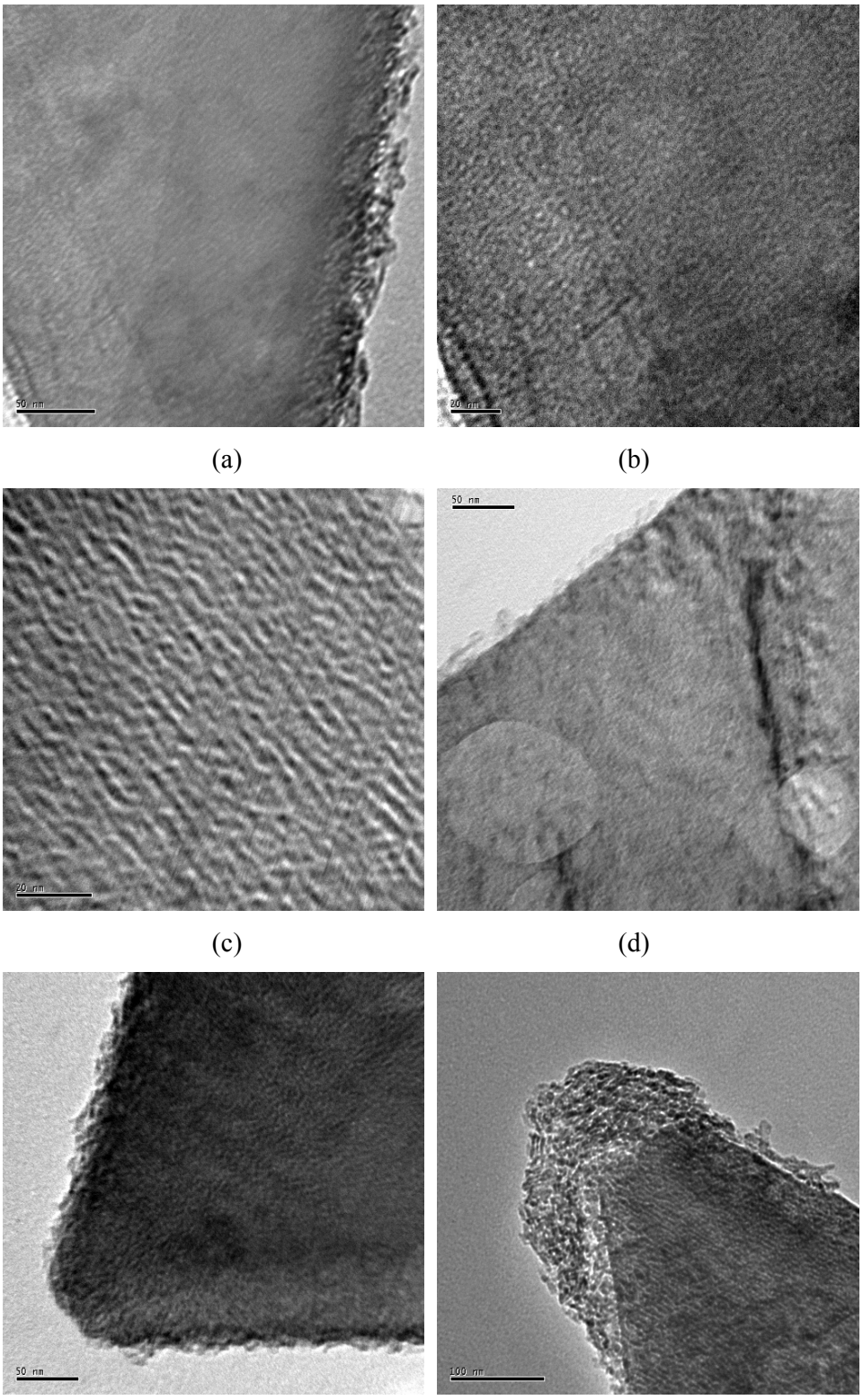

Figure 8.2. Examples of microstructure; (a) and (b): boehmite, (c) and (d): γ-Al_2O_3 formed from boehmite calcined at 500 °C, (e) and (f): γ-Al_2O_3 formed from boehmite calcined at 600 °C.

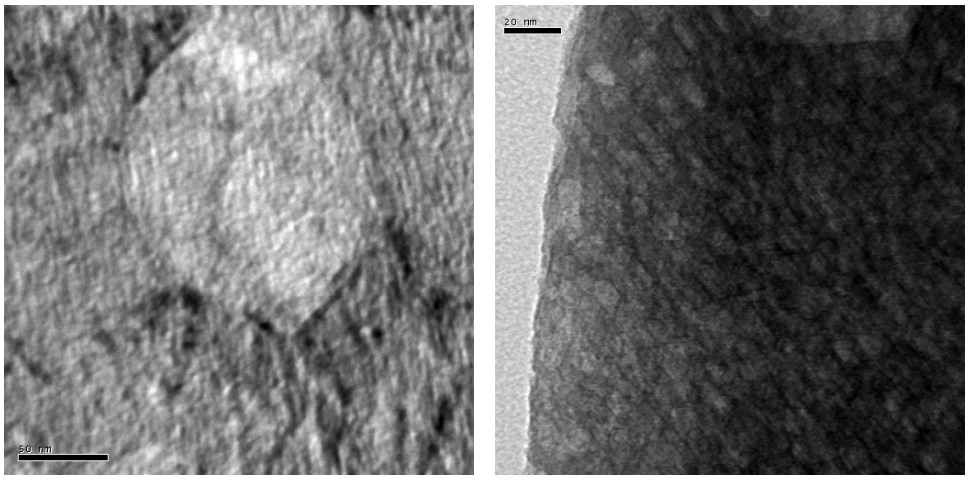

(g) (h)

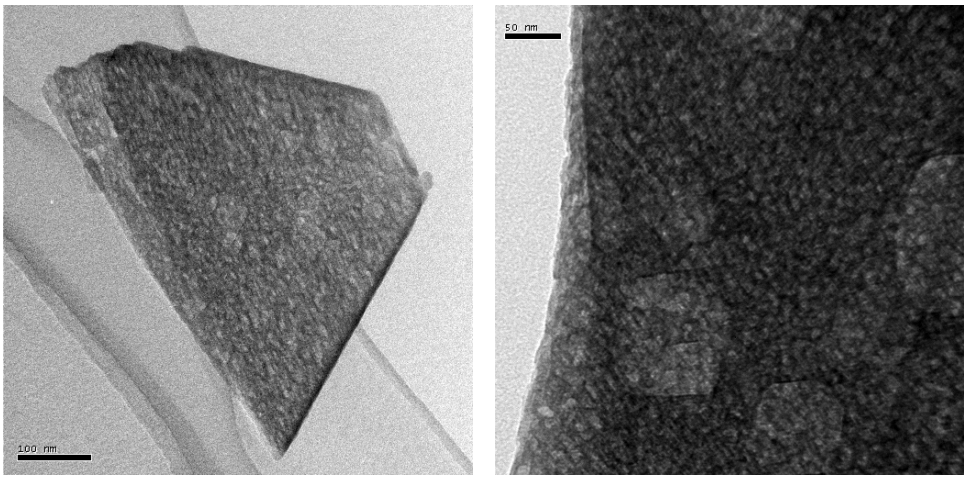

(h) (i)

Figure 8.2 (cont'd). Examples of microstructure; (g): γ-Al_2O_3 formed from boehmite calcined at 700 °C, (h): γ′-Al_2O_3 formed from boehmite calcined at 800 °C (i) and (j): γ′-Al_2O_3 formed from boehmite calcined at 900 °C.

Wilson and McConnell (1980) found no obvious variations in the microstructure of γ-Al_2O_3 (and δ or θ-Al_2O_3) samples, compared with other samples of the same phase, prepared under different conditions from the same well-crystalline boehmite precursor, calcined in air. The morphological TEM analysis performed here concurs with these findings, with no obvious differences in microstructure being observed for the calcination products obtained between 500 and 700 °C or the calcination product obtained between 800 and 900 °C.

Unlike the microstructure, diffraction patterns exhibited different characteristics for each calcination temperature within these ranges. However, the diffraction patterns did display the same features at each particular calcination

temperature for material prepared by different preparation routes from identical precursors.

8.2 Structural Variation with Temperature and the Identification of a New Phase, γ′-Alumina

MAS-NMR spectra of the hydrogenated samples of γ-Al_2O_3 (Figure 8.3) calcined between 500 and 900 °C appear identical for each temperature. As per the findings in *section 7.2* no peaks representative of pentahedrally coordinated cations were observed. The asymmetric tailing of the peaks, indicative of short-range disorder in the structure, was consistent for all temperatures (Phillips *et al.* 1988; Kohn *et al.* 1989; Kohn *et al.* 1991; Kunath *et al.* 1992; Kunath-Fandrei *et al.* 1995). The cation coordination, from peak integration, was determined to be nearly identical for each sample. The 500 °C data yields a coordination distribution of 68(2)% octahedral and 32(2)% tetrahedral for the Al ions. Data for the remaining calcination temperatures yielded a coordination distribution of 69(2)% octahedral and 31(2)% tetrahedral for the Al ions. As temperature increases, fewer octahedral sites are expected to be occupied, particularly after 750 to 800 °C, where the formation of δ-Al_2O_3 is anticipated (Morrissey *et al.* 1985; Repelin and Husson 1990; Wang *et al.* 1998). The model for δ-Al_2O_3 given by Repelin and Husson (1990) indicates that ≈ 38% of the cations are situated in tetrahedral positions, higher than the values shown in the MAS-NMR data here.

XRD patterns measured at room temperature (Figure 8.4) show that γ-Al_2O_3 is present for material calcined between 500 and 700 °C. It can be seen that the peak at $2\theta \sim 46$ ° (004) is split at 500 °C, indicating the tetragonal nature of the structure. The peaks at $2\theta \sim 39$ ° and 67 ° also exhibit splitting. The degree of splitting becomes visibly reduced up to 700 °C, coinciding with a decrease in the tetragonal nature of γ-Al_2O_3 with increasing temperature. However, a cubic γ-Al_2O_3 structure was not observed for the samples examined here. For material calcined at 800 °C the peak splitting at $2\theta \sim 46$ ° becomes more pronounced again, concurrent with an increase in tetragonal distortion. This coincides with the appearance of more peaks as the calcination temperature increases to 900 °C, which have been labelled in Figure 8.4 with a γ′ symbol. The trend of the reduced tetragonal distortion up to

700 °C, and its increase for higher calcination temperatures, is similar to the observations of Wilson (1979a), Wilson and McConnell (1980) and Gan (1996). The diffraction patterns above 800 °C are clearly not characteristic of δ-Al_2O_3 (Repelin and Husson 1990). δ-Alumina has a greater number of peaks, which are also considerably sharp, between 2θ = 30 ° and 2θ = 40 ° than what is observed in Figure 8.4. It is also clear that the structure is not γ-Al_2O_3, although the patterns maintain similar characteristics to γ-Al_2O_3. It is concluded that this is a new phase, which is herein designated γ′-Al_2O_3. It occurs in place of δ-Al_2O_3, between γ and θ-Al_2O_3, in the transformation sequence for the material examined here.

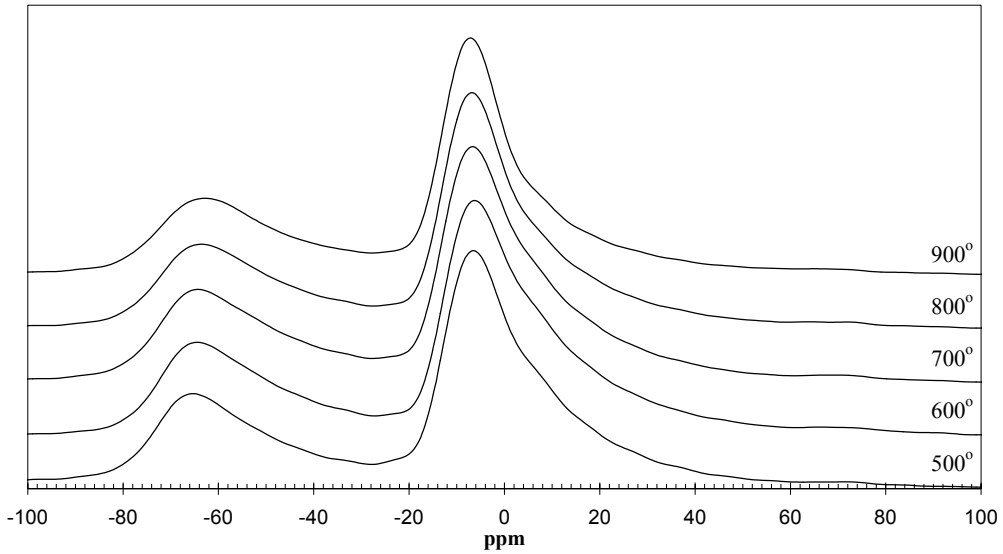

Figure 8.3. ^{27}Al MAS-NMR spectra for γ-Al_2O_3 prepared from hydrogenated boehmite precursor, calcined between 500 and 900 °C.

Similar variations in the diffraction patterns are observed for neutron data. Figure 8.5 shows neutron diffraction patterns of hydrogenated boehmite calcined between 500 and 900 °C. Higher background contributions are characteristic of the data between 500 and 600 °C (although not clear from Figure 8.5). The background is significantly flatter at 650°C, suggesting reduced amorphous content. Beyond 700 °C, there was little change in the background of each neutron diffraction pattern. The tetragonal nature, signified by split peaks, is still evident at 700 °C. At 750 °C the sample is still considered to be γ-Al_2O_3. However, instead of a reduced tetragonal profile at $2\theta \sim 44$ °, the peak is once more increasingly split. This represents the

initial formation of the first γ′-Al_2O_3 peak. The same trends were observed for all neutron data collected, both at room temperature and while heating *in situ*. The only exception is that γ′-Al_2O_3 is clearly formed at 750 °C, instead of 800 °C, for the deuterated boehmite precursor.

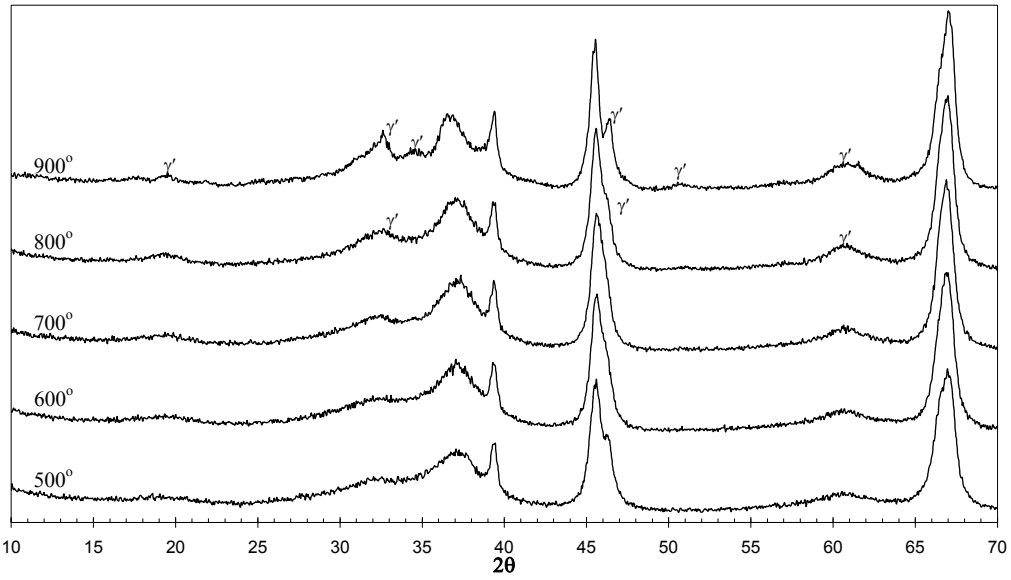

Figure 8.4. XRD patterns for hydrogenated boehmite calcined between 500 and 900 °C. The diffraction patterns from 500 to 700 °C represent γ-Al_2O_3. The diffraction patterns at 800 and 900 °C represent γ′-Al_2O_3. The γ′ symbol indicates emerging peaks that distinguish the material as γ′-Al_2O_3.

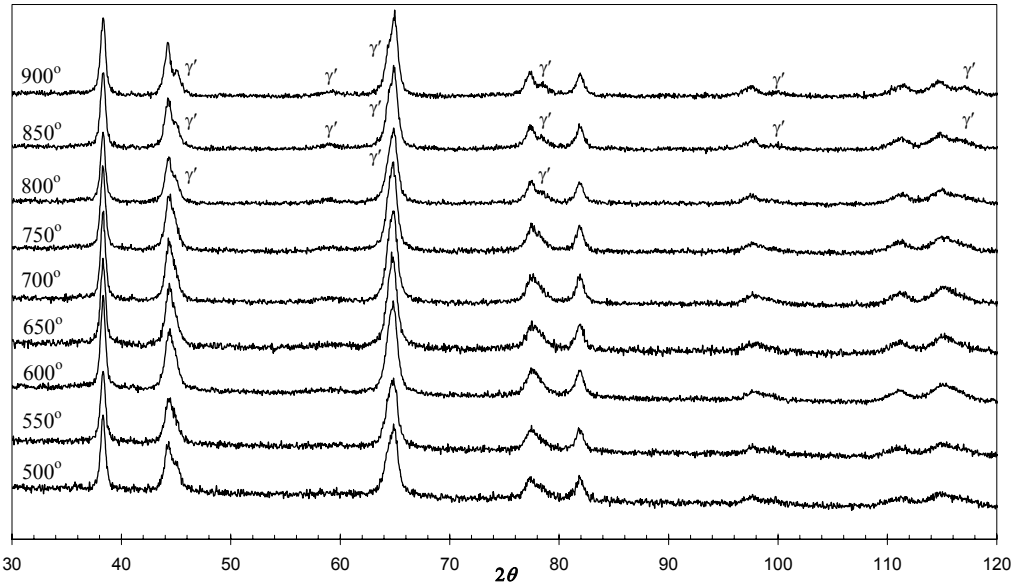

Figure 8.5. HRPD neutron diffraction patterns for hydrogenated boehmite pre-calcined for seven hours at temperatures between 500 and 900 °C. The γ′ symbol indicates emerging peaks that distinguish the material as γ′-Al_2O_3.

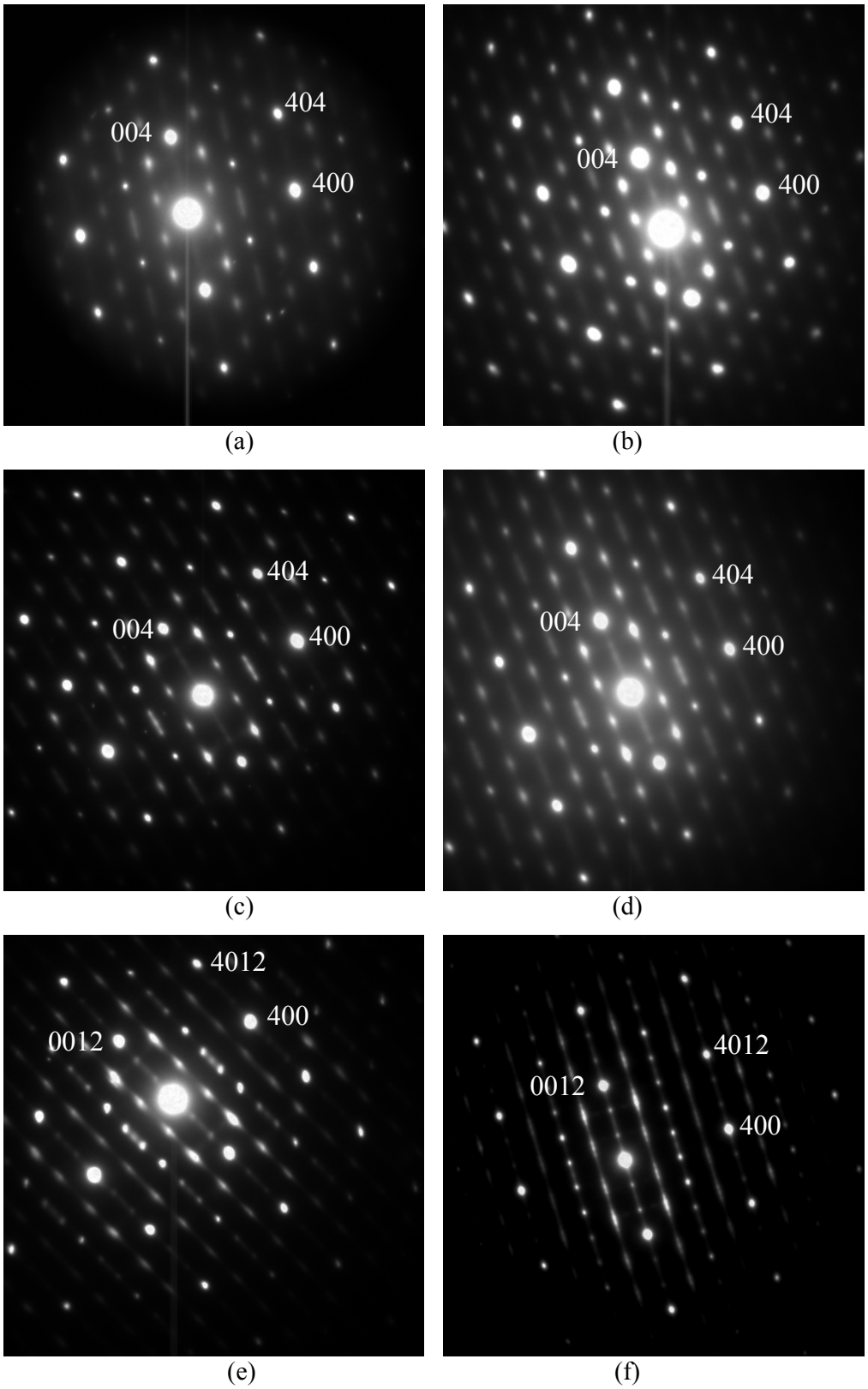

Figure 8.6. SAED patterns, looking down the [0*k*0] zone axis, for hydrogenated boehmite pre-calcined for seven hours at (a): 500 °C, (b): 600 °C, (c): 650 °C, (d): 700 °C, (e): 800 °C, and (f): 900 °C.

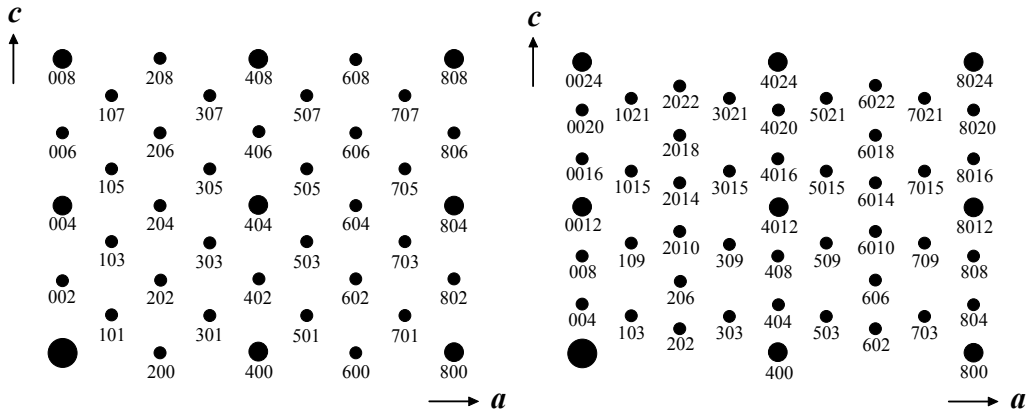

Figure 8.7. Indexing diagrams, using the *I4₁/amd* space group, looking down the [0*k*0] zone axis, for (a): γ-Al_2O_3 and (b): γ′-Al_2O_3.

The continuous change in the diffraction patterns with increasing temperature, the absence of lattice changes in difference plots, the consistency between room temperature and *in situ* data, and the lack of endotherms with marginal mass losses in DTA-TGA curves (*section 6.2.1*) after the formation of γ-Al_2O_3 suggest a higher-order phase transformation. This implies continuous variation of the sub-cell parameters in the transformation from γ-Al_2O_3 (Wilson and McConnell 1980).

The higher-order phase transformation is directly evident from SAED patterns (Figure 8.6), which show increased streaking with increasing calcination temperature between 500 and 700 °C, as shown by the streaking about the *hkl*: $h + k + l = 2n$ reflections, *e.g.* (200). At 700 °C, two peaks can be seen at the extremities of the streak about (200). By 800 °C the reflections exhibit the same characteristics as the lower temperature diffraction patterns. However, additional reflections have appeared and a new symmetry reduced unit cell comprising a triple cell of the original γ-Al_2O_3 unit cell is suggested. The (200) reflection, no longer a defined peak, has split into two (202) peaks of the new γ′-Al_2O_3 phase. By 900 °C the triple cell is the same as that at 800 °C but what was once streaking about the (200) reflection has almost disappeared and the *h*0*l*: $h + l = even$ reflections of the γ′-Al_2O_3 phase, *e.g.* (109), show increased streaking and splitting into multiple peaks. The diffraction pattern at 900 °C shows some characteristics of a δ-Al_2O_3 pattern.

Figure 8.7 shows the indexing diagrams for γ-Al_2O_3 and γ′-Al_2O_3. The diffraction patterns were obtained down the [0*k*0] zone axis. Diffraction patterns down the [00*l*] zone axis could not be obtained as a tilt rotate stage was unavailable.

Lippens and de Boer (1964) showed there are three types of reflections for γ-Al_2O_3. The most diffuse or streaked, the *hkl*: $h + k + l = 2n$ reflections, represent planes with Al ions in tetrahedral positions. The sharpest and most intense peaks, the *hkl*: $h + k + l = 4n$ reflections, *e.g.* (400) and (202), originate from planes with both cations and oxygens. The final type of reflection originates from planes with octahedrally and tetrahedrally coordinated cations. The *h*0*l*: $h + l = even$ reflections, *e.g.* (103), are of this type. These are more diffuse than the sharpest peaks and are not as streaked as those from the tetrahedral sublattice. No reflections originate solely from the octahedral sublattice but it has been deduced that it is more ordered than the tetrahedral sublattice and less ordered than the oxygen sublattice (Zhou and Snyder 1991). Reflection shapes, particularly from the *h*0*l*: $h + l = even$ reflections, were found to vary, indicating some disorder in the cation lattice. However, the oxygen sublattice remains undisturbed with changing calcination temperature, consistent with the findings of other researchers (Morrissey *et al.* 1985; Jayaram and Levi 1989).

Streaking is attributed to stacking faults at cationic vacancies (Cowley 1953). Variation in streak length with temperature represents change in the ordering of Al cations, synonymous with higher-order transformations (Wilson 1979a; Wilson and McConnell 1980). The streaking of the *hkl*: $h + k + l = 2n$ reflections indicate vacancy ordering on tetrahedral positions in γ-Al_2O_3 (Lippens and de Boer 1964). For δ-Al_2O_3, the reflections originating from planes with tetrahedral positions are sharp while those originating from planes with cations in variable coordination become sharp, indicating increased vacancy ordering on the octahedral sites only. A similar phenomenon is observed here for γ′-Al_2O_3 but vacancy ordering on tetrahedral positions is still evident. The diffuseness of the *h*0*l*: $h + l = even$ reflections in γ-Al_2O_3, which clearly increases with calcination temperature, suggests that vacancies are distributed among octahedral positions also. Vacancy distribution among octahedral and tetrahedral sites in γ-Al_2O_3 is also indicated by Rietveld refinements (refer also to *Chapter 7*). The measured coordination distribution from

MAS-NMR data provides further support for vacancies on octahedral and tetrahedral sites for both γ-Al_2O_3 and γ′-Al_2O_3.

8.3 Structural Details of γ-Alumina

The tetragonal model, Tetragonal-8*c*, determined for γ-Al_2O_3 in *section 7.2.2* was most suitable to refine the data obtained for all material calcined between 500 and 750 °C (700 °C for the deuterated material). All refinement data for the Tetragonal-8*c* model at each temperature is presented in *Appendix II*. The Cubic-16*c* model (*section 7.2*), the dual-phase refining approach of Gan (1996; *sections 7.1 and 7.2.2*) and refinements of all structural models with interstitial hydrogen incorporated (*section 7.2.3*), were trialed at all temperatures between 500 and 750 °C also. These structure refinements did not provide fits as good as the Tetragonal-8*c* model. Wilson and McConnell (1980) also did not observe a cubic γ-Al_2O_3, attributing the absence to the process of vacancy ordering on octahedral sites which takes over and causes the increased tetragonal distortion that coincides with the next transition phase (δ-Al_2O_3 in their case).

Lattice expansion caused by the electron beam heating resulted in no observed trend from SAED patterns. The unit cell parameters were essentially constant, with respect to the inherent error associated with selected area electron diffraction. The measured *a* parameter was 5.70 ± 0.5 Å for both γ-Al_2O_3 and γ′-Al_2O_3. For γ-Al_2O_3 the *c* parameter was 8.0 ± 0.8 Å, and for γ′-Al_2O_3 it was 24.0 ± 2.3 Å.

Trends in the lattice parameters were observed from the neutron diffraction data. Figure 8.8 illustrates the change in lattice parameters with calcination temperature from room temperature sample data. There is a small but definite increase in the *c* parameter until 600 °C, after which it remains effectively constant within the limits of the experimental uncertainty. This parameter corresponds to the contracted axis of cubic representations of tetragonally distorted γ-Al_2O_3 and the trend is consistent with these reports, *i.e.* that it coincides with reduced tetragonal distortion (Yanagida and Yamaguchi 1964; Wilson 1979a; Wilson and McConnell 1980). However, the *a* parameter also varies, initially decreasing before becoming effectively level after 600 °C. The net effect is constant volume within the limits of

the uncertainties. For data collected during *in situ* heating there was a continuously increasing trend in cell volume due to the increasing thermal energy within the furnace.

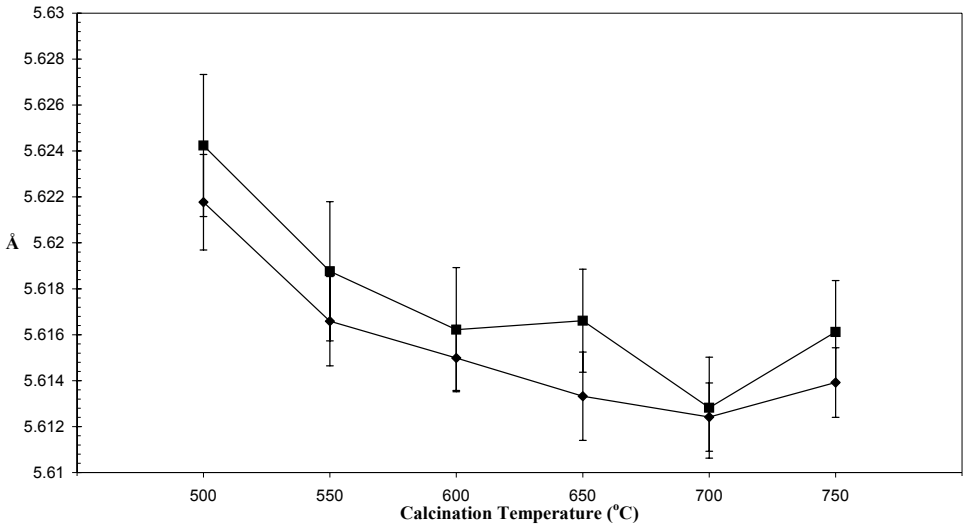

(a)

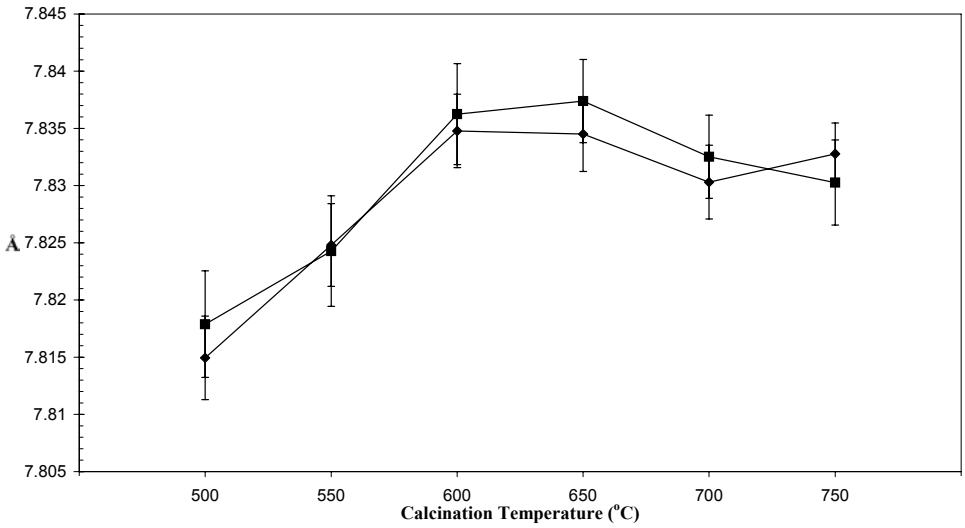

(b)

Figure 8.8. Variation in (a): *a* and (b): *c* parameters for γ-Al_2O_3 from Rietveld refinement of neutron diffraction data collected at room temperature from hydrogenated boehmite calcined for seven hours; ♦ - HRPD, ■ - MRPD.

Variation in the *y* coordinate of the oxygen sublattice asymmetric unit shows convergence of the coordinates with increasing calcination temperature to 650 °C (Figure 8.9). Because the data in Figure 8.9 represents the same material, and even though the uncertainties are large, the trend is significant. The convergence at 650 °C

suggests increased ordering of the oxygen sublattice. By 700 °C the data diverges again as the splitting of the *hkl*: $h + k + l = 2n$ reflections commences and the γ′-Al_2O_3 phase becomes important. Beyond 700 °C the data begins to converge again as the ordering processes, which result in the γ′-Al_2O_3 structure, begin to dominate. Similar trends were observed for the *z* coordinate of the oxygen sublattice asymmetric unit. These trends also correspond to increased Bragg factors for Rietveld refinement of the γ-Al_2O_3 structure above 650 °C, as processes leading to γ′-Al_2O_3 became important.

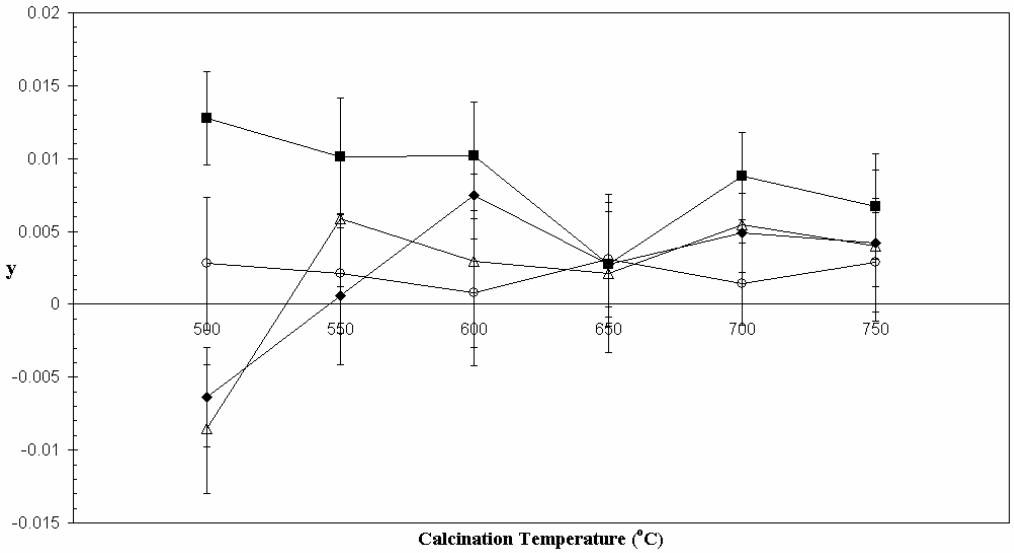

Figure 8.9. Variation in oxygen fractional y coordinate from Rietveld refinement of neutron diffraction data with calcination temperature for various samples; ♦: HRPD data collected from hydrogenated material at room temperature, ■: MRPD data collected from hydrogenated material at room temperature, △ and ○: MRPD data collected during *in situ* heating from hydrogenated material.

The distribution of cations in octahedral and tetrahedral coordination obtained from Rietveld refinements was consistent with the MAS-NMR data at each calcination temperature, with the proportion of cations on octahedral and tetrahedral sites always constant within 3%. From the variation of occupancy with calcination temperature (Figure 8.10) greater fluctuation in the octahedral and tetrahedral site occupancies was observed at lower temperatures, suggesting a lower degree of order. For higher calcination temperatures, the occupancy of tetrahedral sites tended to be constant whereas changes in the ordering between the octahedral site positions was evident. An exception to the constant occupancies of tetrahedral sites was exhibited

by the MRPD data obtained at room temperature; occupancy increased with calcination temperature, which coincides with the increased streaking observed in SAED patterns.

Insight into the causes of the tetragonal nature, and its reduction with higher calcination temperature, is provided by the observed changes in lattice parameters, coordinate positions, and occupancy. Loss of water from the lattice has previously been suggested to cause the reduced tetragonal distortion (Yanagida and Yamaguchi 1964). Water loss is observed here, suggested by the lower background contributions observed with increasing calcination temperature in the neutron diffraction patterns. However, for water loss to be synonymous with the degree of tetragonal distortion, hydrogen must be present within the unit cell. Neutron data Rietveld refinements of the unit cell suggest that the presence of interstitial hydrogen is not likely within the bulk crystalline structure (*section 7.2.3*). Also, from TEM (Figure 8.2), distinct amorphous regions were observed within the γ-Al_2O_3 grains, separate to the lamellar porous microstructure which constitute the crystalline structure. The structural water molecules are most likely to be present in these amorphous regions.

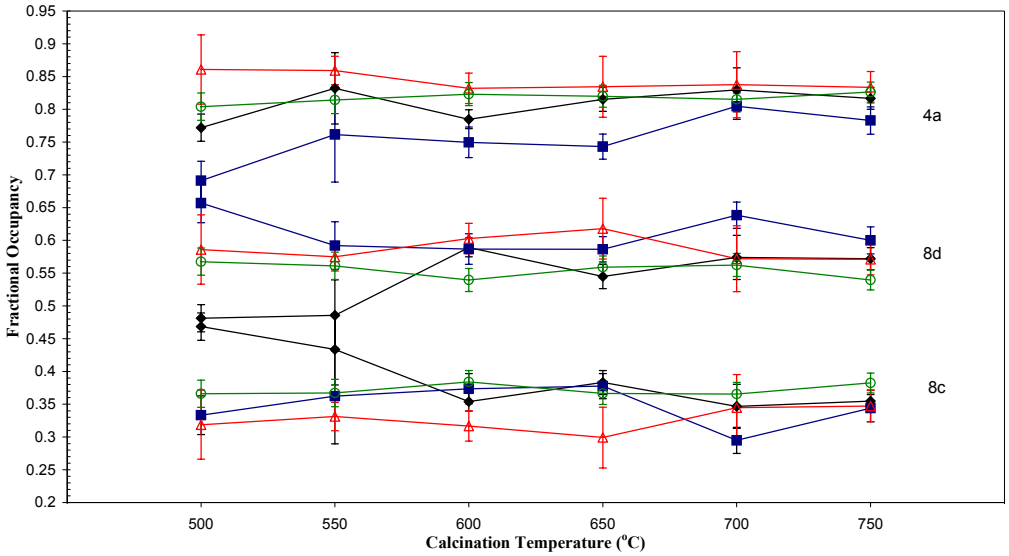

Figure 8.10. Variation in occupancy of octahedral (8*c* and 8*d*) and tetrahedral (4*a*) site positions from Rietveld refinement of neutron diffraction data with calcination temperature for various samples; ♦ (black): HRPD data collected from hydrogenated material at room temperature, ■ (blue): MRPD data collected from hydrogenated material at room temperature, △ (red) and ○ (green): MRPD data collected during *in situ* heating from hydrogenated material. The same colours are used for the 4*a*, 8*c*, and 8*d* occupancies from refinements of the same type of data to aid the visibility of the trends.

Lippens and de Boer (1964) suggested the tetragonal distortion itself is due to shrinkage anisotropy of the lattice parameters during boehmite dehydration. Anisotropic change in the lattice parameters is also observed here after the formation of γ-Al_2O_3 and the lattice parameters become constant as the oxygen sublattice becomes more ordered (Figure 8.8).

It has also been proposed that the reduced tetragonal distortion is due to changes in cation ordering (Wilson 1979a; Wilson and McConnell 1980). Variation in cation ordering is observed here (Figures 8.6 and 8.10). The unit cell of γ-Al_2O_3 is considered to be made up of the skeletal oxygen layers which remain intact after the OH layers of the boehmite precursor are broken down (Lippens and de Boer 1964; Wilson 1979b; Wilson *et al.* 1980). This leaves a cell with, initially, empty inter-skeletal layer regions. It is proposed that short-range ordering occurs within the unit cell whereby cations migrate into site positions within the inter-skeletal layers. The atoms within these regions will initially be rather disordered but increasingly become ordered as the structure evolves with higher temperature treatment. This inter-skeletal layer ordering would cause the variations in the oxygen sublattice seen here (Figure 8.9), which, in turn, causes the observed anisotropy in the lattice parameters followed by them becoming constant (Figure 8.8). More atoms migrate into the inter-skeletal layers as the structure evolves, with the proportion of octahedrally and tetrahedrally coordinated aluminium remaining constant, as per the MAS-NMR spectra (Figure 8.3). This migration accounts for the variations in occupancy observed (Figure 8.10) as atoms move from one site position to another.

8.4 Determination of the Structure of γ'-Alumina

From the diffraction patterns above, cation ordering was more noticeable, and occurred over a shorter temperature range, for γ'-Al_2O_3. Similar to observations in the literature for δ-Al_2O_3 (Wilson 1979a; Wilson and McConnell 1980), the increase in tetragonal distortion in the neutron and X-ray diffraction patterns of γ'-Al_2O_3 coincided with the migration of vacancies to octahedral positions, indicated by the SAED patterns.

The Rietveld refined model of γ-Al_2O_3 was capable of modelling the data for γ'-Al_2O_3, but because of the physical differences known to exist between these

materials it would have been incorrect to follow this path. Determination of the unit cell structure of γ′-Al_2O_3 proceeded by considering a trial structure model, consisting only of oxygen ions as a triple cell of γ-Al_2O_3, as indicated by the SAED results. Based on a physically meaningful distribution and the size of the site positions, a number of octahedral and tetrahedral positions were trialed. The process involved iteratively keeping some cations fixed while others were refined. The refinements presented here represent the best trials (Tables 8.1 and 8.2). All other refinement data for the γ′-Al_2O_3 model at each temperature is presented in *Appendix III*. An example of a refinement fit is shown in Figure 8.11 for MRPD data. From indexing, the oxygen sublattice configuration, and the Al distribution, it became apparent that γ′-Al_2O_3 was represented in the $P\bar{4}m2$ space group. Refinements under this space group best preserved the oxygen lattice while allowing the cations to become more ordered with respect to the γ-Al_2O_3 precursor. The unit cell dimensions and space group obtained are similar to that determined for δ-Al_2O_3 by Repelin and Husson (Repelin and Husson 1990). Both the 800 and 900 °C data refinements yielded 66(3)% octahedral and 34(3)% tetrahedral Al ion coordination. This is in agreement with the MAS-NMR data and supports the plausibility of these structural models.

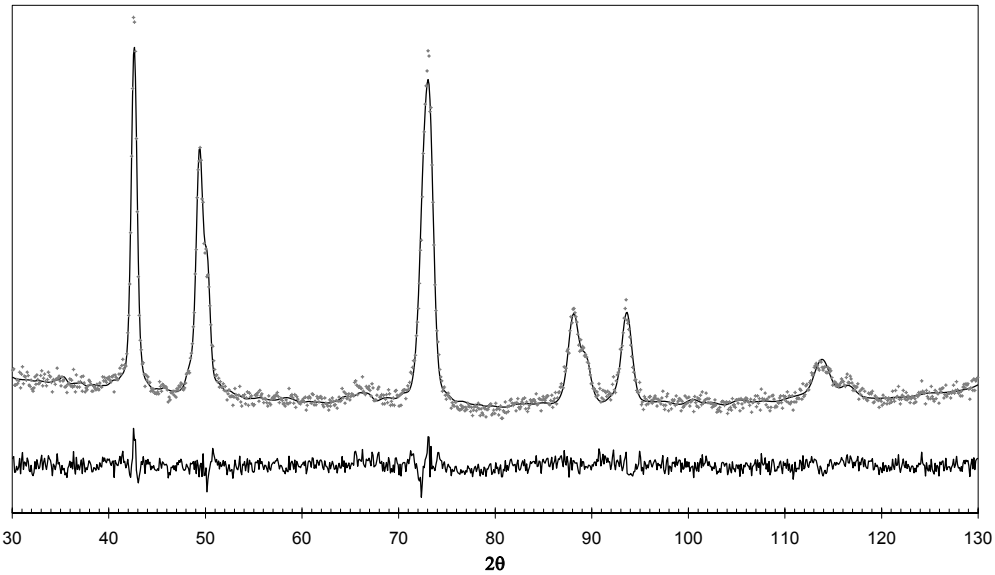

Figure 8.11. Rietveld refinement for γ′-Al_2O_3 formed by calcination of hydrogenated boehmite calcined at 800 °C for seven hours.

Unlike γ-Al_2O_3, the change in the ordering of the sites is obvious when looking directly at the Rietveld structure models of γ′-Al_2O_3 between 800 and 900 °C (Tables 8.1 and 8.2). Cations in octahedral sites are considerably disordered, which is a consequence of the rapid change in the structure of γ′-Al_2O_3 with increasing temperature treatment. It therefore appears that γ′-Al_2O_3 can be considered as a series of transition states within the γ-Al_2O_3 to θ-Al_2O_3 transformation.

A reduced number of occupied site positions were observed with increasing temperature. At 800 °C there are some symmetry-equivalent positions with low occupancy. These low occupancies occur as a result of symmetry. This is to say that occupied symmetry-equivalent site positions in close proximity to each other have low occupancies to maintain physically reasonable average interatomic distances. The atoms were generally found to migrate from symmetry positions with low occupancy to other sites with higher occupancy as treatment temperature increased. By 900 °C the structure is again more ordered with a reduced number of octahedral and tetrahedral sites occupied by cations. The number of occupied site positions approaches that of the δ-Al_2O_3 model of Repelin and Husson (1990). Also at 900 °C, one of the octahedral positions, at (0.1353, 0.5, 0.0013), appears significantly distorted to warrant its consideration as atoms migrating from octahedral to tetrahedral positions. These observations are consistent with the observation by SAED that at 900 °C the structure appears to be approaching that of δ-Al_2O_3.

Table 8.1a. Structural parameters of γ′-Al_2O_3 formed by calcination of hydrogenated boehmite calcined at 800 °C for seven hours. The data was collected at room temperature using MRPD. Uncertainties are to three standard deviations. All uncertainties, where not stated otherwise, are 0.005 for refinable coordinate positions and 0.3 for thermal parameters.

Space group $P\bar{4}m2$, $a = 5.611(3)$, $c = 24.450(12)$, $R_p = 3.51$, $\chi^2 = 1.71$, $R_B = 1.01$.

	Site	x	y	z	B(Å^2)	occupancy
	O (4*j*)	0.2334	0	0.1214	1.5	1.0
	O (4*j*)	0.2621	0	0.2965	1.5	1.0
	O (4*j*)	0.2470	0	0.4572	1.5	1.0
	O (4*j*)	0.2342	0	0.6255	1.5	1.0
	O (4*j*)	0.2294	0	0.7982	1.5	1.0
	O (4*j*)	0.2548	0	0.9581	1.5	1.0
	O (4*k*)	0.2334	0.5	0.1157	1.5	1.0
	O (4*k*)	0.2621	0.5	0.2965	1.5	1.0
	O (4*k*)	0.2470	0.5	0.4572	1.5	1.0
	O (4*k*)	0.2342	0.5	0.6255	1.5	1.0
	O (4*k*)	0.2294	0.5	0.7904	1.5	1.0
	O (4*k*)	0.2548	0.5	0.9581	1.5	1.0
T	Al (2*e*)	0	0	0.2620	1.1	0.25
T	Al (2*f*)	0.5	0.5	0.0882	1.1	0.75
T	Al (2*f*)	0.5	0.5	0.1816	1.1	1.0
T	Al (2*f*)	0.5	0.5	0.4194	1.1	1.0
T	Al (4*i*)	0.2518	0.2513	0.5	1.1	0.25
T	Al (8*l*)	0.2590	0.2546	0.1703	1.1	0.375
T	Al (8*l*)	0.2510	0.2513	0.3297	1.1	0.125
O	Al (4*j*)	0.2490	0	0.1987	1.1	0.75
O	Al (4*j*)	0.2457	0	0.3751	1.1	1.0
O	Al (4*j*)	0.2530	0	0.5536	1.1	0.25
O	Al (4*j*)	0.2457	0	0.8811	1.1	0.5
O	Al (4*k*)	0.2680	0.5	0.0331	1.1	0.125
O	Al (4*k*)	0.2590	0.5	0.2108	1.1	0.5
O	Al (4*k*)	0.2506	0.5	0.3759	1.1	0.875
O	Al (4*k*)	0.2562	0.5	0.7106	1.1	1.0
O	Al (4*k*)	0.2512	0.5	0.8861	1.1	0.25

Table 8.1b. Aluminium – Oxygen bond lengths (Å) and angles (°) for γ′-Al_2O_3 formed by calcination of hydrogenated boehmite calcined at 800 °C for seven hours. The top half of the table reports the Al-O distances within each octahedra and tetrahedra. The bottom half of the table reports the O-Al-O angles within each octahedra and tetrahedra. Repeat values for the distances and angles are only reported once. Uncertainties are to three standard deviations. All uncertainties, where not stated otherwise, are 0.008 for distances and 0.05 for angles.

Al (2e)─O	1.678	1.910		
Al (2f)─O	1.630	1.752		
Al (2f)─O	1.654	2.150		
Al (2f)─O	1.666	1.834		
Al (4i)─O	1.725			
Al (8l)─O	1.590	1.682	1.813	1.901
Al (8l)─O	1.609	1.750		
Al (4j)─O	1.815	1.901	1.925	2.294
Al (4j)─O	1.846	1.905	1.924	1.940
Al (4j)─O	1.691	1.976	1.999	2.260
Al (4j)─O	1.833	1.902	1.921	1.939
Al (4k)─O	1.757	1.905	1.949	2.048
Al (4k)─O	2.009	2.033	2.112	2.235
Al (4k)─O	1.725	2.044	2.048	2.052
Al (4k)─O	1.878	1.919	1.969	1.999
Al (4k)─O	1.832	2.049	2.056	2.104
O─Al(2e)─O	122.38	84.74		
O─Al(2f)─O	133.27	103.46		
O─Al(2f)─O	133.21	88.20		
O─Al(2f)─O	116.92	108.80		
O─Al(4i)─O	109.81	108.82		
O─Al(8l)─O	117.40	101.09		
O─Al(8l)─O	107.53	106.30		
O─Al(4j)─O	179.08	94.57	89.18	
O─Al(4j)─O	176.93	93.72	90.61	
O─Al(4j)─O	175.57	99.83	89.78	
O─Al(4j)─O	177.81	91.44	89.54	
O─Al(4k)─O	171.88	97.91	94.05	90.33
O─Al(4k)─O	176.80	96.08	91.90	81.72
O─Al(4k)─O	178.42	94.40	93.22	87.46
O─Al(4k)─O	171.87	92.38	91.49	87.54
O─Al(4k)─O	178.10	95.08	91.37	86.79

Table 8.2a. Structural parameters of γ′-Al_2O_3 formed by calcination of hydrogenated boehmite calcined at 900 °C for seven hours. The data was collected at room temperature using MRPD. Uncertainties are to three standard deviations. All uncertainties, where not stated otherwise, are 0.005 for refinable coordinate positions and 0.3 for thermal parameters.

Space group $P\bar{4}m2$, $a = 5.617(3)$, $c = 24.405(12)$, $R_p = 4.03$, $\chi^2 = 2.13$, $R_B = 1.70$.

	Site	x	y	z	B(Å^2)	Occupancy
	O (4*j*)	0.2394	0	0.1223	1.1	1.0
	O (4*j*)	0.2708	0	0.2922	1.1	1.0
	O (4*j*)	0.2430	0	0.4566	1.1	1.0
	O (4*j*)	0.2302	0	0.6214	1.1	1.0
	O (4*j*)	0.2298	0	0.7975	1.1	1.0
	O (4*j*)	0.2444	0	0.9575	1.1	1.0
	O (4*k*)	0.2394	0.5	0.1191	1.1	1.0
	O (4*k*)	0.2708	0.5	0.2951	1.1	1.0
	O (4*k*)	0.2430	0.5	0.4566	1.1	1.0
	O (4*k*)	0.2302	0.5	0.6214	1.1	1.0
	O (4*k*)	0.2298	0.5	0.7897	1.1	1.0
	O (4*k*)	0.2444	0.5	0.9575	1.1	1.0
T	Al (2*e*)	0	0	0.3300	0.8	0.375
T	Al (2*f*)	0.5	0.5	0.0882	0.8	0.5
T	Al (2*f*)	0.5	0.5	0.1816	0.8	1.0
T	Al (2*f*)	0.5	0.5	0.4200	0.8	1.0
T	Al (4*i*)	0.2518	0.2513	0.5	0.8	0.1875
T	Al (8*l*)	0.2588	0.2546	0.1703	0.8	0.5625
O	Al (4j)	0.2490	0	0.1987	0.8	0.5
O	Al (4j)	0.2457	0	0.3751	0.8	1.0
O	Al (4j)	0.2457	0	0.8810	0.8	0.6875
O	Al (4k)	0.2590	0.5	0.2108	0.8	0.625
O	Al (4k)	0.2506	0.5	0.3759	0.8	1.0
O	Al (4k)	0.2562	0.5	0.7106	0.8	1.0
O	Al (4k)	0.1353	0.5	0.0013	0.8	0.4375

Table 8.2b Aluminium – Oxygen bond lengths (Å) and angles (°) for γ′-Al_2O_3 formed by calcination of hydrogenated boehmite calcined at 900 °C for seven hours. The top half of the table reports the Al-O distances within each octahedra and tetrahedra. The bottom half of the table reports the O-Al-O angles within each octahedra and tetrahedra. Repeat values for the distances and angles are only reported once. Uncertainties are to three standard deviations. All uncertainties, where not stated otherwise, are 0.008 for distances and 0.05 for angles.

Al(2e)─O	1.722	1.760		
Al (2f)─O	1.633	1.790		
Al (2f)─O	1.660	2.069		
Al (2f)─O	1.679	1.799		
Al (4i)─O	1.733			
Al (8l)─O	1.598	1.799	1.847	1.692
Al (4j)─O	1.789	1.905	1.931	2.192
Al (4j)─O	1.893	1.908	1.929	1.945
Al (4j)─O	1.813	1.962	1.928	1.933
Al (4k)─O	1.973	2.034	2.112	2.150
Al (4k)─O	1.758	2.028	2.078	2.074
Al (4k)─O	1.857	1.884	1.932	2.093
Al (4k)─O	1.194	1.889	2.366	2.681
O─Al(2e)─O	119.68	97.33		
O─Al(2f)─O	127.37	106.69		
O─Al(2f)─O	132.23	90.07		
O─Al(2f)─O	118.59	114.81		
O─Al(4i)─O	112.33	107.81		
O─Al(8l)─O	115.90	102.13		
O─Al(4j)─O	178.50	94.40	91.41	89.70
O─Al(4j)─O	176.29	94.60	87.20	
O─Al(4j)─O	178.61	92.56	89.54	86.48
O─Al(4k)─O	178.99	96.61	91.60	89.07
O─Al(4k)─O	177.49	98.08	93.65	85.25
O─Al(4k)─O	173.80	97.39	88.87	
O─Al(4k)─O	98.92	95.21	81.87	

8.5 Outcomes

The research conducted here has provided insight into the structural evolution of boehmite-derived γ-Al_2O_3 with changing calcination temperature. The main outcomes are summarised below:

- Tetragonal γ-Al_2O_3 was found to be present between 450 and 750 °C. The structure showed a reduction in the tetragonal distortion with increasing temperature but at no stage was cubic γ-Al_2O_3 obtained.

- Neutron data Rietveld refinements of the structural models suggest that hydrogen is not present within the bulk crystalline structure of any of the calcination products.
- Amorphous regions, where hydrogen is most likely to reside in the bulk structure, were observed in TEM micrographs.
- Examination of the progress of cation migration in γ-Al_2O_3 indicates the reduction in the tetragonal nature is due to short-range ordering within inter-skeletal oxygen layers of the unit cell, left over from the breakdown of the hydroxide layers of boehmite when the transformation occurred.
- Above 750 °C, δ-Al_2O_3 was not observed, but a new phase was identified and designated γ′-Al_2O_3. The structure of this phase was determined to be a triple cell of γ-Al_2O_3 and is herein described using the $P\bar{4}m2$ space group. The cation ordering is more obvious in this structure, with fewer site positions being occupied with increasing calcination temperature. Hence the structure of γ′-Al_2O_3 may be considered as a series of transition states within the γ-Al_2O_3 to θ-Al_2O_3 transformation. Some distorted cation positions indicate the onset of migration from octahedral to tetrahedral sites at 900 °C, where the structure approaches the appearance of δ-Al_2O_3. The identification and provision of a structural model for γ′-Al_2O_3 is an important and speedy contribution considering that other transition phases, which have been known of for many years, still have no structural model presented for them.
- Constant cation coordination, of ~ 69% octahedral and ~ 31% tetrahedral, was observed from MAS-NMR spectra of material calcined at temperatures between 500 and 900 °C. These values agree with the cations in octahedral and tetrahedral coordination obtained in the Rietveld refinements, supporting the physical integrity of the structure models.

Chapter 9

Experimental Findings: Consideration of Hydrogen and Surface Effects

The material in this chapter has been published in:

G. Paglia, C.E. Buckley, T.J. Udovic, A.L. Rohl, F. Jones, C.F. Maitland and J. Connolly 2004, "Boehmite derived γ-alumina system, 2: Consideration of hydrogen and surface effects, Chemistry of Materials, ***16****, pp. 1914-1923.*

Preamble

It is well known that hydrogen is present at the surface of metal oxides. However, the role of hydrogen within the bulk structure of γ-Al_2O_3 is uncertain. This is an important consideration as water is a by-product of the dehydration of boehmite and many of the applications of γ-Al_2O_3 are believed to involve hydrogen. The majority of studies involving hydrogen in γ-Al_2O_3 have investigated its presence at the surface and the relationship to Lewis acidity.

The results in *Chapters 7* and *8* suggest that hydrogen is not present interstitially within the bulk crystalline structure. This is investigated further in this chapter. In addition to traditional techniques, PGAA and NVS are used to assess the amount and bonding of hydrogen in the structure of γ-Al_2O_3, and SAXS is used to assess surface characteristics. To the author's knowledge, these techniques have not been used for this purpose before. These features are investigated systematically for different calcination temperatures. It is proposed that the material investigated here has a relatively well ordered bulk crystalline structure which contains no interstitial hydrogen and that hydrogen-containing species are located at the surface and within amorphous regions, which are located in the vicinity of pores.

9.1 Surface Area and Microstructure Trends

It is generally anticipated that the structure of transition aluminas becomes more ordered with increasing calcination temperature. This trend is expected to coincide with an increase in the bulk density, reduced surface area, increased crystallite size and a reduced amount of amorphous content in the material. Soled (1983) attributed these characteristics to the coalescence of adjacent particles (from what has been determined in this work, the particles that Soled refers to are lamellar crystallites; *section 8.1*) that become bridged by terminal oxide ions. As a result the terminal oxides become incorporated within the bulk structure.

The crystallite size for the material examined here has been discussed in *section 8.1*. The observed crystallite size follows the expected trend of increasing size with treatment temperature. The average crystallite size, as determined from analysis of the (220) peak, was ≈ 150 Å for all samples calcined up to, and including, 750 °C, ≈ 185 Å for samples calcined at 800 °C and ≈ 210 Å for samples calcined at 900 °C. In attempting to determine if hydrogen is exclusively at the surface or if it is also located within the bulk structure, it is useful to determine the total volume of the surface and the total amount of hydrogen in the material. Figure 9.1 illustrates the specific surface area measurements from BET and SAXS (Maitland *et al*. 2004). The decrease in surface area with increasing calcination temperature is synonymous with the coalescence of the lamellar porous nanostructure. All BET surface area measurements are below 100 m^2g^{-1}, which is what is expected for γ-Al_2O_3 derived from highly-crystalline boehmite (Wefers and Misra 1987). The surface area measurements from BET are consistently lower than those from SAXS. Gas adsorption measurements have been shown to incompletely fill pores smaller than ≈ 10 Å (Wilson *et al.* 1980; Wilson and Stacey 1981). Higher surface areas from SAXS imply large internal surfaces, very small crystallites and closed porosity.

Preliminary inspection of the SAXS curves (Figure 9.2) shows there is structure on two length scales within the sample (Maitland *et al*. 2004). This is consistent with the observed micron-sized envelope structure of the grains and nano-sized porosity within the grains (*section 8.1*). Also evident from the curves in Figure 9.2, is that the temperature at which the sample is calcined clearly affects the microstructure (nanostructure) of the sample. It is evident that as the temperature

increases, the q value at which the pore scattering becomes significant decreases (Maitland *et al*. 2004). This suggests that the pore size is increasing with temperature.

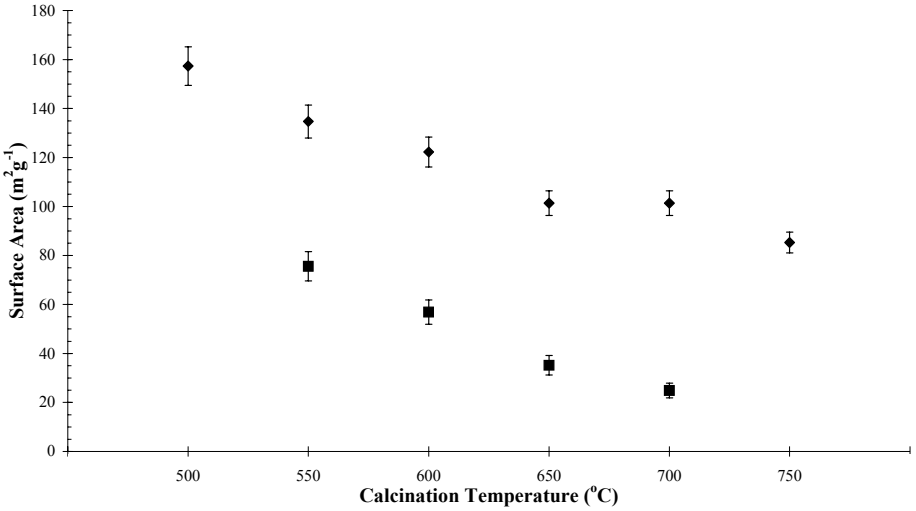

Figure 9.1. Specific surface area measurements from BET, ■, and SAXS, ♦.

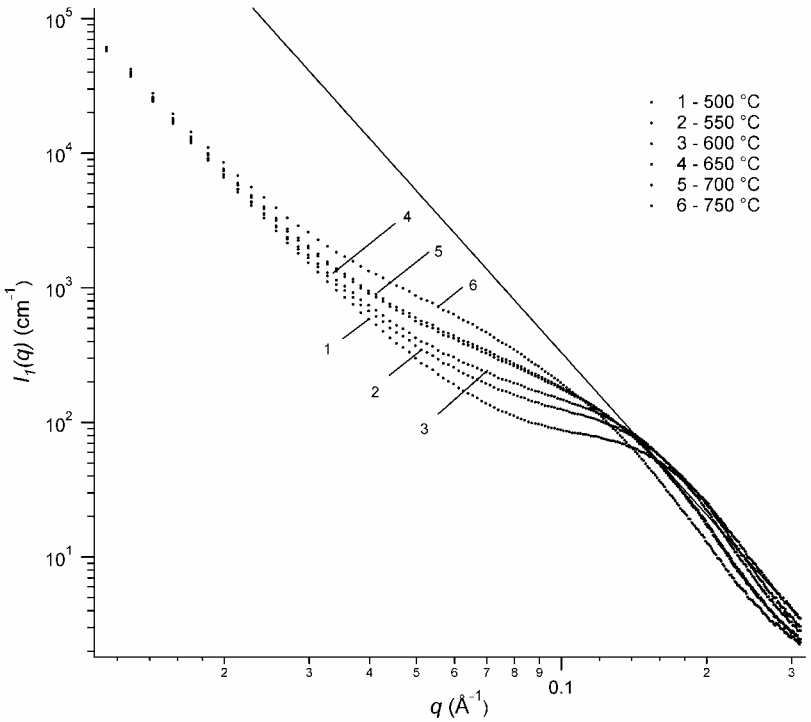

Figure 9.2. The intensities measured by SAXS of the samples calcined at different temperatures (Maitland *et al*. 2004). These plots clearly show that the calcination temperature affects the nanostructure. The line shows scattering that is proportional to q^{-4}.

The Porod plots (Figure 9.3) show significantly increased measured intensities at high q for samples calcined between 650 and 750 ˚C. In these cases, K was calculated from the plateau in the local minimum of $I_1(q)q^4$. The method used here for the determination of K follows that of Schaefer *et al*. (1995). The consequence of this is that any short-scale structure is averaged out of the calculations, which may lead to an underestimation of the actual specific surface area for these particular samples. Using this analysis, the size of the porosity being probed is about 20 Å. The increase of $I_1(q)q^4$ at high q suggests that some small porous structure (r < 10 Å) remains in these samples (Maitland *et al*. 2004).

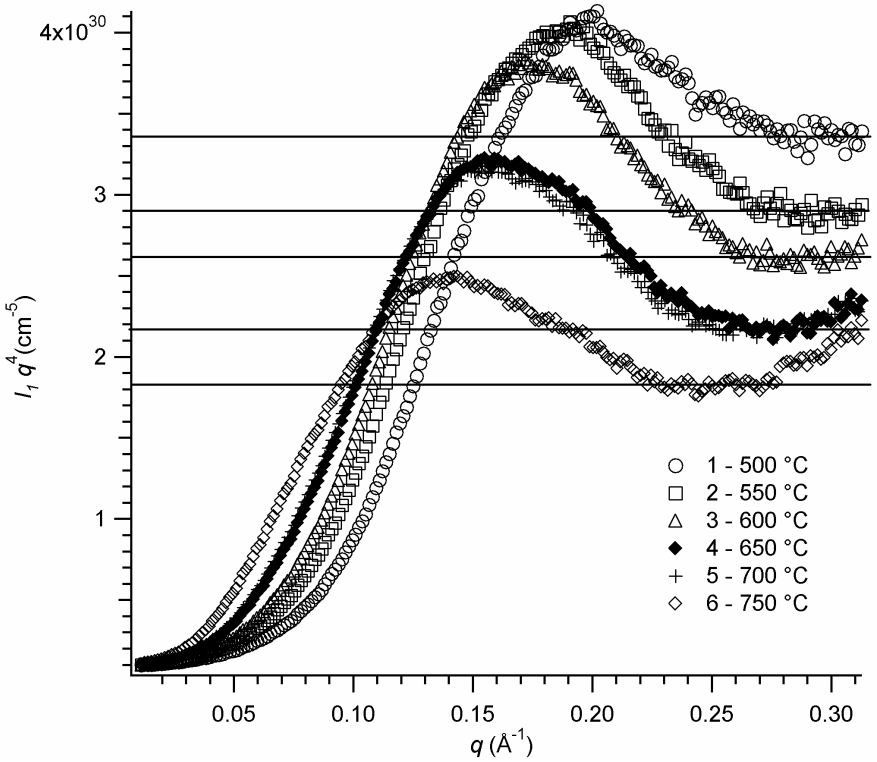

Figure 9.3. Porod plots of the measured intensities. The lines show the fitted values obtained for K (Maitland *et al*. 2004).

From similar lamellar porous microstructures observed by Wilson *et al*. (1979a; 1979c; 1979b), the mean pore widths were determined to be between 8 to 10 Å. From this observation it was determined that the internal surface area of γ-Al_2O_3 derived from highly-crystalline boehmite can theoretically be as high as 560 m^2 g^{-1} (Wilson and Stacey 1981). While it is clear from TEM that the microstructure is lamellar porous with nano-sized pores (Figure 9.4), it is a difficult

task to readily measure pore sizes from the electron micrographs, particularly in the size range specified by Wilson *et al*. (1979a; 1979c; 1979b). All that can be confidently said from the images in Figure 9.4 is that the lamellar shaped pores clearly have dimensions smaller than 40 Å, with pore widths smaller than the pore lengths. These observations are complementary with the SAXS data, which accounts for pore dimensions around 20 Å. This is in contrast to the BET measurements performed here which returned mean pore sizes over 45 Å for all material calcined below 750 °C. The SAXS technique also detects closed pores within the grains that cannot be measured by nitrogen gas adsorption. It is therefore concluded that γ-Al_2O_3 derived from highly-crystalline boehmite has a significantly higher surface area than that measured by BET, due to the presence of closed pores.

The calculated pore volume fractions determined from SAXS analysis of the γ-Al_2O_3 samples showed a constant trend, with values between 0.16 and 0.20. This agrees well with the values obtained from pycnometry of between 0.19 and 0.20. The constant pore volume, coupled with the trend of reduced surface area suggests that the pores are fusing together during calcination and that increased calcination temperature promotes greater fusion of pores as the bridging of crystallites progresses (Soled 1983). Figure 9.5 confirms this, showing increased mean nanopore dimensions with increasing calcination temperature, as the pores fuse together to yield lower surface areas, while the crystallites bridge together and increase in size. The calculated pore sizes from SAXS are between two and three times smaller than those obtained from BET. This is due to the combination of differences in measured specific surface and porosity. The calculations for pore dimension assume a spherical shape to the pores. From TEM it can be seen that the pores are generally lamellar in shape, which is difficult to model. However, the spherical approximation was used so that the calculated sizes from BET and SAXS can be compared and is sufficient to provide an indication of relative trends that are occurring. Given the small change in pore size from 22 to 43 Å for the γ-Al_2O_3 samples calcined at different temperatures between 500 and 750 °C, it is understandable that there is no discernable difference in the nanoporous structure when observed by TEM (Wilson and McConnell 1980; *section 8.1*). The small changes in pore size as they become fused together enables the pore morphology to remain the same (De Boer and Lippens 1964; Lippens and De Boer 1964). The surface area and pore measurements are consistent with

observations that the smallest pores contribute the major part of large specific surface areas (Wefers and Misra 1987).

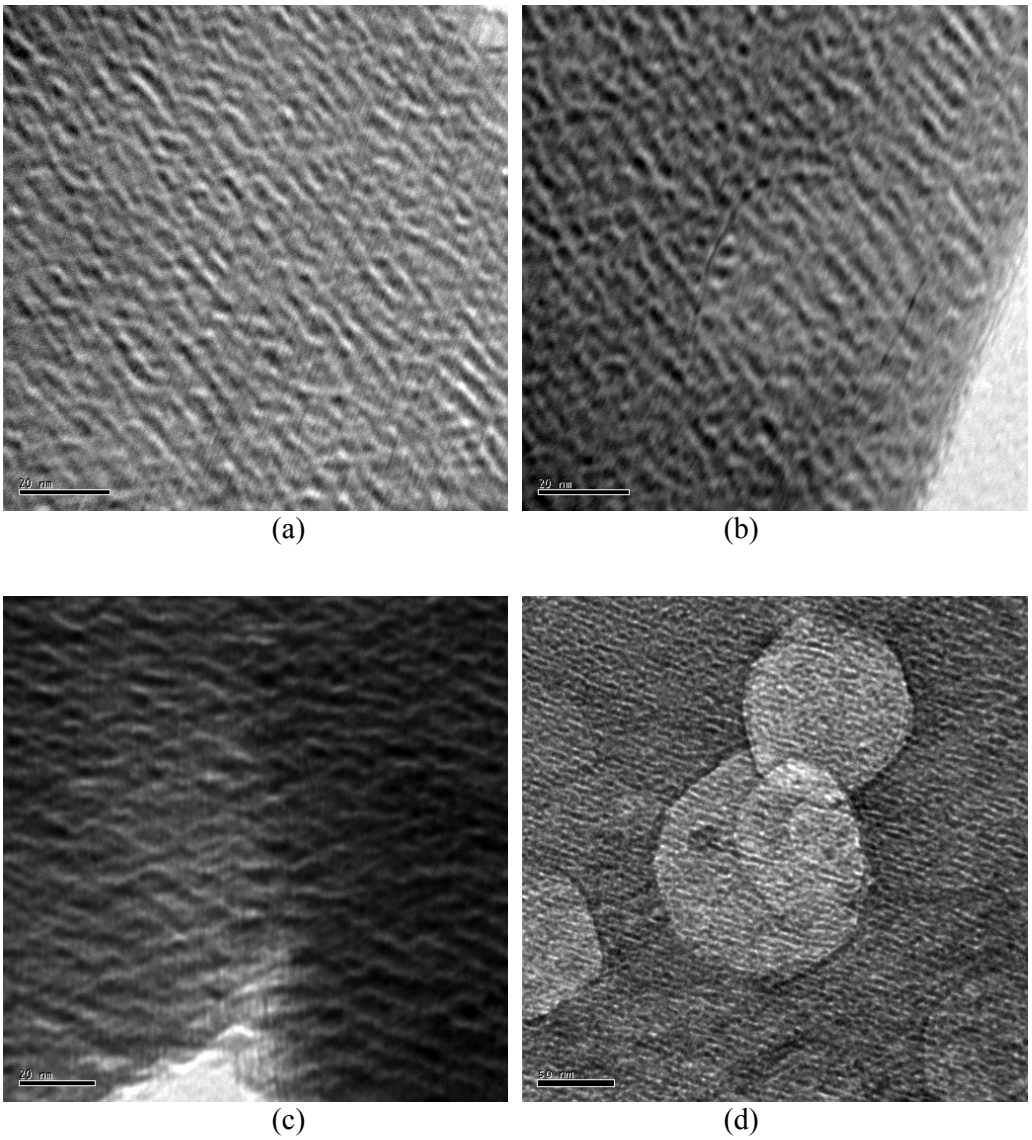

Figure 9.4. TEM images showing the lamellar porous microstructure. (a) and (b): γ-Al_2O_3 formed from boehmite calcined at 500 °C, (c) and (d): γ-Al_2O_3 formed from boehmite calcined at 600 °C.

The lamellar pores result from the loss of water, during boehmite dehydration, from the isovolumetric environment of the grain. The stoichiometric reaction of the boehmite to γ-Al_2O_3 transformation:

$$2\gamma\text{-AlOOH} \rightarrow \gamma\text{-}Al_2O_3 + H_2O \qquad (9.1)$$

indicates that one quarter of the oxygen sublattice is lost during dehydration (Wilson *et al.* 1980). Consequently the total possible pore volume fraction is 0.25. Comparison with the pore volume fractions measured by SAXS and pycnometry indicates that water and amorphous material (described in *section 8.1*) fill up some of the pores.

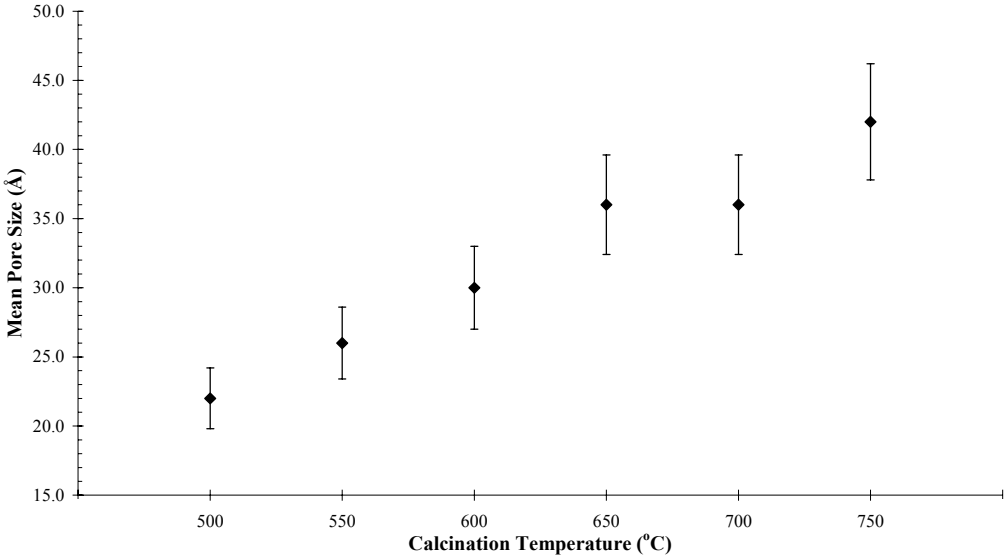

Figure 9.5. Mean pore diameter obtained from SAXS (Maitland *et al*. 2004).

The key question is where in the structure are the hydrogen-containing species and in what quantity? It is generally anticipated that hydrogen-containing species are located predominantly at the surface. Determining the contribution of the surface to the total volume can provide a useful indication of where hydrogen can freely reside. The volume contribution of the surface is determined from the product of the surface area, the surface layer thickness (assumed to be 1.2 Å) and the crystallographic density (Zhou and Snyder 1991).

e.g. at 500 °C, % volume of surface = $1.57 \times 1.2 \times 10^{-10} \times 3.66 \times 10^{6} = 0.069$ or 6.9%

The estimates are reported in Table 9.1. Occupation of the 32*e* site positions by Al ions in the Zhou and Snyder (1991) structural model was suggested to account for the perceived large contribution of the surface to the total volume for highly-crystalline boehmite-derived γ-Al_2O_3. However, the estimates provided in Table 9.1 show that surface volume is not significant and hence does not affect the average bulk structure. Furthermore, the suggestion of the 32*e* site position cannot account for the immense complexities of the γ-Al_2O_3 surface, where in addition to the

traditionally assumed three- and five-coordinated aluminium ions, four- (Coster *et al.* 1994; Kao and Grey 1997; Maresca *et al.* 2000), six- and seven- (Álvarez *et al.* 1995) coordinated aluminium ions have also been reported to exist.

Table 9.1. Calculated contribution of the surface to the total volume.

Calcination Temperature (°C)	Σ_S (m^2g^{-1})	*% volume of surface*
500	157 +/- 8	6.9
550	135 +/- 7	5.9
600	122 +/- 6	5.4
650	101 +/- 5	4.4
700	101 +/- 5	4.4
750	85 +/- 4	3.7

To gain an indication of the quantity of hydrogen species that can be held by the surface, a first order approximation can be made. If monolayer coverage of the entire surface with water is assumed, and each water molecule is assumed spherical with radius 1.1 Å, the surface can hold up to 4.1×10^{21} molecules of water at 500 °C, which equates to 12.3 wt. %. This is a substantial amount, greater than the quantities measured from ignition-loss below. The nature of bonding interactions of hydroxide and water groups to the surface of γ-Al_2O_3 is more complicated than this and has been discussed elsewhere in more detail (Knözinger and Ratnasamy 1978; Zecchina *et al.* 1985; Morterra and Magnacca 1996; Tsyganenko and Mardilovich 1996; Liu and Truitt 1997; Sohlberg *et al.* 1999).

9.2 Measuring the Quantity of Hydrogen in the Structure

The quantity of hydrogen species measured within the structure from ignition-loss measurements and PGAA is presented in Figures 9.6 and 9.7. The amount of water burnt off the surface of the samples before performing ignition-loss was also measured (Figure 9.6). These values are not absolute as the amount of water adsorbed onto the surface of the γ-Al_2O_3 calcination products increased rapidly with time when removed from the desiccator. However, all samples were treated identically and measurements were taken under the same conditions. Hence the values obtained represent the relative difference in surface water adsorbed for the

samples obtained. The reduction in the amount of adsorbed surface species with increasing calcination temperature is consistent with the trend in specific surface area; there is less available surface for adsorbing species to adhere to.

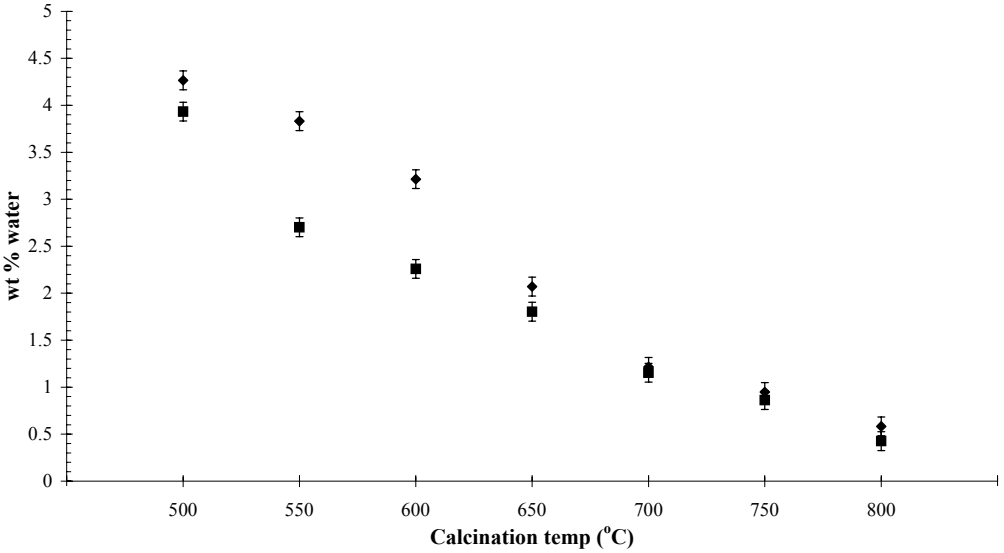

Figure 9.6. Percentage of water contained within the bulk (measured by ignition-loss), ■, and at the surface (measured by weighing the mass lost from pre-heating samples for ignition-loss), ♦, of γ-Al_2O_3 samples.

The reduction of hydrogen-containing species within the bulk structure, from 3.9 wt. % at 500 °C to 0.4 wt. % at 800 °C, indicated by ignition-loss, follows a similar trend to that of the surface species. The determined quantities represent material present in amorphous regions, closed pores, and possibly, crystalline regions. Comparison of the ignition-loss data to PGAA (Figure 9.7) shows that ignition-loss underestimates the total quantity of hydrogen. This is because ignition-loss calculations assume all the material burnt off is composed solely of water. The higher proportion of hydrogen indicated by PGAA suggests the presence of hydroxide and protons, which are not burnt off along with the water within the bulk structure.

In addition to higher calcination temperatures, duration of heat treatment was found to affect the amount of hydrogen-containing species in the material (Wilson 1979a; Wilson and McConnell 1980; Wilson *et al.* 1980). This was measured at 550 °C with a H/Al ratio of 0.153(1) after calcination for 4 hours, 0.147(1) after 7 hours and 0.136(1) after 10 hours.

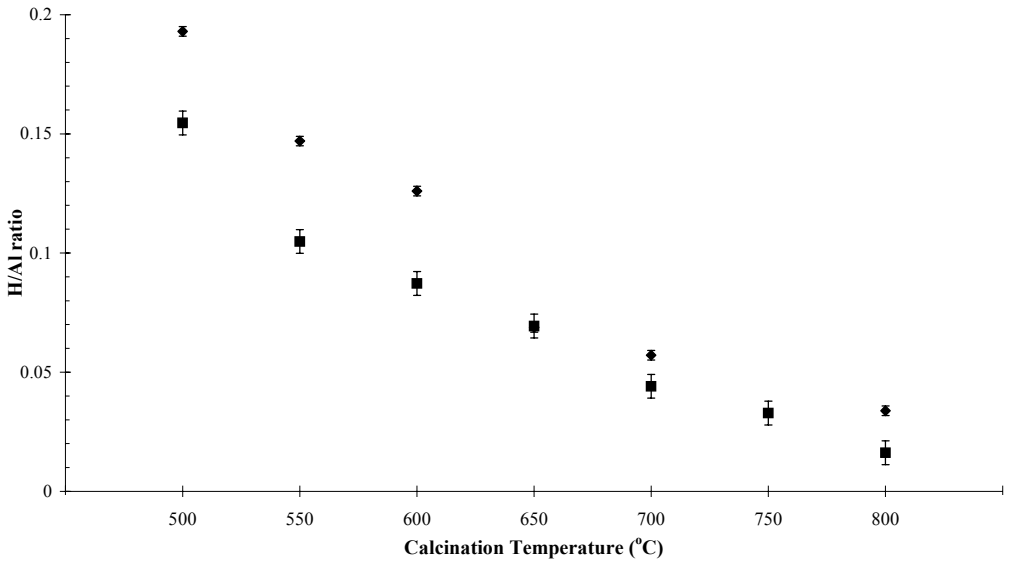

Figure 9.7. Ignition-loss data represented as H/Al ratios, ■, compared with PGAA data, ♦, of γ-Al_2O_3 samples.

Rietveld analysis shows that the presence of interstitial hydrogen within the crystalline bulk structure of γ-Al_2O_3 is unlikely (*Chapters 7* and *8*). This suggests that the presence of protons in the structure, as suggested above, is limited to amorphous regions, which, in addition to hydrogen-containing species, is expected to be comprised of amorphous Al_2O_3 and other AlO species of varying stoichiometries. Protons diffuse through the structure as boehmite is broken down during the transformation to γ-Al_2O_3 (Wilson 1979a; Tsuchida *et al.* 1980). The unit cell of γ-Al_2O_3 is formed from remaining skeletal oxygen layers after the hydroxide layers of the boehmite precursor are broken down (Lippens and de Boer 1964; Wilson 1979a; Wilson and McConnell 1980). To maintain charge neutrality, there is a counter migration of one Al into the inter-skeletal layer regions for every three protons ejected (Lippens and de Boer 1964). The hydrogen is ejected from the broken down regions, which become pores. As these regions break down, the local material forms a melt that becomes the amorphous content from which future crystalline Al_2O_3 nucleates. Protons would, therefore be concentrated within these regions, as suggested by Rietveld analysis. The results from ignition-loss and PGAA indicate that higher temperature or longer periods of heat treatment are required to maximise proton migration out of the pores and nearby amorphous regions through the bulk to the outer surfaces.

9.3 Neutron Vibrational Spectroscopy

Direct insight into the nature of how hydrogen, quantified above, is bonded and where it is located is provided by NVS. Figure 9.8 contains NVS spectra collected from several γ-Al_2O_3 samples, and bulk ice for comparison. The spectra for γ-Al_2O_3 contain two broad hydrogen-related phonon bands reflecting hydrogen bonding interactions in the structure and a third signal, at 293 cm^{-1}, which is mainly due to an Al phonon from the sample can.

The total signal for all the normalized spectra is greatest for the 500 °C sample. At 500 °C there is a significant amount of molecular water in the sample, indicated by the broad H-O-H scissor-mode band centred around ~ 1600 cm^{-1}. There is also a strong, complex O-H bending mode band between 320 - 1120 cm^{-1} that decreases with increasing calcination temperature. These complex bands relate to combinations of OH and non-bulk H_2O. The difference in the shape of the NVS spectrum at 500 °C compared with the spectrum for bulk ice (Figure 9.8) suggests different bonding environments. Bulk ice has sharper edges due to its well-defined hydrogen bonding network. The 500 °C spectrum has broader features due to hydrogen bonding interactions between H_2O and Al_2O_3 surfaces, other H_2O molecules and OH, and the additional presence of OH groups. The broadened scissor-mode band for the 500 °C sample can also mean very small non-bulk ice configurations.

It can be assumed that the water that remains in the sample is trapped inside pores and within amorphous regions, as suggested above. The molecular water contribution to the spectra decreases with increasing temperature. By 650 °C its presence is negligible and by 800 °C it is almost non-existent. This is signified by the reduced intensity in the spectra and the disappearance of the H-O-H scissor-mode. By 800 °C, when the transformation to γ′-Al_2O_3 is complete (*Chapter 8*), the main signals remaining are the complex bands between 320 - 1120 cm^{-1}, which have significantly reduced intensity and are associated with residual surface hydroxyl groups. Although possible vibrational modes from hydrogen occupying interstitial sites may be hidden by the complex O-H bending mode signals, it is more likely that the protons are not located in interstitial octahedral and tetrahedral sites within the bulk structure.

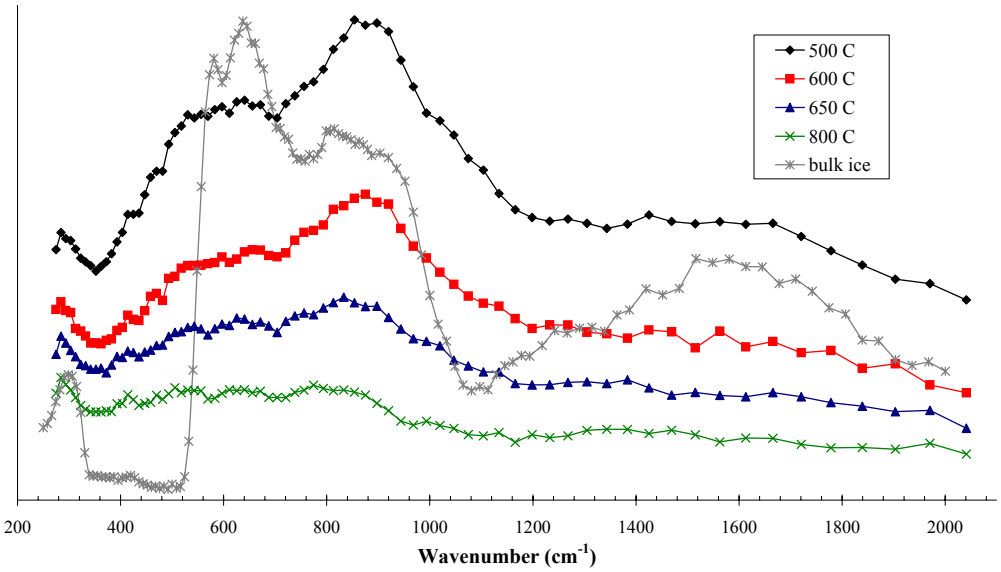

Figure 9.8. Normalized NVS data collected after pre-drying to drive off surface water for boehmite calcined between 500 and 800 °C and bulk ice**.**

The reduction of the overall signal intensity with increasing calcination temperature is synonymous, not only with a reduction in the associated molecular species with each signal, but also a reduction in amorphous content (and surface area). These results complement the observation of amorphous regions in transmission electron micrographs that were also found to decrease with increasing calcination temperature, and reduced background contributions from neutron diffraction data (*Chapter 8*). Soled (1983) suggested that the presence of considerable amorphous content results in non-pure γ-Al_2O_3. It is agreed here that the amorphous material is present, but is proposed that the bulk crystalline structure has Al_2O_3 stoichiometry and contains no interstitial hydrogen. This proposal is based on Rietveld analysis indicating that the presence of hydrogen within the crystalline bulk is unlikely (*Chapters 7* and *8*). Molecular dynamics simulations have also indicated that the bulk structure of γ-Al_2O_3 does not contain hydrogen, is relatively well organized and has few defects (Álvarez *et al.* 1995; Álvarez *et al.* 1993; Álvarez *et al.* 1992). Given the evidence that hydrogen-containing species are present in the structure it can be deduced that there must be amorphous regions to account for these species. The amorphous nature is also evidenced by the absence of a well-defined hydrogen bonding network when the Al_2O_3 NVS spectra is compared to that of bulk ice.

Figure 9.9 illustrates the difference in NVS spectra between the pre-dried and non-pre-dried (wet) samples, with boehmite calcined at 600 °C used as the example. The plot of the difference between the pre-dried and wet samples more dramatically shows the spectrum of only the excess water. The surface water provides a large contribution to the total signal. Comparison with the bulk ice spectrum indicates a non-bulk-like environment characteristic to the water (as per the pre-dried samples), evidenced by the broader features of the difference plot, which signify H_2O bonding interactions with the hydroxylated Al_2O_3 surface. However, the relative signal intensities and positions in the difference plot and the clear appearance of the H-O-H scissor mode band, indicate more obvious similarities of the surface water to the bulk ice spectrum, indicative of the relative quantity of molecular water at the surface. As the calcination temperature increases the difference between the pre-dried and wet spectra diminishes.

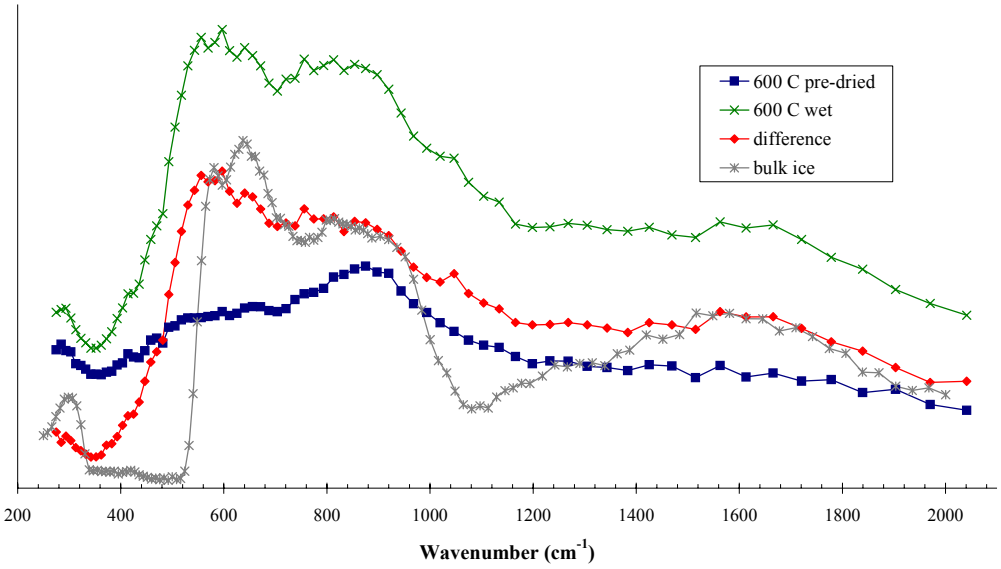

Figure 9.9. Illustration of the difference between the NVS spectra of pre-dried and non-pre-dried (wet) samples of γ-Al_2O_3. This example was taken from boehmite calcined at 600 °C.

9.4 Infrared Analysis

Comparison between DRIFT and transmission IR analysis was used to further investigate the location of hydrogen in the structure. Figure 9.10 shows DRIFT and transmission IR spectra for samples with physisorbed surface water driven off.

Vibrational frequencies below ~ 1000 cm^{-1} represent Al-O interactions in the bulk structure. It has been established that AlO_6 octahedra and AlO_4 tetrahdra are characterized by vibrational frequencies in the range 500 - 700 cm^{-1} and 700 - 900 cm^{-1} respectively (Tarte 1967). The spectra also exhibit an O-H stretching mode, associated with water and hydroxide species, and an H-O-H scissor mode, associated with water species, centered at ~ 3470 cm^{-1} and ~ 1620 cm^{-1} respectively. The signal obtained for the transmission IR spectra predominantly comes from the bulk structure but there is some contribution from the surface. The signal for the DRIFT spectra originates predominantly from the surface, evidenced by the relatively smaller intensity of Al-O vibrations compared to transmission IR.

To investigate whether the spectra obtained could provide information about the location of hydrogen, peak intensity ratios between the AlO_6 and the O-H stretch signals, and the AlO_6 and H-O-H scissor modes, respectively, were measured. O-H/AlO_6 and H-O-H/AlO_6 ratios obtained from the DRIFT spectra were, on average, 2.5 times larger than those obtained from transmission IR spectra. The relatively more intense O-H and H-O-H signals from DRIFT indicate that the majority of hydrogen-containing species lie at the surfaces of the material examined.

The decrease in the intensity of O-H stretch and H-O-H bending mode signals with increasing calcination temperature (Figures 9.10 and 9.11) coincides with the trend in reduced surface area and therefore less access for attachment of hydrogen-containing species. At 800 and 900 °C, when the structure is that of γ′-Al_2O_3 (*Chapter 8*), the O-H stretch remains present. Most of this is associated with OH at the surface because the majority of the water has already been ejected from the structure.

It follows that, since the hydrogen-containing species lie at or near the surface, this is also the case for amorphous regions, as suggested earlier. Further support of amorphous regions lying at or near the surface is provided in Figure 9.11, which shows a decrease in the O-H/AlO_6 and H-O-H/AlO_6 ratios with increasing calcination temperature, following a similar trend as the PGAA and ignition-loss experiments (Figures 9.6 and 9.7).

The reduction in amorphous material in the structure is also signified by the increased sharpness with increased calcination temperature of the signals originating from the Al-O vibrations. Increased signal sharpness also coincides with the

increased structural ordering that occurs as the transition alumina sequence evolves (Baraton and Quintard 1982; Wefers and Misra 1987; Morterra and Magnacca 1996).

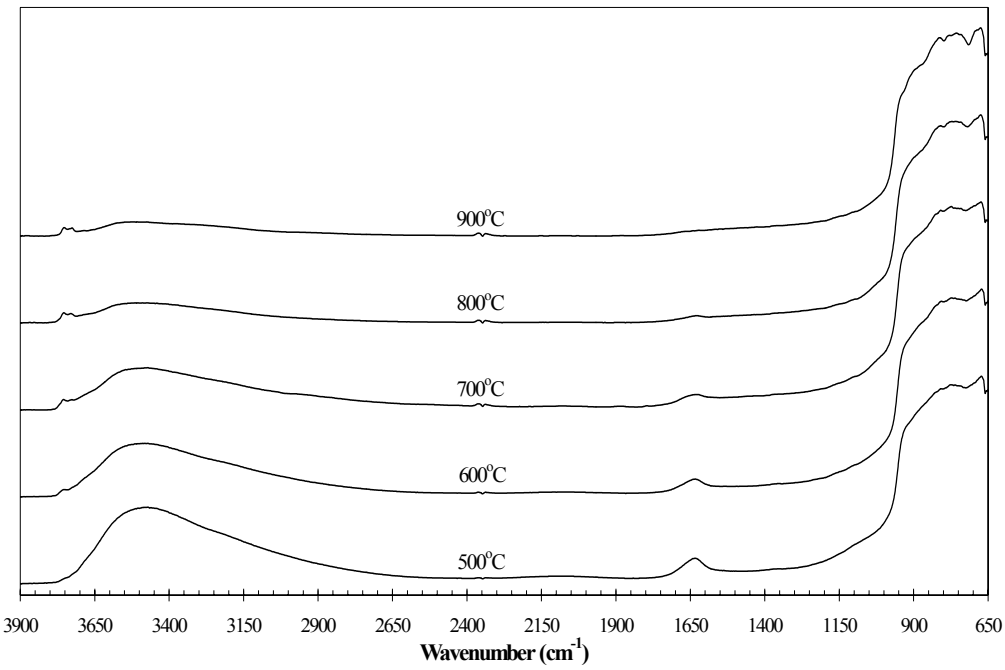

(a)

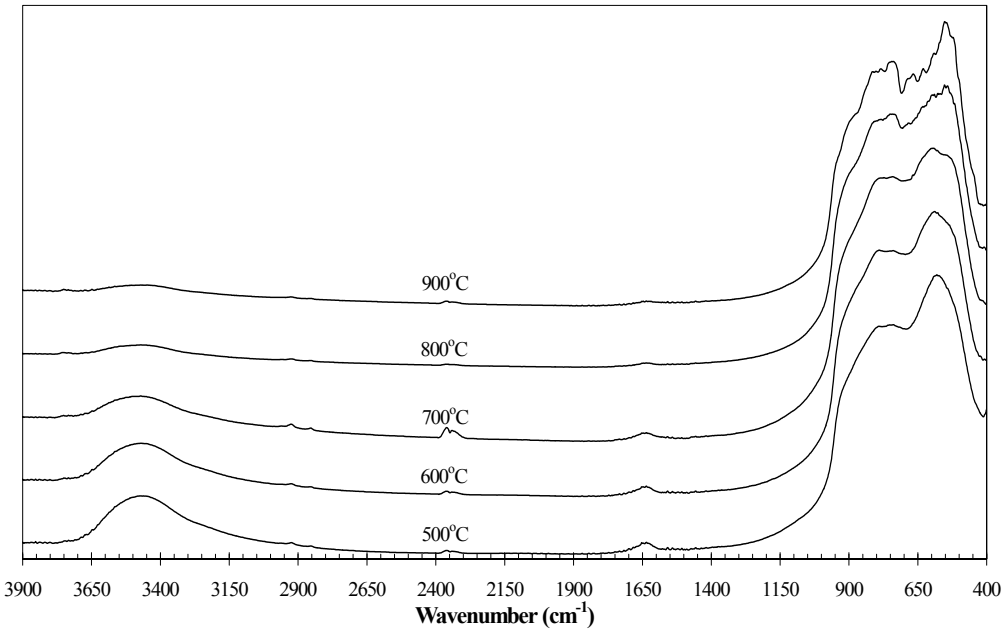

(b)

Figure 9.10. Normalized stack plots of (a): DRIFT and (b): transmission IR spectra collected after surface water was driven off for boehmite calcined between 500 and 900 °C.

Figure 9.11 also shows that IR data can provide an indication of the relative proportion of cations in octahedral and tetrahedral coordinated sites, when used in conjunction with other techniques. The AlO_4/AlO_6 ratio increases to 750 °C, remains level to 800 °C, and then decreases slightly at 900 °C. The increase in the ratio coincides with trends of increased vacancy ordering observed in electron diffraction patterns, which represent an increase in the number of cations occupying tetrahedral site positions (Wilson 1979a; Wilson and McConnell 1980; *section 8.2*). At 800 and 900 °C, the AlO_4 and AlO_6 peak shapes become more complex and the position of the highest adsorption feature shifts because the IR signal is now representative of a different phase, γ'-Al_2O_3 in this case. The levelling off and decrease in the AlO_4/AlO_6 ratios coincides with the vacancy ordering on octahedral sites that occurs for transition phases beyond γ-Al_2O_3 (Wilson 1979a; Wilson and McConnell 1980). The observed trend in the AlO_4/AlO_6 ratio also corresponds to the trends found in cation occupancy, determined from Rietveld refinements on neutron diffraction data obtained at room temperature for the same material (*Chapter 8*).

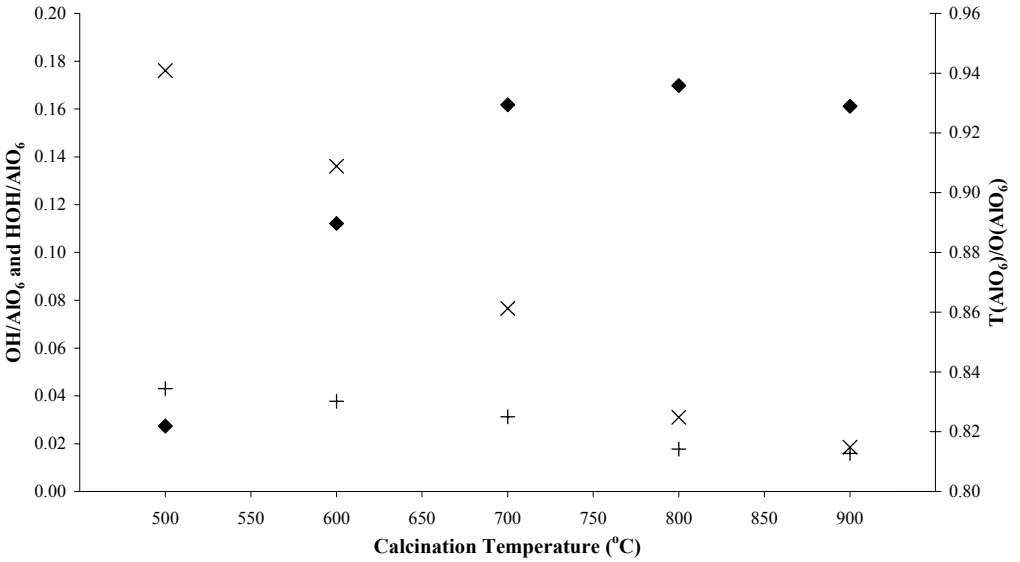

Figure 9.11. O-H/AlO_6, ×, H-O-H/AlO_6, +, and AlO_4/AlO_6, ♦, ratios determined from transmission IR data.

9.5 Outcomes

The research conducted here has provided insight into the quantity and possible location of hydrogen in boehmite-derived γ-Al_2O_3. The main outcomes are summarised below:

- Specific surface area measurements, usually measured using nitrogen absorption techniques, were undertaken with SAXS which indicates that the material examined has a significantly higher surface area than expected for highly-crystalline boehmite derived γ-Al_2O_3. The higher surface area was attributed to the presence of nano-pores and closed porosity, where hydrogen-containing species can also be present.
- After systematic examination of the material with changing calcination temperature, the specific surface area was found to decrease. This trend occurred concurrently with an increase in the mean pore and crystallite size and a reduction in the amount of hydrogen-containing species within the structure and concurs with findings from the literature.
- Loss on ignition experiments, based on the assumption that all hydrogen-containing species driven from the structure are lost in the form of water, were found to underestimate the amount of hydrogen in the material when compared to PGAA. The difference in the measured values is attributed to the presence of hydrogen-containing species such as hydroxide and protons, which are not burnt off along with the water within the bulk structure
- Two signals pertaining to water and hydroxide species were identified using NVS. NVS provided evidence of a reduced amount of amorphous species with increasing calcination temperature, complementing observations made from TEM and neutron diffraction patterns in *Chapter 8*.
- From the mechanism of γ-Al_2O_3 formation from boehmite, the hydrogen-containing species are expected to reside in the vicinity of pores, which make up the bulk of the surface area. Because the pores are remnants of broken down hydroxide layers from boehmite, the amorphous regions are also expected to be located around such regions. This is supported by infrared analysis, where the OH/AlO_6 and $H\text{-}O\text{-}H/AlO_6$ ratios obtained from the DRIFT spectra are 2.5 times larger than those obtained from transmission IR

spectra, indicating that the majority of hydrogen-containing species, and hence amorphous regions, lie at the surface of the material examined.

- It was demonstrated that the AlO_4/AlO_6 ratios obtained from the IR data can provide an indication of the relative proportion of cations in octahedral and tetrahedral coordinated sites, when used in conjunction with other techniques.

It can be concluded from the results obtained here that γ-Al_2O_3 derived from highly-crystalline boehmite has a relatively well ordered bulk crystalline structure which contains little or no interstitial hydrogen and that hydrogen-containing species are located at the surface and within amorphous regions, which are located in the vicinity of pores. There is no evidence either way to suggest that hydrogen does not exist interstitially in crystalline alumina regions near the surface. It would not be surprising if this was the case as diffusion of protons are required to maintain charge neutrality and would occur along surface regions, particularly as the amorphous regions crystallize and become more sparse. More work is required to examine this aspect.

Chapter 10

Computational Findings

The material in this chapter has been submitted for publication as the following paper:

G. Paglia, A.L. Rohl, C.E. Buckley and J.D. Gale 2004 "Determination of the structure of γ-alumina from interatomic potential and first principles calculations - The requirement of significant numbers of non-spinel positions to achieve an accurate structural model," Physical Review B.

Preamble

This chapter provides a crucial contribution from the current research. The molecular modelling performed here allows for exact cation coordinates to be determined, hence permitting direct inspection of the structure. In addition to determining structural details, neutron diffraction patterns generated from the simulated structures are also examined and compared to experimentally observed diffraction patterns. This is imperative to ensure that the simulated structure is consistent with what is experimentally observed. It is a direct way of proving the simulated structure to equate to the real structure.

Here, the optimisation of the starting structural candidates described in *section 5.2* is discussed. It is demonstrated that none of the spinel-based structures exhibited simulated diffraction patterns that were characteristic of γ-Al_2O_3. This is attributed to the cation configurations, which do not agree with those determined in *Chapter 7*. A new set of starting structure candidates is established based on the configurations determined in *Chapter 7*. Optimisation of these *c* symmetry based structures results in simulated diffraction patterns that are characteristic of γ-Al_2O_3. It is also demonstrated that the supercells described allow for more accurate and complete modelling of the defect structure of γ-Al_2O_3 than the single unit cell approach. The Python codes, and associated output files, used to examine the structural configurations are catalogued in *Appendices VII* and *VIII*.

10.1 Spinel-Based Structure Candidates

From the generation of structures and application of selection criteria explained in *section 5.2*, there were 56,064 and 57,763 structures obtained for optimisation from the cubic, $Fd\bar{3}m$, and tetragonal, $I4_1/amd$, symmetry systems respectively. Of these, 55,533 structural configurations of the $Fd\bar{3}m$ system and 56,187 structural configurations of the $I4_1/amd$ system were considered for analysis. The remaining 531 and 1576 configurations were discounted because convergence was proving difficult to achieve, due to discontinuities in the energy surface. The energy of these configurations was relatively high and therefore not likely to be relevant to γ-Al_2O_3. Optimizations using DFT were then carried out on a selection of the lowest energy stable structures to verify that the interatomic potentials return the same trends in relative energies as first principles calculations and that the configurations did not change during the DFT calculations.

When optimising using interatomic potentials, the oxygen sublattice, while remaining relatively stable, showed a tendency to become distorted beyond what is observed experimentally. This artefact of high disorder during optimisation with interatomic potentials was also noticed in the κ-Al_2O_3 study, but is more significant in the case of γ-Al_2O_3 because it was not possible to implement space group symmetry during optimisation (*section 5.3*). This is because the supercells, introduced to ensure that the number of Al ions in the structures is an integer, although related to the symmetry of the original unit cells, result in cells which can no longer be explicitly described by the space group symmetry. The supercells could generally only be described under *P1* symmetry. However, with the exception of a small number of structures, the oxygen sublattice remained satisfactorily ordered (Figure 10.1b). As was the case for κ-Al_2O_3, undertaking DFT calculations was found to reduce the distortion of the oxygen sublattice. The number of cycles required to achieve optimisation with DFT was influenced by the degree of distortion, with greater distortion resulting in longer times before convergence was achieved. Examples of the oxygen sublattice are shown in Figures 10.1 and 10.2. Disorder in the calculated diffraction pattern is observed as greater undulations in the background (e.g. Figure 10.2c exhibits greater undulation than Figure 10.2b). A more disordered oxygen sublattice typically results in total structure diffraction patterns

which exhibit more disorder also (see Figure 10.6d for example). Coincidently, the typical and more significantly disordered oxygen sublattices shown in Figure 10.2 belong to the lowest and second lowest energy structures, respectively. In cases of high oxygen sublattice distortion, the deformation is often due to a small number of severely distorted oxygen atoms while the rest of the sublattice remains relatively well-ordered. There was no apparent correlation between the degree of disorder in the oxygen sublattice and energy relative to the minimum energy.

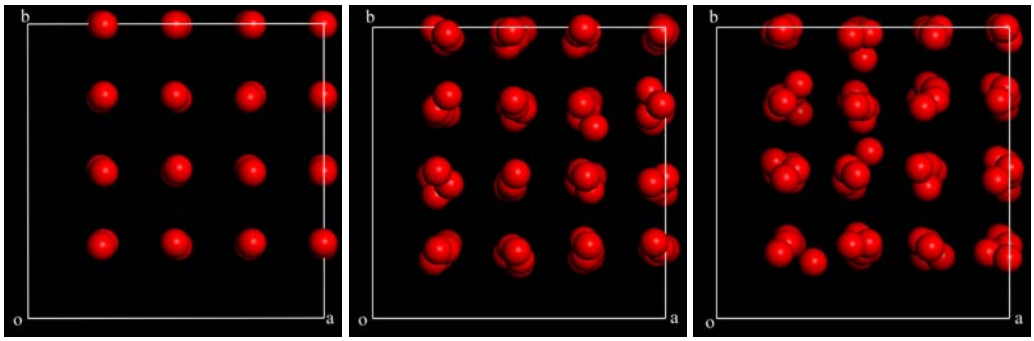

(a) (b) (c)

Figure 10.1. Examples of the oxygen sublattice, viewed down the *c* axis; (a): idealised starting configuration, (b): typical oxygen sublattice after optimisation, (c): oxygen sublattice displaying significant distortion. These examples were taken from the $Fd\bar{3}m$ system structures.

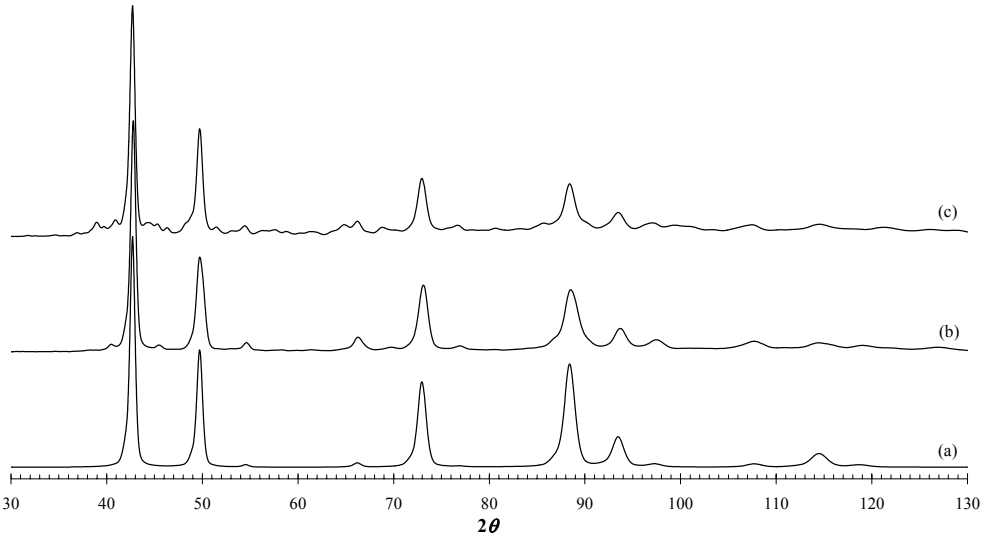

Figure 10.2. Examples of neutron diffraction patterns simulated from just the oxygen sublattice; (a): idealised starting configuration, (b): typical oxygen sublattice after optimisation, (c): oxygen sublattice displaying significant distortion. These examples were taken from the $Fd\bar{3}m$ system structures.

The converged set of structures, yielded 1,161 and 12,573 distinct minimum energies for the $Fd\bar{3}m$ and $I4_1/amd$ systems respectively. This large number of distinct minima suggests that the energy hypersurface of γ-Al_2O_3 is festooned with local minima and thus it is not surprising that such a disordered structure is observed experimentally. Unlike with κ-Al_2O_3 (*section 5.3.4*), configurations with equivalent optimised energies (to 3 decimal places) did not always imply that the structure was the same. Distortions in the oxygen sublattice during the calculations were found to affect the minima. For example, structures were found to have identical Al sublattice configurations, yet different energy due to different distortion in the oxygen sublattice. Structures were also found with identical energy but different Al sublattice configurations.

10.1.1 Structure Analysis

Figure 10.3 illustrates some of the key energetic data obtained from the interatomic potential optimisations regarding the configuration of the cation sublattice. Comparison is made with the energy distribution of the total sample pool and sets of structures. The percentage of each set of structures that exhibits each configurational characteristic is shown above the energy distribution. A lower energy distribution was obtained for the structures of the $Fd\bar{3}m$ system, indicating greater energetic stability. The majority of structural configurations exhibited 65 to 75% of cations on octahedral site positions and 35 to 25% of cations on tetrahedral positions after optimisation, in good agreement with NMR and Rietveld refinements (*Chapters 7* and *8*). Only 15.4% of the $Fd\bar{3}m$ system structures and 52.8% of the $I4_1/amd$ system structures had cations exclusively on spinel site positions after optimisation. These structures were not amongst the lowest energy configurations, implying that spinel structures (those with Al's solely on spinel positions) are not the most energetically favourable.

The majority of optimised structures exhibited occupancy of non-spinel positions, including the lowest energy structural configurations. Although less than half of the $I4_1/amd$ system structures possessed non-spinel site positions, the mean energy of these structures was less than the structures with only spinel-site positions occupied. Most of the structures with non-spinel site occupancy have cations

distributed only among 8*a*/4*a* (*a* symmetry), 16*c*/8*c* (*c* symmetry), and 16*d*/8*d* (*d* symmetry) site positions, which were suggested in the experimental studies reported in *Chapters 7* and *8*. The energies of these structures are also lower than those with cations exclusively situated on spinel sites, but the lowest energy stable structure is not among these structures. Structures that have energies amongst the lowest did have 16c/8c sites occupied, but also tended to have 48*f* positions occupied in $Fd\bar{3}m$-type structures and 16*g* positions in the $I4_1/amd$ system structures. There was generally no occupancy of 8*b* (in the cubic system), and 4*b* and 8*e* (in the tetragonal system) positions in structures amongst the lower energy range.

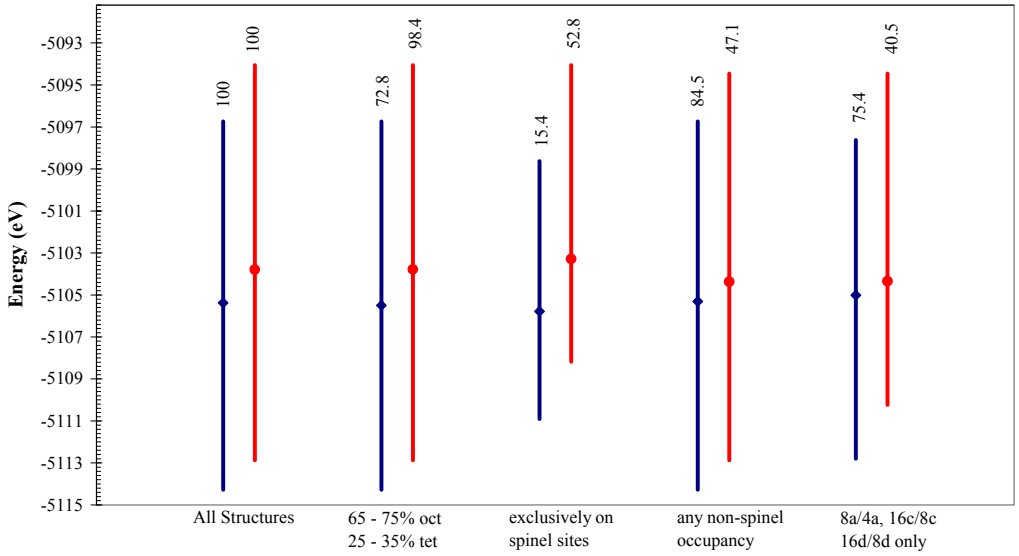

Figure 10.3. Key statistics for occupancy and energy distribution of structures obtained from the optimisation of the cubic $Fd\bar{3}m$, ♦, and tetragonal $I4_1/amd$, •, system structures with interatomic potentials. The ♦ and • symbols indicate the mean energies of the distributions. The values above each energy range is the percentage of the total number of structures that have the configurational characteristic being highlighted.

In Figure 10.4, the number of structures that possess each particular type of site position is indicated. As expected, almost every structure exhibits cation occupancy of *a* and *d* symmetry positions. The occurrence of structures with occupied *b* and *e* site positions is very infrequent, at less than 1 and 2% respectively. The occurrence of structures with any *f* and *g* symmetry positions occupied is also small representing less than 9 and 6% respectively. The low occurrence of cations on

these positions does not support structure models with such symmetry positions occupied.

The number of structures with unassigned site positions is low at less than 2%. Unassigned site positions encompasses any non-tetrahedral or octahedral site position, such as the 32*e* site position proposed by Zhou and Snyder (1991). It can also mean any severely distorted site positions that cannot be assigned to any symmetry position. In most cases, the cations in unassigned positions occurred in regions of severe localized disruption of the oxygen sublattice, resulting in the cation being situated beyond the allowed tolerances (up to 0.7 Å away from the idealized starting position) used to determine site occupation. It is therefore concluded that the 32*e* site position, and any non-tetrahedral or non-octahedral site position, are not likely in γ-Al_2O_3.

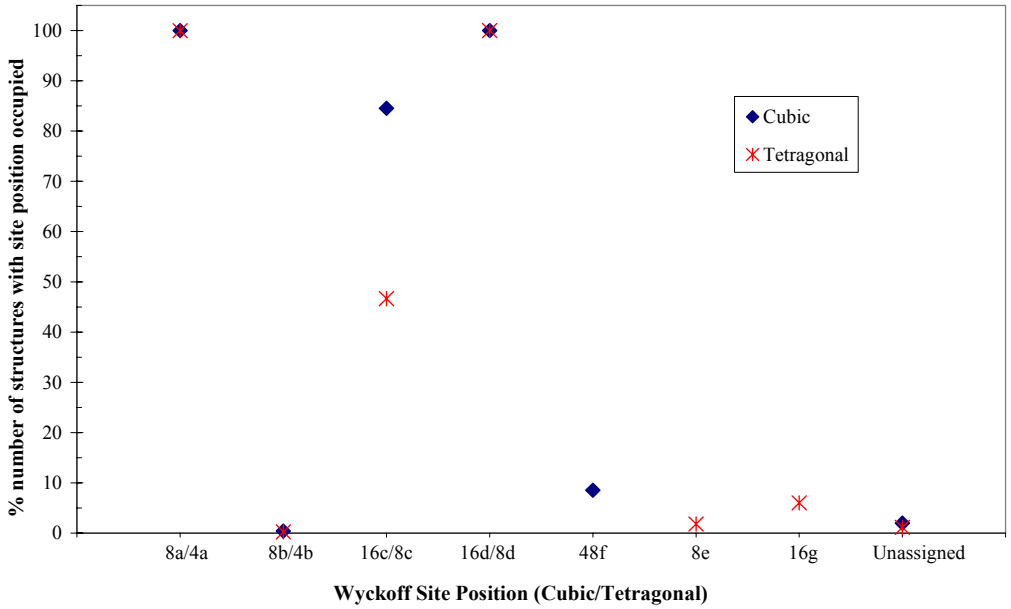

Figure 10.4. Occurrence of each type of site position throughout all optimised structures.

There are a large number of structures with *c* symmetry positions occupied for both the $Fd\bar{3}m$ and $I4_1/amd$ systems, equal to the number of structures with non-spinel site occupancy (Figure 10.4). This is significant, especially given that the cations were restricted to spinel sites in all starting structure models. The high rate of migration to *c* symmetry positions compared to other non-spinel positions further supports the exclusion of *b*, *e*, *f* and *g* symmetry positions from likely structural

models for γ-Al_2O_3. More importantly, the statistics highlighted in Figure 10.3 provide strong evidence that *c* symmetry positions are occupied in γ-Al_2O_3 and supports the Cubic-16*c* and Tetragonal-8*c* structure models presented previously (*Chapter 7*). It also suggests that these models are universal for crystalline γ-Al_2O_3.

Examination of all optimised structures showed that none of the configurations exhibited a cation composition equivalent to that which is experimentally observed (*Chapters 7* and *8*). The fractional cation occupancies obtained in the experimental studies ranged between 0.69 and 0.86 *a* symmetry, 0.30 to 0.45 on *c* symmetry and 0.48 to 0.68 *d* symmetry positions. The limitation of the experimentally derived models is that the occupancies obtained represent an average value distributed over all possible site positions of a particular site. The aim here is to take a closer step towards finding precise cation coordinates of a truly representative structure. In the supercells that have been used in this study, the experimentally determined fractional occupancies equate to Al ions on between (in whole numbers) 17 to 21 *a* symmetry, 14 to 22 *c* symmetry and 23 to 33 *d* symmetry site positions.

The closest that any of the optimised structures came to these experimentally determined values is no more than 4 cations on *c* symmetry site positions, in addition to cations on between 17 to 21 *a* symmetry sites and 39 to 47 *d* sites, with no other site positions being occupied. There were over twice as many structures of the $I4_1/amd$ system with 17 to 21 *a* symmetry sites and 3 to 4 *c* symmetry sites occupied than for the $Fd\bar{3}m$ system (22 to 9). Of the 84.54% of $Fd\bar{3}m$ and 47.12% of $I4_1/amd$ structures with non-spinel site occupancy, the majority have only *a*, *c* and *d* symmetry positions occupied (89.12 and 85.94% respectively), with no other site positions being occupied. On average, structures with these configurational characteristics tended to experience less distortion in the oxygen sublattice, and hence the total diffraction pattern, than most of the other structures. Also, the lowest energy structures do not necessarily result in the most ordered diffraction pattern. In fact, more distortion was observed in diffraction patterns of structures among the lowest energy than those with only *a*, *c* and *d* symmetry positions occupied.

An experimentally determined diffraction pattern of γ-Al_2O_3 is illustrated in Figure 10.5. Anisotropic broadening, synonymous with peak splitting, signifies that the pattern illustrated here corresponds to tetragonally distorted γ-Al_2O_3. If the γ-

Al_2O_3 is purely cubic, there is little difference in the diffraction pattern except that no peak anisotropy is observed. Other variations in the diffraction patterns pertain to the degree of crystallinity, which affects the peak intensity and background contribution but does not affect the number of diffraction peaks. Crystallite size and strain may also affect the breadth of the diffraction peaks. However, none of the optimised structures (or the starting structures) exhibited a diffraction pattern which was characteristic of what is typically observed for γ-Al_2O_3. Figures 10.6 and 10.7 illustrate examples of neutron diffraction patterns generated from the simulated structures. The simulated diffraction patterns have significant peaks which are not present in the experimental pattern. Also the major peaks in the simulated patterns, particularly those at $2\theta \sim$ 43, 49 and 73 °, do not have the same relative intensities exhibited in the experimental pattern.

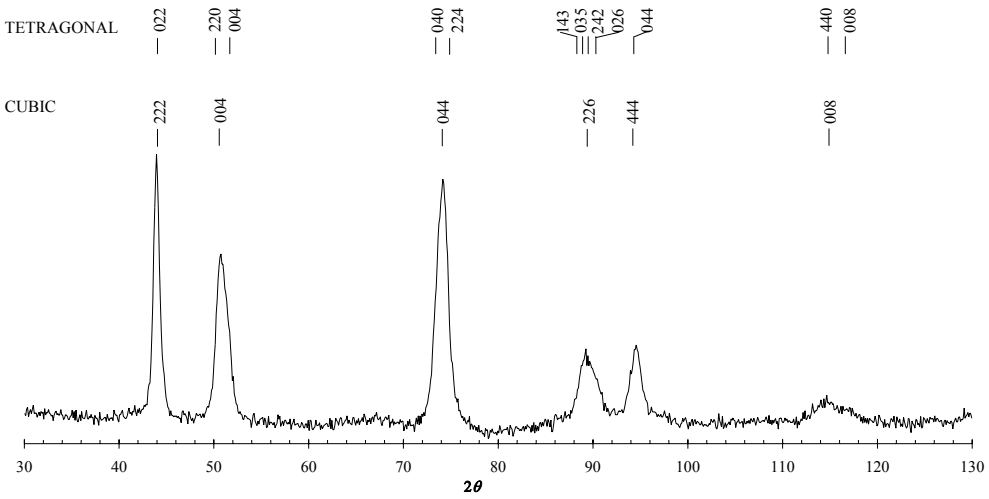

Figure 10.5. A typical experimentally measured neutron diffraction pattern obtained from γ-Al_2O_3 prepared from highly-crystalline boehmite. This example was measured while heating the material *in situ* at 600 °C. Miller indices corresponding to the major peaks are shown for both cubic and tetragonal symmetry groups.

The DFT calculations also fail to yield a more realistic representation of the structure of γ-Al_2O_3 than the interatomic potential optimisations. They mainly served to fine tune the structure and reduce the artificial disorder that accompanies the empirical calculations. Figure 10.8 illustrates an example. The shift in the peaks (Figure 10.8c and d) results from relaxing the unit cell parameters during optimisation. It is therefore concluded that none of the optimised (or starting) structures is representative of the structure of γ-Al_2O_3.

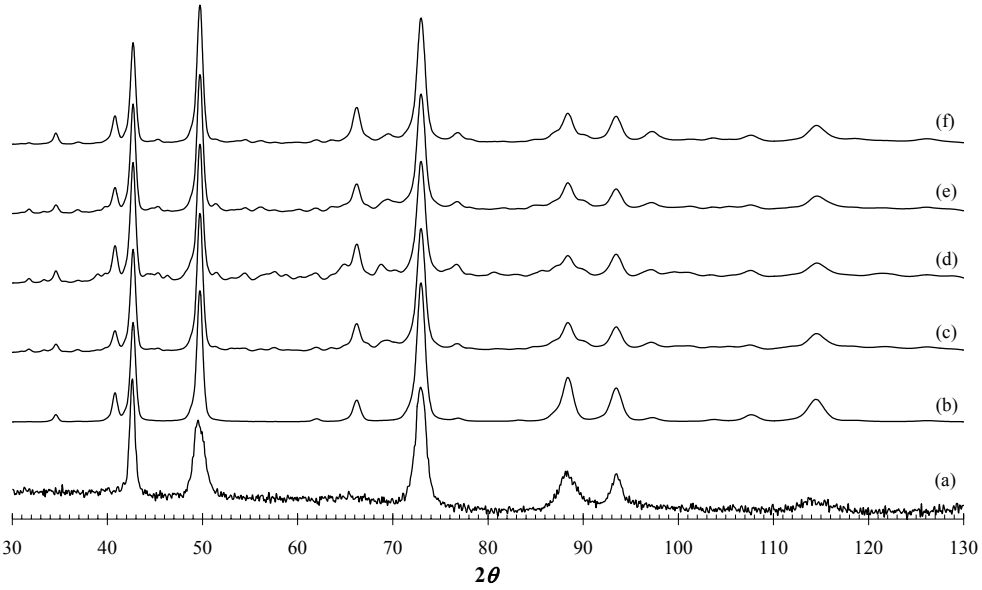

Figure 10.6. Examples of simulated diffraction patterns of structures from the $Fd\bar{3}m$ system; (a): experimental neutron diffraction pattern,[1] (b): starting structural configuration, with 19 cations on 8*a* positions and 45 cations of 16*d*. The cation configurations in (c) – (f) have the site occupancy on each special position given in the following order; 8*a*, 8*b*, 16*c*, 16*d*, 48*f*; (c): the lowest energy structure, with 12, 0, 9, 42, 1, (d): 18, 0, 3, 41, 2, (e): 17, 0, 4, 43, 0, (f): 6, 0, 13, 45, 0.

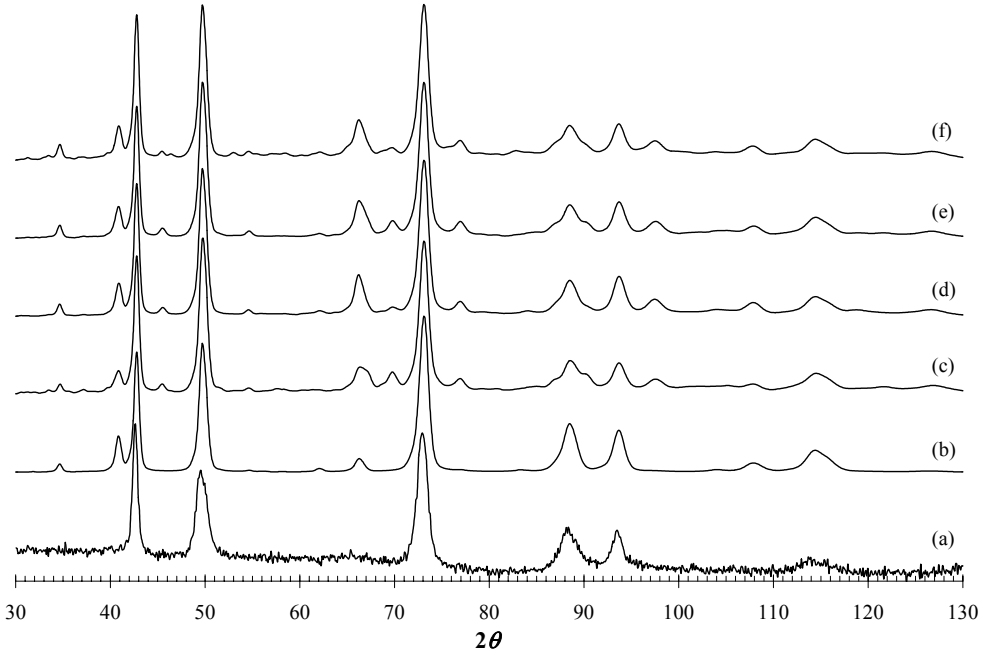

Figure 10.7. Examples of simulated diffraction patterns of structures from the $I4_1/amd$ system; (a): experimental neutron diffraction pattern, (b): starting structural configuration, 19 cations on 4*a* positions and 45 cations of 8*d*. The cation configurations in (c) – (f) have the site occupancy on each special position given in the following order; 4*a*, 4*b*, 8*c*, 8*d*, 8*e*, 16*g*; (c): the lowest energy structure, with 13, 0, 7, 40, 0, 4, (d): 18, 0, 1, 45, 0, 0, (e): 18, 0, 1, 44, 0, 1, (f): 16, 0, 3, 43, 0, 2.

[1] The diffraction pattern shown is overlaid in figures where simulated diffraction patterns are shown for direct comparison. The diffraction pattern was collected at room temperature from γ-Al_2O_3 prepared by calcining highly-crystalline boehmite at 600 °C for seven hours.

As was seen in the κ-Al_2O_3 study (*section 5.3*), interatomic potential calculations allow for significant cation migration. As mentioned earlier, the large number of structures exhibiting cation migration to *c* symmetry site positions suggests that Al ions in these positions are inherent in the structure. However, the discrepancy between the simulated and real structures means that the starting structure models are not close enough to the true structure of γ-Al_2O_3 to facilitate a derivation of its representative configuration. Hence, it follows that the long held belief of γ-Al_2O_3 being a structure where cations are exclusive to spinel site positions can be categorically ruled out.

This finding has implications on all previous computational (and most experimental) studies on γ-Al_2O_3. Seeing that all previous studies invariably began with spinel-based models, it is unlikely that the derived structural configurations would have represented the true structure. This does not mean that these studies have not been excellent contributions. To illustrate this, the calculations of Gutiérrez *et al*. (2002) and Sohlberg *et al*. (1999) were reproduced here, using the Catlow *et al*. (1982) potentials, and the diffraction patterns of the derived structures generated. All 15 possible configurations of the 40 atom cell examined by Gutiérrez *et al*. (2002) were simulated here. The H-O potential of Jones *et al*. (2000) was used to account for hydrogen in the HAl_5O_8 configurations simulated by Sohlberg *et al*. (1999). Six different configurations, one for each possible site on which hydrogen can be located, of the 14 atom HAl_5O_8 cell were examined. The oxygen atoms were restricted to local regions around their starting positions using a harmonic restraint (discussed in *section 10.2.1*). Examples of diffraction patterns obtained from the optimisation of the structures based on these earlier studies are illustrated in Figure 10.9. As expected, none of the patterns obtained is representative of the structure of γ-Al_2O_3. The greatest variation in the diffraction patterns was found for the Sohlberg *et al*. (1999) structures, whereas those from the Gutiérrez *et al*. (2002) structures are all almost identical to each other. The Sohlberg *et al*. (1999) structures were also optimised here using DFT. The diffraction patterns generated from these simulated structures exhibited greater departure from the representative pattern of γ-Al_2O_3 than those simulated from interatomic potentials.

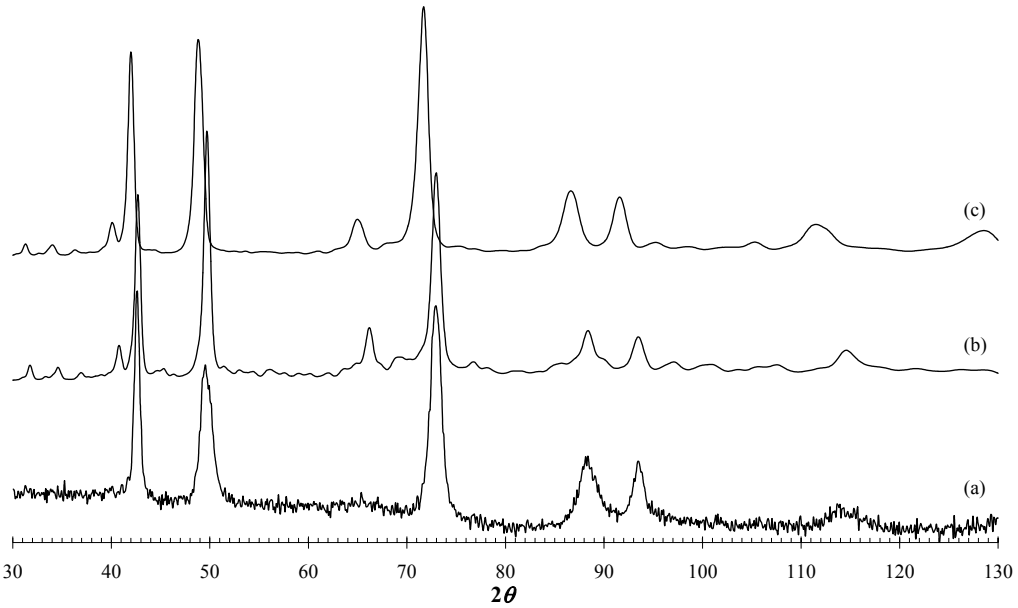

Figure 10.8. Example from the $Fd\bar{3}m$ system of the improvement to the simulated structure provided by DFT calculation; (a): experimental neutron diffraction pattern, (b): diffraction pattern from interatomic potential calculation, (c): using DFT on the $1 \times 1 \times 3$ tetragonal supercell and allowing the cell to relax.

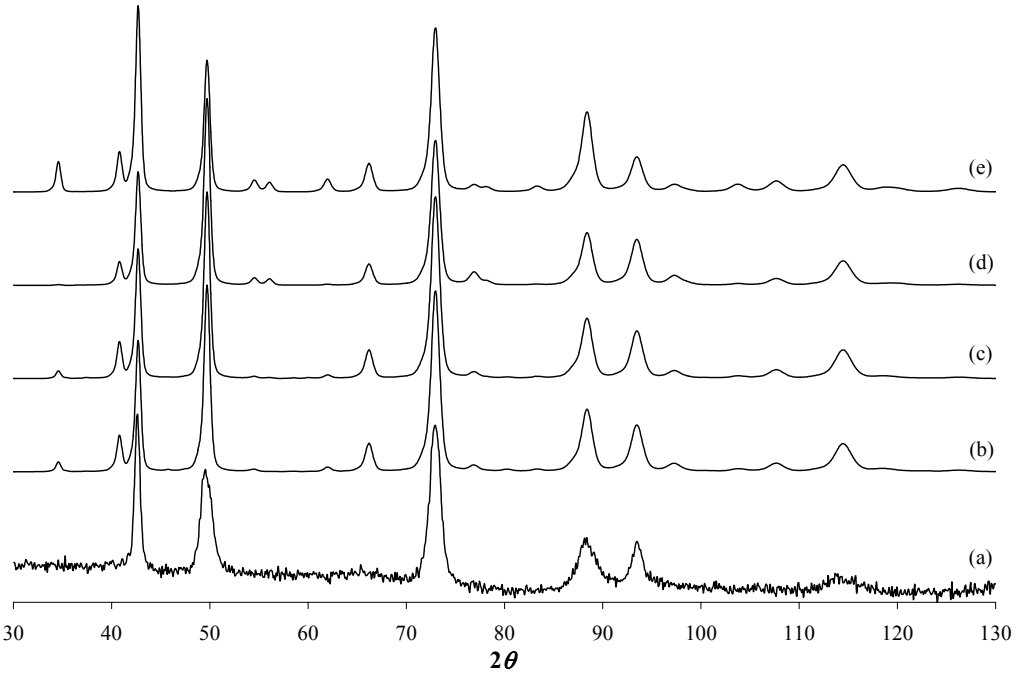

Figure 10.9. Comparison of (a): the experimental diffraction pattern, with example diffraction patterns generated from the reproduced calculations of (b) and (c): the Gutiérrez *et al*. (2002) and (d) and (e): Sohlberg *et al*. (1999). For the Sohlberg *et al*. (1999) based calculations the (d) represents the HAl_5O_8 cell with hydrogen on a tetrahedral position and (e) represents the HAl_5O_8 cell with hydrogen on an octahedral position.

10.2 More Appropriate Starting Models (*c* Symmetry Based)

The key to obtaining a representative structure of any material using molecular modelling is to ensure the starting model is as close to the correct configuration as possible. Fortunately, this computational work was accompanied by a parallel experimental study which has provided useful information. A second series of starting structure models were constructed based on the incorporation of cations on *c* symmetry site positions. Based on the experimental occupancies found (*Chapter 7*), cations were distributed in the supercells as follows; 19 on *a* symmetry positions (occupancy = 0.792), 17 on *c* symmetry positions (occupancy = 0.354), and 28 on *d* symmetry positions (occupancy = 0.583). These are referred to herein as *c* symmetry based structure models.

The starting candidates were generated by fixing the *a* and *d* symmetry position cations in idealized positions, as for the oxygen sublattice, and arranging the 17 cations on *c* symmetry positions in all possible combinations. Three different idealized *a* and *d* symmetry cation configurations were chosen for each of the space group symmetry systems. One configuration was obtained by taking the *a* and *d* symmetry cations from the lowest energy structure of the previous set of optimisations to have 19 *a* symmetry cations and 28 *d* symmetry cations, respectively, and set these to idealized coordinates. The other two configurations were chosen by visual inspection to ensure that the *a* and *d* symmetry cations were distributed as sparsely and physically reasonably, as possible.

This approach yields ${}^{48}C_{17} \approx 4.25 \times 10^{12}$ structural possibilities, an immense quantity to optimise. Each idealised configuration was inspected and restrictions were placed on which *c* symmetry positions Al ions could be situated on, based on nearest neighbour distances to the pre-established *a* and *d* symmetry cations. Care was taken to ensure that the distribution of the *c* symmetry positions was physically sensible. The *c* symmetry cations were placed in positions where no *d* symmetry cation was closer than 2.7 Å. However, all *c* symmetry positions, for both space group structures, lie in close proximity (1.7 Å) to two *a* symmetry positions. Given the number of *a* symmetry cations in the starting structures, it is impossible to avoid placing a *c* symmetry cation in such a close position to another Al ion. It was therefore decided to ensure that *c* symmetry cations were placed such that only one *a*

symmetry position is within 1.7 Å, where possible. Application of these restrictions to the six established idealised configurations (three for each space group symmetry system) yielded 19 possible *c* symmetry positions available for occupation in each structure. This results in $^{19}C_{17} = 171$ possible arrangements for each structure, a total of 513 starting candidates for each space group symmetry system.

Diffraction patterns generated from *c* symmetry based starting configurations are illustrated in Figure 10.10. These diffraction patterns are significantly different to those from the starting configurations with cations exclusive to spinel positions (Figure 10.6b and 10.7b). They are similar to the experimental diffraction pattern (Figure 10.5). The peaks at $2\theta \sim 35$, 41, 55 and 66 ° from the $Fd\bar{3}m$ system diffraction patterns (Figure 10.10b) are more intense than the equivalent peaks in the $I4_1/amd$ system diffraction patterns (Figure 10.10c). This is because the asymmetric unit for the $Fd\bar{3}m$ space group is smaller than that of $I4_1/amd$, and means that the latter can have more atoms in the asymmetric unit. The result is a smaller relative occupancy of the site positions in the $I4_1/amd$ space group (even though on the whole it is the same). Hence, some of the peaks in an $I4_1/amd$ diffraction pattern will be smaller than equivalent peaks in a $Fd\bar{3}m$ pattern.

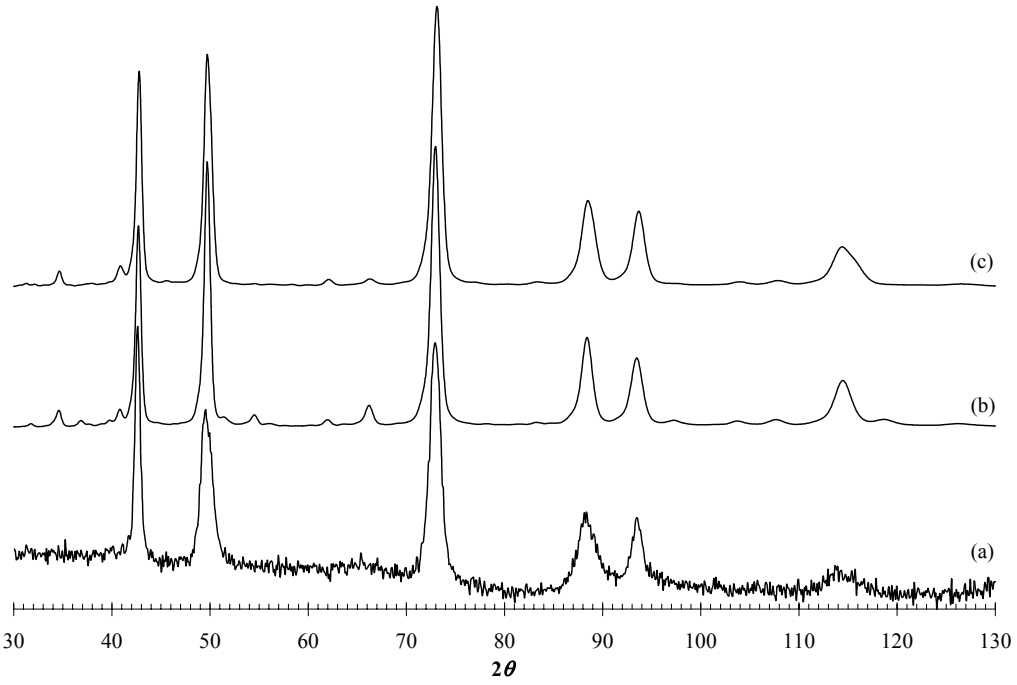

Figure 10.10. Examples of diffraction patterns generated from *c* symmetry based starting structural configurations; (a): experimental neutron diffraction pattern for comparison, (b): from the $Fd\bar{3}m$ system and (c): from the $I4_1/amd$ system of structures.

The smaller peaks at $2\theta \sim 35$, 41, 55 and 66 °, and other peaks of similar or lesser intensity, are largely concealed in the experimental pattern by the background contribution, particularly in the lower 2θ range. In the case of the simulated diffraction pattern peaks at $2\theta \sim 62$ and 66 ° there is a corresponding broad hump in the experimental pattern. The cubic diffraction pattern also exhibits reduced intensity of the peak at $2\theta \sim 43$ °. Discrepancies in the relative intensities of the three most intense peaks are discussed later (*section 10.3*).

10.2.1 Oxygen Sublattice Distortion During Optimisation

Distortion of the oxygen sublattice was far more severe during optimisations of the *c* symmetry based structures, making convergence difficult to achieve. This higher disorder is due to the close proximity of the *c* and *a* site positions. It was therefore decided to apply a harmonic restraint to the oxygen sublattice so that the oxygen ions remain confined close to their initial starting positions:

$$E = \frac{1}{2}k(r - r_o)^2 . \qquad (10.1)$$

Here E is the energy, k is the spring constant (which can be varied) used to dictate how much flexibility the oxygen sublattice ions are given to move about their original positions, r_o is the initial ion position and r is the ion position during optimisation. This approach goes part of the way to enforcing symmetry during optimisation. The degree of distortion in the oxygen sublattice, and the time required to achieve convergence was thereby significantly reduced.

To test if restraining the oxygen sublattice affects the cation configuration, approximately 1000 out of the 57,763 structures from the original *$I4_1/amd$* system were randomly selected and optimised using the approximation. The minimum, mean, and maximum energy of the random sample pool of structures was -5069.89, -5065.78, and -5051.97 eV, representing an increase of 38.02 eV in the mean energy due to the harmonic restraint of the oxygen sublattice. While the range in optimised energies is similar, the harmonic restraint serves to reduce the amount of cation migration to other symmetry positions. This further highlights that starting models with cations exclusive to spinel positions are not close enough to the real structure of γ-Al_2O_3 to facilitate the derivation of its representative configuration. There was no migration of cations to *b*, *e* and *g* (non-*a*, *c* and *d*) symmetry positions or any

unassigned positions. The only cation migration experienced during optimisation was to *c* symmetry positions, indicating, as above, that the structure of γ-Al_2O_3 inherently possesses Al ions on these positions.

After optimisation of the *c* symmetry based structures, selected structures were then re-optimised with the restraint on the oxygen sublattice removed. The oxygen sublattice was found to remain ordered to a similar degree as for the spinel-based structures. Subsequent optimisation using DFT further improved the order and the oxygen sublattice was found to be very similar for all structures. Figure 10.11 contains examples of diffraction patterns from optimisation using interatomic potentials, with the harmonic restraint to the oxygen sublattice, and from DFT.

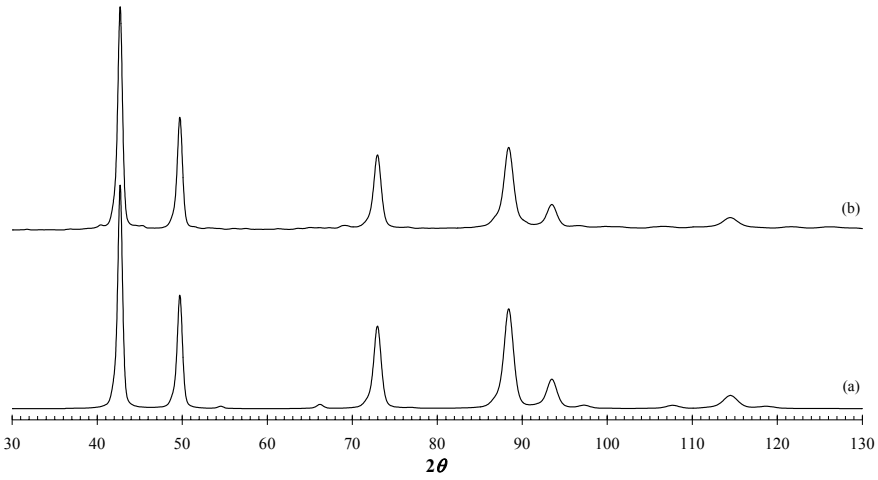

Figure 10.11. Examples of diffraction patterns of the oxygen sublattice; (a): after optimisation using interatomic potentials with the harmonic restraint to the oxygen sublattice, (b): after optimisation with DFT. These examples were taken from the $Fd\bar{3}m$ system structures.

10.3 Results from Optimisation of *c* Symmetry Based Structures

The key results from optimisation of the *c* symmetry based structures are summarized in Figure 10.12 and Table 10.1. As with the previous optimisations, the structures of the $I4_1/amd$ system have higher mean, minimum and maximum energies than the $Fd\bar{3}m$ system. Also, for the characteristics highlighted in Figure 10.12, the differences in the mean energies were smaller for the $I4_1/amd$ system. A greater range in the optimised energies was observed compared with the structures where cations were initially placed on spinel site positions. This greater range in optimised

energy reflects the higher amount of overall cation migration experienced for the *c* symmetry based structures. The majority of structures exhibited an even distribution of cations throughout the optimised supercells. Over two thirds of the structures had either 21 or 22 Al ions within each third of the supercell for the $Fd\bar{3}m$ system structures, and either 10 or 11 Al ions within each sixth of the supercell for the $I4_1/amd$ system structures, maintaining approximate Al_2O_3 stiochiometry in each subcell.

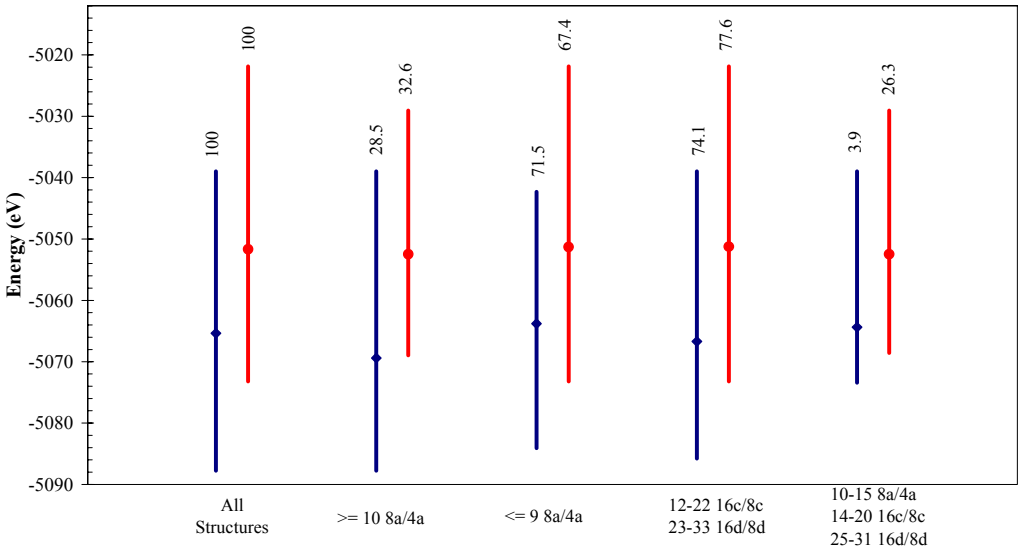

Figure 10.12. Key statistics from optimisations of *c* symmetry based structural configurations of the cubic $Fd\bar{3}m$, ♦, and tetragonal $I4_1/amd$, ●, system structures with interatomic potentials. The ♦ and ● symbols indicate the mean energies of the distributions. The values above each energy range is the percentage of the total number of structures that have the configurational characteristic being highlighted.

After optimisation, every structure in both the $Fd\bar{3}m$ and $I4_1/amd$ symmetry systems possessed cation occupation of non-*a*, *c* or *d* symmetry site positions. There were no cations in unassigned (non-tetrahedral or octahedral) site positions. The cation migration predominantly involves movement of cations away from *a* symmetry positions to other tetrahedral site positions of lower symmetry. The average number of cations in *a* symmetry positions after optimisation is 8 and 9 for the $Fd\bar{3}m$ and $I4_1/amd$ systems (Table 10.1), respectively, representing average occupation of 58 and 53%. The highest number of *a* symmetry site positions occupied in any of the optimised structures, whether from the $Fd\bar{3}m$ or $I4_1/amd$

supercells, was 15. Fewer than one third of the structures in both symmetry systems have ten or more cations in *a* symmetry positions (Figure 10.12). However, the mean energy of this group of structures is less than that for the total sample pool in both symmetry systems. Most of the cation migration was towards the 48*f* symmetry positions in the $Fd\bar{3}m$ system structures. For the $I4_1/amd$ system, the cations were distributed relatively evenly among all the lower symmetry tetrahedral site positions.

The migration to other tetrahedral sites is supposedly due to repulsion between cations in *a* and *c* symmetry positions, which are within 1.7 Å of each other in the starting configurations. Cations migrating away from *a* symmetry positions therefore tend to occupy other tetrahedral positions with fewer *c* and *d* symmetry positions nearby. The *b* symmetry positions are within 1.7 Å of *d* symmetry positions. Migration to these positions is the lowest because *d* symmetry cations are the most populous in the structures. The other tetrahedral positions, *e*, *f* and *g* are also within 1.7 Å of both *c* and *d* symmetry positions. For comparison, distances in the starting configurations between *c* and *d* symmetry positions were 2.7 Å. These cation distances illustrate that migration away from *a* symmetry positions is required to achieve energetically stable structures. To demonstrate this, attempts to optimise the starting structures directly using DFT were made. All of theses attempted DFT optimisations diverged.

The cation migration observed during the simulation of the structures exhibits a logical pattern. Locally, symmetry exclusion rules are obeyed such that if two positions are occupied within a region, nearest neighbour positions are not occupied. The cation migration away from *a* symmetry positions is required for these exclusion rules to be obeyed. When these exclusion rules are obeyed, longer-range ordering results such that positions that are occupied in one subcell of a supercell are not necessarily occupied in the next. There are, for example, many cases where alternate subcells have virtually the same cation configuration, with the separating subcell exhibiting a completely different configuration.

The migration away from *a* symmetry positions means that the configurations closest to the starting configurations had between 10 – 15 *a*, 14 – 20 *c*, and 25 - 31 *d* symmetry sites occupied, representing a variation from the starting configuration of up to 47.4, 1.7, and 1.1% respectively. Only 20 structures of the $Fd\bar{3}m$ system and 135 of the $I4_1/amd$ system lie within this range (Figure 10.12). None of these were

among the lowest energy structures. However, there is comparatively little migration away from the octahedral, *c* and *d* symmetry, site positions. For about three quarters of the structures, the octahedral sites remain within 2.9% of their initial occupancy (Figure 10.12). These structures exhibit the same range in energies as the total sample pool, but have a lower mean energy. Around half of the structures remain within 1.7% of their starting octahedral occupancy.

Table 10.1. Summary of the distribution of cations amongst the possible site positions for all 513 optimised structures of each symmetry system investigated. For each type of Wyckoff symmetry position, the table provides the proportion of structures that have cations occupied in each type of site. The minimum and maximum number of cations occupied in each type of position out of all the structures, the average cation occupation for all the structures, and the 2σ range are also provided. The 2σ range shows the cation occupation range encompassing 90% of structures with a particular type of site position occupied. The table also indicates the number of cations on each type of symmetry position in the starting configuration for comparison.

Wyckoff Symmetry Position	*% Structures With Position Occupied*	*Possible Positions Per Supercell*	*Starting Positions*	*Min. Positions Occupied*	*Max. Positions Occupied*	*Average (site occ.)*	*2σ Range (site occ.)*
			$Fd\bar{3}m$ system				
8*a*	100	24	19	1	15	8 (0.333)	3-14 (0.125-0.583)
8*b*	19	24	0	0	4	1 (0.042)	1 (0.042)
16*c*	100	48	17	6	28	17 (0.375)	10-24 (0.21-0.50)
16*d*	100	48	28	24	36	29 (0.583)	25-32 (0.521-0.667)
48*f*	100	144	0	3	17	9 (0.062)	5-13 (0.035-0.090)
			$I4_1/amd$ system				
4*a*	100	24	19	1	15	9 (0.375)	6-14 (0.25-0.583)
4b	84	24	0	0	7	2 (0.083)	1-3 (0.042-0.125)
8*c*	100	48	17	9	31	20 (0.417)	14-23 (0.292-0.479)
8*d*	100	48	28	17	33	26 (0.542)	23-33 (0.479-0.688)
8*e*	98	48	0	0	10	4 (0.083)	1-6 (0.021-0.125)
16*g*	97	96	0	0	9	3 (0.031)	1-5 (0.010-0.052)

From the $Fd\bar{3}m$ system, the closest configurations to the idealised starting structures and with the least number of non-*a*, *c* or *d* occupied symmetry positions had 10 or less cations on 48*f*, and no cations on 8*b*, symmetry positions (see Figure 10.13b for example). There were only 7 structures within this range. In the $I4_1/amd$ system there were 2 or less cations on the 4*b*, 8*e* and 16*g* symmetry positions in the 11 structures which were closest to the starting configuration (see Figure 10.14b for example).

Irrespective of the differences between the structural configurations, most of the simulated diffraction patterns generated from the optimised structures have similar appearance for both space group systems. Furthermore, they do not differ significantly from the diffraction patterns of the starting structures. Examples of the simulated diffraction patterns obtained are presented in Figures 10.13 and 10.14. These diffraction patterns also provide an excellent match with experimentally obtained diffraction patterns for γ-Al_2O_3 (Figure 10.5).

It is clear from the optimisations that the migration of cations away from *a* symmetry positions does not affect the pattern significantly (Figures 10.13 - 10.15). The most important factor in maintaining a diffraction pattern that is close to experiment is the presence of a sufficient number of occupied *c* symmetry positions. Secondly, a reasonably consistent cation distribution on octahedral sites is required. Only in cases where the structures exhibited significant cation migration away from *c* symmetry positions did the calculated diffraction patterns show noteworthy divergence from the experimental ones. This occurred for structures where the number of cations on *c* symmetry positions was less than 10, of which there were 8 structures for the $Fd\bar{3}m$ system and 1 for the $I4_1/amd$ system. The most extreme cases are shown in Figure 10.15, showing increased intensity of the peaks at $2\theta \sim 41$ and 66 °. In these structures with lower numbers of cations on *c* symmetry positions, there are also higher numbers of cations in *a* symmetry positions. These structures have a higher number of cations in spinel positions, similar to some of the configurations obtained from the optimisation of spinel-based starting candidates. However, the presence of considerable numbers of non-*a*, *c* and *d* symmetry positions prevents the diffraction pattern taking on the appearance of a diffraction pattern obtained from a spinel-based configuration. Irrespective of which tetrahedral site positions are occupied, the ratio of octahedral to tetrahedral cations in the

structures is consistently around 2.33:1, although more structures achieve this for the $I4_1/amd$ system.

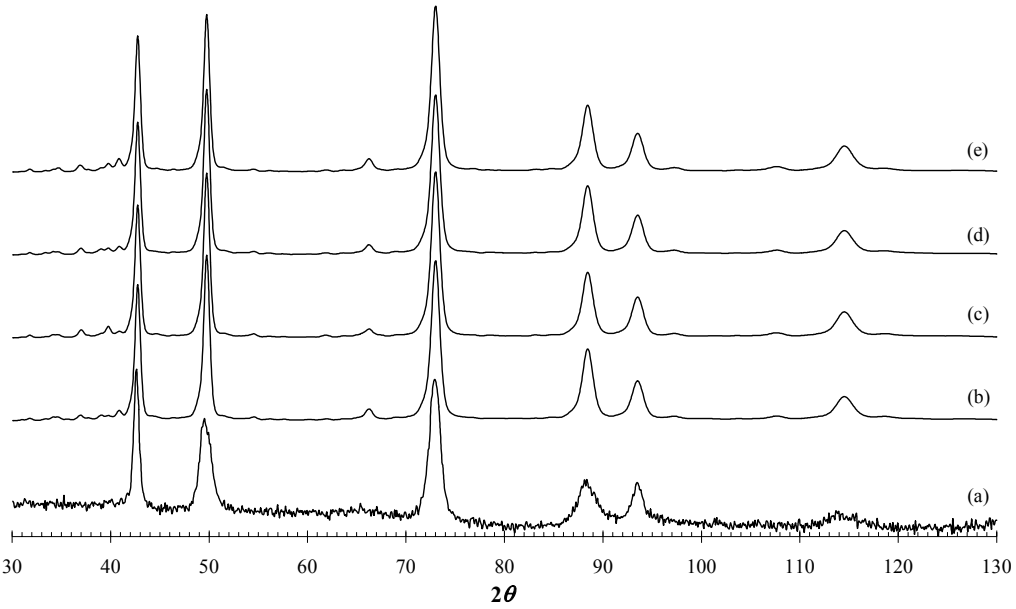

Figure 10.13. Examples of simulated diffraction patterns from *c* symmetry based structures of the $Fd\bar{3}m$ system; (a): experimental neutron diffraction pattern. The cation configurations in (b) – (e) have the site occupancy on each special position given in the following order; 8*a*, 8*b*, 16*c*, 16*d*, 48*f*; (b): closest configuration to starting arrangement (therefore with least amount of non-*a*, *c* and *d* symmetry positions), with 11, 0, 16, 31, 6, (c): 14, 0, 11, 34, 5, (d): 8, 0, 9, 28, 19, (e): 10, 0, 13, 31, 10.

Except for the 9 structures with less than 10 cations on *c* symmetry positions, the only significant discrepancies between the experimental and simulated diffraction patterns lie in the relative peak intensities. In the simulated patterns, the peaks at $2\theta \sim$ 51, 73 and 89 ° are generally more intense than the corresponding peaks in the experimentally measured diffraction pattern. These discrepancies are partly due to preferred orientation in the experimental material. This provides a possible answer for the observed discrepancies between diffraction data and the Rietveld calculated pattern, particularly at $2\theta \sim$ 44 °, in *Chapters 7* and *8*; namely the inability of the Rietveld code used to adequately model preferred orientation. As with the starting structures, the smaller peaks, at $2\theta \sim$ 35, 41, 55 and 66 °, are largely concealed in the experimental pattern by the background contribution.

It should be noted that the disproportionately high intensity of the peak at $2\theta \sim$ 89 ° in the simulated diffraction patterns from interatomic potential optimisation

is due to the restrictions imparted by the harmonic restraint on the oxygen lattice. When the structures are optimised using DFT (Figures 10.16 and 10.17) the peak achieves an intensity comparable to that observed experimentally.

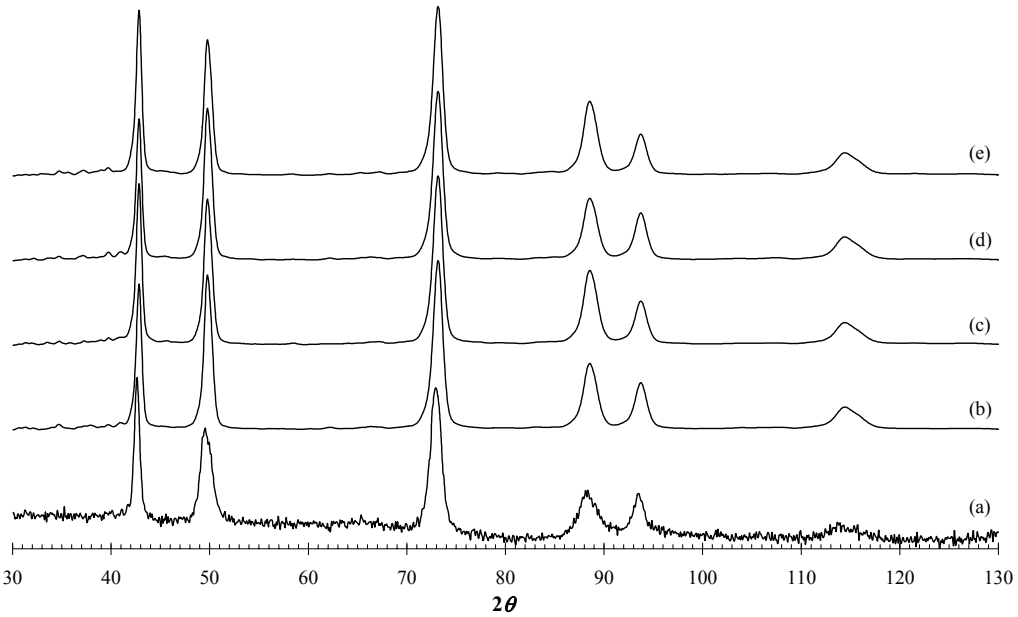

Figure 10.14. Examples of simulated diffraction patterns from *c* symmetry based structures of the $I4_1/amd$ system; (a): experimental neutron diffraction pattern. The cation configurations in (b) – (e) have the site occupancy on each special position given in the following order; 4*a*, 4*b*, 8*c*, 8*d*, 8*e*, 16*g*; (b): among the closest configurations to starting arrangement (therefore with least amount of non-*a*, *c* and *d* symmetry positions), with 11, 2, 20, 28, 2, 1, (c): 8, 1, 17, 27, 5, 6, (d): 10, 1, 17, 30, 3, 2, (e): 8, 5, 20, 21, 5, 5.

The peak at $2\theta \sim 44$ ° has a fairly consistent intensity ratio when compared to the other main peaks for all the simulated diffraction patterns in the $Fd\bar{3}m$ system, but not for the $I4_1/amd$ system. It can be seen from Figure 10.14(c and e) that the relative intensities of the peak at $2\theta \sim 44$ °, when compared to the peaks at 51 and 73 °, approaches that observed in the experimental diffraction patterns. Examining the Miller planes corresponding to the peak at $2\theta \sim 44$ ° in the modelled structures (222 for cubic symmetry and 022 for tetragonal symmetry) indicates a difference in the type of species present. The 222 plane (226 in the 1×1×3 supercell) is predominantly composed of oxygen ions, whereas the 022 plane (026 in the 2×1×3 supercell) also contains a substantial number of cations. The average density of occupied positions on the 022 plane in the modelled $I4_1/amd$ system structures is also higher. Hence the simulated structures from the $I4_1/amd$ system are more

representative of the experimental structure as the 022 peak from the modelling reflects experiment more closely.

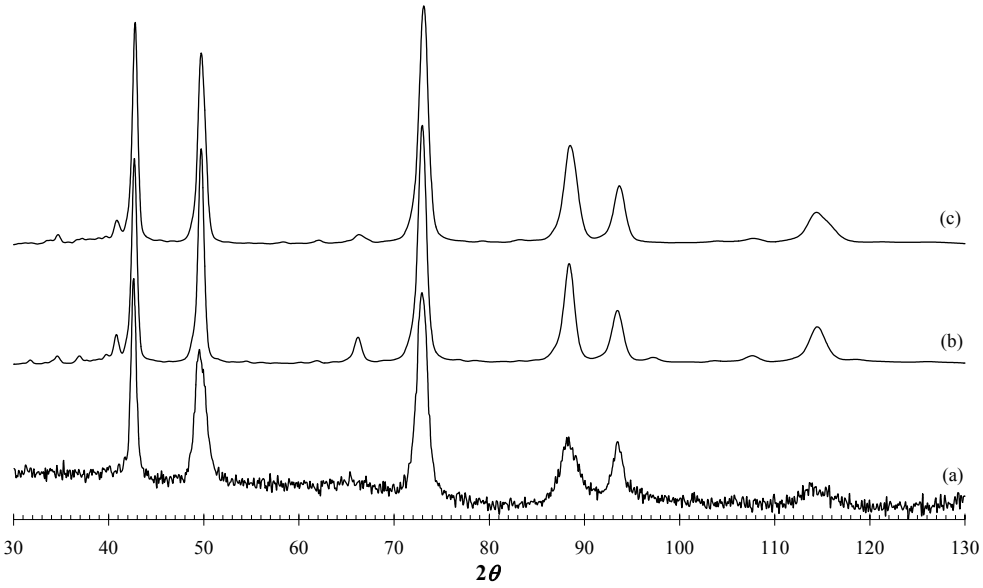

Figure 10.15. Comparison of (a): experimental neutron diffraction pattern, with simulated diffraction patterns exhibiting the greatest difference from experiment for *c* symmetry based structures; (b): from the $Fd\bar{3}m$ system, with 15, 0, 6, 35, and 8 cations on 8*a*, 8*b*, 16*c*, 16*d*, and 48*f* site positions respectively; (c): from the $I4_1/amd$ system, with 15, 1, 9, 33, 2, and 4 cations on 4*a*, 4*b*, 8*c*, 8*d*, 8*e*, and 16*g* site positions respectively.

Furthermore, the anisotropic peak at $2\theta \sim 114$ ° in the experimental pattern tends to be broader than most of the equivalent peaks in simulated patterns, particularly when compared to patterns of the $Fd\bar{3}m$ system. This is indicative of strain in the material. The broadness of the peak(s) at $2\theta \sim 114$ ° in diffraction patterns simulated from the $I4_1/amd$ system is closer to experiment. This is because the tetragonal split (Figure 10.5) shows that some of the strain is being released by changing the lattice relative to the ideal cubic system.

The characteristics mentioned above indicate that configurations from the $I4_1/amd$ system provide a more accurate description of the structure of γ-Al_2O_3 than the $Fd\bar{3}m$ system. This is true for the experimental material examined here (*Chapters 7* and *8*). However, it must be considered that the experimental diffraction pattern can vary slightly depending on the preparation conditions. For example, γ-Al_2O_3 synthesised from amorphous material by chemical vapour deposition (CVD) would not be expected to exhibit the same degree of anisotropic broadening, strain and

preferred orientation observed here, and would have a cubic unit cell (Dragoo and Diamond 1967; Bonevich and Marks 1992; Larsson and Ruppi 2001). In such a case, structural configurations from the $Fd\bar{3}m$ system would provide a more appropriate description of γ-Al_2O_3.

In principle, it does not matter exactly which positions are occupied, as long as the same diffraction pattern is obtained. The simulations illustrate this since there are distinct configurations that result in broadly the same diffraction pattern. Because these theoretically-derived diffraction patterns have the same characteristics as those from experiment, they can be indexed in the same manner. The calculated supercells show that the overall crystal can have variations of configurations from substructure unit to substructure unit (domain structures) as long as it follows the same symmetry rules that are allowed overall (*e.g.* lattice dimensions, extinction rules). The similarities in the diffraction patterns demonstrate that the optimised structures follow these rules.

The variation in the site occupancy, provided there is a reasonably consistent number of cations in *c* symmetry positions, shows that it is more important to have cations on the appropriate Miller planes than it is to have precisely the correct number of cations in particular symmetry positions. This is most easily illustrated by Figure 10.14 (c and e) where there are up to 23 tetrahedrally coordinated cations in the structure corresponding to Figure 10.14e (an extreme case) but the peak intensity ratios are almost identical to those of Figure 10.14c, which corresponds to a more typical configuration.

It is also evident from the modelling that, overall, the structure is ordered, but locally can have regions of varying occupancy. γ-Alumina may therefore be thought of as a structure with a consistent oxygen sublattice and a varying cation configuration. Cations can be located at other site positions (non-*a*, *c* or *d* symmetry) to minimise lattice distortions, and thus the energy, locally. Distortion of octahedra and tetrahedra is present throughout the structures of both the $Fd\bar{3}m$ and $I4_1/amd$ systems. All cations were found to lie within 0.7 Å of the idealised coordinate of the site positions they were situated in.

Each optimised supercell here provides a realistic example of the structure of γ-Al_2O_3 and the data obtained illustrates the variance in the possible cation configurations. It therefore follows that supercells described here allow for more

accurate and complete modelling of the defect structure than the single unit cell approach. The single unit cell approach, namely the Cubic_16c or Tetragonal_8c models, provided in *Chapters 7* and *8* remain a valid portrayal of the structure, but provide only an average description. These models are in turn much better descriptions of the structure than the original cubic spinel description.

10.3.1 Higher Accuracy Structure Examples

When optimising with DFT, the distortions of the octahedra and tetrahedra were found to reduce as the oxygen sublattice was allowed to relax more freely to accommodate cation movement and the cations, generally, moved closer to the ideal positions. The distortion that remains after optimisation with DFT is a realistic feature and, coupled with the varied distribution of cations, provides direct support for the proposed short-range ordering within the inter-skeletal layers of γ-Al_2O_3 in *section 8.3*; distorted octahedra and tetrahedra can occur as a consequence of the incomplete cation migration.

While the results show that almost all of the optimized structure candidates can be considered equally representative of the structure of γ-Al_2O_3, it is appropriate to show the most thermodynamically stable configurations. Simulated diffraction patterns for the lowest energy structures of the $Fd\bar{3}m$ and $I4_1/amd$ systems are shown in Figures 10.16 and 10.17 respectively, which provide comparison between the DFT optimizations and those with the empirical potentials. The undulation of the background is a reflection of the oxygen sublattice being able to relax more freely to accommodate cation migration in DFT than when optimised under the harmonic restraint with interatomic potentials. There is little or no change in the cation positions. The relaxation of the oxygen sublattice results in the peak at $2\theta \sim 89$ ° reducing in intensity and adopting an appearance closer to what is experimentally observed (Figure 10.5). These structures are illustrated in Figure 10.5 and the coordinates are presented in *Appendix IX*. The energy of these structures is 6.20 and 7.60 eV lower than the energies of the structures with configurations closest to the starting structures of the $Fd\bar{3}m$ and $I4_1/amd$ symmetry systems, respectively. The structures that have configurations among the closest to the starting structures, *i.e.* with the least number of occupied non-*a*, *c* or *d* site positions, are representative of

the most ideal cases. The coordinates for the structures with configurations closest to the starting structures are presented in *Appendix IX*.

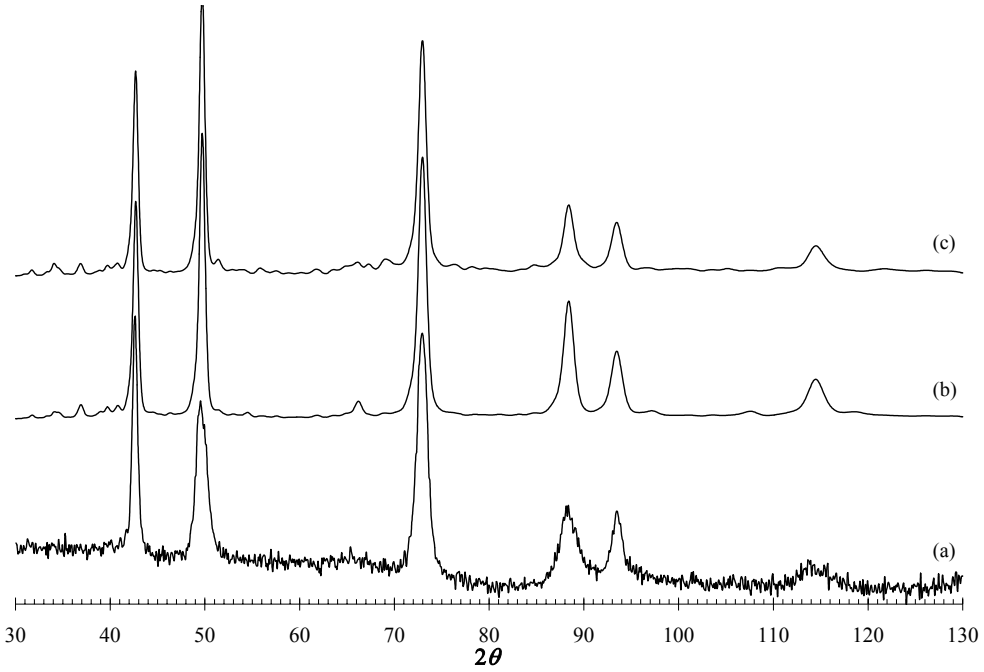

Figure 10.16. Lowest energy supercell structure based on $Fd\bar{3}m$ symmetry, with 9 cations on 8*a*, 14 cations on 16*c*, 28 cations on 16*d* and 13 cations on 48*f* site positions; (a): experimental neutron diffraction pattern, (b): after optimisation with interatomic potentials, (c): after optimising with DFT.

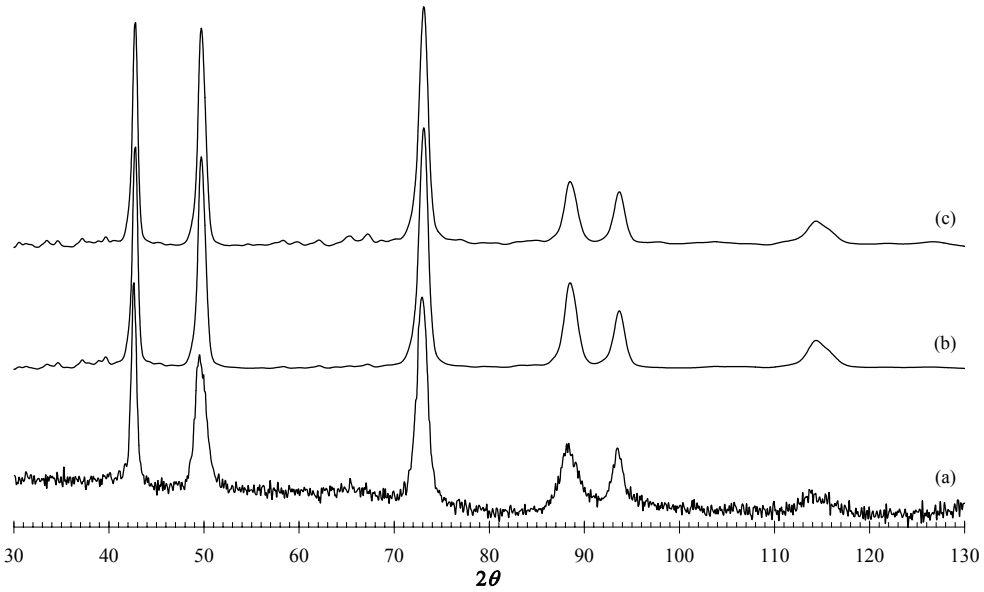

Figure 10.17. Lowest energy supercell structure based on $I4_1/amd$ symmetry, with 9 cations on 4*a*, 4 cation on 4*b*, 18 cations on 8*c*, 25 cations on 8*d*, 4 cations on 8*e* and 4 cations on 16*g* site positions; (a): experimental neutron diffraction pattern, (b): after optimisation with interatomic potentials, (c): after optimising with DFT.

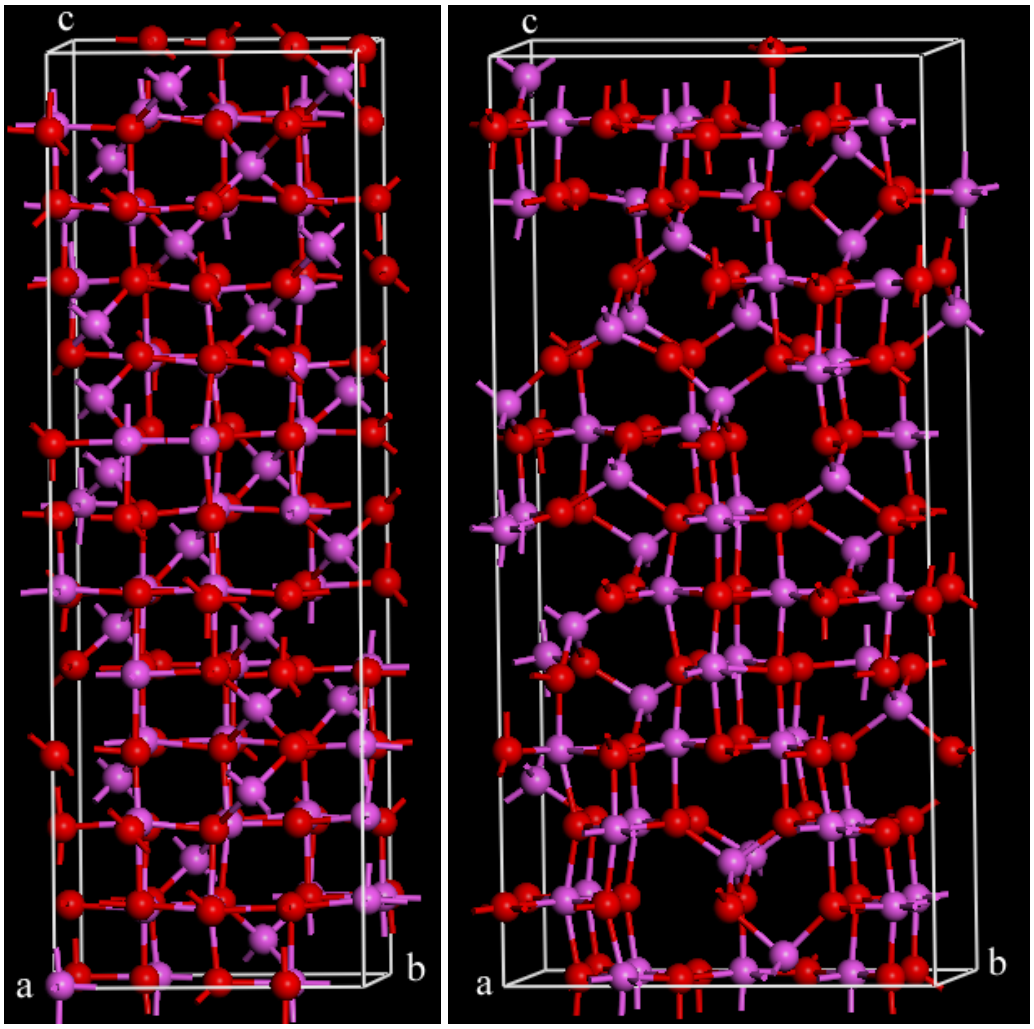

(a) (b)

Figure 10.18. Illustration of (a): $Fd\bar{3}m$ system structure represented in Figure 10.16 and *Appendix IX*, after optimisation of supercell using DFT; (b): $I4_1/amd$ system structure represented in Figure 10.17 and *Appendix IX*, after optimisation of supercell using DFT.

The calculated band gap energy for the $I4_1/amd$ symmetry structure depicted in Figures 10.16 and 10.18b, is 4.2 eV, in excellent agreement with the value of 4.3 eV for γ-Al_2O_3, determined by Costina and Franchy (2001). For the $Fd\bar{3}m$ symmetry structure the calculated band gap energy value was 4.0 eV. However, it should be noted that the agreement of the calculated band gap with experiment may be purely luck as the DFT usually underestimates this by approximately 50%.

10.4 Outcomes

The research conducted here has resulted in a more realistic description of the structure of γ-Al_2O_3. The supercells described here allow for more accurate and complete modelling of the defect structure of γ-Al_2O_3 than the single unit cell approach. The main outcomes are summarised below:

- Optimisation of the spinel-based structural models showed that structures with non-spinel site occupancy were more energetically favourable. However, none of the structural models exhibited a configuration close to those determined from the current experimental studies. None of the theoretical structures yielded a diffraction pattern that was characteristic of γ-Al_2O_3. The spinel-based starting structure models are not close enough to the actual structure to facilitate the derivation of its representative configuration from optimisation.
- The large number of structures which demonstrate migration of cations to *c* symmetry positions provides strong evidence that this tendency is inherent and supports the Cubic-16*c* and Tetragonal-8*c* structure models. It also suggests that these models are universal for crystalline γ-Al_2O_3.
- Optimisation of *c* symmetry based structures, with starting configurations similar to those derived from Rietveld analysis of neutron diffraction data, resulted in simulated diffraction patterns that were characteristic of γ-Al_2O_3. The similarities in the diffraction patterns show that the optimised structures follow the same symmetry rules determined by experiment.
- The occupancy of site positions was found to vary. This variation was predominantly characterised by the migration of cations away from *a* symmetry positions to other tetrahedral sites, which was found not to affect the diffraction pattern.
- The variation in the site occupancy shows that it is more important to have cations on the appropriate Miller planes than it is to have precisely the right number of cations in particular symmetry positions, provided that the number of cations on *c* symmetry site positions remains reasonably consistent.
- Overall, the structure is ordered, but locally regions of varying occupancy can exist. The variation in the cation occupancies follows local symmetry

exclusion rules. This results in the occupancy of non-*a*, *c* or *d* symmetry positions to locally minimise lattice distortions. The observed distortions in octahedra and tetrahedra, coupled with the varied distribution of cations, support the short-range ordering within the inter-skeletal layers of γ-Al_2O_3 proposed in *section 8.3*.

This research also demonstrates that interatomic potentials are suitable for use in investigations where stable structures need to be determined from an enormous number of possibilities. The empirical calculations delivered an acceptable level of accuracy and allowed for a comprehensive survey of possible outcomes using faster methods, before striving to achieve high accuracy for fewer more likely cases.

Chapter 11

Conclusions

The primary objective of this research was to settle some of the ambiguity around the structure of γ-Al_2O_3. This was undertaken through the use of interatomic potential and first principles calculations, and a wide range of supporting experiments. In addition to providing a more realistic representation of the structure, this research has also served to advance knowledge of the evolution of the structure with changing temperature and make new insights regarding the location of hydrogen in γ-Al_2O_3. These contributions are important to the scientific and industrial communities interested in structure and structural phase transitions. Here the conclusions are presented with respect to each individual study performed;

Experimental investigation of structure from single-temperature case (Chapter 7):

Boehmite-derived γ-Al_2O_3, where a tetragonal distortion is observed, is best described using the $I4_1/amd$ space group rather than $Fd\bar{3}m$. This is evident from peak splitting in neutron powder diffraction data and from electron diffraction. It was demonstrated that electron diffraction patterns, typical of γ-Al_2O_3, which have consistently been indexed according to the cubic $Fd\bar{3}m$ space group can be indexed according to the tetragonal $I4_1/amd$ space group. The structure could not be accurately modelled by restricting the Al ions to spinel positions. As a result, occupation of the 8*c* Wyckoff position in addition to the 4*a* and 8*d* is proposed. No evidence of five-coordinated Al atoms within the structure was found in the MAS-NMR data obtained in this study. This and the subsequent Rietveld analysis suggest that the Al ions can only be situated in octahedral or tetrahedral positions. The Tetragonal-8*c* model accommodates the observed peak splitting better than all other models investigated, including the dual-phase refinement approach. The distribution of Al ions determined from the proposed Tetragonal-8*c* structural model is in agreement with the distribution obtained from the MAS-NMR data. Consistency

of this model for all data sets strengthens the argument for one phase as opposed to two phases, as does the presence of only one type of electron diffraction pattern. In this model there is ordering of vacancies on all the site positions, tetrahedral and octahedral. From this it can be seen why ambiguity has arisen in early work as to which sites the vacancies prefer to reside in. It also appears that, for the material examined here, hydrogen is not interstitially present within the crystalline bulk structure, but rather is in the form of water, within the amorphous content.

Cubic γ-Al_2O_3 exhibits a diffraction pattern with the same peak positions as tetragonal γ-Al_2O_3 but no splitting and peak anisotropy. Hence, it is also proposed that the Cubic-16*c* model, which is analogous to Tetragonal-8*c*, is appropriate to describe the structure of γ-Al_2O_3 when no tetragonal distortion is observed.

Evolution of the Structure with Temperature (Chapter 8):

The evolution of the structure of γ-Al_2O_3, derived from highly-crystalline boehmite, calcined at various temperatures in air was investigated. Tetragonal γ-Al_2O_3 was found to be present between 450 and 750 °C. The structure showed a reduction in the tetragonal distortion with increasing temperature but at no stage was cubic γ-Al_2O_3 obtained. Examination of the progress of cation migration indicates the reduction in the tetragonal nature is due to ordering within inter-skeletal oxygen layers of the unit cell, left over from the breakdown of the hydroxide layers of boehmite when the transformation to γ-Al_2O_3 occurred.

Above 750 °C, δ-Al_2O_3 was not observed, but a new phase was identified and designated γ′-Al_2O_3. The structure of this phase was determined to be a triple cell of γ-Al_2O_3 and is herein described using the $P\bar{4}m2$ space group. The cation ordering is more obvious in this structure, with fewer site positions being occupied with increasing calcination temperature. Hence the structure of γ′-Al_2O_3 may be considered as a series of transition states within the γ-Al_2O_3 to θ-Al_2O_3 transformation sequence. Some distorted cation positions indicate the onset of migration from octahedral to tetrahedral sites at 900 °C, where the structure approaches the appearance of δ-Al_2O_3.

Constant cation coordination, of ~ 69% octahedral and ~ 31% tetrahedral, was observed from MAS-NMR spectra of material calcined at temperatures between

500 and 900 °C. These values agree with the cation distribution in octahedral and tetrahedral coordination obtained from the Rietveld refinements, supporting the physical integrity of the structure models.

Neutron data Rietveld refinements of the structural models suggest that hydrogen is not present within the bulk crystalline structure of any of the calcination products. Amorphous regions, where hydrogen in the bulk is most likely to reside, were observed in TEM micrographs. No obvious variations were found in the lamellar porous microstructure and diffraction patterns observed for the calcination products obtained between 500 and 700 °C, and between 800 and 900 °C, for the different preparation routes used.

Consideration of Hydrogen and Surface Effects (Chapter 9):

Systematic research was conducted on boehmite-derived γ-Al_2O_3 to obtain information on the types of hydrogen-containing species present and their possible location within the material. The use of SAXS, PGAA and NVS in conjunction with the traditional techniques utilized provides a more complete picture of the role of hydrogen in the material. Specific surface area measurements, traditionally measured using nitrogen absorption techniques, were undertaken with SAXS and indicate that the material examined has a significantly higher surface area than expected for highly-crystalline boehmite-derived γ-Al_2O_3. The higher surface area is attributed to the presence of nano-pores and closed porosity, where hydrogen-containing species can also be present. Expectedly, the specific surface area was found to decrease with increasing calcination temperature. This trend occurred concurrently with an increase in the mean pore and crystallite size and a reduction in the amount of hydrogen-containing species within the structure.

Loss on ignition experiments, based on the assumption that all hydrogen-containing species driven from the structure are lost in the form of water, were found to underestimate the amount of hydrogen in the material when compared to PGAA. The difference in the measured values is attributed the presence of hydroxide and protons, which are not burnt off along with the water within the bulk structure. Two signals pertaining to water and hydroxide species were identified using NVS. NVS provided evidence of a reduced amount of amorphous species with increasing

calcination temperature, complementing observations made from TEM and neutron diffraction patterns in *Chapter 8*.

From the mechanism of γ-Al_2O_3 formation from boehmite, the hydrogen-containing species are expected to reside in the vicinity of pores, which make up the bulk of the surface area. Because the pores are remnants of broken down hydroxide layers from boehmite, the amorphous regions are also expected to be located around such regions. This is supported by infrared analysis, where the OH/AlO_6 ratios obtained from the DRIFT spectra are 2.5 times larger than those obtained from transmission IR spectra, which indicates that the majority of hydrogen-containing species, and hence amorphous regions, lie at the surface of the material examined.

It can be concluded from the results obtained that γ-Al_2O_3 derived from highly-crystalline boehmite has a relatively well ordered bulk crystalline structure which contains no interstitial hydrogen and that hydrogen-containing species are located at the surface and within amorphous regions, which are located in the vicinity of pores. There is no evidence either way to suggest that hydrogen does not exist interstitially in crystalline alumina regions near the surface. It may not be surprising if this was the case as diffusion of protons are required to maintain charge neutrality and would occur along surface regions, particularly as the amorphous regions crystallize and become more sparse. More work is required to examine this aspect.

Computational Investigation (Chapter 10):

Inspection of ~ 1.47 billion and the simulation of ~ 122,000 structural candidates showed that spinel-based structure models do not yield a characteristic diffraction pattern of the γ-Al_2O_3 and, hence, do not truly reflect the structure. This supports similar findings from Rietveld analysis of neutron diffraction data (*Chapter 7*). The molecular modelling also showed that the spinel-based models were found to be too far from the structure of γ-Al_2O_3 to facilitate optimisation to a truly representative configuration. However, optimisation of these structural configurations showed that structures with some non-spinel site occupancy were more energetically favourable.

The large number of structures which demonstrate migration of cations to *c* symmetry positions provides strong evidence that this tendency is inherent and

supports the Cubic-16*c* and Tetragonal-8*c* structural models presented in *Chapter 7*. It also suggests that these models are universal for crystalline γ-Al_2O_3.

Optimisation of *c* symmetry based structures, with starting configurations based on the experimental findings, resulted in simulated diffraction patterns that were characteristic of γ-Al_2O_3. The similarities in the diffraction patterns show that the optimised structures follow the same symmetry rules determined by experiment. This means that the calculated *c* symmetry based structures are representative of the structure of γ-Al_2O_3. A 2:3 ratio of cations to oxygen ions was found in the subcells of most of the modelled supercells, as was an approximate 2.33:1 ratio of octahedral to tetrahedral cations in the structures. The occupancy of site positions showed variation predominantly characterised by the migration of cations away from *a* symmetry positions to other tetrahedral sites. This was found not to affect the diffraction pattern.

The variation in the site occupancy shows that it is more important to have cations on the appropriate Miller planes than it is to have precisely the correct number of cations in particular symmetry positions, provided that the number of cations on *c* symmetry site positions remains reasonably consistent. Only when there is a significant reduction in the number of occupied *c* symmetry site positions is there deviation of the simulated diffraction patterns away from what was experimentally observed.

Overall, the average structure is ordered, but locally there can be areas of varying occupancy. The variation in the cation occupancies follows local symmetry exclusion rules. This results in the occupancy of non-*a*, *c* or *d* symmetry positions to locally minimise lattice distortions. The observed distortions in octahedra and tetrahedra, coupled with the varied distribution of cations, support the proposed short-range ordering within the inter-skeletal layers of γ-Al_2O_3 (*Chapter 8*).

The supercells described here allow for more accurate and complete modelling of the defect structure of γ-Al_2O_3 than the single unit cell approach. It is hoped that the data can aid in a greater understanding of the transformations to other transition aluminas and the mechanisms by which applications of γ-Al_2O_3 function. This research also demonstrates that interatomic potentials are suitable for use in investigations where stable structures need to be determined from an enormous number of possibilities. The empirical calculations delivered an acceptable level of

accuracy and allowed for a comprehensive survey of possible outcomes using faster methods, before striving to achieve high accuracy for a few promising candidates.

11.1 Recommendations

To facilitate further understanding of the structure of γ-Al_2O_3 the following work is recommended:

1) A computational investigation of the evolution of the structure with temperature. This could entail molecular dynamics or Monte Carlo simulations, to simulate annealing temperature. This should preferably be carried out using DFT as it produces a structure that more accurately represents that of γ-Al_2O_3 than interatomic potentials, although this may not be possible due to limitations of computer power.

2) To model the crystallization process of the amorphous regions to produce Al_2O_3. Pore formation from the phase transformation from boehmite could also be simulated. This should aid in the understanding of transformation mechanisms and proton diffusion.

3) To perform synchrotron radiation diffraction experiments in order to quantify any impurities. It is possible for small amounts of sodium to be present in γ-Al_2O_3 because it is indirectly derived from gibbsite. Synchrotron radiation should have sufficient sensitivity to allow identification of any such impurities.

4) To perform optimization of the structure with impurities present (pending the synchrotron radiation study) to investigate effects on the structural configuration.

5) More extensive neutron vibrational spectroscopy experiments to investigate if hydrogen is present in crystalline alumina regions near the surface.

6) Pending experimental evidence of hydrogen in the structure, computational studies incorporating hydrogen in the crystalline structure could be carried out.

7) To investigate the influence of stacking faults and other defects on the peak anisotropy so that accurate crystallite size distributions can be obtained through improved profile analysis. It would be useful to perform future neutron diffraction experiments at facilities such as ISIS, UK, or any other suitable neutron source, to get better resolution and higher intensity. This will aid in improving the profile analysis. The use of Synchrotron radiation should also yield more detailed profile information.

8) It is difficult to see larger pores and amorphous regions using TEM. Scanning electron microscopy can be used to assist in investigating these features in greater detail.

9) The use different means to crystallize γ-Al_2O_3, for example from an amorphous melt and by the sol-gel method, to comparatively investigate the evolution of the structure with changing temperature.

10) To perform vacuum dehydration experiments on boehmite to investigate the transformation path and see how this compares to previous experiments reported in the literature.

References

Abrams, L. and Low, M.J.D. 1969, Thermal decomposition of Fibrillar Synthetic Boehmite, *Industrial and Engineering Chemistry Product Research and Development*, **8**, pp. 38-39.

Adkins, L. and Adkins, R.A. (Eds.) 1994, *Handbook to Life in Ancient Rome,* Oxford University Press, New York.

Allen, R.E. (Ed.) 1991, *Greek Philosophy: Thales to Aristotle,* The Free Press, New York.

Álvarez, L.J., León, L.E., Sanz, J.F., Capitán, M.J. and Odriozola, J.A. 1995, Computer simulation of γ-Al_2O_3 microcrystal, *Journal of Physical Chemistry*, **99**, pp. 17872-17876.

Álvarez, L.J., Sanz, J.F., Capitan, M.J., Centeno, M.A. and Odriozola, J.A. 1993, Surface models for γ-Al_2O_3 from molecular dynamics simulations, *Journal of the Chemical Society, Faraday Transactions*, **89**, 19, pp. 3623-3628.

Álvarez, L.J., Sanz, J.F., Capitán, M.J. and Odriozola, J.A. 1992, Molecular dynamics studies of the structure of γ-alumina, *Chemical Physics Letters*, **192**, 5,6, pp. 463-468.

Aristotle 350 BC. Mataphysics Transl. Ross, W.D., 1994, The Internet Classics Archive, http://classics.mit.edu//Aristotle/metaphysics.html.

Artacho, E., Sanchez-Portal, D., Ordejon, P., Garcia, A. and Soler, J.M. 1999, Linear-Scaling ab-initio Calculations for Large and Complex Systems, *Physica Status Solidi*, **215**, pp. 809-817.

Bachelet, G.B., Hamann, D.R. and Schluter, M. 1982, Pseudopotentials that Work: From H to Pu, *Physical Review B*, **26**, 8, pp. 4199-4228.

Badmos, A.Y. and Ivey, D.G. 2001, Characterization of structural alumina ceramics used in ballistic armour and wear applications, *Journal of Materials Science*, **36**, pp. 4995-5005.

Balzar, D., Von Dreele, R.B., Bennett, K. and Ledbetter, H. 1998, Elastic-strain tensor by Rietveld refinement of diffraction measurements, *Journal of Applied Physics*, **84**, 9, pp. 4822-4833.

Banerjee, A., Adams, N., Simons, J. and Shepard, R. 1985, Search for stationary points on surfaces, *Journal of Physical Chemistry*, **89**, pp. 52-57.

Baraton, M.I. and Quintard, P. 1982, Infrared evidence of order-disorder phase transitions ($\gamma \rightarrow \delta \rightarrow \alpha$) in Al_2O_3, *Journal of Molecular Structure*, **79**, pp. 337-340.

Barry, T.I., Bayliss, R.K. and Lay, L.A. 1968, Mixed oxides prepared with an induction plasma torch, *Journal of Materials Science*, **3**, pp. 229-238.

Becke, A.D. 1986, Density functional calculations of molecular bond energies, *Journal of Chemical Physics*, **84**, 8, pp. 4524-4529.

Bloch, F. 1929, The electron theory of ferromagnetism and electrical conductivity, *Zeitschrift fur Physik*, **57**, pp. 545-555.

Blonski, S. and Garofalini, S.H. 1993, Molecular dynamics simulations of α-alumina and γ-alumina Surfaces, *Surface Science*, **195**, pp. 263-274.

Bonevich, J.E. and Marks, L.D. 1992, The sintering behavior of ultrafine alumina particles, *Journal of Materials Research*, **7**, 6, pp. 1489-1500.

Born, H. and Oppenheimer, J.R. 1927, Zur quantentheorie der molekeln, *Annalen der Physik*, **84**, p. 457-484.

Born, M. and Mayer, J.E. 1932, Zur gittertheoric der ionenkristalle, *Zeitschrift für Physik*, **75**, pp. 1-18.

Boys, S.F. 1950, Electronic wave functions. I. A general method for calculation of the stationary states or any molecular system, *Proceedings of the Royal Society of London*, **A200**, pp. 542-554.

Brumbaugh, R.S. 1981, *The Philosophers of Greece,* State University of New York, Albany.

Buckingham, R.A. 1938, The classical equation of state of gaseous helium, neon and argon, *Proceedings of the Royal Society of London*, **A168**, pp. 264-283.

Bugosh, J. 1959, Fibrous alumina monohydrate and its production, *U.S. Patent 2,915,475.*

Burke, K., Perdew, J.P. and Levy, M. 1995, Semilocal Local Density Functionals for Exchange and Correlation: Theory and Applications, in *Modern Density Functional Theory: A Tool for Chemistry*, Seminario, J. M. and Politzer, P. (Eds.), Elsevier, Amsterdam.

Busca, G., Lorenzelli, V., Escribano, V.S. and Guidetti, R. 1991, FT-IR study of the surface properties of the spinels $NiAl_2O_4$ and $CoAl_2O_4$ in relation to those of transitional aluminas, *Journal of Catalysis*, **131**, pp. 167-177.

Busca, G., Lorenzelli, V., Ramis, G. and Willey, .J. 1993, Surface sites on spinel-type and corundum-type metal oxide powders, *Langmuir*, **9**, pp. 1492-1499.

Bush, T.S., Catlow, C.R.A. and Battle, P.D. 1995, Evolutionary programming techniques for predicting inorganic crystal-structures, *Journal of Materials Chemistry*, **5**, pp. 1269-1272.

Bush, T.S., Gale, J.D., Catlow, C.R.A. and Battle, P.D. 1994, Self-consistent interatomic potentials for the simulation of binary and ternary oxides, *Journal of Materials Chemistry*, **4**, 6, pp. 831-837.

Caglioti, G., Paoletti, A. and Ricci, F.P. 1958, Choice of collimators for a crystal spectrometer for neutron diffraction, *Nuclear Instruments and Methods*, **3**, pp. 223-228.

Cai, S. and Sohlberg, K. 2003, Adsorption of alcohols on γ-alumina (110C), *Journal of Molecular Catalysis A: Chemical*, **193**, pp. 157-164.

Carter, D.J., Rohl, A.L., Gale, J.D., Fogg, A.M., Gurney, R.W. and Kahr, B. 2003, Adsorption energetics of potassium sulfate dye inclusion crystals, *Journal of Molecular Structure*, **647**, pp. 65-73.

Catlow, C.R.A., Bell, R.G. and Gale, J.D. 1994, Computer modelling as a technique in materials chemistry, *Journal of Materials Chemistry*, **4**, 6, pp. 781-792.

Catlow, C.R.A., Gay, D.H., Rohl, A.L. and Sayle, D.C. 1996, Simulating the structures of crystals and their surfaces, *Topics in Catalysis*, **3**, pp. 135-167.

Catlow, C.R.A., James, R., Mackrodt, W.C. and Stewart, R.F. 1982, Defect energetics in α-Al_2O_3 and rutile TiO_2, *Physical Review B*, **25**, 2, pp. 1006-1026.

Ceperley, D.M. and Alder, B.J. 1980, Ground state of the electron gas by a stochastic method, *Physical Review Letters*, **45**, 7, pp. 566-568.

Che, M. and Bennett, C.O. 1989, The influence of particle size on the catalytic properties of supported metals, *Advances in Catalysis*, **36**, pp. 55-172.

Chen, F.R., Davis, J.G. and Fripiat, J.J. 1992, Aluminum coordination and Lewis acidity in transition aluminas, *Journal of Catalysis*, **133**, pp. 263-278.

Chermette, H. 1998, Density functional theory - A powerful tool for theoretical studies in coordination chemistry, *Coordination Chemistry Reviews*, **178-180**, pp. 699-721.

Chou, T.C. and Nieh, T.G. 1991, Nucleation and concurrent anomolous grain growth of α-Al_2O_3 during $\gamma \rightarrow \alpha$ phase transformation, *Journal of the American Ceramic Society*, **74**, 9, pp. 2270-2279.

Coster, D., Blumenfeld, A.L. and Fripiat, J.J. 1994, Lewis acid sites and surface aluminum in aluminas and zeolites, *Journal of Physical Chemistry*, **98**, pp. 6201-6211.

Costina, I. and Franchy, R. 2001, Band gap of amorphous and well-ordered Al_2O_3 on $Ni_3Al(100)$, *Applied Physics Letters*, **78**, 26, pp. 4139-4141.

Cowley, J.M. 1953, Stacking faults in γ-alumina, *Acta Crystallographica*, **6**, pp. 53-54.

Cullity, B.D. 1978, *Elements of X-ray Diffraction,* 2. Addison-Wesley Publishing Company, Inc., Reading.

Dahl, P.F. 1997, *Flash of the Cathode Rays: A History of J J Thomson's Electron,* Institute of Physics Publishing, London.

Dalton, J., Gay-Lussac, J. and Avogadro, A. 1906, *Foundation of the Molecular Theory: Comprising Papers and Extracts,* The University of Chicago Press, Chicago.

de Boer, J.H. and Houben, G.M.M 1952, *Proceedings of the International Symposium on the Reactivity of Solids (Flanders Boktryckeri Aktieboolag, Göteburg)*, **1**, pp. 237-244.

de Boer, J.H. and Lippens, B.C. 1964, Studies in pore systems of catalysts II. The shapes of pores in aluminum oxide systems, *Journal of Catalysis*, **3**, pp. 38-43.

de Morveau, L.B. 1781, *Encyclopedia Methodoque,* Gryton, Paris.

De Vito, D.A., Gilardoni, F., Kiwi-Minsker, L., Morgantini, P.-Y., Porchet, S., Renkin, A. and Weber, J. 1999, Theoretical investigation of the adsorption of methanol on the (110) surface of γ-alumina, *Journal of Molecular Structure (Theochem)*, **469**, pp. 7-14.

Dick, B.G. and Overhauser, A.W. 1958, Theory of dielectric constants for alkali halide crystals, *Physical Review*, **112**, 1, pp. 90-103.

Digne, M., Sautet, P., Raybaud, P., Euzen, P. and Toulhoat, H. 2002, Hydroxyl groups on γ-alumina surfaces: A DFT study, *Journal of Catalysis*, **211**, pp. 1-5.

Dirac, P.A.M. 1958, *The Principles of Quantum Mechanics,* 4. Clarenden Press, Oxford.

Dowden, D.A. 1950, Heterogeneous catalysis. Part I. Theoretical basis, *Journal of the Chemical Society*, **1-2**, pp. 242-265.

Dragoo, A.L. and Diamond, J.J. 1967, Transitions in vapor-deposited alumina from 300^{o} to 1200^{o}C, *Journal of the American Ceramic Society*, **50**, 11, pp. 568-574.

Drost, M.K., Call, C.J., Cuta, J.M. and Wegeng, R.S. 1997, Microshannel combustor evaporator thermal processes, *Microscale Thermophysical Engineering*, **1**, 4, pp. 321-333.

Dupree, R., Lewis, M.H. and Smith, M.E. 1986, A study of the vacancy distribution in non-stoichiometric spinels by magnetic spinning NMR, *Philosophical Magazine A*, **53**, 2, pp. L17-L20.

Dynys, F.W. and Halloran, J.W. 1982, Alpha alumina formation in alum-derived gamma alumina, *Journal of the American Ceramic Society*, **65**, 9, pp. 442-448.

Ealet, B., Elyakhloufi, M.H., Gillet, E. and Ricci, M. 1994, Electronic and crystallographic structure of γ-alumina thin films, *Thin Solid Films*, **250**, pp. 92-100.

El-Katatny, E.A., Halawy, Samih A., Mohamed, M.A. and Zaki, M.I. 1998, A novel synthesis of high-area alumina via H_2O_2-precipitated boehmite from sodium aluminate solutions, *Journal of Chemical Technology and Biotechnology*, **72**, pp. 320-328.

Ervin, G. and Osborn, E.F. 1951, The system Al_2O_3-H_2O, *Journal of Geology*, **59**, pp. 381-394.

Essmann, U., Perera, L., Berkowitz, M.L., Darden, T., Lee, H. and Pederson, L.G. 1995, A smooth particle mesh Ewald method, *Journal of Chemical Physics*, **103**, 19, pp. 8577-8593.

Everett, D.F., Correll, T.E., Schick, S. and Brown, K.D. 2000, Recovery of the Wide-Field Infrared Explorer Spacecraft, *14th Annual AIAA/USU Conference on Small Satellites (Logan, Utah)*.

Ewald, P.P. 1921, Die berechnung optischer und elektrostatisher gitterpotentiale, *Annalen der Physik*, **64**, pp. 253-287.

Fahy, S., Wang, X.W. and Louie, S.G. 1988, Variational quantum Monte Carlo nonlocal pseudopotential approach to solids: Cohesive and structural properties of diamond, *Physical Review Letters*, **61**, pp. 1631-1634.

Fermi, E. 1927, Un metodo statistice per la determinazione di alcune proprieta dell'atomo, *Atti della Accademia Nazionale dei Lincei. Classe di Scienze Fisiche, Matematiche e Naturali. Rendiconti Lincei*, **6**, pp. 602-607.

Fermi, E. 1928, A statistical method for the determination of some atomic properties and the application of this method to the theory of the periodic system of elements, *Zeitschrift fur Physik*, **48**, pp. 73-79.

Fleisher, M.B., Golender, L.O. and Shimanskaya, M.V. 1991, Electronic charge distribution and Lewis acidity of surface aluminium atoms in γ-Al_2O_3: a quantum-chemical model, *Journal of the Chemical Society, Faraday Transactions*, **87**, pp. 745-748.

Fock, V. 1930, Approximate method for solution of quantum many body problem, *Zeitschrift für Physik*, **61**, pp. 126-148.

Freeman, A.J. and Wimmer, E. 1995, Density functional theory as a major tool in computational materials science, *Annual Reviews of Materials Science*, **25**, pp. 7-36.

French, R.H., Mullejans, H. and Jones, D.J. 1998, Optical properties of aluminum oxide: determined from vacuum ultraviolet and electron energy-loss spectroscopes, *Journal of the American Ceramic Society*, **81**, 10, pp. 2549-2557.

Fu, Q., Cao, C.-B. and Zhu, H.-S. 1999, Preparation of alumina films from a new sol-gel route, *Thin Solid Films*, **348**, pp. 99-102.

Fukuda, T., Saburi, T. and Kamimura, N. 1996, Crystallization and growth of γ-Al_2O_3 in a film prepared by sol-gel method, *Technology Reports of the Osaka University*, **46**, pp. 2247-2266.

Furthmuller, J., Kackell, P. and Bechstedt, F. 2000, Extreme softening of Vanderbilt pseudopotentials: General rules and case studies of first-row and d-electron elements, *Physical Review B*, **61**, 7, pp. 4567-4587.

Gale, J.D. 1996, Empirical potential derivation for ionic materials, *Philosophical Magazine B*, **73**, 1, pp. 3-19.

Gale, J.D. 1997, GULP: A computer program for the symmetry-adapted simulation of solids, *Journal of the Chemical Society, Faraday Transactions*, **93**, 4, pp. 629-637.

Gale, J.D. and Rohl, A.L. 2003, The general utility lattice program (GULP), *Molecular Simulation*, **29**, pp. 291-341.

Gan, B.K. 1996, *Crystallographic Transformations Involved in the decomposition of Gibbsite to Alpha-Alumina*, Ph.D. Thesis, School of Physical Sciences, Curtin University of Technology.

Garn, P.D. 1965, *Thermoanalytical Methods of Investigation,* Academic Press, New York.

Gates, B.C 1995, Supported metal clusters: synthesis, structure, and catalysis, *Chemical Reviews*, **95**, pp. 511-522.

Gentleman, J.F. 1975, Generation of all nCr combinations by simulating nested Fortran DO loops, *Applied Statistics*, **24**, 3, pp. 374-376.

Giacovazzo, C. 1992, Crystallographic Computing, in *Fundamentals of Crystallography*, Giacovazzo, C. (Ed.), Oxford Scientific Publications, Oxford.

Gillespie, A.R., Hyland, M.M. and Metson, J.B. 1999, Irreversible HF adsorption in the dry-scrubbing process, *Journal of Metals*, **51**, 5, pp. 30-34.

Ginsberg, H., Huttig, W. and Strunk-Lichtenberg, G. 1957, *Zeitschrift für Anorganische Chemie*, **293**, 33-46, pp. 204-213.

Goedecker, S. 1999, Linear scaling electronic structure methods, *Reviews of Modern Physics*, **71**, 4, pp. 1085-1123.

Grant, G.H. and Richards, W.G. 1995, *Computational Chemistry,* Oxford University Press, Oxford.

Green, D.J., Hannink, R.H. and Swain, M.V. 1989, *Transformation toughening of Ceramics,* CRC Press, Inc., Boca Raton, pp.157-180.

Grobet, P.J., Geerts, H., Martens, J.A. and Jacobs, P.A. 1987, Correct determination of aluminium in Y zeolites by magic-angle spinning NMR spectroscopy, *Journal of the Chemical Society, Chemical Communications*, 0, pp. 1688-1690.

Gross, H.-L. and Mader, W. 1997, On the crystal structure of κ-alumina, *Chemical Communications*, 1, pp. 55-56.

Gutiérrez, G., Taga, A. and Johansson, B. 2002, Theoretical structure determination of γ-Al_2O_3, *Physical Review B*, **65**, 1, pp. 012201, 1-4.

Hahn, T. (Ed.) 1995, *International Tables of Crystallography,* Kluwer, London.

Halvarsson, M., Langer, V. and Vuorinen, S. 1995, Determination of the thermal expansion of κ-Al_2O_3 by high temperature XRD, *Surface Coatings and Technology*, **76-77**, pp. 358-362.

Halvarsson, M., Langer, V. and Vuorinen, S. 1999, X-Ray powder diffraction data for κ-Al_2O_3, *Powder Diffraction*, **14**, 1, pp. 61-63.

Hansson, P., Halvarsson, M. and Vuorinen, S. 1995, Characterization of the κ-Al_2O_3 → α-Al_2O_3 Transformation in Different Single Layer Coatings of CVD κ-Al_2O_3, *Surface Coatings and Technology*, **76-77**, pp. 256-264.

Hartree, D.R. 1928, The wave mechanics of an atom with an non-Coulomb central field. Part I. Theory and methods., *Proceedings of the Cambridge Philosophical Society*, **24**, pp. 89-110.

Harvey, J., Mathews, H.I. and Wilman, H. 1960, Crystal structure and growth of metallic or metallic-oxide smoke particles produced by elecric arcs, *Chemical Discussions of the Faraday Society*, **30**, pp. 113-123.

Herodotus 425 BC, *The Persian Wars*.

Hill, R.J. 1993, Data collection strategies: fitting the experiment to the need, in *The Rietveld Method*, Young, R. A. (Ed.), International Union of Crystallography, Oxford University Press, New York.

Hille, J., Bollmann, U., Weinhold, W., Becker, K., Bremer, H., Vogt, F. and Berrouschot, H.-D. 1989, Herstellung und eigenschaften von aluminiumaquoxid. I. Böhmit aus aluminiumnitrat und ammoniakwasser, *Zeitschrift für Anorganische und Algemeine Chemie*, **579**, pp. 211-220.

Hind, A.R, Bhargava, S.K. and Grocott, S.C. 1999, The surface chemistry of Bayer process solids: a review, *Colloids and Surfaces A: Physiochemical and Engineering Aspects*, **146**, pp. 359-374.

Hirva, P. and Pakkanen, T.A. 1992, The interaction of amine bases on Lewis acid sites of aluminum oxide - a theoretical study, *Surface Science*, **277**, pp. 389-394.

Hohenberg, P. and Kohn, W. 1964, Inhomogeneous electron gas, *Physical Review*, **136**, pp. B864-B871.

Holland, J.H. 1975, *Adaption in Natural and Artificial Systems,* The University of Michigan Press.

Homsi, P. 1989, Aluminas for modern smelting, *Third Australasian Smelter Technology Course (Sydney, Australia)* pp. 474-506.

Huggins, B.A. and Ellis, P.D. 1992, ^{27}Al nuclear magnetic resonance study of aluminas and their surfaces, *Journal of the American Chemical Society*, **114**, pp. 2098-2108.

Hunter, B.A. 1998, Rietica - A visual Rietveld program, *IUCr Commission on Powder Diffraction Newsletter*, **20**, article 16.

Hunter, B.A. and Kisi, E.H. 2000, *LHPM, A Computer Program for Rietveld Analysis of X-ray and Neutron Diffraction Patterns,* Australian Nuclear Science and Technology Organisation, Sydney.

Jackson, R.A. and Catlow, C.R.A. 1988, Computer simulation studies of zeolite structure, *Molecular Simulations*, **1**, pp. 207-224.

Jackson, R.P.J. 1991, *Doctors and Diseases in the Roman Empire,* The British Museum Company Pty Ltd, London.

Jagodzinski, H. and Saalfield, H. 1958, Kationenverteilung und strukturbeziehungen, *Zeitschrift für Kristallographie*, **110**, pp. 197-218.

Jayaram, V. and Levi, C.G. 1989, The structure of δ-alumina evolved from the melt and the $\gamma \rightarrow \delta$ transformation, *Acta Metallurgica*, **37**, 2, pp. 569-578.

Jenkins, S. 1995. An Introduction to Solid State Many-Body Theory, Available: http://newton.ex.ac.uk/people/jenkins/mbody/index.html.

John, C.S., Alma, N.C.M. and Hays, G.R. 1983, Characterization of transitional alumina by solid-state magic angle aluminium NMR, *Applied Catalysis*, **6**, pp. 341-346.

Jones, F., Rohl, A.L., Farrow, J.B. and van Bronswijk, W. 2000, Molecular modeling of water adsorption on hematite, *Physical Chemistry Chemical Physics*, **2**, pp. 3209-3216.

Jones, R.O. and Gunnarsson, O. 1989, The density functional formalism, its applications and prospects, *Reviews of Modern Physics*, **61**, 3, pp. 689-746.

Junquera, J., Paz, Ó., Sánchez-Portal, D. and Artacho, E. 2001, Numerical atomic orbitals for linear-scaling calculations, *Physical Review B*, **64**, pp. 235111, 1-9.

Kao, H.-C. and Grey, C.P. 1997, Determination of the ^{31}P-^{27}Al *J*-coupling constant in trimethylphosphine bound to the Lewis acid site of zeolite HY, *Journal of the American Chemical Society*, **119**, pp. 627-628.

Kao, H.-C. and Wei, W.-C. 2000, Kinetics and microstructural evolution of heterogeneous transformation of θ-alumina to α-alumina, *Journal of the American Ceramic Society*, **83**, 2, pp. 362-368.

Kaplan, I.G. 1986, *Theory of Molecular Interactions,* Elsevier, Amsterdam.

Kawakami, H. and Yoshida, S. 1986, Quantum chemical studies of alumina, *Journal of the Chemical Society, Faraday Transactions*, **282**, pp. 1385-1397.

Kingery, W.D., Bowen, H.K. and Uhlmann, D.R. 1976, *Introduction to Ceramics,* 2nd Ed. John Wiley and Sons, New York.

Kisi, E.H. 1994, Rietveld analysis of powder diffraction patterns, *Materials Forum*, **18**, pp. 135-153.

Kleinman, L. and Bylander, D.M. 1982, Efficacious form for model pseudopotentials, *Physical Review Letters*, **48**, 20, pp. 1425-1428.

Knözinger, H. 1985, in *Catalysis by Acids and Bases*, Imelik, B., Naccache, C., Coundurier, G., Ben Tarrit, Z. and Vedrine, J. C. (Eds.), Elsevier, Amsterdam.

Knözinger, H. and Ratnasamy, P. 1978, Catalytic aluminas: surface models and characterization of surface sites, *Catalysis Reviews - Science and Engineering*, **17**, 1, pp. 31-70.

Koch, W. and Holthausen, M.C. 2000, *A Chemist's Guide to Density Functional Theory,* Wiley-VCH, Weinheim.

Koeneman, P.B., Busch-Vishniac, I.J. and Wood, K.L. 1997, Feasibility of micro power supplies for MEMS, *Journal of Microelectromechanical Systems*, **6**, 4, pp. 355-362.

Kogure, T. 1999, Dehydration sequence of gibbsite by electron-beam irradiation in a TEM, *Journal of the American Ceramic Society*, **82**, 3, pp. 716-720.

Kohn, S.C., Dupree, R., Mortuza, M.G. and Henderson, C.M.B 1991, NMR evidence for five- and six-coordinated aluminum fluoride complexes in F-bearing aluminosilicate glasses, *American Mineralogist*, **76**, pp. 309-312.

Kohn, S.C., Dupree, R. and Smith, M.E. 1989, A multinuclear magnetic resonance study of the structure of hydrous albite glasses, *Geochimica et Cosmochimica Acta*, **53**, pp. 2925-2935.

Kohn, W. 1996, Density functional and density matrix method scaling linearly with the number of atoms, *Physical Review Letters*, **76**, pp. 3168-3171.

Kohn, W. 1999, Nobel lecture: Electronic structure of matter - wave functions and density functionals, *Reviews of Modern Physics*, **71**, 5, pp. 1253-1266.

Kohn, W. and Sham, L.J. 1965, Self-consistent equations including exchange and correlation effects, *Physical Review*, **140**, pp. A1133-A1138.

Komarneni, S., Roy, R., Fyfe, C.A. and Kennedy, G.J. 1985, Preliminary characterization of gel precursors and their high-temperature products by ^{27}Al magic-angle NMR, *Journal of the American Ceramic Society*, **68**, 9, pp. C243-C245.

Kordes, E. 1935, Ergebnisse de Debye-Scherre-Aufnahmen von kristallinem γ-Al_2O_3, $LiAl_5O_8$ und $MgAl_2O_4$, *Zeitschrift für Kristallographie*, **91**, pp. 202-228.

Krane, K.S. 1988, *Introductory Nuclear Physics,* John Wiley and Sons, Singapore.

Kryukova, G.N., Klenov, D.O., Ivanova, A.S. and Tsybulya, S.V. 2000, Vacancy ordering in the structure of γ-Al_2O_3, *Journal of the European Ceramic Society*, **20**, pp. 1187-1189.

Kunath, G., Losso, P., Schneider, H., Steurnagel, S. and Jäger, C. 1992, ^{27}Al satellite transition spectroscopy (SATRAS) of polycrsyalline aluminium borate $9Al_2O_3.2B_2O_3$, *Solid State Nuclear Magnetic Resonance*, **1**, pp. 261-266.

Kunath-Fandrei, G., Bastow, T.J., Hall, J.S., Jäger, C. and Smith, M.E. 1995, Quantification of aluminium coordinations in amorphous aluminas by combined central and satellite transition magic angle spinning NMR spectroscopy, *Journal of Physical Chemistry*, **99**, pp. 15138-15141.

Larsson, A. and Ruppi, S. 2001, Microstructure and properties of CVD γ-Al_2O_3 coatings, *International Journal of Refractory Metals and Hard Materials*, **19**, pp. 515-522.

Laubengayer, A.W. and Weisz, R.S. 1943, A hydrothermal study of equilibria in the system alumina-water, *Journal of the American Chemical Society*, **65**, 2, pp. 247-250.

Lavalley, J.C. and Benaissa, M. 1984, I.R. spectroscopic evidence for surface vibrational modes upon dehydroxilation of alumina, *Journal of the Chemical Society, Chemical Communications*, 2, pp. 908-909.

Leach, A.R. 2001, *Molecular Modelling: Principles and Applications,* 2^{ed}, Prentice Hall, London.

Lee, C., Yang, W. and Parr, R.G. 1988, Development of the Colle-Salvetti correlation-energy formula into a functional of the electron density, *Physical Review B*, **37**, 2, pp. 785-789.

Lee, M.-H., Cheng, C.-F., Heine, V. and Klinowski, J. 1997, Distribution of tetrahedral and octahedral Al sites in gamma alumina, *Chemical Physics Letters*, **265**, pp. 673-676.

Leech, B.E. (Ed.) 1984, *Applied Industrial Catalysis,* Academic Press, London.

Lennard-Jones, J.E. 1924a, On the determination of molecular fields - II. From the equation of state of a gas, *Proceedings of the Royal Society of London*, **A106**, pp. 463-477.

Lennard-Jones, J.E. 1924b, On the determination of molecular fields - III. From crystal measurements and kinetic theory data, *Proceedings of the Royal Society of London*, **A106**, pp. 709-719.

Lennard-Jones, J.E. 1937, The equation of state of gases and critcal phenomena, *Physica*, **4**, 10, pp. 941-956.

Lennard-Jones, J.E. and Ingham, A.E. 1925, On the calculation of certain crystal potential constants, and on the cubic crystal of least potential energy, *Proceedings of the Royal Society of London*, **A107**, pp. 636-653.

Levin, I., Bendersky, D.G., Brandon, D.G. and Ruhle, M. 1997, Cubic to monoclinic phase transformations in alumina, *Acta Metallurgica*, **45**, 9, pp. 3659-3669.

Levin, I. and Brandon, D. 1998a, Metastable alumina polymorphs: crystal ctructures and transition sequences, *Journal of the American Ceramic Society*, **81**, 8, pp. 1995-2012.

Levin, I. and Brandon, D.G. 1998b, A new metastable alumina polymorph with monoclinic symmetry, *Philosophical Magazine Letters*, **77**, 2, pp. 117-124.

Levin, I., Gemming, Th. and Brandon, D.G. 1998, Some metastable polymorphs and transient stages of transformation in alumina, *Physica Status Solidi*, **166**, pp. 197-218.

Lewis, G.V. and Catlow, C.R.A. 1985, Potential models for ionic oxides, *Journal of Physics C: Solid State Physics*, **18**, pp. 1149-1161.

Li, D.Y., O'Connor, B.H., Roach, G.I.D. and Cornell, J.B. 1990, Structural models for η and γ alumina by x-ray Rietveld Refinement, *XVth Congress of the International Union of Crystallography (Bordeaux)*, **Abstracts volume**, pp. C-61.

Li, X.P., Ceperley, D.M. and Martin, R.M. 1991, Cohesive energy of silicon by the Green's function Monte Carlo method, *Physical Review B*, **44**, pp. 10929-10932.

Liddell, K., 1996, PDF#50-0741, JCPDS Database

Linblad, M. and Pakkanen, T.A. 1993, Cluster models for the interaction of HCl with non-polar surfaces of γ-Al_2O_3, *Surface Science*, **286**, pp. 333-345.

Lippens, B.C. and de Boer, J.H. 1964, Studies on pore systems in catalysts III. Pore-size distribution curves in aluminum oxide systems, *Journal of Catalysis*, **3**, pp. 44-49.

Lippens, B.C. and de Boer, J.H. 1964, Study of phase transformations during calcination of aluminum hydroxides by selected area electron diffraction, *Acta Crystallographica*, **17**, pp. 1312-1321.

Lippens, B.C. and Steggerda, J.J. 1970, Physical and Chemical Aspects of Adsorbents and Catalysts, in *Physical and Chemical Aspects of Adsorbents and Catalysts*, Linsen, B. G. (Ed.), Academic Press, London, ch. 4.

Liu, P. and Skogsmo, J. 1991, Space-group determination and structure model for κ-Al_2O_3 by convergent-beam electron diffraction (CBED), *Acta Crystallographica*, **B47**, pp. 425-433.

Liu, X. and Truitt, R.E. 1997, DRFT-IR studies of the surface of γ-alumina, *Journal of the American Chemical Society*, **119**, 41, pp. 9856-9860.

Lucretius 50 BC. On the Nature of Things, Transl. Leonard, W.E., 1994, The Internet Classics Archive, http://classics.mit.edu//Carus/nature_things.html.

Lux, B., Colombier, C., Altena, H. and Stjernberg, K. 1986, Preparation of alumina coatings by chemical vapour decomposition, *Thin Solid Films*, **138**, 1, pp. 49-64.

MacKenzie, K.J.D., Temuujin, J., Smith, M.E., Angerer, P. and Kameshima, Y. 2000, Effect of mechanochemical activation on thermal reactions of boehmite (γ-AlOOH) and γ-Al_2O_3, *Thermochimica Acta*, **359**, pp. 87-94.

Mackrodt, W.C. and Stewart, R.F. 1979, Defect properties of ionic solids: II. Point defect energies based on modified electron-gas potentials, *Journal of Physics C: Solid State Physics*, **12**, pp. 431-449.

Madelung, E. 1918, Das elektrische feld in systemen von regelmaessig angeordneten punktladungen, *Physikalische Zeitschrift*, **19**, pp. 524-532.

Maitland, G.C., Rigby, M., Smith, E.B. and Wakeham, W.A. 1981, *Intermolecular Forces: Their Origin and Determination,* Oxford Science Publications, Oxford.

Maitland, C.F., Buckley, C.E., Paglia G., and Connolly, J. 2004, Determination of the specific surface of γ-alumina using small angle x-ray scattering, *The Proceedings of the Asian Pacific Nanotechnology Forum (APNF) 2003*, pp. 113-120.

Majors, P.D. and Ellis, P.D. 1987, Surface site distributions by solid-state multinuclear NMR spectroscopy. Pyridine binding to γ-alumina by ^{15}N and ^{2}H NMR, *Journal of the American Chemical Society*, **109**, pp. 1648-1653.

Man, P.P. and Klinowski, J. 1988, Quadrapole nutation ^{27}Al NMR studies of isomorphous substitution of aluminum in the framework of zeolite Y, *Chemical Physics Letters*, **147**, 6, pp. 581-584.

Maple, J., Dinur, U. and Hagler, A.T. 1989, Derivation of force fields for molecular mechanics and dynamics from *ab initio* energy surface, *Proceedings of the National Academy of Sciences, USA*, **85**, pp. 5350-5354.

March, A. 1932, Mathematische theorie der regelung nach der korngestalt bei affiner deformation, *Zeitschrift für Kristallographie*, **81**, pp. 285-297.

Maresca, O., Allouche, A., Aycard, J.P., Rajzmann, M., Clemendot, S. and Hutschka, F. 2000, Quantum study of the active sites of the γ-alumina surface; Chemisorption and adsorption of water, hydrogen sulfide and carbon monoxide on aluminum and oxygen sites, *Journal of Molecular Structure (Theochem)*, **505**, pp. 81-94.

Maresca, O., Ionescu, A., Allouche, A., Aycard, J.P., Rajzmann, M. and Hutschka, F. 2003, Quantum study of the active sites of the γ alumina surface (II): QM/MM (LSCF) approach to water, hydrogen disulfide and carbon monoxide adsorption, *Journal of Molecular Structure (Theochem)*, **620**, pp. 119-128.

Materials Studio version 1.2, Accelrys, San Diego.

McCusker, L.B., Von Dreele, R.B., Cox, D.E., Louer, D. and Scardi, P. 1999, Rietveld refinement guidelines, *Journal of Applied Crystallography*, **32**, pp. 36-50.

McHale, J.M., Auroux, A., Perrotta, A.J. and Navrotsky, A. 1997a, Surface energies and thermodynamic phase stability in nanocrystalline aluminas, *Science*, **277**, pp. 788-791.

McHale, J.M., Navrotsky, A. and Perrotta, A.J. 1997b, Effects of increased surface area and chemiosorbed H_2O on the relative stability of nanocrystalline γ-Al_2O_3 and α-Al_2O_3, *Journal of Physical Chemistry B*, **101**, pp. 602-613.

McPherson, R. 1973, Formation of metastable phases in flame- and plasma-prepared alumina, *Journal of Materials Science*, **8**, pp. 851-858.

McPherson, R. 1980, On the formation of thermally sprayed alumina coatings, *Journal of Materials Science*, **15**, pp. 3141-3149.

Minervini, L., Zacate, M.O. and Grimes, R.W. 1999, Defect cluster formation in M_2O_3-doped CeO_2, *Solid State Ionics*, **116**, pp. 339-349.

Mishra, D., Anand, S., Panda, R.K. and Das, R.P. 2002, Effect of anions during hydrothermal preperation of boehmites, *Materials Letters*, **53**, pp. 133-137.

Mo, S.-D., Xu, Y.-N. and Ching, W.-Y. 1997, Electronic and structural properties of bulk γ-Al_2O_3, *Journal of the American Ceramic Society*, **80**, 5, pp. 1193-1197.

Morrissey, K.J., Czanderna, K.K., Merrill, R.P. and Carter, C.B. 1985, Transition alumina structures studied using HREM, *Ultramicroscopy*, **18**, pp. 379-386.

Morterra, C., Chiorino, A., Ghiotti, G. and Garrone, E. 1979, Surface acidity of η-alumina Part 1. - Pyradine chemiosorption at room temperature, *Journal of the Chemical Society, Faraday Transactions*, **75**, pp. 271-288.

Morterra, C., Ghiotti, G., Boccuzzi, F. and Coluccia, S. 1978, An infrared spectroscopic investigation of the surface properties of magnesium aluminate spinel, *Journal of Catalysis*, **51**, pp. 299-313.

Morterra, C., Ghiotti, G., Garrone, E. and Boccuzzi, F. 1976, Infrared spectroscopic characterization of the α-alumina surface, *Journal of the Chemical Society, Faraday Transactions*, **72**, pp. 2722-2734.

Morterra, C. and Magnacca, G. 1996, A case study: surface chemistry and surface structure of catalytic aluminas, as studied by vibrational spectroscopy and adsorbed species, *Catalysis Today*, **27**, pp. 497-532.

Newton, I. 1687, *Principa Mathematica*.

Neyman, K.M., Nasluzov, V.A. and Zhidomirov, G.M. 1996, A density functional of CO adsorption on three- and five-coordinate Al in oxide systems, *Catalysis Letters*, **40**, pp. 183-188.

Nishio, K., Neo, M., Akiyama, H., Okada, Y., Kokuba, T. and Nakamura, T. 2001, Effects of apatite and wollastonite containing glass-ceramic powder and two types of alumina powder on composites on osteoblastic differentiation of bone marrow cells, *Journal of Biomedical Materials Research*, **55**, pp. 164-176.

Nortier, P., Fourre, P., A.B.M., Saad, Saur, O. and Lavalley, J.C. 1990, Effects of crystallinity and morphology on the surface properties of alumina, *Applied Catalysis*, **91**, 1, pp. 141-160.

Nukui, A., Tagai, H., Morikawa, H. and Iwai, S.-I. 1976, Structural conformation and solidification of molten alumina, *Journal of the American Ceramic Society*, **59**, 11-12, pp. 534-536.

O'Connor, B., Li, D., Gan, B.K., Latella, B. and Carter, J. 1997, Time-resolved studies of alumina ceramics processing with neutron and sychrotron radiation data, *Advances in X-ray Analysis*, **41**, pp. 659-667.

Ollivier, B., Retoux, R., Lacorre, P., Massiot, D. and Ferey, G. 1997, Crystal structure of κ-alumina: an X-ray powder diffraction, TEM and NMR study, *Journal of Materials Chemistry*, **7**, 8, pp. 1049-1056.

Ordejon, P. 2000, Linear Scaling ab initio Calculations in Nanoscale Materials with SIESTA, *Physica Status Solidi (b)*, **217**, 335-356.

Ordejon, P., Artacho, E. and Soler, J.M. 1996, Self-consistent order-N density functional calculations for very large systems, *Physical Review B*, **53**, 16, pp. R10441-R10444.

Ordejon, P., Drabold, D.A., Grumbach, M.P. and Martin, R.M. 1993, Unconstrained minimization approach for electronic computations that scales linearly with system size, *Physical Review B*, **48**, 19, pp. 14646-14649.

Ordejon, P., Drabold, D.A., Martin, R.M. and Grumbach, M.P. 1995, Linear system-size scaling methods for electronic-structure calculations, *Physical Review B*, **51**, 3, pp. 1456-1476.

Ordejon, P., Sanchez-Portal, D., Garcia, A., Artacho, E., Junquera, J. and Soler, J.E. 2000, Large scale DFT calculations with SIESTA, *RIKEN Review*, **29**, pp. 42-44.

Patterson, E.C. 1970, *John Dalton and the Atomic Theory,* Doubleday and Co, Inc., New York.

Paul, R.L., Lindstrom, R.M. and Vincent, D.H. 1994, Cold neutron prompt gamma activation analysis at NIST: A progress report, *Journal of Radioanalytical and Nuclear Chemistry, Articles*, **180**, 2, pp. 263-269.

Pauling, L. 1944, *The Nature of the Chemical Bond, 2nd Ed,* Cornell University, Ithica.

Payne, M.C., Teter, M.P., Allan, D.C., Arias, T.A. and Joannopoulos, J.D. 1992, Iterative minimization techniques for ab-initio total-energy calculations: Molecular dynamics and conjugate gradients, *Reviews of Modern Physics*, **64**, 4, pp. 1045-1097.

Pearson, R.M. 1971, Wide line nuclear magnetic resonance studies on transition aluminas - distribution of protons between surface and bulk phases, *Journal of Catalysis*, **23**, pp. 388-394.

Pecharroman, C., Sobrados, I., Iglesias, J.E., Gonzales-Carreno, T. and Sanz, J. 1999, Thermal evolution of transition aluminas followed by NMR and IR spectroscopy, *Journal of Physical Chemistry B*, **103**, pp. 6160-6170.

Pellet, R.J., Blackwell, C.S. and Rabo, J.A. 1988, Catalytic cracking studies and characterization of steamed Y and LZ-210 zeolites, *Journal of Catalysis*, **114**, pp. 71-79.

Perdew, J.P. 1986, Density-functional approximation for the correlation energy of the inhomogeneous electron gas, *Physical Review B*, **33**, 12, pp. 8822-8824.

Perdew, J.P. 1991, Generalized gradient approximations for exchange and correlation: A look backward and forward, *Physica B*, **172**, pp. 1-6.

Perdew, J.P., Burke, K. and Ernzerhof, M. 1996, Generalized gradient approximation made simple, *Physical Review Letters*, **77**, 18, pp. 3865-3869.

Perdew, J.P. and Kurth, S. 1998, Density Functionals for Non-Relativistic Coulomb Systems, in *Density Functionals: Theory and Applications*, Joubert, D. P. (Ed.), Springer, Berlin.

Perdew, J.P. and Wang, Y. 1986, Accurate and simple density functional for the electronic exchange energy: Generalized gradient approximation, *Physical Review B*, **33**, 12, p. 8800-8802.

Perdew, J.P. and Wang, Y. 1992, Accurate and simple analytic representation of the electron gas correlation energy, *Physical Review B*, **45**, 23, pp. 13244-13249.

Perdew, J.P. and Zunger, A. 1981, Self-interaction correction to density-functional approximations for many-electron systems, *Physical Review B*, **23**, p. 5048-5079.

Peri, J.B. 1965a, Infrared and gravimetric study of the surface of γ-alumina, *Journal of Physical Chemistry*, **69**, pp. 211-219.

Peri, J.B. 1965b, Infrared study of absorption of ammonia on dry γ-alumina, *Journal of Physical Chemistry*, **69**, 1, pp. 231-239.

Peri, J.B. 1965c, A model for the surface of γ-alumina, *Journal of Physical Chemistry*, **69**, 1, pp. 220-230.

Peri, J.B. and Hannan, R.B. 1960, Surface hydroxyl groups on γ-alumina, *Journal of Physical Chemistry*, **64**, pp. 1526-1530.

Perram, J.W., Peterson, H.G. and de Leeuw, S.W. 1988, An algorithm for the simulation of condensed matter which grows as the 3/2 powder of the number of particles, *Molecular Physics*, **65**, 4, pp. 875-893.

Peterson, H.G., Soelvason, D., Perram, J.W. and Smith, E.R. 1994, The very fast multipole method, *Journal of Chemical Physics*, **101**, 10, pp. 8870-8876.

Phillips, B.L., Kirkpatrick, R.J. and Hovis, G.L. 1988, ^{27}Al, ^{29}Si and ^{23}Na MAS NMR study on an Al, Si, ordered alkali feldspar solid solution series, *Physics and Chemistry of Minerals*, **16**, pp. 262-275.

Plinus Secundus, G. 77 AD, *Historia Naturalis*.

Plummer, M. 1958, The formation of metastable aluminas at high temperatures, *Journal of Applied Chemistry*, **8**, pp. 35-44.

Poncelet, G., Jacobs, P.A., Grange, P. and Delmon, B. (eds.) 1991, *Preparation of Catalysts V, Scientific Bases for the Preparation of Heterogeneous Catalysts,* Elsiever, Amsterdam, 95-165.

Pope, M.I. and Judd, M.D. 1977, *Differential Thermal Analysis,* Heyden and Son Ltd., London.

Pople, J.A. 1999, Nobel lecture: Quantum chemical models, *Reviews of Modern Physics*, **71**, 5, pp. 1267-1274.

Porezag, D., Pederson, M.R. and Liu, A.Y. 2000, The accuracy of the pseudopotential approximation within density functional theory, *Physica Status Solidi (b)*, **217**, pp. 219-230.

Porod, G. 1982, General Theory, in *Small Angle X-ray Scattering*, Glatter, O. and O., K. (Eds.), Academic Press, New York, pp. 17-51.

Press, W.H., Teulolsky, S.A., Vatterling, W.T. and Flannery, B.P. 1992, *Numerical Recipes in Fortran: The Art of Scientific Computing*, 2ed, Cambridge University Press, New York.

Repelin, Y. and Husson, E. 1990, Etudes structurales d'alumines de transition. I. Alumines gamma et delta, *Materials Research Bulletin*, **25**, pp. 611-621.

Report, International Aluminium Institute Statistical, form 150, 2001a, International Aluminium Institute, New Zealand house, Haymarket, London.

Report, International Aluminium Institute Statistical, form 650, 2001b, International Aluminium Institute, New Zealand house, Haymarket, London.

Rietveld, H.M. 1969, A profile refinement method for nuclear and magnetic structures, *Journal of Applied Crystallography*, **2**, pp. 65-71.

Rigby, M., Smith, E.B., Wakeham, W.A. and Maitland, G.C. 1986, *The Forces Between Molecules,* Clarendon Press, Oxford.

Rooksby, H.P. and Rooymans, C.J.M. 1961, The formation and structure of delta alumina, *Clay Minerals Bulletin*, **4**, pp. 234-238.

Rooksby, H.P. 1951, Oxides and Hydroxides of Aluminum and Iron, in *X-ray Identification and Crystal Structures of Clay Minerals*, Brindley, G. W. (Ed.), Mineralogical Society, London, p. Chapter 10.

Rosanova, G.G. 1998, Composite bus structure for the SMEX / WIRE satellite, *12th Annual AIAA/USU Conference on Small Satellites (Logan, Utah, 1998)*.

Ruberto, C. 2001, *Metastable Alumina from Theory: Bulk, Surface, and Growth of* κ-Al_2O_3, Thesis, Department of Applied Physics, Chalmers University of Technology and Goteberg University.

Rush, J.J. and Udovic, T.J. 2002, Modern neutron methods for the study of hydrogen in materials, in *EPD Congress 2002 and Fundamentals of Advanced Materials for Energy Conversion*, Taylor, P.R., Chandra, D. and Bautista, R. G. (Eds.), The Minerals, Metals & Materials Society, Warrendale, PA, pp. 161-171.

Rushton, P.P. 2002, *Towards a Non-Local Density Functional Description of Exchange and Correlation*, Department of Physics, University of Durham.

Saalfeld, H. 1958, The dehydration of gibbsite and the structure of a tetragonal γ-Al_2O_3, *Clay Minerals Bulletin*, **3**, pp. 249-257.

Saalfeld, H. 1960, Strukten des hydragillitis und der zwischenstufen beim entwassern, *Neues Jahrburch fuer Mineralogie Abhandlugen*, **95**, 1, pp. 1-87.

Saalfeld, H. and Mehrotra, B. 1965, Elektronenbeugungsuntersuchungen an aluminiumoxiden, *Berichte Deutsche Keramische Gesellschaft*, **42**, pp. 161-165.

Sanchez-Portal, D., Ordejon, P., Artacho, E. and Soler, J.E. 1997, Density-functional method for very large systems with LCAO basis sets, *International Journal of Quantum Chemistry*, **65**, pp. 453-461.

Saniger, J.M. 1995, Al-O infrared vibrational frequencies of γ-alumina, *Materials Letters*, **22**, pp. 109-113.

Sankey, O.F. and Niklewski, D.J. 1989, Ab initio multicenter tight-binding model for molecular-dynamics simulations and other applications in covalent systems, *Physical Review B*, **40**, 6, pp. 3979-3995.

Sanz, J., Fornes, V. and Corma, A. 1988, Extraframework aluminum in steam- and $SiCl_4$-dealuminated Y zeolite, *Journal of the Chemical Society, Faraday Transactions*, **84**, 9, pp. 3113-3119.

Sanz, J., Sobrados, I., Cavalieri, A.L., Pena, P., de Aza, S. and Moya, J.S. 1991, Structural changes induced on mullite precursors by thermal treatment: A ^{27}Al MAS-NMR investigation, *Journal of the American Ceramic Society*, **74**, 10, pp. 2398-2403.

Sato, T. 1962, The thermal transformation of alumina monohydrate, boehmite, *Journal of Applied Chemistry*, **12**, pp. 9-12.

Satterfield, C.N. 1980, *Heterogeneous Catalysis in Practice,* McGraw-Hill, New York.

Schaefer, D.W., Brow, R.K., Olivier, T.R., Beaucage, G., Hrubesh, L. and Lin, S. 1995, Characterisation of porosity in ceramic materials by small-angle scattering, in *Modern Aspects of Small-Angle Scattering*, Brumberger, H. (Ed.), Kluwer Academic Publishers, Netherlands, pp. 299-307.

Shanno, D.F. 1970, Conditioning of quasi-newton methods for function minimization, *Mathematics of Computation*, **24**, pp. 647-656.

Shannon, R.D. 1976, Revised effective ionic radii and systematic studies of interatomic distances in halides and chalcogenides, *Acta Crystallographica A*, **32**, pp. 751-767.

Shelton, J.-A. 1997, *As the Romans Did,* 2. Oxford University Press, New York.

Shi, B. and Davis, B.H. 1995, Alcohol dehydration: mechanism of ether formation using an alumina catalyst, *Journal of Catalysis*, **157**, pp. 359-367.

Shirasuka, K., Yanagida, H and Yamaguchi, G. 1976, The peparation of η-alumina and its structure, *Yogyo Kyokai-shi*, **84**, 12, pp. 610-613.

Sickafus, K.E., Wills, J.M. and Grimes, N.W. 1999, Spinel compounds: structure and property relations, *Journal of the American Ceramic Society*, **82**, 12, pp. 3279-3297.

Simons, J. 1991, An experimental chemist's guide to ab initio quantum chemistry, *Journal of Physical Chemistry*, **95**, pp. 1017-1029.

Simpson, J.A. and Weiner, E.S.C. (Eds.) 1989, *The Oxford English Dictionary,* Clarendon Press, Oxford.

Sinha, K.P. and Sinha, A.P.B. 1957, Vacancy distribution and bonding in some oxides of spinel structure, *Journal of Physical Chemistry*, **61**, pp. 758-761.

Slater, J.C. 1929, The theory of complex spectra, *Physical Review*, **34**, pp. 1293-1322.

Slater, J.C. 1930a, Atomic shielding constants, *Physical Review*, **36**, pp. 57-64.

Slater, J.C. 1930b, Note on Hartree's method, *Physical Review*, **35**, pp. 210-211.

Sohlberg, K., Pantelides, S.T. and Pennycook, S.J. 2001, Surface reconstruction and the difference in surface acidity between γ- and η-alumina, *Journal of the American Chemical Society*, **123**, pp. 26-29.

Sohlberg, K., Pennycook, S.J. and Pantelides, S.T. 1999a, Explanation of the observed dearth of three coordinated Al on γ-alumina surfaces, *Journal of the American Chemical Society*, **121**, 47, pp. 10999-11000.

Sohlberg, K., Pennycook, S.J. and Pantelides, S.T. 1999b, Hydrogen and the structure of the transition aluminas, *Journal of the American Chemical Society*, **121**, 33, pp. 7493-7499.

Soled, S. 1983, γ-Al2O3 viewed as a defect oxyhydroxide, *Journal of Catalysis*, **81**, 252-257.

Soler, J.E., Artacho, E., Gale, J.D., Garcia, A., Junquera, J., Ordejon, P. and Sanchez-Portal, D. 2002, The SIESTA method for *ab initio* order-*N* materials simulation, *Journal of Physics: Condensed Matter*, **14**, pp. 2745-2779.

Souza Santos, P., Souza Santos, H.S. and Toledo, S.P. 2000, Strandard transition aluminas. Electron microscopy studies, *Materials Research*, **3**, 4, pp. 104-114.

Spalla, O., Lyonnard, S. and Testard, F. 2003, Analysis of the small-angle intensity scattered by a porous and granular medium, *Journal of Applied Crystallography*, **36**, pp. 338-347.

Stephens, P.W. 1999, Phenomenological model of anisotropic peak broadening in powder diffraction, *Journal of Applied Crystallography*, **32**, pp. 281-289.

Stratmann, R.E., Scuseria, G.E. and Frisch, M.J. 1996, Achieving linear scaling in exchange-correlation density functional quadratures, *Chemical Physics Letters*, **257**, 213-233.

Streitz, F.H. and Mintmire, J.W. 1999, Energetics of aluminium vacancies in gamma alumina, *Physical Review B*, **60**, 2, pp. 773-777.

Stumpf, H.C., Russell, A.S., Newsome, J.W. and Tucker, C.M. 1950, Thermal transformations of aluminas and alumina hydrates, *Industrial and Engineering Chemistry*, **42**, 7, pp. 1398-1403.

Tachikawa, H. and Tsuchida, T. 1995, The electronic states and Lewis acidity of surface aluminum atoms in γ-Al_2O_3 model cluster: an *ab-initio* study, *Journal of Moelcular Catalysis A: Chemical*, **96**, pp. 277-282.

Tarte, P. 1967, Infra-red spectra of inorganic aluminates and characteristic vibrational frequencies of AlO_4 tetrahedra and AlO_6 octahedra, *Spectrochimica Acta*, **23A**, pp. 2127-2143.

Taylor, K. 1984, in *Catalysis - Science and Technology*, Anderson, J. R. and Moudart, M. (Eds.), Springer-Verlag, Berlin, 5th ed., p. 119.

Taylor, K.C. 1993, Nitric oxide catalysis in automotive exhaust systems, *Catalysis Reviews - Science and Engineering*, **35**, 4, pp. 457-481.

Tepper, F., Lerner, M. and Ginley, D 2001, Nanosized Alumina Fibers, *American Ceramic Society Bulletin*, **80**, 1, pp. 57-60.

Tertian, R. and Papee, D. 1958, Transformations thermiques et hydrothermiques de a'alumine, *Journal de chimie physique et de physico-chimie biologique*, **55**, pp. 341-353.

Thomas, L.H. 1927, The calculation of atomic fields, *Proceedings of the Cambridge Philosophical Society*, **23**, pp. 542-548.

Torrens, I.M. 1972, *Interatomic Potentials,* Academic Press, New York.

Tosi, M.P. 1964, Cohesion of ionic solids in the Born model, *Solid State Physics: Advances in Research and Applications*, **16**, pp. 1-120.

Troullier, N. and Martins, J.L. 1991, Efficient pseudopotentials for plane-wave calculations, *Physical Review B*, **43**, 3, pp. 1993-2006.

Troullier, N. and Martins, J.L. 1990, A straightforward method for generating soft transferable pseudopotentials, *Solid State Communications*, **74**, 7, pp. 613-616.

Tsuchida, T., Furuichi, R. and Ishii, T. 1980, Kinetics of the dehydration of boehmites prepared under different hydrothermal conditions, *Thermochimica Acta*, **39**, pp. 103-115.

Tsyganenko, A.A. and Filimonov, V.N. 1972, Infrared spectra of surface hydroxyl groups and crystalline structure of oxides, *Spectroscopy Letters*, **5**, 12, p. 477.

Tsyganenko, A.A. and Filimonov, V.N. 1973, Infrared spectra of surface hydroxyl groups and crystalline stucture of oxides, *Journal of Molecular Structure*, **19**, pp. 579-589.

Tsyganenko, A.A. and Mardilovich, P.P. 1996, Structure of alumina surfaces, *Journal of the Chemical Society, Faraday Transactions*, **92**, 23, pp. 4843-4852.

Tsyganenko, A.A., Mirnov, K.S.S., Rzhevskij, A.M. and Mardilovich, P.P. 1990, Infrared spectroscopic evidence for the structural OH groups of spinel alumina modifications, *Materials Chemistry and Physics*, **26**, pp. 35-46.

Tung, S.E. and Mcininch, E. 1964, High-purity alumina I. The nature of its surface acid sites and its activity in some hydrocarbon conversion reactions, *Journal of Catalysis*, **3**, pp. 229-238.

Ulrich, F. 1925, Notice regarding the crystal structure of the corundum-hematite group, *Norsk Geologrisk Tidsskrift*, **8**, pp. 115-122.

Ushakov, V.A. and Moroz, E.M. 1984, Structure of low temperature γ- and η-Al_2O_3, *Reaction Kinetics and Catalysis Letters*, **24**, 1-2, pp. 113-118.

van Horn, K.R., Bridenbaugh, P.R. and Staley, J.T. 2002. "Aluminum Processing" *Encyclopedia Britannica* [Online], Available: http://www.britannica.com/eb/article?eu=119891&query=aluminium[2002, Mar. 12].

van Laarhoven, P.J.M. and Aarts, E.H.L. 1987, *Simulated Annealing: Theory and Applications,* Reidel.

Verway, E.J.W. 1935a, The crystal structure of γ-Fe_2O_3 and γ-Al_2O_3, *Zeitschrift für Kristallographie*, **91**, pp. 65-69.

Verwey, E.J.W. 1935b, The structure of electrolytical oxide layer on aluminium, *Zeitschrift für Kristallographie*, **91**, pp. 317-320.

Vosko, S.J., Wilk, L. and Nusair, M. 1980, Accurate spin-dependent electron liquid correlation energies for local spin density calculations: A critical analysis, *Canadian Journal of Physics*, **58**, p. 1200.

Vuorinen, S. and Skogsmo, J. 1990, Characterization of α-Al_2O_3, & κ-Al_2O_3, and α & κ multioxide coatings on cemented carbides, *Thin Solid Films*, **193**, 1-2, pp. 536-546.

Wang, J.A., Bokhimi, X., Morales, A., Novaro, O., Lopez, T. and Gomez, R. 1999, Aluminum local environment and defects in the crystalline structure of sol-gel alumina catalyst, *Journal of Physical Chemistry B*, **103**, pp. 299-303.

Wang, Y.G., Bronsveld, P.M. and DeHosson, J.T.M. 1998, Ordering of octahedral vacancies in transition aluminas, *Journal of the American Ceramic Society*, **81**, 6, pp. 1655-1660.

Watson, G.W. and Willock, D.J. 2001, The enumeration of structure for γ-alumina based on a defective spinel structure, *Chemical Communications*, 12, pp. 1076-1077.

Wefers, K. and Misra, C. 1987, *Oxides and Hydroxides of Aluminum,* Alcoa Laboratories, Pittsburg.

Wei, W.-C., Lu, S.-J. and Hsieh, C.-L. 1996, Colloidal processing and fracture strength of alumina prepared from partially agglomerated theta-phase powder, *Journal of the Ceramic Society of Japan*, **104**, pp. 277-283.

White, C.A., Johnson, B.G., Gill, P.M.W. and Head-Gordon, M. 1996, Linear scaling density functional calculations via the continuous fast multiple method, *Chemical Physics Letters*, **253**, 268-278.

Wilson, S.J. 1979a, The dehydration of boehmite, γ-AlOOH to γ-Al_2O_3, *Journal of Solid State Chemistry*, **30**, pp. 247-255.

Wilson, S.J. 1979b, The development of porous microstructures during the dehydration of boehmite, *Mineralogical Magazine*, **43**, pp. 301-306.

Wilson, S.J. 1979c, Phase transformations and develoment of microstructure in boehmite-derived transition aluminas, *Proceedings of the British Ceramic Society*, **28**, pp. 281-294.

Wilson, S.J. and McConnell, J.D.C. 1980, A kinetic study of the system γ-AlOOH/Al_2O_3, *Journal of Solid State Chemistry*, **34**, pp. 315-322.

Wilson, S.J., McConnell, J.D.C. and Stacey, M.H. 1980, Energetics of formation of lamellar porous microstructures in γ-Al_2O_3, *Journal of Materials Science*, **15**, pp. 3081-3090.

Wilson, S.J. and Stacey, M.H. 1981, The porosity of aluminum oxide phases derived from well-crystallized boehmite: Correlated electron microscope, adsorption, and porosimetry studies, *Journal of Colloid and Interface Science*, **82**, pp. 507-517.

Wimmer, E. 1996, Computational materials design and processing: perspectives for atomistic approaches, *Materials Science and Engineering*, **B37**, pp. 72-82.

Wollaston, W.H. 1813, On a method of freezing at a distance, *Philosophical Transactions*, **103**, pp. 51-63.

Wolverton, C. and Hass, K.C. 2001, Phase stability and structure of spinel-based transition aluminas, *Physical Review B*, **63**, 2, pp. 024102, 1-16.

Xia, W.S., Wan, H.L. and Chen, Y. 1999, Cluster model study on the surface interactions of γ-alumina-supported metal oxides, *Journal of Molecular Catalysis A: Chemical*, **138**, pp. 185-195.

Xu, Z., Xiao, F.-S., Purnell, S.K., Alexeev, O., Kawi, S., Deutsch, S.E. and Gates, B.C 1994, Size-dependent catalytic activity of supported metal clusters, *Nature*, **372**, pp. 346-348.

Yamaguchi, G., Yanagida, H. and Ono, S. 1964, A new alumina hydrate, "tohdite" ($5Al_2O_3.H_2O$), *Bulletin of the Chemical Society of Japan*, **37**, 5, pp. 752-754.

Yamaguchi, G., Yasui, I. and Chiu, W.-C. 1970, A new method for preparing θ-Alumina and the interpretation of its X-ray-powder diffraction pattern and electron diffraction pattern, *Bulletin of the Chemical Society of Japan*, **43**, pp. 2487-2491.

Yanagida, H. and Yamaguchi, G. 1962, On the relation among γ-, η- and δ-Al_2O_3 under hydrothermal condition, *Bulletin of Materials Science*, **35**, pp. 1896-1897.

Yanagida, H. and Yamaguchi, G. 1964, Thermal effects on the lattices of η- and γ-aluminum oxide, *Bulletin of the Chemical Society of Japan*, **37**, 8, pp. 1229-1231.

Young, R.A. 1993a, Introduction to the Rietveld Method, in *The Rietveld Method*, Young, R. A. (Ed.), International Union of Crystallography, Oxford University Press, New York.

Young, R.A. (Ed.) 1993b, *The Rietveld Method,* International Union of Crystallography, Oxford University Press, New York.

Young, R.A. and Wiles, D.B. 1982, Profile shape functions in rietveld refinements, *Journal of Applied Crystallography*, **15**, pp. 430-438.

Yourdshahyan, Y., Engberg, U., Bengtsson, L., Lundqvist, B.I. and Hammer, B. 1997a, Theoretical investigation of the structure of κ-Al_2O_3, *Physical Review B*, **55**, 14, pp. 8721-8725.

Yourdshahyan, Y., Ruberto, C., Bengtsson, L. and Lundqvist, B.I. 1997b, First-principles calculations on the atomic and electronic structure of κ-Al_2O_3, *Physical Review B*, **56**, 16, pp. 8553-8558.

Yourdshahyan, Y., Ruberto, C., Halvarsson, M., Bengtsson, L., Langer, V. and Lundqvist, B.I. 1999, Theoretical structure determination of a complex material: κ-Al_2O_3, *Journal of the American Ceramic Society*, **82**, 6, pp. 1365-1380.

Zecchina, A., Coluccia, S. and Morterra, C. 1985, Infrared spectra of molecules adsorbed on oxide surfaces, *Applied Spectroscopy Reviews*, **21**, 3, pp. 259-310.

Zecchina, A., Platero, E.E. and Areán, C.O. 1987, Low temperature CO adsorption on alum-derived active alumina: an infrared investigation, *Journal of Catalysis*, **107**, pp. 244-247.

Zhou, R.-S. and Snyder, R.L. 1991, Structure and transformation mechanisms of the η, γ & θ transition aluminas, *Acta Crystallographica*, **B47**, pp. 617-630.

Appendix I

Particle Size Analysis Data

Analysis Report

CSIRO
Division of Minerals
Particle Analysis Service

Sample Name:	Synthesized gibbsite
Batch No:	R016416
PAS ID No:	P35842

Dispersant:	Water	**SOP Name:**	
Additives:	10 millilitres Sodium hexametaphosphate	**Analysis Model:**	General purpose
Sonication:	0 minutes in ultrasonic bath	**Result units:**	Volume

Concentration:	0.051 % vol	**Vol. Weighted Mean D[4,3]:**	211.478 µm	**d(0.1):**	102.05
Obscuration:	5.11 %	**Surface Weighted Mean D[3,2]:**	72.059 µm	**d(0.5):**	202.138
Weighted Residual:	0.01 %	**Specific Surface Area:**	0.083265 m^2/cc	**P80:**	0.652
				d(0.9):	346.308

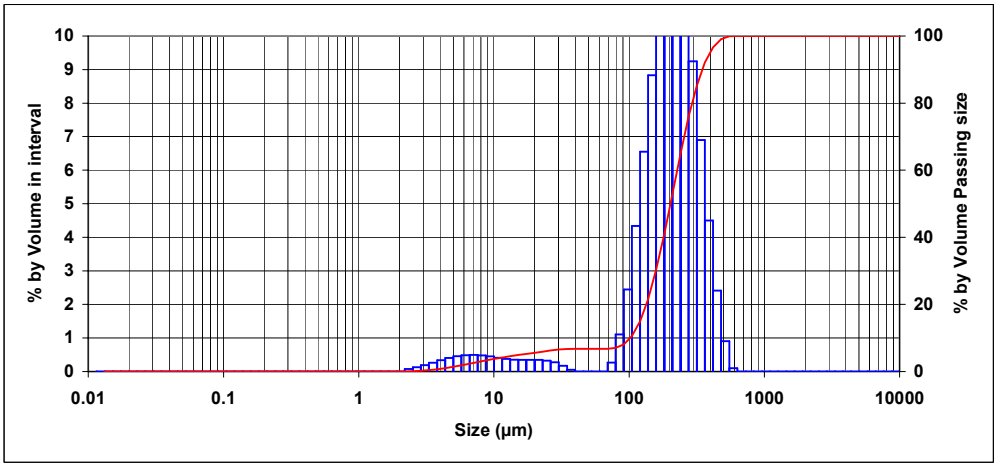

Size (µm)	Vol Under %	Size (µm)	Vol Under %	Size (µm)	Vol Under %	Size (µm)	Vol Under %	Size (µm)	Vol Under %	Size (µm)	Vol Under %
0.011	0.00	0.120	0.00	1.259	0.00	13.183	4.55	138.038	21.47	1445.440	100.00
0.013	0.00	0.138	0.00	1.445	0.00	15.136	4.90	158.489	30.30	1659.587	100.00
0.015	0.00	0.158	0.00	1.660	0.00	17.378	5.25	181.970	41.02	1905.461	100.00
0.017	0.00	0.182	0.00	1.905	0.00	19.953	5.59	208.930	52.89	2187.762	100.00
0.020	0.00	0.209	0.00	2.188	0.00	22.909	5.94	239.883	64.89	2511.886	100.00
0.023	0.00	0.240	0.00	2.512	0.08	26.303	6.27	275.423	75.94	2884.032	100.00
0.026	0.00	0.275	0.00	2.884	0.20	30.200	6.54	316.228	85.19	3311.311	100.00
0.030	0.00	0.316	0.00	3.311	0.40	34.674	6.72	363.078	92.09	3801.894	100.00
0.035	0.00	0.363	0.00	3.802	0.66	39.811	6.76	416.869	96.59	4365.158	100.00
0.040	0.00	0.417	0.00	4.365	1.00	45.709	6.76	478.630	99.00	5011.872	100.00
0.046	0.00	0.479	0.00	5.012	1.40	52.481	6.76	549.541	99.90	5754.399	100.00
0.052	0.00	0.550	0.00	5.754	1.86	60.256	6.76	630.957	100.00	6606.934	100.00
0.060	0.00	0.631	0.00	6.607	2.34	69.183	6.76	724.436	100.00	7585.776	100.00
0.069	0.00	0.724	0.00	7.586	2.84	79.433	7.03	831.764	100.00	8709.636	100.00
0.079	0.00	0.832	0.00	8.710	3.32	91.201	8.14	954.993	100.00	10000.00	100.00
0.091	0.00	0.955	0.00	10.000	3.76	104.713	10.59	1096.478	100.00	0.000	100.00
0.105	0.00	1.096	0.00	11.482	4.17	120.226	14.92	1258.925	100.00		

Analysis Report

CSIRO
Division of Minerals
Particle Analysis Service

Sample Name:	C31 gibbsite
Batch No:	R016416
PAS ID No:	P35843

Dispersant:	Water	**SOP Name:**	
Additives:	10 millilitres Sodium hexametaphosphate	**Analysis Model:**	General purpose
Sonication:	0 minutes in ultrasonic bath	**Result units:**	Volume

Concentration:	0.0386 % vol	**Vol. Weighted Mean D[4,3]:**	81.877 µm	**d(0.1):**	13.179
Obscuration:	12.08 %	**Surface Weighted Mean D[3,2]:**	20.534 µm	**d(0.5):**	78.489
Weighted Residual:	0.01 %	**Specific Surface Area:**	0.292202 m^2/cc	**P80:**	0.591
				d(0.9):	145.598

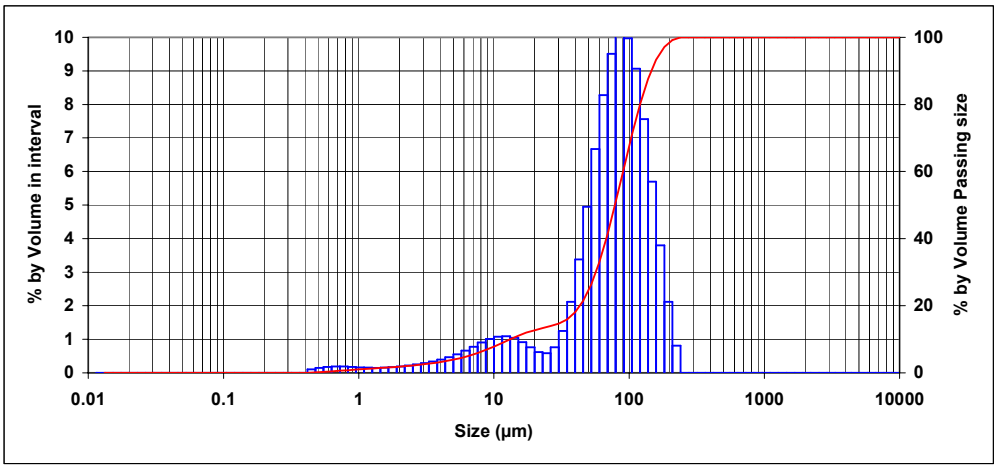

Size (µm)	Vol Under %	Size (µm)	Vol Under %	Size (µm)	Vol Under %	Size (µm)	Vol Under %	Size (µm)	Vol Under %	Size (µm)	Vol Under %
0.011	0.00	0.120	0.00	1.259	1.30	13.183	10.00	138.038	87.57	1445.440	100.00
0.013	0.00	0.138	0.00	1.445	1.45	15.136	11.04	158.489	93.27	1659.587	100.00
0.015	0.00	0.158	0.00	1.660	1.60	17.378	11.96	181.970	97.07	1905.461	100.00
0.017	0.00	0.182	0.00	1.905	1.77	19.953	12.72	208.930	99.19	2187.762	100.00
0.020	0.00	0.209	0.00	2.188	1.96	22.909	13.34	239.883	100.00	2511.886	100.00
0.023	0.00	0.240	0.00	2.512	2.18	26.303	13.93	275.423	100.00	2884.032	100.00
0.026	0.00	0.275	0.00	2.884	2.44	30.200	14.69	316.228	100.00	3311.311	100.00
0.030	0.00	0.316	0.00	3.311	2.73	34.674	15.94	363.078	100.00	3801.894	100.00
0.035	0.00	0.363	0.00	3.802	3.06	39.811	18.06	416.869	100.00	4365.158	100.00
0.040	0.00	0.417	0.00	4.365	3.46	45.709	21.44	478.630	100.00	5011.872	100.00
0.046	0.00	0.479	0.11	5.012	3.92	52.481	26.40	549.541	100.00	5754.399	100.00
0.052	0.00	0.550	0.25	5.754	4.47	60.256	33.06	630.957	100.00	6606.934	100.00
0.060	0.00	0.631	0.43	6.607	5.13	69.183	41.35	724.436	100.00	7585.776	100.00
0.069	0.00	0.724	0.62	7.586	5.91	79.433	50.86	831.764	100.00	8709.636	100.00
0.079	0.00	0.832	0.80	8.710	6.81	91.201	60.98	954.993	100.00	10000.00	100.00
0.091	0.00	0.955	0.98	10.000	7.82	104.713	70.95	1096.478	100.00	0.000	100.00
0.105	0.00	1.096	1.15	11.482	8.91	120.226	80.01	1258.925	100.00		

Analysis Report

CSIRO
Division of Minerals
Particle Analysis Service

Sample Name:	Deuterated boehmite milled 1 min
Batch No:	R016862
PAS ID No:	P37469

Dispersant:	Water	**SOP Name:**	
Additives:	10 millilitres sodium hexametaphosphate	**Analysis Model:**	General purpose
Sonication:	20 minutes in ultrasonic bath	**Result units:**	Volume

Concentration:	0.0026 % vol	**Vol. Weighted Mean D[4,3]:**	4.219 µm	**d(0.1):**	0.528
Obscuration:	15.4 %	**Surface Weighted Mean D[3,2]:**	1.118 µm	**d(0.5):**	1.368
Weighted Residual:	1.172 %	**Specific Surface Area:**	5.37 m^2/cc	**P80:**	3.161
				d(0.9):	11.598

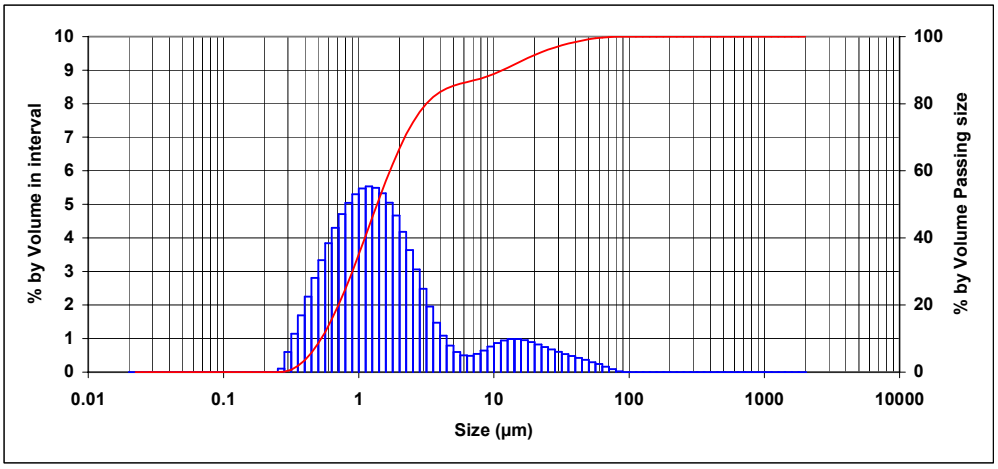

Size (µm)	Vol Under %	Size (µm)	Vol Under %	Size (µm)	Vol Under %	Size (µm)	Vol Under %	Size (µm)	Vol Under %	Size (µm)	Vol Under %
0.020	0.00	0.142	0.00	1.002	35.13	7.096	86.94	50.238	99.19	355.656	100.00
0.022	0.00	0.159	0.00	1.125	40.60	7.962	87.48	56.368	99.49	399.052	100.00
0.025	0.00	0.178	0.00	1.262	46.14	8.934	88.13	63.246	99.72	447.744	100.00
0.028	0.00	0.200	0.00	1.416	51.63	10.024	88.88	70.963	99.89	502.377	100.00
0.032	0.00	0.224	0.00	1.589	56.96	11.247	89.75	79.621	99.98	563.677	100.00
0.036	0.00	0.252	0.00	1.783	62.01	12.619	90.70	89.337	100.00	632.456	100.00
0.040	0.00	0.283	0.11	2.000	66.68	14.159	91.69	100.237	100.00	709.627	100.00
0.045	0.00	0.317	0.70	2.244	70.87	15.887	92.68	112.468	100.00	796.214	100.00
0.050	0.00	0.356	1.84	2.518	74.50	17.825	93.63	126.191	100.00	893.367	100.00
0.056	0.00	0.399	3.54	2.825	77.57	20.000	94.53	141.589	100.00	1002.374	100.00
0.063	0.00	0.448	5.79	3.170	80.05	22.440	95.35	158.866	100.00	1124.683	100.00
0.071	0.00	0.502	8.60	3.557	82.01	25.179	96.10	178.250	100.00	1261.915	100.00
0.080	0.00	0.564	11.93	3.991	83.48	28.251	96.78	200.000	100.00	1415.892	100.00
0.089	0.00	0.632	15.77	4.477	84.56	31.698	97.38	224.404	100.00	1588.656	100.00
0.100	0.00	0.710	20.08	5.024	85.35	35.566	97.92	251.785	100.00	1782.502	100.00
0.112	0.00	0.796	24.78	5.637	85.95	39.905	98.40	282.508	100.00	2000.000	100.00
0.126	0.00	0.893	29.83	6.325	86.45	44.774	98.83	316.979	100.00		

Sample Name:	Hydrogenated boehmite calcined 1 minute
Batch No:	R016862
PAS ID No:	P37468

Dispersant:	Water	**SOP Name:**	
Additives:	10 millilitres sodium hexametaphosphate	**Analysis Model:**	General purpose
Sonication:	20 minutes in ultrasonic bath	**Result units:**	Volume

Concentration:	0.0031 % vol	**Vol. Weighted Mean D[4,3]:**	4.774 µm	**d(0.1):**	0.533
Obscuration:	17.41 %	**Surface Weighted Mean D[3,2]:**	1.164 µm	**d(0.5):**	1.443
Weighted Residual:	1.166 %	**Specific Surface Area:**	5.16 m^2/cc	**P80:**	4.245
				d(0.9):	14.553

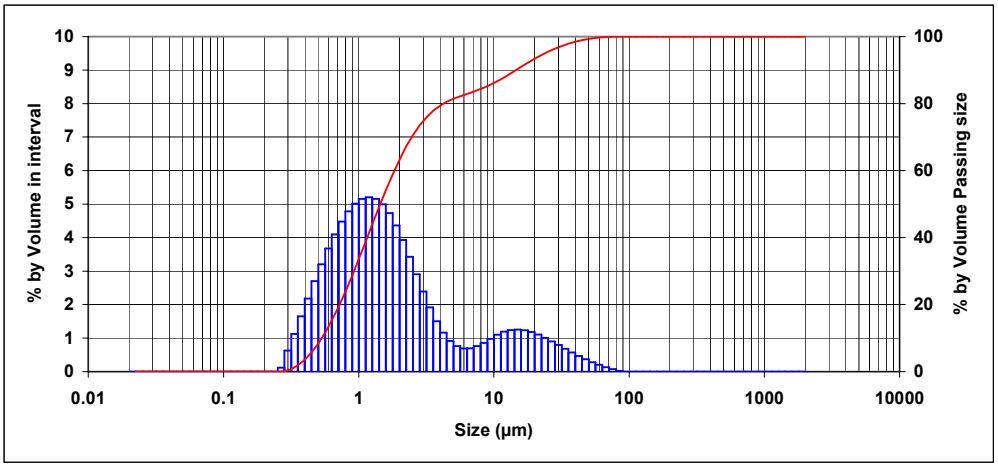

Size (µm)	Vol Under %	Size (µm)	Vol Under %	Size (µm)	Vol Under %	Size (µm)	Vol Under %	Size (µm)	Vol Under %	Size (µm)	Vol Under %
0.020	0.00	0.142	0.00	1.002	33.65	7.096	83.57	50.238	99.29	355.656	100.00
0.022	0.00	0.159	0.00	1.125	38.81	7.962	84.32	56.368	99.57	399.052	100.00
0.025	0.00	0.178	0.00	1.262	44.02	8.934	85.19	63.246	99.77	447.744	100.00
0.028	0.00	0.200	0.00	1.416	49.17	10.024	86.17	70.963	99.90	502.377	100.00
0.032	0.00	0.224	0.00	1.589	54.16	11.247	87.27	79.621	99.98	563.677	100.00
0.036	0.00	0.252	0.00	1.783	58.89	12.619	88.46	89.337	100.00	632.456	100.00
0.040	0.00	0.283	0.12	2.000	63.26	14.159	89.70	100.237	100.00	709.627	100.00
0.045	0.00	0.317	0.74	2.244	67.19	15.887	90.96	112.468	100.00	796.214	100.00
0.050	0.00	0.356	1.87	2.518	70.62	17.825	92.19	126.191	100.00	893.367	100.00
0.056	0.00	0.399	3.52	2.825	73.52	20.000	93.38	141.589	100.00	1002.374	100.00
0.063	0.00	0.448	5.70	3.170	75.92	22.440	94.48	158.866	100.00	1124.683	100.00
0.071	0.00	0.502	8.41	3.557	77.84	25.179	95.49	178.250	100.00	1261.915	100.00
0.080	0.00	0.564	11.61	3.991	79.34	28.251	96.40	200.000	100.00	1415.892	100.00
0.089	0.00	0.632	15.28	4.477	80.50	31.698	97.19	224.404	100.00	1588.656	100.00
0.100	0.00	0.710	19.38	5.024	81.42	35.566	97.88	251.785	100.00	1782.502	100.00
0.112	0.00	0.796	23.86	5.637	82.18	39.905	98.45	282.508	100.00	2000.000	100.00
0.126	0.00	0.893	28.64	6.325	82.87	44.774	98.92	316.979	100.00		

HORIBA LA-910 for Windows(TM) Ver. 1.30 May/29/'200111:06

Laser scattering particle size distribution analyzer

PARTICLE SIZE MEASUREMENT DATA

ID# : 20010529-968 11:06
Filename :
Sample : 0105-301
Material : BOEHMITE -Hydrogenated (as-supplied)

Source : FROM MH-1 LOT 3629
Notes :
Test Number :
Instrument :

Condition
T%(He-Ne) : 78.2% Dist.Form : Std. Sampling times : 10
(LAMP) : 79.9% R.R.Index : 1.22-0.10i ( )
Agitation : 3 Circulation : 3 Ultrasonic : ON(60)

Format
Dist.base : Volume Scaling : Auto Axis : LogX - LinearY

Data
Median : 16.193µm SP.Area : 14586cm²/cm³ S.D. : 8.891µm
Mode : 18.515µm Mean : 16.402µm
C.V. : 54.21% Span : (D 10.0-D 90.0) / D50 = 1.472

Dia. on %(10.0%) : 3.585µm % on Dia.(0.100µm) : 0.0%
Dia. on %(20.0%) : 9.591µm % on Dia.(1.950µm) : 8.2%
Dia. on %(30.0%) : 12.259µm % on Dia.(22.000µm) : 76.6%
Dia. on %(80.0%) : 22.990µm % on Dia.(44.000µm) : 99.4%
Dia. on %(90.0%) : 27.419µm % on Dia.(200.000µm) : 100.0%

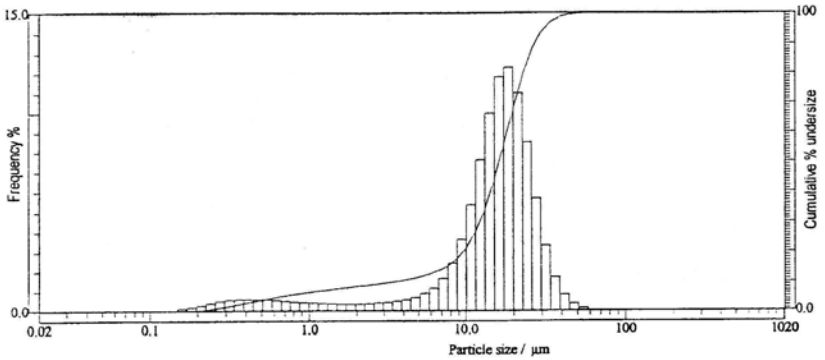

Size(µm)	Freq(%)	Und(%)	Size(µm)	Freq(%)	Und(%)	Size(µm)	Freq(%)	Und(%)
1019.5	0.00	100.00	26.11	8.49	87.96	0.669	0.56	4.95
890.1	0.00	100.00	22.80	11.02	79.47	0.584	0.60	4.39
777.1	0.00	100.00	19.90	12.30	68.45	0.510	0.60	3.80
678.5	0.00	100.00	17.38	11.83	56.15	0.445	0.59	3.20
592.4	0.00	100.00	15.17	9.99	44.32	0.389	0.59	2.61
517.2	0.00	100.00	13.25	7.59	34.33	0.339	0.56	2.02
451.6	0.00	100.00	11.56	5.36	26.74	0.296	0.50	1.46
394.2	0.00	100.00	10.10	3.64	21.38	0.259	0.39	0.96
344.2	0.00	100.00	8.816	2.44	17.74	0.226	0.27	0.57
300.5	0.00	100.00	7.697	1.66	15.30	0.197	0.18	0.29
262.4	0.00	100.00	6.720	1.17	13.64	0.172	0.11	0.11
229.1	0.00	100.00	5.867	0.89	12.48	0.150	0.00	0.00
200.0	0.00	100.00	5.122	0.69	11.59	0.131	0.00	0.00
174.6	0.00	100.00	4.472	0.58	10.89	0.115	0.00	0.00
152.5	0.00	100.00	3.905	0.50	10.31	0.100	0.00	0.00
133.1	0.00	100.00	3.409	0.45	9.82	0.087	0.00	0.00
116.2	0.00	100.00	2.976	0.41	9.37	0.076	0.00	0.00
101.5	0.00	100.00	2.599	0.37	8.96	0.067	0.00	0.00
88.58	0.00	100.00	2.269	0.36	8.59	0.058	0.00	0.00
77.34	0.00	100.00	1.981	0.35	8.23	0.051	0.00	0.00
67.52	0.00	100.00	1.729	0.35	7.88	0.044	0.00	0.00
58.95	0.15	100.00	1.510	0.37	7.53	0.039	0.00	0.00
51.47	0.36	99.85	1.318	0.39	7.16	0.034	0.00	0.00
44.94	0.82	99.48	1.151	0.41	6.78	0.029	0.00	0.00
39.23	1.73	98.66	1.005	0.44	6.36	0.026	0.00	0.00
34.25	3.31	96.93	0.877	0.47	5.93	0.022	0.00	0.00
29.91	5.66	93.62	0.766	0.51	5.46			

Appendix II

Rietveld Refinement Results for the Crystallographic Structure of γ-Alumina

Refinement results for room temperature neutron MRPD data of hydrogenated boehmite pre-calcined for seven hours. Uncertainties are to three standard deviations.

500 °C Refinement:

Space group $I4_1/amd$, a = 5.622(3), c = 7.815(5), R_p = 3.77, χ^2 = 1.38, R_B = 1.13.

Site	x	y	z	B(Å^2)	occupancy
O (16*h*)	0	-0.0064(51)	0.2504(63)	1.2(3)	1.0
Al (4*a*)	0	0.75	0.125	1.5(3)	0.77(2)
Al (8*c*)	0	0	0	1.6(3)	0.47(1)
Al (8*d*)	0	0	0.5	1.6(3)	0.48(1)

Core geometries (distances in Å, angles in °) around Al ions

Al (4*a*)─O	1.684(36)		
Al (8*c*)─O	1.957(48)	1.962(20)	
Al (8*d*)─O	1.951(48)	2.013(20)	
O─Al(4a)─O	109.79(1.50)	108.83(3.00)	
O─Al(8*c*)─O	180.00	90.66(1.62)	89.34(1.62)
O─Al(8*d*)─O	180.00	90.65(1.53)	89.35(1.53)

Resulting cation distribution: 71(3) % octahedrally and 29(3) % tetrahedrally coordinated.

550 °C Refinement:

Space group $I4_1/amd$, a = 5.616(3), c = 7.825(5), R_p = 3.86, χ^2 = 1.28, R_B = 1.11.

Site	x	y	z	B(Å^2)	occupancy
O (16*h*)	0	0.0056(69)	0.2517(60)	1.4(3)	1.0
Al (4*a*)	0	0.75	0.125	1.5(3)	0.83(2)
Al (8*c*)	0	0	0	1.6(3)	0.43(1)
Al (8*d*)	0	0	0.5	1.6(3)	0.49(1)

Core geometries (distances in Å, angles in °) around Al ions

Al (4*a*)─O	1.721(46)		
Al (8*c*)─O	1.969(46)	1.988(27)	
Al (8*d*)─O	1.943(46)	1.983(27)	
O─Al(4a)─O	109.69(2.51)	106.36(1.29)	
O─Al(8*c*)─O	180.00	90.44(1.77)	89.56(1.77)
O─Al(8*d*)─O	180.00	90.44(1.80)	89.56(1.80)

Resulting cation distribution: 69(3) % octahedrally and 31(3) % tetrahedrally coordinated.

600 °C Refinement:

Space group $I4_1/amd$, a = 5.615(1), c = 7.835(4), R_p = 3.35, χ^2 = 1.73, R_B = 0.92.

Site	x	y	z	B(Å^2)	occupancy
O (16*h*)	0	0.0075(48)	0.2514(33)	1.3(3)	1.0
Al (4*a*)	0	0.75	0.125	1.5(3)	0.78(2)
Al (8*c*)	0	0	0	1.6(3)	0.35(1)
Al (8*d*)	0	0	0.5	1.6(3)	0.59(1)

Core geometries (distances in Å, angles in °) around Al ions

Al (4*a*)─O	1.752(15)		
Al (8*c*)─O	1.970(25)	2.015(1)	
Al (8*d*)─O	1.948(25)	1.956(1)	
O─Al(4a)─O	111.19(2.41)	108.62(69)	
O─Al(8*c*)─O	180.00	91.15(72)	86.85(72)
O─Al(8*d*)─O	180.00	90.20(78)	88.80(78)

Resulting cation distribution: 71(3) % octahedrally and 29(3) % tetrahedrally coordinated.

650 °C Refinement:

Space group $I4_1/amd$, a = 5.613(1), c = 7.834(4), R_p = 5.27, χ^2 = 1.38, R_B = 1.77.

Site	x	y	z	B(Å^2)	occupancy
O (16*h*)	0	0.0028(63)	0.2522(57)	1.3(3)	1.0
Al (4*a*)	0	0.75	0.125	1.4(3)	0.81(2)
Al (8*c*)	0	0	0	1.5(3)	0.38(1)
Al (8*d*)	0	0	0.5	1.5(3)	0.55(1)

Core geometries (distances in Å, angles in °) around Al ions

Al (4*a*)─O	1.734(45)		
Al (8*c*)─O	1.976(42)	1.996(2)	
Al (8*d*)─O	1.941(42)	1.974(2)	
O─Al(4a)─O	109.82(1.25)	109.30(1.11)	
O─Al(8*c*)─O	180.00	90.82(1.71)	89.18(1.71)
O─Al(8*d*)─O	180.00	90.17(1.77)	89.17(1.77)

Resulting cation distribution: 70(3) % octahedrally and 30(3) % tetrahedrally coordinated.

700 °C Refinement:

Space group $I4_1/amd$, a = 5.612(1), c = 7.830(4), R_p = 5.28, χ^2 = 1.63, R_B = 2.08.

Site	x	y	z	B(Å^2)	occupancy
O (16*h*)	0	0.0049(49)	0.2524(49)	1.2(3)	1.0
Al (4*a*)	0	0.75	0.125	1.4(3)	0.83(2)
Al (8*c*)	0	0	0	1.5(3)	0.35(1)
Al (8*d*)	0	0	0.5	1.5(3)	0.57(1)

Core geometries (distances in Å, angles in °) around Al ions

Al (4*a*)─O	1.744(30)		
Al (8*c*)─O	1.977(30)	2.004(15)	
Al (8*d*)─O	1.939(30)	1.965(15)	
O─Al(4a)─O	110.22(1.50)	109.10(75)	
O─Al(8*c*)─O	180.00	91.10(1.16)	88.90(1.16)
O─Al(8*d*)─O	180.00	91.13(1.20)	88.87(1.20)

Resulting cation distribution: 69(3) % octahedrally and 31(3) % tetrahedrally coordinated.

750 °C Refinement:

Space group $I4_1/amd$, a = 5.614(1), c = 7.833(4), R_p = 5.45, χ^2 = 1.63, R_B = 2.04.

Site	x	y	z	B(Å^2)	occupancy
O (16*h*)	0	0.0042(45)	0.2524(40)	1.3(3)	1.0
Al (4*a*)	0	0.75	0.125	1.5(3)	0.82(2)
Al (8*c*)	0	0	0	1.6(3)	0.35(1)
Al (8*d*)	0	0	0.5	1.6(3)	0.57(1)

Core geometries (distances in Å, angles in °) around Al ions

Al (4*a*)─O	1.741(31)		
Al (8*c*)─O	1.977(31)	2.002(17)	
Al (8*d*)─O	1.940(31)	1.968(17)	
O─Al(4a)─O	110.08(1.59)	109.17(81)	
O─Al(8*c*)─O	180.00	91.02(1.20)	88.98(1.20)
O─Al(8*d*)─O	180.00	91.04(1.26)	88.96(1.26)

Resulting cation distribution: 70(3) % octahedrally and 30(3) % tetrahedrally coordinated.

Refinement results for room temperature neutron HRPD data of hydrogenated boehmite pre-calcined for seven hours. Uncertainties are to three standard deviations.

500 °C Refinement:

Space group $I4_1/amd$, a = 5.622(3), c = 7.815(5), R_p = 3.77, χ^2 = 1.38, R_B = 1.13.

Site	x	y	z	B(Å^2)	occupancy
O (16*h*)	0	-0.0064(51)	0.2504(63)	1.2(4)	1.0
Al (4*a*)	0	0.75	0.125	1.5(4)	0.77(2)
Al (8*c*)	0	0	0	1.6(4)	0.47(1)
Al (8*d*)	0	0	0.5	1.6(4)	0.48(1)

Core geometries (distances in Å, angles in °) around Al ions

Al (4*a*)─O	1.684(37)		
Al (8*c*)─O	1.957(49)	1.962(21)	
Al (8*d*)─O	1.951(49)	2.013(21)	
O─Al(4a)─O	109.79(1.50)	108.83(1.50)	
O─Al(8*c*)─O	180.00	90.66(1.56)	89.34(1.56)
O─Al(8*d*)─O	180.00	90.65(1.53)	89.35(1.53)

Resulting cation distribution: 74(4) % octahedrally and 26(4) % tetrahedrally coordinated.

550 °C Refinement:

Space group $I4_1/amd$, a = 5.617(1), c = 7.825(4), R_p = 3.86, χ^2 = 1.28, R_B = 1.11.

Site	x	y	z	B(Å^2)	occupancy
O (16*h*)	0	0.0006(69)	0.2517(60)	1.4(4)	1.0
Al (4*a*)	0	0.75	0.125	1.5(4)	0.83(2)
Al (8*c*)	0	0	0	1.6(4)	0.43(1)
Al (8*d*)	0	0	0.5	1.6(4)	0.49(1)

Core geometries (distances in Å, angles in °) around Al ions

Al (4*a*)─O	1.721(47)		
Al (8*c*)─O	1.969(47)	1.988(27)	
Al (8*d*)─O	1.943(47)	1.984(27)	
O─Al(4a)─O	109.69(2.51)	109.36(1.29)	
O─Al(8*c*)─O	180.00	90.44(1.77)	89.56(1.77)
O─Al(8*d*)─O	180.00	90.44(1.80)	89.56(1.80)

Resulting cation distribution: 72(3) % octahedrally and 28(3) % tetrahedrally coordinated.

600 °C Refinement:

Space group $I4_1/amd$, a = 5.615(1), c = 7.835(4), R_p = 3.35, χ^2 = 1.73, R_B = 1.34.

Site	x	y	z	B(Å^2)	occupancy
O (16*h*)	0	0.0075(61)	0.2514(33)	1.3(3)	1.0
Al (4*a*)	0	0.75	0.125	1.5(3)	0.78(2)
Al (8*c*)	0	0	0	1.6(3)	0.35(1)
Al (8*d*)	0	0	0.5	1.6(3)	0.59(1)

Core geometries (distances in Å, angles in °) around Al ions

Al (4*a*)─O	1.752(15)		
Al (8*c*)─O	1.970(27)	2.015(4)	
Al (8*d*)─O	1.948(27)	1.956(4)	
O─Al(4a)─O	111.19(1.51)	108.62(69)	
O─Al(8*c*)─O	180.00	91.15(0.72)	88.85(0.72)
O─Al(8*d*)─O	180.00	91.20(0.78)	88.80(0.78)

Resulting cation distribution: 72(3) % octahedrally and 28(3) % tetrahedrally coordinated.

650 °C Refinement:

Space group $I4_1/amd$, a = 5.613(1), c = 7.834(4), R_p = 5.27, χ^2 = 1.38, R_B = 1.77.

Site	x	y	z	B(Å^2)	occupancy
O (16*h*)	0	0.0027(63)	0.2522(57)	1.3(3)	1.0
Al (4*a*)	0	0.75	0.125	1.4(3)	0.78(2)
Al (8*c*)	0	0	0	1.5(3)	0.35(1)
Al (8*d*)	0	0	0.5	1.5(3)	0.59(1)

Core geometries (distances in Å, angles in °) around Al ions

Al (4*a*)─O	1.752(15)		
Al (8*c*)─O	1.970(27)	2.015(04)	
Al (8*d*)─O	1.948(27)	1.956(04)	
O─Al(4a)─O	109.82(2.25)	109.30(1.11)	
O─Al(8*c*)─O	180.00	90.82(1.71)	89.18(1.71)
O─Al(8*d*)─O	180.00	90.83(1.77)	89.17(1.77)

Resulting cation distribution: 72(3) % octahedrally and 28(3) % tetrahedrally coordinated.

700 °C Refinement:

Space group $I4_1/amd$, a = 5.612(1), c = 7.830(4), R_p = 5.28, χ^2 = 1.63, R_B = 2.08.

Site	x	y	z	B(Å^2)	occupancy
O (16*h*)	0	0.0049(40)	0.2524(39)	1.2(3)	1.0
Al (4*a*)	0	0.75	0.125	1.3(3)	0.83(2)
Al (8*c*)	0	0	0	1.4(3)	0.35(1)
Al (8*d*)	0	0	0.5	1.4(3)	0.57(1)

Core geometries (distances in Å, angles in °) around Al ions

Al (4*a*)─O	1.744(30)		
Al (8*c*)─O	1.977(30)	2.004(15)	
Al (8*d*)─O	1.939(30)	1.965(15)	
O─Al(4a)─O	110.22(1.50)	109.10(75)	
O─Al(8*c*)─O	180.00	91.10(1.14)	89.90(1.14)
O─Al(8*d*)─O	180.00	91.13(1.20)	89.17(1.20)

Resulting cation distribution: 72(3) % octahedrally and 28(3) % tetrahedrally coordinated.

750 °C Refinement:

Space group $I4_1/amd$, a = 5.614(1), c = 7.833(4), R_p = 5.45, χ^2 = 1.63, R_B = 2.04.

Site	x	y	z	B(Å^2)	occupancy
O (16*h*)	0	0.0042(45)	0.2524(40)	1.3(3)	1.0
Al (4*a*)	0	0.75	0.125	1.5(3)	0.82(2)
Al (8*c*)	0	0	0	1.6(3)	0.35(1)
Al (8*d*)	0	0	0.5	1.6(3)	0.57(1)

Core geometries (distances in Å, angles in °) around Al ions

Al (4*a*)─O	1.741(31)		
Al (8*c*)─O	1.977(31)	2.002(16)	
Al (8*d*)─O	1.940(31)	1.968(18)	
O─Al(4a)─O	110.08(1.59)	109.17(81)	
O─Al(8*c*)─O	180.00	91.02(1.20)	89.98(1.20)
O─Al(8*d*)─O	180.00	91.04(1.26)	88.96(1.26)

Resulting cation distribution: 70(3) % octahedrally and 30(3) % tetrahedrally coordinated.

Refinement results for neutron MRPD data of hydrogenated boehmite calcined *in situ*. Uncertainties are to three standard deviations.

500 °C Refinement:

Space group $I4_1/amd$, a = 5.635(3), c = 7.831(6), R_p = 2.27, χ^2 = 2.86, R_B = 1.14.

Site	x	y	z	B(Å^2)	occupancy
O (16*h*)	0	0.0028(60)	0.2509(50)	2.1(4)	1.0
Al (4*a*)	0	0.75	0.125	2.7(4)	0.80(2)
Al (8*c*)	0	0	0	2.8(4)	0.37(1)
Al (8*d*)	0	0	0.5	2.8(4)	0.57(1)

Core geometries (distances in Å, angles in °) around Al ions

Al (4*a*)─O	1.707(42)		
Al (8*c*)─O	1.947(42)	1.990(27)	
Al (8*d*)─O	1.969(42)	1.994(27)	
O─Al(4a)─O	110.91(2.40)	108.76(1.26)	
O─Al(8*c*)─O	180.00	91.37(1.62)	89.63(1.62)
O─Al(8*d*)─O	180.00	90.37(1.59)	89.63(1.59)

Resulting cation distribution: 68(3) % octahedrally and 32(3) % tetrahedrally coordinated.

550 °C Refinement:

Space group $I4_1/amd$, a = 5.634(3), c = 7.839(5), R_p = 2.37, χ^2 = 3.14, R_B = 1.18.

Site	x	y	z	B(Å^2)	occupancy
O (16*h*)	0	0.0032(60)	0.2512(50)	2.2(4)	1.0
Al (4*a*)	0	0.75	0.125	2.8(4)	0.81(2)
Al (8*c*)	0	0	0	2.9(4)	0.34(1)
Al (8*d*)	0	0	0.5	2.9(4)	0.58(1)

Core geometries (distances in Å, angles in °) around Al ions

Al (4*a*)─O	1.736(36)		
Al (8*c*)─O	1.969(39)	2.005(24)	
Al (8*d*)─O	1.951(39)	1.979(24)	
O─Al(4a)─O	110.52(2.52)	108.95(1.23)	
O─Al(8*c*)─O	180.00	90.63(1.32)	89.37(1.32)
O─Al(8*d*)─O	180.00	90.64(1.38)	89.36(1.38)

Resulting cation distribution: 68(3) % octahedrally and 32(3) % tetrahedrally coordinated.

600 °C Refinement:

Space group $I4_1/amd$, a = 5.634(3), c = 7.852(5), R_p = 2.40, χ^2 = 3.09, R_B = 1.64.

Site	x	y	z	B(Å^2)	occupancy
O (16*h*)	0	0.0016(75)	0.2503(54)	2.3(4)	1.0
Al (4*a*)	0	0.75	0.125	3.0(4)	0.75(2)
Al (8*c*)	0	0	0	3.1(4)	0.37(1)
Al (8*d*)	0	0	0.5	3.1(4)	0.59(1)

Core geometries (distances in Å, angles in °) around Al ions

Al (4*a*)─O	1.725(45)		
Al (8*c*)─O	1.966(42)	1.998(30)	
Al (8*d*)─O	1.960(42)	1.986(30)	
O─Al(4a)─O	110.45(2.79)	108.98(1.38)	
O─Al(8*c*)─O	180.00	90.25(1.62)	89.75(1.62)
O─Al(8*d*)─O	180.00	90.26(1.65)	89.74(1.65)

Resulting cation distribution: 69(3) % octahedrally and 31(3) % tetrahedrally coordinated.

650 °C Refinement:

Space group $I4_1/amd$, a = 5.632(3), c = 7.859(5), R_p = 2.50, χ^2 = 3.28, R_B = 1.52.

Site	x	y	z	B(Å^2)	occupancy
O (16*h*)	0	0.0021(48)	0.2511(41)	2.3(4)	1.0
Al (4*a*)	0	0.75	0.125	3.1(4)	0.80(2)
Al (8*c*)	0	0	0	3.2(4)	0.37(1)
Al (8*d*)	0	0	0.5	3.2(4)	0.57(1)

Core geometries (distances in Å, angles in °) around Al ions

Al (4*a*)─O	1.725(45)		
Al (8*c*)─O	1.966(42)	1.997(30)	
Al (8*d*)─O	1.962(42)	1.986(30)	
O─Al(4a)─O	110.49(2.79)	108.98(1.38)	
O─Al(8*c*)─O	180.00	90.35(1.62)	89.78(1.62)
O─Al(8*d*)─O	180.00	90.26(1.65)	89.84(1.65)

Resulting cation distribution: 69(3) % octahedrally and 31(3) % tetrahedrally coordinated.

700 °C Refinement:

Space group $I4_1/amd$, a = 5.634(2), c = 7.860(3), R_p = 2.46, χ^2 = 3.13, R_B = 1.82.

Site	x	y	z	B(Å^2)	occupancy
O (16*h*)	0	0.0029(42)	0.2512(33)	2.4(4)	1.0
Al (4*a*)	0	0.75	0.125	2.8(4)	0.77(2)
Al (8*c*)	0	0	0	2.9(4)	0.37(1)
Al (8*d*)	0	0	0.5	2.9(4)	0.58(1)

Core geometries (distances in Å, angles in °) around Al ions

Al (4*a*)─O	1.736(24)		
Al (8*c*)─O	1.924(27)	2.004(15)	
Al (8*d*)─O	1.956(27)	1.980(15)	
O─Al(4a)─O	110.32(1.68)	109.05(84)	
O─Al(8*c*)─O	180.00	90.61(90)	89.39(90)
O─Al(8*d*)─O	180.00	90.62(90)	89.38(99)

Resulting cation distribution: 69(3) % octahedrally and 31(3) % tetrahedrally coordinated.

750 °C Refinement:

Space group $I4_1/amd$, a = 5.637(2), c = 7.858(4), R_p = 2.42, χ^2 = 2.94, R_B = 1.54.

Site	x	y	z	B(Å^2)	occupancy
O (16*h*)	0	0.0028(51)	0.2521(51)	2.6(4)	1.0
Al (4*a*)	0	0.75	0.125	3.0(4)	0.81(2)
Al (8*c*)	0	0	0	3.1(4)	0.37(1)
Al (8*d*)	0	0	0.5	3.1(4)	0.56(1)

Core geometries (distances in Å, angles in °) around Al ions

Al (4*a*)─O	1.740(31)		
Al (8*c*)─O	1.981(31)	2.004(18)	
Al (8*d*)─O	1.948(31)	1.982(18)	
O─Al(4a)─O	109.93(1.92)	109.24(96)	
O─Al(8*c*)─O	180.00	90.80(1.14)	89.20(1.14)
O─Al(8*d*)─O	180.00	90.81(1.20)	89.19(1.20)

Resulting cation distribution: 69(3) % octahedrally and 31(3) % tetrahedrally coordinated.

Refinement results for neutron MRPD data of deuterated boehmite prepared hydrothermally from hydrogenated gibbsite and calcined *in situ*. Uncertainties are to three standard deviations.

500 °C Refinement:

Space group $I4_1/amd$, $a = 5.661(1)$, $c = 7.845(4)$, $R_p = 2.87$, $\chi^2 = 2.84$, $R_B = 1.10$.

Site	x	y	z	B(Å^2)	occupancy
O (16*h*)	0	0.0103(48)	0.2548(49)	1.9(4)	1.0
Al (4*a*)	0	0.75	0.125	3.2(4)	0.66(2)
Al (8*c*)	0	0	0	3.3(4)	0.38(1)
Al (8*d*)	0	0	0.5	3.3(4)	0.62(1)

Core geometries (distances in Å, angles in °) around Al ions

Al (4*a*)─O	1.791(1)		
Al (8*c*)─O	2.000(2)	2.043(1)	
Al (8*d*)─O	1.925(2)	1.961(1)	
O─Al(4a)─O	110.71(3)	108.86(3)	
O─Al(8*c*)─O	180.00	92.21(3)	87.79(3)
O─Al(8*d*)─O	180.00	92.35(3)	87.65(3)

Resulting cation distribution: 75(4) % octahedrally and 24(4) % tetrahedrally coordinated.

525 °C Refinement:

Space group $I4_1/amd$, $a = 5.659(2)$, $c = 7.854(5)$, $R_p = 3.31$, $\chi^2 = 3.77$, $R_B = 0.71$.

Site	x	y	z	B(Å^2)	occupancy
O (16*h*)	0	0.0094(57)	0.2546(57)	2.0(4)	1.0
Al (4*a*)	0	0.75	0.125	2.9(4)	0.64(2)
Al (8*c*)	0	0	0	3.0(4)	0.36(1)
Al (8*d*)	0	0	0.5	3.0(4)	0.66(1)

Core geometries (distances in Å, angles in °) around Al ions

Al (4*a*)─O	1.786(1)		
Al (8*c*)─O	2.001(2)	2.039(1)	
Al (8*d*)─O	1.928(2)	1.964(1)	
O─Al(4a)─O	110.52(6)	108.95(3)	
O─Al(8*c*)─O	180.00	92.07(3)	87.93(3)
O─Al(8*d*)─O	180.00	92.19(3)	87.81(3)

Resulting cation distribution: 75(4) % octahedrally and 24(4) % tetrahedrally coordinated.

550 °C Refinement:

Space group $I4_1/amd$, a = 5.659(2), c = 7.859(5), R_p = 2.85, χ^2 = 2.73, R_B = 0.92.

Site	x	y	z	B(Å^2)	occupancy
O (16*h*)	0	0.0102(45)	0.2556(45)	1.9(4)	1.0
Al (4*a*)	0	0.75	0.125	3.0(4)	0.68(2)
Al (8*c*)	0	0	0	3.1(4)	0.35(1)
Al (8*d*)	0	0	0.5	3.1(4)	0.65(1)

Core geometries (distances in Å, angles in °) around Al ions

Al (4*a*)─O	1.795(1)		
Al (8*c*)─O	2.010(2)	2.043(1)	
Al (8*d*)─O	1.921(2)	1.961(1)	
O─Al(4a)─O	110.25(3)	109.08(3)	
O─Al(8*c*)─O	180.00	92.38(3)	87.62(3)
O─Al(8*d*)─O	180.00	92.54(3)	87.46(3)

Resulting cation distribution: 75(4) % octahedrally and 24(4) % tetrahedrally coordinated.

600 °C Refinement:

Space group $I4_1/amd$, a = 5.660(2), c = 7.866(4), R_p = 3.12, χ^2 = 2.59, R_B = 0.90.

Site	x	y	z	B(Å^2)	occupancy
O (16*h*)	0	0.0097(51)	0.2540(51)	1.9(4)	1.0
Al (4*a*)	0	0.75	0.125	2.4(4)	0.68(2)
Al (8*c*)	0	0	0	2.5(4)	0.36(1)
Al (8*d*)	0	0	0.5	2.5(4)	0.59(1)

Core geometries (distances in Å, angles in °) around Al ions

Al (4*a*)─O	1.786(1)		
Al (8*c*)─O	1.999(2)	2.041(1)	
Al (8*d*)─O	1.936(2)	1.963(1)	
O─Al(4a)─O	110.74(3)	108.84(3)	
O─Al(8*c*)─O	180.00	91.98(12)	88.02(12)
O─Al(8*d*)─O	180.00	92.10(14)	87.90(15)

Resulting cation distribution: 71(3) % octahedrally and 29(3) % tetrahedrally coordinated.

650 °C Refinement:

Space group $I4_1/amd$, a = 5.662(2), c = 7.867(4), R_p = 3.10, χ^2 = 2.47, R_B = 1.08.

Site	x	y	z	B(Å^2)	occupancy
O (16*h*)	0	0.0079(52)	0.2552(52)	2.1(5)	1.0
Al (4*a*)	0	0.75	0.125	3.0(5)	0.78(2)
Al (8*c*)	0	0	0	3.1(5)	0.35(1)
Al (8*d*)	0	0	0.5	3.1(5)	0.63(1)

Core geometries (distances in Å, angles in °) around Al ions

Al (4*a*)─O	1.784(1)		
Al (8*c*)─O	2.008(2)	2.034(1)	
Al (8*d*)─O	1.926(2)	1.971(1)	
O─Al(4a)─O	109.91(3)	109.25(3)	
O─Al(8*c*)─O	180.00	92.04(3)	87.96(3)
O─Al(8*d*)─O	180.00	92.14(3)	87.86(3)

Resulting cation distribution: 75(4) % octahedrally and 25(4) % tetrahedrally coordinated.

700 °C Refinement:

Space group $I4_1/amd$, a = 5.666(2), c = 7.867(4), R_p = 3.04, χ^2 = 2.39, R_B = 0.97.

Site	x	y	z	B(Å^2)	occupancy
O (16*h*)	0	0.0094(45)	0.2552(45)	2.2(5)	1.0
Al (4*a*)	0	0.75	0.125	3.1(5)	0.72(2)
Al (8*c*)	0	0	0	3.2(5)	0.34(1)
Al (8*d*)	0	0	0.5	3.2(5)	0.64(1)

Core geometries (distances in Å, angles in °) around Al ions

Al (4*a*)─O	1.791(1)		
Al (8*c*)─O	2.008(2)	2.042(1)	
Al (8*d*)─O	1.926(2)	1.967(1)	
O─Al(4a)─O	110.24(3)	109.09(3)	
O─Al(8*c*)─O	180.00	92.04(3)	87.96(3)
O─Al(8*d*)─O	180.00	92.33(3)	87.67(3)

Resulting cation distribution: 73(4) % octahedrally and 27(4) % tetrahedrally coordinated.

Refinement results for neutron MRPD data of deuterated boehmite prepared hydrothermally from deuterated gibbsite and calcined *in situ*. Uncertainties are to three standard deviations.

Includes example refinement of the dual-phase model discussed in *section 7.2.3*.

500 °C Refinement:

Space group $I4_1/amd$, $a = 5.648(3)$, $c = 7.849(6)$, $R_p = 2.51$, $\chi^2 = 2.12$, $R_B = 0.89$.

Site	x	y	z	B(Å^2)	occupancy
O (16*h*)	0	0.0034(60)	0.2541(50)	1.3(3)	1.0
Al (4*a*)	0	0.75	0.125	2.3(3)	0.70(2)
Al (8*c*)	0	0	0	2.4(3)	0.37(1)
Al (8*d*)	0	0	0.5	2.4(3)	0.61(1)

Core geometries (distances in Å, angles in °) around Al ions

Al (4*a*)─O	1.754(42)		
Al (8*c*)─O	1.995(39)	2.011(24)	
Al (8*d*)─O	1.930(39)	1.984(24)	
O─Al(4a)─O	109.50(1.05)	109.41(2.10)	
O─Al(8*c*)─O	180.00	91.30(1.53)	88.70(1.53)
O─Al(8*d*)─O	180.00	91.34(1.62)	88.66(1.62)

Resulting cation distribution: 74(4) % octahedrally and 26(3) % tetrahedrally coordinated.

550 °C Refinement:

Space group $I4_1/amd$, $a = 5.647(3)$, $c = 7.855(5)$, $R_p = 3.31$, $\chi^2 = 1.68$, $R_B = 0.90$.

Site	x	y	z	B(Å^2)	occupancy
O (16*h*)	0	0.0071(30)	0.2538(39)	1.3(3)	1.0
Al (4*a*)	0	0.75	0.125	2.2(3)	0.71(2)
Al (8*c*)	0	0	0	2.3(3)	0.37(1)
Al (8*d*)	0	0	0.5	2.3(3)	0.63(1)

Core geometries (distances in Å, angles in °) around Al ions

Al (4*a*)─O	1.770(33)		
Al (8*c*)─O	1.994(30)	2.025(15)	
Al (8*d*)─O	1.934(30)	1.969(15)	
O─Al(4a)─O	110.25(1.44)	109.41(82)	
O─Al(8*c*)─O	180.00	91.65(1.20)	88.35(1.20)
O─Al(8*d*)─O	180.00	91.73(1.32)	88.27(1.32)

Resulting cation distribution: 75(5) % octahedrally and 25(5) % tetrahedrally coordinated.

600 °C Refinement:

Space group $I4_1/amd$, a = 5.652(1), c = 7.871(5), R_p = 2.47, χ^2 = 1.96, R_B = 0.99.

Site	x	Y	z	B(Å^2)	occupancy
O (16*h*)	0	0.0076(30)	0.2516(40)	1.4(3)	1.0
Al (4*a*)	0	0.75	0.125	2.2(3)	0.78(2)
Al (8*c*)	0	0	0	2.3(3)	0.36(1)
Al (8*d*)	0	0	0.5	2.3(3)	0.58(1)

Core geometries (distances in Å, angles in °) around Al ions

Al (4*a*)─O	1.764(33)		
Al (8*c*)─O	1.981(33)	2.029(18)	
Al (8*d*)─O	1.956(32)	1.968(18)	
O─Al(4a)─O	111.23(1.47)	108.60(72)	
O─Al(8*c*)─O	180.00	91.22(1.26)	88.78(1.26)
O─Al(8*d*)─O	180.00	91.27(1.35)	88.73(1.35)

Resulting cation distribution: 72(3) % octahedrally and 28(3) % tetrahedrally coordinated.

600 °C Dual-Phase Refinement Discussed in *section 7.2.3*:

Figures of Merit: R_p = 2.79, χ^2 = 2.39, R_B (tetragonal) = 1.89, 1.96, R_B (cubic) = 0.56

Space group $I4_1/amd$, a = 5.661(1), c = 7.871(5).

Site	x	y	z	B(Å^2)	Occupancy
O (16*h*)	0	0.0555(35)	0.2507(32)	5.4(1.5)	1.0
Al (4*a*)	0	0.75	0.125	11.0(1.5)	0.90(2)
Al (8*c*)	0	0	0	11.0(1.5)	0.37(1)
Al (8*d*)	0	0	0.5	11.0(1.5)	0.51(1)

Space group $Fd\text{-}3m$, a = 7.938(6).

Site	x	y	z	B(Å^2)	Occupancy
O (32*e*)	0.2581(27)	0.2581(27)	0.2581(27)	5.4(1.5)	1.0
Al (8*a*)	0.125	0.125	0.125	11.0(1.5)	0.95(2)
Al (16*c*)	0	0	0	11.0(1.5)	0.36(1)
Al (16*d*)	0.5	0.5	0.5	11.0(1.5)	0.49(1)

Resulting cation distribution: 65(4) % octahedrally and 35(3) % tetrahedrally coordinated.

Appendix III

Rietveld Refinement Results for the Crystallographic Structure of γ′-Alumina

Refinement results for room temperature neutron MRPD data of hydrogenated boehmite pre-calcined for seven hours. Uncertainties are to three standard deviations. All uncertainties, where not stated otherwise, are 0.005 for refinable coordinate positions, 0.3 for thermal parameters, 0.008 for distances, and 0.05 for angles.

800 °C Refinement:

Space group $P\bar{4}m2$, a = 5.611(3), c = 24.450(12), R_p = 3.51, χ^2 = 1.71, R_B = 1.01.

	Site	x	y	z	B(Å^2)	occupancy
	O (4*j*)	0.2334	0	0.1214	1.5	1.0
	O (4*j*)	0.2621	0	0.2965	1.5	1.0
	O (4*j*)	0.2470	0	0.4572	1.5	1.0
	O (4*j*)	0.2342	0	0.6255	1.5	1.0
	O (4*j*)	0.2294	0	0.7982	1.5	1.0
	O (4*j*)	0.2548	0	0.9581	1.5	1.0
	O (4*k*)	0.2334	0.5	0.1157	1.5	1.0
	O (4*k*)	0.2621	0.5	0.2965	1.5	1.0
	O (4*k*)	0.2470	0.5	0.4572	1.5	1.0
	O (4*k*)	0.2342	0.5	0.6255	1.5	1.0
	O (4*k*)	0.2294	0.5	0.7904	1.5	1.0
	O (4*k*)	0.2548	0.5	0.9581	1.5	1.0
	Al (2*e*)	0	0	0.2620	1.1	0.25
	Al (2*f*)	0.5	0.5	0.0882	1.1	0.75
	Al (2*f*)	0.5	0.5	0.1816	1.1	1.0
T	Al (2*f*)	0.5	0.5	0.4194	1.1	1.0
	Al (4*i*)	0.2518	0.2513	0.5	1.1	0.25
	Al (8*l*)	0.2590	0.2546	0.1703	1.1	0.375
	Al (8*l*)	0.2510	0.2513	0.3297	1.1	0.125
	Al (4*j*)	0.2490	0	0.1987	1.1	0.75
	Al (4*j*)	0.2457	0	0.3751	1.1	1.0
	Al (4*j*)	0.2530	0	0.5536	1.1	0.25
	Al (4*j*)	0.2457	0	0.8811	1.1	0.5
O	Al (4*k*)	0.2680	0.5	0.0331	1.1	0.125
	Al (4*k*)	0.2590	0.5	0.2108	1.1	0.5
	Al (4*k*)	0.2506	0.5	0.3759	1.1	0.875
	Al (4*k*)	0.2562	0.5	0.7106	1.1	1.0
	Al (4*k*)	0.2512	0.5	0.8861	1.1	0.25

Resulting cation distribution: 66(3) % octahedrally and 34(3) % tetrahedrally coordinated.

Aluminium – Oxygen bond lengths (Å) and angles (°) for the 800°C Refinement. The bottom half of the table reports the O-Al-O angles within each octahedra and tetrahedra. Repeat values for the distances and angles are only reported once.

Al (2e)─O	1.678	1.910		
Al (2f)─O	1.630	1.752		
Al (2f)─O	1.654	2.150		
Al (2f)─O	1.666	1.834		
Al (4i)─O	1.725			
Al (8l)─O	1.590	1.682	1.813	1.901
Al (8l)─O	1.609	1.750		
Al (4j)─O	1.815	1.901	1.925	2.294
Al (4j)─O	1.846	1.905	1.924	1.940
Al (4j)─O	1.691	1.976	1.999	2.260
Al (4j)─O	1.833	1.902	1.921	1.939
Al (4k)─O	1.757	1.905	1.949	2.048
Al (4k)─O	2.009	2.033	2.112	2.235
Al (4k)─O	1.725	2.044	2.048	2.052
Al (4k)─O	1.878	1.919	1.969	1.999
Al (4k)─O	1.832	2.049	2.056	2.104
O─Al(2e)─O	122.38	84.74		
O─Al(2f)─O	133.27	103.46		
O─Al(2f)─O	133.21	88.20		
O─Al(2f)─O	116.92	108.80		
O─Al(4i)─O	109.81	108.82		
O─Al(8l)─O	117.40	101.09		
O─Al(8l)─O	107.53	106.30		
O─Al(4j)─O	179.08	94.57	89.18	
O─Al(4j)─O	176.93	93.72	90.61	
O─Al(4j)─O	175.57	99.83	89.78	
O─Al(4j)─O	177.81	91.44	89.54	
O─Al(4k)─O	171.88	97.91	94.05	90.33
O─Al(4k)─O	176.80	96.08	91.90	81.72
O─Al(4k)─O	178.42	94.40	93.22	87.46
O─Al(4k)─O	171.87	92.38	91.49	87.54
O─Al(4k)─O	178.10	95.08	91.37	86.79

900 °C Refinement:

Space group $P\bar{4}m2$, $a = 5.617(3)$, $c = 24.405(12)$, $R_p = 4.03$, $\chi^2 = 2.13$, $R_B = 1.70$.

	Site	x	y	z	B(Å^2)	occupancy
	O (4*j*)	0.2394	0	0.1223	1.1	1.0
	O (4*j*)	0.2708	0	0.2922	1.1	1.0
	O (4*j*)	0.2430	0	0.4566	1.1	1.0
	O (4*j*)	0.2302	0	0.6214	1.1	1.0
	O (4*j*)	0.2298	0	0.7975	1.1	1.0
	O (4*j*)	0.2444	0	0.9575	1.1	1.0
	O (4*k*)	0.2394	0.5	0.1191	1.1	1.0
	O (4*k*)	0.2708	0.5	0.2951	1.1	1.0
	O (4*k*)	0.2430	0.5	0.4566	1.1	1.0
	O (4*k*)	0.2302	0.5	0.6214	1.1	1.0
	O (4*k*)	0.2298	0.5	0.7897	1.1	1.0
	O (4*k*)	0.2444	0.5	0.9575	1.1	1.0
T	Al (2*e*)	0	0	0.3300	0.8	0.375
T	Al (2*f*)	0.5	0.5	0.0882	0.8	0.5
T	Al (2*f*)	0.5	0.5	0.1816	0.8	1.0
T	Al (2*f*)	0.5	0.5	0.4200	0.8	1.0
T	Al (4*i*)	0.2518	0.2513	0.5	0.8	0.1875
T	Al (8*l*)	0.2588	0.2546	0.1703	0.8	0.5625
O	Al (4j)	0.2490	0	0.1987	0.8	0.5
O	Al (4j)	0.2457	0	0.3751	0.8	1.0
O	Al (4j)	0.2457	0	0.8810	0.8	0.6875
O	Al (4k)	0.2590	0.5	0.2108	0.8	0.625
O	Al (4k)	0.2506	0.5	0.3759	0.8	1.0
O	Al (4k)	0.2562	0.5	0.7106	0.8	1.0
O	Al (4k)	0.1353	0.5	0.0013	0.8	0.4375

Resulting cation distribution: 66(3) % octahedrally and 34(3) % tetrahedrally coordinated.

Aluminium – Oxygen bond lengths (Å) and angles (°) for the 900°C Refinement. The bottom half of the table reports the O-Al-O angles within each octahedra and tetrahedra. Repeat values for the distances and angles are only reported once.

Al(2e)─O	1.722	1.760		
Al (2f)─O	1.633	1.790		
Al (2f)─O	1.660	2.069		
Al (2f)─O	1.679	1.799		
Al (4i)─O	1.733			
Al (8l)─O	1.598	1.799	1.847	1.692
Al (4j)─O	1.789	1.905	1.931	2.192
Al (4j)─O	1.893	1.908	1.929	1.945
Al (4j)─O	1.813	1.962	1.928	1.933
Al (4k)─O	1.973	2.034	2.112	2.150
Al (4k)─O	1.758	2.028	2.078	2.074
Al (4k)─O	1.857	1.884	1.932	2.093
Al (4k)─O	1.194	1.889	2.366	2.681
O─Al(2e)─O	119.68	97.33		
O─Al(2f)─O	127.37	106.69		
O─Al(2f)─O	132.23	90.07		
O─Al(2f)─O	118.59	114.81		
O─Al(4i)─O	112.33	107.81		
O─Al(8l)─O	115.90	102.13		
O─Al(4j)─O	178.50	94.40	91.41	89.70
O─Al(4j)─O	176.29	94.60	87.20	
O─Al(4j)─O	178.61	92.56	89.54	86.48
O─Al(4k)─O	178.99	96.61	91.60	89.07
O─Al(4k)─O	177.49	98.08	93.65	85.25
O─Al(4k)─O	173.80	97.39	88.87	

Refinement results for room temperature neutron HRPD data of hydrogenated boehmite pre-calcined for seven hours. Uncertainties are to three standard deviations. All uncertainties, where not stated otherwise, are 0.005 for refinable coordinate positions, 0.3 for thermal parameters, 0.008 for distances, and 0.05 for angles.

800 °C Refinement:

Space group $P\bar{4}m2$, a = 5.611(3), c = 24.444(12), R_p = 6.07, χ^2 = 1.54, R_B = 2.06.

	Site	x	y	z	B(Å^2)	occupancy
	O (4*j*)	0.2334	0	0.1214	1.5	1.0
	O (4*j*)	0.2621	0	0.2965	1.5	1.0
	O (4*j*)	0.2470	0	0.4572	1.5	1.0
	O (4*j*)	0.2342	0	0.6255	1.5	1.0
	O (4*j*)	0.2294	0	0.7982	1.5	1.0
	O (4*j*)	0.2548	0	0.9581	1.5	1.0
	O (4*k*)	0.2334	0.5	0.1157	1.5	1.0
	O (4*k*)	0.2621	0.5	0.2965	1.5	1.0
	O (4*k*)	0.2470	0.5	0.4572	1.5	1.0
	O (4*k*)	0.2342	0.5	0.6255	1.5	1.0
	O (4*k*)	0.2294	0.5	0.7904	1.5	1.0
	O (4*k*)	0.2548	0.5	0.9581	1.5	1.0
T	Al (2*e*)	0	0	0.2620	1.1	0.25
T	Al (2*f*)	0.5	0.5	0.0882	1.1	0.75
T	Al (2*f*)	0.5	0.5	0.1816	1.1	1.0
T	Al (2*f*)	0.5	0.5	0.4194	1.1	1.0
T	Al (4*i*)	0.2518	0.2513	0.5	1.1	0.25
T	Al (8*l*)	0.2590	0.2546	0.1703	1.1	0.375
T	Al (8*l*)	0.2510	0.2513	0.3297	1.1	0.125
O	Al (4*j*)	0.2490	0	0.1987	1.1	0.75
O	Al (4*j*)	0.2457	0	0.3751	1.1	1.0
O	Al (4*j*)	0.2530	0	0.5536	1.1	0.25
O	Al (4*j*)	0.2457	0	0.8811	1.1	0.5
O	Al (4*k*)	0.2680	0.5	0.0331	1.1	0.125
O	Al (4*k*)	0.2590	0.5	0.2108	1.1	0.5
O	Al (4*k*)	0.2506	0.5	0.3759	1.1	0.875
O	Al (4*k*)	0.2562	0.5	0.7106	1.1	1.0
O	Al (4*k*)	0.2512	0.5	0.8861	1.1	0.25

Resulting cation distribution: 66(3) % octahedrally and 34(3) % tetrahedrally coordinated.

Aluminium – Oxygen bond lengths (Å) and angles (°) for the 800°C Refinement. The bottom half of the table reports the O-Al-O angles within each octahedra and tetrahedra. Repeat values for the distances and angles are only reported once.

Al (2e)─O	1.678	1.910		
Al (2f)─O	1.630	1.752		
Al (2f)─O	1.654	2.150		
Al (2f)─O	1.666	1.834		
Al (4i)─O	1.725			
Al (8l)─O	1.590	1.682	1.813	1.901
Al (8l)─O	1.609	1.750		
Al (4j)─O	1.815	1.901	1.925	2.294
Al (4j)─O	1.846	1.905	1.924	1.940
Al (4j)─O	1.691	1.976	1.999	2.260
Al (4j)─O	1.833	1.902	1.921	1.939
Al (4k)─O	1.757	1.905	1.949	2.048
Al (4k)─O	2.009	2.033	2.112	2.235
Al (4k)─O	1.725	2.044	2.048	2.052
Al (4k)─O	1.878	1.919	1.969	1.999
Al (4k)─O	1.832	2.049	2.056	2.104
O─Al(2e)─O	122.38	84.74		
O─Al(2f)─O	133.27	103.46		
O─Al(2f)─O	133.21	88.20		
O─Al(2f)─O	116.92	108.80		
O─Al(4i)─O	109.81	108.82		
O─Al(8l)─O	117.40	101.09		
O─Al(8l)─O	107.53	106.30		
O─Al(4j)─O	179.08	94.57	89.18	
O─Al(4j)─O	176.93	93.72	90.61	
O─Al(4j)─O	175.57	99.83	89.78	
O─Al(4j)─O	177.81	91.44	89.54	
O─Al(4k)─O	171.88	97.91	94.05	90.33
O─Al(4k)─O	176.80	96.08	91.90	81.72
O─Al(4k)─O	178.42	94.40	93.22	87.46
O─Al(4k)─O	171.87	92.38	91.49	87.54
O─Al(4k)─O	178.10	95.08	91.37	86.79

900 °C Refinement:

Space group $P\bar{4}m2$, a = 5.618(3), c = 24.402(12), R_p = 6.50, χ^2 = 1.82, R_B = 2.67.

	Site	x	y	z	B(Å^2)	occupancy
	O (4*j*)	0.2394	0	0.1223	1.1	1.0
	O (4*j*)	0.2708	0	0.2922	1.1	1.0
	O (4*j*)	0.2430	0	0.4566	1.1	1.0
	O (4*j*)	0.2302	0	0.6214	1.1	1.0
	O (4*j*)	0.2298	0	0.7975	1.1	1.0
	O (4*j*)	0.2444	0	0.9575	1.1	1.0
	O (4*k*)	0.2394	0.5	0.1191	1.1	1.0
	O (4*k*)	0.2708	0.5	0.2951	1.1	1.0
	O (4*k*)	0.2430	0.5	0.4566	1.1	1.0
	O (4*k*)	0.2302	0.5	0.6214	1.1	1.0
	O (4*k*)	0.2298	0.5	0.7897	1.1	1.0
	O (4*k*)	0.2444	0.5	0.9575	1.1	1.0
T	Al (2*e*)	0	0	0.3300	0.8	0.375
T	Al (2*f*)	0.5	0.5	0.0882	0.8	0.5
T	Al (2*f*)	0.5	0.5	0.1816	0.8	1.0
T	Al (2*f*)	0.5	0.5	0.4200	0.8	1.0
T	Al (4*i*)	0.2518	0.2513	0.5	0.8	0.1875
T	Al (8*l*)	0.2588	0.2546	0.1703	0.8	0.5625
O	Al (4j)	0.2490	0	0.1987	0.8	0.5
O	Al (4j)	0.2457	0	0.3751	0.8	1.0
O	Al (4j)	0.2457	0	0.8810	0.8	0.6875
O	Al (4k)	0.2590	0.5	0.2108	0.8	0.625
O	Al (4k)	0.2506	0.5	0.3759	0.8	1.0
O	Al (4k)	0.2562	0.5	0.7106	0.8	1.0
O	Al (4k)	0.1353	0.5	0.0013	0.8	0.4375

Resulting cation distribution: 66(3) % octahedrally and 34(3) % tetrahedrally coordinated.

Aluminium – Oxygen bond lengths (Å) and angles (°) for the 900°C Refinement. The bottom half of the table reports the O-Al-O angles within each octahedra and tetrahedra. Repeat values for the distances and angles are only reported once.

Al(2e)─O	1.722	1.760		
Al (2f)─O	1.633	1.790		
Al (2f)─O	1.660	2.069		
Al (2f)─O	1.679	1.799		
Al (4i)─O	1.733			
Al (8l)─O	1.598	1.799	1.847	1.692
Al (4j)─O	1.789	1.905	1.931	2.192
Al (4j)─O	1.893	1.908	1.929	1.945
Al (4j)─O	1.813	1.962	1.928	1.933
Al (4k)─O	1.973	2.034	2.112	2.150
Al (4k)─O	1.758	2.028	2.078	2.074
Al (4k)─O	1.857	1.884	1.932	2.093
Al (4k)─O	1.194	1.889	2.366	2.681
O─Al(2e)─O	119.68	97.33		
O─Al(2f)─O	127.37	106.69		
O─Al(2f)─O	132.23	90.07		
O─Al(2f)─O	118.59	114.81		
O─Al(4i)─O	112.33	107.81		
O─Al(8l)─O	115.90	102.13		
O─Al(4j)─O	178.50	94.40	91.41	89.70
O─Al(4j)─O	176.29	94.60	87.20	
O─Al(4j)─O	178.61	92.56	89.54	86.48
O─Al(4k)─O	178.99	96.61	91.60	89.07
O─Al(4k)─O	177.49	98.08	93.65	85.25
O─Al(4k)─O	173.80	97.39	88.87	

Refinement results for neutron MRPD data of hydrogenated boehmite calcined *in situ*. All uncertainties, where not stated otherwise, are 0.005 for refinable coordinate positions, 0.3 for thermal parameters, 0.008 for distances, and 0.05 for angles.

800 °C Refinement:

Space group $P\bar{4}m2$, $a = 5.633(3)$, $c = 24.538(12)$, $R_p = 2.26$, $\chi^2 = 2.45$, $R_B = 1.04$.

	Site	x	y	z	B(Å^2)	occupancy
	O (4*j*)	0.2334	0	0.1214	1.5	1.0
	O (4*j*)	0.2621	0	0.2965	1.5	1.0
	O (4*j*)	0.2470	0	0.4572	1.5	1.0
	O (4*j*)	0.2342	0	0.6255	1.5	1.0
	O (4*j*)	0.2294	0	0.7982	1.5	1.0
	O (4*j*)	0.2548	0	0.9581	1.5	1.0
	O (4*k*)	0.2334	0.5	0.1157	1.5	1.0
	O (4*k*)	0.2621	0.5	0.2965	1.5	1.0
	O (4*k*)	0.2470	0.5	0.4572	1.5	1.0
	O (4*k*)	0.2342	0.5	0.6255	1.5	1.0
	O (4*k*)	0.2294	0.5	0.7904	1.5	1.0
	O (4*k*)	0.2548	0.5	0.9581	1.5	1.0
T	Al (2*e*)	0	0	0.2620	1.1	0.25
T	Al (2*f*)	0.5	0.5	0.0882	1.1	0.75
T	Al (2*f*)	0.5	0.5	0.1816	1.1	1.0
T	Al (2*f*)	0.5	0.5	0.4194	1.1	1.0
T	Al (4*i*)	0.2518	0.2513	0.5	1.1	0.25
T	Al (8*l*)	0.2590	0.2546	0.1703	1.1	0.375
T	Al (8*l*)	0.2510	0.2513	0.3297	1.1	0.125
O	Al (4*j*)	0.2490	0	0.1987	1.1	0.75
O	Al (4*j*)	0.2457	0	0.3751	1.1	1.0
O	Al (4*j*)	0.2530	0	0.5536	1.1	0.25
O	Al (4*j*)	0.2457	0	0.8811	1.1	0.5
O	Al (4*k*)	0.2680	0.5	0.0331	1.1	0.125
O	Al (4*k*)	0.2590	0.5	0.2108	1.1	0.5
O	Al (4*k*)	0.2506	0.5	0.3759	1.1	0.875
O	Al (4*k*)	0.2562	0.5	0.7106	1.1	1.0
O	Al (4*k*)	0.2512	0.5	0.8861	1.1	0.25

Resulting cation distribution: 66(3) % octahedrally and 34(3) % tetrahedrally coordinated.

Aluminium – Oxygen bond lengths (Å) and angles (°) for the 800°C Refinement. The bottom half of the table reports the O-Al-O angles within each octahedra and tetrahedra. Repeat values for the distances and angles are only reported once.

Al (2e)─O	1.678	1.910		
Al (2f)─O	1.630	1.752		
Al (2f)─O	1.654	2.150		
Al (2f)─O	1.666	1.834		
Al (4i)─O	1.725			
Al (8l)─O	1.590	1.682	1.813	1.901
Al (8l)─O	1.609	1.750		
Al (4j)─O	1.815	1.901	1.925	2.294
Al (4j)─O	1.846	1.905	1.924	1.940
Al (4j)─O	1.691	1.976	1.999	2.260
Al (4j)─O	1.833	1.902	1.921	1.939
Al (4k)─O	1.757	1.905	1.949	2.048
Al (4k)─O	2.009	2.033	2.112	2.235
Al (4k)─O	1.725	2.044	2.048	2.052
Al (4k)─O	1.878	1.919	1.969	1.999
Al (4k)─O	1.832	2.049	2.056	2.104
O─Al(2e)─O	122.38	84.74		
O─Al(2f)─O	133.27	103.46		
O─Al(2f)─O	133.21	88.20		
O─Al(2f)─O	116.92	108.80		
O─Al(4i)─O	109.81	108.82		
O─Al(8l)─O	117.40	101.09		
O─Al(8l)─O	107.53	106.30		
O─Al(4j)─O	179.08	94.57	89.18	
O─Al(4j)─O	176.93	93.72	90.61	
O─Al(4j)─O	175.57	99.83	89.78	
O─Al(4j)─O	177.81	91.44	89.54	
O─Al(4k)─O	171.88	97.91	94.05	90.33
O─Al(4k)─O	176.80	96.08	91.90	81.72
O─Al(4k)─O	178.42	94.40	93.22	87.46
O─Al(4k)─O	171.87	92.38	91.49	87.54
O─Al(4k)─O	178.10	95.08	91.37	86.79

900 °C Refinement:

Space group $P\bar{4}m2$, a = 5.618(3), c = 24.402(12), R_p = 3.10, χ^2 = 2.91, R_B = 2.09.

	Site	x	y	z	B(Å^2)	occupancy
	O (4*j*)	0.2394	0	0.1223	1.1	1.0
	O (4*j*)	0.2708	0	0.2922	1.1	1.0
	O (4*j*)	0.2430	0	0.4566	1.1	1.0
	O (4*j*)	0.2302	0	0.6214	1.1	1.0
	O (4*j*)	0.2298	0	0.7975	1.1	1.0
	O (4*j*)	0.2444	0	0.9575	1.1	1.0
	O (4*k*)	0.2394	0.5	0.1191	1.1	1.0
	O (4*k*)	0.2708	0.5	0.2951	1.1	1.0
	O (4*k*)	0.2430	0.5	0.4566	1.1	1.0
	O (4*k*)	0.2302	0.5	0.6214	1.1	1.0
	O (4*k*)	0.2298	0.5	0.7897	1.1	1.0
	O (4*k*)	0.2444	0.5	0.9575	1.1	1.0
T	Al (2*e*)	0	0	0.3300	0.8	0.375
T	Al (2*f*)	0.5	0.5	0.0882	0.8	0.5
T	Al (2*f*)	0.5	0.5	0.1816	0.8	1.0
T	Al (2*f*)	0.5	0.5	0.4200	0.8	1.0
T	Al (4*i*)	0.2518	0.2513	0.5	0.8	0.1875
T	Al (8*l*)	0.2588	0.2546	0.1703	0.8	0.5625
O	Al (4j)	0.2490	0	0.1987	0.8	0.5
O	Al (4j)	0.2457	0	0.3751	0.8	1.0
O	Al (4j)	0.2457	0	0.8810	0.8	0.6875
O	Al (4k)	0.2590	0.5	0.2108	0.8	0.625
O	Al (4k)	0.2506	0.5	0.3759	0.8	1.0
O	Al (4k)	0.2562	0.5	0.7106	0.8	1.0
O	Al (4k)	0.1353	0.5	0.0013	0.8	0.4375

Resulting cation distribution: 66(3) % octahedrally and 34(3) % tetrahedrally coordinated.

Aluminium – Oxygen bond lengths (Å) and angles (°) for the 900°C Refinement. The bottom half of the table reports the O-Al-O angles within each octahedra and tetrahedra. Repeat values for the distances and angles are only reported once.

Al(2e)─O	1.722	1.760		
Al (2f)─O	1.633	1.790		
Al (2f)─O	1.660	2.069		
Al (2f)─O	1.679	1.799		
Al (4i)─O	1.733			
Al (8l)─O	1.598	1.799	1.847	1.692
Al (4j)─O	1.789	1.905	1.931	2.192
Al (4j)─O	1.893	1.908	1.929	1.945
Al (4j)─O	1.813	1.962	1.928	1.933
Al (4k)─O	1.973	2.034	2.112	2.150
Al (4k)─O	1.758	2.028	2.078	2.074
Al (4k)─O	1.857	1.884	1.932	2.093
Al (4k)─O	1.194	1.889	2.366	2.681
O─Al(2e)─O	119.68	97.33		
O─Al(2f)─O	127.37	106.69		
O─Al(2f)─O	132.23	90.07		
O─Al(2f)─O	118.59	114.81		
O─Al(4i)─O	112.33	107.81		
O─Al(8l)─O	115.90	102.13		
O─Al(4j)─O	178.50	94.40	91.41	89.70
O─Al(4j)─O	176.29	94.60	87.20	
O─Al(4j)─O	178.61	92.56	89.54	86.48
O─Al(4k)─O	178.99	96.61	91.60	89.07
O─Al(4k)─O	177.49	98.08	93.65	85.25
O─Al(4k)─O	173.80	97.39	88.87	

Refinement results for neutron MRPD data of deuterated boehmite prepared hydrothermally from hydrogenated gibbsite and calcined *in situ*. All uncertainties, where not stated otherwise, are 0.005 for refinable coordinate positions, 0.3 for thermal parameters, 0.008 for distances, and 0.05 for angles.

750 °C Refinement:

Space group $P\bar{4}m2$, $a = 5.665(3)$, $c = 24.584(12)$, $R_p = 2.88$, $\chi^2 = 3.19$, $R_B = 1.09$.

	Site	x	y	z	B(Å^2)	occupancy
	O (4*j*)	0.2334	0	0.1214	1.5	1.0
	O (4*j*)	0.2621	0	0.2965	1.5	1.0
	O (4*j*)	0.2470	0	0.4572	1.5	1.0
	O (4*j*)	0.2342	0	0.6255	1.5	1.0
	O (4*j*)	0.2294	0	0.7982	1.5	1.0
	O (4*j*)	0.2548	0	0.9581	1.5	1.0
	O (4*k*)	0.2334	0.5	0.1157	1.5	1.0
	O (4*k*)	0.2621	0.5	0.2965	1.5	1.0
	O (4*k*)	0.2470	0.5	0.4572	1.5	1.0
	O (4*k*)	0.2342	0.5	0.6255	1.5	1.0
	O (4*k*)	0.2294	0.5	0.7904	1.5	1.0
	O (4*k*)	0.2548	0.5	0.9581	1.5	1.0
T	Al (2*e*)	0	0	0.2620	1.1	0.25
T	Al (2*f*)	0.5	0.5	0.0882	1.1	0.75
T	Al (2*f*)	0.5	0.5	0.1816	1.1	1.0
T	Al (2*f*)	0.5	0.5	0.4194	1.1	1.0
T	Al (4*i*)	0.2518	0.2513	0.5	1.1	0.25
T	Al (8*l*)	0.2590	0.2546	0.1703	1.1	0.375
T	Al (8*l*)	0.2510	0.2513	0.3297	1.1	0.125
O	Al (4*j*)	0.2490	0	0.1987	1.1	0.75
O	Al (4*j*)	0.2457	0	0.3751	1.1	1.0
O	Al (4*j*)	0.2530	0	0.5536	1.1	0.25
O	Al (4*j*)	0.2457	0	0.8811	1.1	0.5
O	Al (4*k*)	0.2680	0.5	0.0331	1.1	0.125
O	Al (4*k*)	0.2590	0.5	0.2108	1.1	0.5
O	Al (4*k*)	0.2506	0.5	0.3759	1.1	0.875
O	Al (4*k*)	0.2562	0.5	0.7106	1.1	1.0
O	Al (4*k*)	0.2512	0.5	0.8861	1.1	0.25

Resulting cation distribution: 66(3) % octahedrally and 34(3) % tetrahedrally coordinated.

Aluminium – Oxygen bond lengths (Å) and angles (°) for the 750°C Refinement. The bottom half of the table reports the O-Al-O angles within each octahedra and tetrahedra. Repeat values for the distances and angles are only reported once.

Al (2e)─O	1.678	1.910		
Al (2f)─O	1.630	1.752		
Al (2f)─O	1.654	2.150		
Al (2f)─O	1.666	1.834		
Al (4i)─O	1.725			
Al (8l)─O	1.590	1.682	1.813	1.901
Al (8l)─O	1.609	1.750		
Al (4j)─O	1.815	1.901	1.925	2.294
Al (4j)─O	1.846	1.905	1.924	1.940
Al (4j)─O	1.691	1.976	1.999	2.260
Al (4j)─O	1.833	1.902	1.921	1.939
Al (4k)─O	1.757	1.905	1.949	2.048
Al (4k)─O	2.009	2.033	2.112	2.235
Al (4k)─O	1.725	2.044	2.048	2.052
Al (4k)─O	1.878	1.919	1.969	1.999
Al (4k)─O	1.832	2.049	2.056	2.104
O─Al(2e)─O	122.38	84.74		
O─Al(2f)─O	133.27	103.46		
O─Al(2f)─O	133.21	88.20		
O─Al(2f)─O	116.92	108.80		
O─Al(4i)─O	109.81	108.82		
O─Al(8l)─O	117.40	101.09		
O─Al(8l)─O	107.53	106.30		
O─Al(4j)─O	179.08	94.57	89.18	
O─Al(4j)─O	176.93	93.72	90.61	
O─Al(4j)─O	175.57	99.83	89.78	
O─Al(4j)─O	177.81	91.44	89.54	
O─Al(4k)─O	171.88	97.91	94.05	90.33
O─Al(4k)─O	176.80	96.08	91.90	81.72
O─Al(4k)─O	178.42	94.40	93.22	87.46
O─Al(4k)─O	171.87	92.38	91.49	87.54
O─Al(4k)─O	178.10	95.08	91.37	86.79

Appendix IV

Supercell Coordinates Cubic and Tetragonal γ-Alumina Systems

Tetragonal 1×1×3 supercell for the cubic $Fd\bar{3}m$ system

Oxygen Coordinates

First Third of Supercell			*Second Third of Supercell*			*Final Third of Supercell*		
0.255	0.255	0.085	0.255	0.255	0.418	0.255	0.255	0.752
0.495	0.995	0.252	0.495	0.995	0.585	0.495	0.995	0.918
0.995	0.755	0.165	0.995	0.755	0.498	0.995	0.755	0.832
0.755	0.495	0.332	0.755	0.495	0.665	0.755	0.495	0.998
0.005	0.505	0.082	0.005	0.505	0.415	0.005	0.505	0.748
0.745	0.745	0.248	0.745	0.745	0.582	0.745	0.745	0.915
0.505	0.245	0.002	0.505	0.245	0.335	0.505	0.245	0.668
0.245	0.005	0.168	0.245	0.005	0.502	0.245	0.005	0.835
0.255	0.755	0.252	0.255	0.755	0.585	0.255	0.755	0.918
0.495	0.495	0.085	0.495	0.495	0.418	0.495	0.495	0.752
0.995	0.255	0.332	0.995	0.255	0.665	0.995	0.255	0.998
0.755	0.995	0.165	0.755	0.995	0.498	0.755	0.995	0.832
0.005	0.005	0.248	0.005	0.005	0.582	0.005	0.005	0.915
0.745	0.245	0.082	0.745	0.245	0.415	0.745	0.245	0.748
0.505	0.745	0.168	0.505	0.745	0.502	0.505	0.745	0.835
0.245	0.505	0.002	0.245	0.505	0.335	0.245	0.505	0.668
0.755	0.255	0.252	0.755	0.255	0.585	0.755	0.255	0.918
0.995	0.995	0.085	0.995	0.995	0.418	0.995	0.995	0.752
0.495	0.755	0.332	0.495	0.755	0.665	0.495	0.755	0.998
0.255	0.495	0.165	0.255	0.495	0.498	0.255	0.495	0.832
0.505	0.505	0.248	0.505	0.505	0.582	0.505	0.505	0.915
0.245	0.745	0.082	0.245	0.745	0.415	0.245	0.745	0.748
0.005	0.245	0.168	0.005	0.245	0.502	0.005	0.245	0.835
0.745	0.005	0.002	0.745	0.005	0.335	0.745	0.005	0.668
0.755	0.755	0.085	0.755	0.755	0.418	0.755	0.755	0.752
0.995	0.495	0.252	0.995	0.495	0.585	0.995	0.495	0.918
0.495	0.255	0.165	0.495	0.255	0.498	0.495	0.255	0.832
0.255	0.995	0.332	0.255	0.995	0.665	0.255	0.995	0.998
0.505	0.005	0.082	0.505	0.005	0.415	0.505	0.005	0.748
0.245	0.245	0.248	0.245	0.245	0.582	0.245	0.245	0.915
0.005	0.745	0.002	0.005	0.745	0.335	0.005	0.745	0.668
0.745	0.505	0.168	0.745	0.505	0.502	0.745	0.505	0.835

Possible Aluminium *8a* Coordinates

First Third of Supercell				*Second Third of Supercell*				*Final Third of Supercell*			
a01a	0.125	0.125	0.042	***a01b***	0.125	0.125	0.375	***a01c***	0.125	0.125	0.708
a02a	0.875	0.375	0.125	***a02b***	0.875	0.375	0.458	***a02c***	0.875	0.375	0.792
a03a	0.125	0.625	0.208	***a03b***	0.125	0.625	0.542	***a03c***	0.125	0.625	0.875
a04a	0.875	0.875	0.292	***a04b***	0.875	0.875	0.625	***a04c***	0.875	0.875	0.958
a05a	0.625	0.125	0.208	***a05b***	0.625	0.125	0.542	***a05c***	0.625	0.125	0.875
a06a	0.375	0.375	0.292	***a06b***	0.375	0.375	0.625	***a06c***	0.375	0.375	0.958
a07a	0.625	0.625	0.042	***a07b***	0.625	0.625	0.375	***a07c***	0.625	0.625	0.708
a08a	0.375	0.875	0.125	***a08b***	0.375	0.875	0.458	***a08c***	0.375	0.875	0.792

Possible Aluminium *8b* Coordinates

First Third of Supercell				*Second Third of Supercell*				*Final Third of Supercell*			
b01a	0.375	0.375	0.125	***b01b***	0.375	0.375	0.458	***b01c***	0.375	0.375	0.792
b02a	0.125	0.625	0.042	***b02b***	0.125	0.625	0.375	***b02c***	0.125	0.625	0.708
b03a	0.375	0.875	0.292	***b03b***	0.375	0.875	0.625	***b03c***	0.375	0.875	0.958
b04a	0.125	0.125	0.208	***b04b***	0.125	0.125	0.542	***b04c***	0.125	0.125	0.875
b05a	0.875	0.375	0.292	***b05b***	0.875	0.375	0.625	***b05c***	0.875	0.375	0.958
b06a	0.625	0.625	0.208	***b06b***	0.625	0.625	0.542	***b06c***	0.625	0.625	0.875
b07a	0.875	0.875	0.125	***b07b***	0.875	0.875	0.458	***b07c***	0.875	0.875	0.792
b08a	0.625	0.125	0.042	***b08b***	0.625	0.125	0.375	***b08c***	0.625	0.125	0.708

Possible Aluminium *16c* Coordinates

First Third of Supercell				*Second Third of Supercell*				*Final Third of Supercell*			
c01a	0.000	0.000	0.000	***c01b***	0.000	0.000	0.333	***c01c***	0.000	0.000	0.667
c02a	0.750	0.250	0.167	***c02b***	0.750	0.250	0.500	***c02c***	0.750	0.250	0.833
c03a	0.250	0.500	0.250	***c03b***	0.250	0.500	0.583	***c03c***	0.250	0.500	0.917
c04a	0.500	0.750	0.083	***c04b***	0.500	0.750	0.417	***c04c***	0.500	0.750	0.750
c05a	0.000	0.500	0.167	***c05b***	0.000	0.500	0.500	***c05c***	0.000	0.500	0.833
c06a	0.750	0.750	0.333	***c06b***	0.750	0.750	0.667	***c06c***	0.750	0.750	1.000
c07a	0.250	0.000	0.417	***c07b***	0.250	0.000	0.750	***c07c***	0.250	0.000	1.083
c08a	0.500	0.250	0.250	***c08b***	0.500	0.250	0.583	***c08c***	0.500	0.250	0.917
c09a	0.500	0.000	0.167	***c09b***	0.500	0.000	0.500	***c09c***	0.500	0.000	0.833
c10a	0.250	0.250	0.333	***c10b***	0.250	0.250	0.667	***c10c***	0.250	0.250	1.000
c11a	0.750	0.500	0.417	***c11b***	0.750	0.500	0.750	***c11c***	0.750	0.500	1.083
c12a	0.000	0.750	0.250	***c12b***	0.000	0.750	0.583	***c12c***	0.000	0.750	0.917
c13a	0.500	0.500	0.000	***c13b***	0.500	0.500	0.333	***c13c***	0.500	0.500	0.667
c14a	0.250	0.750	0.167	***c14b***	0.250	0.750	0.500	***c14c***	0.250	0.750	0.833
c15a	0.750	0.000	0.250	***c15b***	0.750	0.000	0.583	***c15c***	0.750	0.000	0.917
c16a	0.000	0.250	0.083	***c16b***	0.000	0.250	0.417	***c16c***	0.000	0.250	0.750

Possible Aluminium *16d* Coordinates

First Third of Supercell				*Second Third of Supercell*				*Final Third of Supercell*			
d01a	0.500	0.500	0.167	***d01b***	0.500	0.500	0.500	***d01c***	0.500	0.500	0.833
d02a	0.250	0.750	0.000	***d02b***	0.250	0.750	0.333	***d02c***	0.250	0.750	0.667
d03a	0.750	0.000	0.083	***d03b***	0.750	0.000	0.417	***d03c***	0.750	0.000	0.750
d04a	0.000	0.250	0.250	***d04b***	0.000	0.250	0.583	***d04c***	0.000	0.250	0.917
d05a	0.500	0.000	0.000	***d05b***	0.500	0.000	0.333	***d05c***	0.500	0.000	0.667
d06a	0.250	0.250	0.167	***d06b***	0.250	0.250	0.500	***d06c***	0.250	0.250	0.833
d07a	0.750	0.500	0.250	***d07b***	0.750	0.500	0.583	***d07c***	0.750	0.500	0.917
d08a	0.000	0.750	0.083	***d08b***	0.000	0.750	0.417	***d08c***	0.000	0.750	0.750
d09a	0.000	0.500	0.000	***d09b***	0.000	0.500	0.333	***d09c***	0.000	0.500	0.667
d10a	0.750	0.750	0.167	***d10b***	0.750	0.750	0.500	***d10c***	0.750	0.750	0.833
d11a	0.250	0.000	0.250	***d11b***	0.250	0.000	0.583	***d11c***	0.250	0.000	0.917
d12a	0.500	0.250	0.083	***d12b***	0.500	0.250	0.417	***d12c***	0.500	0.250	0.750
d13a	0.000	0.000	0.167	***d13b***	0.000	0.000	0.500	***d13c***	0.000	0.000	0.833
d14a	0.750	0.250	0.000	***d14b***	0.750	0.250	0.333	***d14c***	0.750	0.250	0.667
d15a	0.250	0.500	0.083	***d15b***	0.250	0.500	0.417	***d15c***	0.250	0.500	0.750
d16a	0.500	0.750	0.250	***d16b***	0.500	0.750	0.583	***d16c***	0.500	0.750	0.917

Possible Aluminium *48f* Coordinates

First Third of Supercell				*Second Third of Supercell*				*Final Third of Supercell*			
f01a	0.375	0.125	0.042	***f01b***	0.375	0.125	0.375	***f01c***	0.375	0.125	0.708
f02a	0.375	0.125	0.208	***f02b***	0.375	0.125	0.542	***f02c***	0.375	0.125	0.875
f03a	0.125	0.375	0.042	***f03b***	0.125	0.375	0.375	***f03c***	0.125	0.375	0.708
f04a	0.625	0.375	0.042	***f04b***	0.625	0.375	0.375	***f04c***	0.625	0.375	0.708
f05a	0.125	0.125	0.125	***f05b***	0.125	0.125	0.458	***f05c***	0.125	0.125	0.792
f06a	0.125	0.625	0.125	***f06b***	0.125	0.625	0.458	***f06c***	0.125	0.625	0.792
f07a	0.875	0.625	0.125	***f07b***	0.875	0.625	0.458	***f07c***	0.875	0.625	0.792
f08a	0.875	0.625	0.292	***f08b***	0.875	0.625	0.625	***f08c***	0.875	0.625	0.958
f09a	0.125	0.375	0.125	***f09b***	0.125	0.375	0.458	***f09c***	0.125	0.375	0.792
f10a	0.125	0.875	0.125	***f10b***	0.125	0.875	0.458	***f10c***	0.125	0.875	0.792
f11a	0.875	0.375	0.042	***f11b***	0.875	0.375	0.375	***f11c***	0.875	0.375	0.708
f12a	0.375	0.375	0.042	***f12b***	0.375	0.375	0.375	***f12c***	0.375	0.375	0.708
f13a	0.375	0.625	0.208	***f13b***	0.375	0.625	0.542	***f13c***	0.375	0.625	0.875
f14a	0.375	0.625	0.042	***f14b***	0.375	0.625	0.375	***f14c***	0.375	0.625	0.708
f15a	0.125	0.875	0.208	***f15b***	0.125	0.875	0.542	***f15c***	0.125	0.875	0.875
f16a	0.625	0.875	0.208	***f16b***	0.625	0.875	0.542	***f16c***	0.625	0.875	0.875
f17a	0.125	0.625	0.292	***f17b***	0.125	0.625	0.625	***f17c***	0.125	0.625	0.958
f18a	0.125	0.125	0.292	***f18b***	0.125	0.125	0.625	***f18c***	0.125	0.125	0.958
f19a	0.875	0.125	0.292	***f19b***	0.875	0.125	0.625	***f19c***	0.875	0.125	0.958
f20a	0.875	0.125	0.125	***f20b***	0.875	0.125	0.458	***f20c***	0.875	0.125	0.792
f21a	0.125	0.875	0.292	***f21b***	0.125	0.875	0.625	***f21c***	0.125	0.875	0.958
f22a	0.125	0.375	0.292	***f22b***	0.125	0.375	0.625	***f22c***	0.125	0.375	0.958
f23a	0.875	0.875	0.208	***f23b***	0.875	0.875	0.542	***f23c***	0.875	0.875	0.875
f24a	0.375	0.875	0.208	***f24b***	0.375	0.875	0.542	***f24c***	0.375	0.875	0.875
f25a	0.875	0.125	0.208	***f25b***	0.875	0.125	0.542	***f25c***	0.875	0.125	0.875
f26a	0.875	0.125	0.042	***f26b***	0.875	0.125	0.375	***f26c***	0.875	0.125	0.708
f27a	0.625	0.375	0.208	***f27b***	0.625	0.375	0.542	***f27c***	0.625	0.375	0.875
f28a	0.125	0.375	0.208	***f28b***	0.125	0.375	0.542	***f28c***	0.125	0.375	0.875
f29a	0.625	0.125	0.292	***f29b***	0.625	0.125	0.625	***f29c***	0.625	0.125	0.958
f30a	0.625	0.625	0.292	***f30b***	0.625	0.625	0.625	***f30c***	0.625	0.625	0.958
f31a	0.375	0.625	0.292	***f31b***	0.375	0.625	0.625	***f31c***	0.375	0.625	0.958
f32a	0.375	0.625	0.125	***f32b***	0.375	0.625	0.458	***f32c***	0.375	0.625	0.792
f33a	0.625	0.375	0.292	***f33b***	0.625	0.375	0.625	***f33c***	0.625	0.375	0.958
f34a	0.625	0.875	0.292	***f34b***	0.625	0.875	0.625	***f34c***	0.625	0.875	0.958
f35a	0.375	0.375	0.208	***f35b***	0.375	0.375	0.542	***f35c***	0.375	0.375	0.875
f36a	0.875	0.375	0.208	***f36b***	0.875	0.375	0.542	***f36c***	0.875	0.375	0.875
f37a	0.875	0.625	0.042	***f37b***	0.875	0.625	0.375	***f37c***	0.875	0.625	0.708
f38a	0.875	0.625	0.208	***f38b***	0.875	0.625	0.542	***f38c***	0.875	0.625	0.875
f39a	0.625	0.875	0.042	***f39b***	0.625	0.875	0.375	***f39c***	0.625	0.875	0.708
f40a	0.125	0.875	0.042	***f40b***	0.125	0.875	0.375	***f40c***	0.125	0.875	0.708
f41a	0.625	0.625	0.125	***f41b***	0.625	0.625	0.458	***f41c***	0.625	0.625	0.792
f42a	0.625	0.125	0.125	***f42b***	0.625	0.125	0.458	***f42c***	0.625	0.125	0.792
f43a	0.375	0.125	0.125	***f43b***	0.375	0.125	0.458	***f43c***	0.375	0.125	0.792
f44a	0.375	0.125	0.292	***f44b***	0.375	0.125	0.625	***f44c***	0.375	0.125	0.958
f45a	0.625	0.875	0.125	***f45b***	0.625	0.875	0.458	***f45c***	0.625	0.875	0.792
f46a	0.625	0.375	0.125	***f46b***	0.625	0.375	0.458	***f46c***	0.625	0.375	0.792
f47a	0.375	0.875	0.042	***f47b***	0.375	0.875	0.375	***f47c***	0.375	0.875	0.708
f48a	0.875	0.875	0.042	***f48b***	0.875	0.875	0.375	***f48c***	0.875	0.875	0.708

Orthorhombic 2×1×3 supercell for the tetragonal $I4_1/amd$ system

Oxygen Coordinates

First sixth of Supercell			*Second sixth of Supercell*			*Third sixth of Supercell*		
0.000	0.000	0.083	0.500	0.000	0.083	0.000	0.000	0.417
0.250	0.000	0.250	0.750	0.000	0.250	0.250	0.000	0.583
0.125	0.750	0.167	0.625	0.750	0.167	0.125	0.750	0.500
0.125	0.250	0.000	0.625	0.250	0.000	0.125	0.250	0.333
0.250	0.000	0.083	0.750	0.000	0.083	0.250	0.000	0.417
0.000	0.000	0.250	0.500	0.000	0.250	0.000	0.000	0.583
0.125	0.750	0.000	0.625	0.750	0.000	0.125	0.750	0.333
0.125	0.250	0.167	0.625	0.250	0.167	0.125	0.250	0.500
0.250	0.500	0.250	0.750	0.500	0.250	0.250	0.500	0.583
0.000	0.500	0.083	0.500	0.500	0.083	0.000	0.500	0.417
0.375	0.250	0.000	0.875	0.250	0.000	0.375	0.250	0.333
0.375	0.750	0.167	0.875	0.750	0.167	0.375	0.750	0.500
0.000	0.500	0.250	0.500	0.500	0.250	0.000	0.500	0.583
0.250	0.500	0.083	0.750	0.500	0.083	0.250	0.500	0.417
0.375	0.250	0.167	0.875	0.250	0.167	0.375	0.250	0.500
0.375	0.750	0.000	0.875	0.750	0.000	0.375	0.750	0.333

Fourth sixth of Supercell			*Fifth sixth of Supercell*			*Final sixth of Supercell*		
0.500	0.000	0.417	0.000	0.000	0.750	0.500	0.000	0.750
0.750	0.000	0.583	0.250	0.000	0.917	0.750	0.000	0.917
0.625	0.750	0.500	0.125	0.750	0.833	0.625	0.750	0.833
0.625	0.250	0.333	0.125	0.250	0.667	0.625	0.250	0.667
0.750	0.000	0.417	0.250	0.000	0.750	0.750	0.000	0.750
0.500	0.000	0.583	0.000	0.000	0.917	0.500	0.000	0.917
0.625	0.750	0.333	0.125	0.750	0.667	0.625	0.750	0.667
0.625	0.250	0.500	0.125	0.250	0.833	0.625	0.250	0.833
0.750	0.500	0.583	0.250	0.500	0.917	0.750	0.500	0.917
0.500	0.500	0.417	0.000	0.500	0.750	0.500	0.500	0.750
0.875	0.250	0.333	0.375	0.250	0.667	0.875	0.250	0.667
0.875	0.750	0.500	0.375	0.750	0.833	0.875	0.750	0.833
0.500	0.500	0.583	0.000	0.500	0.917	0.500	0.500	0.917
0.750	0.500	0.417	0.250	0.500	0.750	0.750	0.500	0.750
0.875	0.250	0.500	0.375	0.250	0.833	0.875	0.250	0.833
0.875	0.750	0.333	0.375	0.750	0.667	0.875	0.750	0.667

Possible Aluminium *4a* Coordinates

First sixth of Supercell				*Second sixth of Supercell*				*Third sixth of Supercell*			
a1aa	0.000	0.750	0.042	***a1ab***	0.500	0.750	0.042	***a1ba***	0.000	0.750	0.375
a2aa	0.250	0.750	0.125	***a2ab***	0.750	0.750	0.125	***a2ba***	0.250	0.750	0.458
a3aa	0.250	0.250	0.208	***a3ab***	0.750	0.250	0.208	***a3ba***	0.250	0.250	0.542
a4aa	0.000	0.250	0.292	***a4ab***	0.500	0.250	0.292	***a4ba***	0.000	0.250	0.625

Fourth sixth of Supercell				*Fifth sixth of Supercell*				*Final sixth of Supercell*			
a1bb	0.500	0.750	0.375	***a1ca***	0.000	0.750	0.708	***a1cb***	0.500	0.750	0.708
a2bb	0.750	0.750	0.458	***a2ca***	0.250	0.750	0.792	***a2cb***	0.750	0.750	0.792
a3bb	0.750	0.250	0.542	***a3ca***	0.250	0.250	0.875	***a3cb***	0.750	0.250	0.875
a4bb	0.500	0.250	0.625	***a4ca***	0.000	0.250	0.958	***a4cb***	0.500	0.250	0.958

Possible Aluminium *4b* Coordinates

First sixth of Supercell				*Second sixth of Supercell*				*Third sixth of Supercell*			
b1aa	0.000	0.250	0.125	***b1ab***	0.500	0.250	0.125	***b1ba***	0.000	0.250	0.458
b2aa	0.000	0.750	0.208	***b2ab***	0.500	0.750	0.208	***b2ba***	0.000	0.750	0.542
b3aa	0.250	0.750	0.292	***b3ab***	0.750	0.750	0.292	***b3ba***	0.250	0.750	0.625
b4aa	0.250	0.250	0.042	***b4ab***	0.750	0.250	0.042	***b4ba***	0.250	0.250	0.375

Fourth sixth of Supercell				*Fifth sixth of Supercell*				*Final sixth of Supercell*			
b1bb	0.500	0.250	0.458	***b1ca***	0.000	0.250	0.792	***b1cb***	0.500	0.250	0.792
b2bb	0.500	0.750	0.542	***b2ca***	0.000	0.750	0.875	***b2cb***	0.500	0.750	0.875
b3bb	0.750	0.750	0.625	***b3ca***	0.250	0.750	0.958	***b3cb***	0.750	0.750	0.958
b4bb	0.750	0.250	0.375	***b4ca***	0.250	0.250	0.708	***b4cb***	0.750	0.250	0.708

Possible Aluminium *8c* Coordinates

First sixth of Supercell				*Second sixth of Supercell*				*Third sixth of Supercell*			
c1aa	0.000	0.000	0.000	***c1ab***	0.500	0.000	0.000	***c1ba***	0.000	0.000	0.333
c2aa	0.250	0.000	0.167	***c2ab***	0.750	0.000	0.167	***c2ba***	0.250	0.000	0.500
c3aa	0.125	0.750	0.083	***c3ab***	0.625	0.750	0.083	***c3ba***	0.125	0.750	0.417
c4aa	0.125	0.250	0.250	***c4ab***	0.625	0.250	0.250	***c4ba***	0.125	0.250	0.583
c5aa	0.250	0.500	0.167	***c5ab***	0.750	0.500	0.167	***c5ba***	0.250	0.500	0.500
c6aa	0.000	0.500	0.000	***c6ab***	0.500	0.500	0.000	***c6ba***	0.000	0.500	0.333
c7aa	0.375	0.250	0.250	***c7ab***	0.875	0.250	0.250	***c7ba***	0.375	0.250	0.583
c8aa	0.375	0.750	0.083	***c8ab***	0.875	0.750	0.083	***c8ba***	0.375	0.750	0.417

Fourth sixth of Supercell				*Fifth sixth of Supercell*				*Final sixth of Supercell*			
c1bb	0.500	0.000	0.333	***c1ca***	0.000	0.000	0.667	***c1cb***	0.500	0.000	0.667
c2bb	0.750	0.000	0.500	***c2ca***	0.250	0.000	0.833	***c2cb***	0.750	0.000	0.833
c3bb	0.625	0.750	0.417	***c3ca***	0.125	0.750	0.750	***c3cb***	0.625	0.750	0.750
c4bb	0.625	0.250	0.583	***c4ca***	0.125	0.250	0.917	***c4cb***	0.625	0.250	0.917
c5bb	0.750	0.500	0.500	***c5ca***	0.250	0.500	0.833	***c5cb***	0.750	0.500	0.833
c6bb	0.500	0.500	0.333	***c6ca***	0.000	0.500	0.667	***c6cb***	0.500	0.500	0.667
c7bb	0.875	0.250	0.583	***c7ca***	0.375	0.250	0.917	***c7cb***	0.875	0.250	0.917
c8bb	0.875	0.750	0.417	***c8ca***	0.375	0.750	0.750	***c8cb***	0.875	0.750	0.750

Possible Aluminium *8d* Coordinates

First sixth of Supercell				*Second sixth of Supercell*				*Third sixth of Supercell*			
d1aa	0.000	0.000	0.167	***d1ab***	0.500	0.000	0.167	***d1ba***	0.000	0.000	0.500
d2aa	0.250	0.000	0.000	***d2ab***	0.750	0.000	0.000	***d2ba***	0.250	0.000	0.333
d3aa	0.125	0.750	0.250	***d3ab***	0.625	0.750	0.250	***d3ba***	0.125	0.750	0.583
d4aa	0.125	0.250	0.083	***d4ab***	0.625	0.250	0.083	***d4ba***	0.125	0.250	0.417
d5aa	0.250	0.500	0.000	***d5ab***	0.750	0.500	0.000	***d5ba***	0.250	0.500	0.333
d6aa	0.000	0.500	0.167	***d6ab***	0.500	0.500	0.167	***d6ba***	0.000	0.500	0.500
d7aa	0.375	0.250	0.083	***d7ab***	0.875	0.250	0.083	***d7ba***	0.375	0.250	0.417
d8aa	0.375	0.750	0.250	***d8ab***	0.875	0.750	0.250	***d8ba***	0.375	0.750	0.583

Fourth sixth of Supercell				*Fifth sixth of Supercell*				*Final sixth of Supercell*			
d1bb	0.500	0.000	0.500	***d1ca***	0.000	0.000	0.833	***d1cb***	0.500	0.000	0.833
d2bb	0.750	0.000	0.333	***d2ca***	0.250	0.000	0.667	***d2cb***	0.750	0.000	0.667
d3bb	0.625	0.750	0.583	***d3ca***	0.125	0.750	0.917	***d3cb***	0.625	0.750	0.917
d4bb	0.625	0.250	0.417	***d4ca***	0.125	0.250	0.750	***d4cb***	0.625	0.250	0.750
d5bb	0.750	0.500	0.333	***d5ca***	0.250	0.500	0.667	***d5cb***	0.750	0.500	0.667
d6bb	0.500	0.500	0.500	***d6ca***	0.000	0.500	0.833	***d6cb***	0.500	0.500	0.833
d7bb	0.875	0.250	0.417	***d7ca***	0.375	0.250	0.750	***d7cb***	0.875	0.250	0.750
d8bb	0.875	0.750	0.583	***d8ca***	0.375	0.750	0.917	***d8cb***	0.875	0.750	0.917

Possible Aluminium *8e* Coordinates

First sixth of Supercell				*Second sixth of Supercell*				*Third sixth of Supercell*			
e1aa	0.000	0.250	0.042	***e1ab***	0.500	0.250	0.042	***e1ba***	0.000	0.250	0.375
e2aa	0.000	0.750	0.125	***e2ab***	0.500	0.750	0.125	***e2ba***	0.000	0.750	0.458
e3aa	0.250	0.250	0.042	***e3ab***	0.750	0.250	0.042	***e3ba***	0.250	0.250	0.375
e4aa	0.250	0.750	0.042	***e4ab***	0.750	0.750	0.042	***e4ba***	0.250	0.750	0.375
e5aa	0.250	0.750	0.208	***e5ab***	0.750	0.750	0.208	***e5ba***	0.250	0.750	0.542
e6aa	0.250	0.250	0.292	***e6ab***	0.750	0.250	0.292	***e6ba***	0.250	0.250	0.625
e7aa	0.000	0.750	0.208	***e7ab***	0.500	0.750	0.208	***e7ba***	0.000	0.750	0.542
e8aa	0.000	0.250	0.208	***e8ab***	0.500	0.250	0.208	***e8ba***	0.000	0.250	0.542

Fourth sixth of Supercell				*Fifth sixth of Supercell*				*Final sixth of Supercell*			
e1bb	0.500	0.250	0.375	***e1ca***	0.000	0.250	0.708	***e1cb***	0.500	0.250	0.708
e2bb	0.500	0.750	0.458	***e2ca***	0.000	0.750	0.792	***e2cb***	0.500	0.750	0.792
e3bb	0.750	0.250	0.375	***e3ca***	0.250	0.250	0.708	***e3cb***	0.750	0.250	0.708
e4bb	0.750	0.750	0.375	***e4ca***	0.250	0.750	0.708	***e4cb***	0.750	0.750	0.708
e5bb	0.750	0.750	0.542	***e5ca***	0.250	0.750	0.875	***e5cb***	0.750	0.750	0.875
e6bb	0.750	0.250	0.625	***e6ca***	0.250	0.250	0.958	***e6cb***	0.750	0.250	0.958
e7bb	0.500	0.750	0.542	***e7ca***	0.000	0.750	0.875	***e7cb***	0.500	0.750	0.875
e8bb	0.500	0.250	0.542	***e8ca***	0.000	0.250	0.875	***e8cb***	0.500	0.250	0.875

Possible Aluminium *16g* Coordinates

First sixth of Supercell				*Second sixth of Supercell*				*Third sixth of Supercell*			
g01aa	0.125	0.500	0.292	***g01ab***	0.625	0.500	0.292	***g01ba***	0.125	0.500	0.625
g02aa	0.125	0.500	0.125	***g02ab***	0.625	0.500	0.125	***g02ba***	0.125	0.500	0.458
g03aa	0.375	0.000	0.042	***g03ab***	0.875	0.000	0.042	***g03ba***	0.375	0.000	0.375
g04aa	0.375	0.000	0.208	***g04ab***	0.875	0.000	0.208	***g04ba***	0.375	0.000	0.542
g05aa	0.375	0.500	0.042	***g05ab***	0.875	0.500	0.042	***g05ba***	0.375	0.500	0.375
g06aa	0.375	0.500	0.208	***g06ab***	0.875	0.500	0.208	***g06ba***	0.375	0.500	0.542
g07aa	0.125	0.000	0.292	***g07ab***	0.625	0.000	0.292	***g07ba***	0.125	0.000	0.625
g08aa	0.125	0.000	0.125	***g08ab***	0.625	0.000	0.125	***g08ba***	0.125	0.000	0.458
g09aa	0.375	0.000	0.125	***g09ab***	0.875	0.000	0.125	***g09ba***	0.375	0.000	0.458
g10aa	0.375	0.000	0.292	***g10ab***	0.875	0.000	0.292	***g10ba***	0.375	0.000	0.625
g11aa	0.125	0.500	0.208	***g11ab***	0.625	0.500	0.208	***g11ba***	0.125	0.500	0.542
g12aa	0.125	0.500	0.042	***g12ab***	0.625	0.500	0.042	***g12ba***	0.125	0.500	0.375
g13aa	0.125	0.000	0.208	***g13ab***	0.625	0.000	0.208	***g13ba***	0.125	0.000	0.542
g14aa	0.125	0.000	0.042	***g14ab***	0.625	0.000	0.042	***g14ba***	0.125	0.000	0.375
g15aa	0.375	0.500	0.125	***g15ab***	0.875	0.500	0.125	***g15ba***	0.375	0.500	0.458
g16aa	0.375	0.500	0.292	***g16ab***	0.875	0.500	0.292	***g16ba***	0.375	0.500	0.625

Fourth sixth of Supercell				*Fifth sixth of Supercell*				*Final sixth of Supercell*			
g01bb	0.625	0.500	0.625	***g01ca***	0.125	0.500	0.958	***g01cb***	0.625	0.500	0.958
g02bb	0.625	0.500	0.458	***g02ca***	0.125	0.500	0.792	***g02cb***	0.625	0.500	0.792
g03bb	0.875	0.000	0.375	***g03ca***	0.375	0.000	0.708	***g03cb***	0.875	0.000	0.708
g04bb	0.875	0.000	0.542	***g04ca***	0.375	0.000	0.875	***g04cb***	0.875	0.000	0.875
g05bb	0.875	0.500	0.375	***g05ca***	0.375	0.500	0.708	***g05cb***	0.875	0.500	0.708
g06bb	0.875	0.500	0.542	***g06ca***	0.375	0.500	0.875	***g06cb***	0.875	0.500	0.875
g07bb	0.625	0.000	0.625	***g07ca***	0.125	0.000	0.958	***g07cb***	0.625	0.000	0.958
g08bb	0.625	0.000	0.458	***g08ca***	0.125	0.000	0.792	***g08cb***	0.625	0.000	0.792
g09bb	0.875	0.000	0.458	***g09ca***	0.375	0.000	0.792	***g09cb***	0.875	0.000	0.792
g10bb	0.875	0.000	0.625	***g10ca***	0.375	0.000	0.958	***g10cb***	0.875	0.000	0.958
g11bb	0.625	0.500	0.542	***g11ca***	0.125	0.500	0.875	***g11cb***	0.625	0.500	0.875
g12bb	0.625	0.500	0.375	***g12ca***	0.125	0.500	0.708	***g12cb***	0.625	0.500	0.708
g13bb	0.625	0.000	0.542	***g13ca***	0.125	0.000	0.875	***g13cb***	0.625	0.000	0.875
g14bb	0.625	0.000	0.375	***g14ca***	0.125	0.000	0.708	***g14cb***	0.625	0.000	0.708
g15bb	0.875	0.500	0.458	***g15ca***	0.375	0.500	0.792	***g15cb***	0.875	0.500	0.792
g16bb	0.875	0.500	0.625	***g16ca***	0.375	0.500	0.958	***g16cb***	0.875	0.500	0.958

Appendix V

Nearest Neighbour Site Positions Determined for Selection Criteria of Cubic and Tetragonal γ-Alumina Systems

Cubic $Fd\bar{3}m$ system

Nearest neighbour tetrahedral *8c* site positions to each individual tetrahedral *8c* position (*tet-tet*)

First Third of Supercell				
Site Position	***Nearest Neighbour Site positions***			
a01a	*a02a*	*a08a*	*a04c*	*a06c*
a02a	*a01a*	*a03a*	*a05a*	*a07a*
a03a	*a02a*	*a04a*	*a06a*	*a08a*
a04a	*a03a*	*a05a*	*a01b*	*a07b*
a05a	*a02a*	*a04a*	*a06a*	*a08a*
a06a	*a03a*	*a05a*	*a01b*	*a07b*
a07a	*a02a*	*a08a*	*a04c*	*a06c*
a08a	*a01a*	*a03a*	*a05a*	*a07a*

Second Third of Supercell				
Site Position	***Nearest Neighbour Site positions***			
a01b	*a04a*	*a06a*	*a02b*	*a08b*
a02b	*a01b*	*a03b*	*a05b*	*a07b*
a03b	*a02b*	*a04b*	*a06b*	*a08b*
a04b	*a03b*	*a05b*	*a01c*	*a07c*
a05b	*a02b*	*a04b*	*a06b*	*a08b*
a06b	*a03b*	*a05b*	*a01c*	*a07c*
a07b	*a04a*	*a06a*	*a02b*	*a08b*
a08b	*a01b*	*a03b*	*a05b*	*a07b*

Second Third of Supercell				
Site Position	***Nearest Neighbour Site positions***			
a01c	*a04b*	*a06b*	*a02c*	*a08c*
a02c	*a01c*	*a03c*	*a05c*	*a07c*
a03c	*a02c*	*a04c*	*a06c*	*a08c*
a04c	*a01a*	*a07a*	*a03c*	*a05c*
a05c	*a02c*	*a04c*	*a06c*	*a08c*
a06c	*a01a*	*a07a*	*a03c*	*a05c*
a07c	*a04b*	*a06b*	*a02c*	*a08c*
a08c	*a01c*	*a03c*	*a05c*	*a07c*

Nearest neighbour octahedral *16d* site positions to each individual octahedral *16d* position (*oct-oct*)

First Third of Supercell						
Site Position	***Nearest Neighbour Site positions***					
d01a	*d06a*	*d07a*	*d10a*	*d12a*	*d15a*	*d16a*
d02a	*d05a*	*d08a*	*d09a*	*d15a*	*d11c*	*d16c*
d03a	*d05a*	*d08a*	*d10a*	*d12a*	*d13a*	*d14a*
d04a	*d06a*	*d07a*	*d11a*	*d13a*	*d09b*	*d14b*
d05a	*d02a*	*d03a*	*d12a*	*d14a*	*d11c*	*d16c*
d06a	*d01a*	*d04a*	*d11a*	*d12a*	*d13a*	*d15a*
d07a	*d01a*	*d04a*	*d10a*	*d16a*	*d09b*	*d14b*
d08a	*d02a*	*d03a*	*d09a*	*d10a*	*d13a*	*d15a*
d09a	*d02a*	*d08a*	*d14a*	*d15a*	*d04c*	*d07c*
d10a	*d01a*	*d03a*	*d07a*	*d08a*	*d13a*	*d16a*
d11a	*d04a*	*d06a*	*d13a*	*d16a*	*d02b*	*d05b*
d12a	*d01a*	*d03a*	*d05a*	*d06a*	*d14a*	*d15a*
d13a	*d03a*	*d04a*	*d06a*	*d08a*	*d10a*	*d11a*
d14a	*d03a*	*d05a*	*d09a*	*d12a*	*d04c*	*d07c*
d15a	*d01a*	*d02a*	*d06a*	*d08a*	*d09a*	*d12a*
d16a	*d01a*	*d07a*	*d10a*	*d11a*	*d02b*	*d05b*

Second Third of Supercell						
Site Position	***Nearest Neighbour Site positions***					
d01b	*d06a*	*d07a*	*d10a*	*d12a*	*d15a*	*d16a*
d02b	*d06b*	*d07b*	*d10b*	*d12b*	*d15b*	*d16b*
d03b	*d11a*	*d16a*	*d05b*	*d08b*	*d09b*	*d15b*
d04b	*d05b*	*d08b*	*d10b*	*d12b*	*d13b*	*d14b*
d05b	*d06b*	*d07b*	*d11b*	*d13b*	*d09c*	*d14c*
d06b	*d02b*	*d03b*	*d12b*	*d14b*	*d11a*	*d16a*
d07b	*d01b*	*d04b*	*d11b*	*d12b*	*d13b*	*d15b*
d08b	*d01b*	*d04b*	*d10b*	*d16b*	*d09c*	*d14c*
d09b	*d02b*	*d03b*	*d09b*	*d10b*	*d13b*	*d15b*
d10b	*d04a*	*d07a*	*d02b*	*d08b*	*d14b*	*d15b*
d11b	*d01b*	*d03b*	*d07b*	*d08b*	*d13b*	*d16b*
d12b	*d04b*	*d06b*	*d13b*	*d16b*	*d02c*	*d05c*
d13b	*d01b*	*d03b*	*d05b*	*d06b*	*d14b*	*d15b*
d14b	*d03b*	*d04b*	*d06b*	*d08b*	*d10b*	*d11b*
d15b	*d04a*	*d07a*	*d03b*	*d05b*	*d09b*	*d12b*
d16b	*d01b*	*d02b*	*d06b*	*d08b*	*d09b*	*d12b*

Final Third of Supercell						
Site Position	***Nearest Neighbour Site positions***					
d01c	*d06c*	*d07c*	*d10c*	*d12c*	*d15c*	*d16c*
d02c	*d11b*	*d16b*	*d05c*	*d08c*	*d09c*	*d15c*
d03c	*d05c*	*d08c*	*d10c*	*d12c*	*d13c*	*d14c*
d04c	*d09a*	*d14a*	*d06c*	*d07c*	*d11c*	*d13c*
d05c	*d11b*	*d16b*	*d02c*	*d03c*	*d12c*	*d14c*
d06c	*d01c*	*d04c*	*d11c*	*d12c*	*d13c*	*d15c*
d07c	*d09a*	*d14a*	*d01c*	*d04c*	*d10c*	*d16c*
d08c	*d02c*	*d03c*	*d09c*	*d10c*	*d13c*	*d15c*
d09c	*d04b*	*d07b*	*d02c*	*d08c*	*d14c*	*d15c*
d10c	*d01c*	*d03c*	*d07c*	*d08c*	*d13c*	*d16c*
d11c	*d02a*	*d05a*	*d04c*	*d06c*	*d13c*	*d16c*
d12c	*d01c*	*d03c*	*d05c*	*d06c*	*d14c*	*d15c*
d13c	*d03c*	*d04c*	*d06c*	*d08c*	*d10c*	*d11c*
d14c	*d04b*	*d07b*	*d03c*	*d05c*	*d09c*	*d12c*
d15c	*d01c*	*d02c*	*d06c*	*d08c*	*d09c*	*d12c*
d16c	*d02a*	*d05a*	*d01c*	*d07c*	*d10c*	*d11c*

Nearest neighbour octahedral *16d* site positions to each individual tetrahedral *8c* position (*tet-oct*)

First Third of Supercell						
Site Position	***Nearest Neighbour Site positions***					
a01a	*d02a*	*d03a*	*d05a*	*d06a*	*d08a*	*d09a*
	d12a	*d13a*	*d14a*	*d15a*	*d04c*	*d11c*
a02a	*d01a*	*d03a*	*d04a*	*d06a*	*d07a*	*d08a*
	d09a	*d10a*	*d12a*	*d13a*	*d14a*	*d15a*
a03a	*d01a*	*d04a*	*d06a*	*d07a*	*d08a*	*d10a*
	d11a	*d13a*	*d15a*	*d16a*	*d02b*	*d09b*
a04a	*d07a*	*d10a*	*d11a*	*d13a*	*d14a*	*d16a*
	d02b	*d03b*	*d04b*	*d05b*	*d08b*	*d09b*
a05a	*d01a*	*d03a*	*d04a*	*d06a*	*d07a*	*d10a*
	d11a	*d12a*	*d13a*	*d16a*	*d05b*	*d14b*
a06a	*d01a*	*d04a*	*d06a*	*d07a*	*d11a*	*d16a*
	d02b	*d05b*	*d09b*	*d12b*	*d14b*	*d15b*
a07a	*d01a*	*d02a*	*d03a*	*d05a*	*d08a*	*d09a*
	d10a	*d12a*	*d14a*	*d15a*	*d07c*	*d16c*
a08a	*d01a*	*d02a*	*d03a*	*d05a*	*d06a*	*d08a*
	d10a	*d11a*	*d12a*	*d13a*	*d15a*	*d16a*

Second Third of Supercell						
Site Position	***Nearest Neighbour Site positions***					
a01b	*d02b*	*d03b*	*d05b*	*d06b*	*d08b*	*d09b*
	d12b	*d13b*	*d14b*	*d15b*	*d04a*	*d11a*
a02b	*d01b*	*d03b*	*d04b*	*d06b*	*d07b*	*d08b*
	d09b	*d10b*	*d12b*	*d13b*	*d14b*	*d15b*
a03b	*d01b*	*d04b*	*d06b*	*d07b*	*d08b*	*d10b*
	d11b	*d13b*	*d15b*	*d16b*	*d02c*	*d09c*
a04b	*d07b*	*d10b*	*d11b*	*d13b*	*d14b*	*d16b*
	d02c	*d03c*	*d04c*	*d05c*	*d08c*	*d09c*
a05b	*d01b*	*d03b*	*d04b*	*d06b*	*d07b*	*d10b*
	d11b	*d12b*	*d13b*	*d16b*	*d05c*	*d14c*
a06b	*d01b*	*d04b*	*d06b*	*d07b*	*d11b*	*d16b*
	d02c	*d05c*	*d09c*	*d12c*	*d14c*	*d15c*
a07b	*d01b*	*d02b*	*d03b*	*d05b*	*d08b*	*d09b*
	d10b	*d12b*	*d14b*	*d15b*	*d07a*	*d16a*
a08b	*d01b*	*d02b*	*d03b*	*d05b*	*d06b*	*d08b*
	d10b	*d11b*	*d12b*	*d13b*	*d15b*	*d16b*

Final Third of Supercell						
Site Position	***Nearest Neighbour Site positions***					
a01c	*d02c*	*d03c*	*d05c*	*d06c*	*d08c*	*d09c*
	d12c	*d13c*	*d14c*	*d15c*	*d04b*	*d11b*
a02c	*d01c*	*d03c*	*d04c*	*d06c*	*d07c*	*d08c*
	d09c	*d10c*	*d12c*	*d13c*	*d14c*	*d15c*
a03c	*d01c*	*d04c*	*d06c*	*d07c*	*d08c*	*d10c*
	d11c	*d13c*	*d15c*	*d16c*	*d02a*	*d09a*
a04c	*d07c*	*d10c*	*d11c*	*d13c*	*d14c*	*d16c*
	d02a	*d03a*	*d04a*	*d05a*	*d08a*	*d09a*
a05c	*d01c*	*d03c*	*d04c*	*d06c*	*d07c*	*d10c*
	d11c	*d12c*	*d13c*	*d16c*	*d05a*	*d14a*
a06c	*d01c*	*d04c*	*d06c*	*d07c*	*d11c*	*d16c*
	d02a	*d05a*	*d09a*	*d12a*	*d14a*	*d15a*
a07c	*d01c*	*d02c*	*d03c*	*d05c*	*d08c*	*d09c*
	d10c	*d12c*	*d14c*	*d15c*	*d07b*	*d16b*
a08c	*d01c*	*d02c*	*d03c*	*d05c*	*d06c*	*d08c*
	d10c	*d11c*	*d12c*	*d13c*	*d15c*	*d16c*

Tetragonal $I4_1/amd$ system

Nearest neighbour tetrahedral *4c* site positions to each individual tetrahedral *4c* position (*tet-tet*)

First Sixth of Supercell				
Site Position	***Nearest Neighbour Site positions***			
a1aa	*a2aa*	*a2ab*	*a4ca*	*a4ca*
a2aa	*a1aa*	*a3aa*	*a3aa*	*a1ab*
a3aa	*a2aa*	*a2aa*	*a4aa*	*a4ab*
a4aa	*a3aa*	*a3ab*	*a1ba*	*a1ba*

Second Sixth of Supercell				
Site Position	***Nearest Neighbour Site positions***			
a1ab	*a2aa*	*a2ab*	*a4cb*	*a4cb*
a2ab	*a1aa*	*a1ab*	*a3ab*	*a3ab*
a3ab	*a4aa*	*a2ab*	*a2ab*	*a4ab*
a4ab	*a3aa*	*a3ab*	*a1bb*	*a1bb*

Third Sixth of Supercell				
Site Position	***Nearest Neighbour Site positions***			
a1ba	*a2ba*	*a2bb*	*a4aa*	*a4aa*
a2ba	*a1ba*	*a3ba*	*a3ba*	*a1bb*
a3ba	*a2ba*	*a2ba*	*a4ba*	*a4bb*
a4ba	*a3ba*	*a3bb*	*a1ca*	*a1ca*

Fourth Sixth of Supercell				
Site Position	***Nearest Neighbour Site positions***			
a1bb	*a2ba*	*a2bb*	*a4ab*	*a4ab*
a2bb	*a1ba*	*a1bb*	*a3bb*	*a3bb*
a3bb	*a4ba*	*a2bb*	*a2bb*	*a4bb*
a4bb	*a3ba*	*a3bb*	*a1cb*	*a1cb*

Fifth Sixth of Supercell				
Site Position	***Nearest Neighbour Site positions***			
a1ca	*a2ca*	*a2cb*	*a4ba*	*a4ba*
a2ca	*a1ca*	*a3ca*	*a3ca*	*a1cb*
a3ca	*a2ca*	*a2ca*	*a4ca*	*a4cb*
a4ca	*a3ca*	*a3cb*	*a1aa*	*a1aa*

Final Sixth of Supercell				
Site Position	***Nearest Neighbour Site positions***			
a1cb	*a2ca*	*a2cb*	*a4bb*	*a4bb*
a2cb	*a1ca*	*a1cb*	*a3cb*	*a3cb*
a3cb	*a4ca*	*a2cb*	*a2cb*	*a4cb*
a4cb	*a3ca*	*a3cb*	*a1ab*	*a1ab*

Nearest neighbour octahedral *8d* site positions to each individual octahedral *8d* position (*oct-oct*)

First Sixth of Supercell						
Site Position	***Nearest Neighbour Site positions***					
d1aa	*d3aa*	*d4aa*	*d6aa*	*d6aa*	*d7ab*	*d8ab*
d2aa	*d4aa*	*d5aa*	*d5aa*	*d7aa*	*d3ca*	*d8ca*
d3aa	*d1aa*	*d6aa*	*d8aa*	*d8ab*	*d2ba*	*d5ba*
d4aa	*d1aa*	*d2aa*	*d5aa*	*d6aa*	*d7aa*	*d7ab*
d5aa	*d2aa*	*d2aa*	*d4aa*	*d7aa*	*d3ca*	*d8ca*
d6aa	*d1aa*	*d1aa*	*d3aa*	*d4aa*	*d7ab*	*d8ab*
d7aa	*d2aa*	*d4aa*	*d5aa*	*d1ab*	*d4ab*	*d6ab*
d8aa	*d3aa*	*d1ab*	*d3ab*	*d6ab*	*d2ba*	*d5ba*

Second Sixth of Supercell						
Site Position	***Nearest Neighbour Site positions***					
d1ab	*d7aa*	*d8aa*	*d3ab*	*d4ab*	*d6ab*	*d6ab*
d2ab	*d4ab*	*d5ab*	*d5ab*	*d7ab*	*d3cb*	*d8cb*
d3ab	*d8aa*	*d1ab*	*d6ab*	*d8ab*	*d2bb*	*d5bb*
d4ab	*d7aa*	*d1ab*	*d2ab*	*d5ab*	*d6ab*	*d7ab*
d5ab	*d2ab*	*d2ab*	*d4ab*	*d7ab*	*d3cb*	*d8cb*
d6ab	*d7aa*	*d8aa*	*d1ab*	*d1ab*	*d3ab*	*d4ab*
d7ab	*d1aa*	*d4aa*	*d6aa*	*d2ab*	*d4ab*	*d5ab*
d8ab	*d1aa*	*d3aa*	*d6aa*	*d3ab*	*d2bb*	*d5bb*

Third Sixth of Supercell						
Site Position	***Nearest Neighbour Site positions***					
d1ba	*d3ba*	*d4ba*	*d6ba*	*d6ba*	*d7bb*	*d8bb*
d2ba	*d4ba*	*d5ba*	*d5ba*	*d7ba*	*d3aa*	*d8aa*
d3ba	*d1ba*	*d6ba*	*d8ba*	*d8bb*	*d2ca*	*d5ca*
d4ba	*d1ba*	*d2ba*	*d5ba*	*d2ba*	*d7ba*	*d7bb*
d5ba	*d2ba*	*d2ba*	*d4ba*	*d7ba*	*d3aa*	*d8aa*
d6ba	*d1ba*	*d1ba*	*d3ba*	*d4ba*	*d7bb*	*d8bb*
d7ba	*d2ba*	*d4ba*	*d5ba*	*d1bb*	*d4bb*	*d6bb*
d8ba	*d3ba*	*d1bb*	*d3bb*	*d6bb*	*d2ca*	*d5ca*

Fourth Sixth of Supercell						
Site Position	***Nearest Neighbour Site positions***					
d1bb	*d7ba*	*d8ba*	*d3bb*	*d4bb*	*d6bb*	*d6bb*
d2bb	*d4bb*	*d5bb*	*d5bb*	*d7bb*	*d3ab*	*d8ab*
d3bb	*d8ba*	*d1bb*	*d6bb*	*d8bb*	*d2cb*	*d5cb*
d4bb	*d7ba*	*d1bb*	*d2bb*	*d5bb*	*d6bb*	*d7bb*
d5bb	*d2bb*	*d2bb*	*d4bb*	*d7bb*	*d3ab*	*d8ab*
d6bb	*d7ba*	*d8ba*	*d1bb*	*d1bb*	*d3bb*	*d4bb*
d7bb	*d1ba*	*d4ba*	*d6ba*	*d2bb*	*d4bb*	*d5bb*
d8bb	*d1ba*	*d3ba*	*d6ba*	*d3bb*	*d2cb*	*d5cb*

Fifth Sixth of Supercell						
Site Position	***Nearest Neighbour Site positions***					
d1ca	*d3ca*	*d4ca*	*d6ca*	*d6ca*	*d7cb*	*d8cb*
d2ca	*d4ca*	*d5ca*	*d5ca*	*d7ca*	*d3ba*	*d8ba*
d3ca	*d1ca*	*d6ca*	*d8ca*	*d8cb*	*d2aa*	*d5aa*
d4ca	*d1ca*	*d2ca*	*d5ca*	*d6ca*	*d7ca*	*d7cb*
d5ca	*d2ca*	*d2ca*	*d4ca*	*d7ca*	*d3ba*	*d8ba*
d6ca	*d1ca*	*d1ca*	*d3ca*	*d4ca*	*d7cb*	*d8cb*
d7ca	*d2ca*	*d4ca*	*d5ca*	*d1cb*	*d4cb*	*d6cb*
d8ca	*d3ca*	*d1cb*	*d3cb*	*d6cb*	*d2aa*	*d5aa*

Final Sixth of Supercell						
Site Position	***Nearest Neighbour Site positions***					
d1cb	*d7ca*	*d8ca*	*d3cb*	*d4cb*	*d6cb*	*d6cb*
d2cb	*d4cb*	*d5cb*	*d5cb*	*d7cb*	*d3bb*	*d8bb*
d3cb	*d8ca*	*d1cb*	*d6cb*	*d8cb*	*d2ab*	*d5ab*
d4cb	*d7ca*	*d1cb*	*d2cb*	*d5cb*	*d6cb*	*d7cb*
d5cb	*d2cb*	*d2cb*	*d4cb*	*d7cb*	*d3bb*	*d8bb*
d6cb	*d7ca*	*d8ca*	*d1cb*	*d1cb*	*d3cb*	*d4cb*
d7cb	*d1ca*	*d4ca*	*d6ca*	*d2cb*	*d4cb*	*d5cb*
d8cb	*d1ca*	*d3ca*	*d6ca*	*d3cb*	*d2ab*	*d5ab*

Nearest neighbour octahedral *8d* site positions to each individual tetrahedral *4c* position (*tet-oct*)

First Sixth of Supercell						
Site Position	***Nearest Neighbour Site positions***					
a1aa	*d1aa*	*d2aa*	*d4aa*	*d4aa*	*d5aa*	*d6aa*
	d2ab	*d5ab*	*d7ab*	*d7ab*	*d3ca*	*d8cb*
a2aa	*d1aa*	*d2aa*	*d3aa*	*d4aa*	*d4aa*	*d5aa*
	d6aa	*d7aa*	*d7aa*	*d8aa*	*d1ab*	*d6ab*
a3aa	*d1aa*	*d3aa*	*d3aa*	*d4aa*	*d6aa*	*d7aa*
	d8aa	*d8aa*	*d1ab*	*d6ab*	*d2ba*	*d5ba*
a4aa	*d1aa*	*d3aa*	*d3aa*	*d6aa*	*d8ab*	*d8ab*
	d2ba	*d4ba*	*d5ba*	*d2bb*	*d5bb*	*d7bb*

Second Sixth of Supercell						
Site Position	***Nearest Neighbour Site positions***					
a1ab	*d2aa*	*d5aa*	*d7aa*	*d7aa*	*d1ab*	*d2ab*
	d4ab	*d4ab*	*d5ab*	*d6ab*	*d8ca*	*d3cb*
a2ab	*d1aa*	*d6aa*	*d1ab*	*d2ab*	*d3ab*	*d4ab*
	d4ab	*d5ab*	*d6ab*	*d7ab*	*d7ab*	*d8ab*
a3ab	*d1aa*	*d6aa*	*d1ab*	*d3ab*	*d3ab*	*d4ab*
	d6ab	*d7ab*	*d8ab*	*d8ab*	*d2bb*	*d5bb*
a4ab	*d8aa*	*d8aa*	*d1ab*	*d3ab*	*d3ab*	*d6ab*
	d2ba	*d5ba*	*d7ba*	*d2bb*	*d4bb*	*d5bb*

Third Sixth of Supercell						
Site Position	***Nearest Neighbour Site positions***					
a1ba	*d1ba*	*d2ba*	*d4ba*	*d4ba*	*d5ba*	*d6ba*
	d2bb	*d5bb*	*d7bb*	*d7bb*	*d3aa*	*d8ab*
a2ba	*d1ba*	*d2ba*	*d3ba*	*d4ba*	*d4ba*	*d5ba*
	d6ba	*d7ba*	*d7ba*	*d8ba*	*d1bb*	*d6bb*
a3ba	*d1ba*	*d3ba*	*d3ba*	*d4ba*	*d6ba*	*d7ba*
	d8ba	*d8ba*	*d1bb*	*d6bb*	*d2ca*	*d5ca*
a4ba	*d1ba*	*d3ba*	*d3ba*	*d6ba*	*d8bb*	*d8bb*
	d2ca	*d4ca*	*d5ca*	*d2cb*	*d5cb*	*d7cb*

Fourth Sixth of Supercell						
Site Position	***Nearest Neighbour Site positions***					
a1bb	*d2ba*	*d5ba*	*d7ba*	*d7ba*	*d1bb*	*d2bb*
	d4bb	*d4bb*	*d5bb*	*d6bb*	*d8aa*	*d3ab*
a2bb	*d1ba*	*d6ba*	*d1bb*	*d2bb*	*d3bb*	*d4bb*
	d4bb	*d5bb*	*d6bb*	*d7bb*	*d7bb*	*d8bb*
a3bb	*d1ba*	*d6ba*	*d1bb*	*d3bb*	*d3bb*	*d4bb*
	d6bb	*d7bb*	*d8bb*	*d8bb*	*d2cb*	*d5cb*
a4bb	*d8ba*	*d8ba*	*d1bb*	*d3bb*	*d3bb*	*d6bb*
	d2ca	*d5ca*	*d7ca*	*d2cb*	*d4cb*	*d5cb*

Fifth Sixth of Supercell						
Site Position	***Nearest Neighbour Site positions***					
a1ca	*d1ca*	*d2ca*	*d4ca*	*d4ca*	*d5ca*	*d6ca*
	d2cb	*d5cb*	*d7cb*	*d7cb*	*d3ba*	*d8bb*
a2ca	*d1ca*	*d2ca*	*d3ca*	*d4ca*	*d4ca*	*d5ca*
	d6ca	*d7ca*	*d7ca*	*d8ca*	*d1cb*	*d6cb*
a3ca	*d1ca*	*d3ca*	*d3ca*	*d4ca*	*d6ca*	*d7ca*
	d8ca	*d8ca*	*d1cb*	*d6cb*	*d2aa*	*d5aa*
a4ca	*d1ca*	*d3ca*	*d3ca*	*d6ca*	*d8cb*	*d8cb*
	d2aa	*d4aa*	*d5aa*	*d2ab*	*d5ab*	*d7ab*

Final Sixth of Supercell						
Site Position	***Nearest Neighbour Site positions***					
a1cb	*d2ca*	*d5ca*	*d7ca*	*d7ca*	*d1cb*	*d2cb*
	d4cb	*d4cb*	*d5cb*	*d6cb*	*d8ba*	*d3bb*
a2cb	*d1ca*	*d6ca*	*d1cb*	*d2cb*	*d3cb*	*d4cb*
	d4cb	*d5cb*	*d6cb*	*d7cb*	*d7cb*	*d8cb*
a3cb	*d1ca*	*d6ca*	*d1cb*	*d3cb*	*d3cb*	*d4cb*
	d6cb	*d7cb*	*d8cb*	*d8cb*	*d2ab*	*d5ab*
a4cb	*d8ca*	*d8ca*	*d1cb*	*d3cb*	*d3cb*	*d6cb*
	d2aa	*d5aa*	*d7aa*	*d2ab*	*d4ab*	*d5ab*

Appendix VI

Fortran Codes Used to Generate Structures and Perform Analysis of Selection Criteria

In the following tables are lists of the main FORTRAN codes written to determine the number of possible structures, develop selection criteria and generate the starting structures for the interatomic potential calculations. Examples of the most important codes are provided.

All the programs listed here are located on the CD-ROM provided, in the folder titled Appendix_VI.

Programs used to generate the starting structural configurations for κ-Al_2O_3.

These programs are located in the folder \Appendix_VI\6.1.

kappa_bush.f kappa_catlow.f kappa_grimes.f kappa_harwell.f	Each of these programs generate all the possible structures of κ-Al_2O_3 within a series of nested DO loops, and contain IF statements to ensure multiple symmetry equivalent structures are not doubled up. The programs use the potentials of Bush, *et al*. (1994), Catlow *et al*. (1982), Miniverni *et al*. (1999), and Mackrodt and Stewart (1979) respectively.

Example of the nested do loops that generate all possible structural configurations:

```
    do 18 i = 1,9
      do 19 j = i+1,9
        do 20 k = 1,9
          do 21 l = k+1,9

          write (10,40) 'Al core', one(1,i),one(2,i),one(3,i)
          write (10,40) 'Al core', one(1,j),one(2,j),one(3,j)
          write (10,40) 'Al core', two(1,k),two(2,k),two(3,k)
          write (10,40) 'Al core', two(1,l),two(2,l),two(3,l)
40    format (a7,1x,3(e13.6,1x))

21          continue
20        continue
19      continue
18    continue
```

Analysis programs used to count the number of possible structures and test the selection critera for γ-Al_2O_3 (Fd3m signifies that the file considers the cubic structures, I4amd signifies that the file considers tetragonal structures).

These programs are located in the folder \Appendix_VI\6.2.

as88text	Code for simulated nested DO loops
anagammaFd3mtotalcounterTEST.f	Returns total number of structures with no selection criteria being implemented
anagammaFd3m16d2.f anagammaI4amd8d.f	Considers total number of possibilities for the octahedral sublattice and the effect of the *oct-oct* selection criterion
anagammaFd3m8a2.f anagammaI4amd4a.f	Considers total number of possibilities for the tetrahedral sublattice and the effect of the *tet-tet* selection criterion
anagammaFd3m16dadj8a.f	Considers the effect of the *oct-tet* selection criterion
anagammaFd3mALLCONSID.f anagammaI4amdALLCONSID.f	Considers the combined effect of all three selection criteria returns the reduced number of structural possibilities

Reference code of simulated nested DO loops:

```
      subroutine allnr(n, r, j, ifault)
c
c     Algorithm AS 88  Appl. Statist. (1975) Vol.24, No. 3
c
c     When called once, generates all possible combinations
c     from a group of N items.  Each combination (represented in j as
c     r ordered integers between 1 and n) is processed within allnr.
c
c     Parameters:-
c
c     n       integer           input:  The size of the group from which
c                                       the combinations are selected.

c     r       integer           input:  The size of each comination.

c     j       integer array(r)  workspace: Used by allnr to store
c                                       combinations.

c     ifault  integer           output:  Fault indicator, equal to:
c                                       0 if 1 le R le N;
c                                       1 otherwise.
c
```

```
      integer r, j(r)

      ifault = 1
      if (r .lt.1 .or. r .gt. n) return
      ifault = 0
      kount = 0
      nmr = n - r

c     Initialize J(1) to lower limit separately, since lower limit for
c     each index depends on lower limit for previous index

      i = 1
      j(1) = 1

c     Initialize indices for loops i=1,...,r to lower limits

    1 if (i .eq. r) goto 3
      ip1 = i + 1
      do 2 l = ip1, r
    2 j(l) = j(l - 1) + 1

c     Update the count (kount) of combinations and process the current
c     combination.  The call to Subroutine job may be replaced by
c     statements to process the current combination.

    3 kount = kount + 1

      call job(n, r, j, kount)

c     Increment the first possible index (of loop i) among indices of
c     loops R, R-1,...,1
```

Output from the analysis programs (Fd3m signifies that the file considers the cubic structures, I4amd signifies that the file considers tetragonal structures).

These programs and files are located in the folder \Appendix_VI\6.3.

fd3mtetnumbadj i4amdtetnumbadj	Returns the number of different structures which have particular total number of nearest neighbour occupied tetrahedral positions to an occupied tetrahedral position with each structural configuration. Also returns the reduced number of octahedral arrangements after the *tet-tet* criterion is applied.
fd3moctnumbadj i4amdoctnumbadj	Returns the number of different structures which have particular total number of nearest neighbour occupied octahedral positions to an occupied octahedral position with each structural configuration. Also returns the reduced number of octahedral arrangements after the *oct-oct* criterion is applied.
fd3moctadjtet	Returns the number of different structures which have particular total number of nearest neighbour occupied octahedral positions to an occupied tetrahedral position. Also returns the reduced number of octahedral arrangements after the *tet-oct* criterion is applied.
fd3mallconsid i4amdallconsid	Applies all three selection criteria to return the total number of reduced structural possibilities.
fd3mtestconfig.f i4amdtestconfig.f	Returns the number of nearest neighbours for each occupied cation position. Used to test that the selection criteria were coded correctly and the program was generating the correct cation configurations.

Example of output from fd3mtestconfig.f (0 means position not occupied):

structure number: 9574771

OCT adj config:
6 5 6 6 5 6 6 6 6 6 6 6 6 6 6 5 6 6 0 6 5 4 6 6 5 4 6 5 6 6 0 5 5 6 6 5 6 5 6 5 5 5 6 6 5 6 0
sumoct = 252

TET adj config:
0 1 0 2 0 2 4 1 4 4 4 4 4 4 4 4 2 0 2 3 2 3 2 0
sumtet = 56

No. OCT adj 1 TET config:
0 12 0 12 0 12 11 12 12 11 10 10 10 10 12 11 11 0 11 11 11 11 11 0
sumtot = 211

Programs used to generate starting structural configurations.

These programs are located in the folder \Appendix_VI\6.4.

singgammaFd3m8a16d.f singgammaI41amd4a8d.f	Generates the starting structure models for single-point calculation. Used to determine the energies and properties of the starting structural configurations.
fd3m_individ_struct_write_sing.f i4amd_individ_struct_write_sing.f	Generates selected structural configurations for single-point calculation.
singgammaFd3mB_16c.f singgammaFd3mC_16c.f singgammaFd3mD_16c.f singgammaI41amB_8c.f singgammaI41amC_8c.f singgammaI41amD_8c.f	Generates the starting structural configurations that are based on the findings of *Chapter 7* for single-point calculation.
optigammaFd3m8a16d.f optigammaI41amd4a8d.f optigammaI41amd4a8d_random.f	Generates the selected structural configurations for optimisation.
fd3m_individ_struct_write_opti.f i4amd_individ_struct_write_opti.f	Generates selected structural configurations for optimisation.
optigammaFd3mB_16c_einst_k1000.f optigammaFd3mC_16c_einst_k1000.f optigammaFd3mD_16c_einst_k1000.f optigammaI41amB_8c_einst_k1000.f optigammaI41amC_8c_einst_k1000.f optigammaI41amD_8c_einst_k1000.f	Generates the structural configurations that are based on the findings of *Chapter 7* for optimisation.

Example of code to generate structural configurations from optigammaFd3m8a16d.f:

```
      program gamma
      double precision one(3,48)
      double precision two(3,24)
      integer oct(45)
      integer tet(19)
      integer icount
      integer config(48)
      integer neigh(48)
      integer conf(24)
      integer neig(24)
      integer oneig(24)
      common one,two,oct,tet,icount,config,neigh,conf,neig,oneig

c     Possible OCTAHEDRAL positions
c     (Wyckoff 16d)

      one(1,01) = 0.5d0
      one(2,01) = 0.5d0              !d01a
```

```
      one(3,01) = 0.166666667d0
      one(1,02) = 0.25d0
      one(2,02) = 0.75d0              !d02a
      one(3,02) = 0.0d0
.
.
.
c     Possible TETRAHEDRAL positions
c     (Wyckoff 8a)

      two(1,1) = 0.125d0
      two(2,1) = 0.125d0              !a01a
      two(3,1) = 0.041666667d0
      two(1,2) = 0.875d0
      two(2,2) = 0.375d0              !a02a
      two(3,2) = 0.125d0
.
.
.
c     All text for GULP input file to begin writing in here.
c     Must be within loop so that it is written out along side each set
c     of Al configurations (i.e. for each file)

      icount = 1

c     Calling subroutine which performs all the functions required
c     by the program, and calls up other subroutines within itself,
c     in order to perform all necessay operations. This subroutine
c     itself will work out the octahedral combinations.

      call allnroct(48, 45, oct, ifault)

      write(6,*) icount

      stop
      end

****************************************
c     The actual subtroutine is described here. It will call other
c     subroutines from within, which are described below.

      subroutine allnroct(n, r, j, ifault)
      integer r, j(r)
      ifault = 1
      if (r .lt.1 .or. r .gt. n) return
      ifault = 0
      kount = 0
      nmr = n - r
      i = 1
      j(1) = 1
```

```
   1 if (i .eq. r) goto 3
     ip1 = i + 1
     do 2 l = ip1, r
   2 j(l) = j(l - 1) + 1
   3 kount = kount + 1

c      write(*,*) 'joboct called'
c      write (*,*) j

      call joboct(n, r, j, kount)
c
      i = r
   4 if (j(i) .lt. nmr + i) goto 5
     i = i - 1
     if (i .le. 0) return
     goto 4
   5 j(i) = j(i) + 1
     goto 1
     end

**************************************
c     Subroutine which performs the necessary functions within the
c     space equivalent to the first set of loops.

      subroutine joboct(n, r, j, kount)
      integer r, j(r)
      integer sumoct
      double precision one(3,48)
      double precision two(3,24)
      integer oct(45)
      integer tet(19)
      integer icount
      integer config(48)
      integer neigh(48)
      integer conf(24)
      integer neig(24)
      integer oneig(24)
      common one,two,oct,tet,icount,config,neigh,conf,neig,oneig

c     Determination of octahedral configuration and the number of nearest
c     That is: Looking at nearest neighbour octahedrals and hence, the
c     distribution of tetrahedral AL's throughout the lattice

      do i = 1,n
        config(i) = 0
      enddo
      do i = 1,r
        config(j(i)) = 1
      enddo
```

```
c     look at ion 01 (d01a)
      if (config(1).eq.0) then
        neigh(1) = 0
      else
      neigh(1) = config(6)+config(7)+config(10)+config(12)+
     $config(15)+config(16)
      endif

c     look at ion 02 (d02a)
      if (config(2).eq.0) then
        neigh(2) = 0
      else
      neigh(2) = config(5)+config(8)+config(9)+config(15)+
     $config(43)+config(48)
      endif
.
.
.
c     determination of sum of all the nearest neighbour occupied
c     positions, for each occupied position, of each configuration

      sumoct = neigh(1)+neigh(2)+neigh(3)+neigh(4)+
     $neigh(5)+neigh(6)+neigh(7)+neigh(8)+neigh(9)+
     $neigh(10)+neigh(11)+neigh(12)+neigh(13)+neigh(14)+
     $neigh(15)+neigh(16)+neigh(17)+neigh(18)+neigh(19)+
     $neigh(20)+neigh(21)+neigh(22)+neigh(23)+neigh(24)+
     $neigh(25)+neigh(26)+neigh(27)+neigh(28)+neigh(29)+
     $neigh(30)+neigh(31)+neigh(32)+neigh(33)+neigh(34)+
     $neigh(35)+neigh(36)+neigh(37)+neigh(38)+neigh(39)+
     $neigh(40)+neigh(41)+neigh(42)+neigh(43)+neigh(44)+
     $neigh(45)+neigh(46)+neigh(47)+neigh(48)

c     Calling subroutine which will perform tetrahedral combinations.
      if (sumoct.eq.252) then
        call allnrtet(24, 19, tet, ifault)
      endif
      return
      end

****************************************
c     The actual subtroutine is described here. It will call other
c     subroutines from within, which are described below.

c     This subroutine is equivalent to the second set of nested
c     loops in the old progams (...._DEFUNCT.f). This will determine
c     all the combinations of the tetrahedral positions.

      subroutine allnrtet(n, r, k, ifault)
      integer r, k(r)
      ifault = 1
```

```
      if (r .lt.1 .or. r .gt. n) return
      ifault = 0
      kount = 0
      nmr = n - r
      i = 1
      k(1) = 1
   11 if (i .eq. r) goto 13
      ip1 = i + 1
      do 12 l = ip1, r
   12 k(l) = k(l - 1) + 1
   13 kount = kount + 1

      call jobtet(n, r, k, kount)

      i = r
   14 if (k(i) .lt. nmr + i) goto 15
      i = i - 1
      if (i .le. 0) return
      goto 14
   15 k(i) = k(i) + 1
      goto 11
      end

**************************************
c     Subroutine which performs the necessary functions within the
c     space equivalent to the second set of loops. i.e. writing to file.

      subroutine jobtet(n, r, k, kount)
      integer r, k(r)
      integer sumtet
      integer sumtot
      double precision one(3,48)
      double precision two(3,24)
      integer oct(45)
      integer tet(19)
      integer icount
      integer config(48)
      integer neigh(48)
      integer conf(24)
      integer neig(24)
      integer oneig(24)
      common one,two,oct,tet,icount,config,neigh,conf,neig,oneig

c     Determination of tetrahedral configuration and the number of nearest
c     neighbour occupied positions for the octahedral sublattice

      do i = 1,n
        conf(i) = 0
      enddo
      do i = 1,r
```

```
        conf(k(i)) = 1
      enddo

c     Looking at nearest neighbour tetrahedrals and hence, the
c     distribution of tetrahedral AL's throughout the lattice

c     look at ion 01 (a01a)
      if (conf(1).eq.0) then
        neig(1) = 0
      else
      neig(1) = conf(2)+conf(8)+conf(20)+conf(22)
      endif

c     look at ion 02 (a02a)
      if (conf(2).eq.0) then
        neig(2) = 0
      else
      neig(2) = conf(1)+conf(3)+conf(5)+conf(7)
      endif
.
.
.
      sumtet = neig(1)+neig(2)+neig(3)+neig(4)+neig(5)+
     $neig(6)+neig(7)+neig(8)+neig(9)+neig(10)+
     $neig(11)+neig(12)+neig(13)+neig(14)+neig(15)+
     $neig(16)+neig(17)+neig(18)+neig(19)+neig(20)+
     $neig(21)+neig(22)+neig(23)+neig(24)

      if (sumtet.eq.56) then
c     Looking at the 16d's surrounding the 8a's
c     look at ion 01 (a01a)
      if (conf(1).eq.0) then
        oneig(1) = 0
      else
      oneig(1) = config(2)+config(3)+config(5)+config(6)+
     $config(8)+config(9)+config(12)+config(13)+
     $config(14)+config(15)+config(36)+config(43)
      endif

c     look at ion 02 (a02a)
      if (conf(2).eq.0) then
        oneig(2) = 0
      else
      oneig(2) = config(1)+config(3)+config(4)+config(6)+
     $config(7)+config(8)+config(9)+config(10)+
     $config(12)+config(13)+config(14)+config(15)
      endif
.
.
.
```

```
      sumtot = oneig(1)+oneig(2)+oneig(3)+oneig(4)+oneig(5)+
     $oneig(6)+oneig(7)+oneig(8)+oneig(9)+oneig(10)+
     $oneig(11)+oneig(12)+oneig(13)+oneig(14)+oneig(15)+
     $oneig(16)+oneig(17)+oneig(18)+oneig(19)+oneig(20)+
     $oneig(21)+oneig(22)+oneig(23)+oneig(24)

c     Calling subroutine which will write out file
      if (sumtot.eq.210) then
      call jobwrite
      endif

      icount = icount + 1

      if (MOD(icount,1000000).eq.1) then
      write (*,*) icount
      endif
      endif
      return
      end
.
.
.
c     Subroutine which writes out the input file.

      subroutine jobwrite
      character*20 filename
      integer digit
      integer remainder
      double precision one(3,48)
      double precision two(3,24)
      integer oct(45)
      integer tet(19)
      integer icount
      integer config(48)
      integer neigh(48)
      integer conf(24)
      integer neig(24)
      integer oneig(24)
      common one,two,oct,tet,icount,config,neigh,conf,neig,oneig
      filename = 'Fd3mA000000000.gin'
            digit = icount/100000000
c  char(I) command allows integer specification within a character variable
      filename(6:6) = char(digit+ichar('0'))
            remainder = icount - digit*100000000
            digit = remainder/10000000
      filename(7:7) = char(digit+ichar('0'))
            remainder = remainder - digit*10000000
.
.
.
```

```
c     Initialising unit and therefore file. Must be done within loop to allow
c     for different filename to be generated for each file which is generated.

      open(unit = 10, file=filename, status='new')
      if (MOD(icount,1000).eq.1) then
      write(6,*) filename
      endif

      write (10,*) 'conv opti conj comp phonon prop dist'
      write (10,*) 'switch rfo gnorm 0.5'
      write (10,*)
c     Code to designate atomic configuration of starting structure

      write (10,*) 'cell'
      write (10,*) '7.911 7.911 23.733 90.0 90.0 90.0'
      write (10,*) 'fractional'
      write (10,*) 'O core  0.255  0.255  0.085'
      write (10,*) 'O shel  0.255  0.255  0.085'
      write (10,*) 'O core  0.495 -0.005  0.251666667'
      write (10,*) 'O shel  0.495 -0.005  0.251666667'
.
.
.
c     Writing out of Al coordinates

      do i=1,45
      write (10,50) 'Al core', one(1,oct(i)),one(2,oct(i)),one(3,oct(i))
      enddo
      do j=1,19
      write (10,50) 'Al core', two(1,tet(j)),two(2,tet(j)),two(3,tet(j))
      enddo
50    format (a8,1x,3(e13.6,1x))

c     Continuation of GULP input file data.

      write (10,*) 'cuts = 0.8'
      write (10,*) 'buck'
      write (10,*) 'Al core O shell 1460.300 0.29912 0.0 0.0 10.0'
      write (10,*) 'buck'
      write (10,*) 'O shell O shell 22764.000 0.14900 27.87900 0.0 12.0'
      write (10,*) 'spring'
      write (10,*) 'O 74.92'
      write (10,*) 'species'
      write (10,*) 'Al core 3.00000'
      write (10,*) 'O core 0.86902'
      write (10,*) 'O shell -2.86902'
            close (unit=10)
      return
      end
```

Appendix VII

Python Codes Used to Perform Analysis of Optimised Structures and Miscellaneous Tasks (System Administration)

In the following tables are lists of the main PYTHON codes written to perform analysis on the starting and optimised structural configurations, and perform file system administrative functions. Examples of the most important codes are provided.

Note that "p2opti" in the program name refers to programs used for *c* symmetry based structures. Also, "cubic" in the program name refers to supercells derived from $Fd\bar{3}m$ symmetry and "tetrag" refers to supercells derived from $I4_1/amd$ symmetry.

All the programs listed here are located on the CD-ROM provided, in the folder titled Appendix_VII.

Job submission and resubmission.

These programs are located in the folder \Appendix_VII\7.1.

qgulp.py	Submits large numbers of jobs to the queue for GULP optimisation
qgulpmissed.py qgulpmissed_2.py qgulpmissed_3.py qgulpmissed_p2opti_2.py qgulpmissed_p2opti_3.py	Resubmits jobs that did not run to completion or stopped due to some error. Each program resubmits the jobs based on specific attributes.
qgulpinrange.py	Submits jobs to the queue for structures within a desired range of structure number.
zautomated_sequential_operations_cubic.py zautomated_sequential_operations_tetrag.py	Used to run large single-point-calculations on individual processors. These programs performed several additional tasks, including collating structural energies and generating energy lists, determining the maximum, minimum and mean energies and compressing the input and output files.
zmissing_cif_check.py zstructeigen.py zstructwithhighGnorm_1.py zstructwithhighGnorm_2.py zstructwithhighGnorm.py zstructwithhighGnorm_p2opti.py zstructwithhighGnorm_1_p2opti.py zstuctsmissingcifs_p2_opti.py	Used to ensure that the optimised structures reached global minimums. Searches for optimised structures with no corresponding .cif file, unsuitably high Gnorm and positive eigenvalues and resubmits them to the que. The settings in the resubmitted jobs are changed, such as switching optimisers or reducing polarisability to help the structure converge. These files examples provide some examples of what was modified.

System Administration. These programs were written to perform various tasks when the numbers of structures within a folder was greater than 5000, which was typically the case. In many cases the programs emulate standard Unix commands that could not be performed on a large number of files.

These programs are located in the folder \Appendix_VII\7.2.

zcopy.py zcopy_missed.py zcopy_setlist.py zcopy_sorted.py	Copying of files to various different directories. Used for copying all input, output and .cif files, or just one of these three types, a specific few, or input files that did not run to completion.
zgetlist.py zgetlist_2.py	Returns lists of input, output and/or .cif files in a directory.
zcompress.py	Compress groups of files into a single file .
zgzip.py zgzip_1.py zgzip_2.py	Compresses large numbers of individual files. Uses gzip in a loop.
zgunzipBig.py zgunzipBig_gotcif.py	Unzip large numbers of individual files. Uses gunzip in a loop.
zcifdeletionfileBig.py zdeletionfileBig.py zdeletionfileBig_all.py zdeletionfileBig_all_zipped.py zoutdeletionfileBig.py zzippeddelete.py	Deletes large numbers of specified files within folder.
zquedeletion.py	Deletes jobs from que.

Energy Analysis

These programs are located in the folder \Appendix_VII\7.3.

zgrepEBig_sing.py zgrep_optiE_sorted.py zgrep_optiE_sorted_p2opti.py	Returns lists (in a series of output files) that contain the structure (or file) number, the Gnorm (indicates convergence) and the optimised energy. zgrepEBig_sing returns the energy and structure number of the starting structures.
zgrepEBig_kappa.py zgrepEBig_kappa_singELTmean.py zgrepEBig_optigamma_sorted.py zgrepEBig_optigamma_sorted_p2opti.py	Returns lists (in a series of output files) that contain the structure (or file) number, the Gnorm, the starting energy, the optimised energy, and the difference between the starting and optimised energies.
zanalys_energy_list.py zanalys_energy_list_p2opti.py	Returns a list of all the optimised energies in ascending order.
zanalys_no_str_at_optiE_p2opti.py zanalys_no_str_at_optiE.py zanalys_no_str_at_startE_p2opti.py	Returns number of different energies and number of structures at each energy.
zanalys_optiE_1.py zanalys_optiE_1_p2opti.py	Returns the mean, minimum and maximum optimised energies, and Gnorm values, of the files in a directory. Also returns the number of structures at the minimum and maximum energies.
zanalys_gamma_start_final.py zanalys_gamma_start_final_p2opti.py	Returns the mean, minimum and maximum starting energies, optimised energies, and the differences between starting and optimised energies of the files in a directory. Also returns the number of structures at the minimum and maximum energies.

Code for zgrepEBig_optigamma_sorted_p2opti.py:

```
#! /usr/bin/python
import commands, glob, time, os
print 'Processing.....'
files = glob.glob("*.got")

i = j = 0

filelist = []
#out_file_three.write('  Starting Energy       Final Energy     Struct. No.   Struct. no.
with lett.    Difference\n')

for file in files:
  file_str_no = file[5:8]
```

```
  file_str_st = file[4:8]
  file_tuple = (file_str_no, file_str_st)
  filelist.append(file_tuple)

filelist.sort()
print len(filelist)

for file_tuple in filelist:
  if i%10000 == 0:
    j = j + 1
    if j > 1:
      out_file.close()
      time.sleep(2)
    file_name = 'a_B_opti_gam_tetrag%d' % (j,)
    out_file = open(file_name,"w")

  a = commands.getoutput("grep 'Total lattice energy       =' I4am*%s.got | grep 'eV'"
% (file_tuple[1],))
  b = file_tuple[0]
  bb = file_tuple[1]
  c = commands.getoutput("grep 'Final energy = ' I4am*%s.got" % (file_tuple[1],))
  x = eval(a[37:48]) - eval(c[19:30])
  out_file.write('%s      %s      %s      %s      %s\n' % (a[37:48],c[19:30],bb,b,x))
  i = i + 1
print '.....complete!'
```

Extract of code from zanalys_gamma_start_final_p2opti.py:

```
.
.
.
ana_file_name = 'anaBtetrag_E_all_start_final'
out_file = open(ana_file_name,"w")

for file_name in file_names:
  for line in fileinput.input(file_name):
    if len(line) >= 60:
      s_value = eval(line[0:10])
      f_value = eval(line[17:28])
      str_noa = line[34:38]
      str_no = int(line[44:47])
      d_value = eval(line[53:63])
      my_tuple = (str_no, str_noa, s_value, f_value, d_value)
      list.append(my_tuple)
    else:
      print line

list.sort()
for my_tuple in list:
```

```
  struct_list.append(my_tuple[1])
  s_values.append(my_tuple[2])
  f_values.append(my_tuple[3])
  d_values.append(my_tuple[4])

smin_E = min(s_values)
smax_E = max(s_values)
fmin_E = min(f_values)
fmax_E = max(f_values)
dmin = min(d_values)
dmax = max(d_values)

for s in s_values:
  ssum = ssum + s
for f in f_values:
  fsum = fsum + f
for d in d_values:
  dsum = dsum + d
.
.
.
out_file.write('OPTIMISED ENERGIES:\n')
out_file.write('min E = %s\n' % (fmin_E,))
out_file.write('max E = %s\n' % (fmax_E,))
out_file.write('sum E = %s\n' % (fsum,))
out_file.write('count = %s\n' % (len(f_values),))
out_file.write('mean E = %s\n' % (fsum/len(f_values),))
out_file.write('Number of structures with lowest optimised energy = %s\n' %
(f_values.count(fmin_E),))
out_file.write('Number of structures with highest optimised energy = %s\n' %
(f_values.count(fmax_E),))

# determining the sructure numbers to have the lowest energy
for f in f_values:
  if f == fmin_E:
    out_file.write('Structure (number) with lowest optimised energy: = %s\n' %
(struct_list[k],))
  k = k + 1
out_file.write('\n')
# determining the sructure numbers to have the highest energy
for f in f_values:
  if f == fmax_E:
    out_file.write('Structure (number) with highest optimised energy: = %s\n' %
(struct_list[l],))
  l = l + 1
.
.
.
```

Analysis of structural configurations

These programs are located in the folder \Appendix_VII\7.4.

zanalys_singstruct_cubic.py zanalys_singstruct_tetrag.py	Returns a file that contains the site position label for occupied and unoccupied symmetry positions of each starting structure. Also returns the energy.
zanalys_optistruct_cubic_1.py zanalys_optistruct_tetrag_1.py zanalys_optistruct_cubic_1_p2opti.py zanalys_optistruct_tetrag_1_p2opti.py	Returns a file that contains the site position label for occupied and unoccupied symmetry positions of each starting structure. Also returns the starting and optimised energies, and the Gnorm value for each structure.
zanalys_optistruct_cubic_cation_site_distn.py zanalys_optistruct_tetrag_cation_site_distn.py zanalys_optistruct_cubic_cation_site_distn_p2opti.py zanalys_optistruct_tetrag_cation_site_distn_p2opti.py	Returns a file that contains statistical information on the number of structures that have particular cation configurations. Includes of ranges in energy for each type characteristic examined.
zanalys_optistruct_cubic_SIESTA_p2opti.py zanalys_optistruct_tetrag_SIESTA_p2opti.py	Returns a file that contains the site position label for occupied and unoccupied symmetry positions of each structure optimised with DFT. Also returns the cation coordinates corresponding to each site position label.

Extract of code from zanalys_optistruct_cubic_1_p2opti.py:

```
.
.
.

cif_file_names = glob.glob("*.cif")

for cif_file_name in cif_file_names:
  cif_str_mk = cif_file_name[8:9]
  cif_str_st = cif_file_name[10:13]
  cif_tuple = (cif_str_mk, cif_str_st)
  ciflist.append(cif_tuple)
ciflist.sort()

str_ana_file_name = 'anaBcubic_optistruct_pt7Ang_tol_1'
out_file = open(str_ana_file_name,"w")
```

```
# establishing a tolerance for which coordinate can be
tolx = 0.09
toly = 0.09
tolz = 0.03

out_file.write('OPTIMISED STRUCTURE ANALYSIS\n')

for cif_tuple in ciflist:
  i = i + 1
  Al_coords = commands.getoutput("grep 'Al ' opt*%s*%s.cif | cut -c 13-47" %
(cif_tuple[0],cif_tuple[1]))

# The grep command imports the all the Al coordinates as a single string.
# So must break each individual set of coordinates into individual lines:

  crappy = Al_coords.splitlines();

   out_file.write('STRUCTURE NUMBER: %s%s\n' % (cif_tuple[0],cif_tuple[1]))
  a = commands.getoutput("grep 'Total lattice energy       =' Fd3m%s%s.got | grep
'eV'" % (cif_tuple[0],cif_tuple[1]))
  b = commands.getoutput("grep 'Final Gnorm  =' Fd3m%s%s.got" %
(cif_tuple[0],cif_tuple[1]))
  out_file.write('%s %s\n' % (a,b))

# establishing dictionary (associative array) to set up site position labelling
  oct_pos_16c = {'c01a':0,'c02a':0,'c03a':0,…….,'c16c':0}
  oct_pos_16d = {'d01a':0,'d02a':0,'d03a':0,'……..,'d16c':0}
.
.
.
# Determine which Al positions are occupied
  for crap in crappy:
# Need to split up each individual coordinate into components and convert string to
integer.
     coord = crap.split()
     x = eval(coord[0])
     y = eval(coord[1])
     z = eval(coord[2])

# Octahedral coordinates (16d)
     if ((x<0.5+tolx) and (x>0.5-tolx)) and ((y<0.5+toly) and (y>0.5-toly)) and
((z<0.166666667+tolz) and (z>0.166666667-tolz)):
       oct_pos_16d['d01a'] = 1
       first_third_cations['d01a'] = 1
     elif ((x<0.25+tolx) and (x>0.25-tolx)) and ((y<0.75+toly) and (y>0.75-toly)) and
(((z<0+tolz) and (z>0-tolz)) or ((z<1+tolz) and (z>1-tolz))):
       oct_pos_16d['d02a'] = 1
       first_third_cations['d02a'] = 1
.
.
```

```
.

    else:
      out_file.write('unmatched coordinate: %f, %f, %f\n' % (x,y,z))

# loop through the keys to return occupied site positions and occupnacy number
.
.
.
  out_file.write('occupied OCTAHEDRAL site positions:\n')
  out_file.write('occupied 16c site positions: ')
  for key in oct_pos_16c.keys():
    if oct_pos_16c[key] == 1:
      out_file.write('%s ' % (key,))
      j = j + 1
    out_file.write("number of occupied 16c site pos = %s\n" % (j,))
    out_file.write('occupied 16d site positions: ')
  for key in oct_pos_16d.keys():
    if oct_pos_16d[key] == 1:
      out_file.write('%s ' % (key,))
      k = k + 1
.
.
.
  for key in first_third_cations.keys():
    if first_third_cations[key] == 1:
      q = q + 1
  out_file.write('Number of cations in first third of supercell: %s' % (q,))
.
.
.
```

Extract of code from zanalys_optistruct_cubic_cation_site_distn_p2opti.py:

```
.
.
.
cif_file_names = glob.glob("*.cif")

for cif_file_name in cif_file_names:
  cif_str_mk = cif_file_name[8:9]
  cif_str_st = cif_file_name[10:13]
  cif_tuple = (cif_str_mk, cif_str_st)
  ciflist.append(cif_tuple)
ciflist.sort()

str_ana_file_name = 'anaBcubic_struct_cation_site_distn_pt7Ang_tol'
out_file = open(str_ana_file_name,"w")

# establishing a tolerance for which coordinate can be
tolx = 0.09
```

```
toly = 0.09
tolz = 0.03

for cif_tuple in ciflist:
  i = i + 1
  Al_coords = commands.getoutput("grep 'Al ' opt*%s*%s.cif | cut -c 13-47" %
(cif_tuple[0],cif_tuple[1]))

  crappy = Al_coords.splitlines();

# establishing dictionary (associative array) to set up site position labelling
  oct_pos_16c = {'c01a':0,'c02a':0,'c03a':0,……..,'c16c':0}
  oct_pos_16d = {'d01a':0,'d02a':0,'d03a':0,……..,'d16c':0}
.
.
.
# Determine which Al positions are occupied
  for crap in crappy:
# Need to split up each individual coordinate into components and convert string to
integer.
     coord = crap.split()
     x = eval(coord[0])
     y = eval(coord[1])
     z = eval(coord[2])

# Octahedral coordinates (16d)
     if ((x<0.5+tolx) and (x>0.5-tolx)) and ((y<0.5+toly) and (y>0.5-toly)) and
((z<0.166666667+tolz) and (z>0.166666667-tolz)):
       oct_pos_16d['d01a'] = 1
       first_third_cations['d01a'] = 1
     elif ((x<0.25+tolx) and (x>0.25-tolx)) and ((y<0.75+toly) and (y>0.75-toly)) and
(((z<0+tolz) and (z>0-tolz)) or ((z<1+tolz) and (z>1-tolz))):
       oct_pos_16d['d02a'] = 1
       first_third_cations['d02a'] = 1
.
.
  for key in oct_pos_16c.keys():
    if oct_pos_16c[key] == 1:
      j = j + 1
  for key in oct_pos_16d.keys():
    if oct_pos_16d[key] == 1:
      k = k + 1
  for key in tet_pos_8a.keys():
    if tet_pos_8a[key] == 1:
      l = l + 1
  for key in tet_pos_8b.keys():
    if tet_pos_8b[key] == 1:
      m = m + 1
  for key in tet_pos_48f.keys():
    if tet_pos_48f[key] == 1:
```

```
    p = p + 1
  eighta_list.append(l)
  eightb_list.append(m)
  sixteenc_list.append(j)
  sixteend_list.append(k)
  fortyeightf_list.append(p)
  unmatched_list.append(unmatched_count)

  q = 0
  r = 0
  s = 0
  for key in first_third_cations.keys():
    if first_third_cations[key] == 1:
      q = q + 1
  for key in second_third_cations.keys():
    if second_third_cations[key] == 1:
      r = r + 1
  for key in last_third_cations.keys():
    if last_third_cations[key] == 1:
      s = s + 1

  qlist.append(q)
  rlist.append(r)
  slist.append(s)
.
.
.
# 'Number of structures with between 25 and 31 16d, between 10 and 15 8a, between
14and 20 16c, < 3 8b, and, < 3 48f positions occupied, including unmatched:
  if (((l >= 10) and (l <= 15)) and ((k >= 25) and (k <= 31)) and ((j >= 14) and (j <=
20)) and (m == 0) and (p <= 9) and (unmatched_count == 0)):
    T21_count = T21_count + 1
    aa = commands.getoutput("grep 'Final energy =' Fd*%s%s.got | grep 'eV'" %
(cif_tuple[0],cif_tuple[1]))
    T21_list.append(eval(aa[19:29]),)
    aa_tuple = (cif_tuple[0], cif_tuple[1], aa)
    T21_tuple_list.append(aa_tuple)
    T21_tuple_list.sort()
.
.
.
out_file.write('Number of structures with between 25 and 31 16d, between 10 and 15
8a, between 14 and 20 16c, no 8b, and, <= 9 48f positions occupied, excluding
unmatched:  %s\n' % (T21_count,))
if T21_count > 0:
  for num in T21_list:
    sum__T21 = sum__T21 + num
  out_file.write('max E = %s\n' % (max(T21_list),))
  out_file.write('min E = %s\n' % (min(T21_list),))
  out_file.write('mean E = %s\n' % (sum__T21/len(T21_list),))
```

```
  out_file.write("\n")
  lll = 0
  if len(T21_tuple_list) > 10:
    for tuple in T21_tuple_list:
      lll = lll + 1
      if lll%5 == 0:
        out_file.write('Structure no: %s %s   %s\n' % (tuple[0],tuple[1],tuple[2]))
  else:
    for tuple in T21_tuple_list:
      out_file.write('Structure no: %s %s   %s\n' % (tuple[0],tuple[1],tuple[2]))
out_file.write("\n")
out_file.write("\n")
.
.
.
out_file.write('Number of cations in first third of supercell: ')
for num in qlist:
  sum__q = sum__q + num
  if num == 21:
    qa = qa + 1
  if num == 22:
    qb = qb + 1
out_file.write('          max = %s\n' % (max(qlist),))
out_file.write('          min = %s\n' % (min(qlist),))
out_file.write('          mean= %s\n' % (sum__q/len(qlist),))
out_file.write('          no. with 21 cations: %s\n' % (qa,))
out_file.write('          no. with 22 cations: %s\n' % (qb,))
out_file.write("\n")
.
.
.
out_file.write('RANGE OF CATIONS WHICH ACCOUNTS FOR 90% OF
STRUCTURES WITH THESE POSITIONS OCCUPIED\n')
out_file.write("\n")

out_file.write('8a - between 3 and 14, number (out of 513 should = 462) =  %s\n' %
(T55_count,))
out_file.write('Minimum structural energy of struct with 8a:  %s\n' %
(min(T55_list),))
out_file.write("\n")
out_file.write('8b - between 1 and 1, number (out of 95 should = 86) =  %s\n' %
(T56_count,))
out_file.write('Minimum structural energy of struct with 8b:  %s\n' %
(min(T56_list),))
out_file.write("\n")
out_file.write('16c - between 10 and 24, number (out of 513 should = 462) =  %s\n'
% (T57_count,))
out_file.write('Minimum structural energy of struct with 16c:  %s\n' %
(min(T57_list),))
out_file.write("\n")
```

```
out_file.write('16d - between 25 and 32, number (out of 513 should = 462) =  %s\n'
% (T58_count,))
out_file.write('Minimum structural energy of struct with 16d:  %s\n' %
(min(T58_list),))
out_file.write("\n")
out_file.write('48f - between 5 and 13, number (out of 513 should = 462) =  %s\n' %
(T59_count,))
out_file.write('Minimum structural energy of struct with 48f:  %s\n' %
(min(T59_list),))
.
.
.
out_file.write('TOTAL NUMBER OF OCCUPIED CATIONS IN ALL THE
STRUCTURES (use to get average)\n')
out_file.write("\n")
for num in eighta_list:
  bb = float(num)
  sum_8acat = sum_8acat + bb
  cc8a = sum_8acat/eighta_count
out_file.write('Total no. cations on 8a sites:  %s\n' % (sum_8acat,))
out_file.write('Average:  %s\n' % (cc8a,))
out_file.write("\n")
for num in eightb_list:
  bb = float(num)
  sum_8bcat = sum_8bcat + bb
  cc8b = sum_8bcat/eightb_count
out_file.write('Total no. cations on 8b sites:  %s\n' % (sum_8bcat,))
out_file.write('Average:  %s\n' % (cc8b,))
.
.
.
```

Appendix VIII

Output from Analysis of Optimised Structures from the Computational Study

In the following tables are lists of the main output files from the analysis of the optimised structures from the computational study.

Note that "p2opti" in the program name refers to programs used for *c* symmetry based structures. Also, "cubic" in the program name refers to supercells derived from $Fd\bar{3}m$ symmetry and "tetrag" refers to supercells derived from $I4_1/amd$ symmetry.

All the files listed here are located on the CD-ROM provided, in the folder titled Appendix_VIII.

Output from the analysis of *c* symmetry based structures.

These programs are located in the folder \Appendix_VIII\8.1.

a_B_opti_gam_cubic1 a_B_opti_gam_tetrag1	List of the starting and optimised energies for every structure, with the associated structure number. Also lists the difference between the starting and optimised energies.
anaBcubic_Elist_p2opti anaBtetrag_Elist_p2opti	List of all the optimised energies in ascending order with the associated structure number.
anaBcubica_optiE_p2opti anaBtetraga_optiE_p2opti	Lists the mean, minimum, and maximum optimised energies and Gnorm values. Also lists the number of structures at the minimum and maximum energies.
anaBcubic_E_all_start_final_p2opti anaBtetrag_E_all_start_final_p2opti	Lists the mean, minimum and maximum starting energies, optimised energies, and the differences between starting and optimised energies of the files in a directory. Also lists the number of structures at the minimum and maximum energies.
anaBcubic_optistruct_pt9Ang_tol_1_p2opti anaBtetrag_optistruct_pt9Ang_tol_1_p2opti	Lists the site position label for occupied and unoccupied symmetry positions of each optimised structure. Also returns the starting and optimised energies, and the Gnorm value for each structure.
anaBcubic_struct_cation_pt9Ang_tol_p2opti anaBtetrag_struct_cation_pt9Ang_tol_p2opti	Contains statistical information on the number of structures that have particular cation configurations. Includes of ranges in energy for each type characteristic examined.

Output from the analysis of spinel-based structures.

These programs are located in the folder \Appendix_VIII\8.2.

a_210opti_gam_cub1 a_210opti_gam_cub2 a_210opti_gam_cub3 a_210opti_gam_cub4 a_210opti_gam_cub5 a_210opti_gam_cub6 a_210opti_gam_tetrag1 a_210opti_gam_tetrag2 a_210opti_gam_tetrag3 a_210opti_gam_tetrag4 a_210opti_gam_tetrag5 a_210opti_gam_tetrag6	List of the starting and optimised energies for every structure, with the associated structure number. Also lists the difference between the starting and optimised energies.
ana210cubic_Elist ana210tetrag_Elist	List of all the optimised energies in ascending order with the associated structure number.
ana210cubic_optiE ana210tetrag_optiE	Lists the mean, minimum, and maximum optimised energies and Gnorm values. Also lists the number of structures at the minimum and maximum energies.
ana210tetrag_E_all_start_final ana210cubic_E_all_start_final	Lists the mean, minimum and maximum starting energies, optimised energies, and the differences between starting and optimised energies of the files in a directory. Also lists the number of structures at the minimum and maximum energies.
ana210cubic_optistruct_pt7Ang_tol_1.zip ana210tetrag_optistruct_pt7Ang_tol_1.zip	Lists the site position label for occupied and unoccupied symmetry positions of each optimised structure. Provides the number of cations within each subcell of the supercell. Also lists the starting and optimised energies, and the Gnorm value for each structure.
ana210cubic_struct_cation_site_distn_pt7Ang_tol ana210tetrag_struct_cation_site_distn_pt7Ang_tol	Contains statistical information on the number of structures that have particular cation configurations. Includes of ranges in energy for each type characteristic examined.

Extract from anaBcubic_optistruct_pt9Ang_tol_1_p2opti:

OPTIMISED STRUCTURE ANALYSIS

STRUCTURE NUMBER: B001
Total lattice energy = -4440.04368656 eV
Total lattice energy = -5057.58347575 eV Final Gnorm = 0.00000600
occupied OCTAHEDRAL site positions:
occupied 16c site positions: c11c c03a c03c c13a c13c c05c c05a c09b c15a c10a c02b c06a c16b c11b c14b c08b
number of occupied 16c site pos = 16

occupied 16d site positions: d15b d05c d05b d01c d01a d07b d03b d11b d08a d08c d16a d01b d13b d06c d06a d16c d04a d04c d12c d12b d12a d14a d14c d10a d10c d10b d02c d02a d09b
number of occupied 16d site pos = 29

occupied TETRAHEDRAL site positions:
occupied 8a site positions: a04c a05c a07b a08c a08a a03b a04b a01a a01c
number of occupied 8a site pos = 9

occupied 8b site positions:
number of occupied 8b site pos = 0

occupied 48f site positions: f40b f39a f20a f15a f33a f20c f44c f15c f22b f02a
number of occupied 48f site pos = 10

octahedral (16c & 16d) vacancies: 16c vacancies: c01b c01c c01a c03b c15c c07a c07b c07c c13b c05b c15b c10c c09c c09a c02a c12b c12c c12a c02c c10b c06c c06b c14c c11a c04a c04c c04b c16c c16a c14a c08a c08c
16d vacancies: d15c d15a d05a d13a d13c d07a d07c d03a d03c d11c d11a d16b d08b d06b d04b d14b d02b d09c d09a

tetrahedral (8a) vacancies: a05a a04a a02a a02c a02b a06a a06c a06b a05b a07a a08b a03c a07c a03a a01b

Number of cations in first third of supercell: 22
Number of cations in second third of supercell: 21
Number of cations in final third of supercell: 21

Appendix IX

Optimised Structural Coordinates

All supercell lattice parameters were kept fixed at $a = b = 7.911$ Å and $c = 23.733$ Å for the $Fd\bar{3}m$ system, and $a = 5.600$ Å, $b = 11.200$ Å and $c = 23.562$ Å for the $I4_1/amd$ system.

In the following tables are structural coordinates from the lowest energy structures of γ-Al_2O_3 for both symmetry systems, described in *section 10.3.1*. They are provided as an example of the configurations obtained, after using DFT.

Cation coordinates for the lowest energy structure from $Fd\bar{3}m$ system, represented in Figures 10.16 and 10.18a.

Site Position	x	y	z	*Site Position*	x	y	z
	Octahedral Coordinates			*d14c*	0.7777	0.2323	0.6583
c01a	0.0029	0.9975	0.9995	*d16c*	0.5047	0.7333	0.9191
c03a	0.2359	0.5075	0.2493				
c05a	0.9541	0.4905	0.1695		***Tetrahedral Coordinates***		
c10a	0.2400	0.2528	0.3293	*a04a*	0.8324	0.8758	0.2913
c16a	0.9863	0.2406	0.0850	*a05a*	0.6197	0.1092	0.2023
c02b	0.7646	0.2541	0.5013	*a07a*	0.6122	0.6113	0.0417
c08b	0.4986	0.2472	0.5800	*a08a*	0.3674	0.8743	0.1222
c11b	0.7665	0.4988	0.7408	*a03b*	0.1442	0.6420	0.5411
c16b	0.9939	0.2521	0.4137	*a08b*	0.3708	0.8820	0.4588
c03c	0.2634	0.4861	0.9254	*a07b*	0.6033	0.6396	0.3726
c05c	0.0063	0.4970	0.8308	*a04b*	0.9121	0.8755	0.6240
c09c	0.4919	0.9892	0.8289	*a01c*	0.1463	0.1074	0.7086
c13c	0.5007	0.5046	0.6593				
c15c	0.7457	0.9936	0.9189	*f15a*	0.1098	0.8723	0.2101
				f33a	0.6166	0.3736	0.2900
d01a	0.5056	0.4892	0.1662	*f07b*	0.8746	0.6302	0.4572
d02a	0.2593	0.7511	0.0008	*f16b*	0.6329	0.8813	0.5443
d03a	0.7269	0.9896	0.0774	*f22b*	0.1373	0.3749	0.6250
d04a	0.9719	0.2336	0.2519	*f40b*	0.1239	0.8819	0.3673
d06a	0.2403	0.2319	0.1702	*f01c*	0.8868	0.6186	0.9577
d08a	0.9896	0.7439	0.0838	*f15c*	0.1306	0.8715	0.8748
d10a	0.7349	0.7547	0.1676	*f20c*	0.8675	0.1230	0.7918
d12a	0.4782	0.2325	0.0783	*f27c*	0.6218	0.3726	0.8730
d14a	0.7360	0.2592	0.9983	*f32c*	0.3740	0.6076	0.7867
d15a	0.2386	0.4901	0.0787	*f39c*	0.6228	0.8774	0.7044
d16a	0.4824	0.7603	0.2500	*f44c*	0.3764	0.1118	0.9597
d01b	0.4977	0.5225	0.5035				
d03b	0.7463	0.9948	0.4145				
d05b	0.4876	0.0034	0.3292				
d07b	0.7782	0.5173	0.5843				
d09b	0.9751	0.5178	0.3285				
d11b	0.2605	0.0045	0.5835				
d12b	0.4935	0.2560	0.4201				
d13b	0.0139	0.0055	0.5010				
d15b	0.2443	0.5208	0.4153				
d02c	0.2608	0.7476	0.6657				
d04c	0.0032	0.2474	0.9194				
d06c	0.2523	0.2392	0.8289				
d08c	0.0163	0.7534	0.7474				
d10c	0.7510	0.7433	0.8310				
d12c	0.5006	0.2377	0.7404				

Oxygen coordinates for the lowest energy structure from $Fd\bar{3}m$ system, represented in Figures 10.16 and 10.18a.

x	y	z	x	y	z
0.7622	0.5057	0.835	0.2728	0.5085	0.6643
0.0052	0.7568	0.0020	0.5093	0.7485	0.8358
0.2726	0.2419	0.5874	0.7417	0.2367	0.4197
0.5249	0.0097	0.7543	0.0197	0.0066	0.5783
0.2665	0.9838	0.6644	0.7621	0.0061	0.4965
0.4951	0.2319	0.8330	0.0082	0.2451	0.6697
0.0144	0.4855	0.9140	0.5234	0.4793	0.7498
0.7595	0.7437	0.7531	0.2579	0.7664	0.5878
0.7590	0.0075	0.9955	0.2429	0.9973	0.5022
0.9994	0.2586	0.1646	0.5325	0.2615	0.6646
0.2452	0.7456	0.7515	0.7183	0.7556	0.2428
0.4922	0.5023	0.9140	0.0000	0.5014	0.4097
0.2455	0.4809	0.8375	0.7397	0.5092	0.3310
0.4916	0.7423	0.9968	0.0042	0.7599	0.4970
0.9742	0.9931	0.0765	0.4995	0.0196	0.5784
0.7572	0.2404	0.9177	0.2442	0.2812	0.4082
0.2407	0.5187	0.0010	0.7317	0.5202	0.1615
0.4936	0.7337	0.1640	0.9874	0.7519	0.3262
0.7494	0.2588	0.7480	0.2425	0.2522	0.9167
0.9891	0.0043	0.9181	0.4929	0.0019	0.0789
0.7428	0.9868	0.8390	0.2326	0.9804	0.9941
0.9812	0.2357	0.9989	0.4830	0.2469	0.1602
0.4796	0.4792	0.0845	0.9941	0.4838	0.2461
0.2584	0.7316	0.9185	0.7496	0.7520	0.0808
0.2648	0.0087	0.8407	0.7220	0.0059	0.3367
0.5040	0.2437	0.0007	0.9884	0.2374	0.4894
0.7634	0.7502	0.5860	0.2321	0.7373	0.0807
0.9872	0.5192	0.7571	0.4790	0.5032	0.2455
0.7500	0.4840	0.6645	0.2558	0.4767	0.1654
0.9915	0.7402	0.8358	0.4900	0.7671	0.3265
0.5103	0.9801	0.9141	0.9896	0.0078	0.4130
0.2717	0.2384	0.7534	0.7400	0.2516	0.2436
0.7496	0.5024	0.5024	0.2206	0.4952	0.3275
0.0220	0.7546	0.6727	0.5150	0.7546	0.4972
0.2183	0.2603	0.2478	0.7406	0.2297	0.0757
0.4993	0.0173	0.4139	0.9715	0.0023	0.2483
0.2540	0.0228	0.3312	0.7304	0.9815	0.1553
0.5214	0.2808	0.4986	0.9955	0.2699	0.3308
0.0096	0.5059	0.5815	0.4885	0.4972	0.4164
0.7446	0.7571	0.4140	0.2510	0.7350	0.2423
0.7671	0.0009	0.6654	0.2328	0.9989	0.1639
0.0069	0.2532	0.8381	0.4809	0.2496	0.3338
0.2548	0.7547	0.4099	0.7468	0.7512	0.9145
0.5277	0.4931	0.5817	0.0050	0.4962	0.0896
0.2689	0.5278	0.4931	0.7509	0.4934	0.9981
0.4971	0.7289	0.6732	0.9793	0.7363	0.1631
0.0089	0.9933	0.7568	0.4920	0.9954	0.2490
0.7492	0.2687	0.5809	0.2352	0.2548	0.0861

Cation coordinates for the lowest energy structure from *$I4_1/amd$* system, represented in Figures 10.17 and 10.18b.

Site Position	x	y	z	*Site Position*	x	y	z
Octahedral Coordinates				*d05cb*	0.7454	0.5141	0.6613
c02aa	0.2628	0.0063	0.1680	*d07cb*	0.8854	0.2669	0.7502
c03aa	0.1223	0.7583	0.0857				
c04aa	0.1116	0.2611	0.2500	***Tetrahedral Coordinates***			
c05aa	0.2628	0.5142	0.1671	*a02ba*	0.2619	0.7800	0.4574
c07aa	0.3791	0.2636	0.2569	*a03ba*	0.2560	0.2642	0.5450
c02ab	0.7603	0.0169	0.1706	*a04ba*	0.0009	0.2606	0.6208
c04ab	0.6280	0.2623	0.2544	*a02bb*	0.7561	0.7520	0.4545
c05ab	0.7594	0.5043	0.1663	*a03bb*	0.7594	0.2616	0.5412
c06ab	0.5058	0.5096	0.0066	*a04bb*	0.4940	0.2639	0.6239
c08ab	0.8829	0.7650	0.0808	*a01ca*	0.9955	0.7653	0.7100
c01ba	0.0174	0.9669	0.3382	*a01cb*	0.5098	0.7763	0.7073
c01bb	0.4948	0.0034	0.3421	*a02cb*	0.7564	0.7682	0.7834
c06bb	0.5016	0.5262	0.3421				
c02ca	0.2394	0.9854	0.8254	*b01ab*	0.5072	0.2584	0.1278
c04ca	0.1326	0.2532	0.9242	*b02aa*	0.0053	0.7655	0.2075
c07ca	0.3818	0.2496	0.9178	*b03aa*	0.2578	0.7690	0.2947
c04cb	0.6280	0.2662	0.9102	*b04ca*	0.2451	0.2367	0.7019
c07cb	0.8794	0.2529	0.9252				
				e02ab	0.5044	0.7603	0.1266
d02aa	0.2758	0.0089	0.0099	*e04ca*	0.2501	0.7349	0.7046
d04aa	0.1198	0.2589	0.0875	*e07ca*	0.0100	0.7538	0.9631
d05aa	0.2585	0.5033	0.0066	*e05cb*	0.7471	0.7740	0.8913
d03ab	0.6080	0.7636	0.2498				
d05ab	0.7550	0.5170	0.0036	*g14ab*	0.6482	0.0075	0.0320
d07ab	0.8807	0.2597	0.0808	*g16ab*	0.8746	0.4900	0.2926
d01ba	0.0162	0.0133	0.4900	*g12ba*	0.1273	0.4569	0.3785
d03ba	0.1350	0.7651	0.5855	*g15ca*	0.3801	0.4802	0.7966
d06ba	0.0131	0.5055	0.4962				
d07ba	0.3611	0.2571	0.4204				
d08ba	0.3826	0.7632	0.5872				
d01bb	0.5117	0.0033	0.5027				
d02bb	0.7605	0.9727	0.3321				
d04bb	0.6345	0.2647	0.4181				
d06bb	0.5112	0.5207	0.5028				
d07bb	0.8823	0.2702	0.4131				
d08bb	0.8728	0.7653	0.5787				
d01ca	0.9960	0.9984	0.8353				
d06ca	0.0246	0.5062	0.8330				
d08ca	0.3826	0.7467	0.9181				
d01cb	0.5136	0.9796	0.8315				
d02cb	0.7457	0.0157	0.6625				
d04cb	0.6181	0.2761	0.7559				

Oxygen coordinates for the lowest energy structure from *$I4_1/amd$* system, represented in Figures 10.17 and 10.18b.

x	y	z	x	y	z
0.8669	0.7631	0.6638	0.3923	0.7603	0.3317
0.9011	0.2673	0.8403	0.3912	0.2648	0.4985
0.7530	0.4896	0.7475	0.2584	0.5095	0.4180
0.4949	0.4905	0.9241	0.0020	0.5340	0.5782
0.8723	0.7642	0.8411	0.3938	0.7623	0.5017
0.8679	0.2652	0.6689	0.3929	0.2676	0.3349
0.5082	0.5255	0.7552	0.9980	0.4977	0.4187
0.7544	0.4910	0.9234	0.2543	0.5404	0.5810
0.6103	0.2474	0.8352	0.1202	0.2610	0.5045
0.6436	0.7643	0.6709	0.1284	0.7252	0.3341
0.4963	0.0083	0.9132	0.0026	0.9887	0.5779
0.7534	0.0464	0.7471	0.2564	0.0286	0.4163
0.6323	0.2660	0.6694	0.1168	0.2351	0.3266
0.6407	0.7661	0.8365	0.1222	0.7608	0.4993
0.7494	0.0488	0.9238	0.2549	0.9871	0.5806
0.5145	0.0153	0.7560	0.9923	0.0263	0.4136
0.3814	0.7610	0.6661	0.8775	0.7512	0.0035
0.3676	0.2162	0.8387	0.8631	0.2585	0.1600
0.2535	0.4901	0.7522	0.7688	0.5190	0.0847
0.0113	0.4886	0.9197	0.5101	0.4942	0.2567
0.3729	0.7587	0.8395	0.8700	0.7641	0.1639
0.3807	0.2587	0.6711	0.8679	0.2797	0.0041
0.9888	0.5179	0.7575	0.5047	0.5072	0.0848
0.2627	0.4865	0.9257	0.7405	0.5100	0.2473
0.1287	0.2320	0.8449	0.6362	0.2614	0.1713
0.1198	0.7590	0.6651	0.6295	0.7288	0.0018
0.0046	0.0248	0.9228	0.5052	0.0328	0.2546
0.2462	0.9866	0.7503	0.7648	0.0058	0.0854
0.1131	0.2609	0.6679	0.6255	0.2831	0.9978
0.1158	0.7750	0.8396	0.6365	0.7584	0.1703
0.2648	0.0103	0.9266	0.7325	0.0047	0.2500
0.9834	0.0084	0.7577	0.5224	0.0111	0.0835
0.8803	0.7635	0.3277	0.3768	0.7407	0.0001
0.8891	0.2567	0.4955	0.3781	0.2609	0.1710
0.7554	0.4815	0.4160	0.2358	0.5077	0.0861
0.4970	0.5184	0.5802	0.9960	0.4931	0.2436
0.8887	0.7610	0.4990	0.3711	0.7618	0.1644
0.8710	0.2254	0.3328	0.3804	0.2676	0.0029
0.5060	0.4835	0.4179	0.0055	0.5122	0.0860
0.7658	0.5147	0.5845	0.2558	0.4964	0.2475
0.6261	0.2597	0.4981	0.1505	0.2591	0.1677
0.6194	0.7731	0.3292	0.1442	0.7584	0.0065
0.4972	0.0079	0.5802	0.0158	0.0022	0.2527
0.7523	0.0204	0.4112	0.2378	0.0089	0.0868
0.6242	0.2423	0.3349	0.1507	0.2498	0.0050
0.6236	0.7615	0.4942	0.1411	0.7602	0.1650
0.7654	0.0121	0.5855	0.2591	0.0288	0.2476
0.5057	0.0437	0.4185	0.0040	0.0082	0.0849

In the following tables are structural coordinates from example structures, those with configurations closest to the starting configurations of both symmetry systems. These example configurations were obtained after using DFT.

Cation coordinates for the $Fd\bar{3}m$ symmetry structure, with configuration closest to the initial. The structure has 10 cations on 8*a*, 19 cations on 16*c*, 30 cations on 16*d*, and 5 cations on 48*f* site positions.

Site Position	**x**	**y**	**z**	*Site Position*	**x**	**y**	**z**
	Octahedral Coordinates			*d05c*	0.4657	0.0167	0.6614
c02a	0.7474	0.2315	0.1713	*d07c*	0.7419	0.4618	0.9244
c03a	0.2172	0.4983	0.2496	*d09c*	0.9936	0.5099	0.6648
c05a	0.9874	0.5382	0.1644	*d10c*	0.7551	0.7447	0.8260
c07a	0.2465	0.9705	0.4251	*d11c*	0.2518	0.0228	0.9163
c08a	0.5013	0.2204	0.2528	*d13c*	0.9948	0.0234	0.8290
c10a	0.2042	0.2201	0.3242	*d15c*	0.2360	0.4814	0.7416
c11a	0.7749	0.5098	0.4191	*d16c*	0.5081	0.7516	0.9193
c14a	0.2873	0.7728	0.1531				
c16a	0.9554	0.2775	0.0896		***Tetrahedral Coordinates***		
c02b	0.7828	0.2089	0.5092	*a01a*	0.1329	0.1134	0.0351
c03b	0.2732	0.4708	0.6020	*a04a*	0.8873	0.8730	0.2885
c06b	0.7469	0.7135	0.6782	*a07a*	0.6347	0.6190	0.0472
c08b	0.5460	0.2681	0.5929	*a03b*	0.1098	0.6573	0.5411
c09b	0.4937	0.9804	0.5064	*a04b*	0.8978	0.8899	0.6198
c13b	0.5091	0.5267	0.3289	*a01c*	0.1213	0.1145	0.7023
c16b	0.9837	0.2155	0.4168	*a02c*	0.8798	0.3763	0.7880
c04c	0.4670	0.7614	0.7395	*a04c*	0.8728	0.9067	0.9652
c12c	0.0311	0.7142	0.9102	*a05c*	0.6361	0.1280	0.8773
c14c	0.2285	0.7509	0.8213	*a06c*	0.3851	0.3736	0.9628
d01a	0.5085	0.5019	0.1656	*f43a*	0.3883	0.1280	0.1248
d02a	0.2542	0.7571	0.0104	*f39b*	0.6157	0.8765	0.3731
d03a	0.7525	0.9876	0.0808	*f01c*	0.6229	0.3736	0.7057
d05a	0.5199	0.0367	0.0055	*f28c*	0.1244	0.3684	0.8753
d07a	0.7846	0.5217	0.2590	*f43c*	0.3764	0.1253	0.7892
d09a	0.9847	0.4884	0.0040				
d10a	0.7142	0.7822	0.1746				
d11a	0.2722	0.9785	0.2488				
d13a	0.0071	0.9974	0.1711				
d15a	0.2684	0.4849	0.0816				
d01b	0.5079	0.5171	0.4999				
d02b	0.2424	0.7578	0.3295				
d04b	0.9930	0.2272	0.5927				
d06b	0.2287	0.2294	0.5084				
d08b	0.9824	0.7755	0.4130				
d10b	0.7714	0.7684	0.5085				
d12b	0.5081	0.2395	0.4121				
d14b	0.7802	0.2212	0.3238				
d15b	0.2293	0.5130	0.4201				
d16b	0.4801	0.7526	0.5891				
d01c	0.4990	0.4791	0.8309				
d03c	0.7636	0.0207	0.7418				

Oxygen coordinates for the $Fd\bar{3}m$ symmetry structure, with configuration closest to the initial. The structure has 10 cations on 8*a*, 19 cations on 16*c*, 30 cations on 16*d*, and 5 cations on 48*f* site positions.

x	y	z	x	y	z
0.7445	0.4931	0.8359	0.9793	0.0208	0.7548
0.0365	0.7374	0.9963	0.7318	0.2513	0.5721
0.2765	0.2612	0.576	0.2284	0.4967	0.6756
0.5065	0.9872	0.7474	0.5068	0.7203	0.8368
0.2482	0.9927	0.6731	0.7542	0.2598	0.4153
0.4947	0.2390	0.8365	0.0087	0.0611	0.5837
0.9957	0.5050	0.9223	0.7269	0.9882	0.4968
0.7189	0.7590	0.7522	0.9797	0.2750	0.6708
0.7567	0.9828	0.0047	0.4866	0.4970	0.7534
0.9912	0.2582	0.1645	0.2548	0.7004	0.5802
0.2612	0.7265	0.7608	0.2751	0.9934	0.4903
0.5169	0.4970	0.9151	0.5035	0.2326	0.6589
0.2604	0.4994	0.8361	0.7723	0.7402	0.2483
0.5050	0.7452	0.9962	0.0052	0.4899	0.4166
0.0097	0.0238	0.0863	0.7430	0.4870	0.3344
0.7629	0.2439	0.9187	0.9807	0.7560	0.4928
0.2542	0.4977	0.0031	0.4808	0.9923	0.5815
0.5018	0.7275	0.1699	0.2555	0.2474	0.4051
0.7229	0.2421	0.7527	0.7625	0.5060	0.1758
0.0163	0.9967	0.9183	0.0098	0.7540	0.3349
0.7594	0.9805	0.8315	0.2512	0.2439	0.9197
0.0196	0.2457	0.0097	0.5178	0.9903	0.0811
0.5104	0.4890	0.089	0.2818	0.9739	0.9945
0.2650	0.7638	0.9139	0.5259	0.2672	0.1736
0.2430	0.9904	0.8367	0.0225	0.4954	0.2418
0.5074	0.2265	0.9980	0.7561	0.7566	0.0948
0.7389	0.7591	0.5846	0.7578	0.9991	0.3304
0.0053	0.5065	0.7537	0.9936	0.2422	0.4952
0.7542	0.5022	0.6723	0.2706	0.7175	0.0821
0.0028	0.7683	0.8431	0.4933	0.4799	0.2513
0.5053	0.9800	0.9181	0.2633	0.5073	0.1661
0.2411	0.2546	0.7535	0.4812	0.7335	0.3365
0.7299	0.5071	0.4896	0.0284	0.0084	0.4158
0.9626	0.7439	0.6631	0.7468	0.2727	0.2528
0.2700	0.2539	0.2557	0.2655	0.4956	0.3318
0.4928	0.0057	0.4155	0.5171	0.7443	0.5056
0.2597	0.9962	0.3310	0.7467	0.2228	0.0944
0.5191	0.2439	0.4936	0.0410	0.0041	0.2442
0.0278	0.4791	0.5855	0.7841	0.9950	0.1666
0.7562	0.7438	0.4145	0.9918	0.2496	0.3401
0.7393	0.9757	0.6677	0.4934	0.4789	0.4135
0.9926	0.2458	0.8372	0.2587	0.7415	0.2504
0.2286	0.7468	0.4083	0.2598	0.9886	0.1653
0.4921	0.4923	0.5784	0.5226	0.2594	0.3345
0.2648	0.5022	0.4887	0.7543	0.7242	0.9098
0.5029	0.7565	0.6661	0.0300	0.4802	0.0848
0.4978	0.0163	0.2429	0.7734	0.5070	1.0000
0.2678	0.2427	0.0887	0.0341	0.7534	0.1631

Cation coordinates for the *I4$_1$/amd* symmetry structure, with configuration closest to the initial. The structure has 11 cations on 4*a*, 1 cation on 4*b*, 18 cations on 8*c*, 30 cations on 8*d*, 1 cation on 8*e*, and 3 cations on 16*g* site positions.

Site Position	x	y	z	*Site Position*	x	y	z
	Octahedral Coordinates						
c02aa	0.2490	0.9952	0.1718	d03ca	0.1286	0.7865	0.9262
c03aa	0.1111	0.7695	0.0724	d05ca	0.2277	0.4971	0.6592
c05aa	0.2278	0.4834	0.1717	d07ca	0.3789	0.2746	0.7449
c07aa	0.3881	0.2424	0.2479	d01cb	0.4970	0.9449	0.8300
c08aa	0.3716	0.7526	0.0831	d03cb	0.6263	0.6966	0.9073
c01ab	0.4929	0.9825	0.9905	d04cb	0.6285	0.2458	0.7533
c02ab	0.7526	0.9981	0.1689	d05cb	0.7461	0.4648	0.6635
c03ab	0.6262	0.7496	0.0856	d07cb	0.8970	0.2666	0.7506
c04ab	0.6338	0.2147	0.2524	d08cb	0.8805	0.6711	0.9245
c05ab	0.7724	0.4862	0.1739				
c06ab	0.5110	0.4922	0.9937		***Tetrahedral Coordinates***		
c08ab	0.8761	0.6826	0.0687	a04aa	0.9932	0.2578	0.2906
c08ba	0.4110	0.7659	0.4081	a01ba	0.9963	0.7488	0.3770
c06bb	0.5126	0.4932	0.3383	a02ba	0.2351	0.7447	0.4632
c02ca	0.2430	0.0072	0.8284	a03ba	0.2568	0.2478	0.5439
c03ca	0.1248	0.7089	0.7482	a04ba	0.9979	0.2557	0.6275
c04ca	0.0981	0.2656	0.9151	a02bb	0.7510	0.7412	0.4606
c05ca	0.2605	0.5254	0.8312	a03bb	0.7501	0.2465	0.5431
c07ca	0.3885	0.2540	0.9096	a04bb	0.5014	0.2565	0.6262
c08cb	0.9049	0.7643	0.7307	a01cb	0.4996	0.7435	0.7079
				a02cb	0.7413	0.7559	0.7966
d01aa	0.9989	0.0893	0.1605	a03cb	0.7485	0.2416	0.8728
d03aa	0.1091	0.7361	0.2514				
d05aa	0.2373	0.4819	0.9968	b02ab	0.5020	0.7487	0.2110
d07aa	0.3688	0.2400	0.0866				
d02ab	0.7744	0.0412	0.9894	e01aa	0.9998	0.2533	0.0368
d04ab	0.6400	0.2558	0.0829				
d08ab	0.8653	0.7791	0.2577	g14bb	0.6270	0.0026	0.3735
d01ba	0.0057	0.9931	0.5070				
d02ba	0.2575	0.0018	0.3314				
d04ba	0.1329	0.2517	0.4187				
d05ba	0.2501	0.4983	0.3326				
d06ba	0.0015	0.5071	0.5074				
d08ba	0.3653	0.7522	0.5856				
d01bb	0.5054	0.0254	0.4977				
d03bb	0.6325	0.7809	0.5915				
d05bb	0.7564	0.5196	0.3376				
d06bb	0.5082	0.4824	0.4960				
d07bb	0.8620	0.2360	0.4151				
d08bb	0.8897	0.7721	0.5956				
d01ca	0.9803	0.0022	0.8356				
d02ca	0.2303	0.0021	0.6670				

Oxygen coordinates for the *I4$_1$/amd* symmetry , with configuration closest to the initial. The structure has 11 cations on 4*a*, 1 cation on 4*b*, 18 cations on 8*c*, 30 cations on 8*d*, 1 cation on 8*e*, and 3 cations on 16*g* site positions.

x	y	z	x	y	z
0.8495	0.7119	0.6605	0.3687	0.7360	0.3358
0.8755	0.2628	0.8342	0.3876	0.2486	0.4994
0.7464	0.4649	0.7520	0.2380	0.4913	0.4142
0.5036	0.4771	0.9263	0.9786	0.4965	0.5804
0.8688	0.7827	0.8452	0.3800	0.7584	0.4929
0.8769	0.2349	0.6805	0.3675	0.2588	0.3273
0.4970	0.4576	0.7481	0.0046	0.4709	0.4212
0.7503	0.4916	0.9182	0.2566	0.5148	0.5822
0.6147	0.1836	0.8305	0.1208	0.2402	0.4989
0.6126	0.7040	0.6637	0.1333	0.7478	0.3307
0.4878	0.9901	0.9181	0.9775	0.0056	0.5827
0.7481	0.9673	0.7522	0.2538	0.9727	0.4132
0.6265	0.2351	0.6701	0.1350	0.2372	0.3368
0.6116	0.7153	0.8397	0.1035	0.7438	0.5031
0.7349	0.9751	0.925	0.2589	0.9922	0.5841
0.4922	0.9966	0.7525	0.0057	0.0077	0.4203
0.3607	0.7546	0.6629	0.8631	0.7817	0.9972
0.3632	0.2606	0.8313	0.8717	0.2359	0.1614
0.2444	0.5134	0.7491	0.7393	0.5066	0.0891
0.0234	0.5530	0.9236	0.5044	0.4737	0.2550
0.3568	0.7797	0.8325	0.8720	0.7625	0.1727
0.3612	0.2579	0.6674	0.8780	0.2640	0.0113
0.9729	0.6267	0.7487	0.5050	0.4803	0.0857
0.2549	0.5015	0.9188	0.7546	0.4971	0.2511
0.1307	0.2746	0.8389	0.6476	0.2554	0.1686
0.1310	0.7723	0.6720	0.6108	0.7438	0.0044
0.0119	0.0116	0.9150	0.5060	0.0243	0.2472
0.2465	0.0265	0.7484	0.7324	0.9921	0.0850
0.1323	0.2633	0.6600	0.6158	0.2165	0.0117
0.1290	0.7853	0.8297	0.6342	0.7447	0.1648
0.2447	0.0394	0.9119	0.7527	0.9980	0.2459
0.9983	0.0568	0.7583	0.4949	0.9862	0.0849
0.8741	0.7461	0.3317	0.3894	0.7073	0.0122
0.8835	0.2404	0.4956	0.3597	0.2417	0.1693
0.7637	0.4862	0.4146	0.2631	0.4891	0.0880
0.4940	0.5216	0.5772	0.9971	0.5267	0.2525
0.8816	0.7397	0.5028	0.3737	0.7257	0.1697
0.8756	0.2619	0.3377	0.3838	0.2454	0.0072
0.4890	0.5283	0.4144	0.0104	0.5049	0.0778
0.7415	0.4976	0.5854	0.2454	0.4932	0.2518
0.6190	0.2608	0.5017	0.136	0.2158	0.1689
0.6262	0.7202	0.3351	0.1586	0.7523	0.0053
0.4976	0.9847	0.5800	0.0043	0.9874	0.2464
0.7581	0.9891	0.4188	0.2648	0.9620	0.0938
0.6314	0.2648	0.3299	0.1439	0.2610	0.9965
0.6102	0.7454	0.5013	0.1384	0.7395	0.1693
0.7439	0.9614	0.5765	0.2551	0.9858	0.2522
0.5143	0.0237	0.4177	0.0155	0.9822	0.0895

Appendix X

Publication List

All works that have reached publication are located on the CD-ROM provided, in the folder titled Appendix_X.

As of May 5 2004 the following journal and conferences papers have been published:

Paglia, G., Rohl, A.L., Buckley, C.E. and Gale, J.D. 2001 "A computational investigation of the structure of κ-alumina using interatomic potentials," *Journal of Materials Chemistry,* **11**, pp. 3310-3316.

Paglia, G., Buckley, C.E., Rohl, A.L., O'Connor, B.H., van Riessen, A. and Gale. J.D. 2001 "The determination of the structure of γ-alumina using empirical and first principle calculations and supporting experiment." *Proceedings of the 2001 Joint Conference: Australian X-Ray Analytical Association (WA) Inc. and WA Society for Electron Microscopy, Mandurah, Australia, September 21-23,* pp. 143-156.

Paglia, G., Buckley, C.E., Rohl, A.L., van Riessen, A. and Gale. J.D. 2002 "Theoretical and Experimental Structure Determination of γ-Alumina." *AUSTCERAM 2002 Transactions* (Australasian Ceramic Society), September 30 – October 4, 2002, pp. 213-214.

Paglia, G., Buckley, C.E., Rohl, A.L., and Byrne, L.T. 2002, "Towards the determination of the structure of γ-alumina," *Journal of the Australasian Ceramics Society*, **38**, 1, pp. 92-98.

Paglia, G., Buckley, C.E., Rohl, A.L., Hunter, B.A., Hart, R.D., Hanna, J.V. and Byrne, L.T. 2003, "Tetragonal structure model for boehmite-derived γ-alumina," *Physical Review B,* **68**, 14, pp.144110, 1-11.

Maitland, C.F., Buckley, C.E., Paglia G., and Connolly, J. 2004, "Determination of the specific surface of γ-alumina using small angle x-ray scattering," *Proceedings of the Second Annual Conference of Asian Pacific Nanotechnology Forum (APNF) 2003*, Cairns, Australia, November 19-21, 2003.

Paglia, G., Buckley, C.E., Rohl, A.L., Hart, R.D., Winter, K., Studer, A.J., Hunter, B.A. and Hanna, J.V. 2004, "Boehmite derived γ-alumina system, 1: Structural evolution with temperature, with the identification and structural determination of a new transition phase, γ′-alumina," *Chemistry of Materials*, **16**, pp. 220-236.

Paglia, G., Buckley, C.E., Udovic, T.J., Rohl, A.L., Jones, F., Maitland, C.F. and Connolly, J. 2004, "Boehmite derived γ-alumina system, 2: Consideration of hydrogen and surface effects," *Chemistry of Materials*, **16**, 1914-1923.

Papers that have been submitted for publication:

Paglia, G., Rohl, A.L., Buckley, C.E. and Gale, J.D. 2004 "Determination of the structure of γ-alumina from interatomic potential and first principles calculations - The requirement of significant numbers of non-spinel positions to achieve an accurate structural model," *Physical Review B*.

Papers in preparation:

Paglia, G., Rohl, A.L., Buckley, C.E., Gale, J.D., 2004 "Consideration of hydrogen in the structure of γ-alumina from computer simulation," *Chemistry of Materials*.

Maitland, C.F., Connolly, J., Paglia, G. and Buckley, C.E., "Investigation of the nanostructure of γ-alumina from SAXS," *International Journal of Solids and Structures*.

This page has been left blank deliberately.